

Energy, Environment, and Sustainability

Series Editors: Avinash Kumar Agarwal · Ashok Pandey

Kalyan Kumar Srinivasan  
Avinash Kumar Agarwal  
Sundar Rajan Krishnan  
Vincenzo Mulone *Editors*

# Natural Gas Engines

For Transportation and Power  
Generation



 Springer

# **Energy, Environment, and Sustainability**

## **Series editors**

Avinash Kumar Agarwal, Department of Mechanical Engineering, Indian Institute of Technology Kanpur, Kanpur, Uttar Pradesh, India

Ashok Pandey, Distinguished Scientist, CSIR-Indian Institute of Toxicology Research, Lucknow, Uttar Pradesh, India

This books series publishes cutting edge monographs and professional books focused on all aspects of energy and environmental sustainability, especially as it relates to energy concerns. The Series is published in partnership with the International Society for Energy, Environment, and Sustainability. The books in these series are editor or authored by top researchers and professional across the globe. The series aims at publishing state-of-the-art research and development in areas including, but not limited to:

- Renewable Energy
- Alternative Fuels
- Engines and Locomotives
- Combustion and Propulsion
- Fossil Fuels
- Carbon Capture
- Control and Automation for Energy
- Environmental Pollution
- Waste Management
- Transportation Sustainability

More information about this series at <http://www.springer.com/series/15901>

Kalyan Kumar Srinivasan  
Avinash Kumar Agarwal  
Sundar Rajan Krishnan · Vincenzo Mulone  
Editors

# Natural Gas Engines

For Transportation and Power Generation

 Springer

*Editors*

Kalyan Kumar Srinivasan  
Department of Mechanical Engineering  
The University of Alabama  
Tuscaloosa, AL, USA

Sundar Rajan Krishnan  
Department of Mechanical Engineering  
The University of Alabama  
Tuscaloosa, AL, USA

Avinash Kumar Agarwal  
Department of Mechanical Engineering  
Indian Institute of Technology Kanpur  
Kanpur, Uttar Pradesh, India

Vincenzo Mulone  
Department of Industrial Engineering  
University of Rome Tor Vergata  
Rome, Italy

ISSN 2522-8366 ISSN 2522-8374 (electronic)  
Energy, Environment, and Sustainability  
ISBN 978-981-13-3306-4 ISBN 978-981-13-3307-1 (eBook)  
<https://doi.org/10.1007/978-981-13-3307-1>

Library of Congress Control Number: 2018961728

© Springer Nature Singapore Pte Ltd. 2019

This work is subject to copyright. All rights are reserved by the Publisher, whether the whole or part of the material is concerned, specifically the rights of translation, reprinting, reuse of illustrations, recitation, broadcasting, reproduction on microfilms or in any other physical way, and transmission or information storage and retrieval, electronic adaptation, computer software, or by similar or dissimilar methodology now known or hereafter developed.

The use of general descriptive names, registered names, trademarks, service marks, etc. in this publication does not imply, even in the absence of a specific statement, that such names are exempt from the relevant protective laws and regulations and therefore free for general use.

The publisher, the authors and the editors are safe to assume that the advice and information in this book are believed to be true and accurate at the date of publication. Neither the publisher nor the authors or the editors give a warranty, express or implied, with respect to the material contained herein or for any errors or omissions that may have been made. The publisher remains neutral with regard to jurisdictional claims in published maps and institutional affiliations.

This Springer imprint is published by the registered company Springer Nature Singapore Pte Ltd. The registered company address is: 152 Beach Road, #21-01/04 Gateway East, Singapore 189721, Singapore

# Preface

Energy demand has been rising remarkably due to increasing population and urbanization. Global economy and society are significantly dependent on the energy availability because it touches every facet of human life and its activities. Transportation and power generation are two major examples. Without the transportation by millions of personalized and mass transport vehicles and availability of  $24 \times 7$  power, human civilization would not have reached contemporary living standards.

The International Society for Energy, Environment and Sustainability (ISEES) was founded at Indian Institute of Technology Kanpur (IIT Kanpur), India, in January 2014 with the aim of spreading knowledge/awareness and catalysing research activities in the fields of energy, environment, sustainability and combustion. The society's goal is to contribute to the development of clean, affordable and secure energy resources and a sustainable environment for the society and to spread knowledge in the above-mentioned areas and create awareness about the environmental challenges, which the world is facing today. The unique way adopted by the society was to break the conventional silos of specializations (engineering, science, environment, agriculture, biotechnology, materials, fuels, etc.) to tackle the problems related to energy, environment and sustainability in a holistic manner. This is quite evident by the participation of experts from all fields to resolve these issues. ISEES is involved in various activities such as conducting workshops, seminars and conferences in the domains of its interest. The society also recognizes the outstanding works done by the young scientists and engineers for their contributions in these fields by conferring them awards under various categories.

The second international conference on “Sustainable Energy and Environmental Challenges” (SEEC-2018) was organized under the auspices of ISEES from 31 December 2017 to 3 January 2018 at J N Tata Auditorium, Indian Institute of Science Bangalore. This conference provided a platform for discussions between eminent scientists and engineers from various countries including India, USA, South Korea, Norway, Finland, Malaysia, Austria, Saudi Arabia and Australia. In this conference, eminent speakers from all over the world presented their views

related to different aspects of energy, combustion, emissions and alternative energy resources for sustainable development and a cleaner environment. The conference presented five high-voltage plenary talks from globally renowned experts on topical themes, namely “Is It Really the End of Combustion Engines and Petroleum?” by Prof. Gautam Kalghatgi, Saudi Aramco; “Energy Sustainability in India: Challenges and Opportunities” by Prof. Baldev Raj, NIAS Bangalore; “Methanol Economy: An Option for Sustainable Energy and Environmental Challenges” by Dr. Vijay Kumar Saraswat, Hon. Member (S&T), NITI Aayog, Government of India; “Supercritical Carbon Dioxide Brayton Cycle for Power Generation” by Prof. Pradip Dutta, IISc Bangalore; and “Role of Nuclear Fusion for Environmental Sustainability of Energy in Future” by Prof. J. S. Rao, Altair Engineering.

The conference included 27 technical sessions on topics related to energy and environmental sustainability including 5 plenary talks, 40 keynote talks and 18 invited talks from prominent scientists, in addition to 142 contributed talks, and 74 poster presentations by students and researchers. The technical sessions in the conference included Advances in IC Engines: SI Engines, Solar Energy: Storage, Fundamentals of Combustion, Environmental Protection and Sustainability, Environmental Biotechnology, Coal and Biomass Combustion/Gasification, Air Pollution and Control, Biomass to Fuels/Chemicals: Clean Fuels, Advances in IC Engines: CI Engines, Solar Energy: Performance, Biomass to Fuels/Chemicals: Production, Advances in IC Engines: Fuels, Energy Sustainability, Environmental Biotechnology, Atomization and Sprays, Combustion/Gas Turbines/Fluid Flow/Sprays, Biomass to Fuels/Chemicals, Advances in IC Engines: New Concepts, Energy Sustainability, Waste to Wealth, Conventional and Alternate Fuels, Solar Energy, Wastewater Remediation and Air Pollution. One of the highlights of the conference was the rapid-fire poster sessions in (i) Energy Engineering, (ii) Environment and Sustainability and (iii) Biotechnology, where more than 75 students participated with great enthusiasm and won many prizes in a fiercely competitive environment. More than 200 participants and speakers attended this four-day conference, which also hosted Dr. Vijay Kumar Saraswat, Hon. Member (S&T), NITI Aayog, Government of India, as the chief guest for the book release ceremony, where 16 ISEES books published by Springer, under a special dedicated series “Energy, Environment, and Sustainability” were released. This is the first time that such significant and high-quality outcome has been achieved by any society in India. The conference concluded with a panel discussion on “Challenges, Opportunities & Directions for Future Transportation Systems”, where the panellists were Prof. Gautam Kalghatgi, Saudi Aramco; Dr. Ravi Prashanth, Caterpillar Inc.; Dr. Shankar Venugopal, Mahindra and Mahindra; Dr. Bharat Bhargava, DG, ONGC Energy Centre; and Dr. Umamaheshwar, GE Transportation, Bangalore. The panel discussion was moderated by Prof. Ashok Pandey, Chairman, ISEES. This conference laid out the road map for technology development, opportunities and challenges in energy, environment and sustainability domains. All these topics are very relevant for the country and the world in the present context. We acknowledge the support received from various funding agencies and organizations for the successful conduct of the second ISEES

conference SEEC-2018, where these books germinated. We would therefore like to acknowledge SERB, Government of India (special thanks to Dr. Rajeev Sharma, Secretary); ONGC Energy Centre (special thanks to Dr. Bharat Bhargava); TAFE (special thanks to Sh. Anadrao Patil); Caterpillar (special thanks to Dr. Ravi Prashanth); Progress Rail, TSI, India (special thanks to Dr. Deepak Sharma); Tesscorn, India (special thanks to Sh. Satyanarayana); GAIL, Volvo; and our publishing partner Springer (special thanks to Swati Meherishi).

The editors would like to express their sincere gratitude to a large number of authors from all over the world for submitting their high-quality work in a timely manner and revising it appropriately at short notice. We would like to express our special thanks to Prof. Mirko Baratta, Prof. Antonio Carlucci, Prof. Vincenzo Mulone, Prof. Sundar Krishnan, Prof. Kalyan Srinivasan, Mr. Prabhat Ranjan Jha, Mr. Hamidreza Mahabadipour, Mr. Kendyl Partridge, Mr. Gaurav Guleria and Mr. Aimilios Sofianopoulos, who reviewed various chapters of this book and provided very valuable suggestions to the authors to improve their draft manuscripts.

The book covers different aspects of advanced combustion engines that utilize natural gas as a primary fuel. The principal objective of this book is to fulfil an important global need in presenting the state of the art in natural gas engine technologies for transportation and power generation. We believe that this book will be useful to early-career researchers, academicians, professional engineers and scientists across the globe who work in the area of natural gas utilization for internal combustion engines. Chapter 2 presents a general overview of various natural gas combustion technologies including spark ignited, dual fuel, prechamber ignition, homogeneous charge compression ignition. Chapters 3 through 6 discuss various spark-ignited natural gas combustion technologies including direct injection natural gas engines. Chapter 7 discusses the techno-economic impacts of using natural gas engines for marine applications, and it serves as a segue between SI and CI engine combustion technologies. Chapters 8 through 12 focus on opportunities and challenges associated with dual-fuel natural gas engines. Chapter 13 presents an overview of emission control technologies for natural gas-fired engines. Finally, Chap. 14 presents a unique perspective of high-efficiency natural gas-fired residential genset technologies.

Tuscaloosa, USA  
Kanpur, India  
Tuscaloosa, USA  
Rome, Italy

Kalyan Kumar Srinivasan  
Avinash Kumar Agarwal  
Sundar Rajan Krishnan  
Vincenzo Mulone



# Contents

<b>1</b>	<b>Introduction to Advanced Combustion Technologies: The Role of Natural Gas in Future Transportation and Power Generation Systems</b> . . . . .	<b>1</b>
	Kalyan Kumar Srinivasan, Avinash Kumar Agarwal, Sundar Rajan Krishnan and Vincenzo Mulone	
<b>2</b>	<b>Low-Temperature Natural Gas Combustion Engines</b> . . . . .	<b>7</b>
	Sotirios Mamalis	
<b>3</b>	<b>The Ultra-Lean Partially Stratified Charge Approach to Reducing Emissions in Natural Gas Spark-Ignited Engines</b> . . . . .	<b>29</b>
	L. Bartolucci, E. C. Chan, S. Cordiner, R. L. Evans and V. Mulone	
<b>4</b>	<b>Simulation and Modeling of Direct Gas Injection through Poppet-type Outwardly-opening Injectors in Internal Combustion Engines</b> . . . . .	<b>65</b>
	Abhishek Y. Deshmukh, Mathis Bode, Tobias Falkenstein, Maziar Khosravi, David van Bebber, Michael Klaas, Wolfgang Schröder and Heinz Pitsch	
<b>5</b>	<b>Prospects and Challenges for Deploying Direct Injection Technology for Compressed Natural Gas Engines</b> . . . . .	<b>117</b>
	Rajesh Kumar Prasad, Tanmay Kar and Avinash Kumar Agarwal	
<b>6</b>	<b>Effects of EGR on Engines Fueled with Natural Gas and Natural Gas/Hydrogen Blends</b> . . . . .	<b>143</b>
	Luigi De Simio, Michele Gambino and Sabato Iannaccone	
<b>7</b>	<b>Natural Gas Combustion in Marine Engines: An Operational, Environmental, and Economic Assessment</b> . . . . .	<b>169</b>
	Roussos G. Papagiannakis, Theodoros C. Zannis, Efthimios G. Pariotis and John S. Katsanis	

<b>8</b>	<b>Advanced Combustion in Natural Gas-Fueled Engines</b> .....	215
	Ulugbek Azimov, Nobuyuki Kawahara, Kazuya Tsuboi and Eiji Tomita	
<b>9</b>	<b>Advances of the Natural Gas/Diesel RCCI Concept Application for Light-Duty Engines: Comprehensive Analysis of the Influence of the Design and Calibration Parameters on Performance and Emissions</b> .....	251
	Giacomo Belgiorno, Gabriele Di Blasio and Carlo Beatrice	
<b>10</b>	<b>Design and Calibration Strategies for Improving HCCI Combustion in Dual-Fuel Diesel–Methane Engines</b> .....	267
	A. P. Carlucci, A. Ficarella, D. Laforgia and L. Strafella	
<b>11</b>	<b>Dual Fuel (Natural Gas Diesel) for Light-Duty Industrial Engines: A Numerical and Experimental Investigation</b> .....	297
	Enrico Mattarelli, Carlo Alberto Rinaldini and Tommaso Savioli	
<b>12</b>	<b>Cyclic Combustion Variations in Diesel–Natural Gas Dual Fuel Engines</b> .....	329
	Kalyan Kumar Srinivasan, Sundar Rajan Krishnan, Prabhat Ranjan Jha and Hamidreza Mahabadipour	
<b>13</b>	<b>Emissions Control Technologies for Natural Gas Engines</b> .....	359
	A. Wahbi, A. Tsolakis and J. Herreros	
<b>14</b>	<b>A Review of Residential-Scale Natural Gas-Powered Micro-Combined Heat and Power Engine Systems</b> .....	381
	Gokul Vishwanathan, Julian Sculley, David Tew and Ji-Cheng Zhao	

# Editors and Contributors

## About the Editors



**Kalyan Kumar Srinivasan** is an associate professor in the Department of Mechanical Engineering at the University of Alabama, USA. He completed his M.S. and Ph.D. from the University of Alabama in 2002 and 2006, respectively. His interests include research and development of novel low-temperature combustion concepts to minimize pollution formation and increase thermal efficiency of internal combustion engines for transportation, development of laser-based diagnostics to measure temperature and species in open flames and internal combustion engines, investigation of energy destruction in combustion and thermodynamic processes and combined first and second law analyses to design/analyse bottoming. He has authored 1 chapter, 20 conference papers and more than 35 journal articles.



**Avinash Kumar Agarwal** is a professor in the Department of Mechanical Engineering at Indian Institute of Technology Kanpur. His areas of interest are IC engines, combustion, alternative fuels, conventional fuels, optical diagnostics, laser ignition, HCCI, emission and particulate control, and large bore engines. He has published 24 books and more than 230 international journal and conference papers. He is a fellow of SAE (2012), ASME (2013), ISEES (2015) and INAE (2015). He has received several awards such as prestigious Shanti Swarup Bhatnagar Award-2016 in engineering sciences, Rajib Goyal Prize-2015,

NASI-Reliance Industries Platinum Jubilee Award-2012, INAE Silver Jubilee Young Engineer Award-2012, SAE International's Ralph R. Teetor Educational Award-2008, INSA Young Scientist Award-2007, UICT Young Scientist Award-2007 and INAE Young Engineer Award-2005.



**Sundar Rajan Krishnan** is an associate professor in the Department of Mechanical Engineering at the University of Alabama, USA. He received his M.S. and Ph.D. in mechanical engineering from the University of Alabama in 2001 and 2005, respectively, and has subsequently worked in Argonne National Laboratory (USA), Mississippi State University (USA) and University of Rome (Italy). His research interests include performance and emission analysis of internal combustion engines, advanced combustion strategies and developing alternative fuels and waste energy recovery. He has authored 7 technical reports, 18 conference papers and 24 journal articles.



**Vincenzo Mulone** is an associate professor at the University of Rome "Tor Vergata", from where he has also done his Ph.D. His research activities are mainly concerned with the fluid dynamics of energy conversion processes and their impact on environment, especially focusing on the analysis of internal combustion engines, aftertreatment components and systems, fuel cells and renewables. He has authored more than 100 publications.

## Contributors

**Avinash Kumar Agarwal** Engine Research Laboratory, Department of Mechanical Engineering, Indian Institute of Technology Kanpur, Kanpur, Uttar Pradesh, India

**Ulugbek Azimov** University of Northumbria, Newcastle upon Tyne, UK

**L. Bartolucci** Department of Industrial Engineering, University of Rome Tor Vergata, Rome, Italy

**Carlo Beatrice** Istituto Motori, Consiglio Nazionale Delle Ricerche, Naples, Italy

**Giacomo Belgiojorno** Istituto Motori, Consiglio Nazionale Delle Ricerche, Naples, Italy

**Mathis Bode** Institute for Combustion Technology, RWTH Aachen University, Aachen, Germany

**A. P. Carlucci** Department of Engineering for Innovation (DII), University of Salento, Lecce, Italy

**E. C. Chan** Institute for Advanced Sustainability Studies, Potsdam, Germany

**S. Cordiner** Department of Industrial Engineering, University of Rome Tor Vergata, Rome, Italy

**Abhishek Y. Deshmukh** Institute for Combustion Technology, RWTH Aachen University, Aachen, Germany

**Luigi De Simio** Istituto Motori, National Research Council, Naples, Italy

**Gabriele Di Blasio** Istituto Motori, Consiglio Nazionale Delle Ricerche, Naples, Italy

**R. L. Evans** Department of Mechanical Engineering, The University of British Columbia, Vancouver, BC, Canada

**Tobias Falkenstein** Institute for Combustion Technology, RWTH Aachen University, Aachen, Germany

**A. Ficarella** Department of Engineering for Innovation (DII), University of Salento, Lecce, Italy

**Michele Gambino** Istituto Motori, National Research Council, Naples, Italy

**J. Herreros** Mechanical Engineering, University of Birmingham, Birmingham, UK

**Sabato Iannaccone** Istituto Motori, National Research Council, Naples, Italy

**Prabhat Ranjan Jha** Department of Mechanical Engineering, The University of Alabama, Tuscaloosa, AL, USA

**Tanmay Kar** Engine Research Laboratory, Department of Mechanical Engineering, Indian Institute of Technology Kanpur, Kanpur, India

**John S. Katsanis** Hellenic Naval Academy, Piraeus, Attiki, Greece

**Nobuyuki Kawahara** Okayama University, Okayama, Japan

**Maziar Khosravi** Ford Research and Advanced Engineering, Ford Werke GmbH, Cologne, Germany

**Michael Klaas** Institute of Aerodynamics, RWTH Aachen University, Aachen, Germany

**Sundar Rajan Krishnan** Department of Mechanical Engineering, The University of Alabama, Tuscaloosa, AL, USA

**D. Laforgia** Department of Engineering for Innovation (DII), University of Salento, Lecce, Italy

**Hamidreza Mahabadipour** Department of Mechanical Engineering, The University of Alabama, Tuscaloosa, AL, USA

**Sotirios Mamalis** Stony Brook University, Stony Brook, NY, USA

**Enrico Mattarelli** Modena & Reggio Emilia University, Modena, Italy

**Vincenzo Mulone** Department of Industrial Engineering, University of Rome Tor Vergata, Rome, Italy

**Roussos G. Papagiannakis** Hellenic Air Force Academy, Dekelia, Attiki, Greece

**Efthimios G. Pariotis** Hellenic Naval Academy, Piraeus, Attiki, Greece

**Heinz Pitsch** Institute for Combustion Technology, RWTH Aachen University, Aachen, Germany

**Rajesh Kumar Prasad** Engine Research Laboratory, Department of Mechanical Engineering, Indian Institute of Technology Kanpur, Kanpur, India

**Carlo Alberto Rinaldini** Modena & Reggio Emilia University, Modena, Italy

**Tommaso Savioli** Modena & Reggio Emilia University, Modena, Italy

**Wolfgang Schröder** Institute of Aerodynamics, RWTH Aachen University, Aachen, Germany

**Julian Sculley** Booz Allen Hamilton, Washington, DC, USA

**Kalyan Kumar Srinivasan** Department of Mechanical Engineering, The University of Alabama, Tuscaloosa, AL, USA

**L. Strafella** Department of Engineering for Innovation (DII), University of Salento, Lecce, Italy

**David Tew** Department of Energy, Advanced Research Projects Agency-Energy (ARPA-E) United States, Washington, DC, USA

**Eiji Tomita** Okayama University, Okayama, Japan

**A. Tsolakis** Mechanical Engineering, University of Birmingham, Birmingham, UK

**Kazuya Tsuboi** Okayama University, Okayama, Japan

**David van Bebber** Ford Research and Advanced Engineering, Ford Werke GmbH, Cologne, Germany

**Gokul Vishwanathan** Booz Allen Hamilton, Washington, DC, USA

**A. Wahbi** Mechanical Engineering, University of Birmingham, Birmingham, UK

**Theodoros C. Zannis** Hellenic Naval Academy, Piraeus, Attiki, Greece

**Ji-Cheng Zhao** Department of Energy, Advanced Research Projects Agency-Energy (ARPA-E) United States, Washington, DC, USA; Department of Materials Science and Engineering, The Ohio State University, Columbus, OH, USA

# Chapter 1

## Introduction to Advanced Combustion Technologies: The Role of Natural Gas in Future Transportation and Power Generation Systems



**Kalyan Kumar Srinivasan, Avinash Kumar Agarwal,  
Sundar Rajan Krishnan and Vincenzo Mulone**

**Abstract** Among the many alternatives to gasoline and diesel, natural gas is considered a viable fuel for future transportation and power generation applications. The present chapter provides an introductory overview of the role of natural gas in future transportation and power generation systems. Current and projected trends (up to 2040) for global energy consumption and the associated contribution of natural gas in various sectors (industrial, transportation, residential, etc.) are discussed. The advantages and challenges of natural gas as a combustion fuel, natural gas fuel storage and transportation challenges (as compressed natural gas and liquefied natural gas), and natural gas utilization in internal combustion (IC) engines are reviewed. Advanced natural gas low-temperature combustion (LTC) strategies for IC engines, natural gas combustion in spark ignition (SI) engines with a specific focus on direct injection of natural gas, natural gas utilization in marine SI and compression ignition (CI) engines, natural gas utilization in light-duty, heavy-duty, industrial, and marine engines, emissions control technologies for natural gas-fueled engines, and a review of natural gas-powered residential scale micro-combined heating and power (CHP) systems are the major topics explored in the book. The organizational rationale of the book is discussed, and brief summaries of various chapters in the book are provided.

**Keywords** Natural gas · Low-temperature combustion · Advanced combustion  
Dual fuel · Spark ignition

---

K. K. Srinivasan (✉) · S. R. Krishnan  
Department of Mechanical Engineering, The University of Alabama,  
Tuscaloosa, AL 35487, USA  
e-mail: [ksrinivasan@eng.ua.edu](mailto:ksrinivasan@eng.ua.edu)

A. K. Agarwal  
Department of Mechanical Engineering, Indian Institute of Technology Kanpur,  
Kanpur 208016, Uttar Pradesh, India

V. Mulone  
Department of Industrial Engineering, University of Rome Tor Vergata, 00141 Rome, Italy



## 1.1 Introduction

With increasing global population and economic development, energy consumption is expected to increase significantly, while the energy resource portfolio is expected to become increasingly diverse. According to the 2018 International Energy Outlook (IEO 2018) provided by the US Energy Information Administration (EIA 2018), the world energy consumption is projected to increase from about 575 quadrillion British Thermal Units (BTUs) in 2015 to 739 quadrillion BTU by 2040. Of this, natural gas accounts for a significant fraction as an energy source. For example, while natural gas accounted for about 125 quadrillion BTU ( $\sim 22\%$  of total) of the energy consumption in 2015, it is projected to increase to 182 quadrillion BTU (nearly 25% of total) of the energy consumption in 2040, likely accounting for the largest increase in global primary energy consumption by source. Global natural gas consumption statistics in 2015 (IEA 2017) indicated that nearly 38% of the total was utilized in the industrial sector, 30% in the residential sector, while the remainder was used in transportation (7%), commercial and public service (13%), and non-energy sector, agriculture, fishing, etc. (12%). One of the challenges of using natural gas, especially in transportation applications, is onboard natural gas storage. Two options for natural gas storage are in compressed natural gas (CNG) form (typically at 3600 psig or 250 bar) or in liquefied natural gas (LNG) form at  $-260\text{ }^\circ\text{F}$  (or  $-160\text{ }^\circ\text{C}$ ) (US DOE 2018). Although cryogenic natural gas storage as LNG is technically more complicated and economically more demanding, it is clearly advantageous in terms of substantially lower storage space and weight requirements and significantly longer durations between fuel refueling compared to CNG (because of higher fuel energy density for a given storage volume when stored in liquefied form). With the increasing market penetration of LNG transported via ships to different parts of the world, it is natural to consider LNG (and CNG) as a primary fuel in marine applications.

Natural gas has several inherent advantages that augur well for its being adapted for transportation and power generation applications. For example, natural gas typically exhibits high resistance to autoignition (high octane number, allowing the use of higher compression ratios), lower carbon-to-hydrogen ratio (leading to lower post-combustion  $\text{CO}_2$  emissions), suitability for lean combustion (leading to higher fuel conversion efficiencies), and a well-established infrastructure for production and distribution in many parts of the world.

Considering the general energy trends discussed above and some of the advantages of natural gas compared to other fuels, it is clear that natural gas is (and will continue to be) a significant energy resource in a variety of sectors, including transportation, industrial power generation, and residential applications (e.g., home heating). For transportation and industrial power generation applications, combustion of natural gas in internal combustion (IC) engines will remain an important energy conversion strategy for the foreseeable future. This book focuses on advanced natural gas combustion and emissions control technologies, including

both transportation applications (including light-duty, heavy-duty, and marine) and stationary power generation for residential applications.

## 1.2 Organization of the Book

The book is organized as follows. Chapter 2 provides a discussion of advanced natural gas low-temperature combustion (LTC) strategies for IC engines. Chapters 3 through 6 deal with the fundamentals and applications of natural gas combustion in spark ignition (SI) engines with a specific focus on direct injection of natural gas. Natural gas utilization in marine SI and compression ignition (CI) engines is discussed in Chap. 7. Chapters 8 through 12 deal with natural gas utilization in light-duty, heavy-duty, industrial, and marine engines. Chapter 13 discusses emissions control technologies for natural gas-fueled engines, while Chap. 14 presents a review of natural gas-powered residential-scale micro combined heating and power (CHP) systems. Both experimental and computational analyses of natural gas combustion, performance, and emissions are covered.

Natural gas combustion in IC engines can occur over a wide range of operating conditions. Depending on the type of engine, the combustion strategy utilized, and the application, natural gas combustion can occur at different compression ratios (higher for CI compared to SI), overall fuel–air equivalence ratios (lower for CI), injection strategies (port injection vs. direct injection), in-cylinder fuel stratification (homogeneous vs. heterogeneous), and in-cylinder conditions of temperature and pressure. Various natural gas combustion strategies have been investigated over the past several decades. These include lean-burn natural gas combustion using a variety of ignition systems (e.g., spark ignition, laser ignition, turbulent jet ignition with pre-chambers), conventional diesel-ignited natural gas dual-fuel combustion, homogeneous charge compression ignition (HCCI) combustion of natural gas, dual-fuel LTC of premixed natural gas with diesel pilot or diesel micro-pilot ignition, high-pressure direct injection (HPDI) of natural gas and diesel leading to stratified diesel-ignited natural gas dual-fuel combustion, and reactivity controlled compression ignition (RCCI) combustion. Naturally, the chapters in this book present an eclectic mix of different current approaches as well as promising natural gas combustion and emissions control technologies for the future.

For example, Chap. 2 reviews advanced natural gas LTC concepts such as HCCI and RCCI and discusses their potential benefits (e.g., low emissions of oxides of nitrogen ( $\text{NO}_x$ ), particulate matter (PM), and  $\text{CO}_2$ ) and important challenges (e.g., unburned hydrocarbons (UHC), knock).

Partially stratified combustion of natural gas in SI engines is dealt with in Chap. 3. A combined experimental and computational fluid dynamics (CFD) approach is adopted to analyze natural gas PSC in both a constant volume combustion chamber (CVCC) and a single-cylinder research engine (SCRE). A large eddy simulation (LES), coupled with a partially stirred reactor model for considering the non-resolved turbulence-chemistry interaction, is first validated

with Schlieren images obtained in the CVCC and subsequently used for extensive numerical analysis of PSC in the SCRE. With detailed CFD simulations and partial fuel stratification, ultra-lean SI combustion of natural gas is demonstrated with improved engine performance on the SCRE.

Natural gas DI technology is explored numerically in Chap. 4 as a means to improve volumetric and brake thermal efficiencies in natural gas-fueled SI engines. Volumetric efficiency and engine brake power are improved in natural gas DISI by obviating intake air displacement and throttling losses due to manifold induction or port fuel injection (PFI) of natural gas. Modeling strategies for natural gas DI are reviewed, followed by detailed studies of the gas injection process through poppet-type outwardly opening injectors. Specifically, the effect of gas injection on the in-cylinder flow field (e.g., the occurrence of compression shocks, expansion fans, jet collapse) and fuel–air mixing is studied using high-fidelity LES and unsteady Reynolds-averaged Navier–Stokes (URANS) CFD models.

The prospects and challenges of natural gas DI combustion in SI engines in comparison with natural gas PFI are presented in Chap. 5. After a discussion of DI nozzle geometry, the performance of natural gas DI injectors is investigated using Schlieren and planar laser-induced fluorescence (PLIF) imaging. The effect of start of injection (SOI) of natural gas, brake mean effective pressure (BMEP), and equivalence ratio on natural gas DI operation are studied on an SCRE.

Chapter 6 examines the effects of EGR on the performance of SI engines fueled by natural gas and natural gas–hydrogen blends (with 40% v/v of hydrogen). Based on experimental results obtained from a naturally aspirated light-duty SI engine and a turbocharged heavy-duty SI engine, the authors show that EGR can be utilized to yield high specific power and improved fuel conversion efficiency with lower thermal stress. It is shown that hydrogen-enriched natural gas can counteract the reduction of combustion rates with EGR (especially at high EGR levels) and also mitigate the adverse impact of EGR on UHC emissions.

Chapter 7 forms a sort of natural transition between natural gas-fueled SI and CI engines. It presents an operational, environmental, and economic assessment of natural gas-fueled, two-stroke, and four-stroke dual-fuel CI engines and four-stroke SI engines used in marine applications. Fuel conversion efficiency, power density, ignition stability, knocking tendency, and exhaust emissions are considered for both SI and dual-fuel CI engines, and the inherent trade-offs in adapting natural gas as a primary fuel for marine applications are discussed.

Advanced combustion and ignition technologies for natural gas-fueled CI and SI engines are dealt with in Chap. 8. Natural gas-fueled HCCI, RCCI, and dual-fuel LTC strategies are reviewed, and the PREmixed Mixture Ignition in the End gas Region (PREMIER) combustion concept is presented in significant detail. With control of pilot fuel injection quantity and pressure, pilot fuel injection timing, gaseous fuel equivalence ratio, and exhaust gas recirculation (EGR) levels, it is shown that a reasonable compromise can be achieved between fuel conversion efficiency and exhaust emissions using the PREMIER concept. In addition, advanced ignition systems such as laser ignition and plasma-assisted ignition of

lean natural gas–air mixtures at relatively high compression ratios are also reviewed.

In Chap. 9, a parametric analysis is performed for diesel–natural gas RCCI in a light-duty CI engine. Specifically, the impact of natural gas substitution, EGR, compression ratio on RCCI performance and emissions is presented. The authors show that, by optimizing the combustion chamber and the aforementioned dual-fuel engine operating parameters, it is possible to reduce engine-out exhaust emissions (UHC emissions, in particular) while simultaneously improving fuel conversion efficiency.

Design and calibration strategies for improving diesel–methane dual-fuel HCCI engines are described in Chap. 10. Results from a full factorial design-of-experiments study of the effects of compression ratio, intake pressure, diesel pilot injection timing and injection pressure, and methane substitution on combustion evolution, engine performance, and pollutant emissions are presented. The results show that dual-fuel HCCI combustion can be achieved both with early and late SOIs when combined with high intake pressures to yield very low  $\text{NO}_x$  emissions and maximum pressure rise rates with very little penalty on fuel conversion efficiency, HC, and carbon monoxide (CO) emissions.

Chapter 11 presents results from a combined experimental and computational investigation of diesel–natural gas dual-fuel combustion in a light-duty industrial engine. The authors leverage calibrated CFD and 1D models of dual-fuel combustion and experiments at different engine loads and speeds to optimize dual-fuel operation (without EGR) and demonstrate virtual elimination of soot, significant  $\text{NO}_x$  and  $\text{CO}_2$  reduction, and improvements in brake fuel conversion efficiency. The authors report higher engine-out UHC and CO emissions, which may be eliminated with an effective exhaust oxidation catalyst.

One of the challenges in conventional diesel–natural gas dual-fuel combustion and dual-fuel LTC is unstable engine operation, especially at low loads. Cyclic combustion variations, which lead to engine instabilities and high UHC and CO emissions in dual-fuel LTC, are discussed in Chap. 12. Inconsistent fuel–air mixing from one engine cycle to another, leading to cyclic inconsistencies in ignition and combustion phasing as well as combustion duration, may be an important cause of cyclic combustion variations in dual-fuel LTC. Therefore, strategies to mitigate cyclic combustion variations may include ensuring appropriate local stratification of diesel-to-methane fractions such that the combustion process is just sufficiently premixed to achieve low  $\text{NO}_x$  and soot emissions without compromising engine stability.

A review of the performance, combustion-generated emissions, and emissions control strategies, and exhaust aftertreatment technologies used for natural gas-fueled CI and SI engines is provided in Chap. 13. In particular, lean-burn vs. stoichiometric operation, the impact of EGR with hydrogen enrichment, the importance of spark timing, performance enhancement with hydrogen addition, and aftertreatment systems (e.g., performance of three-way catalytic converters) for natural gas SI engines are discussed. Similarly, for CI engines operating on dual-fuel combustion, the benefits of EGR, pilot fuel quantity and type, and pilot injection timing on mitigating exhaust emissions are also reviewed.

Finally, Chap. 14 presents a detailed review of the state of the art in residential-scale, natural gas-powered CHP systems utilizing IC engines, Stirling engines, Brayton cycle engines, and micro-Rankine cycle engines as prime movers. The authors conclude that natural gas-fueled reciprocating IC engines provide the best benefits vis-à-vis fuel conversion efficiency and load-following, but they also face technical hurdles in terms of heat transfer, incomplete combustion, and pumping and friction losses, which become more pronounced for small-scale engines.

## References

- Energy Information Administration. International Energy Outlook 2018; Released on July 24, 2018; [https://www.eia.gov/pressroom/presentations/capuano\\_07242018.pdf](https://www.eia.gov/pressroom/presentations/capuano_07242018.pdf). Accessed Aug 18, 2018
- International Energy Agency. Key World Energy Statistics 2017; <http://www.iea.org/publications/freepublications/publication/KeyWorld2017.pdf>. Accessed Aug 18, 2018
- US Department of Energy, Office of Fossil Energy (2018). Liquefied Natural Gas. <https://www.energy.gov/fe/science-innovation/oil-gas/liquefied-natural-gas> Accessed Aug 19, 2018

# Chapter 2

## Low-Temperature Natural Gas Combustion Engines



Sotirios Mamalis

**Abstract** Advanced or low-temperature combustion engines have shown the potential to achieve high fuel conversion efficiency with minimal emissions formation and therefore can provide solutions for future powertrain systems. Numerous advanced combustion concepts have been explored, including both spark-ignited and compression-ignited concepts, and each one has been investigated using different liquid or gaseous fuels. This chapter will discuss the potential of using natural gas as a fuel for future advanced combustion engines and will present the associated benefits and challenges. The low carbon-to-hydrogen atom ratio of natural gas can enable a highly efficient combustion process with low CO<sub>2</sub> formation; its chemical composition mitigates soot formation during combustion, and its high octane number enables high compression ratio operation of spark-ignited engines with good knock resistance. However, the low reactivity of natural gas inhibits the compression ignition of lean fuel–air mixtures, and any combustion inefficiency may result in direct methane emissions in the exhaust. These characteristics have led researchers to investigate lean natural gas combustion using prechambers (jet ignition), high-pressure direct injection (HPDI) of diesel and natural gas mixtures, micro-pilot injection concepts with premixed natural gas and direct-injected diesel fuel, as well as kinetically controlled and low-temperature combustion concepts such as Homogeneous Charge Compression Ignition (HCCI) and Reactivity Controlled Compression Ignition (RCCI) combustion. This chapter will discuss the use of natural gas in the HCCI and RCCI combustion concepts and analyze the associated benefits and challenges.

**Keywords** Natural gas · Low-temperature combustion · Advanced combustion Internal combustion engines

---

S. Mamalis (✉)  
Stony Brook University, Stony Brook, NY, USA  
e-mail: [sotirios.mamalis@stonybrook.edu](mailto:sotirios.mamalis@stonybrook.edu)

© Springer Nature Singapore Pte Ltd. 2019  
K. K. Srinivasan et al. (eds.), *Natural Gas Engines*, Energy, Environment,  
and Sustainability, [https://doi.org/10.1007/978-981-13-3307-1\\_2](https://doi.org/10.1007/978-981-13-3307-1_2)

## 2.1 Introduction

Worldwide fuel economy and emissions regulations have prompted research and development on internal combustion engines that can achieve higher fuel conversion efficiency and lower emissions formation compared to currently available spark-ignition (SI) and diesel engines. Numerous advanced combustion concepts have been proposed in the literature, primarily originating from Homogeneous Charge Compression Ignition (HCCI), which was first proposed by Najt and Foster in 1983 (Najt and Foster 1983). The HCCI concept combines the homogeneous charge of premixed SI engines with the compression ignition of diesel engines to create a lean burn concept that can achieve high thermal efficiency. The lean mixture also results in low burned gas temperature, thus preventing thermal  $\text{NO}_x$  formation during combustion. The low burned gas temperature has led many researchers to use the term “low-temperature combustion” to describe this concept, which has since been used to encompass other combustion concepts of similar nature as well. HCCI combustion is achieved by creating a homogeneous and lean fuel–air mixture and compressing it until the point of autoignition, which results in a heat release process initiated and controlled by chemical kinetics. This process is different from the heat release in SI engines, which is controlled by turbulent flame propagation, as well as from the heat release in diesel engines, which is controlled by diffusion mixing between the direct-injected fuel and the surrounding air. The absence of a spark or direct fuel injection results in having no *direct* control of the start of combustion in HCCI engines. Therefore, ignition timing can only be controlled *indirectly*, by controlling the air/fuel ratio of the mixture, the dilution level, and the initial mixture temperature.

The HCCI concept has been demonstrated through experimental testing in single-cylinder optical and metal engines (Epping et al. 2002; Sjöberg et al. 2004; Sjöberg and Dec 2004, 2005, 2007; Silke et al. 2009), as well as in light-duty and heavy-duty commercial engine platforms (Christensen et al. 1997; Olsson et al. 2001, 2002; Christensen and Johansson 2000; Hyvönen et al. 2003; Haraldsson et al. 2002, 2003, 2004; Zhao et al. 2003) using gasoline and diesel fuels. Experimental results have shown that HCCI combustion can be achieved at very lean mixtures with high compression ratio resulting in high thermal efficiency as well as low  $\text{NO}_x$  and no soot formation. However, the homogeneous nature of the mixture results in bulk autoignition, and rapid heat release rate and pressure rise rate in the cylinder, which limits the maximum attainable load. In addition, igniting a lean fuel–air mixture by compression alone requires charge heating, which can be accomplished either by intake air preheating or by residual gas trapping in the cylinder (Chang et al. 2007; Babajimopoulos et al. 2009; Olesky et al. 2012; Mamalis et al. 2012).

In order to mitigate the high heat release rates of HCCI combustion, researchers have proposed techniques to introduce thermal and compositional stratification to the mixture and thus stagger the autoignition process. Partial fuel stratification (PFS) is one technique proposed by Dec et al. (2011, 2015), Sjöberg and Dec

(2006), Yang et al. (2011a, b, 2012) which utilizes split fuel injections directly into the cylinder. By splitting the injection process into one early and one late injection, the mixture becomes compositionally and thermally stratified resulting in staggered autoignition throughout the combustion chamber. Direct water injection is another technique proposed by Lawler et al. (2017), Boldaji et al. (2017, 2018), which injects water in a premixed fuel–air mixture to forcefully stratify the thermal field in the cylinder through the latent heat of vaporization of water and thus stagger the autoignition process.

In addition to the methods described above, researchers have proposed the use of two fuels to control the heat release rates of low-temperature combustion engines. The Reactivity Controlled Compression Ignition (RCCI) concept that was proposed by Kokjohn et al. (2011a, b), Splitter (2011), Hanson et al. (2011) combines a low reactivity fuel injected at the port (e.g., gasoline) with a high reactivity fuel injected directly into the cylinder to create a compositional stratification in the combustion chamber. The mixing between the two different fuels in the combustion chamber creates zones of different reactivity resulting in staggered autoignition and lower heat release rates compared to HCCI. The RCCI combustion concept has been demonstrated in light- and heavy-duty engines and has shown good controllability and fuel conversion efficiency comparable to diesel engines (Hanson et al. 2012; Splitter et al. 2011; Klos et al. 2015; Kokjohn and Reitz 2013; Kavuri et al. 2016; Lim et al. 2014). The lean, low-temperature combustion process prevents thermal  $\text{NO}_x$  formation; however, the direct fuel injection of the high reactivity liquid fuel results in some particulate emissions albeit at considerably lower levels than conventional diesel combustion.

Research on low-temperature combustion concepts such as HCCI and RCCI has been primarily focused on using gasoline and diesel fuels due to their widespread commercial use. However, a number of studies have focused on exploring advanced combustion with natural gas, as an alternative to liquid fuels that can provide solutions for sustainable future transportation and power generation.

### *Natural Gas HCCI Combustion*

HCCI combustion with natural gas has been explored for use in heavy-duty vehicles, locomotives, and stationary power generation. However, the high Research Octane Number (RON) of natural gas requires higher compression ratio and/or higher heat addition to the fuel–air mixture to achieve autoignition compared to gasoline. Aceves et al. performed CFD simulations with detailed chemistry of a supercharged HCCI engine using methane and investigated the effect of compression ratio on combustion (Aceves et al. 1999). It was found that combustion could be well controlled through equivalence ratio and the trapped Residual Gas Fraction (RGF), but high-speed cylinder pressure sensing was necessary for control. The high load limit of the engine was posed by peak cylinder pressure and  $\text{NO}$  formation. Flowers et al. continued this modeling study using actual natural gas composition and investigated the effect of varying fuel composition on HCCI combustion (Flowers et al. 2001). HCCI combustion was found to be sensitive to natural gas composition, and active control is required in order to compensate for



changes in composition typical throughout the world. Changes in natural gas composition may shift the peak heat release timing by as much as 10 Crank Angle Degrees (CADs), with significant effects on efficiency and emissions formation. The concentration of propane and butane present in natural gas can significantly affect HCCI combustion. Three control strategies were proposed: (i) adding Dimethyl Ether (DME) to the fuel–air mixture, (ii) intake gas preheating, and (iii) using hot Exhaust Gas Recirculation (EGR), which were found to be effective in controlling the heat release rate over a wide range of operating conditions.

Fiveland et al. performed experimental testing and modeling on a heavy-duty natural gas HCCI engine operating at 1000 rev/min and  $\phi$  of 0.3 in order to examine the sensitivity of HCCI combustion to fuel composition (Fiveland et al. 2001). The presence of higher order hydrocarbons increased the reactivity of the mixture and reduced the temperature of autoignition. Butane had a sensitivity of 2.5 °C/%, propane had 1.5 °C/%, and ethane had 1.0 °C/%. Based on the experimental results, it was concluded that fluctuations in natural gas composition may result in high-speed or low-speed effects on engine performance.

Olsson et al. performed a similar experimental study using a Volvo TD100 heavy-duty engine modified for natural gas HCCI combustion and also performed modeling of the same engine to study the effect of compression ratio on combustion (Olsson et al. 2002). Hydrogen enrichment was used to control combustion phasing on a cycle basis. Compression ratio was varied from 15:1 to 21:1, but was found to have a small effect on the heat release rate. High compression ratio resulted in higher peak cylinder pressures but also enabled the engine to operate leaner and reduce NO<sub>x</sub> formation. Overall, the compression ratio should be high enough to enable lean operation with low NO<sub>x</sub> at high load, but also offer good control authority at maximum load.

Yap et al. studied the effects of hydrogen addition on natural gas HCCI combustion using a light-duty research engine with residual gas trapping (Yap et al. 2004). The hydrogen was produced using an exhaust-assisted reformer, and it was introduced into the cylinder as hydrogen-rich EGR. The addition of hydrogen in the fuel–air mixture resulted in lower intake air preheating requirement for autoignition. However, even with the addition of hydrogen, some intake air preheating was required in combination with residual gas trapping. The benefit of hydrogen in reducing the autoignition temperature was more effective at low loads; however, the addition of hydrogen resulted in higher cylinder temperatures at high load and higher NO<sub>x</sub> compared to pure natural gas HCCI. In subsequent experiments, Yap et al. utilized low-temperature exhaust gas fuel reforming to produce reformat gas with up to 16% hydrogen by volume (Yap et al. 2006). This reformat gas was recirculated to the intake and mixed with the fresh natural gas–air mixture to control autoignition. It was confirmed that the addition of hydrogen reduced the intake air preheating requirement for autoignition.

The engine-reformer closed-loop operation showed that the hydrogen addition also promoted stable HCCI operation and extended the low load limit without reducing combustion efficiency. NO<sub>x</sub> emissions decreased with the addition of hydrogen-rich reformat gas; however, CO and unburned hydrocarbon emissions

(UHC) increased. The addition of hydrogen also had minor benefits on the indicated specific fuel consumption (Fig. 2.1). The water content in the exhaust gas contributes to the increase of hydrogen production in the reformer and thus offsets the energy loss due to the oxidation reactions.

Soylu modeled a natural gas HCCI engine using a zero-dimensional model to investigate the combustion characteristics and phasing strategies (Soylu 2005). Controlling the equivalence ratio, and temperature and pressure conditions at Intake Valve Closing (IVC), is critical for controlling combustion phasing and can be achieved through Variable Valve Actuation (VVA), Variable Compression Ratio (VCR), and EGR. However, increasing the EGR fraction was found to reduce the maximum attainable thermal efficiency and load. The addition of propane to natural gas–air mixtures was also found to be effective in controlling combustion phasing, albeit being a low-speed control alternative. Provided that good combustion phasing control is achieved, fuel conversion efficiency of 45% can be achieved at IMEPn of 4–5 bar.

Natural gas HCCI engines have also been considered for stationary power generation, including distributed generation and Combined Heat and Power (CHP) systems. Kobayashi et al. investigated the potential of using a 50 kW natural gas HCCI engine in a CHP system and performed experimental testing, first on a single-cylinder research engine and then on a four-cylinder turbocharged engine (Kobayashi et al. 2011). Experimental results indicated that the load range of turbocharged HCCI can exceed that of naturally aspirated SI engines (Fig. 2.2). When the peak cylinder pressure is limited, high thermal efficiency with extremely low  $\text{NO}_x$  can be achieved by raising the engine compression ratio and limiting the boost pressure. The four-cylinder turbocharged HCCI engine achieved 43.3% brake thermal efficiency at 0.98 MPa bar Brake Mean Effective Pressure (BMEP) with 13.8 ppm of engine-out  $\text{NO}_x$  emissions (Fig. 2.3), which confirmed the potential of

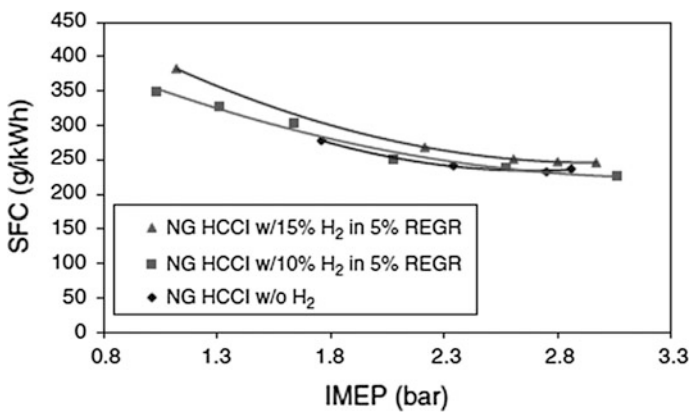


**Fig. 2.1** Specific fuel consumption for natural gas HCCI combustion supplemented with 10 and 15% hydrogen, as presented by Yap et al. (2006)

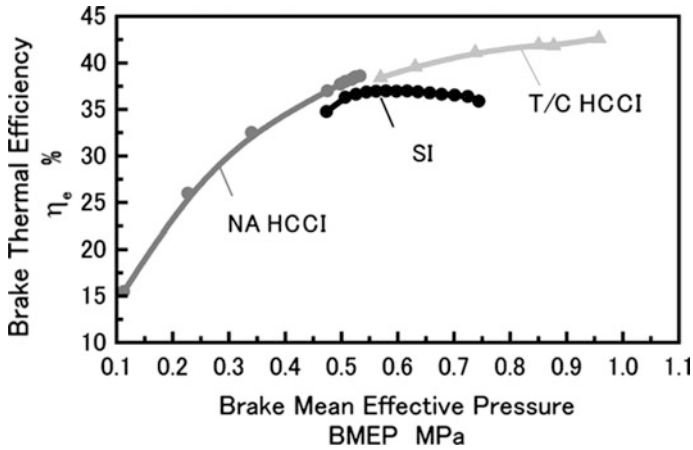
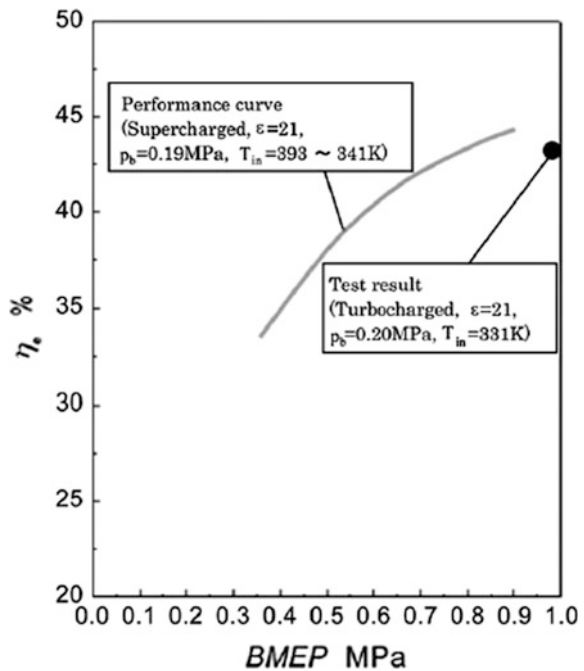


Fig. 2.2 Brake thermal efficiency and load range for naturally aspirated SI, HCCI, and boosted HCCI operation, as presented by Kobayashi et al. (2011)

Fig. 2.3 Performance of a four-cylinder, natural gas, turbocharged HCCI engine, at 1800 rev/min, compression ratio 21:1, and intake pressure of 2 bar, as presented by Kobayashi et al. (2011)



natural gas HCCI to provide high efficiency and low emissions for CHP applications.

Djermouni et al. investigated turbocharged natural gas engines by performing thermodynamic analysis including energy and exergy calculations (Djermouni and

Quadha 2014). Increasing the compressor pressure ratio resulted in increased thermal and exergetic efficiencies; however, increasing the intake temperature to facilitate autoignition resulted in reducing both efficiencies. The lean, low-temperature HCCI combustion resulted in high exergy loss during combustion, thus increasing the equivalence ratio increased the exergetic efficiency. Overall, exergy analysis was useful in understanding the losses associated with the gas exchange and combustion processes and designing natural gas HCCI engines for maximum efficiency.

Judith et al. also performed numerical simulations of a light-duty, natural gas HCCI engine for cogeneration applications and focused on identifying the interactions between engine speed, compression ratio, air/fuel ratio, residual gas trapping, and intake air preheating on enabling HCCI combustion over a wide operating range (Judith et al. 2017). Model predictions showed that natural gas HCCI combustion could be achieved at compression ratio of 25:1 to 31:1, but ignition timing at the highest compression ratios was more difficult to control. By varying the air/fuel ratio and the Residual Gas Fraction, the autoignition timing was greatly influenced by the heat capacity of the mixture, its reactivity, and the oxygen concentration. In a similar fashion to HCCI combustion with liquid fuels, operation with natural gas depended heavily on compression ratio and intake temperature.

Sofianopoulos et al. also investigated natural gas HCCI combustion for distributed power using a small free-piston linear alternator concept (Sofianopoulos et al. 2017). The free-piston engine was modeled using three-dimensional Computational Fluid Dynamics (CFD) with detailed chemistry in order to identify the gas exchange, mixture preparation, and combustion processes required for HCCI combustion with natural gas. The free-piston engine was modeled to operate at a constant frequency of 20 Hz, which resulted from the mass of the reciprocating components as well as from the requirements posed by the linear alternator. The ports of the free-piston engine were designed to eliminate short-circuiting of fresh mixture from the intake to the exhaust and to trap more than 50% of residual gas in order to enable autoignition of the lean natural gas-air mixture. Natural gas HCCI operation was simulated for ten consecutive cycles, and the heat release rate and cylinder pressure are shown in Fig. 2.4. The free-piston engine was operated at effective equivalence ratio of 0.32 with residual gas trapping, which resulted in modeled combustion efficiency of 97.3% and gross indicated efficiency of 38.1% at 1 kW power output.

### *Dual-Fuel Advanced Natural Gas Combustion*

Although HCCI combustion with natural gas has been demonstrated experimentally and its efficiency and emissions benefits have been documented, the high heat release rates during combustion limit the achievable upper and lower engine load. In order to reduce the heat release rates, researchers have utilized dual-fuel combustion that introduces compositional stratification to the air-fuel mixture and results in a staggered autoignition process. Stanglmaier et al. performed experimental testing on a heavy-duty, John Deere 8.1 L PowerTech natural gas engine, which was modified to operate on dual-fuel HCCI combustion at low to moderate

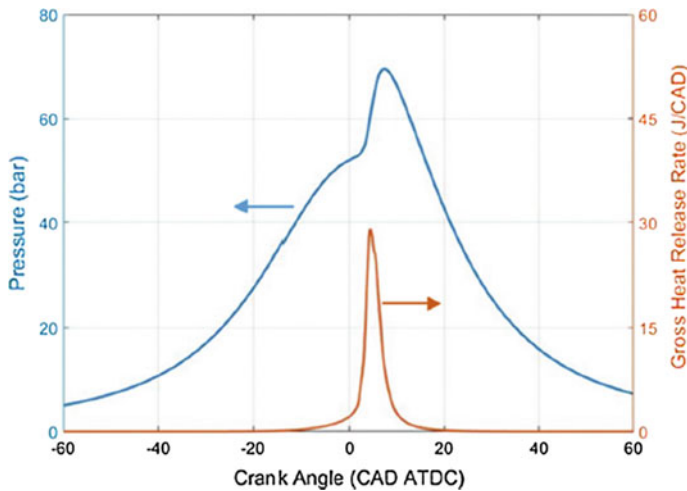


**Fig. 2.4** Simulated cylinder pressure and heat release rate of a single-cylinder, natural gas, free-piston HCCI engine operating with residual gas trapping at effective equivalence ratio of 0.32, as presented by Sofianopoulos et al. (2017)

loads (Stanglmaier et al. 2001). The engine was equipped with port fuel injectors, which were used to inject Fischer–Tropsch (FT) naphtha fuel enhanced with 1000 ppm of Ethyl Hexyl Nitrate (EHN) to improve its autoignition characteristics. The liquid fuel supplemented the lean natural gas–air mixture introduced upstream in the intake manifold. Dual-fuel HCCI operation was achieved from idle to 5.5 bar BMEP, which corresponded to about 35% of the peak engine torque. Fuel blending was an effective way to control the heat release rates in HCCI mode, which were considerably higher than SI operation. HCCI operation resulted in up to 15% fuel conversion efficiency benefits compared to SI operation and a simultaneous reduction of  $\text{NO}_x$  by 95–99%. However, HCCI operation resulted in higher CO and UHC emissions than SI operation at the same conditions.

Papagiannakis et al. performed experimental testing of dual-fuel natural gas–diesel combustion on a single-cylinder DI diesel engine (Papagiannakis and Hountalas 2004). The engine was operated using a premixed natural gas–air mixture and direct injection of a small amount of diesel fuel to control autoignition. Dual-fuel operation resulted in lower heat release rate and pressure rise rate compared to conventional diesel combustion. At low loads, dual-fuel operation showed lower fuel conversion efficiency than diesel, but high load operation was equally efficient. In all cases, dual-fuel operation exhibited low-temperature combustion characteristics, which resulted in lower  $\text{NO}_x$  formation compared to conventional diesel combustion.

Kong studied natural/DME HCCI combustion using CFD with detailed chemical kinetics and compared the modeling results against experimental data from a single-cylinder Yanmar diesel engine modified for dual-fuel operation (Kong 2007).

Natural gas and DME were premixed upstream in the engine intake manifold, and DME was used as an additive to the fuel–air mixture to promote autoignition. Modeling results showed that HCCI combustion is facilitated by the addition of DME, and by increasing the DME concentration, the low-temperature heat release increases and drives the autoignition of the mixture. The modeling results were used to establish engine operating limits at different concentrations of natural gas and DME in the mixture (Fig. 2.5). As the natural gas concentration increased, the operating range becomes narrower and HCCI combustion becomes unstable.

Nieman et al. performed CFD simulations of a heavy-duty RCCI engine operated with natural gas and diesel (Nieman et al. 2012). Natural gas was used as a replacement for gasoline as the low reactivity fuel, because its higher RON created larger reactivity gradient between the two fuels when mixed in the cylinder. A broad speed and load range were investigated; six operating points from 4 to 23 bar IMEPn and 800 to 1800 rev/min were optimized, which represent typical heavy-duty engine operating conditions. Using a compression ratio of 16:1, it was determined that operation up to 13.5 bar IMEP can be achieved without EGR, while still maintaining high efficiency and low emissions. Natural gas/diesel operation was compared against gasoline/diesel operation at 9 bar IMEPn and was found that in the natural gas/diesel gases 90–95% of UHC emissions were methane. The sensitivity of high load RCCI combustion to injection parameters was examined, and the results showed that precise injection control is necessary.

Fathi et al. performed experimental testing on a single-cylinder CFR engine operated in HCCI mode with n-heptane/natural gas fuel (Fathi et al. 2011) and focused on understanding the effects of EGR on combustion phasing control. The

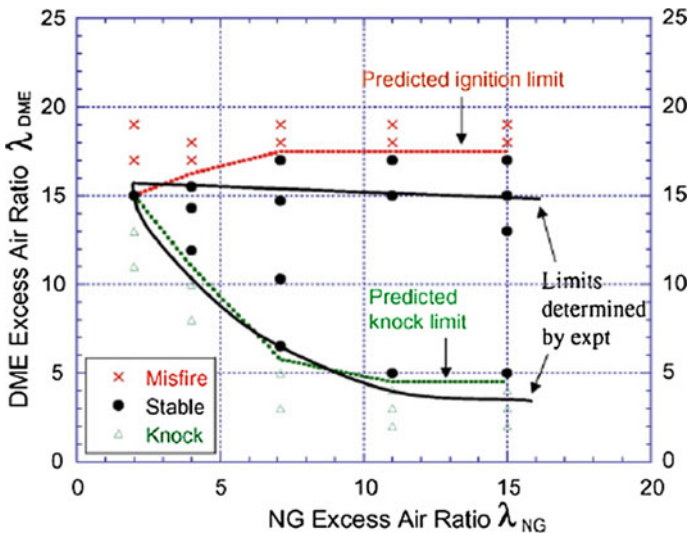


**Fig. 2.5** Predicted operating limits for a dual-fuel natural gas–DME HCCI engine at different natural gas and DME concentrations, as presented by Kong (2007)

fuel blend was premixed and introduced at the engine intake manifold. Experimental data showed that EGR reduced the bulk cylinder temperature as well as the pressure rise rate and peak pressure during combustion. EGR also delayed autoignition and increased the burn duration due to its effect on the physical and chemical properties of the mixture (Fig. 2.6). However, in the cases where EGR resulted in considerably delayed combustion phasing, the thermal efficiency was reduced. Although EGR reduced the peak cylinder temperatures and thus reduced  $\text{NO}_x$  formation, it had an adverse effect on CO and UHC emissions.

Doosje et al. also performed experimental testing of RCCI combustion in a six-cylinder, 8.0 L, heavy-duty engine, using natural gas as the low reactivity fuel and cooled EGR (Doosje et al. 2014). The engine was used to explore the operating limits of RCCI combustion. Experimental results showed that RCCI operation could be achieved between 1200 and 1800 rev/min, 2 and 9 bar BMEP, with engine-out  $\text{NO}_x$  and soot emissions that satisfied the Euro VI emissions regulations. UHC emissions were high, but the high exhaust gas temperature was suitable for using an oxidation catalytic converter. The effect of diesel injection timing on the

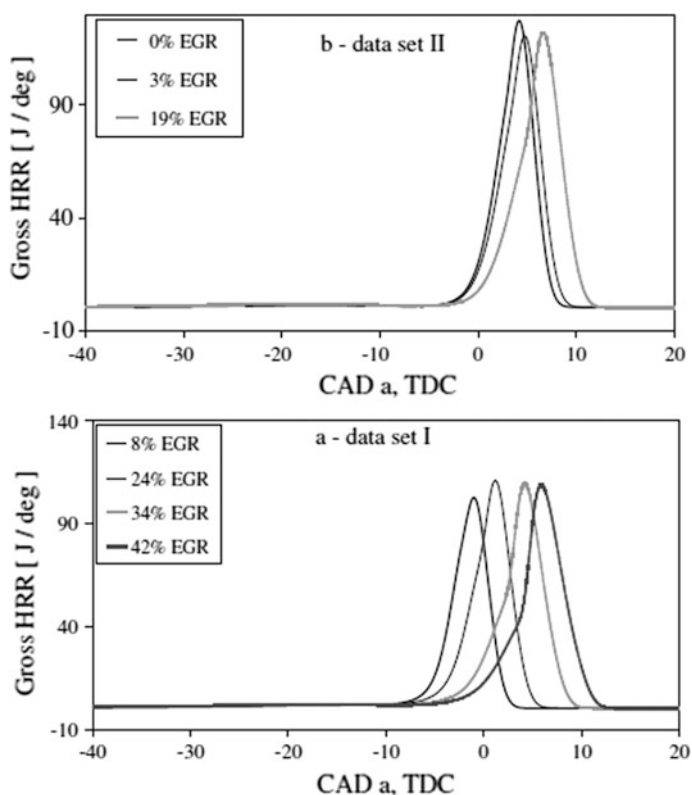


**Fig. 2.6** Effect of EGR on the heat release rate of n-heptane/natural gas HCCI combustion, as presented by Fathi et al. (2011)

heat release was investigated, and experimental results showed that when the start of injection (SOI) was advanced beyond 34 CAD before TDC, further advancement resulted in delayed heat release rate, an indication of operation in the RCCI regime. For all operating points considered, the engine thermal efficiency in RCCI mode was comparable to or better than conventional diesel combustion. Total UHC was high, but 80–85% of them comprised of methane. For the operating conditions examined, any methane number (MN) variation in the 70–100 range had negligible effects on RCCI combustion.

Zoldak et al. performed a computational study on RCCI combustion using natural gas as the low reactivity fuel on a 15.0 L heavy-duty diesel engine (Zoldak et al. 2014). The trade-offs between fuel consumption, pressure rise rate, peak cylinder pressure, and emissions formation were examined, and the results showed that RCCI combustion had the potential for 17.5%  $\text{NO}_x$  reduction, 78% soot reduction, and 24% decrease in fuel consumption compared to conventional diesel combustion at the rated power condition using the same air–fuel ratio and EGR level. Modeling results showed that the amount of diesel fuel injected directly into the cylinder dictated the mixture reactivity and thus the combustion phasing and pressure rise rate. The maximum pressure rise rate and peak pressure increased compared to conventional diesel combustion, but both were within acceptable limits for engine durability. The large reduction in soot formation in RCCI mode resulted from the lower level of mixture stratification compared to conventional diesel, as well as from having natural gas as the low reactivity fuel.

Similar studies were performed by Dahodwala et al., who focused on analyzing experimental RCCI combustion data on a heavy-duty diesel engine operated at 6 bar BMEP and different speeds (Dahodwala et al. 2014, 2015). The study evaluated the impact of various control variables, such as natural gas substitution rate, EGR rate, and injection strategy on achieving RCCI combustion, and thereby establishing a framework for identifying the in-cylinder mixture properties required for RCCI. Experimental data were also collected at 14 bar BMEP in order to investigate high load RCCI operation as well. A CFD model with detailed chemistry was also used to support the analysis of experimental data. Increasing the natural gas substitution resulted in delayed combustion phasing and lower burn rate, and also increased CO and UHC emissions. Combustion phasing and burn duration could also be controlled through the EGR rate, although increasing EGR resulted in lower combustion efficiency. Increasing the amount of diesel fuel injected in the cylinder led to more mixture stratification and advanced combustion phasing. The injection strategy dictates the combustion mode of the engine, and the timing of injection changes with engine speed. For conventional diesel combustion,  $\text{NO}_x$  emissions were higher at lower engine speeds. However, for RCCI combustion  $\text{NO}_x$  emissions were higher at higher engine speeds. Reduced engine speed in RCCI mode also reduced CO and UHC emissions.

Kakae et al. used CFD modeling to study the effects of natural gas composition and engine speed on combustion and emission characteristics of natural gas/diesel RCCI combustion (Kakae et al. 2015). RCCI combustion was found to be sensitive to fuel composition and engine speed. Specifically, the Wobbe number



(WN) of the fuel affected the ignition timing and burn rates. Higher WN resulted in higher peak cylinder pressure and temperature, higher  $\text{NO}_x$  emissions, but lower CO and UHC emissions. Gas with lower WN exhibited lower heat release rate, which resulted in lower combustion efficiency at high engine speeds. Overall, gas with higher WN was found to be beneficial for efficiency and emissions at high engine speed operation. The same group studied the effects of piston bowl geometry on combustion and emissions of natural gas/diesel RCCI engine using CFD modeling (Kakaee et al. 2016). Three different piston bowl geometries were studied: a conventional reentrant bowl for diesel operation, a bathtub-shaped, and a cylindrical bowl (Fig. 2.7). Modeling results showed that the piston bowl geometry did not affect RCCI combustion at low engine speeds, but had an increasing effect as engine speed increased. By increasing the bowl depth, cylinder pressure and temperature increased, which in turn increased  $\text{NO}_x$  emissions. CO and UHC emissions were minimized at bowl depth of 1 mm. Also, by increasing the piston chamfer size, the cylinder pressure and temperature increased, which again increased  $\text{NO}_x$  but also increased the gross indicated efficiency. Using a chamfered ring-land can reduce UHC emissions particularly at chamfer sizes greater than 3 mm.

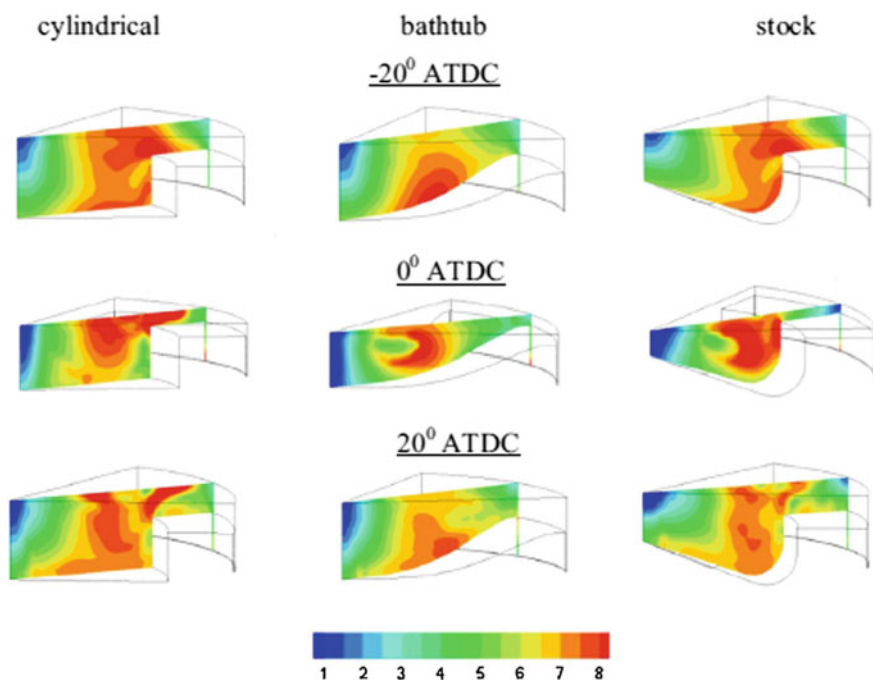


**Fig. 2.7** Simulated cylinder velocity (m/s) cutplanes at  $-20^\circ$  ATDC, TDC, and  $20^\circ$  ATDC, for three different piston bowl profiles for natural gas/diesel RCCI combustion, as presented by Kakaee et al. (2016)

Jia et al. performed experimental testing of natural gas/diesel RCCI combustion on a single-cylinder AVL 501 heavy-duty diesel engine and focused on analyzing the effects of diesel injection timing and duration on combustion at 1200 rev/min and 9 bar BMEP (Jia and Denbratt 2015). Experiments were conducted at two compression ratio levels, 14:1 and 17:1. It was found that reducing the compression ratio to 14:1 had favorable effects on combustion phasing control and  $\text{NO}_x$  emissions, but increased UHC emissions. The lower compression ratio resulted in longer ignition delay times, longer combustion duration, and also lower heat release rate. Delaying the injection of diesel fuel made the fuel–air mixture more stratified, which reduced the ignition delay and increased the burn rate. Overall, it was shown that RCCI combustion with low  $\text{NO}_x$  and almost zero soot emissions can be achieved, albeit with high UHC emissions which can be treated in the emissions control system.

Paykani et al. performed a similar study on investigating injection strategies for natural gas/diesel RCCI combustion, using CFD modeling (Paykani et al. 2015). Direct-injected diesel was split into two injections, and it was shown that the timing of each injection as well as the fuel fraction split has significant effects on RCCI combustion. Delaying the second injection was found to increase mixture stratification, local fuel reactivity, and burned gas temperatures, which advanced combustion phasing and increased NO and soot emissions as well as the ringing intensity. Similar effects were seen by increasing the amount of diesel fuel injected in the second injection. The injection timing and duration also played a role when engine speed was increased, because the available time for fuel–air mixing was reduced. Therefore, as engine speed increased, the peak pressure and temperature decreased, which resulted in later combustion phasing and increased CO and UHC emissions. The simulated mid-load case had over 50% gross indicated efficiency, with low  $\text{NO}_x$  and soot without using EGR. Combustion phasing could be accurately controlled through the ratio of the natural gas and diesel, as well as through the ratio of diesel fuel split between the two direct injections. Additionally, it was found that the large difference in reactivity between natural gas and diesel helped the engine to achieve low pressure rise rate.

Ansari et al. used experimental testing of a 1.9 L diesel engine and CFD modeling to map the efficiency and emissions of light-duty natural gas/diesel RCCI combustion (Ansari et al. 2016). The engine was operated at speeds of 1300–2500 rev/min and loads of 1–7 bar BMEP. Operation was limited to 10 bar/deg of maximum pressure rise rate and 6% Coefficient of Variation (COV) of IMEP. The engine operating envelope was explored by varying the natural gas/diesel blend ratio, the diesel injection fuel split and timing, and the EGR amount. More than 80% of the required fuel energy input in RCCI mode was provided from natural gas. Experimental results showed that the pressure rise rate is very sensitive to the pilot injection timing and the fuel split ratio between the two direct injections. At low loads, RCCI combustion provided brake thermal efficiency equivalent to or lower than diesel; however, as speed and load increased, the efficiency increased as well. The maximum recorded brake efficiency for RCCI combustion was 39% at 2500 rev/min and 6 bar BMEP, compared to 34% for conventional diesel

combustion. Up to 92% reduction in  $\text{NO}_x$  was achieved through precise control of the injection parameters. The majority of the RCCI operating points had exhaust gas temperature below 450 °C, which is a typical light-off temperature for methane oxidation catalysts. Therefore, the low exhaust gas temperature and the high CO and UHC emissions present a major challenge for the commercial adoption of natural gas/diesel RCCI engines.

Hockett et al. focused on developing a reduced chemical kinetics mechanism for performing detailed chemistry calculations of natural gas/diesel dual-fuel engines (Hockett et al. 2016). In this mechanism, natural gas is modeled as a mixture of methane, ethane, and propane, while diesel is modeled as n-heptane. The mechanism consists of 141 species and 709 reactions and has been validated against experimental premixed laminar flame speed measurements of  $\text{CH}_4/\text{O}_2/\text{He}$  mixtures, ignition delay and lift-off length from a diesel spray experiment in a constant volume chamber, and also against dual-fuel engine experiments using CFD simulations. The results showed that this mechanism accurately reproduces the chemical kinetic behavior of larger detailed mechanisms and captures the laminar flame speeds at high pressure, the ignition delay and lift-off length of the diesel experiment, and the heat release rate in the engine experiments. Also, this reduced mechanism is able to accurately model varying natural gas reactivity without relying on rate constant tuning.

Poorghasemi et al. performed CFD simulations with detailed chemical kinetics to study the effect of diesel injection strategies on natural gas/diesel RCCI combustion in a light-duty engine (Poorghasemi et al. 2017). The parameters that were varied in the simulations included the premixed ratio of natural gas, the diesel fuel fraction split between the first and second injection, the timing of the two injections, the injection pressure, and the spray included angle. The modeling results showed that by increasing the premixed ratio of natural gas, the mixture reactivity is reduced, resulting in increased ignition delay and lower heat release rates. The diesel injection strategy has significant effects on RCCI combustion because it controls the local reactivity of the mixture. As the direct injections are moved toward TDC, the local reactivity of the mixture increases the temperature during combustion by raising the local equivalence ratio. Increasing the amount of diesel fuel injected in the first pulse resulted in higher heat release rates and cylinder pressure. However, more diesel fuel is accumulated in the crevice volume and on the cylinder wall, which increased CO and UHC emissions. By increasing the spray angle, more fuel was burned in the centerline of the spray and the squish region of the combustion chamber. However, by decreasing the spray angle, more fuel was burned in the cylinder bulk. The latter results in higher CO and UHC emissions generated near the cylinder walls, as well as higher  $\text{NO}_x$  formation due to locally richer zones that result in higher burned gas temperature.

Rahnama et al. used CFD modeling to investigate natural gas/diesel RCCI combustion in a heavy-duty engine and focused on investigating the effects of using hydrogen, reformer gas, and nitrogen on combustion (Rahnama et al. 2017). The lower reactivity of natural gas compared to gasoline resulted in compromised engine performance at low loads, but the addition of hydrogen or syngas (reformer

gas) as additives can improve the combustion process at low loads (Fig. 2.8). They can increase the combustion and thermal efficiencies and significantly reduce the UHC and CO formation. However, high values of hydrogen and syngas were found to increase cylinder temperature and thus  $\text{NO}_x$  emissions.

The modeling results showed that adding hydrogen or syngas to RCCI combustion increases the combustion efficiency and is more favorable than increasing the fuel fraction of the direct-injected diesel, because the latter increases soot formation. The ignition delay and start of combustion were not significantly affected by the addition of hydrogen or syngas, and it can be well controlled by the diesel fuel fraction and the intake temperature. Medium load operation was not greatly benefited by the additive gases, despite the fact that thermal efficiency was increased, and UHC and CO emissions were reduced compared to the baseline RCCI engine.

Gharehghani et al. performed an experimental study of RCCI combustion with natural gas and biodiesel derived from waste fish oil, using a single-cylinder Ricardo E6 diesel engine (Gharehghani et al. 2015). The properties of the biodiesel used in their study are shown in Table 2.1, along with diesel and natural gas.

The waste fish oil biodiesel has higher cetane number and oxygen content than conventional diesel, which resulted in higher heat release rates and more stable combustion in natural gas/biodiesel RCCI operation. Figure 2.9 shows the heat release rates for conventional diesel and RCCI combustion modes using diesel, biodiesel, and natural gas. The higher heat release rate in natural gas/biodiesel RCCI combustion led to 1.6% higher gross thermal efficiency than the natural gas/

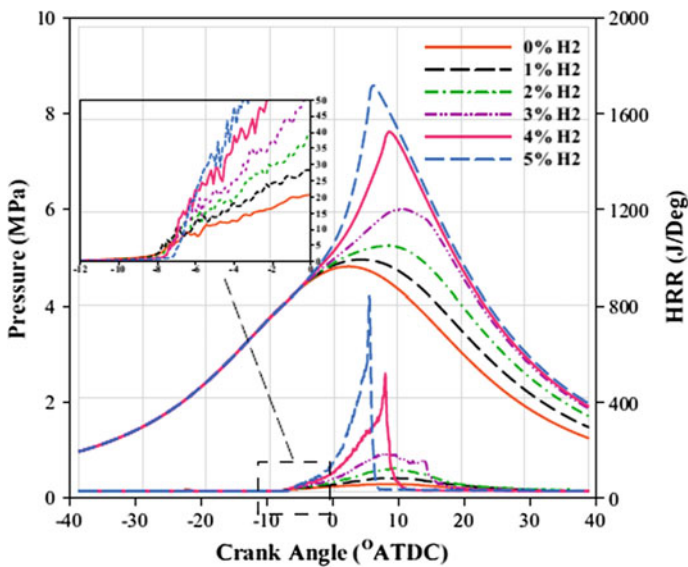


**Fig. 2.8** Impact of hydrogen addition on the heat release rate and cylinder pressure of a heavy-duty natural gas/diesel RCCI engine, as presented by Rahnama et al. (2017)

**Table 2.1** Properties of waste fish oil biodiesel, diesel, and natural gas used for RCCI engine experiments, as presented by Gharehghani et al. (2015)

Parameter	Biodiesel	Diesel	NG
Content of C (%)	82.06	84.2	–
Content of H (%)	8.64	15.7	–
Content of O (%)	9.3	<0.1	–
Flash point (PM, °C)	164–173	74–76	–
Density (15 °C, kg/m <sup>3</sup> )	870–880	830	–
Kinematic viscosity (40 °C, mm <sup>2</sup> /s)	4.142	3.4	–
Cetane index	51.5	50	–
Low heating values (MJ/kg)	41	43.15	45
Methane (Mole. %)	–	–	90.30
Ethane (Mole. %)	–	–	4.28
Propane (Mole. %)	–	–	0.63
Butane (Mole. %)	–	–	0.08
Nitrogen (Mole. %)	–	–	3.6

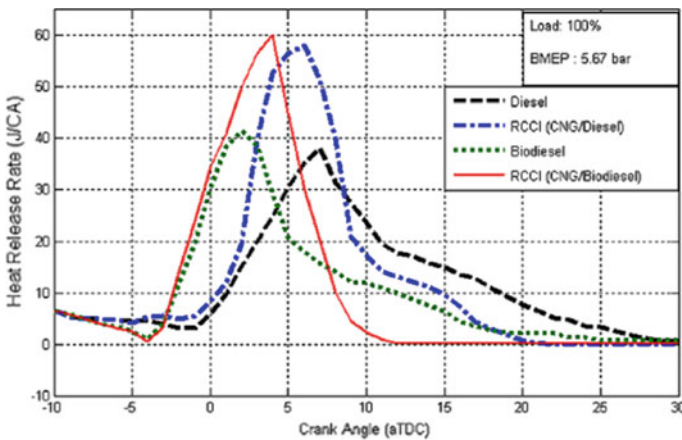


**Fig. 2.9** Heat release rate for conventional diesel and RCCI combustion modes in a single-cylinder engine, using diesel, biodiesel, and natural gas, as presented by Gharehghani et al. (2015)

diesel RCCI, as well as higher combustion efficiency and marginally lower heat transfer losses.

Based on experimental results, the waste fish oil biodiesel was found to be a good alternative to diesel, with great potential for CO reduction in RCCI mode, especially at medium and high loads. RCCI combustion using premixed natural gas with either diesel or biodiesel was found to have significantly lower NO<sub>x</sub> formation than conventional diesel combustion.

Bekdemir et al. performed multi-zone modeling of natural gas/diesel RCCI combustion and focused on deriving real-time, map-based models that can be used for RCCI control system development (Bekdemir et al. 2015). The multi-zone model was used to extract trends of control-relevant quantities, such as CA10, CA50, peak cylinder pressure, peak pressure rise rate, and NO<sub>x</sub> emissions, as functions of the start of injection, fuel blend ratio, and engine speed. Overall, the model was able to capture the right trends as functions of the control variables, which can be used for future control system development. However, the model showed sensitivity to the initial temperature of the mixture, which can be addressed by investigating cylinder-to-cylinder and cycle-to-cycle variations.

Advanced and dual-fuel combustion concepts using natural gas have shown great potential for efficiency gains and emissions reduction, but are also susceptible to abnormal combustion phenomena such as knock and Low-Speed Pre-Ignition (LSPI). LSPI has typically been associated with downsized, boosted SI engines, but Zaccardi et al. discussed the occurrence of LSPI in diesel–methane CI engines (Zaccardi and Serrano 2014). The LSPI occurrence in dual-fuel engines has been linked to the diesel pilot start of injection, which can vary and thus affect the temperature of exhaust gases and in-cylinder trapped burned gases. However, the causes of LSPI in CI engines can be multiple and complex to identify. The combustion process of CI dual-fuel engines is radically different than SI engines in terms of mixture preparation and ignition, thus the mechanisms causing LSPI in SI engines (overheated spark plugs, liquid fuel films, and fuel–oil interactions) may not necessarily apply to CI engines. The sources of LSPI in CI diesel–methane engines have been mainly associated with local spontaneous gas phase autoignition, originating from hot residual gases and temperature heterogeneity in the combustion chamber (Zaccardi and Serrano 2014).

Kirsten et al. presented a study on advanced knock detection in diesel/natural gas engines and introduced a novel methodology using the in-cylinder pressure and the knock sensor data (Kirsten et al. 2016). Their methodology accounted for variation in multiple parameters such as diesel rail pressure, start of injection, amount of fuel injected, equivalence ratio, intake air temperature, methane number, compression ratio, and load. Based on these parameters, they developed an algorithm that can distinguish between individual knocking and normal cycles, while considering the premixed and diffusion phases of CI combustion.

## 2.2 Summary and Future Outlook

The experimental and modeling studies discussed in this chapter have shown that natural gas can be used as a fuel for low-temperature combustion engine concepts such as HCCI and RCCI. Specifically, the lower reactivity of natural gas compared to gasoline makes it suitable for dual-fuel advanced combustion concepts, in which the natural gas is paired with a high reactivity fuel such as diesel or biodiesel. In these applications, natural gas can be used to create a background fuel–air mixture

for lean, low-temperature combustion with high thermal efficiency and low soot,  $\text{NO}_x$ , UHC, and CO formation. These characteristics can enable advanced natural gas and dual-fuel engines to provide solutions for future transportation and power generation systems. The low reactivity of natural gas makes the implementation of single-fuel HCCI engines challenging; however, dual-fuel diesel/natural gas engines are already used in stationary power generation and locomotive applications and have strong potential to be used in heavy-duty on-highway and off-highway applications.

The main challenge of advanced natural gas combustion is associated with unburned fuel (or natural gas slip), which is manifested as methane emissions in the exhaust and needs to be treated in low-temperature aftertreatment systems. Another challenge is the identification and prevention of abnormal combustion phenomena such as knock and LSPI, which are different in nature than those observed in SI engines. Despite these challenges, advanced natural gas engines have strong potential for use in transportation and power generation in the future. Making advanced natural gas engines widely commercially available will result in direct reduction of  $\text{CO}_2$  emissions, as well as reduced dependence on liquid petroleum fuels.

## References

- Aceves SM, Smith JR, Westbrook CK, Pitz WJ (1999) Compression ratio effect on methane HCCI combustion. *J Eng Gas Turbines Power* 121(3):569–574
- Ansari E, Poorghasemi K, Irdmousa BK, Shahbakhti M, Naber J (2016) Efficiency and emissions mapping of a light duty diesel-natural gas engine operating in conventional diesel and RCCI modes. SAE Technical Paper No. 2016-01-2309
- Babajimopoulos A, Challa VP, Lavoie GA, Assanis DN (2009) Model-based assessment of two variable cam timing strategies for HCCI engines: recompression vs. rebreathing. In: ASME 2009 Internal combustion engine division spring technical conference. American Society of Mechanical Engineers, pp 597–610
- Bekdemir C, Baert R, Willems F, Somers B (2015) Towards control-oriented modeling of natural gas-diesel RCCI combustion. SAE Technical Paper No. 2015-01-1745
- Boldaji MR, Sofianopoulos A, Mamalis S, Lawler B (2017) CFD simulations of the effect of water injection characteristics on TSCI: a new, load-flexible, advanced combustion concept. In: ASME 2017 internal combustion engine division fall technical conference. American Society of Mechanical Engineers, pp V001T03A019–V001T03A019
- Boldaji MR, Sofianopoulos A, Mamalis S, Lawler B (2018) Computational fluid dynamics investigations of the effect of water injection timing on thermal stratification and heat release in thermally stratified compression ignition combustion. *Int J Engine Res* 1468087418767451
- Chang K, Lavoie GA, Babajimopoulos A, Filipi Z, Assanis DN (2007) Control of a multi-cylinder HCCI engine during transient operation by modulating residual gas fraction to compensate for wall temperature effects. SAE Technical Paper No. 2007-01-0204
- Christensen M, Johansson B (2000) Supercharged homogeneous charge compression ignition (HCCI) with exhaust gas recirculation and pilot fuel. SAE Technical Paper No. 2000-01-1835
- Christensen M, Johansson B, Einewall P (1997) Homogeneous charge compression ignition (HCCI) using isoctane, ethanol and natural gas—a comparison with spark ignition operation. SAE Technical Paper No. 972874

- Dahodwala M, Joshi S, Koehler EW, Franke M (2014) Investigation of diesel and CNG combustion in a dual fuel regime and as an enabler to achieve RCCI combustion. SAE Technical Paper No. 2014-01-1308
- Dahodwala M, Joshi S, Koehler E, Franke M, Tomazic D (2015) Experimental and computational analysis of diesel-natural gas RCCI combustion in heavy-duty engines. SAE Technical Paper No. 2015-01-0849
- Dec JE, Yang Y, Dronniou N (2011) Boosted HCCI-controlling pressure-rise rates for performance improvements using partial fuel stratification with conventional gasoline (No. SAND2011-0200C). Sandia National Laboratories (SNL-CA), Livermore, CA (United States)
- Dec JE, Yang Y, Dermotte J, Ji C (2015) Effects of gasoline reactivity and ethanol content on boosted, premixed and partially stratified low-temperature gasoline combustion (LTGC). SAE Int J Engines 8(3):935–955
- Djermouni M, Ouadha A (2014) Thermodynamic analysis of an HCCI engine based system running on natural gas. Energy Convers Manag 88:723–731
- Doosje E, Willems F, Baert R (2014) Experimental demonstration of RCCI in heavy-duty engines using diesel and natural gas. SAE Technical Paper No. 2014-01-1318
- Epping K, Aceves S, Bechtold R, Dec JE (2002) The potential of HCCI combustion for high efficiency and low emissions. SAE Technical Paper No. 2002-01-1923
- Fathi M, Saray RK, Checkel MD (2011) The influence of exhaust gas recirculation (EGR) on combustion and emissions of n-heptane/natural gas fueled Homogeneous Charge Compression Ignition (HCCI) engines. Appl Energy 88(12):4719–4724
- Fiveland SB, Agama R, Christensen M, Johansson B, Hiltner J, Maus F, Assanis DN (2001) Experimental and simulated results detailing the sensitivity of natural gas HCCI engines to fuel composition. SAE Technical Paper No. 2001-01-3609
- Flowers D, Aceves S, Westbrook CK, Smith JR, Dibble R (2001) Detailed chemical kinetic simulation of natural gas HCCI combustion: gas composition effects and investigation of control strategies. J Eng Gas Turbines Power 123(2):433–439
- Gharehghani A, Hosseini R, Mirsalim M, Jazayeri SA, Yusaf T (2015) An experimental study on reactivity controlled compression ignition engine fueled with biodiesel/natural gas. Energy 89:558–567
- Hanson R, Kokjohn S, Splitter D, Reitz RD (2011) Fuel effects on reactivity controlled compression ignition (RCCI) combustion at low load. SAE Int J Engines 4:394–411
- Hanson R, Curran S, Wagner R, Kokjohn S, Splitter D, Reitz RD (2012) Piston bowl optimization for RCCI combustion in a light-duty multi-cylinder engine. SAE Int J Engines 5 (2012-01-0380):286–299
- Haraldsson G, Tunestål P, Johansson B, Hyvönen J (2002) HCCI combustion phasing in a multi cylinder engine using variable compression ratio. SAE Technical Paper No. 2002-01-2858
- Haraldsson G, Tunestål P, Johansson B, Hyvönen J (2003) HCCI combustion phasing with closed-loop combustion control using variable compression ratio in a multi cylinder engine. SAE Technical Paper No. 2003-01-1830
- Haraldsson G, Tunestål P, Johansson B, Hyvönen J (2004) HCCI closed-loop combustion control using fast thermal management. SAE Technical Paper No. 2004-01-0943
- Hockett A, Hampson G, Marchese AJ (2016) Development and validation of a reduced chemical kinetic mechanism for computational fluid dynamics simulations of natural gas/diesel dual-fuel engines. Energy Fuels 30(3):2414–2427
- Hyvönen J, Haraldsson G, Johansson B (2003) Supercharging HCCI to extend the operating range in a multi-cylinder VCR-HCCI engine. SAE Technical Paper No. 2003-01-3214
- Jia Z, Denbratt I (2015) Experimental investigation of natural gas-diesel dual-fuel RCCI in a heavy-duty engine. SAE Int J Engines 8(2015-01-0838):797–807
- Judith J, Neher D, Kettner M, Klaisle M, Kozarac D (2017) Numerical investigations of the auto-ignition ranges of a natural gas fueled HCCI engine. SAE Technical Paper No. 2017-32-0073



- Kakaee AH, Rahnama P, Paykani A (2015) Influence of fuel composition on combustion and emissions characteristics of natural gas/diesel RCCI engine. *J Nat Gas Sci Eng* 25:58–65
- Kakaee AH, Nasiri-Toosi A, Partovi B, Paykani A (2016) Effects of piston bowl geometry on combustion and emissions characteristics of a natural gas/diesel RCCI engine. *Appl Therm Eng* 102:1462–1472
- Kavuri C, Paz J, Kokjohn SL (2016) A comparison of reactivity controlled compression ignition (RCCI) and gasoline compression ignition (GCI) strategies at high load, low speed conditions. *Energy Convers Manag* 127:324–341
- Kirsten M, Pirker G, Redtenbacher C, Wimmer A et al (2016) Advanced knock detection for diesel/natural gas engine operation. *SAE Int J Engines* 9(3):1571–1583. <https://doi.org/10.4271/2016-01-0785>
- Klos D, Janeczek D, Kokjohn S (2015) Investigation of the combustion instability- $\text{NO}_x$  tradeoff in a dual fuel reactivity controlled compression ignition (RCCI) engine. *SAE Int J Engines* 8 (2015-01-0841):821–830
- Kobayashi K, Sako T, Sakaguchi Y, Morimoto S, Kanematsu S, Suzuki K et al (2011) Development of HCCI natural gas engines. *J Nat Gas Sci Eng* 3(5):651–656
- Kokjohn SL, Reitz RD (2013) Reactivity controlled compression ignition and conventional diesel combustion: a comparison of methods to meet light-duty  $\text{NO}_x$  and fuel economy targets. *Int J Engine Res* 14(5):452–468
- Kokjohn SL, Hanson RM, Splitter DA, Reitz RD (2011a) Fuel reactivity controlled compression ignition (RCCI): a pathway to controlled high-efficiency clean combustion. *Int J Engine Res* 12 (3):209–226
- Kokjohn S, Hanson R, Splitter D, Kaddatz J, Reitz RD (2011b) Fuel reactivity controlled compression ignition (RCCI) combustion in light-and heavy-duty engines. *SAE Int J Engines* 4 (2011-01-0357):360–374
- Kong SC (2007) A study of natural gas/DME combustion in HCCI engines using CFD with detailed chemical kinetics. *Fuel* 86(10–11):1483–1489
- Lawler B, Splitter D, Szybist J, Kaul B (2017) Thermally stratified compression ignition: a new advanced low temperature combustion mode with load flexibility. *Appl Energy* 189:122–132
- Lim JH, Walker NR, Kokjohn S, Reitz RD (2014) High speed dual-fuel RCCI combustion for high power output. *SAE Technical Paper No.* 2014-01-1320
- Mamalis S, Babajimopoulos A, Guralp O, Najt P (2012) Optimal use of boosting configurations and valve strategies for high load HCCI-A modeling study. *SAE Technical Paper No.* 2012-01-1101
- Najt PM, Foster DE (1983) Compression-ignited homogeneous charge combustion. *SAE Technical Paper No.* 830264
- Nieman DE, Dempsey AB, Reitz RD (2012) Heavy-duty RCCI operation using natural gas and diesel. *SAE Int J Engines* 5(2012-01-0379):270–285
- Olesky LM, Vavra J, Assanis D, Babajimopoulos A (2012) Effects of charge preheating methods on the combustion phasing limitations of an HCCI engine with negative valve overlap. *J Eng Gas Turbines Power* 134(11):112801
- Olsson JO, Tunestål P, Johansson B (2001) Closed-loop control of an HCCI engine. *SAE Technical Paper No.* 2001-01-1031
- Olsson JO, Tunestål P, Johansson B, Fiveland S, Agama R, Willi M, Assanis DN (2002) Compression ratio influence on maximum load of a natural gas fueled HCCI engine. *SAE Technical Paper No.* 2002-01-0111
- Papagiannakis RG, Hountalas DT (2004) Combustion and exhaust emission characteristics of a dual fuel compression ignition engine operated with pilot diesel fuel and natural gas. *Energy Convers Manag* 45(18–19):2971–2987
- Paykani A, Kakaee AH, Rahnama P, Reitz RD (2015) Effects of diesel injection strategy on natural gas/diesel reactivity controlled compression ignition combustion. *Energy* 90:814–826
- Poorghasemi K, Saray RK, Ansari E, Irdmousa BK, Shahbakhti M, Naber JD (2017) Effect of diesel injection strategies on natural gas/diesel RCCI combustion characteristics in a light duty diesel engine. *Appl Energy* 199:430–446

- Rahnama P, Paykani A, Reitz RD (2017) A numerical study of the effects of using hydrogen, reformer gas and nitrogen on combustion, emissions and load limits of a heavy duty natural gas/diesel RCCI engine. *Appl Energy* 193:182–198
- Silke EJ, Pitz WJ, Westbrook CK, Sjöberg M, Dec JE (2009) Understanding the chemical effects of increased boost pressure under HCCI conditions. *SAE Int J Fuels Lubricants* 1(1):12–25
- Sjöberg M, Dec JE (2004) An investigation of the relationship between measured intake temperature, BDC temperature, and combustion phasing for premixed and DI HCCI engines. SAE Technical Paper No. 2004-01-1900
- Sjöberg M, Dec JE (2005) Effects of engine speed, fueling rate, and combustion phasing on the thermal stratification required to limit HCCI knocking intensity. SAE Technical Paper No. 2005-01-2125
- Sjöberg M, Dec JE (2006) Smoothing HCCI heat-release rates using partial fuel stratification with two-stage ignition fuels. SAE Technical Paper No. 2006-01-0629
- Sjöberg M, Dec JE (2007) EGR and intake boost for managing HCCI low-temperature heat release over wide ranges of engine speed. SAE Technical Paper No. 2007-01-0051
- Sjöberg M, Dec JE, Babajimopoulos A, Assanis DN (2004) Comparing enhanced natural thermal stratification against retarded combustion phasing for smoothing of HCCI heat-release rates. SAE Technical Paper No. 2004-01-2994
- Sofianopoulos A, Zhou Y, Lawler B, Mamalis S (2017) Gas exchange processes of a small HCCI free piston engine—a computational study. *Appl Therm Eng* 127:1582–1597
- Soylu S (2005) Examination of combustion characteristics and phasing strategies of a natural gas HCCI engine. *Energy Convers Manag* 46(1):101–119
- Splitter, D et al (2011) Reactivity controlled compression ignition (RCCI) heavy-duty engine operation at mid- and high-loads with conventional and alternative fuels. SAE Technical Paper No. 2011-01-0363
- Splitter D, Hanson R, Kokjohn S, Wissink M, Reitz RD (2011) Injection effects in low load RCCI dual-fuel combustion. SAE Technical Paper No. 2011-24-0047
- Stanglmaier RH, Ryan TW, Souder JS (2001) HCCI operation of a dual-fuel natural gas engine for improved fuel efficiency and ultra-low NO<sub>x</sub> emissions at low to moderate engine loads. SAE Technical Paper No. 2001-01-1897
- Yang Y, Dec JE, Dronniou N, Sjöberg M (2011a) Tailoring HCCI heat-release rates with partial fuel stratification: Comparison of two-stage and single-stage-ignition fuels. *Proc Combust Inst* 33(2):3047–3055
- Yang Y, Dec JE, Dronniou N, Sjöberg M, Cannella W (2011b) Partial fuel stratification to control HCCI heat release rates: fuel composition and other factors affecting pre-ignition reactions of two-stage ignition fuels. *SAE Int J Engines* 4(2011-01-1359):1903–1920
- Yang Y, Dec JE, Dronniou N, Cannella W (2012) Boosted HCCI combustion using low-octane gasoline with fully premixed and partially stratified charges. *SAE Int J Engines* 5 (2012-01-1120):1075–1088
- Yap D, Megaritis A, Peucheret S, Wyszynski ML, Xu H (2004). Effect of hydrogen addition on natural gas HCCI combustion. SAE Technical Paper No. 2004-01-1972
- Yap D, Peucheret SM, Megaritis A, Wyszynski ML, Xu H (2006) Natural gas HCCI engine operation with exhaust gas fuel reforming. *Int J Hydrogen Energy* 31(5):587–595
- Zaccardi J, Serrano D (2014) A comparative low speed pre-ignition (LSPI) study in downsized SI gasoline and CI diesel-methane dual fuel engines. *SAE Int J Engines* 7(4):1931–1944. <https://doi.org/10.4271/2014-01-2688>
- Zhao F, Asmus TN, Assanis DN, Dec JE, Eng JA, Najt PM (2003) Homogeneous charge compression ignition (HCCI) engines. SAE Technical Paper No. PT-94
- Zoldak P, Sobiesiak A, Bergin M, Wickman DD (2014) Computational study of reactivity controlled compression ignition (RCCI) combustion in a heavy-duty diesel engine using natural gas. SAE Technical Paper No. 2014-01-1321

# Chapter 3

## The Ultra-Lean Partially Stratified Charge Approach to Reducing Emissions in Natural Gas Spark-Ignited Engines



L. Bartolucci, E. C. Chan, S. Cordiner, R. L. Evans and V. Mulone

**Abstract** Lean-burn natural gas engines can be used to reduce exhaust emissions significantly. However, as the mixture is leaned out, the occurrence of extinction and incomplete combustion increases, resulting in poor performance and stability, as well as elevated levels of unburned hydrocarbon (UHC) and nitrogen oxides ( $\text{NO}_x$ ) emissions. The partially stratified charge (PSC) method can be used to mitigate these issues, while extending the lean misfire limit (LML) beyond its equivalent, homogeneous level. In this chapter, the PSC ignition and combustion processes are examined following a comprehensive experimental and numerical approach. Experiments are conducted in an idealized PSC configuration, using a constant volume combustion chamber (CVCC), to identify the principle enabling mechanisms of the PSC methodology. Engine tests conducted in a single-cylinder research engine (SCRE) demonstrate the feasibility of various PSC implementations in improving performance and emission characteristics in real-world settings. Complementary numerical analyses for the CVCC are obtained through large eddy simulations (LES), while Reynolds-averaged Navier–Stokes (RANS) simulations are conducted for SCRE with reduced chemical kinetics. The corresponding simulated results provide additional insights in characterizing the effect of fuel stratification on flame kernel maturation and flame propagation, the interplay between chemistry and turbulence at different overall air–fuel ratios, as well as formation of major pollutant species.

---

L. Bartolucci (✉) · S. Cordiner · V. Mulone  
Department of Industrial Engineering, University of Rome “Tor Vergata”, Rome, Italy  
e-mail: [l.bartolucci@ing.uniroma2.it](mailto:l.bartolucci@ing.uniroma2.it)

E. C. Chan (✉)  
Institute for Advanced Sustainability Studies, Potsdam, Germany  
e-mail: [Edward.Chan@iass-potsdam.de](mailto:Edward.Chan@iass-potsdam.de)

R. L. Evans  
Department of Mechanical Engineering, The University of British Columbia,  
Vancouver, BC, Canada

**Keywords** Natural gas combustion · Spark ignition (SI) engine  
Lean combustion · Stratified charge · High efficiency · Low emissions

### Roman Symbols

$D_o$	Injector nozzle diameter (mm)
$E$	Energy (kJ)
$f$	Arbitrary function
$H$	Energy content of air–fuel mixture (kJ)
$k$	Turbulent kinetic energy ( $\text{m}^2/\text{s}^2$ )
$K_e$	Jet entrainment constant (–)
$L_e$	Turbulent integral length scale (mm)
$m_e$	Entrained jet mass (mg)
$m_{\text{fuel}}$	Mass of fuel (in air–fuel mixture) (mg)
$m_o$	Injected jet mass (mg)
$p$	Pressure (bar)
$p$	Power in $L^p$ combination (–)
$S_L$	Laminar flame speed (m/s)
$t$	Time (s)
$t_0$	Time at start of injection (s)
$T$	Temperature (K)
$u'$	Turbulent velocity fluctuation (m/s)
$U_o$	Jet velocity at nozzle (m/s)
$V$	Volume (cc)
$z$	Jet penetration distance (mm)
$Z$	Normalized energy release (–)

### Greek Symbols

$\gamma$	Ratio of specific heats (–)
$\Gamma$	Jet penetration constant (–)
$\delta_L$	Laminar flame brush thickness (m)
$\varepsilon$	Dissipation rate of turbulent kinetic energy ( $\text{m}^2/\text{s}^3$ )
$\phi$	Fuel–air ratio relative to stoichiometric level (–)
$\lambda$	Air–fuel ratio relative to stoichiometric level (–)
$\mu$	Mean value of an observable
$\mu_j$	Mixing ratio between entrained and injected mass (–)
$\rho_\infty$	Density of ambient gas ( $\text{kg}/\text{m}^3$ )
$\rho_0$	Density of injected gas ( $\text{kg}/\text{m}^3$ )
$\rho_b$	Density of burned gas ( $\text{kg}/\text{m}^3$ )
$\rho_u$	Density of unburned gas ( $\text{kg}/\text{m}^3$ )
$\sigma$	Standard deviation of an observable
$\tau$	Normalized time (–)

**Acronyms and Abbreviations**

abs	Absolute (pressure level)
AMR	Adaptive mesh refinement
AS	After spark onset
ASOI	After start of injection (ms)
BFSC	Brake-specific fuel consumption (g/kWh)
BMEP	Brake-specific mean effective pressure (bar)
B/ATDC	Before/after top dead center
CAD	Crank angle degree (°)
CFD	Computational fluid dynamics
(C)NG	(Compressed) natural gas
CoV	Coefficient of variation (%)
CVCC	Constant volume combustion chamber
DNS	Direct numerical simulation
HR(R)	Heat release (Rate) (kJ (/s))
I/EVC	Intake/exhaust valve closed
I/EVO	Intake/exhaust valve open
IMEP	Indicated mean effective pressure (bar)
LES	Large eddy simulation
LML	Lean misfire limit (–)
LPG	Liquefied petroleum gas
MBT	Mean best torque
MFB	Mass fraction burned (%)
NO <sub>x</sub>	Nitrogen oxides (i.e., NO + NO <sub>2</sub> )
PaSR	Partially stirred reactor
PM	Particulate matter
PSC	Partially stratified charge
RANS	Reynolds-averaged Navier–Stokes
RNG	Renormalization group
RPM	Revolutions per minute
S/EOI	Start/end of injection (ms)
SCRE	Single-cylinder research engine
T/BDC	Top/bottom dead center
TCI	Turbulence chemistry interaction
TKE	Turbulent kinetic energy (m <sup>2</sup> /s <sup>2</sup> )
(U)HC	(Unburned) hydrocarbon
WOT	Wide-open throttle

### 3.1 Introduction

Natural gas (NG; CNG for the compressed variety) is a viable alternative to conventional fossil fuels. Passenger vehicles fueled with CNG produce over 25% less carbon dioxide ( $\text{CO}_2$ ) per driven kilometer than its gasoline counterpart (Helmers 2009; Prieur and Tilagone 2007). For heavy-duty applications, CNG engines are shown have significant reductions in specific emissions for regulated and non-regulated pollutants compared to their diesel equivalents. Particularly for nitrogen oxides ( $\text{NO}_x$ ), the emission level can be decreased from 2.79 g/kWh for Diesel to 0.992 g/kWh for CNG. Similar improvements can also be seen for particulate matters (PM), which can be reduced from 79.5 mg/kWh (Diesel) to 1.53 mg/kWh (CNG) (Ntziachristos and Samaras 2016). The introduction of lean-burn strategies in natural gas combustion processes further minimizes  $\text{CO}_2$  and other emissions, while extending operating range with limited power losses through throttling.

The main challenge, however, pertains to stabilizing CNG combustion processes beyond its lean misfire limit (LML). Promoting turbulent mixing, for instance, through modifying piston bowl topology, may partially address the issue (Evans and Blaszczyk 1998). A more common approach, however, involves facilitating a rich fuel region and igniting the mixture in its vicinity. This allows a more sustainable flame kernel development, as the excess energy release from the richer mixture provides support to the flame propagating into the leaner, unburned mixture. Normally, fuel stratification is achieved by staging the ignition in a small segregated region, known as the prechamber, connected to the combustion chamber (Esfahanian et al. 2017; Shah et al. 2015). This has been shown to stabilize lean natural gas combustion substantially, through turbulence production (Arcoumanis et al. 1997) from the resulting flame jet and the availability of reactive radicals (Chung et al. 2003) in the combustion chamber. Alternatively, fuel stratification can also take place in the absence of the prechamber. In the partially stratified charge (PSC) ignition strategy (Evans 2000), a small amount of fuel is injected near the ignition zone in the combustion chamber. Thus, stabilization of flame kernel growth and subsequent flame propagation can be achieved with a higher level of fuel stratification. A number of studies (Chicka 2012; Logan 2011; Reynolds and Evans 2004) have demonstrated the feasibility of the PSC methodology, in various implementations, on extending the lean operating range without throttling under engine conditions.

This chapter details a comprehensive experimental and numerical approach on the fundamentals and application of PSC, beginning with an overview on engine combustion stability and its stochastic treatment. This is followed by a discussion of the principal enabling mechanisms of the PSC technology, or more generally, spark ignition in a spatially stratified environment, as well as the aero- and thermodynamic interactions between the stratified fuel injection and the ambient environment. An idealized PSC arrangement is then examined experimentally in a constant volume combustion chamber (CVCC), where accompanying results obtained through large eddy simulations (LES) provide additional insights in terms of mixture formation mechanisms and flame front development. The experimental and

numerical analyses will be further applied to an engine environment, in which the PSC system is deployed to a single-cylinder research engine (SCRE), along with results from various PSC implementations.

### 3.2 Lean Misfire Limit

Misfire is a phenomenon occurring in spark-ignited engines where the combustion process is prematurely terminated, either due to extinction before the end of the combustion cycle or when the combustion process is still ongoing when the charge is evacuated into the exhaust stream. Misfires have a negative impact on engine power output and produce additional unburned hydrocarbon (UHC) and nitrogen oxides ( $\text{NO}_x$ ). In engine conditions, it is often instructive to define a misfire limit as a statistical diagnostic indicator, where the occurrences of misfire over a representative number of engine cycles are deemed significant. A common definition for the misfire limit is based on the coefficient of variation (CoV) of engine performance indicators such as indicated mean effective pressure (IMEP), as shown in Eq. (3.1):

$$\text{CoV}_{\text{IMEP}} = \left( \frac{\sigma}{\mu} \right)_{\text{IMEP}} \quad (3.1)$$

where  $\mu$  and  $\sigma$  are the mean and standard deviation, respectively, for an observable parameter, in this case the IMEP. A generally accepted criterion for misfire consists of a threshold, usually set to 10% (Heywood 1989) or 5% (Reynolds and Evans 2004) of the CoV, sometimes thresholds as low as 2% (Daniels and Scilzo 1996) can also be used.

Under identical engine configuration and operating conditions, the CoV is likely to be higher while running on leaner air–fuel mixtures than in near stoichiometric mixtures. The available heat released from the combustion process and the associated reaction rate decrease in leaner mixtures, leading to a reduction in flammability and flame front stability (Ahmed and Mastorakos 2006; Ahmed et al. 2007). The maximum air–fuel ratio above which the misfire limit is exceeded is known as the lean misfire limit, or LML. Figure 3.1 shows a typical CoV on the IMEP over a range of relative air–fuel ratios ( $\lambda$ ) for a natural gas spark-ignited engine, where the LML determined to be  $\lambda = 1.58$  for the 10% CoV criterion, and 1.55 for the 5% criterion. It can be seen from Fig. 3.1 that the transition from stable to unstable combustion is rapid and distinct as the relative air–fuel ratio increases. Therefore, the onset of misfire can be determined by using an  $L^p$  combination of the asymptotic parameterization for the pre- and post-misfire behaviors of the CoV (Churchill and Usagi 1972):

$$\text{CoV}(\lambda) = [f_0^p(\lambda) + f_1^p(\lambda)]^{\frac{1}{p}}, \quad (3.2)$$

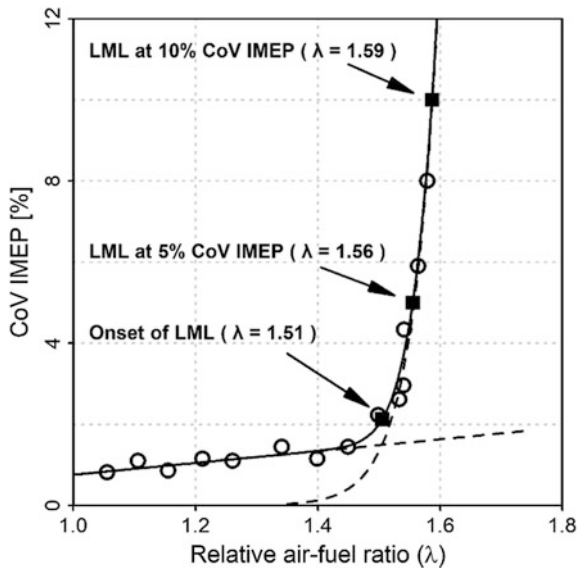


**Fig. 3.1** Determining the LML of an exemplary spark-ignited natural gas engine using CoV IMEP. The onset for misfire, as well as the 5 and 10% LML criterion, has been identified. Key: ○: Test bench measurements, ■: identified misfire limits, - -: asymptotic pre- and post-misfire parameterizations, —:  $L^p$  combination of parameterized asymptotes

where  $f_0(\lambda)$  and  $f_1(\lambda)$  are the parameterized functions for the pre- and post-misfire regions, respectively, and  $p$  is an arbitrary blending coefficient, and it is equal to two in this case. The value of  $\lambda$  at the intersection between  $f_0(\lambda)$  and  $f_1(\lambda)$  can be interpreted as the onset of misfire, and the CoV can be determined evaluating Eq. (3.2) at the corresponding  $\lambda$  value. Using this method, the onset is found to be located at  $\lambda = 1.51$ , with a corresponding CoV of 2.12%. This is also close to the 2% misfire criterion used in reference (Daniels and Scilzo 1996).

A more comprehensive approach, however, involves inspecting the distribution of IMEP and timing of cylinder peak pressure, as shown in Fig. 3.2, where the data of a spark-ignited, homogeneous charge natural gas engine operating at 2000 RPM at different air–fuel ratios (Reynolds and Evans 2004) are presented. The corresponding values for CoV on IMEP are 0.9% for  $\lambda = 1$  and 21.6% for  $\lambda = 1.54$ . The individual misfired engine cycles from the sample can be identified using statistical classification techniques such as  $k$ -means clustering (Lloyd 1982). The number of misfired cycles for  $\lambda = 1.54$  is determined to be 24% of all cycles, while the associated CoV on IMEP is 21.6%, well beyond the standard criteria for misfires (i.e., 5% and 10% CoV). In addition, these misfired cycles correspond to two modes. First are misfires due to ignition failure, characterized by a near-zero IMEP. This implies inability for the flame kernel to reach maturity and propagate into the bulk mixture. The second mode is partial combustion due to a slow burn rate, as suggested by low-to-moderate IMEP values for the corresponding combustion cycles.



### 3.3 Strategies for Combustion Stabilization

Based on the observations from Fig. 3.2, stabilizing combustion in lean-burn conditions requires a combination of mitigating strategies aimed at reducing the two modes of misfires. First and more obvious, thermal support must be provided to foster flame kernel maturation to prevent ignition failure. Furthermore, additional measures should be in place to promote penetration of the flame front into the bulk mixture once the flame kernel reaches maturity. These theoretical considerations will be discussed below.

#### 3.3.1 Stabilizing Flame Kernel Maturation

During the initial stages of spark ignition, the electric spark produces a high-temperature plasma at the ignition zone and forms an expanding flame front, initiating the combustion process. This developing flame front is known as the flame kernel. As it expands, the growth rate of the flame kernel is sensitive to the local flow and mixture composition in its vicinity (Abdel-Gayed and Bradley 1985; Johansson et al. 1995). Thus, the term *flame kernel maturity* (Eichengerber and Roberts 1999) is used to describe this phase of combustion process. The maturity of the flame kernel can be rudimentarily inferred from the pressure history of the combustion event, defined by an arbitrary but reasonable level of initial mass fraction burned (MFB) (Aleiferis et al. 2003; Kalghatgi 1985). Typically, this corresponds to the first 5 to 10% of MFB.

Alternatively, flame kernel maturity can be conceptualized to be bounded by the Kolmogorov and integral length scales (Herweg and Maly 1992), which supports the

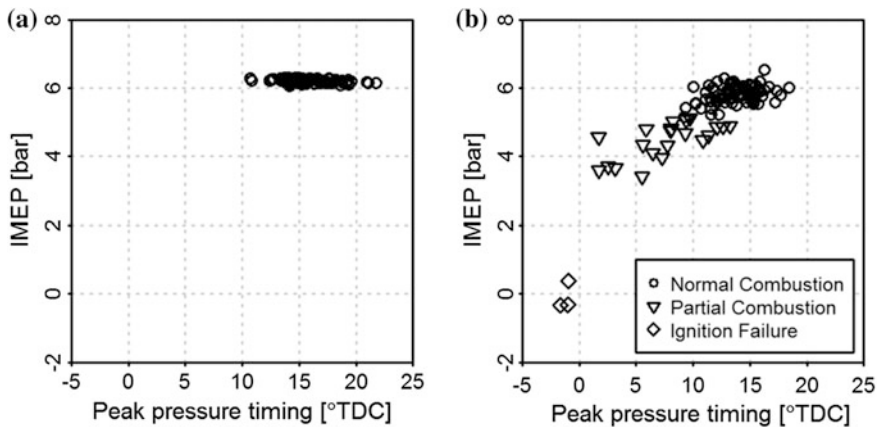


**Fig. 3.2** Distribution of IMEP and peak pressure crank angle of 100 consecutive engine cycles for a homogeneous charge, spark-ignited natural gas engine operating at 2000 RPM with **a**  $\lambda = 1.00$  at half throttle and **b**  $\lambda = 1.61$  at full throttle. The coefficients of variation on the IMEP are 0.90 and 21.6% respectively. Adopted from (Reynolds and Evans 2004)

notion that a matured flame kernel further expands at a fully-developed turbulent flame speed (Bradley et al. 1994; Tan and Reitz 2006). Therefore, the flame kernel is considered to have reached maturity when it is sufficiently large to be advected to the remaining mixture in a self-sustained manner (Chen and Ju 2007; Deshaies and Joulin 1984). This critical size can be based on a characteristic length scale (Herweg and Maly 1992; Tan and Reitz 2006) or volume (Andreassi et al. 2003; Kuo and Reitz 1992). In the presence of turbulence, this critical scale can be derived from the integral length scale (Fan and Reitz 2000; Song and Sunwoo 2000).

The initial spherical flame kernel undergoes deformation, known as wrinkling, in the turbulent flow field (Eichengerber and Roberts 1999), and the likelihood of extinction increases as the flame kernel grows and becomes progressively sensitive to turbulent vortices at the lower frequency spectrum (Jenkins et al. 2006). Further, since the kernel expansion speed depends in part on the laminar flame speed, turbulence is more likely to hinder flame kernel development in lean-burn than in stoichiometric conditions (Ho and Santavicca 1987). Based on studies on ignition limits in homogeneous charge under turbulence (Abdel-Gayed and Bradley 1985; Herweg and Maly 1992), a criterion for stable flame kernel maturation for natural gas/air mixtures is derived (Chan et al. 2011):

$$\left(\frac{\delta_L}{15L_e}\right)^{\frac{1}{2}}\left(\frac{u'}{S_L}\right)^{\frac{3}{2}} < 1, \quad (3.3)$$

where  $\delta_L$  is the laminar thickness of the kernel flame front,  $L_e$  is the local integral length scale,  $u'$  is the local mean turbulent fluctuation, and  $S_L$  is the local laminar flame speed. The time for a flame kernel to reach maturity asymptotically increases as the criterion set forth in Eq. (3.3) approaches unity, indicating that wrinkling is too severe to sustain flame kernel growth (Chan et al. 2011).

Traditionally, this has been remedied through the use of stratified charge ignition methods, that is, the flame is initiated at a location of favorable fuel concentration and propagated over an adverse concentration gradient. A number fundamental studies involving spark ignition in stratified environments (Kang and Kyritsis 2005; Pires da Cruz et al. 2000; Richardson et al. 2010) indicated that the heat released from the richer mixture upstream provides enhancement, termed back support, to the advancing flame front, which results in a higher effective flame speed than the mixture at its equivalent, homogeneous concentration. This enhancement is particularly effective in stratified methane–air flames than heavier hydrocarbon such as propane and n-heptane (Pires da Cruz et al. 2000; Shi et al. 2017). This is due to a local increase in production of H and OH radicals, as well as intermediate hydrocarbon species such as  $\text{CH}_2\text{O}$ , resulting from the high ratio of hydrogen-to-carbon atoms, thus providing additional reaction pathways. Consequently, the combination of these mechanisms also extends the lean flammability limit of the air–fuel mixture in a stratified environment. For laminar methane–air flames, an extension of the lean limit to  $\lambda = 2.85$  can be observed (Kang and Kyritsis 2005), while for the turbulent natural gas flame jets, an extension from  $\lambda = 1.6$  to beyond  $\lambda = 2.0$  is achieved (Chan 2010).

### 3.3.2 Stratified Air–Fuel Mixture Formation

While typical spark-ignited engines operate in homogeneous mixtures, spatial and temporal variations of fuel concentration can be introduced directly to the engine cylinder under stratified operation. In particular, for the PSC operation, pilot fuel is injected in the vicinity of the ignition zone, producing a fuel-rich region along the trajectory of the injection. In addition to providing thermal back support, as previously discussed, the injection also results in flame stretch and wrinkling, which could further affect combustion quality.

Gaseous fuel injection is a transient, compressible, and turbulent phenomenon, where the injected fuel mass has a different composition than the ambient mixture. For ease of understanding the physical processes of mixture formation, the fuel injection could be conceptualized as a spheroidal “vortex ball” containing both the injected fuel and entrained ambient gas, trailed by a conical jet (Turner 1963), such as that illustrated in Fig. 3.3. The evolution of the injection can be summarily described by its penetration length, its maximum extent from the center of the injection nozzle. The entrainment of the fuel jet can be effectively regarded as the mixing ratio between the injected fuel mass and the mass of entrained ambient gas. At the early stages of the injection process, the injected fuel mass is greater than the entrained mass, and the mixing of the injected fuel with ambient gas takes place at the tip of the injection (Cossali et al. 2001), which forms a vortex ring. As the injection proceeds, the entrained mass begins to dominate the jet composition, and the entrainment mechanism shifts from the mixing at the tip vortex to shear interaction in the trailing jet. Toward this limit, the jet also exhibits self-similar behavior. In an axisymmetric geometry, this self-similarity phase takes place from 10 to 20 nozzle diameters downstream of the jet nozzle, as observed by the empirical studies (Hill 1972; Ouellette and Hill 2001; Witze 1980).

Universal profiles can be derived to describe its mean radial velocity and concentration profiles at any point of time along the central axis (Hussein et al. 1994;

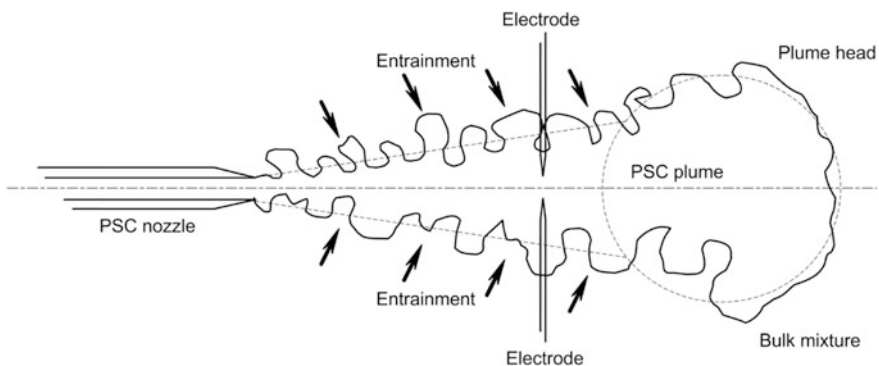


**Fig. 3.3** An idealized illustration of a fuel jet with the vortex ball interpretation

Wynanski and Fiedler 1969). In particular, an analytical model for jet penetration has been proposed for a self-similar turbulent gaseous axisymmetric jet for a wide-range injection-to-ambient pressure ratio, including underexpanded jets (Ouellette and Hill 2001):

$$z = \Gamma \left[ \left( \frac{\pi}{4} \right)^{\frac{1}{2}} \left( \frac{\rho_0}{\rho_\infty} \right)^{\frac{1}{2}} D_0 U_0 t \right]^{\frac{1}{2}}, \quad (3.4)$$

where  $z$  is the axial penetration of the jet relative from a virtual origin, the geometrical apex of the conical jet,  $\rho_0$  and  $\rho_\infty$  are the densities of the injected gas and the ambient mixture, respectively,  $D_0$  is the nozzle diameter,  $U_0$  is the velocity of the jet at the nozzle,  $t$  is the time elapsed from the start of injection, and  $\Gamma$  is a penetration factor and is reported to be 3.08 (Ouellette and Hill 2001). Note that the term  $(\rho_0/\rho_\infty)^{1/2}D_0$  is also known as *equivalent diameter*, an effective length scale accounting for difference in said densities. Further, based on empirical observations on steady, turbulent jets (Ricou and Spalding 1973), a linear relationship between penetration and entrainment, termed *entrainment coefficient*,  $K_e$ , has been proposed (Hill 1972):

$$K_e = \left( \frac{dm_e}{dz} \right) \left( \frac{\rho_0}{\rho_\infty} \right)^{\frac{1}{2}} \left( \frac{D_0}{\dot{m}_0} \right), \quad (3.5)$$

which is dependent on the injection mass flowrate,  $\dot{m}_0$ , as well as the aforementioned equivalent diameter. In the axisymmetric, self-similar limit,  $K_e$  can be shown to assume a constant value of 0.32 (Hill 1972). This is later also confirmed to be the asymptotic limit for transient jets (Cossali et al. 2001).

In addition to stratification of fuel concentration, i.e., back support, the injection also introduces aerodynamic strain of the flame front. The intermittent nature of fuel pocket distribution is reflected in the stochastic treatment of ignition behavior (Alvani and Fairweather 2002; Birch et al. 1981; Effelsberg and Peters 1983). Accordingly, this affects the probability of flame kernel maturation and the subsequent flame propagation of the mixture at a local level (Ahmed et al. 2007). For laminar jet flames, negative flame stretch can be observed in cases where a rich mixture is injected into a lean, homogeneous mixture, effectively increasing flame propagation rate and thus with a stabilizing effect (Balusamy et al. 2014). Similar observations are also made with the direct numerical simulation (DNS) of a lifted jet flame (Ruan et al. 2014). However, in a bluff-body configuration (Ahmed and Mastorakos 2006; Ahmed et al. 2007), for a non-premixed gaseous fuel jet, the probability of ignition, that is, whether the ignition results into a sustained flame propagation, rapidly decreases downstream of the stoichiometric contour formed by the jet and surrounding mixture, particularly near the vortex tip of the jet, due to local straining and dilution.

### 3.4 Idealized PSC Injection/Ignition Process

To observe and identify the principal enabling mechanisms of the PSC ignition technique, and more generally non-premixed spark-ignited combustion, in a quantifiable and adjustable manner, an optically accessible, constant volume combustion chamber (CVCC) is constructed, such that the PSC injection and ignition processes can take place in an idealized, controlled environment. The fuel mixture stratification occurs solely between the PSC injection and the initially quiescent, bulk homogeneous mixture. In order to reduce geometrical interference as well as minimizing conduction heat loss, particularly during flame kernel maturation, sharpened thin-wire electrodes are used in lieu of an automotive spark plug. The ignition zone is kept along the axis of symmetry of the PSC jet to minimize effects of intermittent fuel concentration near the edge of the PSC jet (Ahmed and Mastorakos 2006; Smith et al. 1988). This also preserves the symmetry of the injection and subsequent combustion characteristics. A schematic of the idealized PSC system is presented in Fig. 3.3.

#### 3.4.1 Constant Volume Combustion Chamber

The interior of the CVCC consists of a cylindrical volume with a bore of 80 mm and a height of 50.8 mm. The total displacement of the CVCC is 369 cm<sup>3</sup>. Four optical ports are in orthogonal arrangement around the cylindrical central axis. The PSC injection and spark ignition also take place along this axis. The PSC fuel is injected through a capillary tube of diameter 0.571 mm into the combustion chamber. The electrodes (0.406 mm diameter), located 10 mm downstream of the capillary tube nozzle, maintain a 1 mm spark gap to ascertain sufficient energy to reach electrical breakdown (Paschen 1889). The operative dimensions of the CVCC are summarized in Table 3.1.

Figure 3.4 shows the general schematic of the mixture preparation and fuel delivery system for the CVCC. Both air and CNG originate from intensified sources. A partial pressure approach is used to prepare the bulk mixture and obtain the target overall air-to-fuel ratio. The pressure of the bulk mixture is kept at 7 bar

**Table 3.1** Operative dimensions of the CVCC

Bore diameter (mm)	80
Bore height (mm)	50.8
Chamber volume (cc)	369
Number of view ports	4
View port diameter (mm)	50.8
PSC injector nozzle diameter (mm)	0.571
Spark electrode gap (mm)	1
Spark location from nozzle (mm)	10

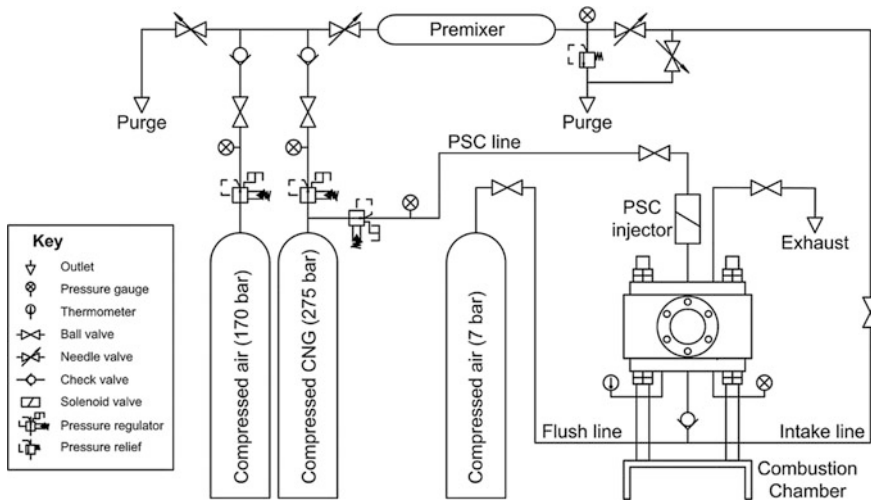


**Fig. 3.4** Schematic of the CVCC fuel and air delivery system

(abs.). The CNG composition is obtained daily using a gas chromatography analyzer. The pressure of the PSC fuel line is regulated at 10 bar (abs.) throughout. Based on mass flow measured data (see following section), the amount of PSC charge injected is 0.35 mg, that is less than 0.6% of the bulk charge at  $\lambda = 2.0$ . The PSC injection and ignition events are captured visually using Z-type Schlieren motion photography at a frame rate of 0.1 ms. The instantaneous chamber pressure is measured and recorded through static and dynamic pressure transducers.

### 3.4.2 Preignition Characterization of PSC Injection

The mass of PSC fuel injected from a line pressure of 10 bar (abs.) into a bulk mixture at 7 bar (abs.) is equal to 0.354 mg. Using the Schlieren images, the preignition characteristics of the PSC fuel jet can be visually inspected. The extent of the fuel jet at each recorded time can be identified in an automated manner using common image processing techniques such as edge detection (Canny 1986). The injection duration of the PSC jet under said CVCC operating conditions is 9.9 ms over 120 samples. The Schlieren images of the PSC injections at various stages are presented in Fig. 3.5. It can be seen that early in the injection, the jet exhibits near cylindrical trailing core and a substantially larger vortex tip section, suggesting entrainment at the tip. This persists until about 1.0 ms, in which the trailing section begins to assume a conic shape, reminiscent of entrainment in the jet tail. By 2.0 ms, the PSC jet transitions into the fully-developed regime.

Figure 3.6 shows the quantification of the mean penetration history over 120 PSC injection events in the CVCC. The injection time (after SOI) is normalized by

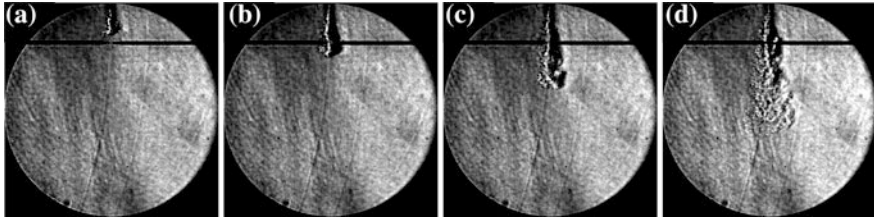


**Fig. 3.5** Schlieren images of a PSC injection event in the CVCC at **a** 0.5 ms, **b** 1.0 ms, **c** 2.0 ms, and **d** 4.0 ms after SOI

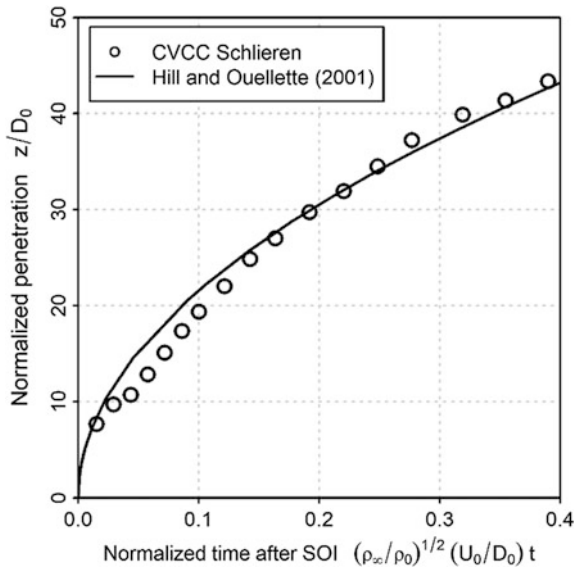


**Fig. 3.6** Normalized penetration history of the PSC jet. Key:  $\circ$  CVCC Schlieren visualization, — self-similar jet penetration model in Eq. (3.4)

a time constant,  $(\rho_0/\rho_\infty)^{1/2} D_0/U_0$ , based on the effective diameter and the injection velocity at the nozzle. Meanwhile, the jet penetration is normalized by the nozzle diameter. The analytical jet penetration model (Ouellette and Hill 2001) in Eq. (3.4) is also included for comparison. It can be seen that, for the PSC jet, the transition to a self-similar regime takes place at approximately 20 nozzle diameters, as indicated by the comparison with the analytical model.

### 3.4.3 Enhancement Strategies of PSC Combustion

The test scenarios for the CVCC ignition experiments are summarized in Table 3.2. A range of overall air–fuel ratios between 1.2 and 2.0 is considered. A set of homogeneous cases (NO PSC) serves as baseline to the PSC runs. To successfully

**Table 3.2** Test matrix for the PSC CVCC experiments

$\lambda$	1.2	1.4	1.6	1.8	2.0
NO PSC	×	×	×	–	–
SOI	×	×	×	×	×
EOI $\times$ 1	×	×	×	×	×
EOI $\times$ 2	–	–	×	×	×

ignite the CVCC bulk mixture with the PSC injection, two spark timings are contemplated: at the start of injection (SOI) and at the end of injection (EOI  $\times$  1). An additional PSC ignition strategy is also introduced (EOI  $\times$  2), in which a second PSC injection takes place 10 ms following spark ignition at the EOI  $\times$  1 timing. Note that for the homogeneous scenarios, the spark-ignited flame kernel fails to reach maturity at  $\lambda = 1.8$  and 2.0. Further, for the EOI  $\times$  2 cases, no significant improvement can be observed in relation to the corresponding EOI  $\times$  1 cases for cases where  $\lambda < 1.6$ . These results are not presented.

The instantaneous pressure history and the corresponding Schlieren motion images of each sample point are recorded. The energy release during combustion process is calculated with the following relationship for a constant volume process:

$$\Delta E = \left( \frac{V}{\gamma - 1} \right) \int_{t_0}^t \frac{d}{dt} p(t) dt, \quad (3.6)$$

where  $\Delta E$  is the sensible energy release,  $V$  is the volume of the CVCC,  $\gamma$  is the ratio of specific heats for natural gas ( $\gamma = 1.32$ ),  $p(t)$  is the instantaneous pressure, and  $t_0$  is the time of spark onset. As no energy is released from the air–fuel mixture prior to ignition (i.e.,  $t \leq t_0$ ), the integration constant for Eq. (3.6) is zero. The heat release results are then normalized to the following dimensionless terms:

$$\tau = \left[ \frac{1}{2} \left( \frac{\rho_b}{\rho_u} \right) \left( \frac{V^{1/3}}{S_L} \right) \right]^{-1} t, \quad (3.7)$$

and

$$\dot{Z} = \left[ \frac{1}{2} \left( \frac{\rho_b}{\rho_u} \right) \left( \frac{V^{1/3}}{S_L} \right) \right] \left( \frac{\Delta \dot{E}}{H} \right), \quad (3.8)$$

where  $\dot{Z}$  stands for the normalized energy release rate,  $H$  is the energy content of the overall mixture in the CVCC, while  $\rho_b/\rho_u$  denote the ratio between the burned and unburned gas densities, and  $S_L$  is the laminar flame speed of the overall mixture. The mixture-specific quantities,  $S_L$ ,  $H$ , and  $\rho_b/\rho_u$ , are calculated for the experimental operating temperature, pressure and air–fuel ratios. These are shown in Table 3.3. Also note that, as the PSC fuel mass is 0.534 mg, the PSC injection represents about 0.4% of the total fuel mass at  $\lambda = 2.0$ , and about 0.25% at  $\lambda = 1.2$ .



**Table 3.3** CVCC combustion characteristics at different air–fuel ratios at a chamber pressure of 7 bar (abs.)

$\lambda$	1.2	1.4	1.6	1.8	2.0
$m_{\text{fuel}}$ (mg)	145.8	126.5	111.6	99.91	90.42
$S_L$ (cm/s)	11.62	7.026	4.543	3.092	2.192
$H$ (kJ)	7.159	6.209	5.481	4.906	4.440
$\rho_b/\rho_u$ ( )	0.1372	0.1353	0.1360	0.1784	0.1913

**Table 3.4** Normalized energy release for all cases

$\lambda$	1.2	1.4	1.6	1.8	2.0
NO PSC	0.6259	0.5484	0.4801	–	–
SOI	0.6377	0.5859	0.5940	0.2837	0.08,698
EOI $\times$ 1	0.6299	0.5822	0.5481	0.4333	0.2994
EOI $\times$ 2	–	–	0.5797	0.4980	0.3568

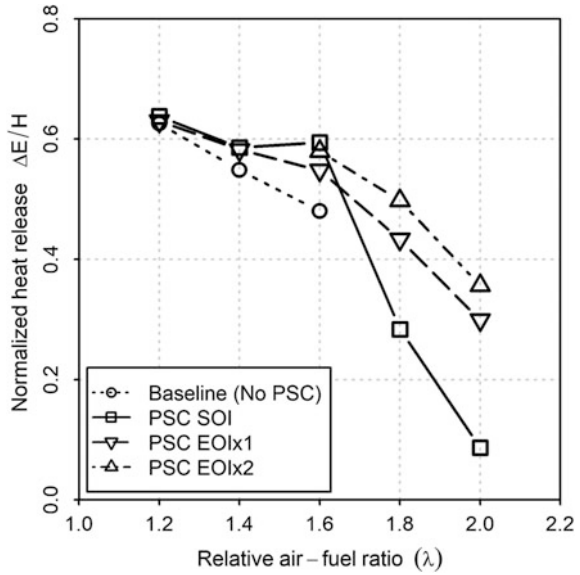
For the EOI  $\times$  2 scenarios, the level of stratification through PSC is accordingly doubled.

Table 3.4 shows the normalized energy release for all cases obtained by Eq. (3.6) and is illustrated in Fig. 3.7. The normalized energy release is indicative of the amount of total available energy that has been converted through the combustion process. There are two factors accounting for the rapid decrease of heat release with increasing air–fuel ratios. First is the increased heat loss to the surrounding unburned mixture and the combustion chamber surface due to a slower burn rate. The second factor is that the combustion process can be prematurely terminated. This is particularly prominent in the SOI cases, where the energy release is drastically diminished beyond  $\lambda = 1.6$ , while both EOI cases achieve substantially higher levels.

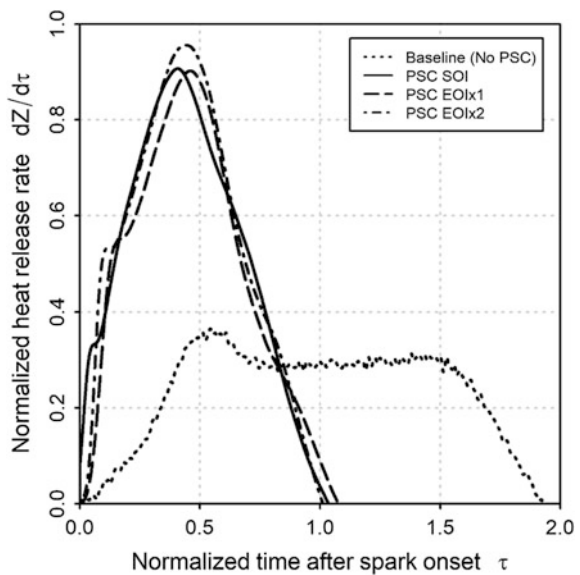
The energy release rate profiles can be further explained from the instantaneous energy release rates as shown in Figs. 3.8 and 3.9. For  $\lambda = 1.6$  (Fig. 3.8), the initial flame kernel growth is comparatively slower in the EOI  $\times$  1 spark timing, due to a much richer but relatively slow-moving mixture near the spark ignition zone, reducing the flame speed. However, as the flame kernel approaches maturity, the existing stratified mixture field from the PSC injection forms a preferential propagation path for the flame front. Nevertheless, both PSC cases have a peak energy release rate lower than the homogeneous case. On the other hand, based on the total energy release data on Table 3.4, the final heat release for all cases is very close together, suggesting that the decrease in the peak heat release rate in the homogeneous case is a result of a laminar flame development slower, than the PSC cases.

The benefits of the PSC injection become more apparent as  $\lambda$  is further increased. Upon ignition, the flame propagates again along the preferential fuel concentration gradient set forth by the PSC jet at  $\lambda = 1.6$  (Fig. 3.8), instead of directly expanding through the bulk mixture. This gives rise to a first, lower peak in energy release rate. As expected, the SOI injection allows a faster rise to the peak,

**Fig. 3.7** Normalized heat release of the CVCC experiment across different air–fuel ratios

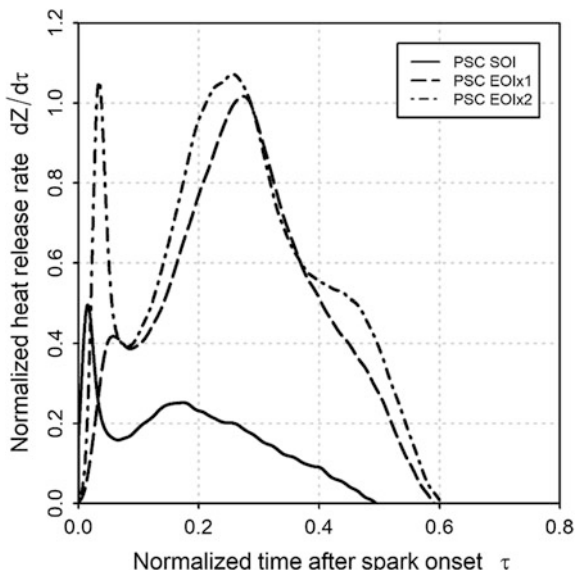


**Fig. 3.8** Instantaneous CVCC energy release rate for all cases at  $\lambda = 1.6$



and the  $EOI \times 1$  reaches peak pressure somewhat later due to the lack of aerodynamic momentum from the injection, though both result in significant boost in bulk mixture energy release rate, as indicated by the second peak, compared to the homogeneous case. Under  $EOI \times 2$ , however, the second PSC injection provides additional fuel as well as momentum for the existing flame front, increasing the

**Fig. 3.9** Instantaneous CVCC energy release rate for all cases at  $\lambda = 2.0$



peak bulk mixture energy release rate. While the normalized combustion duration for the homogeneous case is 1.945 (566.2 ms), in the PSC cases the reduction in combustion duration is nearly twofold, down to 1.072 (312.2 ms) for SOI and  $\text{EOI} \times 1$ , and 0.992 (288.9 ms) for  $\text{EOI} \times 2$ .

This trend continues to  $\lambda = 2.0$  (Fig. 3.9), where the homogeneous case data are unavailable due to failure for the flame kernel reach maturity. The seemingly shorter combustion duration for the SOI indicates premature termination. Again, the two peaks appear again in all PSC cases, signifying the primary ignition of the PSC jet and the subsequent propagation of the flame front into the bulk air–fuel mixture. This is particularly important for air–fuel ratios under which stable combustion cannot be achieved with a homogeneous mixture. Also, as shown from the difference in heat release rate behavior between SOI and  $\text{EOI} \times 1$ , back support remains a primarily enabling factor, where the initial peak in heat release rate for the  $\text{EOI} \times 1$  case almost equals that of the second peak. The aerodynamic forces, indicative by the second injection of the  $\text{EOI} \times 2$  case, provide additional enhancement.

### 3.4.4 Large Eddy Simulation of Idealized PSC Injection and Ignition

Experimental observations on the CVCC are complemented with results obtained from detailed computational fluid dynamics (CFD) analyses, using the large eddy simulation (LES) approach to provide additional information in mixture formation and flame front development. To this aim, the open source code OpenFOAM

(Weller et al. 1998) is used. To model combustion reactions numerically, methane is used as the working fuel, and a single-step reaction mechanism is considered (Westbrook and Dryer 1984). The computational domain for the CVCC is represented by an unstructured mesh with different levels of local refinement. The computational mesh used for modeling the injection consists of 3.4 million cells, with the cell size of 0.015 mm at the finest level. A much finer grid is used for combustion modeling, with cell sizes ranging from 0.03 mm to 0.48 mm, giving a total of 10.5 million cells. Further information about the numerical setup can be found in Bartolucci et al. (2018).

Figure 3.10 shows the comparison between the experimental Schlieren images and the numerical density gradient from the LES simulations for homogeneous spark ignition. The numerically computed isotherms at 900 K, the autoignition temperature of methane, are superimposed on the Schlieren images representing the flame front location. Both sets of results are in excellent agreement. Continuing with the comparison, Fig. 3.11 shows the LES results with corresponding Schlieren results for the PSC scenarios from  $\lambda = 1.2$  and  $\lambda = 2.0$  for the  $\text{EOI} \times 1$  case. As with Fig. 3.10, the 900 K isotherms have been superimposed on the corresponding Schlieren images, and the numerical results are illustrated using simulated Schlieren (i.e., density gradient). Excellent agreement can again be observed between the two sets of results. More importantly, this is indicative of the ability of the LES approach to capture the flame front development as it transitions from a laminar to a turbulent flow regime. At the same air–fuel ratio and timing after spark ignition, it is evident that the flame surface area under PSC is much larger than that of the homogeneous case. The flame topology is also elongated and corrugated resulting from the PSC jet. Figure 3.11 also shows similar enhancement characteristics for the  $\lambda = 1.8$  and  $\lambda = 2.0$ , where extinction occurs in homogeneous conditions.

To further understand the stabilizing effects of the PSC injection, ensemble data are obtained from eight LES runs at  $\lambda = 1.6$ . Random, low-intensity turbulent vortices have been introduced as perturbations for the initially quiescent flow field. The radial turbulent kinetic energy (TKE) distributions 11 mm below of the PSC injection nozzle for the different simulations are presented in Fig. 3.12 at different times after the start of the injection. Although the ensemble average data, evaluated only with eight samples, begin to exhibit a Gaussian profile, the intermittency in the TKE profiles for each individual simulation is evident, confirming previous observations (Alvani and Fairweather 2002; Effelsberg and Peters 1983). More importantly, the variation in turbulent kinetic energy at the ignition zone changes the wrinkling which the flame kernel undergoes during expansion, affecting its likelihood to reach maturity (Chan et al. 2011). In other words, different spark timings during the injection period, which in ensemble indicate stable flame kernel maturation, could lead to extinction on an individual basis.

Figure 3.13 illustrates the individual LES cases at  $\lambda = 1.6$  and their comparison to the experimental results. The numerical results are different due to the perturbations in boundary conditions, and similar general topologies are retained across all simulations, however. The dispersion of the flame front between the different LES simulations also increased as the flame expanded over time, indicative of the

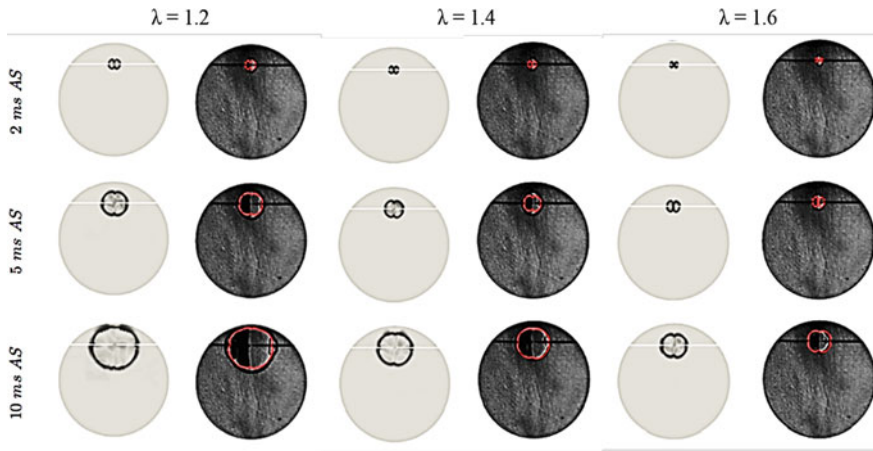


**Fig. 3.10** Comparison between experimental and simulated Schlieren results for homogeneous cases at (left)  $\lambda = 1.2$ , (middle)  $\lambda = 1.4$ , and (right)  $\lambda = 1.6$ . Computed isotherms at 900 K have been superimposed on the experimental images (Bartolucci et al. 2018)

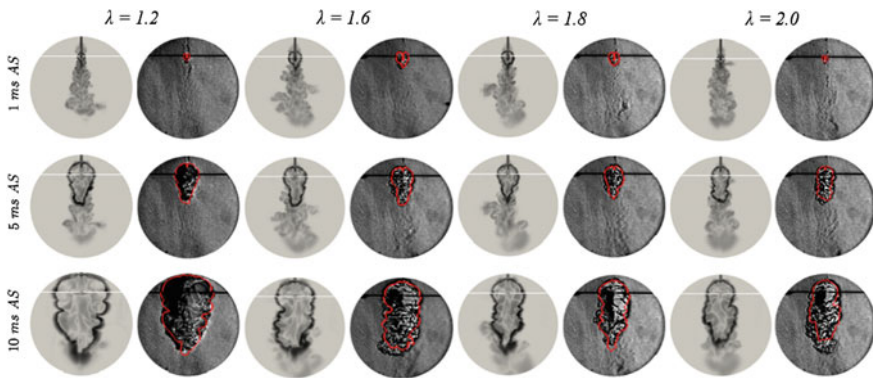


**Fig. 3.11** Comparison between experimental and simulated Schlieren results for PSC cases from  $\lambda = 1.2$  to  $\lambda = 2.0$ . Computed isotherms at 900 K have been superimposed on the experimental images (Bartolucci et al. 2018)

thermal diffusion, that is, thickening of the flame brush at leaner mixtures. In addition, the comparison with the corresponding Schlieren images shows very good agreement. It is worth mentioning that, despite possible stochastic effects between different LES simulations, a reasonable prediction of the flame front can still be achieved using a single LES realization (Bartolucci et al. 2018).

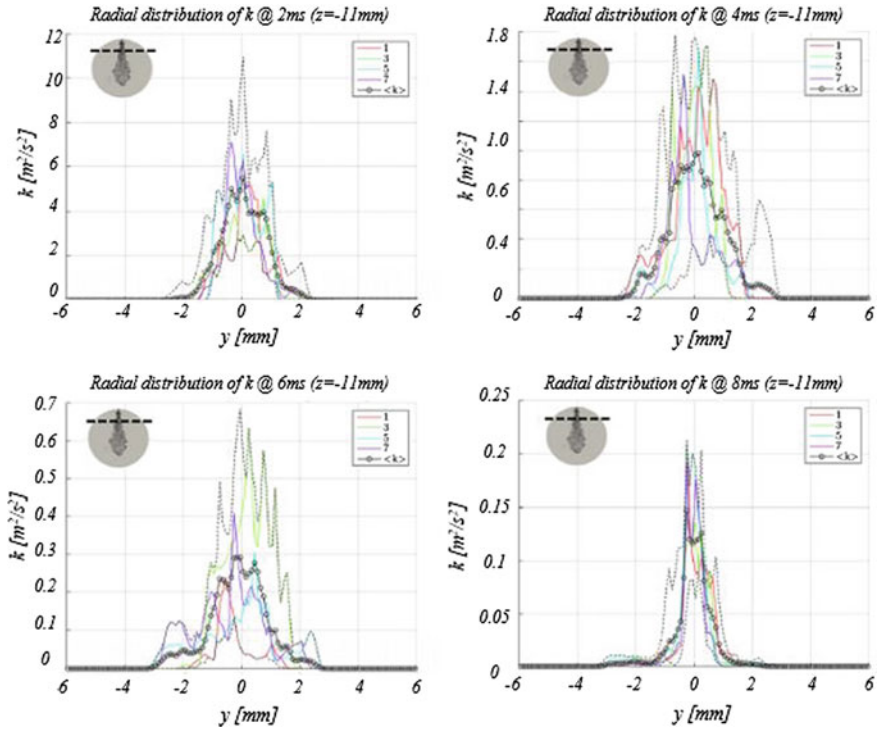


**Fig. 3.12** Radial distribution of TKE at different times after SOI, evaluated at 11 mm from the PSC injector nozzle. Colored lines denote individual runs with randomized initial low-intensity turbulent vortices. Black lines represent (solid) ensemble average and (dotted) standard deviation

### 3.5 PSC Implementation in Engine Conditions

The PSC ignition concept has been implemented for use under engine conditions with different configurations, which have been tested on a Ricardo Hydra single-cylinder research engine (SCRE). A first-generation implementation, consisting of a modified automotive spark plug for PSC injection, has been contemplated in various works (Reynolds and Evans 2004; Reynolds et al. 2005). This subsequently led to further numerical studies, validated using measurement to provide additional information such as engine performance and pollutant formation. Additional design modifications have also been introduced to improve PSC performance. This included the *PSC insert* (Logan 2011), allowing better mixture characteristics of the PSC charge around the spark ignition zone without modifying the spark plug. Meanwhile, the application of the double-injection technique (Chan 2010; Chicka 2012) has been shown to further extend the lean misfire limit than existing PSC implementations.

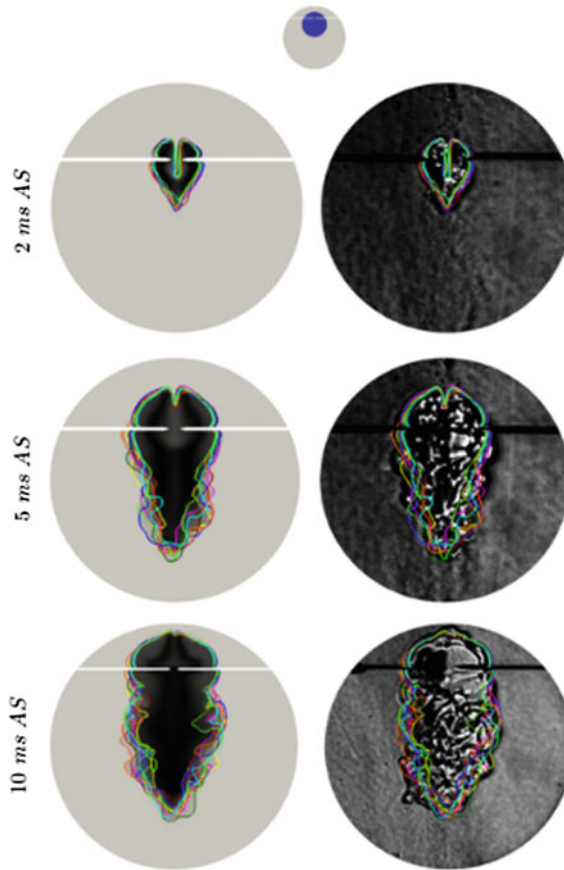


**Fig. 3.13** Comparison between experimental and simulated Schlieren results for PSC  $EOI \times 1$  operation at  $\lambda = 1.6$ . Computed isotherms for individual cases have been superimposed on both sets of images (Bartolucci et al. 2018)

### 3.5.1 First-Generation PSC Design

The first generation of PSC injection/ignition system consists of a modified automotive spark plug, allowing CNG fuel to be delivered directly to the spark ignition zone through a capillary tube, metered by a solenoid valve. The overall implementation of said PSC system can be found in Fig. 3.14, and a summary of the general parameters for the SCRE under homogeneous charge and PSC operating conditions is presented in Tables 3.5 and 3.6. The PSC injection settings are calibrated to 10 CAD before spark onset to minimize brake-specific fuel consumption (BSFC) at a given overall air–fuel ratio, while the spark timing is so determined for each engine speed to obtain the mean maximum torque. All the conditions homogeneous and PSC, are performed with wide-open throttle (WOT) to reduce

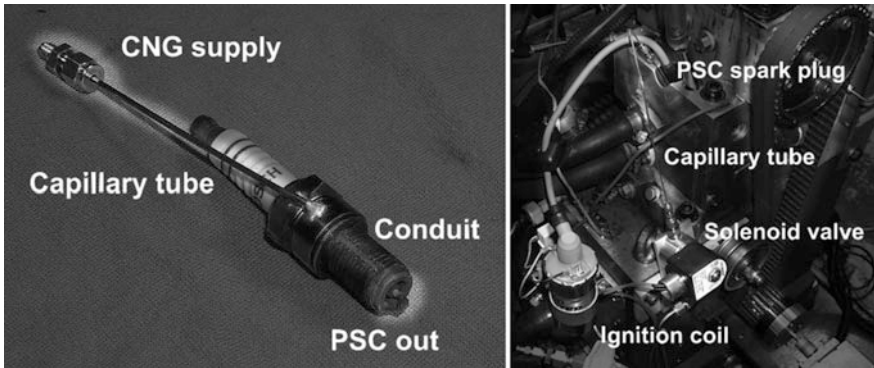


**Fig. 3.14** Schematic of the first-generation PSC spark ignition system and its implementation in the Ricardo Hydra SCRE. From Reynolds and Evans. Adopted from (Reynolds et al. 2005; Reynolds and Evans 2004)

**Table 3.5** General specifications of the Ricardo Hydra SCRE

Working fuel	CNG
Number of valves	4
Firedeck geometry	Flat
Bore × stroke (mm)	81.4 × 88.9
Connecting rod (mm)	158.0
Compression ratio (mm)	9.25
Displacement (cm <sup>3</sup> )	463.3
Clearance volume (cm <sup>3</sup> )	54.7

**Table 3.6** First-generation PSC injection parameters (Fig. 3.14)

Working fuel (no mixture)	CNG
Capillary tube length (mm)	480
Capillary tube diameter (mm)	0.571
Inlet pressure (bar)	25
Mean mass flowrate (g/h)	40
EOI before spark (°)	10
Injection signal width (°)	8

power losses. The amount of PSC fuel injected into the engine is typically no more than 5% of the total fuel mass.

The engine results are summarized in Fig. 3.15. A 10% extension of the LML, defined at a 5% threshold on the CoV IMEP, at 2000 RPM is achieved with the first-generation PSC implementation, from  $\lambda = 1.54$  to  $\lambda = 1.71$  (Reynolds and Evans 2004). A corresponding increase in WOT operating range can also be observed in terms of the brake mean effective pressure (BMEP), with little penalty on the brake-specific fuel consumption (BSFC). In terms of emissions, the



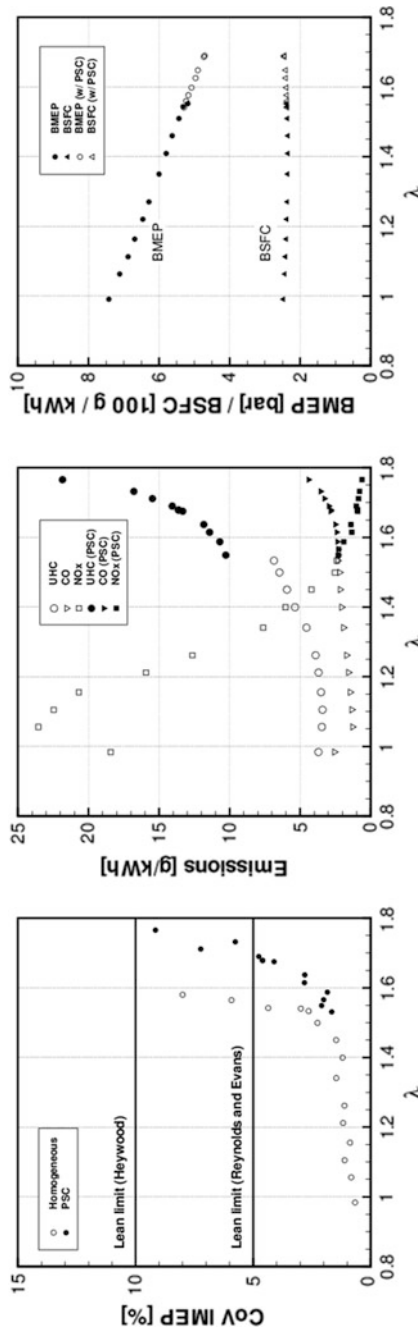


**Fig. 3.15** Performance and emission of the Ricardo Hydra SCRE with and without PSC, based on the first-generation implementation (Reynolds and Evans 2004). (Left) CoV on IMEP, showing an extension of LML; (middle) Brake-specific emissions, showing continued NO<sub>x</sub> reduction; (right) BMEP versus BSFC, with extended operating range

power-specific CO increases slightly with the introduction of PSC, although the overall CO emission level remains low. This is likely a result of a fuel-rich region resulting from the PSC injection, which is responsible for the majority of the CO at the inception of the combustion process (Bikas and Michos 2018). However, a continued reduction of  $\text{NO}_x$  emissions in the PSC-extended operating range can be noted. This is a major departure from conventional stratified charge technologies, where  $\text{NO}_x$  emissions are elevated through ignition of rich mixtures in the prechamber (Michos et al. 2016; Thomas and Staunton 1999). The introduction of PSC results in a sudden increase in UHC. This could be due to a lowering of combustion temperature during lean operation, in which not all of the natural gas in the overall mixture could be consumed. In addition, residual CNG could accidentally enter the combustion chamber through the PSC injector. Future PSC designs are therefore contemplated to improve the injection process.

### 3.5.2 Numerical Simulation of First-Generation PSC Engine Cases

A numerical framework used for the analysis is presented. The simulations are performed with the commercial CFD package CONVERGE (Convergent Science 2008). A Reynolds-averaged Navier–Stokes (RANS) approach has been adopted for turbulence modeling, and the renormalization group (RNG)  $k-\varepsilon$  (Yakhot et al. 1992) model is used for closure. This has been shown to produce robust results in typical engine simulations (Tanner et al. 2001). For modeling reaction chemistry, a partially stirred reactor (PaSR) combustion model is chosen to account for the turbulence chemistry interaction (TCI). A reduced methane mechanism (Lu and Law 2008) involving 30 chemical species and 184 reactions has been chosen to represent chemical kinetics. Mesh refinements are introduced near critical regions, and adaptive mesh refinement (AMR) has been introduced to capture more accurately the flame front. The base mesh resolution is 3 mm, with the finest grid size set to 0.094 mm (PSC spark plug) and 0.375 mm (valve gap and flame front).

Simulations are conducted at  $\lambda = 1.53$  and  $\lambda = 1.68$  under homogeneous and PSC conditions. The intake and exhaust pressure profiles are obtained from 1D thermodynamic analysis. Each simulation is conducted for three engine cycles, where the residual gas fraction has reached a steady value. Figure 3.16 shows the in-cylinder pressure and heat release for all three cases. In terms of pressure trace, the numerical data are in excellent agreement with the engine measurements. There are, however, slight differences in the heat release. This might be due to a number of factors, ranging from the estimation of the mixture composition in the CFD model to the treatment of the numerical integration in the experimental model. It is worth noting that no model calibration has been performed for the simulations.

Looking into details of flame kernel growth under PSC, Fig. 3.17 shows the evolution of the fuel flow during the injection process. A large recirculation region

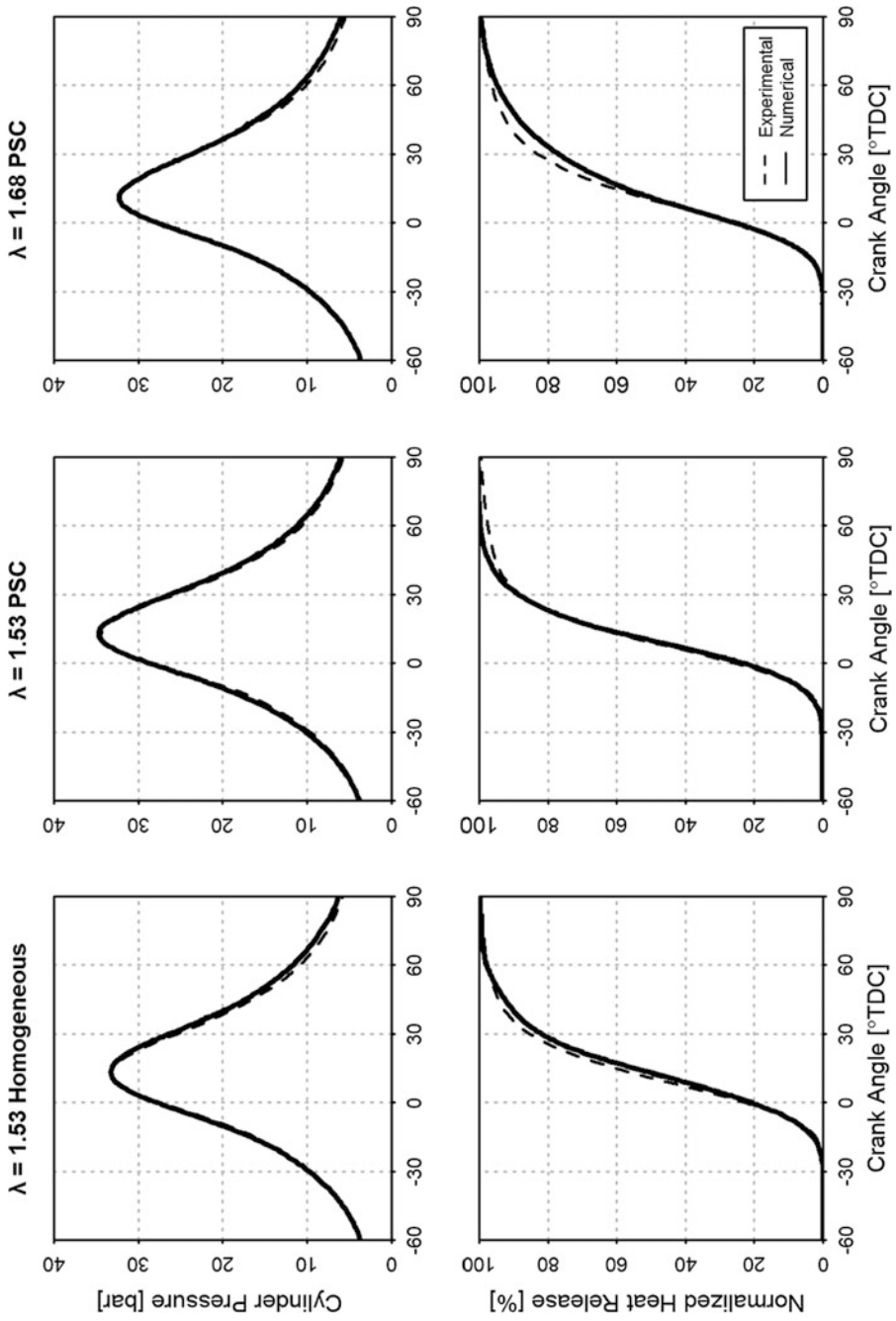
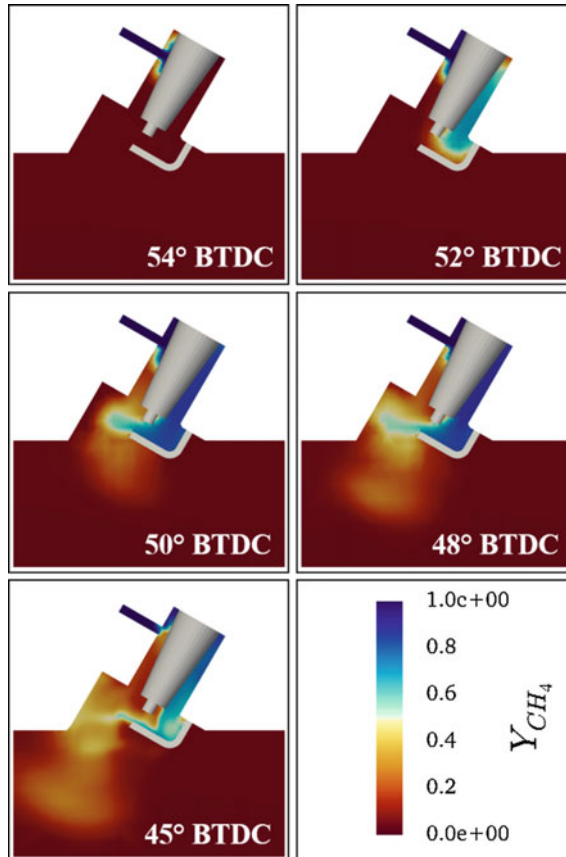


Fig. 3.16 Comparison between SCR experimental and numerical results for (top) pressure trace and (bottom) normalized heat release



**Fig. 3.17** Formation of the fuel-rich region during PSC injection

is formed in the vicinity of the spark plug as the PSC injected fuel flows around the spark plug. This recirculation zone is further sustained by the upward movement of the piston, thus facilitating the formulation of a fuel-rich region. As the charge is ignited, the additional heat released from the rich mixture provides back support to stabilize flame kernel maturation, allowing the flame to propagate faster than under equivalent lean homogeneous conditions. This effect is shown in Fig. 3.18a. Furthermore, as illustrated in Fig. 3.18b, c, the PSC injection also introduces additional turbulence and fresh fuel to support flame kernel growth at the local scale (Bartolucci et al. 2015) until it reaches maturity, as shown in Fig. 3.18d. The evolution of the main combustion event for the PSC cases is depicted in Fig. 3.19. Initially, the rich fuel cloud near the spark plug forms a preferential path and directs the flame toward the center of the cylinder, as indicated in Fig. 3.19a, b, thus promoting the penetration of the flame front into the bulk mixture. Since the flame

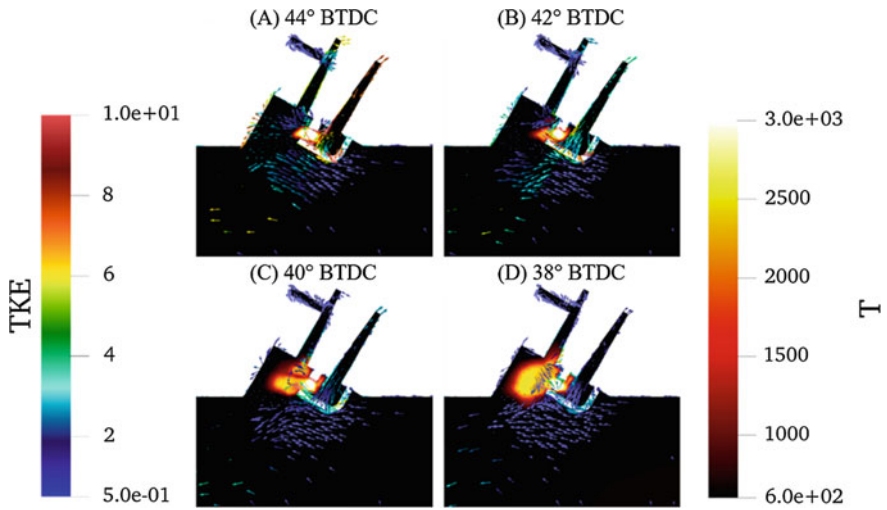


Fig. 3.18 Numerical representation of the charge ignition process

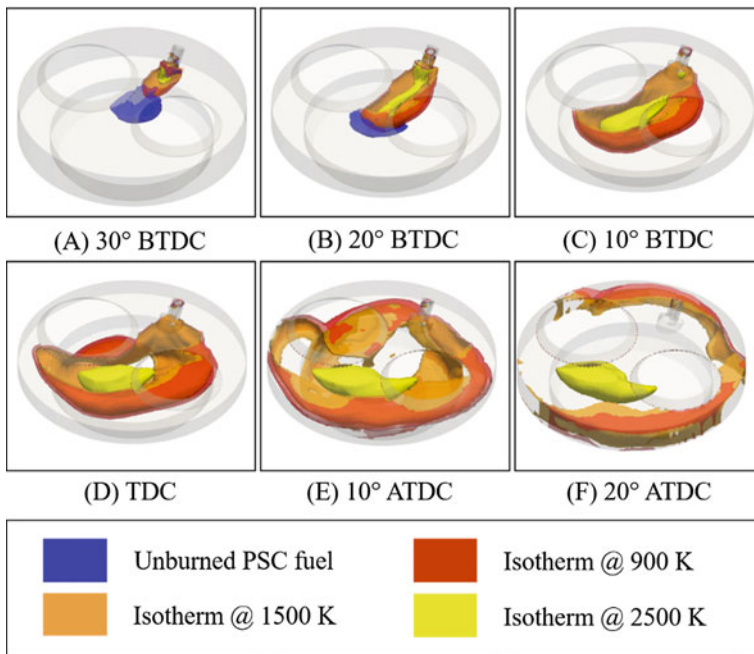


Fig. 3.19 Numerical results for flame propagation. In blue is reported the unburnt PSC fuel, in red the flame front location (defined as the isotherm at 900 K), in orange the isotherm at 1500 K while in yellow the high reactivity area represented by the isotherm at 2500 K

is still traveling at high temperature and relatively high speed, the flame penetrates the lean bulk mixture quickly, as shown in Figs. 3.19c, d. Thermal back support persists until the end of the combustion cycle, where the flame front reaches the cylinder walls, as indicated in Figs. 3.19e, f.

In terms of aggregated engine behavior, Table 3.7 shows a comparison between the in-cylinder peak pressures obtained from the numerical tested cases. With a homogeneous mixture strategy, the performance deteriorates as the charge is leaned out. On the other hand, the peak pressure is increased for both the air-to-fuel ratios considered under PSC, indicative of improved engine power output. However, the improvement in peak pressure at  $\lambda = 1.53$  (4.27%) is much lower than at  $\lambda = 1.68$  (43.08%). The simulated mass fraction burned (MFB) results are shown in Table 3.8. The durations of 0–5% MFB and the 5–95% MFB, representing kernel maturation and flame propagation, are presented. All MFB durations decreased through the deployment of PSC at both air–fuel ratios. Though the 5–95% MFB shows a 10 CAD reduction for  $\lambda = 1.53$ , the improvements in 0–5% are slight. On the other hand, the reduction is particularly evident with  $\lambda = 1.68$ , where the 0–95% MFB is reduced from 154 CAD to 115 CAD. The results presented indicate the benefit of the PSC strategy in aiding flame penetration into the bulk mixture for moderately lean operations, and additionally in stabilizing flame kernel maturation for ultra-lean operations.

The power-specific engine-out emissions for the major pollutants are reported in Table 3.9, evaluated at exhaust valve opening (EVO). The amount of  $\text{NO}_x$  generated is increased under PSC as compared to homogeneous cases, as the combustion process under PSC can be maintained at a higher temperature. Despite a significantly lower  $\text{NO}_x$  output, the engine performance under homogeneous operation is much poorer, particularly reflected into the UHC emissions at  $\lambda = 1.68$ , where it is 74.1 g/kWh. Further, there is a slight increase in UHC for  $\lambda = 1.53$  under PSC. The additional UHC is likely to originate from the rich PSC mixture, in which there is insufficient oxygen available. A similar trend can also be observed for CO emissions. As cylinder temperature is relatively low at the ultra-lean case ( $\lambda = 1.68$ ), the CO oxidation into  $\text{CO}_2$  is almost frozen during the expansion stroke. The deployment of PSC enables combustion to take place at higher cylinder temperature, subsequently allowing the more CO to be converted into  $\text{CO}_2$  (Bikas and Michos 2018). Nevertheless, for the moderately lean case ( $\lambda = 1.53$ ), a greater amount of CO is produced under PSC than homogeneous operations. This is due to the absence of oxygen in the fuel-rich PSC injection region. Lastly, the power-specific  $\text{CO}_2$  production is indicative of the combustion efficiency for the four cases. At  $\lambda = 1.53$ , the higher combustion temperature under PSC allows for

**Table 3.7** Peak pressure improvement generated by PSC ignition strategy

Peak pressure (bar)	Homo.	PSC	Change (%)
$\lambda = 1.53$	33.26	34.68	4.27
$\lambda = 1.68$	22.54	32.25	43.08

**Table 3.8** Combustion duration for all the simulated cases

MFB Duration (CAD)	0–5%	5–95%
$\lambda = 1.53$ Homogeneous	39	62
$\lambda = 1.53$ PSC	34	52
$\lambda = 1.68$ Homogeneous	55	99
$\lambda = 1.68$ PSC	41	74

**Table 3.9** Specific exhaust emissions for all simulated cases

Specific emissions (g/kWh)	NO <sub>x</sub>	UHC	CO	CO <sub>2</sub>
$\lambda = 1.53$ Homogeneous	2.46	0.18	0.04	543.00
$\lambda = 1.53$ PSC	5.23	0.20	0.19	548.00
$\lambda = 1.68$ Homogeneous	0.10	74.10	2.82	684.00
$\lambda = 1.68$ PSC	1.49	1.74	0.41	573.00

longer period for CO oxidation, thereby increasing the CO<sub>2</sub> production slightly. For the homogeneous case at  $\lambda = 1.68$ , engine performance has been compromised due to misfires. Hence, the specific CO<sub>2</sub> production is increased drastically. The application of PSC lowers the CO<sub>2</sub> emission to a nominal level.

The following conclusions can be drawn from the numerical simulations. First, when the relative air-to-fuel ratio is below the LML, the PSC injection aids the propagation of the flame into the bulk mixture. This results into a slightly higher peak pressure, but also increases engine-out emissions at the same time. Second, when the relative air-to-fuel ratio lies beyond the LML for homogeneous combustion, the application of PSC improves engine performance significantly due to additional stabilization of flame kernel maturation, and greatly reduces HC and CO emissions. Engine-out NO<sub>x</sub> emissions are, however, increased as a result of higher in-cylinder temperatures. The advantages of PSC are much more evident under ultra-lean-burn conditions, where the combustion behavior would otherwise be unstable at an equivalent, homogeneous air-fuel ratio.

### 3.5.3 Further Developments on PSC Implementation

While the first-generation PSC has demonstrated its ability to extend the LML under engine conditions, and consequently the engine load control without throttling losses, additional measures have been introduced to further improve the PSC to bulk fuel stratification level, as well as to reduce UHC emissions under ultra-lean operation. Initial attempts have been made, in which a mixture of varying air-fuel ratio has been used for the PSC injection using a first-generation implementation (Reynolds et al. 2005). Engine test results indicate a monotonic progression in all performance and emission observables between homogeneous and pure CNG PSC

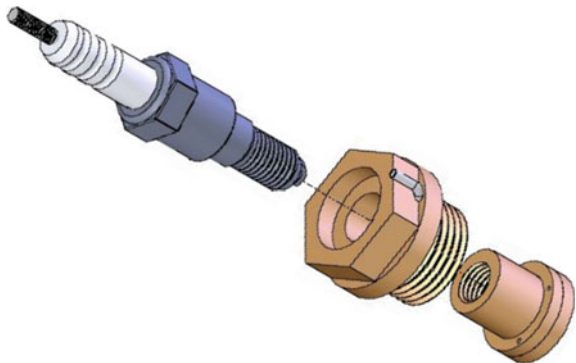
(PSC injection at  $\lambda = 0$ ) engine conditions, with the most desirable outcomes obtained using pure CNG in the PSC injection.

Following the preignition characterization of the first-generation PSC injector (Chan et al. 2007), additional efforts have been made to improve the interaction between the PSC jet and the bulk charge. An adjustable distributed PSC injection mechanism, termed *PSC insert*, has been designed (Logan 2011). A removable insert provides flow channels to supply PSC fuel around the perimeter of the spark ignition region in various injection patterns, allowing better control of mixture formation in its immediate vicinity. A schematic of the PSC insert design is presented in Fig. 3.20. An extension of LML from  $\lambda = 1.53$  to 1.67 can be observed with the PSC insert while the maximum PSC fuel mass is decreased by 36.8% (Logan 2011).

In addition, the effectiveness of the double PSC injection strategy (Chan 2010) is has also been investigated in the Ricardo Hydra SCRE (Chicka 2012). Tests have been performed under homogeneous, single (PSC  $\times$  1) and double (PSC  $\times$  2) PSC injection using the insert design (Logan 2011). The stability of combustion at both engine speeds and PSC injection strategies are presented in Fig. 3.21. The  $L^p$  combination of asymptotic parameterizations (Churchill and Usagi 1972) is used to identify the LML on CoV IMEP at the 5% threshold. At 1500 RPM (Fig. 3.21a), the LML is extended to  $\lambda = 1.75$  for PSC  $\times$  1 and  $\lambda = 1.79$  for PSC  $\times$  2. A slightly reversed trend is observed at 3000 RPM, where the LML is  $\lambda = 1.72$  for PSC  $\times$  1 and  $\lambda = 1.71$  for PSC  $\times$  2.

This reduction can be explained in part by examining the distributions of IMEP over the peak pressure timing (Fig. 3.22) for the two injection schemes at 1500 RPM. For PSC  $\times$  1, the CoV is 19.6% at  $\lambda = 1.81$  and 18.6% at  $\lambda = 1.84$  for PSC  $\times$  2. Misfired cycles, identified using *k*-means clustering (Lloyd 1982), represent 32% of total engine cycles for both cases. Compared to PSC  $\times$  1, the PSC  $\times$  2 strategy produces a higher IMEP for the normal (5.33 bar vs. 4.97 bar) as well as partial combustion cycles (4.22 bar vs. 3.35 bar). The normal combustion cycles for the PSC  $\times$  2 case are much more tightly clustered, where the standard

**Fig. 3.20** Schematic of the PSC insert





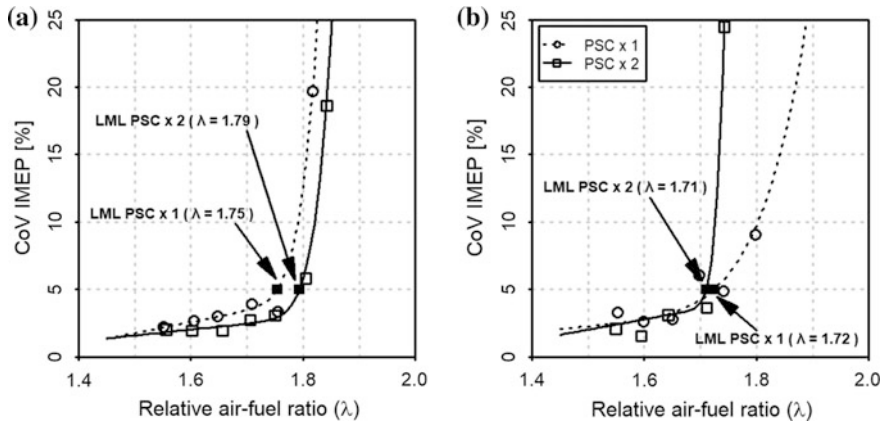


**Fig. 3.21** LML for single (PSC  $\times$  1) and double (PSC  $\times$  2) injection strategies at **a** 1500 RPM and **b** 3000 RPM. Adopted from (Chicka 2012)

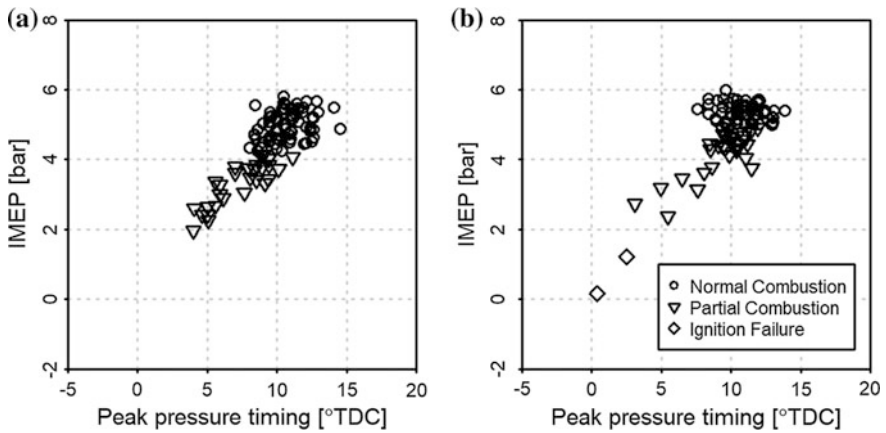


**Fig. 3.22** Distribution of IMEP and peak pressure crank angle of 100 consecutive engine cycles for **a** PSC  $\times$  1 and **b** PSC  $\times$  2 at  $\lambda = 1.8$  and 1500 RPM, respectively. The CoV for both cases is 19.8% for PSC  $\times$  1 and 18.4% for PSC  $\times$  2, respectively. The corresponding IMEPs are 4.49 bar and 4.87 bar. Adopted from (Chicka 2012)

deviation is 0.25 bar, as opposed to 0.41 bar in the PSC  $\times$  1 case. On the other hand, the standard deviation among the misfired cycles in the PSC  $\times$  2 case is increased relative to PSC  $\times$  1 from 0.62 bar to 1.04 bar, thus indicating a decrease of the combustion stability overall combustion stability. This issue could be remedied by further improving the injection timing and duration of the PSC injection, particularly for the second injection.

### 3.6 Concluding Remarks

The role of the partially stratified charge (PSC) injection and ignition technique in extending the lean misfire limit (LML) of natural-gas-fueled engines is presented, to which a comprehensive experimental and numerical approach is adopted. The fundamental enabling mechanisms of PSC are identified in an optically accessible constant volume combustion chamber (CVCC) under idealized conditions. Different spark timings and injection strategies are considered, and stable combustion can be achieved for an air–fuel ratio of  $\lambda = 2.0$ . The energy released from the richer region under PSC provides back support to the flame front. The PSC injection also forms a preferential path through which the flame front penetrates into the unburned mixture, further improving the combustion characteristics of ultra-lean mixtures. Thus, the flame propagation of ultra-lean mixtures under PSC can take place at a greater speed than its equivalent, homogeneous air-fuel ratio level. Corresponding numerical results obtained from large eddy simulations (LES) further highlight the effect of turbulence on the stability of flame kernel maturation and robustness of the flame front topology.

The PSC methodology is then applied to engine conditions in a single-cylinder research engine (SCRE). Using a first-generation PSC implementation, an extension of LML from  $\lambda = 1.53$  to  $\lambda = 1.71$  can be observed at 2000 RPM. This extension of the operating range, though results in a slight increase in carbon monoxide (CO) production, as well as a reduction of nitrogen oxides ( $\text{NO}_x$ ) emissions. Multi-cycle simulations of the SCRE are conducted using a Reynolds-averaged Navier–Stokes (RANS) approach and reduced chemical kinetics for methane combustion. Very good agreement with the test bench results can be achieved without model calibration. The numerical results indicate PSC enhancement through flame propagation in moderately lean mixtures, and additionally through stabilization of flame kernel maturation in ultra-lean mixtures. Subsequent modifications, namely the PSC insert and the double-injection technique, are introduced. The operating range is further extended, with the LML increased to  $\lambda = 1.79$  at 1500 RPM and to  $\lambda = 1.72$  at 3000 RPM.

### References

- Abdel-Gayed RG, Bradley D (1985) Criteria for turbulent propagation limits of premixed flames. *Combust Flame* 62(1):61–68
- Ahmed SF, Mastorakos E (2006) Spark-ignition of lifted turbulent jet flames. *Combust Flame* 146:215–231
- Ahmed SF, Balachandran R, Marchione T, Mastorakos E (2007) Spark ignition of turbulent non-premixed bluff-body flames. *Combust Flame* 151:366–385
- Aleiferis PG, Hardalupas Y, Taylor AMKP, Ishii K, Urata Y (2003) Flame chemiluminescence studies of cyclic combustion variations and air-to-fuel ratio of the reacting mixture in a lean-burn stratified-charge spark-ignition engine. *Combust Flame* 136(1–2):72–90

- Alvani RF, Fairweather M (2002) Ignition characteristics of turbulent jet flows. *Chem Eng Res Des* 80(8):917–923
- Andreassi L, Cordiner S, Rocco V (2003) Modelling the early stage of spark ignition engine combustion using the KIVA-3 V code incorporating an ignition model. *Int J Engine Res* 4 (3):179–192
- Arcoumanis C, Hull DR, Whitelaw JH (1997) Optimizing local charge stratification in a lean-burn spark-ignition engine. *Proc IMechE Part D: J Automobile Eng* 211(2):145–154
- Balusamy S, Cessou A, Lecordier B (2014) Laminar propagation of lean premixed flames ignited in stratified mixture. *Combust Flame* 161:427–437
- Bartolucci L, Cordiner S, Mulone V, Rocco V (2018) Natural gas partially stratified lean combustion: analysis of the enhancing mechanisms into a constant volume combustion chamber. *Fuel* 211:737–753
- Bartolucci L, Cordiner S, Mulone V, Rocco V, Chan EC (2015) Partially stratified charge natural gas combustion: the impact of uncertainties on LES modeling. *SAE Technical Paper* 2015-24-2409
- Bikas G, Michos K (2018) Carbon monoxide emissions model for data analytics in internal combustion engine applications derived from post-flame chemical kinetics. *SAE Technical Paper* 2018-01-1153
- Birch AD, Brown DR, Dodson MG (1981) Ignition probabilities in turbulent mixing flows. *Int Symp Combust* 18(1):1775–1780
- Bradley D, Lawes M, Scott MJ, Mushi EMJ (1994) Afterburning in spherical premixed turbulent explosions. *Combust Flame* 99(3–4):581–590
- Canny JF (1986) A computational approach to edge detection. *IEEE Trans Pattern Anal Mach Intell* 8(6):679–698
- Chan EC, Davy MH, de Simone G, Mulone V (2011) Numerical and experimental characterization of a natural gas engine with partially stratified charge spark ignition. *ASME J Eng Gas Turbines Power* 133(2)
- Chan EC, Evans RL, Davy MH, Cordiner S (2007) Pre-ignition characterization of partially stratified natural gas injection. *SAE Technical Paper* 2007-01-1913
- Chan EC (2010) Spark ignition of partially stratified gaseous fuel-air mixtures. Doctoral Thesis, The University of British Columbia
- Chen Z, Ju Y (2007) Theoretical analysis of the evolution from ignition kernel to flame ball and planar flame. *Combust Theor Model* 11(3):427–453
- Chicka AS (2012) Performance of a lean-burn natural gas engine using a double-pulse partially stratified charge ignition system. M.A.Sc. Thesis, The University of British Columbia
- Chung S, Ha J, Park J, Lee M, Yeom JK (2003) Rapid bulk combustion of lean premixture by using radical injection method and an application to an actual engine. *SAE Technical Paper* 2003-01-3212
- Churchill SW, Usagi R (1972) A general expression for the correlation of rates of transfer and other phenomena. *AIChE J* 18(6):1121–1128
- Convergent Science (2008) CONVERGE CFD [Online]. Available: <https://convergecf.com/>
- Cossali GE, Coghe A, Araneo L (2001) Near-field entrainment in an impulsively started turbulent gas jet. *AIAA J* 39(6):1113–1122
- Daniels C, Scilzo B (1996) The effects of electrode design on mixture ignitability. *SAE Technical Paper* 960606
- Deshaies B, Joulin G (1984) On the initiation of a spherical flame kernel. *Combust Sci Technol* 37 (3–4):99–116
- Effelsberg E, Peters N (1983) A composite model for the conserved scalar PDF. *Combust Flame* 50:351–360
- Eichengerber DA, Roberts WL (1999) Effect of unsteady stretch on spark-ignited flame kernel survival. *Combust Flame* 118(3):469–478
- Esfahanian V, Salahi MM, Gharehghani A, Mirsalim M (2017) Extending the lean operating range of a premixed charged compression ignition natural gas engine using a pre-chamber. *Energy* 119:1181–1194






- Evans RL (2000) A control method for spark ignition engines, US Patent 6032640
- Evans RL, Blaszyk J (1998) Fast-burn combustion chamber design for natural gas engines. ASME J Eng Gas Turbines Power 120(1):232–236
- Fan L, Reitz RD (2000) Development of an ignition and combustion model for spark-ignition engines. SAE Technical Paper 2000-01-2809
- Helmers E (2009) Das Auto der Zukunft. Wiley-VCH, Weinheim
- Herweg R, Maly R (1992) A fundamental model for flame kernel formation. SAE Technical Paper 922243
- Heywood JB (1989) Internal combustion engine fundamentals. Wiley, New York
- Hill BJ (1972) Measurement of local entrainment rate in the initial region of axisymmetric turbulent air jets. J Fluid Mech 51(4):773–779
- Ho C, Santavicca D (1987) Turbulence effects on early flame kernel growth. SAE Technical Paper 872100
- Hussein HJ, Capp SP, George WK (1994) Velocity measurements in a high Reynolds number momentum conserving axisymmetric turbulent jet. J Fluid Mech 258:31–75
- Jenkins KW, Klein M, Chakraborty N, Cant RS (2006) Effects of strain rate and curvature on the propagation of a spherical flame kernel in the thin-reaction-zones regime. Combust Flame 145 (1–2):415–434
- Johansson B, Neij H, Aldén M, Juhlin G (1995) Investigations of the influence of mixture preparation on cyclic variations in a SI-engine using laser induced fluorescence. SAE Technical Paper 950108
- Kalghatgi GT (1985) Early flame development in a spark-ignition engine. Combust Flame 60 (3):299–308
- Kang T, Kyritsis DC (2005) Methane flame propagation in compositionally stratified gases. Combust Sci Technol 177:2191–2210
- Kuo TW, Reitz RD (1992) Three-dimensional computations of combustion in premixed-charge and direct-injected two-stroke engines. SAE Trans 101:679–695
- Lloyd SP (1982) Least squares quantization in PCM. IEEE Trans Inf Theory 28:129–137
- Logan JMS (2011) Evaluation of a partially stratified-charge insert in a natural-gas engine. M.A. Sc. Thesis, The University of British Columbia
- Lu T, Law CK (2008) A criterion based on computational singular perturbation for the identification of quasi steady state species: a reduced mechanism for methane oxidation with NO chemistry. Combust Flame 154(4):761–774
- Michos K, Bikas G, Vlaskos I (2016) A new global algebraic model for NO<sub>x</sub> emissions formation in post-flame gases—application to lean premixed combustion systems. SAE Technical Paper 2016-01-0803
- Ntziachristos L, Samaras Z (2016) Exhaust emissions from road transport. EMEP/EEA air pollutant emission inventory guidebook
- Ouellette P, Hill PG (2001) Turbulent transient gas injections. ASME J Fluids Eng 122(4):743–752
- Paschen F (1889) Über die zum Funkenübergang in Luft, Wasserstoff und Kohlensäure bei verschiedenen Drucken erforderliche Potentialdifferenz. Ann Phys 273(5):69–75
- Pires da Cruz A, Dean AM, Grenda JM (2000) A numerical study of the laminar flame speed of stratified methane/air flames. Proc Combust Inst 28:1925–1932
- Prieur A, Tilagone R (2007) A detailed well to wheel analysis of CNG compared to diesel oil and gasoline for the French and the European Markets. SAE Technical Paper 2007-01-0037
- Reynolds CCOB, Evans RL (2004) The low NO<sub>x</sub> potential of partially stratified-charge combustion in a natural gas engine. In: Proceedings of the combustion institute Canadian section spring technical meeting
- Reynolds CCO, Evans RL, Andreassi L, Mulone V, Cordiner S (2005) The effect of varying the injected charge stoichiometry in a partially stratified charge natural gas engine. SAE Technical Paper 2005-01-0247
- Reynolds CCOB, Evans RL (2004b) Improving emissions and performance characteristics of lean burn natural gas engines through partial stratification. Int J Engine Res 5(1):105–114

- Richardson ES, Granet VE, Eyssartier A, Chan JH (2010) Effects of equivalence ratio variation on lean, stratified methane-air laminar counterflow flames. *Combust Theor Model* 14(6):775–792
- Ricou FP, Spalding DB (1973) Measurements of entrainment by axisymmetric turbulent jets. *J Fluid Mech* 59(4):21–32
- Ruan S, Swaminathan N, Mizobuchi Y (2014) Investigation of flame stretch in turbulent lifted jet flame. *Combust Sci Technol* 186(3):243–272
- Shah A, Tunestal P, Johansson B (2015) Effect of pre-chamber volume and nozzle diameter on pre-chamber ignition in heavy duty natural gas engines. SAE Technical Paper 2015-01-0867
- Shi X, Chen JY, Chen Y (2017) Laminar flame speeds of stratified methane, propane and *n*-heptane flames. *Combust Flame* 176:38–47
- Smith MTE, Birth AD, Brown DR, Fairweather M (1988) Studies of ignition and flame propagation in turbulent jets of natural gas, propane and a gas with high hydrogen content. *Int Symp Combust* 21(1):1403–1408
- Song J, Sunwoo M (2000) A modeling and experimental study of initial flame kernel development and propagation in SI engines. SAE Technical Paper 2000-01-0960
- Tan Z, Reitz RD (2006) An ignition and combustion model based on the level-set method for spark ignition engine multidimensional modeling. *Combust Flame* 145(1–2):1–15
- Tanner FX, Zhu GS, Reitz RD (2001) A turbulence dissipation correction to the *k*-epsilon model and its effect on turbulence length scales in engine flows. In: Proceedings of the international multidimensional engine modeling user's group meeting at the SAE Congress
- Thomas J, Staunton R (1999) What fuel economy improvement technologies could aid the competitiveness of light-duty natural gas vehicles? SAE Technical Paper 1999-01-1511
- Turner JS (1963) The motion of buoyant elements in turbulent surroundings. *J Fluid Mech* 16(1):1–16
- Weller HG, Tabor G, Jasak H, Fureby C (1998) A tensorial approach to computational continuum mechanics using object-oriented techniques. *Comput Phys* 12(6):620–631
- Westbrook CK, Dryer FL (1984) Chemical kinetic modelling of hydrocarbon combustion. *Prog Energy Combust Sci* 10:1–57
- Witze PO (1980) The impulsively started incompressible turbulent jet. Sandia National Laboratory Technical Report SAND80-8617
- Wynanski I, Fiedler H (1969) Some measurements in the self-preserving jet. *J Fluid Mech* 38(3):577–612
- Yakhot V, Orszag SA, Thangam S, Gatski TB, Speziale CG (1992) Development of turbulence models for shear flows by a double expansion technique. *Phys Fluids A* 4(7):1510–1520

# Chapter 4

## Simulation and Modeling of Direct Gas Injection through Poppet-type Outwardly-opening Injectors in Internal Combustion Engines



Abhishek Y. Deshmukh , Mathis Bode, Tobias Falkenstein ,  
Maziar Khosravi , David van Bebbber, Michael Klaas ,  
Wolfgang Schröder and Heinz Pitsch 

**Abstract** The obligation for the development of highly efficient and low-emission combustion engines has renewed interest in compressed natural gas (CNG) engines using a direct injection (DI) system. CNG has high knock resistance, and with the use of DI, the volumetric efficiency can be increased compared to port-injected CNG engines. Additionally, carbon dioxide and particulate emissions are lower due to a high hydrogen-to-carbon ratio. Therefore, the DI-CNG technology has the potential to surpass the thermal efficiency of conventional gasoline spark-ignition

---

A. Y. Deshmukh (✉) · M. Bode · T. Falkenstein · H. Pitsch  
Institute for Combustion Technology, RWTH Aachen University,  
Templergraben 64, 52062 Aachen, Germany  
e-mail: [a.deshmukh@itv.rwth-aachen.de](mailto:a.deshmukh@itv.rwth-aachen.de)

M. Bode  
e-mail: [m.bode@itv.rwth-aachen.de](mailto:m.bode@itv.rwth-aachen.de)

T. Falkenstein  
e-mail: [t.falkenstein@itv.rwth-aachen.de](mailto:t.falkenstein@itv.rwth-aachen.de)

H. Pitsch  
e-mail: [h.pitsch@itv.rwth-aachen.de](mailto:h.pitsch@itv.rwth-aachen.de)

M. Khosravi · D. van Bebbber  
Ford Research and Advanced Engineering, Ford Werke GmbH,  
Henry-Ford Str. 1, 50725 Cologne, Germany  
e-mail: [maziar.k@gmail.com](mailto:maziar.k@gmail.com)

D. van Bebbber  
e-mail: [dvanbebb@ford.com](mailto:dvanbebb@ford.com)

M. Klaas · W. Schröder  
Institute of Aerodynamics, RWTH Aachen University,  
Wüllnerstr. 5a, 52062 Aachen, Germany  
e-mail: [m.klaas@aia.rwth-aachen.de](mailto:m.klaas@aia.rwth-aachen.de)

W. Schröder  
e-mail: [office@aia.rwth-aachen.de](mailto:office@aia.rwth-aachen.de)

engines while producing lower emissions. However, the design of DI-CNG engines is challenging because of gaseous and, hence, highly compressible fuel running through small injector passages, which results in complex supersonic flows with shocks. The supersonic gas jets emerging from the injector outlet interact with the in-cylinder flow field, which has an impact on fuel–air mixing and combustion. Therefore, it is essential to understand the fundamental physics of the injection process to develop modeling strategies for DI-CNG systems and further study the influence of direct gas injection on the in-cylinder flow field and mixing. To this end, the current chapter is dedicated to the fundamental understanding of the gas injection process through poppet-type outwardly-opening injectors. The DI modeling strategies are discussed for the application in engine simulations. Furthermore, the impact of gas injection on the in-cylinder flow field and fuel–air mixing is analyzed for centrally-mounted injector configurations.

**Keywords** Compressed natural gas · Direct injection · Poppet-type outwardly-opening injector · Supersonic flow · Shocks · Modeling

## 4.1 Introduction

Internal combustion engines (ICEs) are currently the primary power source for ground transportation and will continue to power, at least, heavy-duty vehicles and off-road applications in the future (Eilts 2016). With increasing restrictions on emissions for the transportation sector, research and development efforts must be directed toward significantly reducing engine-out emissions and improvement of the overall efficiency of ICEs through several viable options such as efficient combustion, exhaust after-treatment, or use of low carbon fuels. Compressed natural gas (CNG) is a highly attractive alternative low carbon fuel with high hydrogen-to-carbon ratio and has a potential for efficient combustion.

### 4.1.1 Direct Gas Injection

CNG engines with port fuel injection (PFI) technology have existed for a long time. However, CNG engines have not fully exploited their potential because of some limitations of PFI technology, e.g., reduced drivability and potential methane slip. The reason for reduced drivability of a PFI-CNG vehicle is lower part-load torque compared with gasoline or diesel ICEs, which is caused by the reduction in volumetric efficiency due to the displacement of air as CNG is injected into the manifold. Furthermore, during the valve overlap period, the unburnt methane–air mixture may be passed directly to the exhaust ports resulting in methane slip. The direct injection (DI) of CNG into the cylinder shows the potential to outperform PFI (Husted et al. 2014). Recent work, e.g., the InGas Collaborative Project (INGAS 2017), focused on the development of innovative technologies for CNG engines

such as operating PFI and DI engines under stoichiometric and lean burn conditions to improve efficiency. The present focus, e.g., within the GasOn project by the European Council for Automotive Research & Development (EUCAR) (European Council for Automotive R&D 2018), is to develop CNG-only engines to achieve stricter emission targets.

Despite clear advantages, DI-CNG engines are not predominantly used so far because of the challenges in their design and development. The main challenges in the design process come from the direct gaseous fuel injection, which appears simpler than liquid fuel injection, but is, in fact, a complex process because of the compressible nature of the gas (Müller et al. 2013) and small complex geometries of the injector nozzles. The gas flowing through the injector nozzle with changing area of cross section accelerates to supersonic speeds if the pressure ratios across the nozzle exceed critical values (typically 2–2.5). Moreover, the effects of gas injection on well-established design strategies for conventional ICEs are not well understood. For example, the intake ports of conventional SI engines are optimized to generate a strong tumble vortex in the cylinder. The tumble vortex accelerates by spin-up effect and breaks into a large number of smaller eddies by piston compression, which results in high turbulence near ignition timing, leading to faster combustion (Arcoumanis et al. 1990; He et al. 2007). On the other hand, in a compression ignition (CI) engine, a swirling flow field is desired and generated by the swirl intake ports to aid mixing and diffusion-controlled combustion of the injected fuel by enhancing oxidizer entrainment (Fuchs and Rutland 1998; McCracken and Abraham 2001). Regardless of the potential application of direct gas injection, either in an SI or in a CI engine, e.g., in a dual-fuel application, the high-momentum gas jet strongly affects the in-cylinder flow field and mixing (Chiodi et al. 2006; Baratta et al. 2017; Sevik et al. 2016). Therefore, it is crucial to fundamentally understand the process of gas injection and its consequences on the overall engine performance with existing engine designs, which will then help to devise new design strategies for DI-CNG engines. However, the experimental investigations of the nozzle flow and the near-nozzle gas jet are difficult due to small injector geometries and very small flow timescales. Furthermore, the injected gas jet is highly fluctuating and dynamically interacts with the in-cylinder flow field, making it difficult to measure the velocity field and mixing experimentally. Therefore, predictive simulations are integral to the design and development of DI-CNG systems. A first step toward the understanding of the direct gas injection is to perform resolved simulations of the injector nozzle flow, near-nozzle flow, far-field development of the gas jet in order to characterize the gas jet behavior of DI-CNG injectors in detail.

### ***4.1.2 Design Considerations for Direct Gas Injector***

From a practical point of view, the design and development of the direct gas injector require several considerations as studied by Husted et al. (2014). As



opposed to injectors for liquid fuels, the gas injector lacks lubrication by the fuel, requiring additional means of lubrication to extend the durability. Additionally, a high mass flow rate is desired to inject a sufficient amount of gas in each engine cycle depending on the operation condition. For higher mass flow rate, either the flow area needs to be large or the injection pressure must be high. High pressure also promotes mixing, but on the other hand, to maximize the vehicle range, lower injection pressure is required so that the maximum amount of CNG can be obtained from the pressurized tank before the tank pressure falls below the desired injection pressure. It should be noted that the current design assumption of CNG engines omits the use of high-pressure fuel pump as used in DI gasoline and diesel applications. For example, current PFI systems use injection pressure of around 8 bar and can use more than 96% of CNG from the tank. Using the same injection pressure in the DI system would significantly limit the peak power of the engine or put too many constraints on the design of the injector. Increasing injection pressure to 15 bar will reduce the vehicle range by  $\sim 3\%$ , and a further increase of injection pressure to 30 bar will decrease the vehicle range by  $\sim 9\%$ . Therefore, for a chosen CNG direct injector, the optimum injection pressure is a trade-off between the engine output at the desired operating conditions and the vehicle range. The trade-off can be shifted favorably by careful design of the injector nozzle by maximizing the flow area.

There are mainly three types of injector designs currently used, namely an inwardly-opening needle with a multi-hole tip for diesel, an inwardly opening needle with counterbore cylindrical holes for gasoline direct injection (GDI), and an outwardly-opening poppet-type needle for GDI applications. The selection of the injector nozzle design for DI-CNG applications is primarily driven by the pressure difference across the nozzle in the operating range. In diesel or GDI engines, the injection pressure ( $>100$  bar) is much higher than the peak cylinder pressures during the entire engine cycle, whereas it is significantly lower in DI-CNG ( $<20$  bar) to achieve maximum vehicle range as described before. Therefore, inwardly opening DI-CNG injectors could be inadvertently opened at high in-cylinder pressures. On the other hand, the outwardly-opening poppet-type valves are sealed by the cylinder pressure (see Fig. 4.1), and therefore, the outwardly-opening poppet-type valves have become a natural choice for DI-CNG applications.

### ***4.1.3 Flow Through Poppet-Type/Outwardly Opening Injectors***

The nozzle geometry of outwardly opening poppet-type injectors (henceforth called poppet-type injectors) is complex, and compressible gas flow through the small and complex passages can be rich in physical phenomena. Compared to cylindrical nozzles, there have been relatively a few experimental and simulation studies of outwardly opening poppet-type nozzle designs in the literature. Kim et al. (2004)

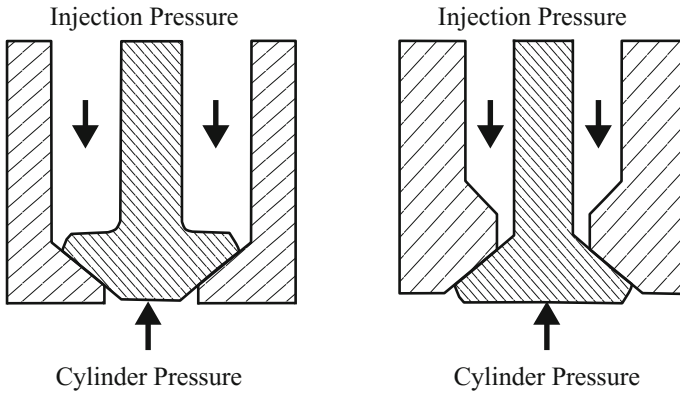


**Fig. 4.1** Schematic of design of inwardly (*left*) and outwardly (*right*) opening injector nozzles

carried out URANS simulations of direct natural gas (NG) injection through shrouded and unshrouded poppet-type nozzle geometries in a large bore, low-speed two-stroke ICE. At lower injection pressure ( $\sim 4$  bar), the injection resulted in a collapsed gas jet, whereas at higher pressure ( $\sim 35$  bar) the gas jet did not collapse, but instead attached to the walls of the cylinder head resulting in a Coanda-type flow. With the use of a shrouded poppet-type nozzle, the gas jet was forced to collapse at higher pressure. The authors also analyzed the effect of these nozzle designs on the mixing performance, combustion efficiency, and susceptibility to pollutant formation and found that high injection pressure with shrouded nozzle resulted in a higher flammability of the mixture. Baratta et al. (2011) showed for a poppet-type injector that the wave propagation inside the injector and the needle motion affect the mass flow rate and the resulting gas jet before collapsing. They suggested the use of fixed needle lift with a ramp of injection pressure to mimic the effects of needle opening. Kuensch et al. (2014) studied a far-field gas jet development in a constant pressure chamber emerging from a piezoelectrically actuated poppet-type injector. They used a planar laser-induced fluorescence (PLIF) technique with acetone as a tracer to track the injected nitrogen gas in the chamber filled with air. The temporal development of the gas jet was visualized, which showed a two-stage gas jet evolution. In the first stage, a hollow cone was formed, which, in the second stage, collapsed into a single jet penetrating the chamber along the axial direction. It was observed that the injection pressures and needle lifts controlled the collapsing tendency of the hollow cone, with higher injection pressure and needle lift lowering the collapsing tendency.

Keskinen et al. (2016) carried out URANS simulations to investigate the gas jet from a cylindrical as well as a poppet-type nozzle. They compared different turbulence models and observed that the jet tip penetration was overpredicted by the RNG  $k-\epsilon$  model, whereas the quadratic  $k-\epsilon$  model resulted in a better agreement with the experimental data. Therefore, the quadratic  $k-\epsilon$  model was chosen for further DI engine simulations. The results showed different mixing mechanisms for

different nozzle designs. The gas jet from the poppet-type nozzle predominantly showed free jet mixing, whereas the cylindrical nozzle favored the mixing induced by impingement of the jet on the piston. As a consequence, a faster mixing was observed with the poppet-type nozzle for early injection timing, while, for late injection timing, the cylindrical nozzle resulted in faster mixing due to impingement of the gas jet on the piston top. Detailed X-ray radiography experiments were performed by Bartolucci et al. (2016) in a nitrogen-filled chamber using a poppet-type injector with nitrogen as the injected gas. The flow around the pintle of the nozzle and the subsequent gas jet development was investigated using the URANS simulations, and a good agreement was observed between simulations and experiments. A mesh resolution study was also carried out that suggested the use of fine mesh resolution for such simulations. However, a detailed upstream geometry of the injector except the pintle was unknown in this case, which is very important for accurate prediction of the development of the gas jet. Besides, with increasing mesh resolution, the computational cost increases significantly. Therefore, to reduce the computational expenses, some modeling approaches to replace poppet-type injectors have been suggested in the literature, e.g., a converging–diverging nozzle approximation for a shrouded poppet-type valve by Kim et al. (2007), a source modeling approach by Baratta et al. (2011), and a mapped boundary condition (MBC) approach by Deshmukh et al. (2016).

So far, most studies using poppet-type injectors have focused on full engine URANS simulations including either fully resolved simulations of the injectors or models of the injectors to overcome computational challenges. The turbulence models have been used in these simulations with little validation against higher fidelity methods such as LES. Provided a sufficient mesh resolution is used, an accurate time-resolved flow field can be obtained using a high-fidelity LES. Along with turbulent mixing characteristics, the classical features of high Mach flows can also be observed for poppet-type injectors, e.g., annular Mach disks and barrel shocks. Furthermore, the effects of the initial condition and needle motion are reported to be very important but have not been quantified in terms of jet characteristics.

#### **4.1.4 Scope**

This chapter aims to introduce the reader to a systematic characterization of the gas jet emerging from a poppet-type injector using LES, which may further provide insights into the fundamental physical processes and the effects. The LES simulations are used to characterize the nozzle flow, near-nozzle gas jet, and the far-field gas jet in detail. A few turbulence models are compared against the LES, and a possible choice for URANS is suggested. The effects of initial conditions in the nozzle and the needle motion are discussed, and recommendations for further engine simulations are provided. The modeling approaches for poppet-type injectors are discussed in detail. The recent MBC modeling approach is then

demonstrated for *quasi*-steady and engine configurations. The idea is to provide comprehensive simulation and modeling approaches of the chosen poppet-type injector used for DI-CNG application in ICEs.

In the following, resolved numerical simulations of the poppet-type injector using both LES and URANS methods are discussed in Sect. 4.2. The challenges in the use of a resolved simulation approach in real engine applications are described, which motivate the development of models for injector nozzles. Previously developed models are discussed briefly in Sect. 4.3. The recently developed MBC approach is applied to quasi-steady-state and full engine configurations, and the results are discussed in Sect. 4.4. The impact of direct gas injection on the in-cylinder flow and mixing is discussed in Sect. 4.5. The chapter is summarized in Sect. 4.6, and future challenges are discussed in Sect. 4.7.

## 4.2 Simulations of Gas Injection Through Poppet-Type Injectors: A Case Study

### 4.2.1 Numerical Challenges

From a numerical point of view, resolved simulations of the poppet-type injector are challenging because of small and complex gas passages of the order of micrometers and high-speed flow with shocks and discontinuities typical in supersonic regimes. LES provides a feasible approach to obtain highly accurate flow field simulations in complex industrial geometries. Especially for flows with high Mach numbers and Reynolds numbers, where the computational cost of DNS is high, LES can be a practical alternative. LES of flows with shocks requires special numerical schemes with the capability to capture shocks and remain stable at the same time. The numerical stability can be obtained by adding numerical dissipation. However, this must be limited to areas of shocks and discontinuities to avoid dissipation of physical turbulent flow structures. A shock detector is required to add numerical dissipation just locally and conserve turbulent flow structures. The shock detector determines gradients in the velocity and scalar field and activates the shock-capturing scheme in the regions of high gradients. In addition, supersonic velocities in combination with grid cell sizes of the order of micrometers result in time steps on the order of 100 picoseconds. A high-fidelity full engine LES simulation with a fully resolved gas injector simulation may need years to complete one or more cycles. Nevertheless, a fully resolved LES of the gas jet from the injector is still feasible for a simplified case, such as a constant pressure or constant volume chamber because the run-times are shorter due to the reduced domain of interest compared to full engine simulations.

On the other hand, URANS simulations may be computationally cheaper due to lower mesh resolution requirements compared to LES. However, since the energy-containing turbulent scales are also modeled, the accuracy of the solution

needs to be carefully evaluated. Also, most of the turbulence models for URANS have been developed for specific applications and may generally not be applied to direct gas injection studies. Nevertheless, the turbulence models are extensively used in industry for different applications including direct gas injection. The URANS approach is very dissipative as it adds a high amount of eddy viscosity to the molecular viscosity, and therefore, central difference numerical schemes may remain stable in the presence of shocks. However, a drawback is that the shocks and discontinuities are dissipated quickly and do not survive for longer times.

## 4.2.2 Case Description

Recently, Deshmukh et al. (2018a, b) performed LES of a helium gas jet from a poppet-type injector in a closed chamber to obtain an accurate time-resolved flow field along with turbulent mixing characteristics. This is considered as a case study here to understand physical and numerical aspects in the simulation of gas injection through poppet-type injectors. First, the nozzle flow and near-nozzle gas jet development are discussed, and then, the far-field jet evolution is validated with the experimental data.

**Experimental Data.** Delphi has developed a fourth-generation electromagnetically actuated solenoid injector for DI-CNG applications (Husted et al. 2014). It is an outwardly opening poppet-type injector. A helium gas jet through the injector was characterized experimentally at Delphi. The schematic of the experimental setup is shown in Fig. 4.2. Helium at a pressure of 16 bar and ambient temperature was injected into the ambient air, and the Schlieren imaging technique, which can capture density gradients in a flow field, was used to visualize the temporal evolution of the gas jet. The selection of helium in this study was driven by the consideration that the Schlieren measurement technique requires high gradients in the density field to work well. This study aimed to investigate the fundamental physical processes behind the hollow-cone gas jet formation and the characterization in terms of global parameters.

**Simulation Methods.** The state-of-the-art compressible solver Compressible High-speed Reactive Solver (CHRIS), which is developed by Cascade Technologies Inc., is used for high-fidelity LES (Brès et al. 2012). CHRIS uses an unstructured mesh to solve the compressible Navier–Stokes equations along with scalars in the conservative form using a novel low-dissipation and low-dispersion finite volume method (Khalighi et al. 2011). A third-order total variation diminishing (TVD) Runge–Kutta scheme is used to explicitly solve the equations in time (Shu and Osher 1988). The essentially non-oscillatory (ENO) scheme (Shu and Osher 1988) is used together with a shock detector to capture shocks and discontinuities. Shock detectors based on the normalized flow solution and based on the absolute pressure dilatation are available in CHRIS. The ENO scheme is used in the regions of shocks identified by a shock detector to ensure the stability of the

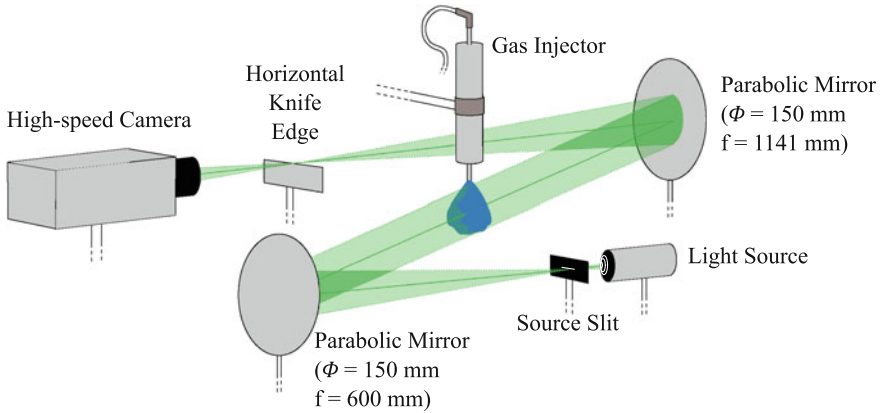


**Fig. 4.2** Schematic of the experimental setup at Delphi

numerical scheme by adding local numerical dissipation. The energy-containing turbulent structures are resolved by the low-dissipation scheme away from the shocks, and sub-filter scales are modeled using the Vreman model (Vreman et al. 1995). The ideal gas (IG) equation of state (EOS) is used to calculate pressure from temperature and density. For detailed governing equations and used parameters, the reader is referred to Deshmukh et al. (2018a).

For URANS simulations, the commercial Computational Fluid Dynamics (CFD) code CONVERGE (version 2.3.9) by Convergent Science Inc. (Richards et al. 2016) is used. CONVERGE is a compressible 3D flow solver, specifically developed for the computation of steady-state or transient flows in complex and moving geometries. In this study, a spatially second-order central difference numerical scheme was selected. A first-order Euler backward scheme is used to solve the equations in time, which results in fully implicit time integration. The pressure is calculated from density and temperature using the Redlich-Kwong (RK) EOS. The system of equations is solved using a modified pressure implicit with splitting operators (PISO) algorithm. For detailed equations and used numerical schemes, the reader is referred to the CONVERGE manual (Richards et al. 2016), whereas for details on parameters used in this study the reader is referred to Deshmukh et al. (2018a).

*Equation of State.* The IG EOS is used in the LES, which is justified because the compressibility factors for the gases involved in the study, namely helium, nitrogen, and oxygen, do not significantly diverge from 1.0 in the relevant operating range (Van Sciver 2012; Jensen et al. 1980). On the other hand, the RK EOS, which follows real gas behavior, is chosen for the URANS simulations. The choice is motivated by the subsequent applicability of the results of the fundamental investigations to full engine simulations. A real gas EOS is required in URANS simulations of a full engine configuration because the in-cylinder pressure during an engine cycle varies in the range, where the real gas effects become significant.

Therefore, the RK EOS is used in the current setup. The compressibility factor of the in-cylinder gas mixture in the engine simulations reported in the next sections varied between 0.98 and 1.004. Nevertheless, the RK EOS should ideally approach the IG EOS under the conditions considered in this study. To verify that, a comparison of the density of helium computed with the IG EOS and RK EOS at injection pressure and ambient pressure for a relevant range of temperatures was performed. The relative error in density is less than 0.025%, which substantiates the presumed convergence of RK EOS toward IG EOS under the conditions relevant to this study.

**Simulation Setup.** A cylindrical domain with a diameter of 75 mm and a height of 82.5 mm, which are typical dimensions for a downsized engine cylinder of a passenger car, is used for the numerical simulations (see Fig. 4.3a). The injector is placed at the top, on the axis of this cylinder, but is not shown here. The meshes used in the simulations are shown on a representative plane ( $Y = 0.0$ ) through the domain.

The ANSYS Meshing software (ANSYS<sup>®</sup> Meshing 2013) is used to generate a hybrid mesh, which comprises stretched prism layers attached to the walls and hexagonal cells away from the walls. The hybrid mesh is used for LES and contains approximately 24 million cells. The mesh inside the injector nozzle contains 5 stretched prism layers with a stretching factor of 1.2 on each side at the wall and 10–20 hexagonal cells across the gaps between the prism layers. A highly refined mesh is generated near the nozzle exit, and the mesh size is gradually increased in a concentric manner away from the nozzle, which helps to capture the shocks and pressure waves traveling concentrically outward from the injector nozzle. The minimum and maximum cell sizes of hexagonal cells in the domain are approximately 18.75 and 600  $\mu\text{m}$ , respectively. The resulting downstream mesh is shown in Fig. 4.3b.

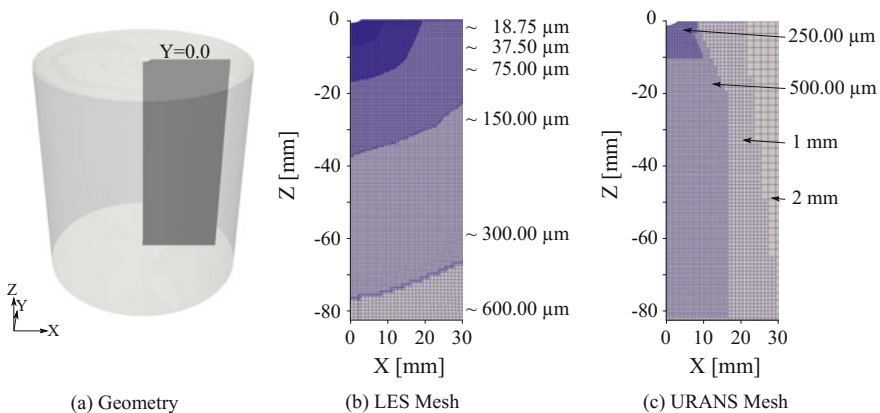


**Fig. 4.3** Computational domain and mesh for LES and URANS simulations depicted on a representative plane

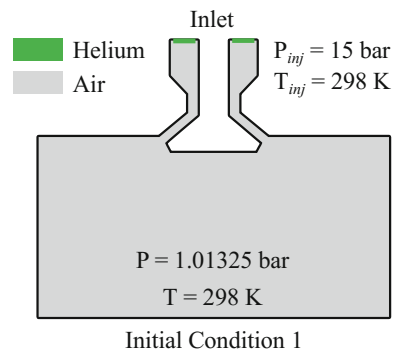
The mesh resolution study by Bartolucci et al. (2016) suggested the use of highly refined meshes for the gas jet URANS simulations. However, the computational costs for such resolutions can be intractable for practical engine simulations. Therefore, the mesh size in the URANS simulations is chosen such that it is directly applicable in the subsequent engine simulations. CONVERGE generates a Cartesian cut-cell mesh at run-time. The base size for the mesh is set to 2 mm. The near-nozzle and upstream region are refined using several successive embedded regions, which results in the smallest cell size of  $64.5 \mu\text{m}$  within the nozzle gaps (not shown here). CONVERGE has an adaptive mesh refinement (AMR) capability. However, for comparison with LES, which has a fixed mesh, the AMR is switched off in all URANS. The resulting mesh (see Fig. 4.3c) is used in all URANS simulations in this study.

A Courant–Friedrichs–Lewy (CFL) number of 1.0 is set in the LES, which is the limit for the used explicit third-order TVD Runge–Kutta scheme. In the URANS, an implicit solver is available, which allows a CFL of 2.0 to speed up the simulations. The results with a CFL of 1.0 in the URANS were not significantly different.

*Initial Conditions.* The initial conditions in the computational domain are shown schematically in Fig. 4.4. The injector needle is set in an open position with the needle lift of  $300 \mu\text{m}$ , which is fixed throughout the simulation and is less than the maximum lift of  $350 \mu\text{m}$ . The resulting mass flow rate in the LES is close to the measured mass flow ( $\sim 3.5 \text{ g/s}$ ) of helium through the injector. Initially, the domain is filled with air (77%  $\text{N}_2$  and 23%  $\text{O}_2$  by mass) at a pressure of 1.01325 bar and a temperature of 298 K, which is referred to as initial condition 1 (or briefly as IC1). The region is set to zero velocity.

*Boundary Conditions.* A total pressure of 15 bar, temperature of 298 K, and helium mass fraction of 1.0 are set at the inlet of the nozzle for all simulations. Remaining boundaries are treated as adiabatic, no-slip walls. Some differences between the simulation and experimental conditions must be noted; e.g., the injection pressure in experiments was maintained at 16 bar, although the predetermined operating pressure is 15 bar, which was used in simulations. Despite differences in the injection pressure and the needle lift, the mass flow rate in the simulations is slightly

**Fig. 4.4** Schematic diagram of initial condition 1





higher than the measured mass flow rate. The second difference is that the measurements were carried out in open ambient conditions, whereas the simulations were performed in a closed chamber. However, it has been shown that due to the short duration of injection of 700  $\mu\text{s}$ , these differences have insignificant effects on the intended study and conclusions (Deshmukh et al. 2018a).

The duration of injection (DOI) is fixed to 700  $\mu\text{s}$  for all simulations. During the injection period, the gas jet reaches close to the opposite boundary of the computational domain. Detailed qualitative and quantitative analyses of the nozzle flow, near-nozzle, and far-field gas jet are carried out using the data generated in LES and URANS simulations.

### 4.2.3 Nozzle Flow

The nozzle flow is one of the most critical processes of gas injection because the pressurized gas undergoes expansion in the nozzle and accelerates to supersonic speeds depending on the geometry of the nozzle. The geometry of the nozzle and the pressure ratio essentially determine the flow conditions at the nozzle exit. Further gas jet evolution depends on the flow properties at the nozzle exit. In the poppet-type injector nozzle, the gas passages frequently change the direction of the flow. Also, the gas flow, in general, encounters the converging and diverging sections (see Fig. 4.5). Such a geometric configuration with the higher than critical pressure ratio across the nozzle drives the gas flow to first sonic speeds and then to supersonic speeds. Because of changing direction, a boundary layer separation occurs within and at the exit of the nozzle and recirculation regions form. To capture these viscous effects, a no-slip boundary condition is applied at the nozzle walls. A schematic diagram of the nozzle flow and the initial development of the helium gas jet are shown in Fig. 4.5. To analyze the nozzle flow, five locations are chosen considering the axisymmetric geometry of the nozzle. These are location 1, which is near the inlet, location 2 in the converging section, location 3 approximately located at the throat, and location 4 corresponding to the nozzle exit, and the centerline of the nozzle gap.

Considering the geometrical symmetry about the axis and steady-state condition of the flow in the nozzle, a combined azimuthal and time-averaging (Farrace et al. 2015) is used to compute the averaged velocity profiles, and the statistical information is obtained. For the statistical independence of the samples in space and time, the integral length and timescales are estimated carefully (Deshmukh et al. 2018b), which resulted in the azimuthal angle of  $30^\circ$  with 12 planes for spatial averaging and a sampling frequency of 67 kHz for time-averaging. A total of 492 individual samples are used to obtain the averaged velocity profiles in the nozzle at different locations after a steady-state flow condition is reached. The resulting averaged velocity profiles and the individual samples are shown in Fig. 4.6. The symbols are an indicator of the mesh density at the given location. Close to the nozzle inlet, i.e., the location 1, the W-velocity shows a flat averaged velocity

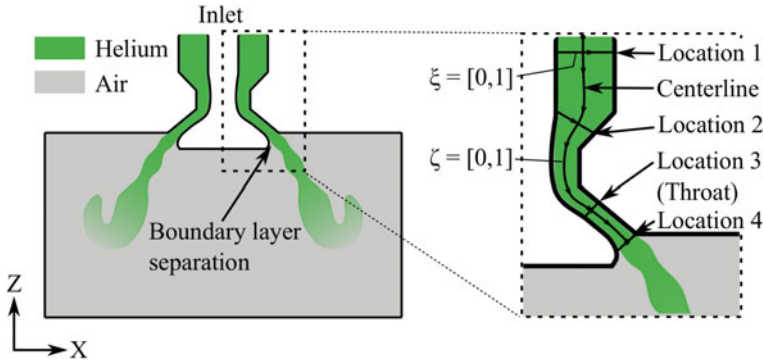


**Fig. 4.5** Schematic diagram for the analysis of nozzle flow

profile, whereas the other two components are almost zero. At location 2, substantial variation can be observed on the right boundary, which is because the flow speed increases in the converging section and the direction also changes, resulting in a recirculation region in the corner. At location 3, which is almost the throat section, the velocities reach sonic levels and further accelerate to supersonic levels as the gas passages diverge after the throat. A boundary layer separation occurs at location 4 as the boundaries diverge further near the exit, which can be seen in the velocity profiles. The flow separation on the poppet boundary causes the formation of a recirculating region resulting in highly varying velocity profiles.

The resolved turbulent kinetic energy (TKE) can be estimated from the individual velocity profiles at four locations. Figure 4.7 shows the resolved TKE at four locations with multiplying factors to visualize all plots on the same scale. As expected, the locations with high variability, i.e., location 2 and location 4, show high TKE near the boundaries. The local bulk Reynolds number and  $y^+$  at the first cell are calculated at the chosen locations. Maximum Reynolds number of 20,400 and maximum  $y^+$  value of 21 are observed at location 3, which is expected because the bulk velocities are high. At location 4, the  $y^+$  value is  $\sim 7$  and the Reynolds number is 16,211, which is lower due to reduced density and reduced bulk velocity as a result of flow separation.

The averaged steady-state profiles of Mach number, pressure, temperature, and density on the centerline of the nozzle passage are depicted in Fig. 4.8. As the nozzle passage acts as a converging–diverging nozzle, the gas accelerates to supersonic velocities with Mach numbers higher than 2.0 close to nozzle exit. After the throat, the continuously changing direction of the flow leads to an isentropic expansion fan on the poppet boundary and a nearly isentropic compression shock on the outer boundary. The compression shock is visible near the nozzle exit. Temperature and density decrease continuously along the centerline of the nozzle passage and increase at the compression shock but are still below the ambient conditions. The pressure at the nozzle exit is higher than the ambient pressure, which causes further expansion of the gas to the ambient conditions. Overall, the nozzle operates under moderately under-expanded conditions.

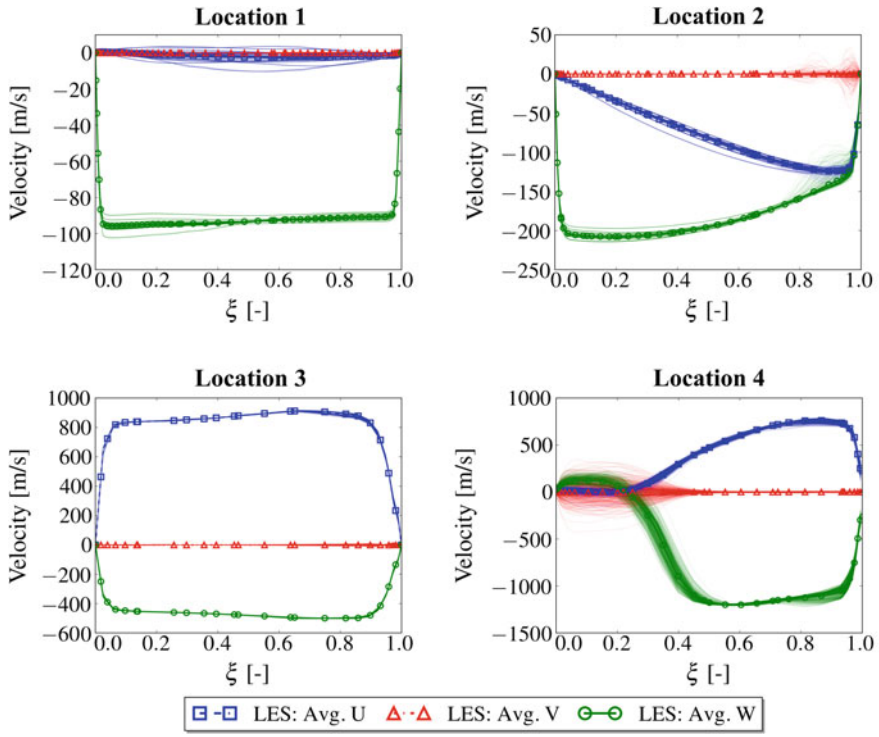


**Fig. 4.6** Steady-state velocity profiles at four chosen locations in the nozzle (*thin lines: individual profiles; thick lines: averaged profiles*)

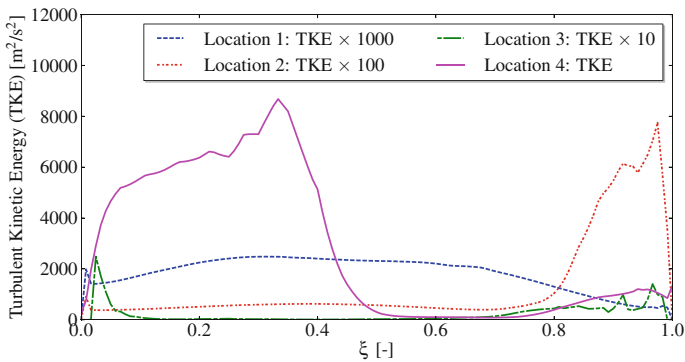


**Fig. 4.7** Resolved turbulent kinetic energy at four chosen locations in the nozzle

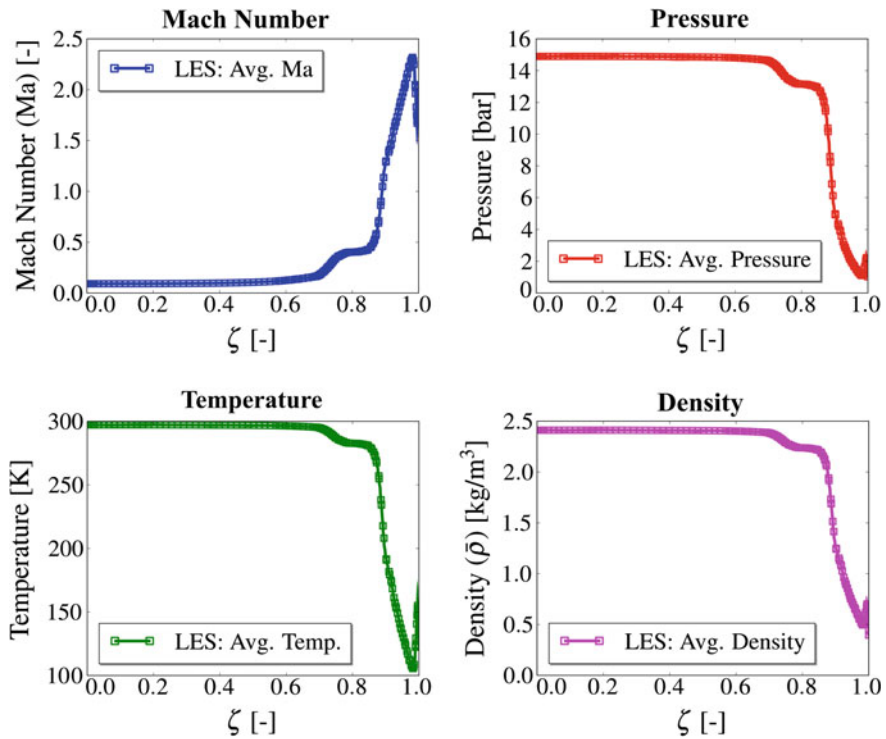


**Fig. 4.8** Averaged steady-state profiles of Mach number, pressure, temperature, and density on the centerline inside the nozzle (*inlet*:  $\zeta = 0.0$ ; *exit*:  $\zeta = 1.0$ )

#### 4.2.4 Near-Nozzle Gas Jet

The gas leaves the nozzle with supersonic velocity through the annular nozzle exit. Figure 4.9 shows a section through the domain at  $Y = 0.0$  depicting the very early phases of the development of the gas jets through contours of Mach number. The bow shocks can be seen clearly in the first frame. The annular bow shocks merge to form a complex interaction of waves behind the shock. The Mach disk and shock cells in the annular shape begin to form as a part of the hollow cone. The reflected shocks keep the hollow cone intact. Instabilities develop further downstream due to shear between helium and air, resulting in the formation of vortical structures similar to those in the wake of a bluff body. The initial bow shocks also interact with the gas jets during the early development phase, destabilizing them. The near-nozzle flow reaches steady state within  $60 \mu\text{s}$ .

Similar to the nozzle flow, a statistical characterization of near-nozzle jet formation can be performed. The near-nozzle jet statistics are computed using the combined azimuthal and time-averaging procedure described previously. The averaged steady-state velocity magnitude and the standard deviation for the jet are

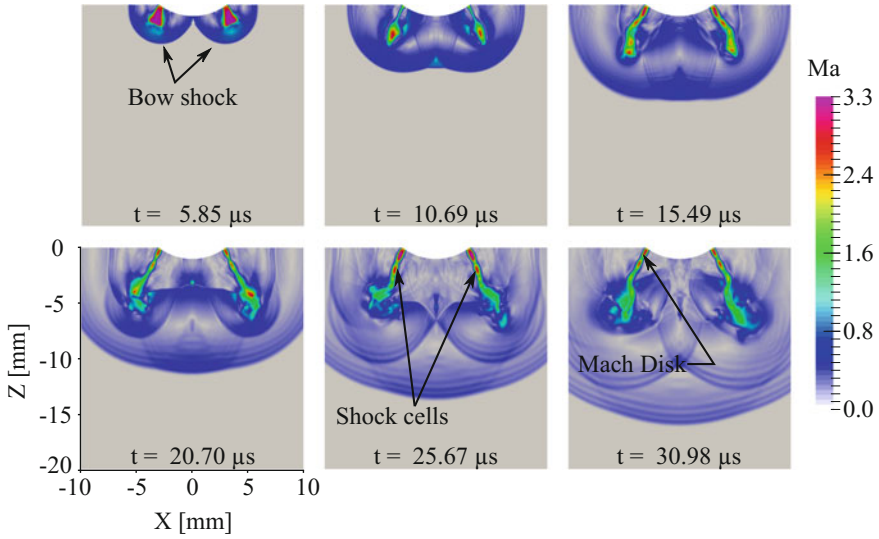


**Fig. 4.9** Initial development of the gas jet in terms of Mach number close to the nozzle exit and classical features of supersonic jets (*LES: Y = 0.0 plane*)

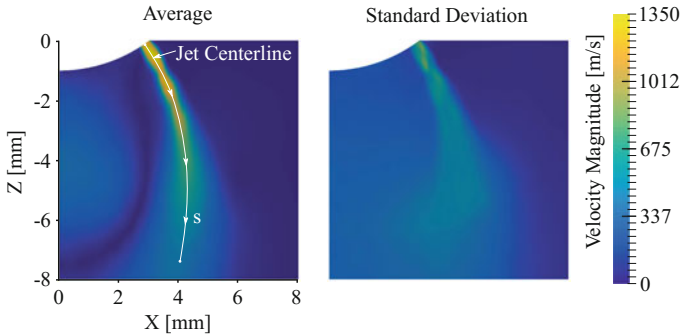


**Fig. 4.10** Near-nozzle steady-state averaged velocity magnitude and standard deviation in the LES

shown in Fig. 4.10. The near-nozzle mesh resolution used in this study cannot sharply resolve the typical structures of the supersonic gas jets. However, the formation of shock cells can be observed. As the pressure in the region below the poppet is low, the jet bends toward the axis of the injector. A highly fluctuating flow field near the nozzle results in the high standard deviation, particularly in the jet core near the nozzle exit. Nevertheless, the jet core mostly remains intact within the shock cells. The mixing of helium begins at the edges of the jet core, and mixing layers form on the inner edge and the outer edge (see Fig. 4.11). The thickness of both mixing layers gradually increases, and the two layers merge away from the

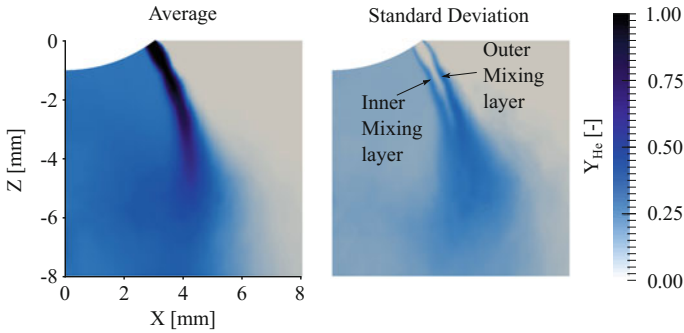


**Fig. 4.11** Near-nozzle steady-state helium mass fraction and standard deviation in the LES

nozzle exit. The helium–air mixture moves into the low-pressure region below the poppet, eventually increasing the helium concentration there.

The averaged steady-state profiles of different flow variables are plotted along the jet centerline in Fig. 4.12 along with the standard deviation ( $\sigma$ ) about the mean. The distance along the jet centerline is non-dimensionalized with the needle lift ( $L = 300 \mu\text{m}$ ) as a characteristic length scale. The average Mach number at the nozzle exit is approximately 2.0, and the average pressure is slightly above ambient. The helium expands into the ambient air, the average pressure drops, and the average Mach number increases up to  $\sim 2.6$ . After that, the pressure recovers and exceeds ambient pressure, and the Mach number drops. The cycle repeats until a distance of  $\sim 12$  times the needle lift. After initial fluctuations in the shock cells, the temperature remains stable at  $\sim 200 \text{ K}$  before the average Mach number drops below 1.0. Thereafter, the temperature begins recovering toward ambient conditions. The standard deviations of Mach number and pressure do not change significantly, although the absolute values are quite high. On the other hand, the standard deviation of density increases continuously, indicating mixing of helium with air, and the standard deviation of temperature first increases and begins decreasing after a distance of  $\sim 12$  times the needle lift. The average temperature in the near-nozzle gas jet is very low compared to ambient conditions.

### 4.2.5 Far-Field Gas Jet Evolution

The far-field gas jet development was analyzed using both experimental measurements and simulation data. The top row in Fig. 4.13 shows the visualization from the Schlieren experiments, while an isosurface corresponding to helium mass fraction of 0.003 from the LES is shown in the bottom row for the same instants as those of the experiments for direct comparison. The time shown here is relative to the instant when the gas jet first emerges from the injector.

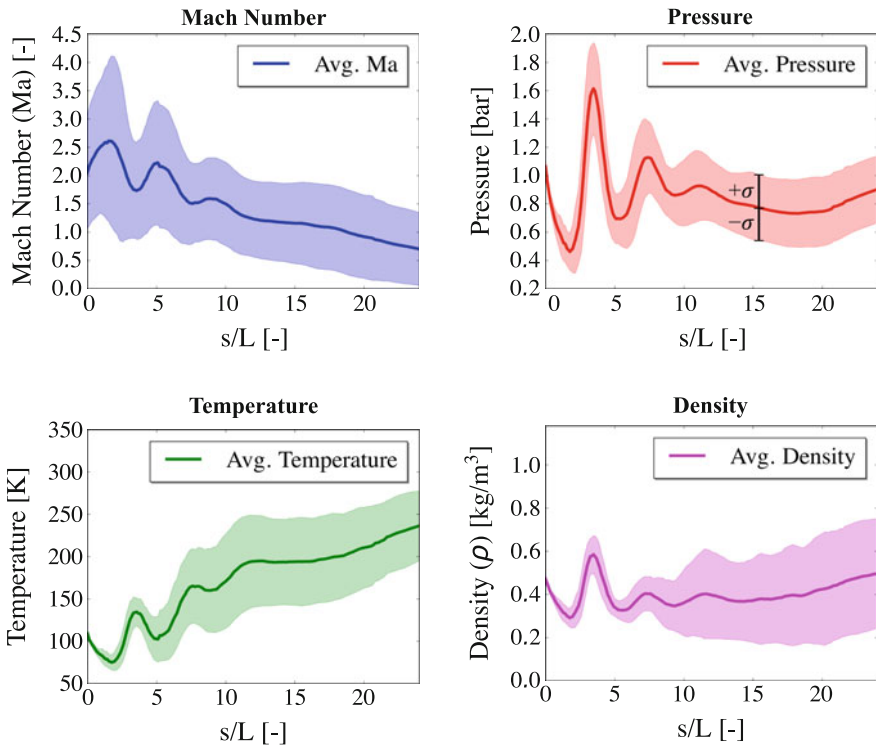


**Fig. 4.12** Near-nozzle steady-state profiles of Mach number, pressure, temperature, and density along the centerline of the gas jet

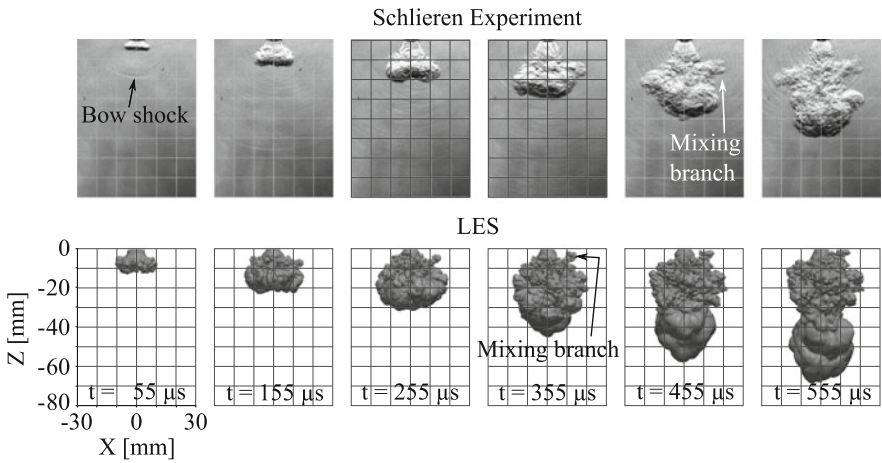


**Fig. 4.13** Comparison of the temporal development of the gas jet in Schlieren experiment (top row) and LES (bottom row: isosurface of  $Y_{\text{He}} = 0.003$ )

The initial bow shock is visible in the first and second Schlieren frame, and the pressure waves emitted from the jet are seen in the later frames. The gas jet continuously mixes with the ambient gas forming a cloud-like structure. A similar development can also be observed in the corresponding LES time frames. The range of length scales of the flow features observed in the experiments is qualitatively represented in the LES. The mixing branches of the gas jet moving in the transverse direction can be found in the experiment as well as the LES. The gas jet penetration in the experiments is shorter than in the LES. The reasons for the overprediction are the assumption of a fixed needle lift in the simulations and will be discussed later. However, a detailed view of the near-nozzle flow features is not available in the experimental data presented here.

From the simulation data, information on the mixing of the gas jet with surrounding gas can be obtained. For example, Fig. 4.14 shows the contours of the helium mass fraction at different time instants. As the gas jet develops, a hollow cone is formed initially. The high-speed gas flow entrains the surrounding gas, both from inside and from outside of the cone, which causes a pressure drop inside the cone below the poppet leading to the collapse of the hollow cone and formation of the single gas jet. It is possible to detect the collapsing event by monitoring the pressure below the poppet during the injection. The instantaneous pressure as shown in Fig. 4.15 is highly fluctuating, and a clear trend is not visible. Therefore, it is filtered to remove high-frequency oscillations. The filtered pressure values decrease after  $\sim 255 \mu\text{s}$  and fluctuate around lower levels when the hollow cone collapses.

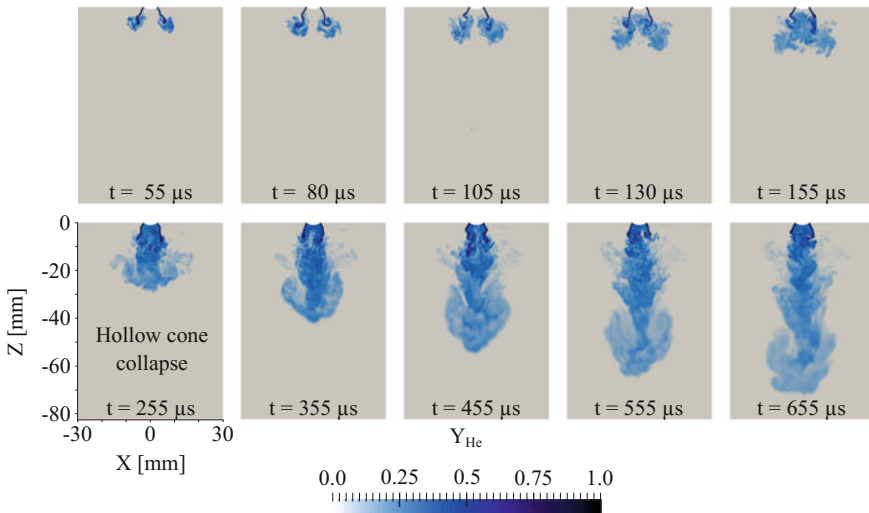


**Fig. 4.14** Development of the gas jet and mixing behavior as observed in  $Y = 0$  plane



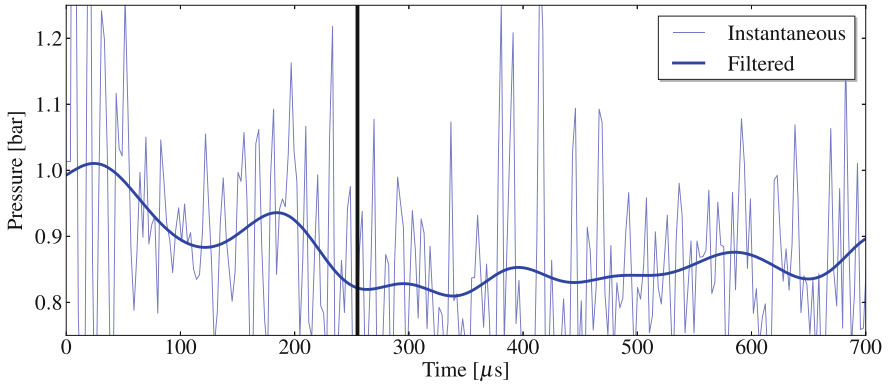


**Fig. 4.15** Pressure monitor below the poppet in LES; vertical black line  $t = 255 \mu\text{s}$  denotes the time of hollow-cone collapse

The far-field gas jet development and mixing can be characterized quantitatively in terms of different parameters, which are commonly used in the literature for liquid or gaseous fuel jets. These are:

- Axial penetration length (APL)
- Maximum width (MW)
- Area of the jet (AJ)
- Volume of the jet (VJ)
- Mass-weighted probability density function (PDF) of helium mass fraction within the volume of jet

Some of the parameters, such as axial penetration length, maximum width, and area of the jet, can be obtained from the experimental data, which are Schlieren images in this case. The Schlieren images are first converted into a binary image as shown in Fig. 4.16a ( $t = 455 \mu\text{s}$ ) using common image processing techniques. On the other hand, the simulations can provide information on additional parameters such as the volume of the jet and mixing statistics (see Fig. 4.16b, c, d) and help in gaining further insights into the mixture formation. The axial penetration length and maximum width provide spatial extents of the gas jet within the domain, while the area of the jet and the volume of the jet can be an indicator of the amount of entrainment of ambient gas. The mixing statistics determine the mixture quality and can establish the flammability limits of the mixture in a typical partially premixed combustion case. To compute the mixing statistics, one can either use normalized cumulative volume fraction plotted versus equivalence ratio (Sukumaran 2010) or compute mass-weighted PDF of the mass fraction of the injected gas within the jet volume (Vuorinen et al. 2014). The first method is preferable for full engine cases as the volume is fixed by walls of the combustion chamber, while the second method is appropriate for the free gas jets.

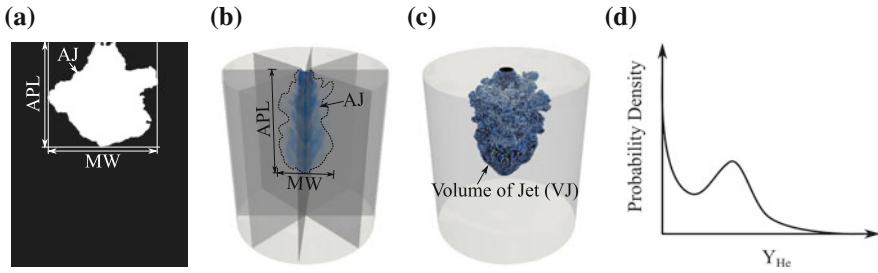


**Fig. 4.16** Methods of calculation of characterizing parameters from experiments (a) and simulations (b, c, d)

In the simulations, the characterizing parameters are computed from the computational domain using a threshold for the mass fraction of helium. The threshold value is selected based on the convergence of the parameters. In this study, the threshold value of 0.001 was found to be sufficient (Deshmukh et al. 2018a). The volume of the jet is computed by adding all cell volumes with helium mass fraction above the chosen threshold. The length of the bounding box of the jet volume along the axis of the jet constitutes the axial penetration length. The lateral penetration of the gas jet is different in different directions, and thus, the maximum width and the area of the jet depend on the plane of computation. Therefore, in this study, 24 planes with an angle of  $7.5^\circ$  between each other are selected passing through the axis of the cylindrical domain to calculate the maximum width and the area of the jet. As a result, a range of values is obtained for these parameters at a particular instant in time. It is important to note that different path lengths in the transverse direction are not the effect of directional sensitivity to the underlying Cartesian mesh. The mass-weighted PDF of helium mass fraction is computed from the volume of the jet. The statistical information such as mean, standard deviation, and skewness can be calculated from the PDF over time.

Figure 4.17 shows the comparison of all quantitative parameters from the LES with some of the available measured values. The axial penetration length is over-predicted in the simulations, although the slope of the line matches at later times. A nonlinear behavior is predicted in the initial phases of the jet development, which results in higher axial penetration in the beginning. Similar nonlinear behavior was observed in the experimental studies of the hollow-cone gas jets by Kuensch et al. (2014), and a 0.8 power law of the axial penetration length was fitted to the data. In this study, two-stage power laws are observed before and after the collapse of the hollow cone. The slight depression in the axial penetration plot shows the collapsing events consistent with the previous observations. A 0.65 power law is observed during the initial development phases when the hollow cone remains intact, whereas later a 0.8 power law fits well. For the maximum width, a range of values is obtained as discussed before. The range widens as the jet develops and can be as large as 15 mm away from the nozzle. While Kuensch et al. (2014) found a 0.2 power law of the maximum width, in this study, two-stage power laws are

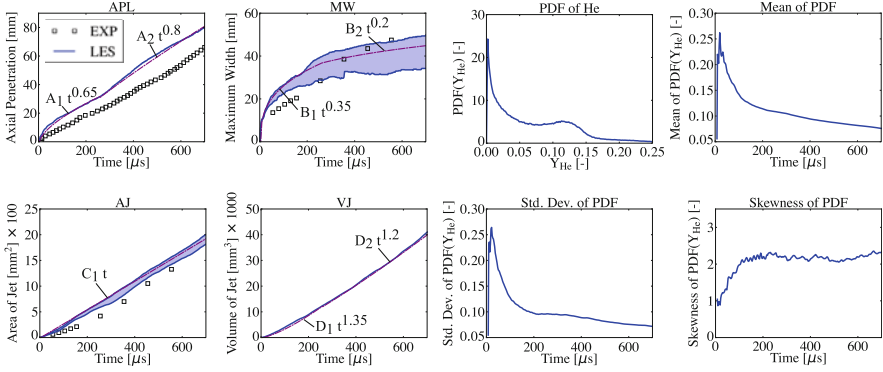


**Fig. 4.17** Comparison of characterizing parameters between experiment and LES

observed with an initial 0.35 power law behavior and 0.2 power law after the collapsing event. The area of the jet increases linearly with time, which is also consistent with the product of power laws of the axial penetration length and the maximum width. In summary, this leads to

$$AJ \sim APL_{1,2} \cdot MW_{1,2} = C_1 t \quad (4.1)$$

$$VJ_1 \sim APL_1 \cdot MW_1 \cdot MW_1 = D_1 t^{1.35} \quad (4.2)$$

$$VJ_2 \sim APL_2 \cdot MW_2 \cdot MW_2 = D_2 t^{1.2} \quad (4.3)$$

The subscripts, 1 and 2, denote the first and the second stage of the jet evolution, respectively. The jet volume increases continuously as the jet entrains ambient gas into the jet volume. The product of the power laws of the maximum width and the axial penetration (Eqs. 4.2 and 4.3) follow the LES predictions quite well. These scaling laws can be used for getting the first estimates of the probable gas jet behavior. However, the constants of proportionality must be known beforehand. The mass-weighted PDF of the helium mass fraction at  $t = 700 \mu\text{s}$  is also shown in Fig. 4.17. The probability of finding no helium anywhere in the jet volume is zero because the jet volume is obtained with the chosen threshold of 0.001 for helium mass fraction ( $Y_{\text{He}}$ ). A bimodal PDF can be observed. The statistics of the PDF, mean, standard deviation, and skewness provide information on the quality of the mixture. These are plotted for the duration of the simulation. The mean values are the indicators of the average helium mass fraction within the jet volume. The mean of the PDF increases to a peak value very quickly after the start of injection (SOI) indicating a very rich mixture. As more and more ambient air is entrained and mixed with helium, the mean value decreases nonlinearly. The standard deviation quantifies the degree of mixing. Higher standard deviation indicates less homogeneous mixture and vice versa. The standard deviation of the PDF shows a similar trend to that of the mean and is of the same order, implying a high degree of

inhomogeneities in the mixture. The third standardized moment of the PDF, skewness, is the indicator of pockets of lean or rich mixture. Positive values show the presence of pockets of rich mixture, while negative values show the presence of lean regions in the jet volume. Here, the skewness of the PDF is very high initially and positive, which drops quickly and again increases gradually. Initial large positive values are expected because the mixing of helium has not started yet. With the progress of mixing, the skewness drops. The gradual increase of the skewness indicates the increasing presence of unmixed rich regions of helium.

Overall, the macroscopic characteristics such as the axial penetration, the maximum width, and the collapsing event of the hollow cone can be reasonably predicted by the LES with the used mesh resolution. The LES was run on 1024 cores for 131 h, which is quite expensive for such a short duration of injection. Therefore, the potential reasons for the discrepancies between experiment and simulation are investigated using a computationally less expensive URANS approach. However, URANS requires modeling of energy-containing turbulent scales, and several turbulence models have been developed for different applications. Some of them have become a standard in industrial simulations, e.g., RNG  $k-\varepsilon$ , realizable  $k-\varepsilon$ , and SST  $k-\omega$ . Before applying these in the simulations of the gas injection, these turbulence models are evaluated in terms of macroscopic characteristics against the LES, which relies on the Vreman model for the sub-filter eddy viscosity.

#### 4.2.6 Choice of Turbulence Model

The RNG  $k-\varepsilon$  model has been developed from the Navier–Stokes equations through the renormalization group (RNG) theory (Yakhot and Orszag 1986). The renormalization group method is based on statistical averaging of fluctuations on all scales, ranging from the smallest scale to successively larger scales, which is particularly appropriate for the description of turbulence involving a wide range of scales (Wilson 1983). Therefore, the effects of different length scales on turbulent diffusion are intrinsically modeled by the RNG  $k-\varepsilon$  model. Also, the model constants are deduced analytically. The realizable  $k-\varepsilon$  model ensures physically realistic values of the turbulent kinetic energy by constraining the positivity of normal Reynolds stresses and obeying the Schwarz’s inequality for turbulent shear stresses (Shih et al. 1995). The realizable  $k-\varepsilon$  model performs well for rotational flows. The shear stress transport (SST)  $k-\omega$  model by Menter (1994) is the combination of the standard  $k-\varepsilon$  model and the standard  $k-\omega$  model, which has the benefits of both models. The standard  $k-\omega$  model is advantageous for boundary layer flows and modeling of the near-wall viscous regions. A blending function is used, which is zero close to walls, activating the  $k-\omega$  model, and unity away from walls, leading to the  $k-\varepsilon$  model. The effects of high-pressure gradients are also considered for calculating the eddy viscosity. The SST  $k-\omega$  model is well suited for external flows, such as in aerodynamic applications. Nevertheless, it is investigated in this study

because high-pressure gradients and flow separation occur near the exit of the nozzle.

The initial and boundary conditions for the URANS simulations are maintained as in the LES for a direct comparison. The temporal jet evolution is investigated with the turbulence models. A quantitative analysis of the performance of URANS models is made and compared with the LES (see Fig. 4.18). The experimental values are plotted for reference. Compared to the LES, all turbulence models used here predict the initial axial penetration length reasonably, although the collapsing instant as indicated by the depression in the plots is slightly delayed. The maximum width is predicted well; however, the range of values is smaller at later times. More substantial differences between the turbulence models can be observed in the area of the jet and are more prominent in the volume of the jet. Comparing the volume of the jet, the RNG  $k-\varepsilon$  model is the closest to the LES, which is very important for mixing as the amount of entrained ambient air affects the mixture quality. This is reflected in the mean of the PDF of  $Y_{He}$ , which is lower for all turbulence models compared to the LES due to a higher amount of air entrainment. Again, the RNG  $k-\varepsilon$  model comes closer to the LES. The standard deviation shows a distinct bump in the URANS results, which is the effect of the hollow-cone collapse. The skewness of the PDFs shows a similar trend in the URANS compared to the LES. However, the development of the trend is delayed, and the absolute values are high with all turbulence models, which implies a high probability of finding rich helium regions in the jet volume. It can be distinctly observed that the mixing statistics, in general, can be entirely different although other global characteristics are very similar. Based on the overall performance with respect to macroscopic characteristics on the typical mesh resolutions used in the full engine simulations, the RNG  $k-\varepsilon$  model can be a good choice compared to the other two models considered here and is chosen for further URANS simulations in this study.

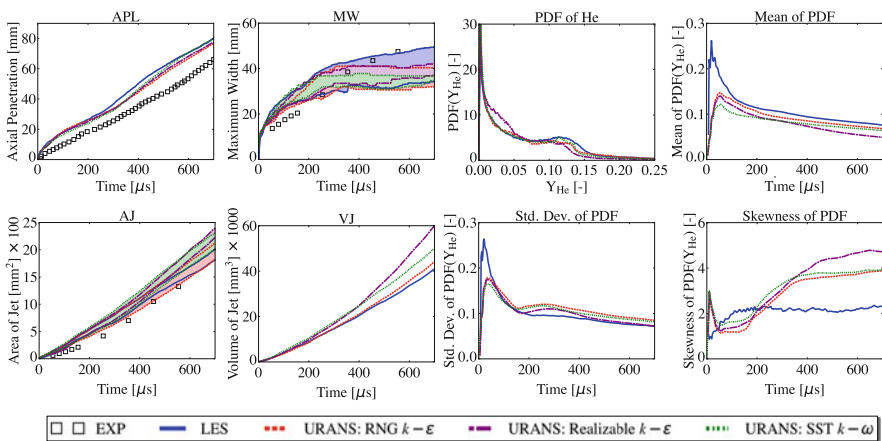


**Fig. 4.18** Comparison of characterizing parameters obtained with different URANS turbulence models and LES

### 4.2.7 Needle Motion and Initial Conditions

The initial nonlinear behavior of the temporal gas jet development observed in the LES caused an overprediction of the axial penetration. In the LES, the needle lift is fixed resulting in a higher mass flow rate from the beginning. In practice, the needle does not open instantly. There is always a delay in opening; depending on the type of injector used, the opening can be very fast as in piezoelectric injectors, or it can be relatively slow as in solenoid injectors. Since the injector in this study is of the solenoid type, the opening profile is expected to be gradual. The needle lift profile is shown in Fig. 4.19a, where the opening delay is  $\sim 100 \mu\text{s}$ . Initially, the needle is in a closed position, and the domain is divided into two regions: a high-pressure upstream region with helium at a pressure of 15 bar and a temperature of 298 K and a low-pressure downstream region. A second initial condition (IC2) for the fixed needle case (keeping the same needle lift) is also considered in this study because it is more similar to the initial conditions in the injector with a closed needle. The domain is divided into two regions at the valve seat location as shown in Fig. 4.19b. The IC2 mimics the sudden opening of the needle.

URANS simulations with the needle lift profile are carried out, and as expected, the linear behavior in the initial stages of the gas jet development is reproduced well by the simulation with needle motion (see Fig. 4.20). However, the plot diverges from the experimental values after  $400 \mu\text{s}$ , probably due to the collapse of the hollow cone. To investigate the deviation, the pressure below the poppet is monitored and plotted in Fig. 4.21. The collapsing event in the simulation with needle lift is delayed significantly, causing more than 50% decrease in the axial penetration length compared to the fixed needle simulations with IC1. In contrast to this study, Kuensch et al. (2014) reported a nonlinear behavior of the axial penetration in the experiments with the hollow-cone injector. However, a piezoelectric injector was used in their investigations, which is very fast compared to the solenoid-actuated Delphi injector. Therefore, for piezoelectric injectors, it may be concluded that the

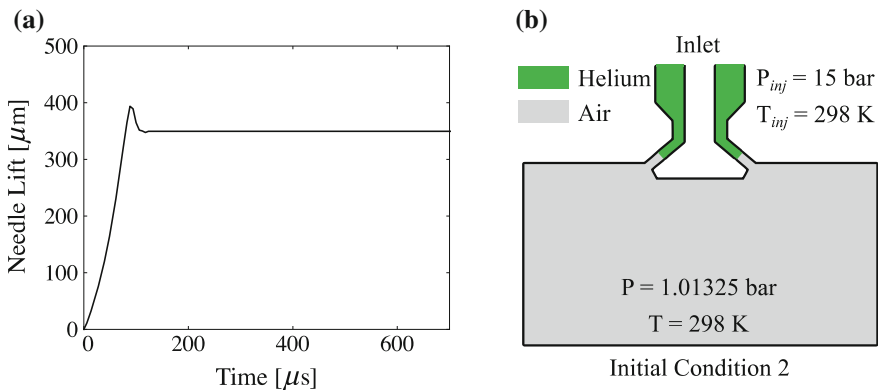


**Fig. 4.19** Needle lift profile (a) and initial condition 2 (b) in the nozzle

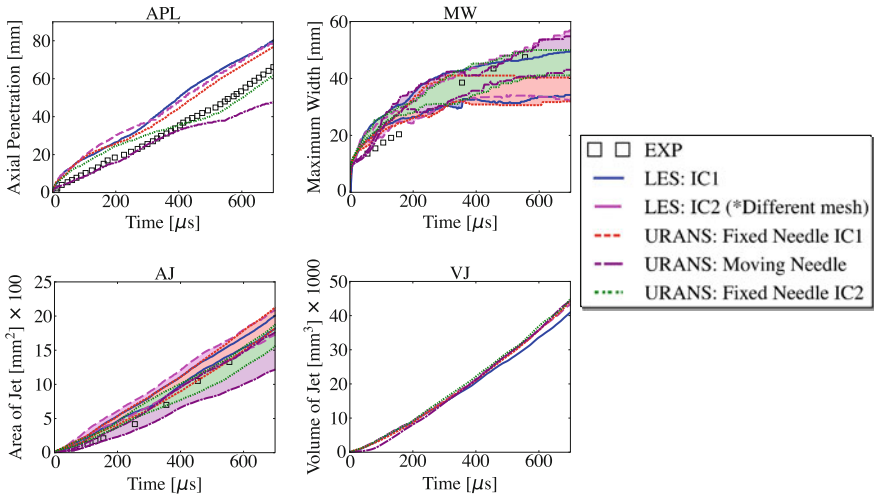


**Fig. 4.20** Effect of initial conditions and the needle motion on the characterizing parameters

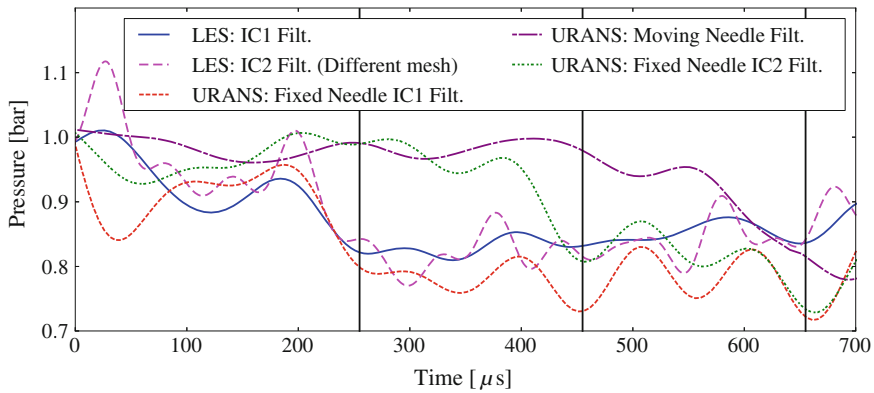


**Fig. 4.21** Pressure monitor below the poppet: vertical black lines  $t = 255 \mu\text{s}$ ,  $t = 455 \mu\text{s}$ ,  $t = 655 \mu\text{s}$  indicate the event of hollow-cone collapse for respective cases

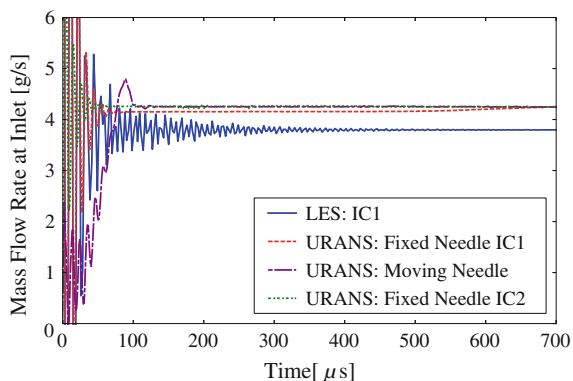
needle motion may not be important for prediction of the initial phase of the gas jet development. The second initial condition, IC2, was tested using URANS and LES with a mesh resolution lower than used before. The URANS simulations with IC2 predict the initial nonlinear behavior similar to that observed with IC1. However, as the hollow-cone collapse is delayed (see Fig. 4.21), the axial penetration drops. After the collapse, the single coherent gas jet follows a linear increase in the axial direction. The maximum width and the area of the jet closely follow the experimentally measured values for the case with needle motion and fixed needle with IC2. For the moving needle case, the volume of the jet increases slowly but later

converges to the other URANS cases, indicating similar air entrainment for all URANS cases. To verify the effect of initial conditions on the collapsing behavior of the jet, an LES with IC2 is performed. However, a lower mesh resolution was used in this case to keep the computational costs lower. In contrast to the corresponding URANS case, the LES with IC2 shows a very similar axial penetration to that with IC1, and the collapsing event is only slightly delayed.

The needle motion and initial conditions influence the mass flow rate through the nozzle during the initial phases. The mass flow rate at the inlet of the nozzle for different cases is shown in Fig. 4.22. The shock/pressure waves propagating inside the nozzle and their reflections from the complex internal geometry cause the initial fluctuations. The waves survive for long times in the LES due to low-dissipation numerical schemes and dissipate quickly in the URANS simulations. The viscous boundary layer flow is resolved better in the LES using a high-resolution stretched grid near the walls, whereas the near-wall velocities are modeled with log law in the URANS simulations with a coarse cut-cell Cartesian grid. Therefore, the values of the mass flow rate in the LES are lower than those in the URANS simulations. Initially, the mass flow rate in the URANS simulation with initial condition IC1 is marginally lower but later merges with the mass flow rates for the cases with needle motion and initial condition IC2.

The consideration of the needle motion is crucial for accurate resolved simulations of the poppet-type gas injectors, particularly for solenoid-actuated injectors. For piezoelectrically actuated poppet-type injectors, the fixed needle approach may be sufficient. The initial conditions in the nozzle are important for the further development of the gas jet. With the chosen mesh resolution and turbulence model, the URANS simulations showed sensitivity to different initial conditions, whereas the LES did not predict such distinction. The URANS computations required 8–25 h on 24 cores, which is less by, at least, a factor of 200 compared to the LES. Further investigations using high-fidelity LES with a moving needle are necessary to identify the reasons for the discrepancies with respect to the experiments. Moreover, the sensitivities of the URANS approach to the initial conditions in the nozzle need to be examined.

**Fig. 4.22** Mass flow rate at the inlet in LES and URANS with different initial conditions and the needle motion





## 4.3 Modeling of Poppet-Type Gas Injectors

### 4.3.1 *Challenges in Numerical Simulations*

Resolved simulations of the poppet-type gas injectors have already been described as challenging and computationally very expensive mainly because of different length and timescales present inside the injector and the cylinder. Therefore, it is important to reduce the simulation run-time to be able to use numerical simulations in the engine design process that motivates the splitting of the full simulation considering it as a multi-scale problem and development of simplified models for the process with smaller timescales. There have been a few attempts in the literature for the development of such models. A computational model was developed for a cylindrical orifice by Johnson et al. (1995) for hydrogen gas injection and combustion. The model was based on the inflow conditions calculated from choked nozzle flow dynamics. The model replaced the nozzle flow dynamics and reduced the run-time of the full simulation by a factor of 10. Another model for high-speed jets was developed by Mather and Reitz (2000), which was based on compressible under-expanded nozzle flow with a barrel shock and a Mach disk. Sonic flow was assumed at the Mach disk, and the diameter of the Mach disk (called equivalent diameter) was calculated from the nozzle exit pressure and ambient gas pressure. The jet exit velocity and density were obtained from an isentropic expansion process and used as the inflow boundary condition. The jet penetration was found to be dependent on the momentum injection rate by Ouellette and Hill (1999). They proposed to simply impose momentum as a boundary condition at the nozzle exit. Most models were developed for cylindrical orifices, while the modeling efforts for the poppet-type outwardly opening design have been relatively scarce due to the more complex geometry. Some of the models are described in the following sections.

### 4.3.2 *Converging–Diverging Nozzle Approximation*

Considering the similarity between high-speed round jets and the resulting single gas jet from a shrouded poppet-type valve, Kim et al. (2007) proposed to use a simplified converging–diverging nozzle design. The throat area of the simplified nozzle and modified injection pressure were obtained using quasi-one-dimensional isentropic flow relations from the downstream characteristic Mach number and fuel mass flow rate corresponding to the original valve. However, this model is limited to shrouded poppet-type nozzles.

### 4.3.3 Source Modeling Approach

A virtual injector model for a poppet-type valve based on the source terms in the governing equations was developed by Baratta et al. (2011). In this model, the injector needle is opened to the maximum lift and the geometry upstream of the throat section is removed from the computational domain. The mesh cells at the throat section are treated as the injection source cells. The source terms in the governing equations are computed as  $S_\phi = \dot{m}\Phi$ , where  $\dot{m}$  is the mass flow rate through the injector and  $\Phi$  is the flux in each of the equations. This approach is valid for supersonic injection velocities as downstream conditions do not affect upstream flow properties in supersonic flows. However, the approach does not include the effects of upstream nozzle geometry, which are typically important.

### 4.3.4 Mapped Boundary Condition Approach

The mapped boundary condition (MBC) approach was recently proposed by Deshmukh et al. (2016), where the simulation is split into two parts: nozzle flow and in-cylinder flow. This approach retained the geometrical information of the nozzle and provided accurate boundary conditions for the in-cylinder flow simulation. In this approach, a stand-alone nozzle simulation, either LES or URANS, is carried out for a desired pressure ratio. The nozzle flow and near-nozzle flow reach a steady state within a short time compared to the duration of injection. The injector nozzle is decoupled from the cylinder by slicing it from the computational domain along an arbitrary surface, which is treated as the mapping boundary on the cylinder. Since the flow at the nozzle exit is supersonic due to high-pressure ratio, the downstream flow conditions have no effect on the upstream flow field. On the other hand, under subsonic conditions, the upstream flow field depends on downstream flow conditions, and hence, the one-way mapping is not accurate. Therefore, the MBC approach is physically more accurate under supersonic nozzle flow conditions. The flow variables in the nozzle simulation are recorded at the mapping boundary and then transferred onto the corresponding inflow boundary of the full-scale simulation. The approach is illustrated in Fig. 4.23.

The location of the mapping boundary is selected based on two opposing criteria:

1. The mapping boundary should be far off from the nozzle exit so that the velocity is small enough to increase the time step significantly.
2. The mapping boundary should be close to the nozzle exit to avoid removal of a large volume from the computational domain.

An ideal mapping location is at the end of the Mach disk, which is consistent with the models reported in the literature (Johnson et al. 1995; Mather and Reitz 2000; Ouellette and Hill 1999). However, in this study, the mapping boundary is

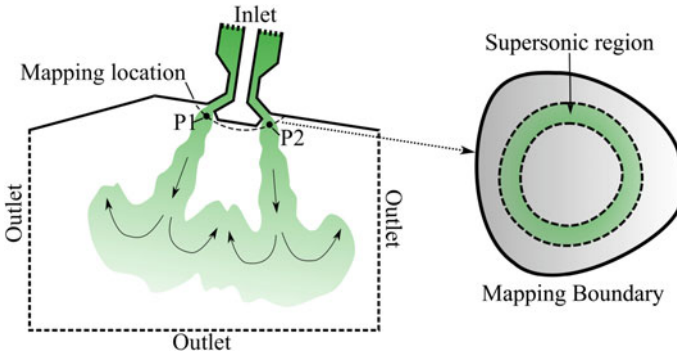


**Fig. 4.23** Sketch illustrating the mapped boundary condition approach

located at 1 mm downstream of the nozzle to avoid cutting into the cylinder volume. This location is found to be sufficient to obtain large time steps and reasonably accurate predictions of the in-cylinder flow fields. Nevertheless, further work is necessary to determine the optimum location for the mapping boundary.

To generate the mapped boundary condition, a stand-alone nozzle flow simulation is performed. The injector needle is opened to its maximum lift and the domain is initialized into two regions with an initial discontinuity at the valve seat. The upstream region containing helium is set to the specified injection pressure and temperature, and the downstream region is initialized with a low pressure corresponding to ambient conditions. A total pressure boundary condition is set at the inlet, and a non-reflecting characteristic boundary condition is applied at the outlet. Remaining boundaries are treated as no-slip, adiabatic walls. The simulation is run and continued until statistically stationary conditions are reached at the mapping location. It can be verified whether the near-nozzle flow has reached a statistically stationary condition. For example, Fig. 4.24 shows the plot of velocity magnitude at two locations, P1 and P2, on the mapping surface over time for pressure ratios of 15 and 8. The instantaneous signal is fluctuating; therefore, it is filtered to get the mean velocity magnitude. The mean velocity magnitude becomes steady after  $\sim 60 \mu\text{s}$ . The interaction of shock waves and the geometrical features of the cylinder head are also captured.

The flow field variables downstream of the nozzle exit for two pressure ratios are shown in Fig. 4.25 in the  $Y = 0.0$  plane at time  $t = 75 \mu\text{s}$ . A dashed line indicates the mapping location. The flow variables such as velocity, density, temperature, and mass fractions at the mapping location are recorded and stored. The flow variables are mapped only in the supersonic regions, which is geometrically marked based on the mass fraction of injected gas. Here, it is observed that the entrainment of ambient gas in the supersonic gas jet at the mapping location is negligible. The threshold helium mass fraction to mark the supersonic region is chosen based on a trade-off between the thickness of the supersonic region and mesh resolution. For example, it is set to 0.7 for the pressure ratio of 15 and 0.6 for the pressure ratio of

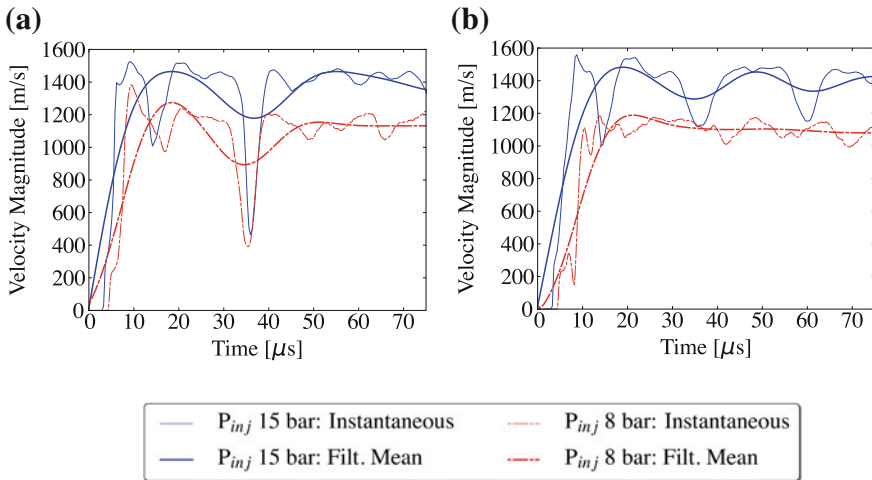


**Fig. 4.24** Velocity magnitude monitored at location P1 (a) and P2 (b) on the mapping surface

8. After the mean flow quantities reach a statistically stationary state, they are averaged in time. The resulting inflow profiles of different flow variables on the inflow boundary are also shown in Fig. 4.25. The remaining area outside the supersonic region should mimic a wall boundary and is set to zero velocity and a fixed temperature avoiding additional inflow through this area. A zero-gradient condition for pressure is required over the mapping boundary to get constant mass flow across it. The effects of needle motion are important for solenoid-actuated injectors as shown before, especially at high engine speeds. These can be considered by gradually ramping up the velocity components at the mapping boundary. At relatively lower engine speeds (e.g., 1000–2000 RPM in this study), the needle opening period in terms of crank angles is small enough and does not largely affect subsequent mixture formation. Moreover, the conditions at the mapping location do not change significantly during the injection period at lower engine speeds. Therefore, the inflow profiles are fixed in time.

For a supersonic inflow boundary, all characteristic waves enter the flow domain; therefore, all information should come from outside of the domain (Hirsch 1994). For a system of compressible Navier–Stokes equations with a non-reacting scalar, at least six flow variables, namely density, three components of velocity, temperature, the mass fraction of helium, are required. Neglecting the contribution of sub-filter scales, these are sufficient for an LES. However, for a URANS simulation, two additional equations for the turbulence model need turbulent kinetic energy (TKE) and turbulent dissipation rate to be specified at the inflow boundary. Depending on the method used for the stand-alone nozzle flow simulation, some variables are directly available, and the rest need to be estimated from the available ones and specified as a constant value in the supersonic region. For example, a mapping from a stand-alone nozzle flow LES to an LES of full-scale simulation (LES-to-LES mapping) or URANS-to-URANS mapping will not require any

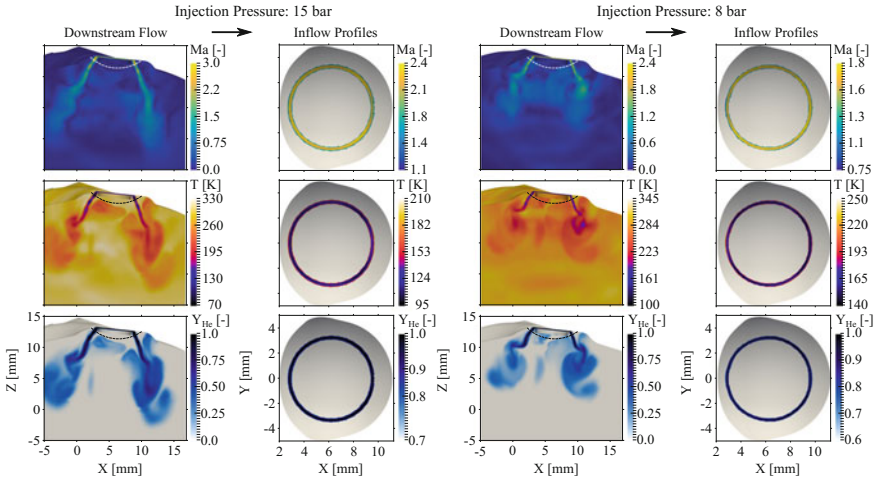


**Fig. 4.25** Downstream spatial distribution of Mach number ( $Ma$ ), temperature ( $T$ ), and helium mass fraction ( $Y_{He}$ ) in  $Y = 0.0$  clip plane and resulting inflow profiles at time  $t = 75 \mu s$  in nozzle simulations for injection pressures 15 bar (*left*) and 8 bar (*right*)

estimation, whereas for the LES-to-URANS mapping the TKE is estimated from the fluctuating velocity components obtained from the time-averaged mean velocity profile from the LES. The turbulent dissipation rate is calculated using Eq. 4.4 from the TKE and an appropriate length scale ( $le$ ), which is chosen as a fraction of the maximum valve lift.

$$\varepsilon = \frac{c_{\mu}^{3/4} k^{3/2}}{le} \quad (4.4)$$

where  $c_{\mu}$  ( $=0.09$ ) is a model constant. The TKE could also be specified in terms of estimated turbulent intensity and an appropriate dissipation length scale. However, the sensitivity of the results to the estimated kinetic energy and dissipation rates needs further investigation in the future.

## 4.4 Application of Mapped Boundary Condition Approach

### 4.4.1 Case Description

The MBC approach is demonstrated in a quasi-steady-state flow configuration and a full-cycle engine configuration. For validation, the in-cylinder velocity field is measured for an optically accessible single-cylinder research engine. All of the experimental data has been measured at the Institute of Aerodynamics (AIA) of RWTH Aachen University. The injector was provided by Delphi, and helium was

**Table 4.1** Engine specifications

Displaced volume	364 cc
Bore	75 mm
Stroke	82.5 mm
Connecting rod	146 mm
Compression ratio	7.4
Number of valves	4
Valve lift	9 mm
Exhaust valve open	250° BTDC
Exhaust valve close	33° ATDC
Inlet valve open	34° BTDC
Inlet valve close	250° ATDC

used for injection. The physical properties of helium are different from natural gas. Based on isentropic flow calculations, helium results in 46% lower mass flow and 13% higher momentum flow compared to natural gas through the injector at a given pressure ratio. Nevertheless, this study can reasonably provide an insight into the underlying processes occurring due to gas injection and their impact on the in-cylinder flow field and mixture formation. Table 4.1 shows the engine specifications. The valve opening and closing events are with reference to the non-firing TDC, which is set to 0° crank angle.

The velocity field has been measured using state-of-the-art time-resolved stereoscopic particle image velocimetry (PIV) (see the experimental setup in Fig. 4.26a). The measurement cases chosen for comparison with the simulations are shown in Table 4.2. The poppet-type injector is positioned between the two intake valves inclined at an angle of 6° with an offset of 6 mm from the axis of the cylinder. The maximum needle lift of the injector is 350 μm in all measurement cases. For the steady-state measurement of the velocity field, helium at a pressure of 15 bar is injected for one second in a fully closed cylinder with the piston at the bottom dead center (BDC). Initially, the cylinder is at atmospheric pressure and temperature. The velocity field is measured in two planes passing through the injector and perpendicular to each other as shown in Fig. 4.26b. During the injection, 500 samples of the velocity field are recorded, beginning at 100 ms after SOI until 167 ms at a frequency of 750 Hz. The sampling starts 100 ms after SOI to obtain a fully developed mixture of the injected and the in-cylinder gas. For the full engine cases (transient 1–3), the measurements are carried out on two planes except for case transient 3, where the velocity field is measured only in the  $Y = 0.0$  plane. Three hundred and twenty-one consecutive cycles are recorded during the measurements to obtain a high convergence of the data. In one cycle, 17 images are recorded with an interval of 16° crank angle with a sampling frequency of 375 Hz for the engine speed of 1000 RPM and 750 Hz for the engine speed of 2000 RPM. Measurements are performed only during the intake and compression phase, beginning at a crank angle of 72° ATDC until 328° ATDC.

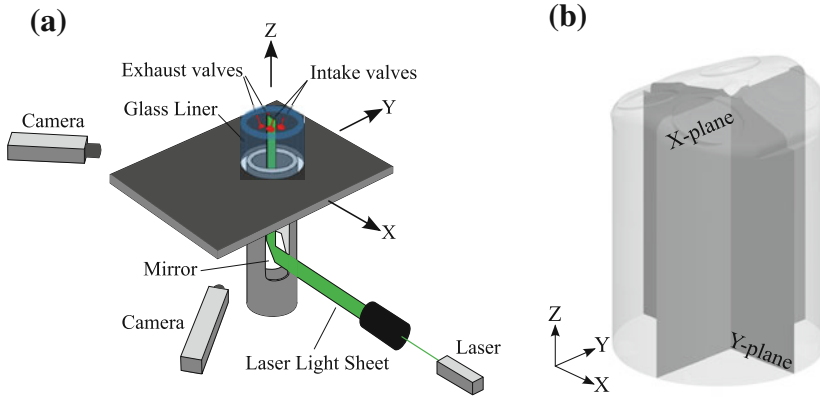


**Fig. 4.26** Experimental setup (a) and measurement planes (b) for time-resolved stereoscopic PIV

**Table 4.2** PIV measurement cases

Case	Engine speed (RPM)	$P_{inj}$ (bar)	SOI (ms)	DOI (ms)	SOI (CA°)	DOI (CA°)
Steady	0	15	0	1000	–	–
Transient 1	2000	15	–	6	90	72
Transient 2	1000	15	–	6	90	36
Transient 3	2000	8	–	3	135	36

### 4.4.2 Steady-State Configuration

The measurements of the velocity field begin 100 ms after SOI, and as shown in Fig. 4.27, the pressure in the cylinder rises continuously from 1 to 5.5 bar up to the start of measurement as the valves are closed. Therefore, the simulation, if begun from the start of injection, would have to be run for more than 100 ms to capture this pressure rise, which is impractical from a numerical point of view. The initial estimate of the time required for running one such LES without any modeling of nozzle flow was in the order of months on the available computing resources, which is unrealistic. A more practical approach is considered here. Because of the inherent transient nature of the physical process, it cannot reach a steady state. Therefore, a timescale is defined based on the physical dimensions of the domain and the speed of sound in the fluid, here air, in the domain. The timescale is used to roughly estimate the time required for the velocity field to reach a *quasi*-steady state. In this case, the maximum dimension is along the axis of the cylinder ( $\sim 0.1$  m). Speed of sound in air is  $\sim 343$  m/s. So, the time required for a pressure wave to reach the bottom of the cylinder is approximately 0.3 ms. It is assumed that a *quasi*-steady state is reached when the pressure waves have traveled across the cylinder multiple times so that they no longer change the flow field significantly. Hence, the actual simulation time to reach the *quasi*-steady state is assumed to be in multiples of the

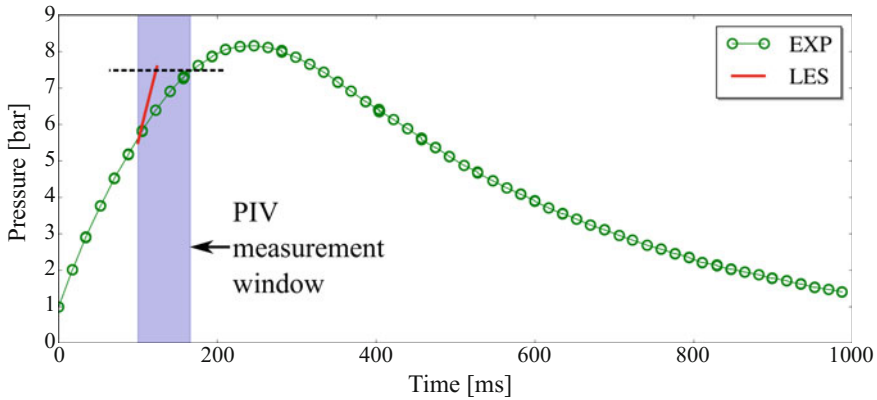


**Fig. 4.27** Chamber pressure measured during PIV with  $P_{inj}$  15 bar

characteristic time  $T$  ( $\approx 0.3$  ms), and  $70 * T \sim 21$  ms was found to be sufficient in this study. The simulation is directly started 100 ms after the SOI with the initial cylinder pressure of  $\sim 5.5$  bar. Within the measurement window, the pressure rises up to  $\sim 7.5$  bar. Both LES and URANS simulations were carried out and compared with velocity field measurements. The LES shows the pressure rise of  $\sim 2$  bar in the time required to reach the *quasi*-steady-state (21 ms) compared to 67 ms required for the same pressure rise in the experiment. This is because blow-by losses were not considered in the simulations. An unstructured mesh was used with the high-fidelity compressible LES solver (CHRIS), and a Cartesian cut-cell mesh was used in CONVERGE for the URANS, which are not shown here for brevity. With this simulation approach, it was possible to reduce the simulation run-time significantly, from the order of months to the order of days.

The instantaneous and time-averaged velocity magnitude in the  $X$ - and  $Y$ -plane is shown in Fig. 4.28. The gas jet penetrates the cylinder, hits the bottom, and reverses resulting in a recirculation zone moving it sideways in the  $X$ -plane. As said before, the simulation required 70 characteristic times, i.e., 21 ms, to reach a *quasi*-steady-state. This can be verified by monitoring the velocity components at different points in the cylinder. For example, four points are monitored in the  $Y$ -plane, and the velocity components at these points are plotted in Fig. 4.29. The instantaneous signals are filtered to get mean values to identify trends. It can be observed that the mean signal does not change significantly after 21 ms. The simulation is continued until 80 characteristic time units, i.e., 24 ms, and a window of 3 ms is used for time-averaging.

A direct comparison of instantaneous  $W$ -velocity from the LES and PIV in the  $X$ -plane is shown in Fig. 4.30. Qualitatively, the LES predicts the gas jet location and sideways motion. After analyzing the experimental data, it was found that the jet is not visible in all of the measured samples because it fluctuates vigorously and moves out of the measurement plane. In fact, only selected samples show the gas



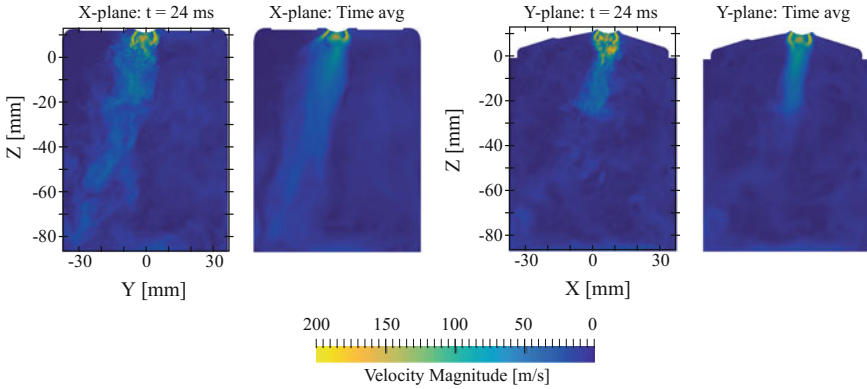


**Fig. 4.28** Velocity magnitude in LES on two planes; instantaneous field at  $t = 24$  ms and time-averaged field ( $t = 21$ – $24$  ms)

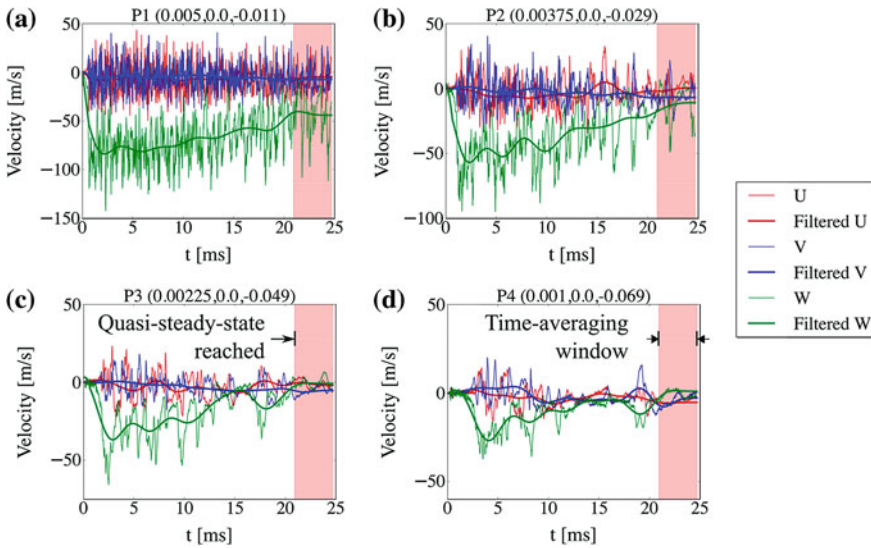


**Fig. 4.29** Velocity components monitored at four locations in the Y-plane

jet, indicating a large variability in the measurements. This is important when averaging the experimental data.

On the other hand, the time-averaged velocity field from the LES can be directly compared with that from the URANS simulation (see Fig. 4.31) because URANS ideally should provide ensemble-averaged results. The URANS predicts velocity magnitudes qualitatively similar to the LES. The strong sideways movement of the gas jet is not predicted in the URANS simulation, although the flow field is asymmetric. URANS cannot be expected to capture the dynamic large-scale

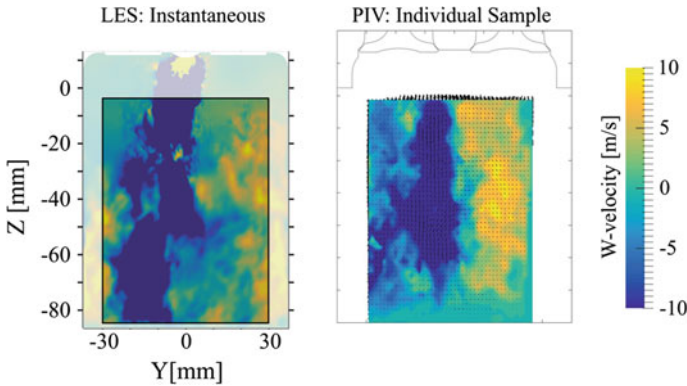


**Fig. 4.30** Comparison of LES (*left*) and PIV experiment (*right*) in the X-plane (*instantaneous fields*)

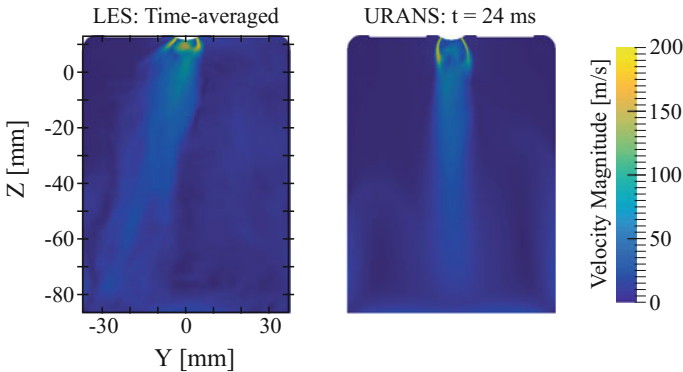


**Fig. 4.31** Comparison of time-averaged ( $t = 21\text{--}24$  ms) velocity magnitude in the LES (*left*) and the instantaneous one at  $t = 24$  ms in the URANS simulation (*right*) in the X-plane

motions of the gas jet due to the inherent modeling of energy-containing turbulent length scales.

For a more quantitative comparison, the velocity magnitude from the simulations and the experiments is plotted at certain locations in the cylinder (see Fig. 4.32) in the X-plane and the Y-plane. The gray curves in the background indicate instantaneous velocity magnitudes in LES, while gray symbols indicate the individual experimental snapshots only where the gas jet is present in the plane. Red curves show time-averaged LES, blue curves show URANS results, and green symbols are ensemble averages of individual experiments. The LES can reasonably capture the ensemble-averaged velocity field as well as the instantaneous fluctuations. On the other hand, URANS predicts the magnitudes of the ensemble-averaged velocity field, although the peak locations are not predicted. This is again because of the

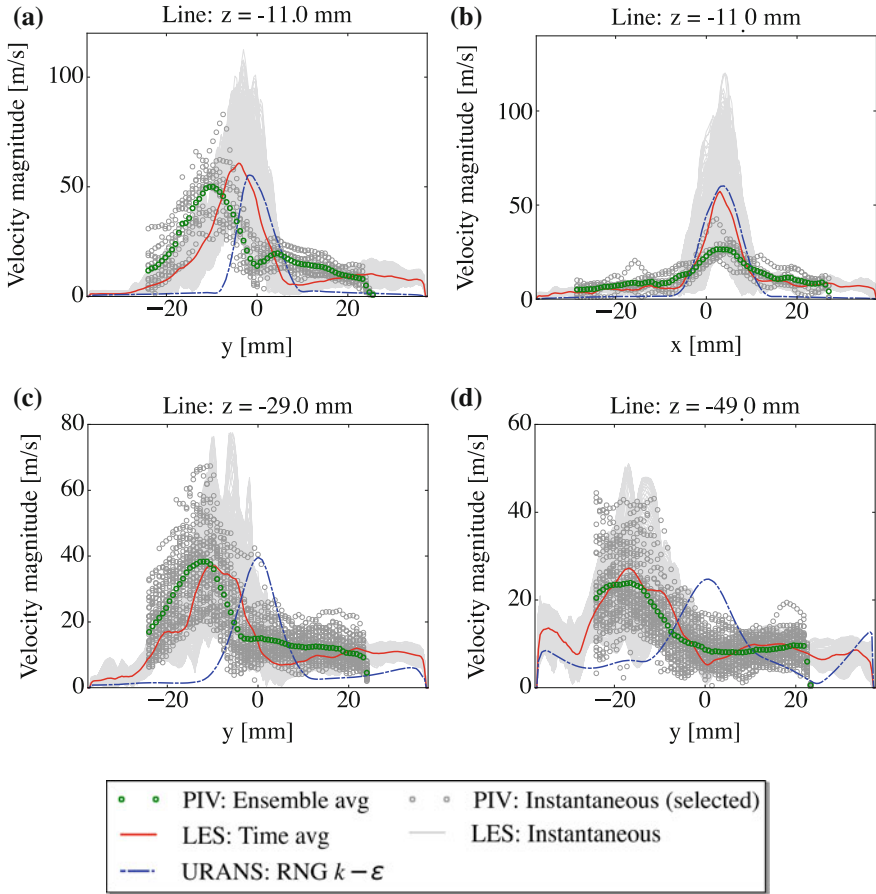


**Fig. 4.32** Comparison of LES and URANS with PIV experiments at different locations

intrinsic limitations of the URANS turbulence modeling. In the  $Y$ -plane, the gas jet is not fully visible due to sideways movement in the  $X$ -plane. Therefore, only one location is plotted in Fig. 4.32b.

### 4.4.3 Full Engine Configuration

**Simulation Setup.** The simulation setup for the engine simulation is shown in Fig. 4.33a. The domain is split into three regions: cylinder, exhaust, and intake. The injector is sliced out from the computational domain for the MBC approach. CONVERGE generates a Cartesian cut-cell mesh at run-time. The base mesh size of 4 mm is used, and embedded refinement regions are placed in the cylinder, which results in a mesh size of 1 mm. The AMR is activated to capture gradients in

velocity and scalar fields. The mesh is refined at certain boundaries and/or regions to capture the physical fields and their gradients accurately. A representative mesh in the simulation during the intake stroke is shown in Fig. 4.33b.

Initially, a simulation of a full engine cycle is performed without injection for two engine speeds, 1000 and 2000 RPM, with air as a working fluid. To avoid the effects of initial quiescent conditions, the simulation is run for four cycles to set up a tumble flow field inside the cylinder. For the simulations with injections, the computational domain is initialized with the flow field just before the SOI.

A total pressure boundary condition is applied at the hemispherical inlet with a pressure of 101.325 kPa and a temperature of 298 K. A time-varying pressure boundary condition based on measured data is imposed at the outlet of the exhaust pipe. Gradients of velocity and temperature at the exhaust pipe are set to zero. Other boundaries are modeled as no-slip walls with a fixed temperature of 298 K. For further details on the simulation setup, initial and boundary conditions, the reader is referred to Deshmukh et al. (2018c).

The MBC approach is used in place of the injector. The MBCs are generated for two injection pressures, 15 and 8 bar, using the LES solver. As the URANS solver of CONVERGE is used for the engine simulations, this is an LES-to-URANS mapping for MBC. Therefore, the TKE and turbulent dissipation rates are required to be estimated from the LES data at the mapping location. The time-averaging is performed on the inflow profiles to obtain the TKE. The turbulent dissipation rate is computed using Eq. 4.4. The length scale ( $l_e$ ) is chosen as  $\sim 15\%$  of the maximum valve lift resulting in the values reported in Table 4.3 for two injection pressures.

The injection mass flow rates across the mapped boundary for injection pressures of 15 and 8 bar are shown in Table 4.4. For comparison, the injector mass flow rates measured in separate constant volume chamber experiments at the injection pressures of 16 and 11.8 bar are provided. Additionally, the mass flow rates from isentropic flow calculations are given for reference. In general, the isentropic calculations predict higher mass flow rates compared to the measured values and those from the LES, except for the injection pressure of 8 bar.

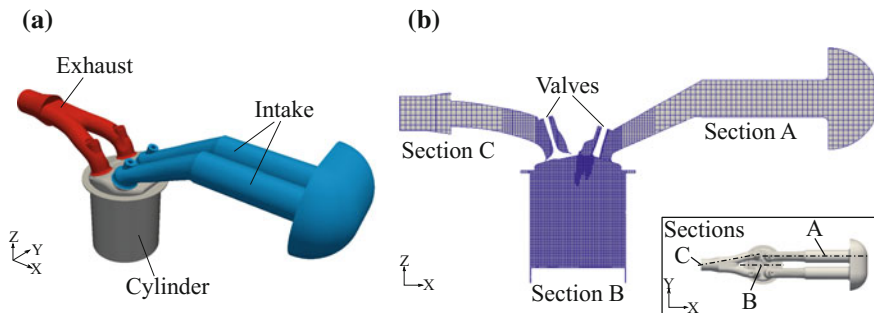


**Fig. 4.33** Computational domain (a) and representative mesh (b)

**Table 4.3** TKE and turbulent dissipation rate estimated for two injection pressures

Injection pressure (bar)	TKE ( $\text{m}^2/\text{s}^2$ )	Turbulent dissipation rate ( $\text{m}^2/\text{s}^3$ )
15	$6.001 \times 10^4$	$4.423 \times 10^{10}$
8	$2.979 \times 10^4$	$2.194 \times 10^{10}$

**Table 4.4** Measured and calculated mass flow rates through the injector for different injection pressures

Injection pressure (bar)	Measured (g/s)	LES (g/s)	Isentropic calculations (g/s)
16.07	3.5	–	4.45
15	–	3.8	4.15
11.79	2.5	–	3.26
8	–	2.3	2.21

For validation of the MBC approach for full-cycle engine simulations, a direct comparison can be made between PIV measurements and simulations in terms of velocity magnitude. Alternatively, derived quantities of interest, such as the tumble number, can be compared. The tumble number is a quantitative measure of the in-cylinder charge motion about the instantaneous volumetric center of the cylinder relative to the engine speed. The following expression is used for the calculation of a planar tumble number from both PIV data and simulations:

$$\text{Tumble Number} = \frac{\sum_{i=0}^n [(Z_i - Z_{ca})U_i - (X_i - X_{ca})W_i]}{\omega_{\text{crank}} \sum_{i=0}^n [(Z_i - Z_{ca})^2 + (X_i - X_{ca})^2]} \quad (4.5)$$

where

$\omega_{\text{crank}} = \frac{2\pi N}{60}$  (Hz), angular speed of the crankshaft

$N$  = engine speed (RPM)

$U_i, W_i$  = X- and Z-components for velocity at point  $i$  (m/s)

$X_i, Z_i$  = X- and Z-coordinates of point  $i$  (m)

$X_{ca}, Z_{ca}$  = X- and Z-coordinates of the center of area of the FOV (m)

**Results and Discussion.** A comparison of velocity magnitude between measurements and simulations in the Y-plane is shown in Fig. 4.34 for the first transient case. The experimental contours are ensemble averages of 321 cycles. Also, the plots at certain locations are shown for quantitative comparison. The flow field before the SOI shows an anticlockwise tumble vortex in both experiments and simulations. The vortex is more smeared out due to averaging of cycles with highly fluctuating velocities as seen from the plots at a location 10 mm downstream of the cylinder head. After SOI, the high-speed gas jet penetrates the tumble vortex destroying the overall tumble motion in the cylinder. As seen in the steady-state

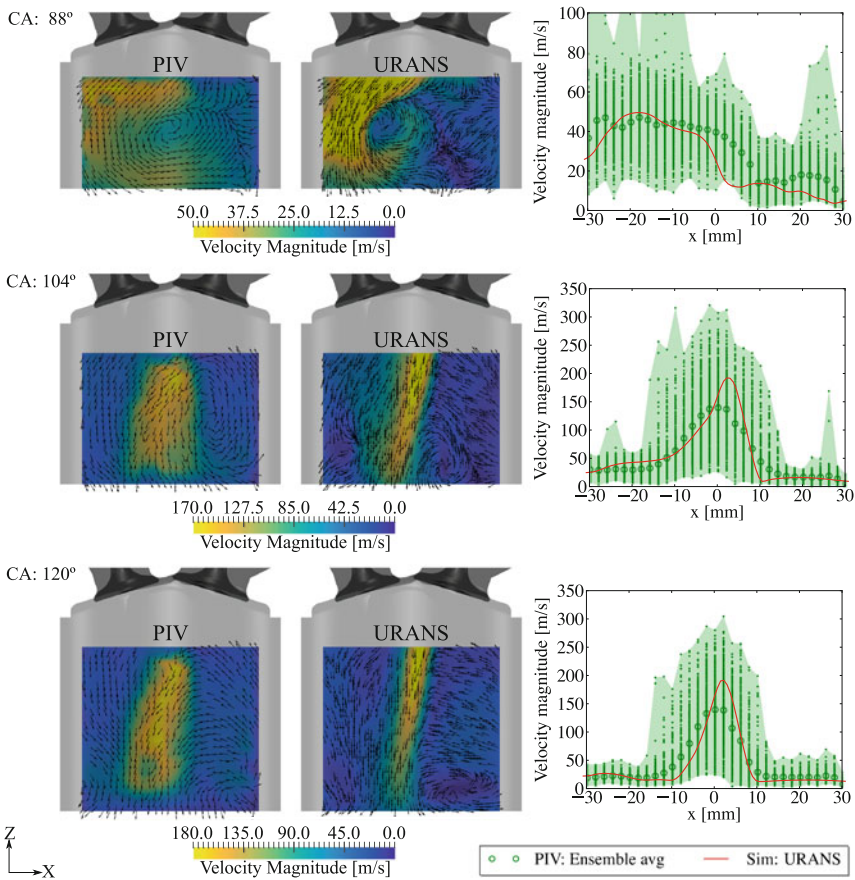


**Fig. 4.34** Contour plots for transient case 1: comparison of velocity magnitude, ensemble-averaged PIV (left) and URANS (right) in  $Y = 0.0$  plane at a crank angle  $88^\circ$  (before SOI),  $104^\circ$ , and  $120^\circ$  ATDC (after SOI); line plots: CA  $88^\circ$ — $Z = -10$  mm, CA  $104^\circ$ — $Z = -15$  mm, CA  $120^\circ$ — $Z = -15$  mm

configuration, the gas jet is highly fluctuating due to the complex interaction of the flow field and shocks/discontinuities and their reflections from the walls of the combustion chamber resulting in high variability in the experimental data ranging, for example, from 25 to 310 m/s. Nevertheless, the URANS simulations reasonably capture the ensemble-averaged velocity magnitude.

The tumble number comparison between the simulations and experiments provides an integral validation over a range of crank angles. In the experiments, the field of view (FOV) is limited due to practical limitations. Therefore, in both simulations and experiments, the planar tumble number is calculated using the velocity field in the same FOV (see Fig. 4.35a). The comparison between the

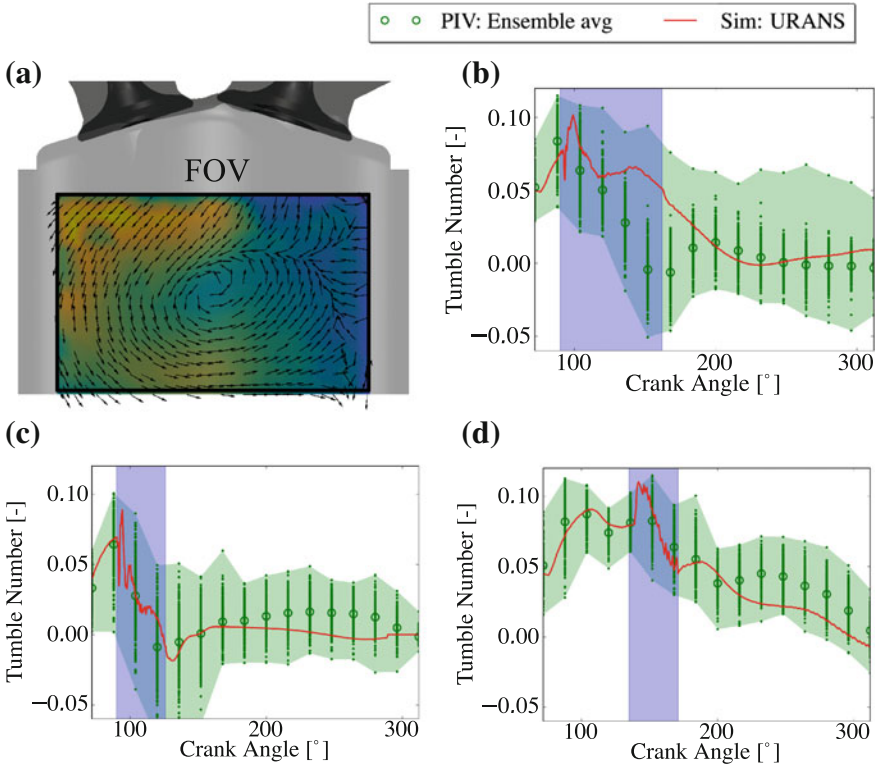


**Fig. 4.35** a Field of view for the calculation of tumble number; Comparison of tumble number in  $Y = 0.0$  plane for transient cases with **b** 2000 RPM-15 bar, **c** 1000 RPM-15 bar, **d** 2000 RPM-8 bar (injection period is indicated by vertical shaded region)

tumble number from URANS simulations and ensemble-averaged tumble number from PIV experiments for all transient cases (Fig. 4.35b, c, d) is reasonable despite the restrictive FOV. As a common observation, the tumble number decreases sharply after the injection starts, which is consistent with the observations made from contour plots, i.e., destruction of tumble vortex by the gas jet. Depending on the DOI, SOI, and injection pressure, the tumble vortex is destroyed either completely as in transient case 1 and 2 or partly as in transient case 3. With lower injection pressure in case 3, the mass flow rate is lower, reducing the overall momentum of the gas jet. In this case, the tumble vortex partly survives due to lower momentum combined with shorter duration of injection.

Thus, the MBC model for poppet-type injectors has been successfully validated against the in-cylinder PIV measurements. The model reduced the simulation run-times for full engine cycle with injection from the order of months to the order of weeks on the same computational resource, at the same time ensuring the reasonable accuracy of the predicted results.

## 4.5 Impact of Direct Gas Injection on the In-Cylinder Flow Field and Mixing

After the validation of the full engine simulation data, the impact of direct gas injection on the in-cylinder flow field is investigated using integral quantities such as mass-averaged tumble number and mass-averaged TKE. The mass-averaged quantities provide more information than the plane-averaged quantities, which were available in the experiments. Without direct gas injection, the mass-averaged tumble number follows an M-shape behavior, which is typical for spark-ignition (SI) engines (see Fig. 4.36a). On the other hand, with gas injection, the tumble number drops sharply for the cases with higher injection pressure. For the case with lower injection pressure, some of the tumble motion still survives because of the lower momentum of the gas jet. For the same injection pressure of 15 bar, the rate of decrease of the tumble number in a crank angle space is higher for lower engine speed. This is because the absolute in-cylinder flow velocities are lower for lower engine speed, and the gas jet has more time to interact with the tumble vortex.

The in-cylinder tumble flow has a special significance for SI engines (Arcoumanis et al. 1990; He et al. 2007). The tumble vortex is intentionally generated in the cylinder and acts as a storage of kinetic energy. The piston motion compresses the vortex as it moves toward TDC, which increases its angular speed (spin-up effect). Close to firing TDC, the tumble vortex breaks up releasing the kinetic energy in the form of turbulence, which is required for faster flame propagation. Figure 4.36b shows the mass-averaged TKE for the simulations considered here. As expected, without injection, the TKE levels are higher for higher engine speed. However, during the injection, the gas jet introduces very high amounts of TKE until the end of injection (EOI), which is the result of high velocities of the jet as well as the destruction of the tumble vortex. The highest maximum TKE is

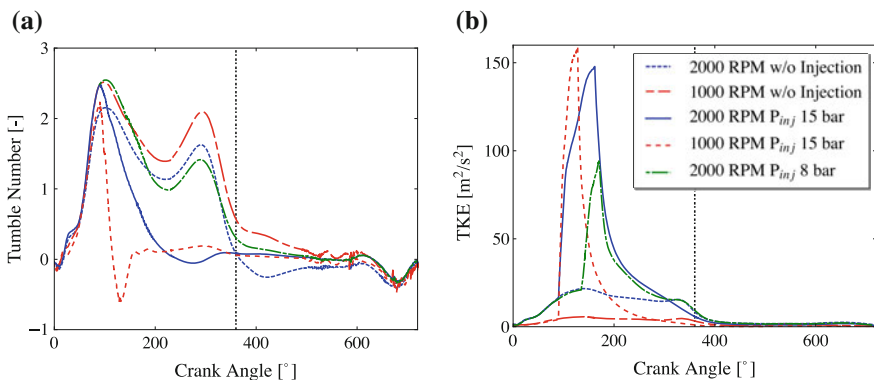


**Fig. 4.36** Comparison of the in-cylinder mass-averaged tumble number (a) and mass-averaged TKE (b) without injection (*fourth engine cycle*) and with injection (*fifth engine cycle*) for two injection pressures (vertical dashed lines indicate the crank angle of firing TDC)

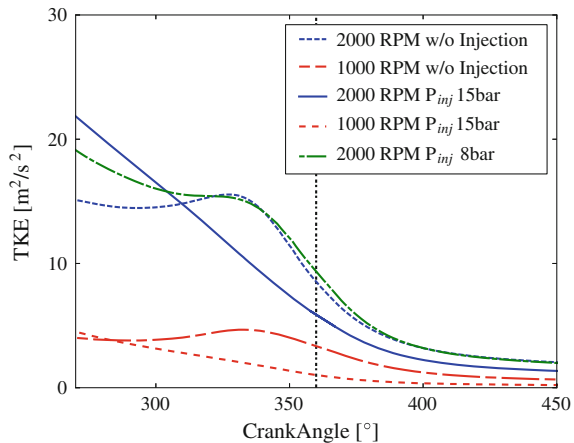


observed for the case with high injection pressure and low engine speed. The maximum TKE is the lowest for low injection pressure and high engine speed among the considered cases. In this case, the surviving tumble vortex breaks up near firing TDC, resulting in the late increase in the TKE. Once the injection has ended, the TKE shows exponential decay as there is no production mechanism left in the absence of tumble motion, except the case with high engine speed and low injection pressure. The amount of TKE available near the firing TDC can be closely examined from Fig. 4.37. Except for 2000 RPM-8 bar case, the direct gas injection results in lower TKE levels than without injection. One of the major reasons for this is the centrally mounted injector configuration. If the injector is side-mounted or inclined in an angle that results in the gas jet assisting the in-cylinder tumble motion, the turbulence levels may be maintained or even be higher than without injection. Therefore, it is imperative to investigate the influence of direct gas injection on the in-cylinder flow and then optimize the injector configuration to obtain the desired turbulence levels for faster combustion.

High turbulence levels due to direct injection have a strong impact on the in-cylinder mixing. The mixture quality in the full engine case can be well described by the normalized cumulative volume fraction (CVF) of the injected gas. An ideal mixture is defined as a mixture with a constant mass fraction of the injected gas throughout the cylinder. The CVF is computed by adding the cylinder volume up to a certain mass fraction, which results in a monotonically increasing curve as shown in Fig. 4.38a. The ideal mixture is represented by a vertical line. The mixture quality for all the cases at firing TDC deviates from the ideal one. To quantify the deviation, more statistical information can be obtained from the CVF. A PDF is derived from the CVF (see Fig. 4.38b), and the mean, standard deviation, coefficient of variation, and skewness of the PDF are calculated.

Table 4.5 shows the statistical parameters computed for the mixture at firing TDC. The ideal mass fraction is computed from the total injected mass of helium divided by the total cylinder mass after the intake valve closing (IVC). The mean

**Fig. 4.37** Comparison of the in-cylinder mass-averaged TKE with and without injection at two injection pressures near firing TDC (vertical dashed line denotes the crank angle of firing TDC)



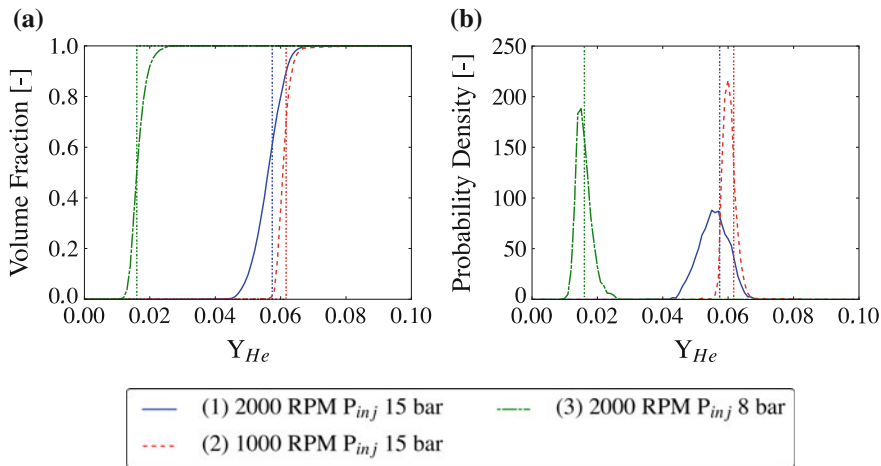


**Fig. 4.38** Mixture quality in terms of CDFs (a) and PDFs (b) at firing TDC for three cases (vertical dashed lines correspond to the mass fraction in case of ideal mixing)

**Table 4.5** Statistical parameters computed from the PDFs for three transient cases at firing TDC

Transient case	Ideal $Y_{He}$	Mean	Standard deviation	Coefficient of variation (%)	Skewness
1	0.05742	0.05554	0.004497	8.10	-0.05627
2	0.06170	0.06044	0.002305	3.81	2.3143
3	0.01592	0.01589	0.0024795	15.6	0.90298

values of the PDFs are lower than the ideal mass fraction because some of the injected helium is transported in the intake port before IVC. The standard deviation quantifies the degree of mixing. However, the standard deviation relative to the mean value, also known as the coefficient of variation (CoV), is more useful to compare mixture quality under different conditions. The lower the CoV, the higher the mixture quality. Case 2 with high injection pressure and low engine speed has the lowest CoV of helium mass fraction and hence the highest mixture quality. Case 3 with low injection pressure and high engine speed has a standard deviation similar to that of case 2; however, it has the lowest mixture quality, although visually the mixture looks more homogeneous (see Fig. 4.39). The mixture quality of the transient case correlates with the peak turbulence levels. Higher peak TKE is accompanied by a higher degree of mixing. A high positive skewness combined with a low CoV of the mass fraction implies that the volume contains pockets of a rich mass fraction, which can also be observed in the contour plots. The negative skewness in case 1 indicates the presence of regions with lean mass fractions, which can also be verified from the contour plots.

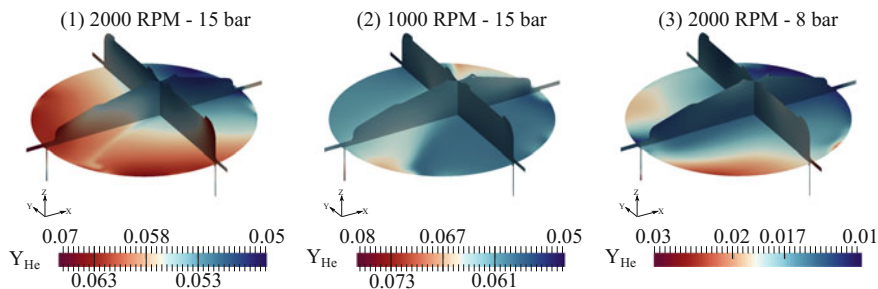


**Fig. 4.39** Helium mass fraction at firing TDC in three cases

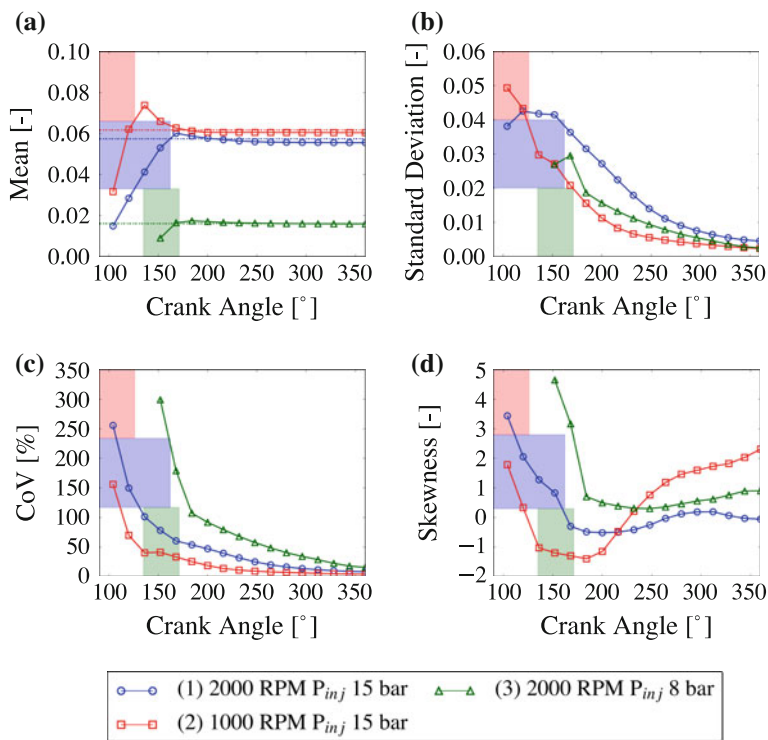


**Fig. 4.40** Evolution of mixing statistics over a crank angle (*filled regions indicate injection period for the respective cases, and horizontal dashed lines correspond to the ideal mass fraction after IVC*)

The mixing statistics can be tracked over a crank angle to assess the progress of mixing through the engine cycle (see Fig. 4.40). The mean of the PDFs increases during the injection and, after the EOI, approaches a constant value, which is close to the ideal one. All three cases have a high positive skewness at the beginning,

which is expected as the gas jet with rich helium mass fraction is concentrated in a very small region near the injection boundary. The skewness fluctuates throughout the mixing process and can be regarded as an indicator of the presence of rich or lean unmixed regions.

## 4.6 Summary

This chapter focuses on resolved simulations and modeling of poppet-type injectors and the potential impact of the direct gas injection on mixing and combustion. The resolved simulations of the poppet-type injector were performed using a high-fidelity LES solver, which provided detailed physical insights into the nozzle flow, near-nozzle flow, and the global hollow-cone jet characteristics. Specifically, complex gas passages in the injector nozzle lead to compression shocks and expansion fans causing a flow separation at the nozzle exit. The near-nozzle gas jet at steady state is inclined toward the poppet due to locally low pressure. The jet core remains intact despite the high standard deviation of the velocity field. Two distinct mixing layers develop on the inner and outer edge of the hollow cone and merge away from the nozzle. On the macroscopic level, the gas jet develops in two stages. The first stage involves the formation of a hollow cone, which then collapses and forms a single gas jet in the second stage. Turbulence models in URANS simulations are evaluated against the LES data, and it is found that the RNG  $k$ - $\epsilon$  model is suitable for the URANS simulations with respect to global characteristics and mixing behavior, which are important for general engine simulations. Therefore, it may be recommended for use in engine simulations with direct gas injection.

Injector needle motion essentially needs to be considered for resolved simulations of electromagnetically actuated solenoid injectors. The gradual opening of the needle results in a linear increase of axial penetration during the initial phase as observed in the experiments. Initial conditions in the injector may influence the global gas jet evolution and subsequent mixing. In the URANS simulations, different initial conditions lead to different collapsing instants, eventually affecting the overall development of the jet. However, the sensitivity to the initial conditions in the LES simulations is less prominent.

As the full engine simulations with detailed injector geometries are computationally expensive, the development of models for poppet-type injectors is necessary. However, there are currently only a few modeling approaches for such injectors in the literature. The recently developed MBC model considers the full geometry of the injector nozzle and is accurate. It is validated with PIV measurements in a steady-state flow configuration and full-cycle engine cases. URANS simulations and LES with MBC model for the injector predict similar levels of velocity magnitudes in *quasi*-steady-state simulations, although the LES also predicts highly fluctuating and dynamic interaction with the surrounding flow field. In the engine configuration, there is a reasonable agreement between the velocity field in URANS simulations and the ensemble-averaged velocity field in PIV

measurements. The MBC model reduced the simulation run-time to the order of weeks while enabling reasonably accurate simulations for further design and analysis.

Using the URANS simulation data, the impact of the gas jet on the in-cylinder flow field and mixing is analyzed. The direct gas injection introduces high turbulence in the cylinder potentially destroying the tumble vortex. High injection pressure at lower engine speeds results in high amounts of TKE because the high momentum of the gas jet breaks the weaker tumble motion at lower engine speeds. The TKE levels dissipate rapidly and may result in overall lower values with injection than without. The lower TKE values near firing TDC may lead to slower combustion if the engine is fired. Therefore, analysis of the DI-injector configuration must be performed, and ways to assist the tumble motion and maintain high turbulence levels until firing TDC must be investigated. The mixture quality is quantified by statistical parameters such as mean, standard deviation, CoV, and skewness of the PDFs derived from the CVFs of the in-cylinder mixture. As expected, higher TKE leads to lower CoV of the PDFs indicating a higher degree of mixing among the considered cases.

## 4.7 Future Work and Challenges

In the future, high-fidelity simulations with the LES approach including needle motion are required to verify the conclusions of the URANS approach and accurately predict the initial stages of the hollow-cone gas jet formation. The sensitivities of the URANS simulations to the initial conditions in the nozzle need to be scrutinized. To resolve the near-nozzle supersonic jet features in detail and investigate resulting instabilities, a higher mesh resolution is required.

The MBC model has some limitations. The inflow profiles are generated for a given pressure ratio across the nozzle and, for the cases considered in this chapter, the nozzle pressure ratio does not change significantly, as the injection occurs during the intake stroke. However, the nozzle pressure ratio may change depending on the SOI if the cylinder pressure fluctuates during the engine cycle, particularly at high engine speeds. In such cases, the nozzle may operate in under-expanded, perfectly expanded, overexpanded, or subsonic regimes, which will require dynamic mapping of inflow profiles, which is currently challenging. Additionally, the mesh resolution at the mapping boundary needs to be high enough to map the highly accurate boundary conditions from the nozzle flow simulation and obtain reasonably accurate in-cylinder flow fields. This has direct implications on the possibilities of further reduction of the simulation run-times.

**Acknowledgements** This work was performed within the Ford RWTH-Aachen Research Alliance Project FA-0099 funded by the Ford Motor Company. The authors would like to thank Delphi Automotive PLC for providing the injector and the appropriate control unit for the experimental measurements. The authors gratefully acknowledge the support and computing

resources provided by JARA-HPC partition of RWTH Compute Cluster under project JARA0117. The authors would like to thank Cascade Technologies Inc. for providing the license for the compressible LES solver CHRIS. The authors are also thankful to Convergent Science Inc. for providing the license for CONVERGE and support during the project.

## References

- ANSYS® Meshing (Release 15.0) (2013) Computer Software. ANSYS, Inc., Canonsburg, PA
- Arcoumanis C, Hu Z, Vafidis C, Whitelaw J (1990) Tumbling motion: a mechanism for turbulence enhancement in spark-ignition engines. SAE technical paper 900060. <https://doi.org/10.4271/900060>
- Baratta M, Catania AE, Pesce FC (2011) Multidimensional modeling of natural gas jet and mixture formation in direct injection spark ignition engines—development and validation of a virtual injector model. *ASME J Fluids Eng* 133(4):041304–041304-14. <https://doi.org/10.1115/1.4003877>
- Baratta M, Misul D, Xu J, Fuerhapter A et al (2017) Development of a high performance natural gas engine with direct gas injection and variable valve actuation. *SAE Int J Engines* 10 (5):2535–2551
- Bartolucci L, Scarcelli R, Wallner T, Swantek A et al (2016) CFD and X-ray analysis of gaseous direct injection from an outward opening injector. SAE technical paper 2016-01-0850. <https://doi.org/10.4271/2016-01-0850>
- Brès G, Ham F, Le H, Shoeybi M (2012) User's and developer's manual. Jefferson Release Version 4.0.4
- Chiodi M, Berner H, Bargende M (2006) Investigation on different injection strategies in a direct-injected turbocharged CNG-engine. SAE technical paper 2006-01-3000. <https://doi.org/10.4271/2006-01-3000>
- Deshmukh AY, Mayer D, Bode M, Falkenstein T et al (2016) LES of direct gas injection in internal combustion engines. Presented at LES for internal combustion engine flows LES4ICE, France, Nov 30–Dec 1, 2016
- Deshmukh A, Vishwanathan G, Bode M, Pitsch H et al (2018a) Characterization of hollow cone gas jets in the context of direct gas injection in internal combustion engines. SAE technical paper 2018-01-0296. <https://doi.org/10.4271/2018-01-0296>
- Deshmukh A, Vishwanathan G, Bode M, Pitsch H et al (2018b) Characterization of hollow cone gas jets in the context of direct gas injection in internal combustion engines. *SAE Int J Fuels Lubr* (accepted 2018)
- Deshmukh A, Falkenstein T, Pitsch H, Khosravi M et al (2018c) Numerical investigation of direct gas injection in an optical internal combustion engine. SAE technical paper 2018-01-0171. <https://doi.org/10.4271/2018-01-0171>
- Eilts P (2016) Future of the internal combustion engine. *ATZoffhighway Worldwide* 9(3):50. <https://doi.org/10.1007/s41321-016-0524-8>
- European Council for Automotive R&D. EUCAR Project Book. [http://www.eucar.be/wp-content/uploads/2016/12/Projectbook\\_2017\\_WEB.pdf](http://www.eucar.be/wp-content/uploads/2016/12/Projectbook_2017_WEB.pdf). Accessed July 2018
- Farrace D, Panier R, Schmitt M, Boulouchos K et al (2015) Analysis of averaging methods for large eddy simulations of diesel sprays. *SAE Int J Fuels Lubr* 8(3):568–580. <https://doi.org/10.4271/2015-24-2464>
- Fuchs T, Rutland C (1998) Intake flow effects on combustion and emissions in a diesel engine. SAE technical paper 980508. <https://doi.org/10.4271/980508>
- He Y, Selamet A, Reese R, Vick R et al (2007) Impact of tumble on combustion in SI engines: correlation between flow and engine experiments. SAE technical paper 2007-01-4003. <https://doi.org/10.4271/2007-01-4003>

- Hirsch C (1994) Numerical computation of internal and external flows: volume 2: Computational methods for inviscid and viscous flows. Wiley, Chichester, pp 344–401. ISBN: 0471923516
- Husted H, Karl G, Schilling S, Weber C (2014) Direct injection of CNG for driving performance with low CO<sub>2</sub>. Presented at 23rd Aachen colloquium automobile and engine technology, Germany, 6–8 Oct 2014
- INGAS—Integrated GAS Powertrain. Project Final Report. [http://www.ingas-eu.org/docs/INGAS\\_PROJECT\\_FINAL\\_REPORT\\_31May2012.pdf](http://www.ingas-eu.org/docs/INGAS_PROJECT_FINAL_REPORT_31May2012.pdf). Accessed Sept 2017
- Jensen JE, Tuttle WA, Stewart RB, Brechna H et al (1980) Brookhaven National Laboratory selected cryogenic data notebook, vol 1, Sections 1–9, United States
- Johnson NL, Amsden AA, Naber JD, Siebers DL (1995) Three-dimensional computer modeling of hydrogen injection and combustion. Presented at '95 SMC simulation multiconference, Phoenix, Arizona, USA, 9–13 April 1995
- Keskinen K, Kaario O, Nuutinen M, Vuorinen V et al (2016) Mixture formation in a direct injection gas engine: numerical study on nozzle type, injection pressure and injection timing effects. *Energy* 94:542–556. <https://doi.org/10.1016/j.energy.2015.09.121>
- Khalighi Y, Ham F, Nichols J, Lele S et al (2011) Unstructured large eddy simulation for prediction of noise issued from turbulent jets in various configurations. In: 17th AIAA/CEAS aeroacoustics conference (32nd AIAA aeroacoustics conference), aeroacoustics conferences, Portland, Oregon. <https://doi.org/10.2514/6.2011-2886>
- Kim G, Kirkpatrick A, Mitchell C (2004) Computational modeling of natural gas injection in a large bore engine. *ASME J Eng Gas Turbines Power* 126(3):656–664. <https://doi.org/10.1115/1.1762906>
- Kim G, Kirkpatrick A, Mitchell C (2007) Supersonic virtual valve design for numerical simulation of a large-bore natural gas engine. *ASME J Eng Gas Turbines Power* 129(4):1065–1071. <https://doi.org/10.1115/1.2747251>
- Kuensch Z, Schlatter S, Keskinen K, Hulkkonen T et al (2014) Experimental investigation on the gas jet behavior for a hollow cone piezoelectric injector. SAE technical paper 2014-01-2749. <https://doi.org/10.4271/2014-01-2749>
- Mather DK, Reitz RD (2000) Modeling the effects of auxiliary gas injection on diesel engine combustion and emissions. SAE technical paper 2000-01-0657. <https://doi.org/10.4271/2000-01-0657>
- McCracken M, Abraham J (2001) Swirl-spray interactions in a diesel engine. SAE technical paper 2001-01-0996. <https://doi.org/10.4271/2001-01-0996>
- Menter FR (1994) Two-equation eddy-viscosity turbulence models for engineering applications. *AIAA J* 32(8):1598–1605. <https://doi.org/10.2514/3.12149>
- Müller F, Schmitt M, Wright Y, Boulouchos K (2013) Determination of supersonic inlet boundaries for gaseous engines based on detailed RANS and LES simulations. *SAE Int J Engines* 6(3):1532–1543. <https://doi.org/10.4271/2013-24-0004>
- Ouellette PP, Hill PG (1999) Turbulent transient gas injections. *ASME J Fluids Eng* 122(4):743–752. <https://doi.org/10.1115/1.1319845>
- Richards KJ, Senecal PK, Pomraning E (2016) CONVERGE (v2.3), Convergent Science, Madison, WI
- Sevik J, Pamminger M, Wallner T, Scarcelli R et al (2016) Influence of injector location on part-load performance characteristics of natural gas direct-injection in a spark ignition engine. *SAE Int J Engines* 9(4):2262–2271. <https://doi.org/10.4271/2016-01-2364>
- Shih TH, Liou WW, Shabbir A, Yang Z, Zhu J (1995) A new k- $\epsilon$  eddy viscosity model for high reynolds number turbulent flows. *Comput Fluids* 24(3):227–238. [https://doi.org/10.1016/0045-7930\(94\)00032-T](https://doi.org/10.1016/0045-7930(94)00032-T)
- Shu C-W, Osher S (1988) Efficient implementation of essentially non-oscillatory shock-capturing schemes. *J Comput Phys* 77(2):439–471. [https://doi.org/10.1016/0021-9991\(88\)90177-5](https://doi.org/10.1016/0021-9991(88)90177-5)
- Sukumaran S (2010) Numerical study on mixture formation characteristics in a direct-injection hydrogen engine. Master thesis, Mechanical Engineering Department, Iowa State University, Ames, Iowa

- Van Sciver SW (2012) Helium cryogenics. International cryogenics monograph series. Springer Science+Business Media, LLC. <https://doi.org/10.1007/978-1-4419-9979-5>
- Vreman B, Geurts B, Kuerten H (1995) Subgrid-modelling in LES of compressible flow. *Appl Sci Res* 54(3):191–203. <https://doi.org/10.1007/BF00849116>
- Vuorinen V, Wehrfritz A, Duwig C, Boersma BJ (2014) Large-eddy simulation on the effect of injection pressure and density on fuel jet mixing in gas engines. *Fuel* 130:241–250. <https://doi.org/10.1016/j.fuel.2014.04.045>
- Wilson KG (1983) The renormalization group and critical phenomena. *Rev Mod Phys* 55(3):583–600. <https://doi.org/10.1103/RevModPhys.55.583>
- Yakhot V, Orszag SA (1986) Renormalization group analysis of turbulence. I. Basic theory. *J Sci Comput* 1(1):3–51. <https://doi.org/10.1007/BF01061452>



# Chapter 5

## Prospects and Challenges for Deploying Direct Injection Technology for Compressed Natural Gas Engines



Rajesh Kumar Prasad, Tanmay Kar and Avinash Kumar Agarwal

**Abstract** In this chapter, prospects and challenges of direct injection (DI) compressed natural gas (CNG) engine technology are dealt with and compared with conventional port fuel injection (PFI) technology used for CNG induction. DI injector nozzle geometries are discussed along with their performance using optical diagnostics tools such as Schlieren imaging and planar laser-induced fluorescence (PLIF) technique. Different CNG induction methodologies are compared along with different fueling arrangements such as induction of 100% natural gas (NG), bi-fuel, and dual-fuel systems. DI and PFI engines are compared for volumetric efficiency for varying fuel injection timings. In a single-cylinder prototype engine, engine parameters are analyzed for a different start of injection (SOI) timings with varying brake mean effective pressure (BMEP) and equivalence ratio ( $\Phi$ ). Advanced SOI reduced the brake-specific fuel consumption (BSFC), increased the brake thermal efficiency (BTE), and reduced the emissions.

**Keywords** Compressed natural gas · Injector geometry · Planar laser-induced fluorescence · Direct injection spark ignition · Emissions

### 5.1 Introduction

NG is a non-renewable, naturally occurring gaseous fossil fuel, which became popular after World War II because of development of efficient fuel storage systems in Europe. NG does not require any refining as the petroleum products, and it exists as a gas under pressures along with oil, deep in the earth's crust. Compressed and liquefied forms of NG can be directly used for transportation. In the last 20 years, new reserves of NG have been discovered and NG reserves have now increased (by 51%) from 123.5 trillion cubic meters (Tcm) to 186.6 Tcm between 1996 and 2016

---

R. K. Prasad · T. Kar · A. K. Agarwal (✉)  
Engine Research Laboratory, Department of Mechanical Engineering,  
Indian Institute of Technology Kanpur, Kanpur 208016, India  
e-mail: [akag@iik.ac.in](mailto:akag@iik.ac.in)

(BP P.L.C. 2017). NG can also be extracted from methane hydrates such as methane clathrate ( $\text{CH}_4 \cdot 5.75\text{H}_2\text{O}$ ) or ( $4\text{CH}_4 \cdot 23\text{H}_2\text{O}$ ), which also called natural gas hydrate or gas hydrate (Methane Clathrate 2017; Lüthi et al. 2008), and this could be potentially an inexhaustible source of NG in the future. NG can be used in vehicles either in NG-fueled SI engines (dedicated engines), bi-fuel mode SI engines, or dual-fuel mode compression ignition (CI) engines. NG-fueled vehicles reduce GHG emission (especially  $\text{CO}_2$  emissions) by  $\sim 20\%$  compared to conventional gasoline engines (BP P.L.C. 2017; Methane Clathrate 2017). NG is non-toxic and has wider flammability limits, lower density, and high autoignition temperature ( $\sim 550\text{--}600^\circ\text{C}$ ) (BP P.L.C. 2017; Methane Clathrate 2017). It is reported that properly optimized CNG DI engine performs identical to a modern gasoline direct injection (GDI) engine and is relatively more efficient thermodynamically (Durgada and Lappas 2017; Sevik et al. 2016; Sankesh et al. 2017).

### 5.1.1 Methodology to Introduce NG into Vehicles

Various NG induction technologies are used worldwide, which basically differ in the way fuel is introduced into the engine cylinder. These three are the main CNG engine technologies:

- Port injection technology
- Dual-fuel technology
- Direct injection technology.

#### *Port fuel injection technology*

Figure 5.1a illustrates the CNG port fuel injection (PFI) technology. In this technology, CNG is introduced close to the intake port of the cylinder at a certain time, where it is mixed with ambient air to form a premixed NG–air mixture before the combustion. The CNG–air mixture is then inducted into the combustion chamber, and compressed and ignited before the top dead center by a spark plug. This technology is relatively easier to implement by employing appropriate ‘conversion kits’ but has some shortcomings when applied to automotive engines. Major shortcomings are relatively lower power output due to reduced volumetric efficiency and thermal efficiency, engine knocking restriction, and unavoidable throttling of the intake to maintain the premixed air–fuel ratio within combustible limits at part-load conditions (Gunawan 1992).

#### *Dual-fuel technology*

Figure 5.1b illustrates the CNG dual-fuel technology. The operating mode of this technology is based on the ignition of homogeneous CNG–air mixture by pilot injection of diesel just before TDC. Exclusion of spark plug allows this technology to reduce cyclic variations during engine operation up to a certain level. However,

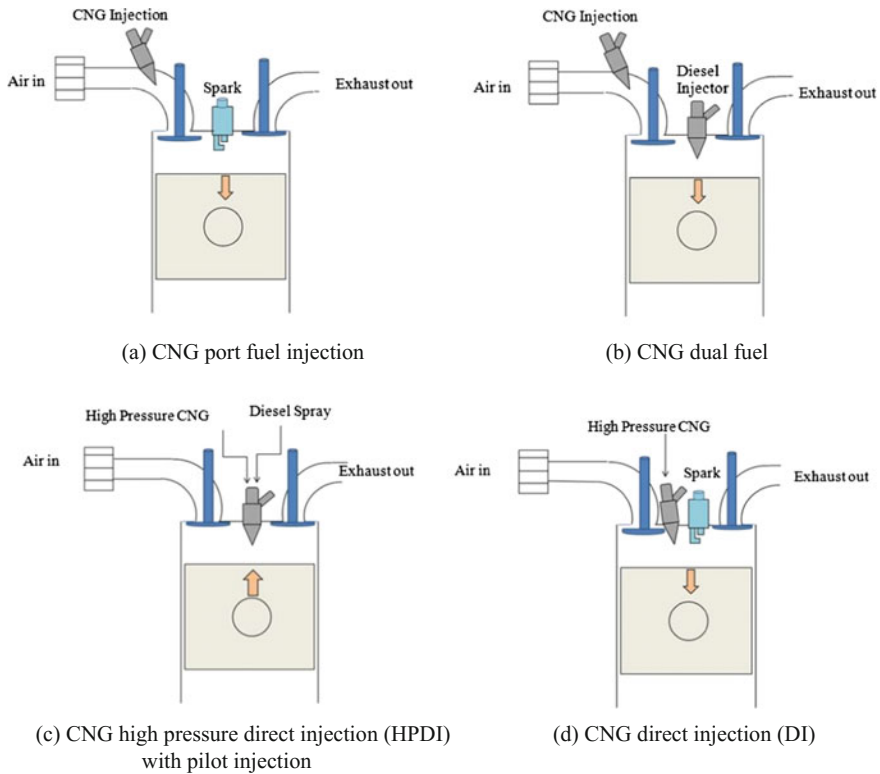


**Fig. 5.1** CNG injection technology options

this technology also suffers from high pumping losses due to unavoidable throttling at the intake and harmful emissions associated with diesel.

### *Direct injection technology*

Recently, Westport Isuzu has developed high-pressure direct injection (HPDI) engine technology (Fig. 5.1c), in which CNG is introduced directly into the engine combustion chamber at a very high pressure during compression stroke, and this mixture is ignited by a pilot injection of diesel just before the TDC. This engine does not experience throttling losses and, therefore, avoids knocking restrictions. This is an excellent technology; however, it needs two fuel supply systems, which makes it a very complicated and expensive technology which still has issues such as high HC emissions. To overcome the drawbacks of port and dual-fuel technologies, the focus of recent research tends to be on the development of dedicated CNG direct injection technology. It was demonstrated that increasing pilot diesel quantity enhanced the combustion and reduced  $\text{NO}_x$  emissions (Pirouzpanah and Khoshbakhti 2006). Effect of cold EGR was studied using CFD code (AVL FIRE) by Jafarmadar et al. (2010), and they reported that 10% EGR reduced the  $\text{NO}_x$  and

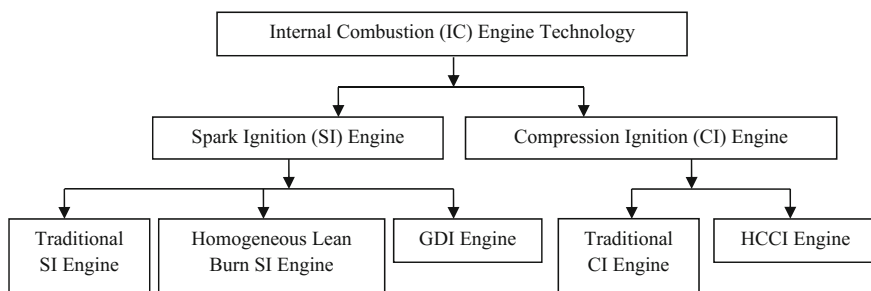
soot emissions, instead of 15% EGR. It was also reported that increasing intake swirl and intake pressure reduces the  $\text{NO}_x$  emissions and increases power loss and resistance to knock (Gharehghani et al. 2012). Heated inlet air temperature with EGR reduced the BTE as well as  $\text{NO}_x$ , unburned hydrocarbon, and CO emissions (Paykani et al. 2012).

Figure 5.1d shows CNG DI technology schematically. In this method, CNG is injected directly into the combustion chamber at a high pressure. The air–fuel mixture is then compressed and ignited by the spark plug just before TDC. Introduction of CNG directly into the combustion chamber leads to a significant improvement in volumetric efficiency and reduces pumping losses. Exclusion of diesel spray also permits reduction in unburned hydrocarbon emissions. Richards et al. (Heywood 1988) investigated the performance of direct injection CNG engine and noticed higher power output and thermal efficiency than a conventional SI NG-fueled engine due to its relatively higher compression ratio and lower pumping losses at part-load conditions. Ikeda et al. (Richards 1992) reported doubling the BMEP using CNG DI technology compared to conventional SI CNG engine technology.

### 5.1.2 Classifications of CNG Engine Technology

Internal combustion (IC) engine technology is one of the most exciting segments for advanced mobility development, even in present times. Figure 5.2 shows various IC engine technologies, either available or being developed/improved further for large-scale deployment in the transport sector.

In SI engines, either a homogeneous mixture of NG and air or gasoline and air is inducted into the engine, and then compressed and ignited using a spark plug. SI engines dominate the passenger car market due to its high specific power output; however, they suffer from the problem of lower thermal efficiency as a result of unavoidable throttling and engine knocking. In CI engines, only air is introduced into the engine and compressed to a higher temperature. Fuel, typically diesel, is injected into the hot compressed air, where it vaporizes, mixes with air, and



**Fig. 5.2** IC engine technology landscape

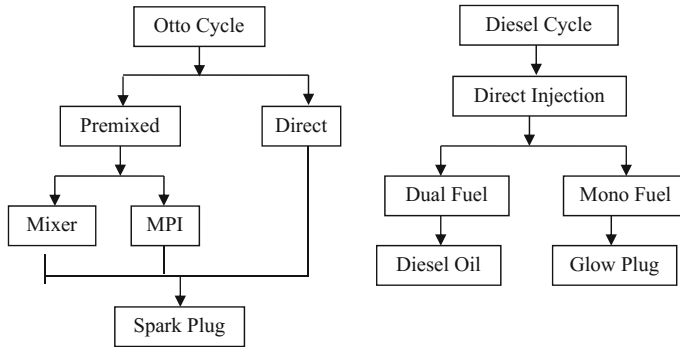


**Fig. 5.3** Basic CNG engine technology landscape (Ikeda et al. 1995)

spontaneously ignites at multiple locations. CI engines dominate the heavy-duty engine market due to their higher efficiency; however, they face the problem of higher particulate and  $\text{NO}_x$  emissions. Therefore, comprehensive research was required to meet the stringent emission legislation as well as to improve the fuel economy of the engine. In the last few decades, CNG has emerged as one of the most potential alternatives to meet these conflicting requirements. Figure 5.3 illustrates the basic structure of the existing CNG engine technologies. Each of the techniques has unique feature/specific strategies of mixture preparation, combustion control, and emission reduction, under the overall common goal of fuel economy improvement.

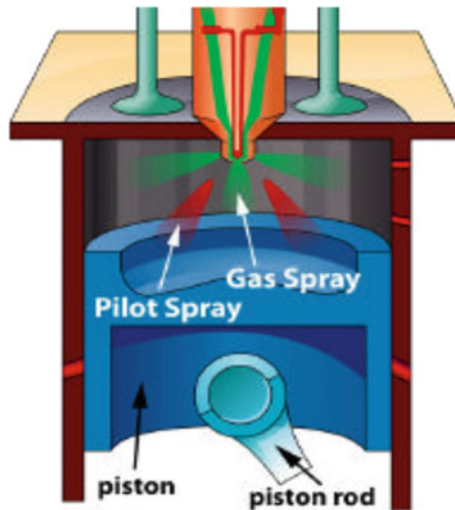
### 5.1.3 CNG Charge Preparation Techniques

Higher fuel efficiency can be obtained by developing/employing effective CNG charge preparation, which reduces engine emissions. CNG–air mixture preparation techniques can be classified into three main categories: port fuel injection (mixture prepared externally), dual fueling, and in-cylinder fuel injection technique (internal mixture preparation during compression stroke).

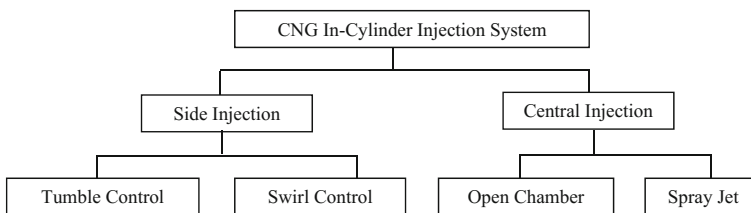
In port fuel injection system, CNG is injected upstream of the intake valve, where it mixes with air before entering the cylinder. This method provides an opportunity to form a homogeneous fuel–air mixture before its entry into the combustion chamber. Reduction in volumetric efficiency due to the displacement of intake air and lower part-load efficiency due to throttling of intake air are two major shortcomings of the port fuel injection strategy for CNG (Hassan et al. 2009).

Figure 5.4 illustrates dual-fuel injection technique schematically. There are two different types of dual-fuel injection systems: with pilot fuel injection and mixing fuel injection (MFI) systems.

In pilot fuel injection, a pilot quantity of mineral diesel is injected after the main injection of CNG in the engine cylinder, whereas in MFI system a small quantity of



**Fig. 5.4** Dual-fuel injection strategy



**Fig. 5.5** In-cylinder injection technique (Miyake et al. 1983)

mineral diesel is injected in advance into the CNG, so that pilot fuel and CNG are introduced together into the cylinder in a mixed form. Generally, pilot fuel injection strategy needs smaller pilot fuel quantity compared to MFI; however, it requires more complicated and evolved dual-fuel injector and control systems (Dunn 2003).

Figure 5.5 illustrates CNG in-cylinder fuel injection techniques.

The side injection system has the direction of injection jet toward the wall of the piston bowl. This system can be classified into two:

- **Tumble Control Side Injection:** CNG–air mixture motion perpendicular to cylinder axis is termed as tumble motion. The design of piston bowl supports this motion and diverts the direction of motion near the spark plug.
- **Swirl Control Side Injection:** Swirl air motion is parallel to the cylinder axis, and piston wall interaction is used to prepare and transport ignitable mixture near the spark plug.

In central injection of CNG, injection direction is toward the center of the piston bowl. It consists of the following two methods:

- Open-Chamber Central Injection: Air does not have any special motion. Only the movement of the piston is used to prepare a homogeneous mixture.
- Spray Jet Central Injection: Piston bowl is used to control the mixture with spark ignition trailing the edge of the spray.

However, in-cylinder CNG injection process is actually limited by lack of availability of suitable fuel injector. An open-chamber high-pressure central injection system along with simple bowl-type piston recess on top of the piston can be adapted as a mean for achieving reasonably good in-cylinder mixture homogeneity.

#### ***5.1.4 CNG DI Engine Technology: Hurdles and Challenges***

CNG DI technology is still in the research and development stage, and its development cost is quite high, making it difficult to initially compete with the existing after-market conversions. Development of CNG DI engine technology faces major challenges in the following aspects.

##### **A. Modification of the existing cylinder head**

- For accommodating fuel injector, spark plug, and a pressure transducer, engine cylinder head needs to be modified carefully so that it can withstand high stresses due to combustion.

##### **B. Development of dedicated CNG injectors**

- The durability of injectors due to exposure of dry gas is challenging.
- Maintenance of the injector turndown ratio to cope with adequate fuel flow rates from high to low engine loads is challenging.
- Quick transmission of fuel injection pressures due to compressible nature of natural gas makes it challenging.

##### **C. Development of a flexible electronic circuit and closed-loop engine management system is essential.**

## **5.2 Parameters Influencing Combustion and Emissions from DI CNG-Fueled Engines**

Combustion and emissions from engines are mainly depended on the fuel–air mixing as well as on fuel injection parameters like fuel injection duration, injection delivery pressure, nozzle geometry, the design of piston-cylinder and turbulence

within the chamber and engine structure (Hajjalimohammadi et al. 2014). From engine structure point of view, the throat diameter at the inlet valve seat to the cylinder bore ratio must be gradually reduced in order to achieve optimum brake thermal efficiency (BTE) (Yan et al. 2017). Ignition delay and combustion duration both decrease with increasing chamber reentrant level of 0.5 rather than 0.46 to reduced knock, heat rejection, and higher BTE ( $\sim 1.5\%$  at full load and 3% at medium to high load). Higher chamber reentrant level results in increased flame surface wrinkles due to a higher level of turbulence (Hajjalimohammadi et al. 2014). The nozzle having  $55^\circ$  hollow cone angle is most effective for mixing of CNG–air at the end of the compression stroke with early injection (Keskinen et al. 2016). On the other hand, impingement-induced mixing of CNG–air is more dominant with the circular nozzle with  $45^\circ$  hollow cone nozzle with a late injection. It promotes the toroidal vortex in the piston bowl, resulting in lower HC emissions (Keskinen et al. 2016). Location or configuration of spark plug electrode inside the engine cylinder is another essential factor, which affects the combustion duration. Central spark plugs (CSPs), appropriate equivalence ratio ( $\Phi$ ), and spark plug configurations of the SI system are effective parameters to reduce the combustion duration. Central spark plug location for  $\Phi = 1.0$  gives least combustion duration. Both Wobbe Index (WI) and maximum combustion potential (MCP) are indicators of the performance of fuel–air mixture in IC engines (Min et al. 2002; Kakaee et al. 2014). MCP is an index of combustion speed for gaseous fuel, and it is expressed by the following equation:

$$\text{MCP} = \frac{0.1\text{H}_2 + 0.6(\text{CO} + C_m\text{H}_N) + 0.3\text{CH}_4}{\sqrt{d}} \quad (5.1)$$

In Eq. (5.1), the numerator indicates the summations of various fractions of constituents of NG and in the denominator ‘ $d$ ’ represents the specific gravity of the typical NG. The WI compares the combustion energy output of different compositions of fuel gas, and MCP is the indicator of the combustion characteristics of the engines. It is reported that THC decreases and  $\text{NO}_x$  slightly increases with increasing WI and MCP (Min et al. 2002).

### 5.3 Optical Diagnostic Techniques for CNG Induction

Many engine researchers investigated the CNG jet structure (such as jet penetration and jet cone angle) using different optical diagnostic techniques: Schlieren and Shadowgraphy (Hajjalimohammadi et al. 2013, 2016; Petersen and Ghandhi 2006; Chitsaz et al. 2013; Erfan et al. 2015), PLIF (Rubas et al. 1998), and visualization by injection in liquid ambient. Few experimental studies (Chitsaz et al. 2013; Rubas et al. 1998; Chiodi et al. 2006; Yu et al. 2012; Mohamad et al. 2010) are concentrated on the structure of a jet produced by multi-hole nozzles. For direct injector, the injection pressure, at which the fuel is injected into the cylinder,



depends on many parameters. Taha et al. (2017) experimented with Bosch HDEV 1.2 injector, which was designed for GDI engine, and the maximum fuel injection pressure was  $\sim 200$  bar. It was reported that fuel injection pressure was varied between 20 and 60 bar for CNG (Taha et al. 2017). The injection pressure was dependent on in-cylinder pressure at the time of injection as well as the pulse width of the injection. High pressure was used for obtaining very high injection rates for small pulse width.

### ***5.3.1 Schlieren Technique for Visualization of Direct Injection of Hydrogen***

In Schlieren technique, an optical inhomogeneity was observed due to a change in refractive index of the medium. Refractive index varies linearly with the density. There is a change in density of the fuel delivered from the fuel nozzle due to the presence of higher pressure or temperature compared to ambient, which affects the light exposure to the camera. In one study, four identical prototype injectors (except a number of holes) were developed and tested under transient gaseous jets for high pressure ( $\geq 100$  bar) by Westport Innovations, Canada (Petersen 2006).

#### *Jet Pattern Visualizations:*

The jet pattern visualization of different number of nozzle holes was done using Schlieren in a constant volume chamber by injecting hydrogen at 104 bar in quiescent inert medium of nitrogen. The Schlieren end view and side views were captured at 8200 and 4800 fps, respectively. It was reported that 3-hole and 7-hole injectors showed irregularities between exiting jets, while 9- and 13-hole injector jets interact with each other and formed fuel-rich regions, which restricted the fuel-air mixing compared to a 3-hole injector (Petersen 2006).

#### *Under-expansion Features:*

One-, 3-, 7-, and 9-hole injectors produced spray of barrel structure for their individual jets, while the individual structures produced by the 13-hole injector appear to coalesce and create a single larger spray structure (Petersen 2006).

### ***5.3.2 Schlieren Technique for Visualization of Direct Injection of NG***

Figure 5.6 shows the Schlieren optical setup, in which two mirrors are arranged in Z-type. This setup consists of two identical parabolic mirrors, which were placed in such a way that both were in opposite direction and free from optical aberration. An outward-opening GDI injector was fitted on the top of constant volume chamber

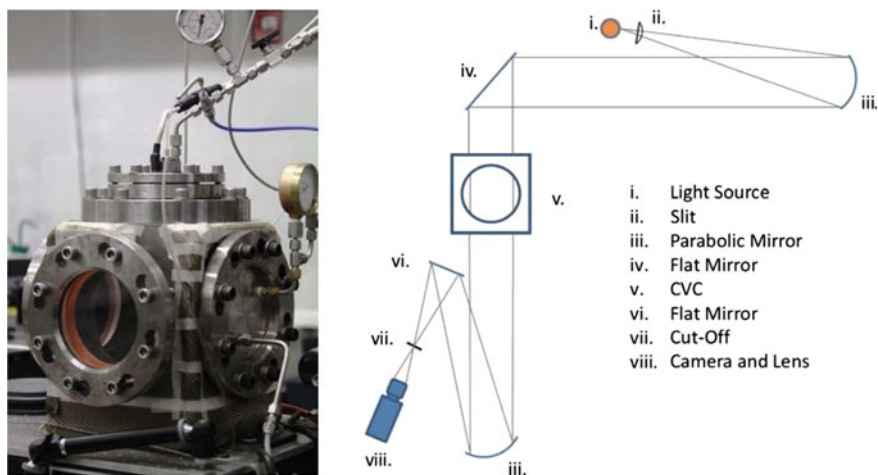


**Fig. 5.6** Schlieren imaging setup of CVC using folded Z-type mirrors (Rogers 2014)

(CVC). A schematic of the cross section of outward-opening injector nozzle is shown in Fig. 5.7. The included angle of the nozzle seat was  $\sim 90^\circ$ . The injector was placed on the top of the CVC having 7L capacity and four optical accesses (Fig. 5.6). The fused silica optical windows used in CVC were 40 mm thick and 150 mm in diameter.

In this experimental study, CNG was injected into the CVC, which was maintained at atmospheric pressure. Images of flow near-field from a  $90^\circ$  conical annular nozzle were investigated using Schlieren imaging. Experiments were performed in 20 bar steps, starting from 20 to 160 bar. It was reported that at the exit of injector, immediately downstream of the nozzle, a hollow conical gas jet was formed, which was followed by a toroidal vortex.

The gas jet emitted from the nozzle took the shape of annulus as depicted in Fig. 5.7a. A toroidal vortex was formed just after gas exit from the nozzle, as shown in Fig. 5.7b. It was reported that just after jet exit from the nozzle, with increasing pressure, the vortex size increased first and then slowly retarded. Large regions of recirculation were formed as the gas jet filled up the void present inside the cone and collapsed along the injector's axis (Fig. 5.8).

Initially, Ouellette and Hill validated (Ouellette and Hill 2000) these conditions and various injection parameters used by them are included in Table 5.1.

The numerical model with the given conditions was developed in AVL FIRE software, and injection modeling of methane gas into air was simulated. A snapshot of flow field near-nozzle exit is shown in Fig. 5.9b. Exit gas flow of Mach number 1.0 occurred at the inlet boundary 1 mm downstream of the nozzle, with a complex flow pattern, and the maximum exit Mach number obtained was 3.24. Therefore, injection process is a strongly transient phenomenon because of needle bounces and this conclusion was strongly supported by the simulation model. Yadollahi and

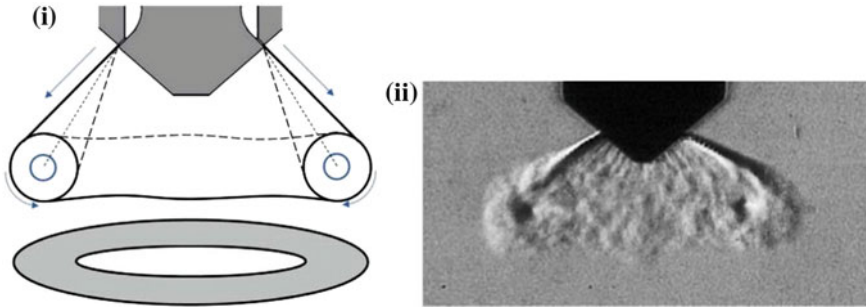


**Fig. 5.7** **a** Cross section of hollow conical jet. **b** Image of nozzle near-field at 140,000 fps, pressure ratio = 20 (Sankesh et al. 2018)

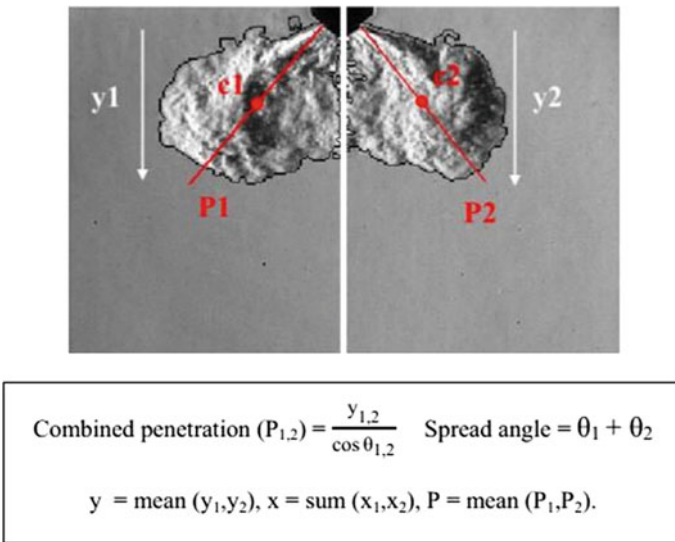


**Fig. 5.8** **a** Image showing jet penetration (P) and spread angle (Sankesh et al. 2018)

**Table 5.1** Injection conditions used by Ouellette and Hill (2000)

Chamber dimension radius (mm)	20 mm
Chamber dimension length (mm)	90 mm
Injection pressure (MPa) and temperature (K)	$P_{0_{inj}} = 15 \text{ MPa}, T_{0_{inj}} = 350 \text{ K}$
Chamber pressure (MPa) and temperature (K)	$P_{0_{ch}} = 5, T_{0_{ch}} = 850 \text{ K}$
Wall temperature (K)	$T_w = 450(\text{K})$
Nozzle diameter (mm)	$d_N = 0.5 \text{ (mm)}$
Injected mass (mg)	3.5(mg)
Turbulence level ( $\text{m}^2/\text{s}^2$ )	1.5 ( $\text{m}^2/\text{s}^2$ )

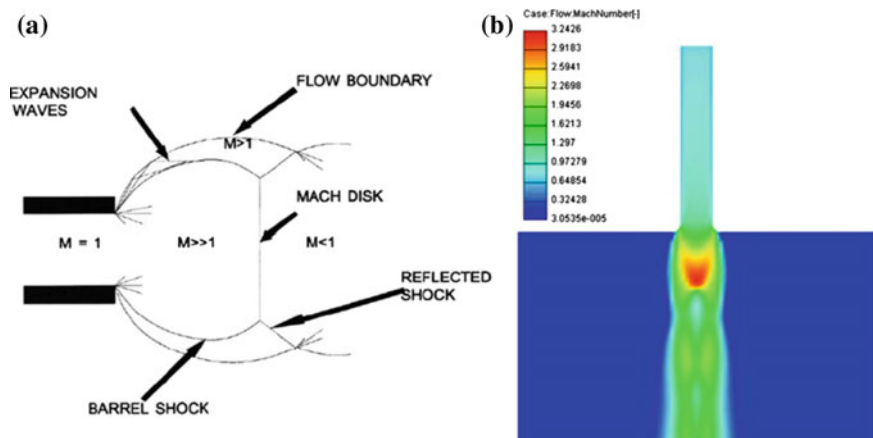


**Fig. 5.9** Flow pattern in under-expansion flow: **a** graphical representation, (Ouellette and Hill 2000) and **b** numerical simulation (Yadollahi and Boroomand 2013)

**Table 5.2** Inputs for injection modeling (Yadollahi and Boroomand 2013)

Injected fluid	Methane
Chamber fluid	Air
Fuel rail pressure	8 bar
Chamber pressure	1 bar
Chamber temperature	300 K
Duration of injection	10 ms
Fuel mass flow	270 mg/s

Boroomand (2013) also performed numerical modeling of CNG injector, and the inputs for it are given in Table 5.2.

It was reported that single-hole nozzle injector produced much more fuel-rich zones compared to multi-hole nozzle injector (Fig. 5.10).

It was reported that a wider nozzle angle produces deeper jet propagation radially, compared to axially. Both axial and radial penetration depths were measured using the centroid of the jet's projected area. This type of penetrations can also be used for irregular jet nozzles. It was reported that low penetration rate could be better for centrally mounted outward-opening injectors for the stratified mode in spray-guided DISI engines.

Erfan et al. (2017) performed experiments to determine the effect of chamber pressure (5–15 bar) on the fuel jet tip penetration depth with 40 bar fuel injection pressure. It was found to be an inverse relation between tip penetration and pressure of the chamber. It was noted that jet penetration was affected more by the chamber pressure than the fuel injection pressure. The fuel injection pressure and ambient pressure inside the chamber have a positive and negative impact on the jet penetration. The jet penetration depth was found to increase with increasing fuel injection pressures and with lower chamber pressures.

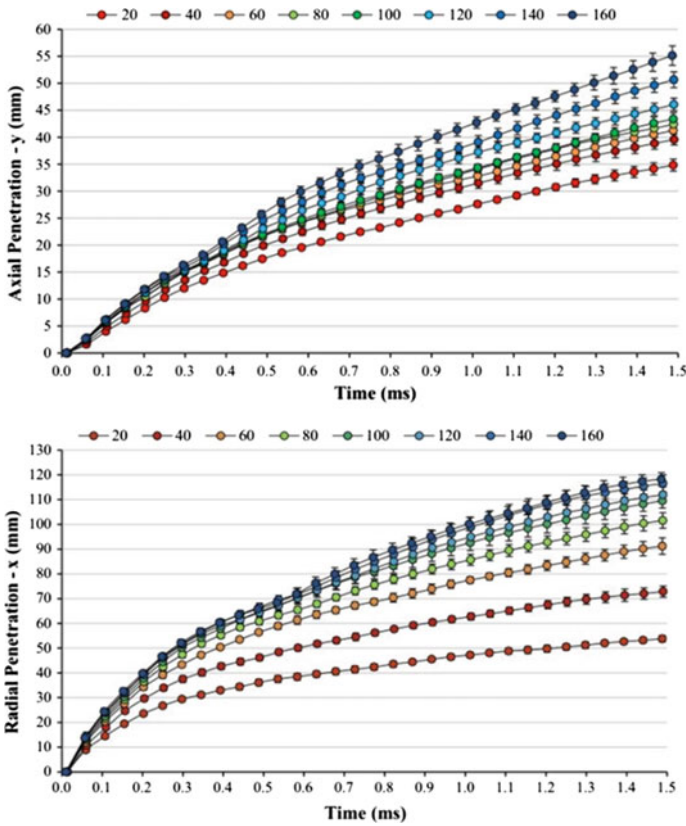


**Fig. 5.10** Mean combined penetration depth for pressure ratio (PR) 20–160 in steps of 20 bar. Fuel injection pressure ( $P_o$ ) = 20–160 bar. Chamber pressure ( $P_a$ ) = 1 bar.  $T_a = T_o = 294$  K. (Sankesh et al. 2018)

### 5.3.3 Investigation of CNG Sprays Using Planar Laser-Induced Fluorescence (PLIF)

Figure 5.11 shows a schematic of a typical PLIF experimental setup, which was used to investigate various parameters of spray. The PLIF setup consists of a fuel delivery system, a solid-state Nd:YAG laser (266 nm/40 mJ), sheet optics, a digital-pulse generator, and a CCD camera. For safety reasons, instead of natural gas, compressed nitrogen was injected and acetone was used as a tracer by simple bubbling because it has low boiling point temperature and no toxicity (Fig. 5.12).

The numerical simulation of gaseous fuel spray results was by and large in agreement. Few researchers performed a numerical simulation of gaseous fuel injection using the KIVA-3 V (Release 2) code. It was concluded that the core region (near the nozzle exit) has an effect on the gas fuel penetration, which is mainly dependent on the nozzle hole size. The modified RNG  $k-\epsilon$  turbulence model was used during

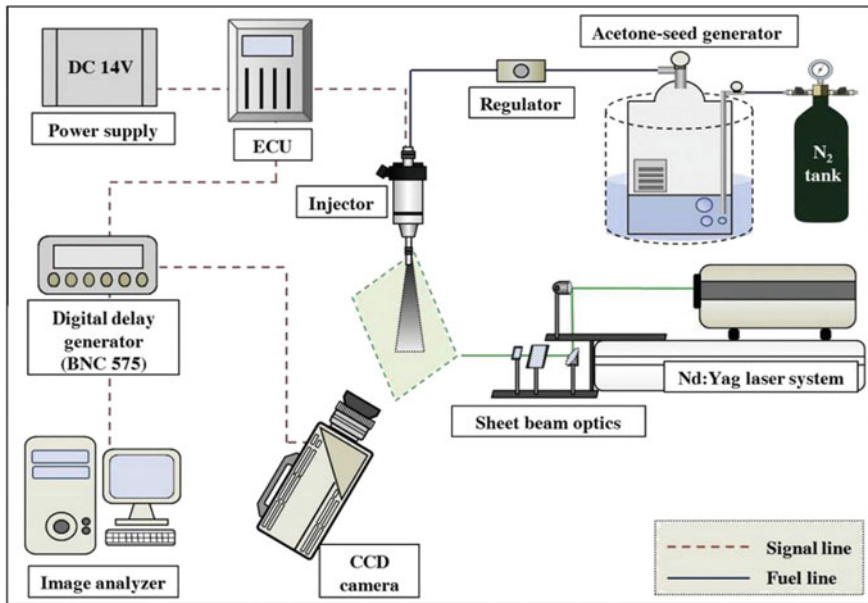


Fig. 5.11 Schematic of PLIF arrangement for CNG DI spray visualization.  $P_{inj} = 2, 4.5$  Mpa;  $P_{amb} = 1$  MPa;  $T_{amb} = 288$  K;  $Inj_{time} = 1.5$  ms;  $d_{nozzle} = 0.14$  mm (Choi et al. 2015)

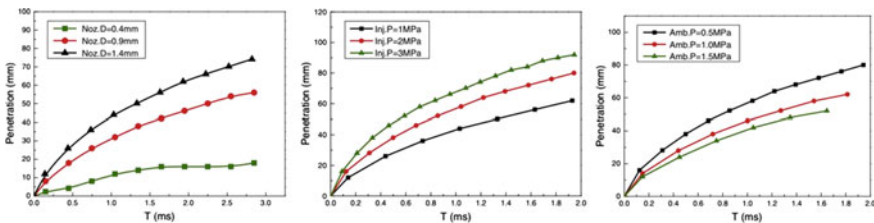
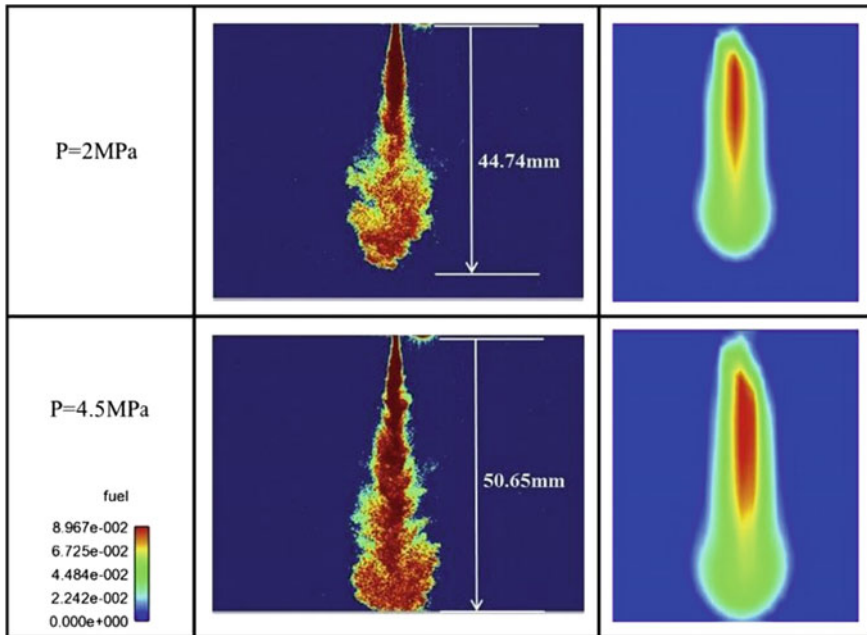


Fig. 5.12 Gas jet penetration as a function of the nozzle hole diameter, injection pressure, and ambient pressure (Choi et al. 2015)

the injection period, and after that, the conventional RNG  $k-\epsilon$  turbulence model was used.

ent with the experimental results obtained by PLIF (refer Fig. 5.13). The cross-sectional image of nozzle of the gas injector could be captured by CCD camera. It was observed that simulation results could not predict quite appropriately using a coarse mesh. Gas jet diffusion is an important aspect in simulation and is taken care off near the nozzle tip in order to predict the diffusion and penetration. Gaseous fuel injection model can be used for gaseous fuel injection, CNG direct injection as well as combustion using a coarse mesh.



**Fig. 5.13** Comparison of simulation results with experimental results of gas jet penetration at different pressures (Choi et al. 2015)

#### 5.4 Comparative Analyses of DI and PFI CNG Injection on Engine

Figure 5.14 shows the engine experimental setup with DI injection as well as PFI injection of CNG into the engine combustion chamber. In both PFI and DI engines, CNG–air mixture quality and homogeneity before the spark were better than those of conventional gasoline–air mixture, which led to more complete combustion relatively. Due to complete combustion, BSFC, HC, and CO emissions reduced. Lower C/H ratio of CNG reduced the CO<sub>2</sub> emission. NO<sub>x</sub> emitted from CNG bi-fuel engines was obviously higher than gasoline fueling, because of higher BTE and higher combustion temperature. Since gasoline is a liquid fuel, it cools the intake charge during mixture preparation; hence, lower peak temperature is attained during combustion, and thus, lower NO<sub>x</sub> formation takes place in case of gasoline combustion vis-à-vis CNG. PFI technique uses low injection pressure but early fuel induction during suction, while in case of DI higher fuel injection pressure was used for fuel induction during compression stroke for better atomization and improved fuel–air mixture quality (Lee and Park 2014a, b). The injected fuel absorbs latent heat of vaporization from pressurized air in the combustion chamber, and thus charge cooling enhances volumetric efficiency of the engine. Better volumetric efficiency results in improved engine power because more air is inducted into the

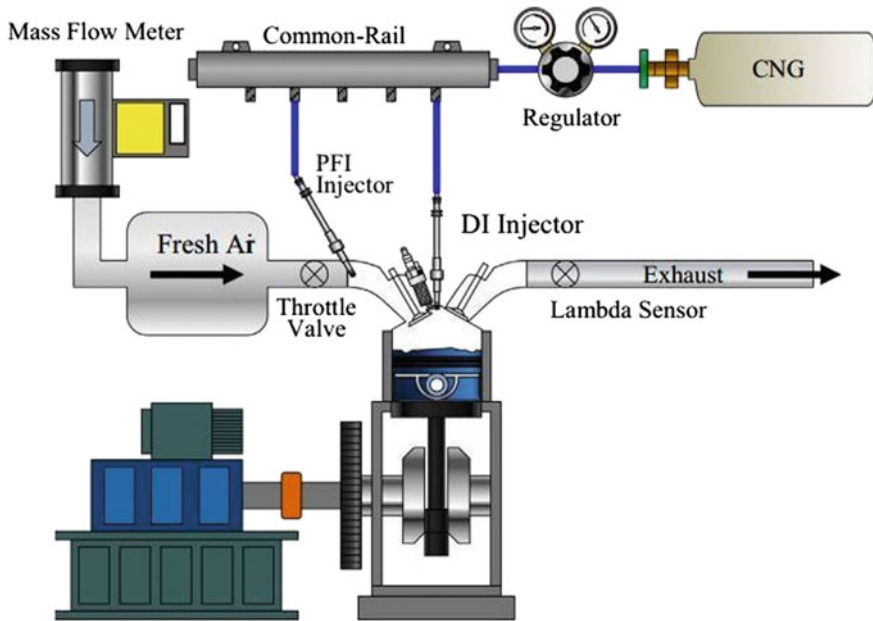


Fig. 5.14 Engine experimental setup with DI and PFI induction techniques (Song et al. 2017)

cylinder and hence more fuel (Movahed et al. 2014). In addition, a properly designed DI system allows the fuel saving during deceleration (Alkidas and El Tahry 2003; Fansler et al. 2009; Zhao et al. 1999).

#### 5.4.1 Volumetric Efficiency for DI and PFI Systems

Figure 5.15a shows the comparison between DI and PFI systems for volumetric efficiency by varying SOI timings at  $\lambda = 1.0$  and  $20^\circ$  CA bTDC spark timing. SOI timing was varied from  $330^\circ$  CA bTDC to  $120^\circ$  CA bTDC during the experiment. The volumetric efficiencies of DI and PFI were almost similar for early fuel injection before the IVC. For the SOI timings varied from  $330^\circ$  CA bTDC to  $120^\circ$  CA bTDC, the volumetric efficiencies of DI and PFI were both  $\sim 38.62 \pm 0.2\%$  standard deviations. The numerical simulation results depicted that the fuel intake flow was influenced by the fuel injection pressure, regardless of its position. Late DI, near the IVC, increased the volumetric efficiency. This strategy showed optimized torque due to higher volumetric efficiency and turbulence, hence faster combustion. This optimized strategy resulted in stable  $COV_{IMEP} (<1.5\%)$ . Faster combustion is supposed to improve BSFC under idle engine operating condition.



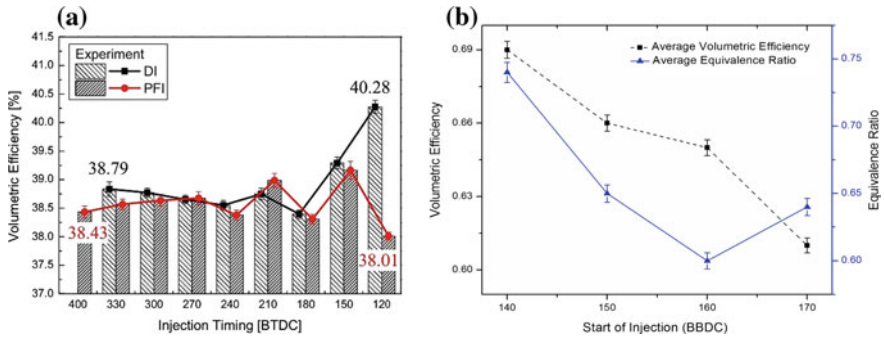


**Fig. 5.15** **a** Volumetric efficiency versus SOI; displacement volume 338.27 ml; 1700 rpm;  $P_{inj} = 1.4$  MPa; DI: bTDC 330–120° CA; PFI: bTDC 400–120° CA;  $\Phi = 1.0$ ; CR = 11.5 (Song et al. 2017) and **b** volumetric efficiency versus  $\Phi$  and SOI; 1500 rpm; 50 bar injection pressure; 948 CC engine capacity; CR = 9.5 (Kar and Agarwal 2015)

Figure 5.15b depicts the effect of SOI timings and  $\Phi$  on the volumetric efficiency of the CNG-fueled DI engine. It was reported that retarded SOI timing increased the volumetric efficiency of CNG-fueled DI engine. A similar observation was reported by Goto (Goto 1999). This was because pressurized CNG displaced a high volume of air during fuel induction and suction.

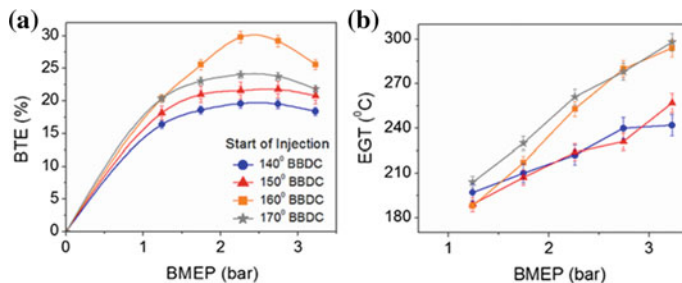
### 5.4.2 CNG DI Engine Performance Characteristics

Engine performance in terms of its brake thermal efficiency (BTE), brake-specific fuel consumption (BSFC), and exhaust gas temperature (EGT) was investigated by several engine researchers with varying engine operating conditions. The engine specifications used for this study are given in Table 5.3.

Figure 5.16 shows DI engine performance characteristics curves for a different SOI at varying BMEP at 1500 rpm and 50 bar CNG injection pressure.

**Table 5.3** Engine specifications after modifications (Kar and Agarwal 2015)

Make	Kirloskar
Model	DM-10
Bore	102 mm
Stroke	115 mm
Displacement	948 CC
Compression ratio	9.5
Combustion chamber	$\omega$ Bowl
CNG injection pressure	50 bar
Ignition source	Spark plug



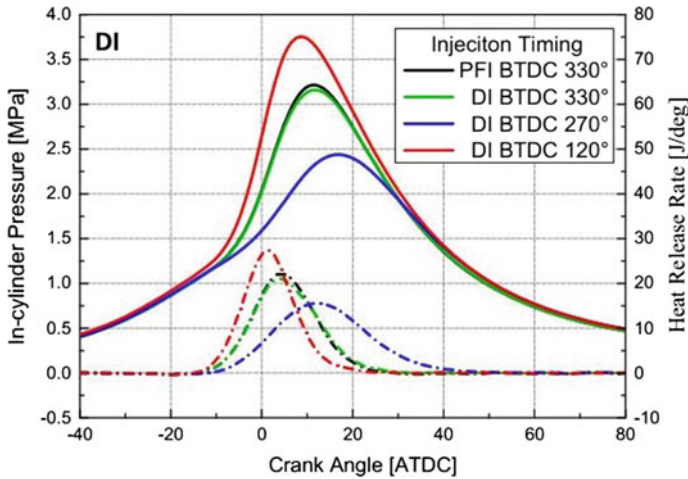
**Fig. 5.16** DI engine performance characteristics for varying SOI timings: **a** BTE versus BMEP and **b** EGT versus BMEP (Kar and Agarwal 2015)

Figure 5.16a shows variation of BTE w.r.t. varying BMEP and SOI. It was reported that for all SOI timings, BTE was higher for higher BMEP, and it reached a maximum at intermediate load and then started reducing with further increased BMEP. Among all SOI timings tested, 160° bBDC resulted in higher BTE under all operating conditions. It was noted that BSFC was relatively lower at intermediate loads compared to low load and high load conditions. Similar results were also reported by Hassan et al. (2009) and Aslam et al. 2006 (Goto 1999). At high engine loads, more fuel–air mixture was required to generate higher power output; however, large pumping losses were observed at low engine loads, which increased the BSFC. The lowest BSFC was 0.26 kg/kWh obtained at 2.5 bar BMEP (for 160° bBDC SOI). Figure 5.16b shows the variation of EGT with BMEP for different SOI timings. EGT was lower at lower BMEP, which increased with increasing BMEP, and the maximum was reported at 170° bBDC SOI. The engine operated in CNG DI configuration with advanced SOI timings resulting in relatively lower BSFC, higher BTE and EGT and vice versa. Retarded SOI timings reduced the time available for fuel–air mixing and reduced the fuel jet penetration distance toward the end of injection in the later part of injection or after the intake valve closing. This happens because of the presence of higher cylinder pressures near TDC, which offered resistance to the fuel injected. This finally resulted in relatively inhomogeneous CNG–air mixing hence relatively inferior engine combustion and performance.

### 5.4.3 CNG DI Engine Combustion Characteristics

The in-cylinder pressure–crank angle history ( $P$ – $\theta$  diagram) was obtained at different engine loads for CNG DI engine at various SOI conditions. Figure 5.17 shows variations of in-cylinder pressures and heat release rates (HRRs) for varying SOI strategies.

The in-cylinder pressure at SOI at 120° CA bTDC was significantly higher ( $\sim 3.75$  MPa) compared to other SOI conditions. This was due to relatively higher



**Fig. 5.17** In-cylinder pressure and HRR for different SOI; MBT timing 20° CA bTDC (Song et al. 2017)

flame speed rather than a large amount of injected fuel. The HRR curve in Fig. 5.17 was used to compare the flame speed by analyzing the combustion duration. It was reported that the combustion duration at SOI of 120° CA bTDC was much shorter compared to other SOI timings. As the charge was consumed and flame front propagated toward the piston, HRR curve increased steeply and reached a maxima at ~1.5° CA aTDC before further reducing to zero at ~20° CA aTDC (Song et al. 2017). Combustion duration reported (between the sparks initiated to the end of combustion) was ~40° CA. On the other hand, SOI of 270° CA bTDC showed relatively longer combustion duration. Figure 5.18a shows that in-cylinder pressure increased with engine load for all SOI strategies. With increasing BMEP, more CNG was combusted, which improved the volumetric efficiency in the DI CNG engine. Advanced SOI timings (160 and 170° bBDC) produced higher in-cylinder

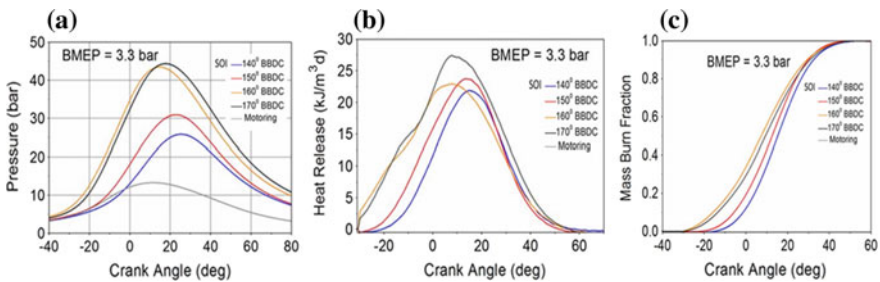


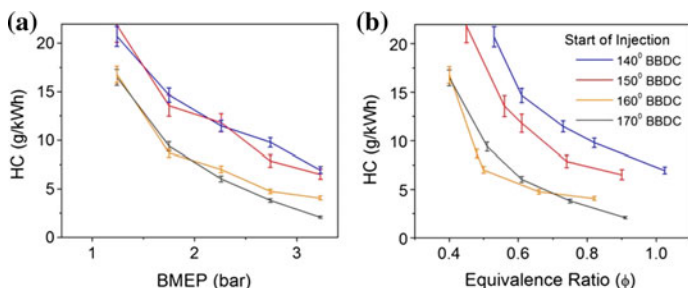
**Fig. 5.18** Engine combustion characteristics curves: **a** pressure versus SOI, **b** heat release rate versus SOI, **c** mass burn fraction versus SOI; 1500 rpm; 50 bar injection pressure; 948 CC engine capacity (Kar and Agarwal 2015)

pressures at all BMEP. Advanced SOI timing resulted in superior homogeneous mixture formation and improved combustion. Figure 5.18b, c shows the variations of heat release rate (HRR) and mass burn fraction w.r.t. crank angle for different SOI timings.

It was reported that HRR increased with increasing BMEP as well as retarded SOI. This was because of more CNG injected and faster combustion rates at high BMEP. For all BMEP, advanced SOI timings ( $160^\circ$  and  $170^\circ$  BBDC) resulted in higher HRR compared to retarded SOI timings; however, 2.8 bar BMEP resulted in identical HRR curves. At all engine BMEPs, advanced SOI timing shifted the maximum HRR closer to the TDC as compared to the retarded SOI timings. Moving closer to TDC pointed at possibly faster flame speeds and reduced the combustion duration for advanced injections. Figure 5.18c shows the percentage of mass burn fraction (MBF) at different SOI timings. It was reported that advanced SOI timings resulted in relatively earlier SOC and vice versa.

#### 5.4.4 CNG DI Engine Emission Characteristics

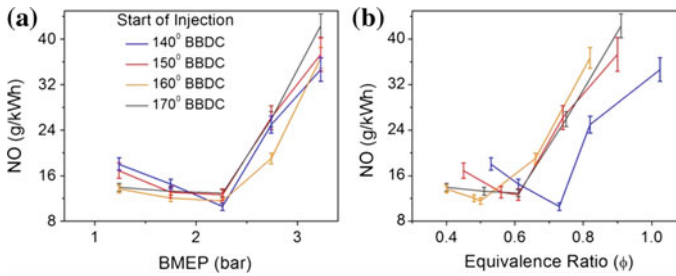
Figure 5.19a shows the variations of HC mass emissions with BMEP, and corresponding  $\Phi$  is indicated in Fig. 5.19b for different SOI timings. It was reported that either at lower BMEP or at lower  $\Phi$ , HC emissions were higher, and they decreased with increasing BMEP and  $\Phi$ . At lower BMEP, relatively slower flame speed of CNG–air mixture was unable to burn the charge completely, which led to increased HC emissions. On the other side, at higher BMEP, lack of oxygen in rich CNG–air mixtures resulted in incomplete combustion and increased unburned HC emissions. The unburned HC emitted in case of CNG-fueled DI engine for all operating conditions varied between 2.0 and 20.7 g/kWh. It was also noticed that retarded SOI timings increased the HC emissions compared to advanced injection timings. Advanced SOI timing provided adequate time for mixture preparation, leading to relatively superior combustion (Goto 1999).



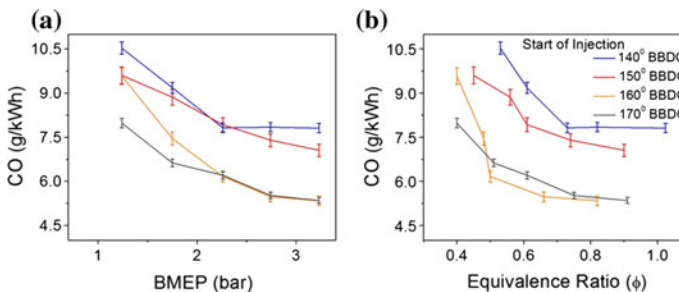
**Fig. 5.19** Unburnt HC emissions for different SOI timings: **a** mass emissions of HC versus BMEP and **b** mass emissions of HC versus equivalence ratio; 1500 rpm; 50 bar injection pressure; 948 CC engine capacity (Kar and Agarwal 2015)

Figure 5.20 depicts variations of NO w.r.t. BMEP and  $\Phi$  for different SOI timings at 1500 rpm and 50 bar CNG injection pressure. It was reported that at a relatively lower engine load and lower  $\Phi$ , marginally lower NO was produced due to low combustion temperature, which increased exponentially with increasing  $\Phi$  up to 0.9. However, at higher BMEP with  $\Phi$  in the range of 0.8–0.9, higher combustion temperature and the presence of sufficient excess oxygen produced higher NO. Experimental data showed that NO varied in the range of 12–42 g/kWh. It was also observed from Fig. 5.20 that NO emission increased with advanced SOI timing due to relatively faster flame speed and more complete combustion and vice versa (Goto 1999).

Figure 5.21 shows the variation of CO w.r.t. BMEP and  $\Phi$  at 1500 rpm and for different SOI timings. CO emitted from DI engine combustion is strongly influenced by CNG–air mixture strength. It was reported that engine operating at higher BMEP produced higher CO, and at higher equivalence ratio, it produced lower CO due to combustion of relatively leaner mixture. However, CO emission increased with increasing  $\Phi$  because of formation of localized rich zones. Different SOI timings showed minor variations in CO, which lies between 0.05 and 0.1% (v/v),



**Fig. 5.20** NO<sub>x</sub> emissions for different SOI timings: **a** mass emissions of NO versus BMEP and **b** mass emissions of NO versus equivalence ratio; 1500 rpm; 50 bar injection pressure; 948 CC engine capacity (Kar and Agarwal 2015)



**Fig. 5.21** CO emissions for different SOI timings: **a** mass emission of CO versus BMEP and **b** raw emission of CO versus  $\Phi$ ; 1500 rpm; 50 bar injection pressure; 948 CC engine capacity (Kar and Agarwal 2015)

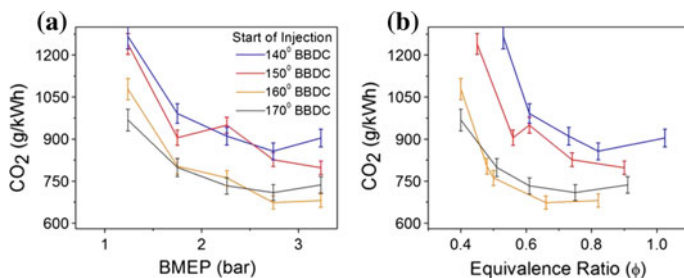


**Fig. 5.22** CO<sub>2</sub> emissions for different SOI timings: **a** mass emissions of CO<sub>2</sub> versus BMEP and **b** mass emissions of CO<sub>2</sub> versus  $\Phi$ ; 1500 rpm; 50 bar injection pressure; 948 CC engine capacity (Kar and Agarwal 2015)

which was relatively lower compared to conventional gasoline-fueled engines. Inferior combustion was reported in case of retarded SOI timings, which resulted in relatively higher CO emission compared to that of advanced SOI timings.

Figure 5.22 shows the variation of CO<sub>2</sub> emissions w.r.t. BMEP and  $\Phi$  from CNG–air engine under different SOI timings. It was noticed that CO<sub>2</sub> emissions reduced with increasing BMEP due to the requirement of lower CNG quantity to produce higher power output and it varied from 4–8% (v/v). On comparing CO<sub>2</sub> emissions with typical gasoline SI engine, CNG DI engines produced roughly 20% lesser CO<sub>2</sub> emissions (Aslam et al. 2006). This was due to lower carbon-to-hydrogen ratio of natural gas compared to gasoline. CO<sub>2</sub> emissions increased with retarded SOI timing in spite of its inferior combustion characteristics because the CNG mass required to meet a particular load was higher in retarded SOI timing compared to an advanced SOI timing.

## 5.5 Conclusions

CNG DI technology is effective for enhancing the volumetric efficiency of the engine; hence, greater power output can be extracted from the vehicle. Different relevant cases were discussed in detail to understand the effect of injector nozzle parameters on engine performance using various optical tools, and thereafter, engine experimental investigations were performed to assess the performance, emissions, and combustion characteristics of a CNG DI engine operated under different SOI timings for varying BMEP. The following conclusions were drawn:

1. Schlieren images from CVC showed that at the start of injection, a hollow conical gas jet was formed, followed by a toroidal vortex. The wide nozzle angle  $\sim 90^\circ$  resulted in greater jet propagation radially than axially.
2. Nozzle with outward-opening injectors would be suitable for stratified mixture in spray-guided engine with lower spray penetration.

3. The injection pressure has an influence on the jet penetration and penetration length increased with an increasing fuel injection pressure, while chamber pressure had an opposite impact on the jet tip penetration.
4. The volumetric efficiency of CNG DI reduced at advanced SOI timings. Advanced SOI timings such as  $170^\circ$  reduced the BSFC and increased the BTE compared to retarded SOI timings at all engine loads.
5. Advanced SOI timings resulted in relatively lower unburned HC and higher NO emissions.
6. At moderate BMEP, BSFC and BTE were relatively lower.
7. Unburned HC emissions decreased with increasing engine BMEP up to an equivalence ratio of 0.9 but simultaneously increased NO and CO<sub>2</sub> emissions.
8. Retarded SOI strategies resulted in relatively lower peak in-cylinder pressure and maximum HRR compared to the advanced SOI timings.

Overall, CNG DI technology offers a host of advantages; however, the engine performance, combustion, and emissions need to be adequately optimized using flexible injection control systems.

## References

- Alkidas AC, El Tahry SH (2003) Contributors to the fuel economy advantage of DISI engines over PFI engines. SAE Technical Paper
- Aslam MU, Masjuki HH, Kalam MA, Abdesselam H, Mahlia TM, Amalina MA (2006) An experimental investigation of CNG as an alternative fuel for a retrofitted gasoline vehicle. *Fuel* 85(5–6):717–724
- BP P.L.C. (2017) BP Statistical Review of World Energy 2015–2017
- Chiodi M, Berner HJ, Bargende M (2006) Investigation on different injection strategies in a direct-injected turbocharged CNG-engine. SAE Technical Paper, 14 Sep 2006
- Chitsaz I, Saidi MH, Mozafari AA, Hajjalimohammadi A (2013) Experimental and numerical investigation on the jet characteristics of spark ignition direct injection gaseous injector. *Appl Energy* 1(105):8–16
- Choi M, Lee S, Park S (2015) Numerical and experimental study of gaseous fuel injection for CNG direct injection. *Fuel* 15(140):693–700
- Dunn M (2003) State of the art and future developments in natural gas engine technologies. Cummins Westport Inc. (US), 24 Aug 2003
- Durgada S, Lappas P (2017) Natural-gas direct-injection for spark-ignition engines—a review on late-injection studies. SAE Technical Papers, pp 1–3
- Erfan I, Chitsaz I, Ziabasharhagh M, Hajjalimohammadi A, Fleck B (2015) Injection characteristics of gaseous jet injected by a single-hole nozzle direct injector. *Fuel* 15(160):24–34
- Erfan I, Hajjalimohammadi A, Chitsaz I, Ziabasharhagh M, Martinuzzi RJ (2017) Influence of chamber pressure on CNG jet characteristics of a multi-hole high pressure injector. *Fuel* 1(197):186–193
- Fansler TD, Drake MC, Gajdeczko B, Düwel I, Koban W, Zimmermann FP, Schulz C (2009) Quantitative liquid and vapor distribution measurements in evaporating fuel sprays using laser-induced exciplex fluorescence. *Meas Sci Technol* 20(12):125401

- Gharehghani A, Mirsalim SM, Jazayeri SA (2012) Numerical and experimental investigation of combustion and knock in a dual fuel gas/diesel compression ignition engine. *J Combust* (Hindawi Publishing Corporation) (504590):10. <http://dx.doi.org/10.1155/2012/504590>
- Goto Y (1999) Mixture formation and ignition in a direct injection natural gas engine. *JSME Int J, Ser B* 42(2):268–274
- Gunawan H (1992) Performance and combustion characteristics of a diesel-pilot gas injection engine. Doctoral dissertation, University of British Columbia
- Hajjalimohammadi A, Honnery D, Abdullah A, Mirsalim MA (2013) Time resolved characteristics of gaseous jet injected by a group-hole nozzle. *Fuel* 1(113):497–505
- Hajjalimohammadi A, Abdullah A, AghaMirsalim M, Chitsaz I (2014) Experimental and numerical investigation on the macroscopic characteristics of the jet discharging from gaseous direct injector. *J Mech Sci Technol* 28(2):773–781
- Hajjalimohammadi A, Edgington-Mitchell D, Honnery D, Montazerin N, Abdullah A, Mirsalim MA (2016) Ultra high speed investigation of gaseous jet injected by a single-hole injector and proposing of an analytical method for pressure loss prediction during transient injection. *Fuel* 184:100–109
- Hassan MH, Kalam MA, Mahlia TI, Aris I, Nizam MK, Abdullah S, Ali Y (2009a) Experimental test of a new compressed natural gas direct injection engine. *Energy Fuels* 23(10):4981–4987
- Hassan MK, Aris I, Mahmud S, Sidek R (2009b) An experimental result of exhaust emission concentration relative to various injection timing of CNG fuelled direct injection engine. *Eur J Sci Res* 25(3):405–416
- Heywood JB (1988) *Internal combustion engine fundamentals*. McGraw-Hill, New York, p 915
- Ikeda K, Hashimoto T, Sumie Y, Ishibashi K, Komoda T, Beppu O (1995) Develop of the high efficient gas injection diesel engine. In: IGRC Conference
- Jafarmadar S, Zehni A (2010) Modeling the effect of EGR on combustion and pollution of dual fuel engines with flow field model. *Int J Energy Environ Eng* 1(1):19–26
- Kakaee AH, Paykani A, Ghajar M (2014) The influence of fuel composition on the combustion and emission characteristics of natural gas fueled engines. *Renew Sustain Energy Rev* 1(38):64–78
- Kar T, Agarwal AK (2015) Development of a single cylinder CNG direct injection engine and its performance, emissions and combustion characteristics. *Int J Oil Gas Coal Technol* 10(2):204–220
- Keskinen K, Kaario O, Nuutinen M, Vuorinen V, Künsch Z, Liavåg LO, Larmi M (2016) Mixture formation in a direct injection gas engine: numerical study on nozzle type, injection pressure and injection timing effects. *Energy* 1(94):542–556
- Lee S, Park S (2014a) Experimental study on spray break-up and atomization processes from GDI injector using high injection pressure up to 30 MPa. *Int J Heat Fluid Flow* 1(45):14–22
- Lee S, Park S (2014b) Spray atomization characteristics of a GDI injector equipped with a group-hole nozzle. *Fuel* 1(137):50–59
- Lüthi D, Le Floch M, Bereiter B, Blunier T, Barnola JM, Siegenthaler U, Raynaud D, Jouzel J, Fischer H, Kawamura K, Stocker TF (2008) High-resolution carbon dioxide concentration record 650,000–800,000 years before present. *Nature* 453(7193):379
- Methane Clathrate (2017) Wikipedia. Retrieved from: [https://en.wikipedia.org/wiki/Methane\\_clathrate](https://en.wikipedia.org/wiki/Methane_clathrate)
- Min BH, Chung JT, Kim HY, Park S (2002) Effects of gas composition on the performance and emissions of compressed natural gas engines. *KSME Int J* 16(2):219–226
- Miyake M, Biwa T, Endoh Y, Shimotsu M, Murakami S, Komoda T (1983) The development of high output, highly efficient gas burning diesel engines. CIMAC paper D11-2
- Mohamad TI, Harrison M, Jermy M, How HG (2010) The structure of the high-pressure gas jet from a spark plug fuel injector for direct fuel injection. *J Visual* 13(2):121–131
- Movahed MM, Tabrizi HB, Mirsalim M (2014) Experimental investigation of the concomitant injection of gasoline and CNG in a turbocharged spark ignition engine. *Energy Convers Manag* 1(80):126–136
- Ouellette P, Hill PG (2000) Turbulent transient gas injections. *ASME Trans J Fl Eng* 122:743–753



- Paykani A, Khoshbakhti Saray R, Shervani-Tabar MT, Mohammadi-Kousha A (2012) Effect of exhaust gas recirculation and intake pre-heating on performance and emission characteristics of dual fuel engines at part loads. *J Central South Univ* 19(5):1346–1352
- Petersen BR (2006) Transient high-pressure hydrogen jet measurements. Master of Science thesis, University of Wisconsin-Madison
- Petersen BR, Ghandhi JB (2006) Transient high-pressure hydrogen jet measurements. SAE Technical Paper, 3 Apr 2006
- Pirouzpanah V, Khoshbakhti Saray R (2006) A predictive model for the combustion process in dual fuel engines at part loads using a quasi-dimensional multi zone model and detailed chemical kinetics mechanism. *Int J Eng Trans B* 19(1):83–98
- Richards BG (1992) Direct gas injection with glow plug ignition. Interim report (Phases 2 and 3), February 1988–October 1992. Caterpillar, Inc., Peoria, IL (United States), 1 Oct 1992
- Rogers T (2014) Mixture preparation of gaseous fuels for internal combustion engines using optical diagnostics. Ph.D. RMIT University, Melbourne
- Rubas PJ, Paul MA, Martin GC, Coverdill RE, Lucht RP, Peters JE, DelVecchio KA. Methane jet penetration in a direct-injection natural gas engine. SAE Technical Paper, 1 Feb 1998
- Sankesh D, Edsell J, Mazlan S, Lappas P (2017) Comparative study between early and late injection in a natural-gas fuelled spark-ignited direct-injection engine. *Energy Procedia* 1 (110):275–280
- Sankesh D, Petersen P, Lappas P (2018) Flow characteristics of natural-gas from an outward-opening nozzle for direct injection engines. *Fuel* 15(218):188–202
- Sevik J, Pamminer M, Wallner T, Scarcelli R, Reese R, Iqbal A, Boyer B, Wooldridge S, Hall C, Miers S (2016) Performance, efficiency and emissions assessment of natural gas direct injection compared to gasoline and natural gas port-fuel injection in an automotive engine. *SAE Int J Engines* 9(2):1130–1142
- Song J, Choi M, Park S (2017) Comparisons of the volumetric efficiency and combustion characteristics between CNG-DI and CNG-PFI engines. *Appl Therm Eng* 5(121):595–603
- Taha Z, Rahim MA, Mamat R (2017) Injection characteristics study of high-pressure direct injector for compressed natural gas (CNG) using experimental and analytical method. In: IOP conference series: materials science and engineering, vol 257, no 1. IOP Publishing, p 012057, Oct 2017
- Yadollahi B, Boroomand M (2013) The effect of combustion chamber geometry on injection and mixture preparation in a CNG direct injection SI engine. *Fuel* 1(107):52–62
- Yan B, Tong L, Wang H, Zheng Z, Qin Y, Yao M (2017) Experimental and numerical investigation of the effects of combustion chamber reentrant level on combustion characteristics and thermal efficiency of stoichiometric operation natural gas engine with EGR. *Appl Therm Eng* 1(123):1473–1483
- Yu J, Vuorinen V, Hillamo H, Sarjoavaara T, Kaario O, Larmi M (2012) An experimental study on high pressure pulsed jets for DI gas engine using planar laser-induced fluorescence. SAE Technical Paper, 10 Sep 2012
- Zhao F, Lai MC, Harrington DL (1999) Automotive spark-ignited direct-injection gasoline engines. *Prog Energy Combust Sci* 25(5):437–562

# Chapter 6

## Effects of EGR on Engines Fueled with Natural Gas and Natural Gas/Hydrogen Blends



Luigi De Simio , Michele Gambino  and Sabato Iannaccone 

**Abstract** The exhaust gas recirculation can be used in a stoichiometric engine, for suppressing knocking and increasing efficiency, without a significant impact on pollutant emissions, since charge dilution is obtained with inert gases, allowing closed-loop control operations. However, relatively high EGR rates make worse the combustion process. This chapter deepens the effects of EGR on the performance of gaseous powered engines. In particular, the experimental data have been obtained fueling two engines with NG and NG/H<sub>2</sub> mixtures until 40% by volume of hydrogen, at steady state for different loads, measuring emissions upstream and downstream the three-way catalyst and analyzing the combustion process. A naturally aspirated light-duty spark ignition engine and a turbocharged heavy-duty one were tested. The results obtained with the two engines were consistent with each other. In particular, EGR could be utilized to have high specific power, with reduced thermal stress, but also to increase engine efficiency. Moreover, NG fueling permits a large flexibility in EGR system design, due to very clean engine-out exhaust gas, without visible particles. H<sub>2</sub> added to NG allows to mitigate the effect of EGR in reducing combustion speed. The positive effect of H<sub>2</sub> as combustion booster is more evident at EGR rate increasing. Nevertheless, with EGR, an increment of raw THC emission has been observed. Moreover, for the lower exhaust gas temperatures, oxidation of THC in the catalyst could result less effective. For these reasons, the blends with high hydrogen content, allowing a significant reduction of THC formation directly in the combustion chamber, can be usefully utilized for engines optimization with high EGR rates.

**Keywords** Natural gas · Hydrogen · Exhaust gas recirculation

---

L. De Simio (✉) · M. Gambino · S. Iannaccone  
Istituto Motori, National Research Council, Via Marconi 4, 80125 Naples, Italy  
e-mail: [l.desimio@im.cnr.it](mailto:l.desimio@im.cnr.it)

© Springer Nature Singapore Pte Ltd. 2019  
K. K. Srinivasan et al. (eds.), *Natural Gas Engines*, Energy, Environment,  
and Sustainability, [https://doi.org/10.1007/978-981-13-3307-1\\_6](https://doi.org/10.1007/978-981-13-3307-1_6)

### List of Acronyms

ATDC	After top dead center
BMEP	Brake mean effective pressure
BSFC	Brake specific fuel consumption
BTDC	Before top dead center
COV	Coefficient of variation
CR	Compression ratio
ECU	Electronic control unit
EGR	Exhaust gas recirculation
HD	Heavy duty
HR	Heat release
ID	Incubation duration
IMEP	Indicated mean effective pressure
LHV	Lower heating value
LPR	Low-pressure route
MAP	Manifold absolute pressure
MCD	Main combustion duration
NG	Natural Gas
NG <sub>up</sub>	Natural gas unburned percentage
PWM	Pulse-width modulation
SAFR	Stoichiometric air to fuel ratio
SI	Spark ignition
ST	Spark timing
THC	Total hydrocarbons
TP	Throttle valve position
TWC	Three-way catalyst
WG	Wastegate
WHTC	World harmonized transient cycle test
WOT	Wide open throttle

### List of Symbols

CA50	Crank angle for 50% heat release ATDC
EGR%	EGR rate
<i>M</i>	Molecular weight
<i>m</i>	Mass flow rate
<i>P</i>	Power
<i>W<sub>c</sub></i>	Water content
<i>y<sub>H<sub>2</sub></sub></i>	Mass fraction of H <sub>2</sub> in the NG/H <sub>2</sub> blend

## 6.1 Introduction

Comparing stoichiometric and lean burn technologies, the first allows to realize spark ignition (SI) engine with very low emissions, while the second allows lower thermal load and fuel consumption, but with worse emissions (Corbo et al. 1995). In particular, a three-way catalyst (TWC), which allows very low THC, CO, and NO<sub>x</sub> emissions with stoichiometric fueling, is not able to reduce NO<sub>x</sub> in lean condition. Moreover, simple and cheap after-treatment systems to reduce NO<sub>x</sub> are not available. With natural gas engine, also the emissions of unburned methane could be a problem with lean mixtures, due to the lower exhaust temperatures, which could affect methane conversion efficiency. To reduce engine thermal load and improve fuel specific consumption, exhaust gas recirculation (EGR) could be used. EGR technology consists in bringing a part of the exhaust gas to the intake manifold. Exhaust gas, in the case of stoichiometric fueling, is composed by CO<sub>2</sub>, N<sub>2</sub>, and H<sub>2</sub>O; therefore, EGR implies the dilution of the intake charge with inert gases that do not influence closed-loop control for stoichiometric fueling which is necessary for proper working of the TWC.

EGR strategy was initially developed for compression ignition engine, as shown, for example, in the articles Bae (1995) and Kohketsu et al. (1997), to reduce NO<sub>x</sub> emission, thanks to the dilution effect (reductions in O<sub>2</sub> available) and thermal effect (increases in the specific heat capacity of in-cylinder working gas) of inert species (Ladommatos et al. 1996), which achieve a reduction of in-cylinder maximum temperature, on which NO<sub>x</sub> emissions strongly depend. A lot of commercial diesel engines are nowadays equipped with EGR due to the effectiveness and to the cheapness of this technology.

EGR has been also proposed for optimizing gaseous fueling of compression ignition engine with pilot injection (dual-fuel technology). In these dual-fuel engines, EGR could improve such a complex combustion process, as shown for example in the articles (Dishy et al. 1995) and (Millo et al. 2000) to achieve a more smoothed combustion or in De Simio et al. (2007) to allow the optimization of low loads with a throttle valve. More recently, EGR has been studied as a parameter on which to act for affecting chemical kinetics of the auto-ignition process of natural gas as in Singh Kalsi and Subramanian (2016) and Jamsran and Lim (2016).

Focusing on SI natural gas (NG) engines, EGR strategy has been analyzed with different purposes. Since SI NG engines produce very negligible soot at the exhaust gas, any of the possible EGR routes can be utilized without the inconvenience to dirty the intake manifold or the compressor or to lock the EGR valve. The exhaust gas can be spilled before or after the turbine and can be introduced into the intake manifold before or after the compressor. Moreover, EGR can be cooled or not.

When exhaust gases are taken upstream the turbine and mixed with fresh air downstream the compressor, a high-pressure route is followed, while when exhaust comes from tailpipe to the engine intake, it follows a low-pressure route. Mixed solutions are also possible.

In De Simio et al. (2009), three EGR routes are compared with the scope to achieve the highest possible EGR rate for a six-cylinder, turbocharged gas engine. The best setup, which allows to introduce the highest EGR quantities, to provide the best reduction of the thermal load at rated power, was found to be a cooled low-pressure route (LPR) EGR. However, high–low-pressure route could give the possibility to increase engine efficiency by modulating the power output in the widest un-throttled range operation. In Li et al. (2014), intake dilution of a six-cylinder, turbocharged, intercooler, and large-powered NG engine was obtained with inert addition like  $\text{CO}_2$  and  $\text{N}_2$  instead of by re-cycling exhaust gas, to evaluate the effect of each component on  $\text{NO}_x$  emissions. They found that  $\text{CO}_2$  is more effective than  $\text{N}_2$  in reducing  $\text{NO}_x$  emission. In addition, with reference to the diluent and to the thermal effects, they are almost comfortable in the view of reducing  $\text{NO}_x$  emissions for both  $\text{N}_2$  and  $\text{CO}_2$ . In Ibrahim and Bari (2008), a numerical model was developed for a single cylinder research SI engine fueled with NG. The engine employs a stoichiometric mixture with EGR dilution. In particular, it has been predicted the minimum dilution value of EGR that could prevent knocking at high compression ratio (CR). In Ibrahim and Bari (2010), on the same engine, the author found that the engine tolerance to EGR increases with the raise of inlet pressure. In Zhang et al. (2016), a turbocharged SI NG engine for heavy-duty trucks, with TWC and cooled EGR, adopted stoichiometric combustion. EGR was optimized on the whole engine map with a generally positive trend, increasing EGR rate with engine load. The author found that the Euro VI emission standard for  $\text{NO}_x$  emissions (0.46 g/kWh on the WHTC, world harmonized transient cycle test) can be achieved without difficulties, while engine-out CO emissions could increase, in particular in high-speed/high-load regions with high EGR rates. In Zhang et al. (2017), they found high THC emissions in the late stages of the rural subcycle and in the whole motorway subcycle, due to rapid torque change of the WHTC cycle test and the fact that EGR rate changes accordingly, giving less combustion stability. In Feng et al. (2018), the effects of increasing CR and intake boosting when operating engine with cooled EGR are characterized and compared in a single cylinder research engine equipped with a variable CR mechanism. They assess that combing either intake boosting or increased CR with cooled EGR can further improve engine performance within acceptable regulated emissions. In Yan et al. (2017), on a six-cylinder heavy-duty engine, the author test, in addition to a CR increasing and EGR, the use of late intake valve closing to obtain expansion stroke longer than compression one and further increase engine efficiency. In Sen et al. (2011), the authors investigated the effect of EGR on the cycle-to-cycle variations in a three-cylinder light-duty NG SI engine. The paper investigates the frequency variations of the indicated mean effective pressure (IMEP) time series, highlighting the fact that EGR promotes low-frequency oscillation. On the same engine, the authors in Hu et al. (2009) studied also NG-hydrogen blends combined with EGR. The engine was fueled with mixture up to 40% by volume of hydrogen increasing EGR rate up to 40%, founding, in particular, that the coefficient of variation of the indicated mean effective pressure, which increases with the increase of EGR rate, could be reduced with hydrogen addition.

In this chapter, using experimental campaigns carried out on both a light-duty and a heavy-duty engine fueled with stoichiometric mixtures, a discussion will be carried out on the effects that the addition of recycled gas and hydrogen have on the completeness of the NG combustion. To evaluate in a direct and effective way the opposite effects coming from these factors, hydrogen which tends to promote combustion and EGR which, on the contrary, tends to oppose it, two parameters have been carefully calculated: the EGR rate and the NG unburned percentage.

### 6.1.1 EGR Rate

The EGR rate (EGR%), which is the percentage of engine exhaust in the mixture entering the engine, as defined in Eq. (6.1), is often estimated with the formula (6.2), (Kohketsu et al. 1997), in which the increased CO<sub>2</sub> concentration at the inlet manifold, with respect to the ambient concentration (roughly 400 ppm), is directly related to the share of exhaust gas recycled.

$$\text{EGR}\% = \frac{m_{\text{EGR}}}{m_{\text{EGR}} + m_{\text{air}}} \times 100 \quad (6.1)$$

$$\text{EGR}\% = \frac{[\text{CO}_2]_{\text{intake}} - [\text{CO}_2]_{\text{ambient}}}{[\text{CO}_2]_{\text{exhaust}} - [\text{CO}_2]_{\text{ambient}}} \times 100 \quad (6.2)$$

This estimation does not take into account the injected fuel, which alters the mass balance between engine intake and exhaust, or the different density and the mixture composition which influence the molar concentration of the involved species. While the formula could result sufficiently approximated for diesel engine running with high air dilution, for stoichiometric engine, the EGR rate could be underestimated. For NG engines, this underestimation could be up to a 15–20%.

A more approximated evaluation could be obtained performing a mass balance of the gaseous flows between the engine intake and the exhaust, the measurement of composition in each section through sampling analysis, and water production calculation.

The mass flow of EGR gas can be obtained by calculating separately the flow rate of dry gas and that of the water vapor. This separation is made necessary by the fact that from the gas analyzers, it is possible to derive the exhaust composition, on a dry basis, as O<sub>2</sub>, CO<sub>2</sub>, and consequentially N<sub>2</sub>. Air mass flow rate and humidity are commonly measured at the engine intake, respectively, with mass flow meters and hygrometers; therefore, water vapor content can be calculated and consequently the dry air mass flow rate. The water produced during the fuel combustion can be calculated directly from the fuel composition and the fuel mass flow rate. From these parameters, and measuring the dry composition at the intake and the exhaust, it is possible to obtain the EGR rate.

In the following,  $M$  is the molecular weight,  $m$  the mass flow rate, concentration in bracket the molar fraction, while the suffix *wc* stands for water content.

$\text{CO}_2$  entering the engine both with the intake air and with the recycled exhaust gas can be calculated with the Eq. (6.3):

$$m_{\text{CO}_2, \text{air, dry}} + m_{\text{CO}_2, \text{EGR, dry}} = [\text{CO}_2]_{\text{intake, dry}} \frac{M_{\text{CO}_2}}{M_{\text{intake, dry}}} (m_{\text{air, dry}} + m_{\text{EGR, dry}}) \quad (6.3)$$

Parameter in Eq. (6.3) can be calculated with the followings formulas.

$$M_{\text{intake, dry}} = [\text{CO}_2]_{\text{intake, dry}} M_{\text{CO}_2} + [\text{N}_2]_{\text{intake, dry}} M_{\text{N}_2} + [\text{O}_2]_{\text{intake, dry}} M_{\text{O}_2} \quad (6.4a)$$

$$m_{\text{CO}_2, \text{air, dry}} = [\text{CO}_2]_{\text{ambient}} \frac{M_{\text{CO}_2}}{M_{\text{air, dry}}} m_{\text{air, dry}} \quad (6.4b)$$

$$m_{\text{CO}_2, \text{EGR, dry}} = [\text{CO}_2]_{\text{exhaust, dry}} \frac{M_{\text{CO}_2}}{M_{\text{exhaust, dry}}} m_{\text{EGR, dry}} \quad (6.4c)$$

$$M_{\text{exhaust, dry}} = [\text{CO}_2]_{\text{exhaust, dry}} M_{\text{CO}_2} + [\text{N}_2]_{\text{exhaust, dry}} M_{\text{N}_2} + [\text{O}_2]_{\text{exhaust, dry}} M_{\text{O}_2} \quad (6.4d)$$

In formulas (6.4a, b, c, d),  $[\text{CO}_2]_{\text{ambient}}$  is the  $\text{CO}_2$  molar fraction in ambient air and was assumed to be  $4 \times 10^{-4}$  (i.e., 400 ppm), considering the available literature data with a single significant digit.

The only unknown parameter of Eq. (6.2), the dry mass flow rate of EGR, can be calculated with the Eq. (6.5), obtained substituting (6.4b) and (c) in (6.3):

$$m_{\text{EGR, dry}} = \frac{[\text{CO}_2]_{\text{intake, dry}} \frac{M_{\text{CO}_2}}{M_{\text{intake, dry}}} - [\text{CO}_2]_{\text{ambient}} \frac{M_{\text{CO}_2}}{M_{\text{air, dry}}}}{[\text{CO}_2]_{\text{exhaust, dry}} \frac{M_{\text{CO}_2}}{M_{\text{exhaust, dry}}} - [\text{CO}_2]_{\text{intake, dry}} \frac{M_{\text{CO}_2}}{M_{\text{intake, dry}}}} m_{\text{air, dry}} \quad (6.5)$$

It is possible to note that approximated Eq. (6.2) can be obtained substituting Eq. (6.5) in (6.1), neglecting water content in EGR, if  $\text{CO}_2$  concentration is measured on a dry basis, and assuming:  $M_{\text{intake, dry}} \approx M_{\text{air, dry}} \approx M_{\text{exhaust, dry}}$ .

As regards the water vapor content in the EGR, as the percentage of dry exhaust gas recycled must be the same of the percentage of water in the exhaust gas recycled, the Eq. (6.6), in which  $f$  is a constant, can be written:

$$\frac{m_{\text{EGR, dry}}}{m_{\text{exhaust, dry}}} = \frac{m_{\text{EGR, wc}}}{m_{\text{exhaust, wc}}} = f \quad (6.6)$$

Therefore, the recycled water can be calculated with the Eq. (6.7) obtained from the Eq. (6.6), sorting all the sources of water in the exhaust and calculating water from combustion as the mass of water produced per mass of fuel burned.

$$\begin{aligned}
 m_{\text{EGR,wc}} &= f \times (m_{\text{air,wc}} + m_{\text{EGR,wc}} + m_{\text{combustion,wc}}) \\
 &= \frac{f}{1-f} (m_{\text{air,wc}} + m_{\text{combustion,wc}})
 \end{aligned}
 \tag{6.7}$$

The total mass of exhaust gas recycled is given by the Eqs. (6.5) and (6.7).

## 6.2 NG Unburned Percentage

To evaluate the effect of EGR and H<sub>2</sub> addition on the combustion a parameter, defined in De Simio et al. (2016), was used.

$$NG_{\text{up}} = \frac{m_{\text{THC}}}{m_{\text{NG}}} = \frac{m_{\text{THC}}/P}{\text{BSFC}(1 - \gamma_{\text{H}_2})} \times 100 [\%]
 \tag{6.8}$$

$NG_{\text{up}}$ , which stands for “natural gas unburned percentage,” evaluates the exhaust THC mass flow rate with respect to the NG consumption. Unburned H<sub>2</sub>, that is not taken into account by THC measurement device, does not affect  $NG_{\text{up}}$ ; therefore, with NG/H<sub>2</sub> blends, a less value of  $NG_{\text{up}}$  clearly shows a more complete NG combustion, reduces THC emissions achieved with H<sub>2</sub> addition.

In the case of full natural gas running, the parameter coincides with the combustion efficiency; therefore, an increasing of  $NG_{\text{up}}$  with EGR rate indicates a worse combustion condition.

## 6.3 Experimental Setup

Tests with some NG/H<sub>2</sub> blends were carried out on two engines: a light duty and a heavy duty. To the HD SI turbocharged engine (main characteristics in Table 6.1) was added a cooled LPR EGR, in which the exhaust gases come from the turbine outlet at the compressor inlet. The EGR rate was set with a valve using a pulse-width modulation (PWM) signal. An electronic control unit (ECU) enabled to

**Table 6.1** Main characteristics of the reference HD SI NG engine

Type	Six-cylinder in-line
Displacement	7800 cm <sup>3</sup>
Bore × stroke	115 × 125 mm
CR	11:1
Rated power	200 kW @ 2100 rpm
Max. torque	1100 Nm @ 1100–1650 rpm
Boost pressure	0.8 relative bar, with wastegate valve
NG feeding system	Electronic timed multi-point injection



set the main operating parameters (air/fuel mixture, spark timing, wastegate valve duty cycle, etc.). The apparent heat release (HR) curves were calculated from a mean over 100 consecutive pressure cycles to identify the incubation duration (ID), angular interval between the spark and 10% HR; the main combustion duration (MCD), angular interval between 10 and 90% HR, and the crank angle for 50% heat release (CA50), as the angle at which 50% of heat is released. The spark timing (ST) was set to have a CA50 close to  $8\text{--}10^\circ$  after top dead center (ATDC), which is commonly considered a condition for the best thermal conversion efficiency at fixed engine brake torque.

For the light-duty naturally aspirated engine, which main characteristics are shown in Table 6.2, the exhaust gas was taken before the catalyst and reintroduced after the throttle valve.

Moreover, the exhaust gas recycled has been cooled using the engine liquid coolant. The EGR control valve was similar to that used for the HD engine, but with feedback on working position to be sure of the absence of any uncertainty in the valve position. This was necessary, because the EGR route does not always exhibit a strong difference in the pressure between the inlet and the outlet section. Due to the complex fluid dynamic of a reciprocating engine and the mutual influence that have both the intake and the exhaust pressure on the EGR line, also the position of the throttle valve strongly affected the EGR rate. Therefore, the rate of EGR can be significantly different if a given position of the valve is reached in closing or opening maneuvers and also if the given position is reached more slowly or more quickly. For this reason, to find a prefixed EGR rate, the position of the EGR valve has been varied for further approximation very accurately, using the feedback position signal. In particular, the points at low EGR rate were more difficult to perform, for finding the required EGR rate. This behavior, not observed on the HD turbo engine, made the experimental activity on LD engine longer than that on the HD one.

The installed EGR valve is closed with a PWM duty cycle of 97.5%, and fully open at 0%. It worked properly. In fact, at a fixed PWM signal, no EGR variation was observed over the time and no EGR rate was measured when the EGR valve was closed. Anyway, a specified EGR rate did not correspond to a given position of the valve. In Fig. 6.1, the results at different EGR rate, for two engine throttle valve positions (TP), are reported for three repetitions (series 1–3). Since there is not a

**Table 6.2** Main characteristics of the reference LD SI NG engine

Type	Four-cylinder in-line
Displacement	1596 cm <sup>3</sup>
Bore × stroke	80.5 × 78.4 mm
CR	10.5:1
Rated power	76 kW @ 5750 rpm
Max. torque	144 Nm @ 4000 rpm
Boost pressure	Naturally aspirated
NG feeding system	Electronic timed multi-point injection

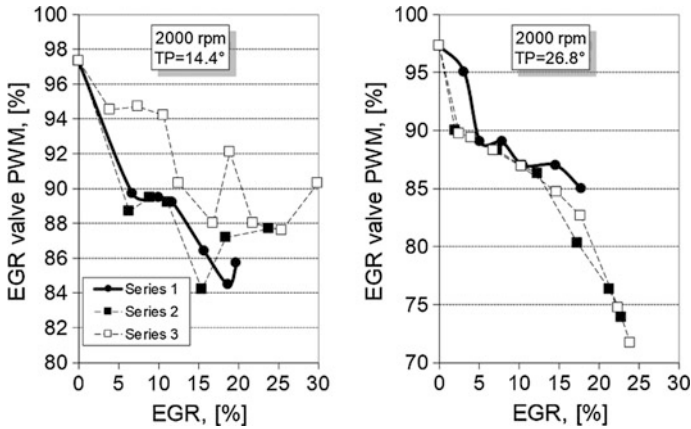


Fig. 6.1 EGR rate at different PWM values at 2000 rpm for all the test conditions

Table 6.3 Instrumentation for emissions and performance measurement

Unit	Type	Range	Accuracy
Air flow	ABB sensy flow P (HD)	1200 kg/h	±1% of reading
	Laminar flow meter cussons (LD)	0 ÷ 350 l/s	±1% of reading
Fuel	Micro motion elite	50 kg/h	<1% of reading
THC	Multifid 14 EGA	0 ÷ 10,000 ppm C <sub>3</sub>	0.5% of range
CO	URAS 14 EGA	0 ÷ 10%	<1% of range
NO <sub>x</sub>	CLD ecophysics	0 ÷ 5000	<1% of range
CO <sub>2</sub>	URAS 14 EGA	0 ÷ 20%	1% of range
O <sub>2</sub>	MACROS 16 EGA	0 ÷ 25%	0.5% of range
In-cylinder pressure	Piezoelectric pressure transducer	0 ÷ 250 bar	0.1% of range

close correlation between the measured EGR rate and the PWM duty cycle set, this means that the amount of EGR in steady state does not depend mainly on the position of the EGR valve, but it depends also on the story of the EGR valve changing. Also for the LD engine, test cases refer to the optimal ST phasing.

A list of the main instrumentation used for both HD and LD engines is reported in Table 6.3.

The experimental activity has been carried out with NG and two blends containing a nominal 20 and 40% of hydrogen by volume, with and without EGR, at steady state in different engine conditions, measuring emissions upstream and downstream the catalyst and analyzing the combustion behavior through the study

**Table 6.4** Tested fuel composition

Fuel	CH <sub>4</sub>	H <sub>2</sub>	C <sub>2</sub> H <sub>6</sub>	C <sub>3</sub> H <sub>8</sub>	CO <sub>2</sub> + N <sub>2</sub>
	% vol	% vol	% vol	% vol	% vol
NG	85.36	0.00	9.47	1.75	3.40
NG/H <sub>2</sub> 20%	69.89	18.20	6.86	1.40	3.65
NG/H <sub>2</sub> 40%	50.55	37.87	6.80	1.33	3.44

**Table 6.5** Tested fuel characteristics

Fuel	SAFR	LHV	$y_{H_2}$	H/C	CO <sub>2</sub>	H <sub>2</sub> O
	kg/kg	MJ/kg	kg/kg		g/MJ	kg/kg
NG	15.89	46.27	0.00	3.71	57.07	2.01
NG/H <sub>2</sub> 20%	16.16	47.56	0.02	4.09	53.89	2.15
NG/H <sub>2</sub> 40%	16.56	49.44	0.06	4.79	48.70	2.36

of pressure cycles inside the combustion chamber. An EGR mass percentage until a maximum of 25–30% was tested.

All the fuels were analyzed, and the results are shown in Table 6.4, while the main characteristics of the fuels, like stoichiometric air to fuel ratio (SAFR) or water production through combustion, have been calculated and reported in Table 6.5.

In the following, the experimental activity on the HD engine and on the LD engine and a comparison among the results is shown.

## 6.4 Experimental Activity on the Heavy-Duty Engine

A first experimental activity was carried out only with NG, at SAFR condition with closed-loop control, at different engine speeds and loads, adding EGR, without changing the ST. The main results of this activity are reported in Fig. 6.2, as the effect on ID and MCD. Each point of the lines in Fig. 6.2 is an average value obtained from points with different loads (from 170 to 850 Nm), but at the same speed. It resulted in quite representative of the behavior of the engine at each speed, being the relative standard deviation of the data at different load less than 5 and 15%, respectively, for ID and MCD. It is possible to note that both ID and MCD are not strongly affected by the speed at each EGR rate. From the above two mean trend lines, main combustion duration is almost not affected by the speed at EGR increasing.

Therefore, as a first wider approximation, to make possible a simple evaluation of EGR effect on combustion development, it can be assumed that ID and MCD are almost not affected by engine load and speed at each EGR rate. In Fig. 6.2, also the relationship between combustion parameters and EGR rate with relative correlation factors is reported.

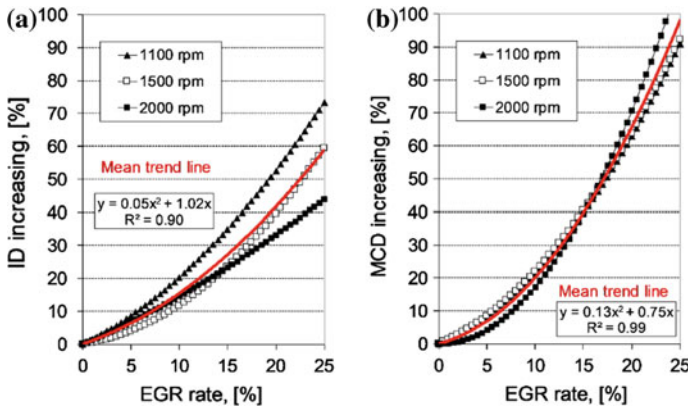


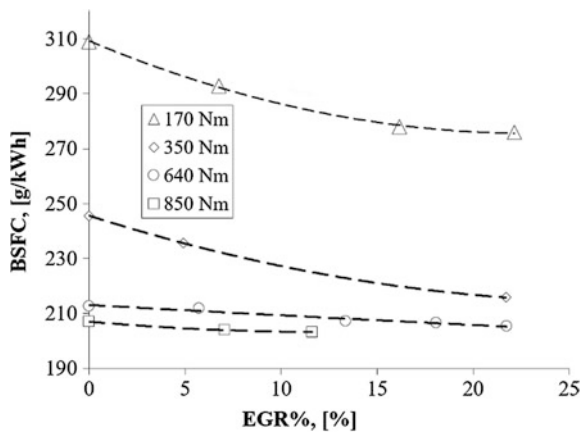
Fig. 6.2 Effect of EGR on ID (a) and MCD, (b) for the HD engine, without changing the ST

### 6.4.1 Effect of EGR on HD Engine BSFC

The tests on the HD engine have revealed the possibility to reduce fuel consumption by means of EGR, when a spark timing optimization is made, to compensate the lower flame combustion speed and achieving the maximum thermal efficiency at a given engine brake torque. The results, reported in Fig. 6.3, are consistent with this trend, especially at low loads.

The fuel consumption reduction can be related to both a lower pumping work and a lower heat loss (thermal exchanges through walls, sensible heat of the exhaust gases). A lower pumping work implies a lower active work at the same engine torque, while a lower heat loss requires lower fuel to burn to retain the same in-cylinder pressure.

Fig. 6.3 EGR effect on BSFC at 1100 rpm for the HD engine (ST optimized)



The fraction related to the pumping work could be very small or negligible. Actually, the indicated work ( $W_i$ ) can be expressed as:

$$W_i = W_a + W_p$$

where  $W_a$  is the active work ( $W_a > 0$ ) and  $W_p$  is the pumping work.

Generally,  $W_p < 0$ , although at full load and with turbocharger, it is possible to have  $W_p > 0$ . If  $W_p < 0$ , a positive effect of the EGR on  $W_p$  would imply a decrease of  $|W_p|$  due to higher throttle valve opening angles, while it would imply an increase, if  $W_p > 0$ , due to higher boost pressure (i.e., higher mass flow rate to the turbine). At the same operating conditions, and therefore at the same  $W_i$ , a positive effect of the EGR on  $W_p$  would cause a  $W_a$  reduction. Such a  $W_a$  decrease would determine the same reduction of consumption, assuming negligible the effects of a different cycle development/peak pressure positioning, for pressure cycles with optimized ST.

Figure 6.4 shows some indicated pressure cycles during the phases of the change of charge. It is notable that at low load (a), although the mean pressure into the cylinder increases with EGR, there is no effect of the EGR on the  $W_p$ , while at mean load (b), the  $W_p$  increases from negative to positive values, due to a higher boost pressure and therefore of the net work acting on the piston also during the change of the charge. However, this work is of small entity (about 0.5%) respect the  $W_a$ .

Therefore, it is reasonable to think that the lower fuel consumption found in the case of EGR is mainly due to a reduction of the heat exchange. This reduction is always present with EGR, and it allows to increase the indicated active efficiency and therefore to decrease the natural gas quantity for each cycle necessary to reach the required indicated torque.

To verify and deepen the experimental results, the EGR effect on the consumption has been analyzed through a mono-dimensional numeric model. To do this, the engine has been modeled both with and without EGR, on all the operating conditions. The EGR% has been set at the maximum possible value, for each

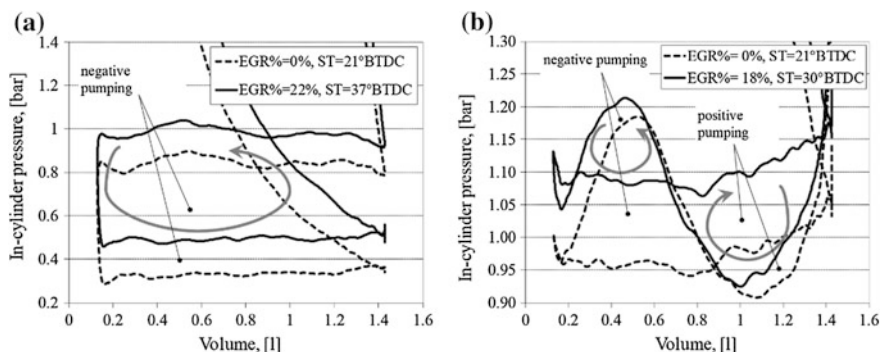


**Fig. 6.4** EGR effect on pumping cycle at 1100 rpm and 170 Nm (a) or 640 Nm, (b) for the HD engine (ST optimized)

condition, without overcoming the 25% threshold. At low load, this result has been reached increasing the throttle valve opening, while at medium–high loads acting also on the wastegate valve (WG), to increase the turbocharging and so allow to introduce EGR, besides the air, to obtain the required torque. The model has ignored the EGR effect on the combustion efficiency, and it has been considered the optimization of the spark timing, both with and without EGR, to have an optimal burner center gravity, considering a lower combustion speed, with EGR, according to the trend of Fig. 6.2. More details about the numeric model construction are reported in De Simio et al. (2009). The results of the model, useful to analyze the BSFC, are reported in Figs. 6.5, 6.6 and 6.7.

Figure 6.5 shows the BSFC percentage reduction of the engine with LPR EGR compared to the base configuration (without EGR). The possibility of obtaining a reduction in consumption of up to 7% in any operating condition of the engine is evident.

The effect of the pumping on fuel consumption reduction ( $I_{W_p/\Delta BSFC}$ ) has been evaluated as:

$$I_{W_p/\Delta BSFC} = \frac{\Delta W_a}{\Delta BSFC} \times 100 [\%] \tag{6.9}$$

where  $\Delta BSFC$  represents the consumption percentage reduction in the case of LPR with respect to the base case, and  $\Delta W_a$  represents the active work percentage variation in the case of LPR with respect to the base case. As before mentioned, the Eq. (6.9) was written assuming that for a given  $W_a$  percentage reduction, and there

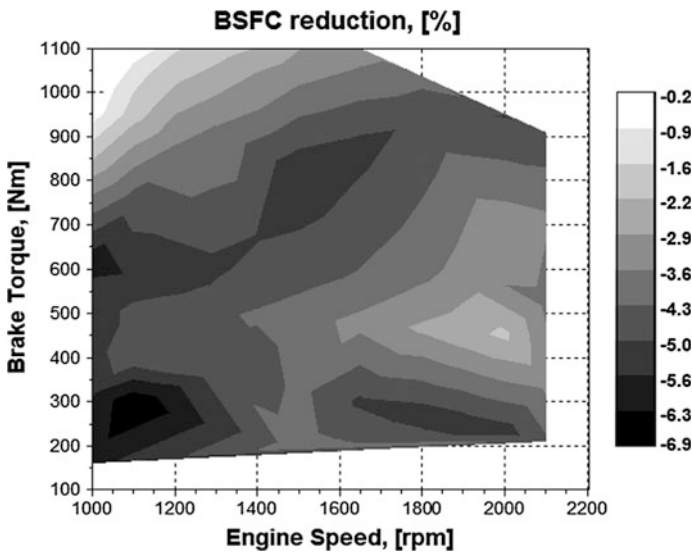


Fig. 6.5 Calculated BSFC percentage reduction achievable switching from the base case to the LPR EGR case on the whole HD engine map (ST optimized)

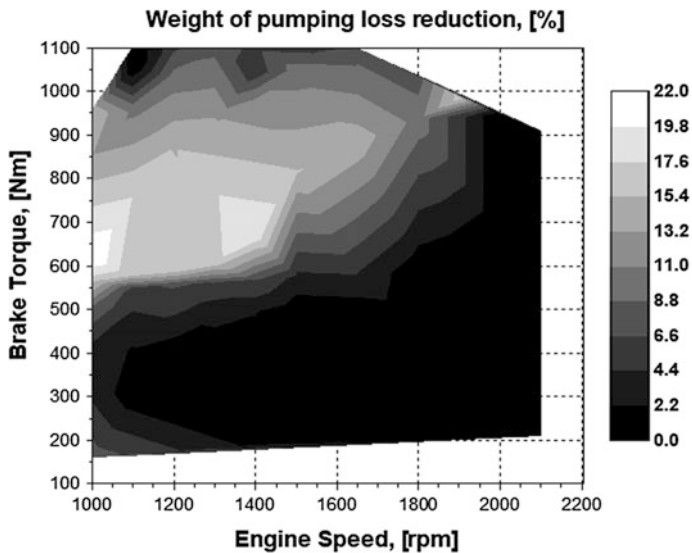


Fig. 6.6 Calculated weight of pumping loss reduction on BSFC percentage reduction achievable switching from the base case to the LPR EGR case on the whole HD engine map (ST optimized)

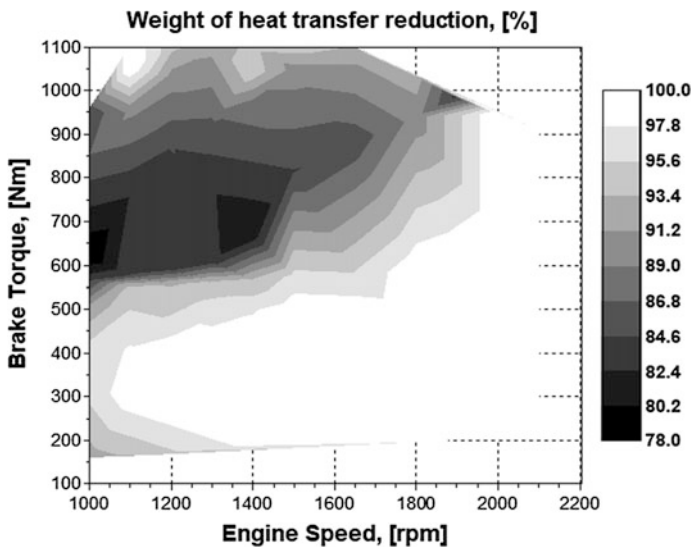


Fig. 6.7 Calculated weight of heat transfer reduction on BSFC percentage reduction achievable switching from the base case to the LPR EGR case on the whole HD engine map (ST optimized)

should be about the same percentage of consumption reduction. Therefore, the positive influence of pumping work reduction on the BSFC reduction is directly related to the active work reduction percentage (i.e.,  $I_{W_p/\Delta BSFC}$  is 0% if there is not a reduction in the active work in the EGR case, and it is 100% if the active work percentage reduction is the same as BSFC one). This parameter is shown in Fig. 6.6. It is notable that the influence of the pumping work on the fuel consumption reduction does not exceed 22%, while exists a zone, at high speeds and low/medium loads, where the pumping work is even increased when the EGR is used. Therefore, in that zone, the effect of EGR on the consumption is zeroed because of the EGR flow requires more active work, due to the increase of gas speed through engine valves, which is not balanced by lower-pressure drops through the throttle valve.

The effect of the lesser heat exchange on fuel consumption reduction ( $I_{Q/\Delta BSFC}$ ) has been valued, instead, as complement to 100%, with Eq. (6.10):

$$I_{Q/\Delta BSFC} = 100 - I_{W_p/\Delta BSFC} [\%] \quad (6.10)$$

Equation (6.10) assumes negligible the effect of unburned fuel, and combustion phasing on the BSFC. Therefore, lower BSFC, in the case of EGR, which is not related to a lower pumping work, must be related to lower in-cylinder wall heat losses, which implies less fuel for retaining the engine torque at the same level without EGR. These conditions, that have been considered in the model, could be realistic if not high EGR rate is achieved, being small the worsening of combustion and the difference in cycle development, once the ST is adapted. This effect, reported in Fig. 6.7, clearly shows that the lower fuel consumption calculated with EGR is mainly due to the reduction in heat exchange with the walls. The influence of minor thermal exchange on the consumption reduction ranges between 75 and 100%. In particular, where the pumping work increases with EGR, it is the same possible to have a reduction of the fuel consumption, thanks to less heat exchanges.

### 6.4.2 Combined Effect of EGR and H<sub>2</sub> Addition

The main activity was performed changing the ST with EGR and adding H<sub>2</sub>. The engine was tested with the WG valve fully open and at wide open throttle (WOT). Engine speed was set at 1100 and 1500 rpm.

At increasing EGR, the substitution of part of the inlet air with exhaust gases causes a BMEP reduction at fixed SAFR, Fig. 6.8. Comparing the three blends, only negligible reductions of BMEP were observed with H<sub>2</sub> admission, due to the small reduction of the heat content of the stoichiometric mixture. In the same figure, also the manifold absolute pressure (MAP) is reported. Although the less air entering the engine, MAP is not much influenced by EGR, because the gas mass flow rate expanding into the turbine is more or less the same at EGR increasing,



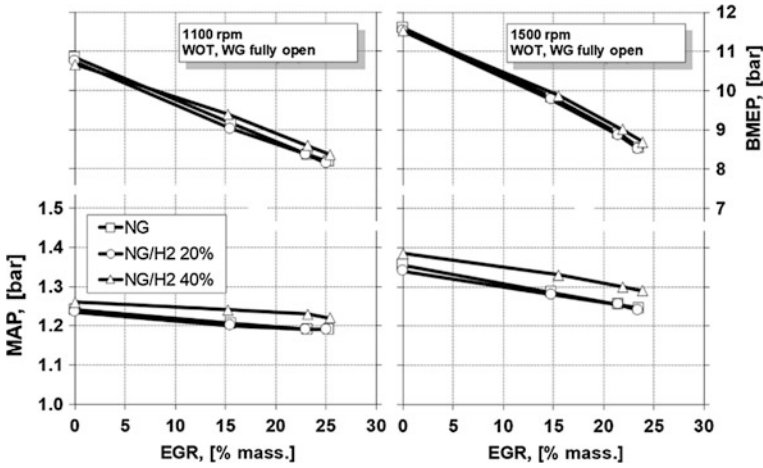


Fig. 6.8 BMEP and MAP at the two tested speeds varying EGR rate and H<sub>2</sub> for the HD engine

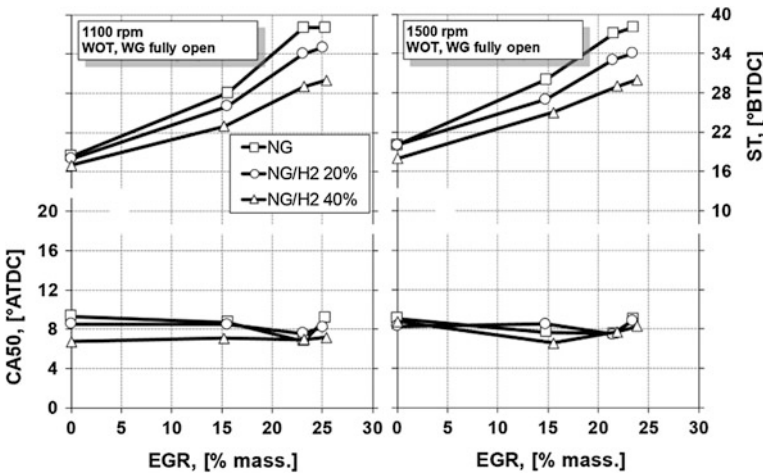


Fig. 6.9 ST and CA50 at the two tested speeds varying EGR rate and H<sub>2</sub> for the HD engine

even if at lower temperatures. As a result, the boost pressure decreases, but less than the load does.

The ST for proper CA50 phasing has to be increased with EGR and decreased with H<sub>2</sub>, Fig. 6.9.

The addition of H<sub>2</sub> causes the combustion to be faster, in particular at lower range speed during the first stage of combustion (ID). On the contrary, the combustion propagation becomes worse with high EGR rate. In these last conditions, a more positive effect of H<sub>2</sub> on the start of the ignition process can be noted,

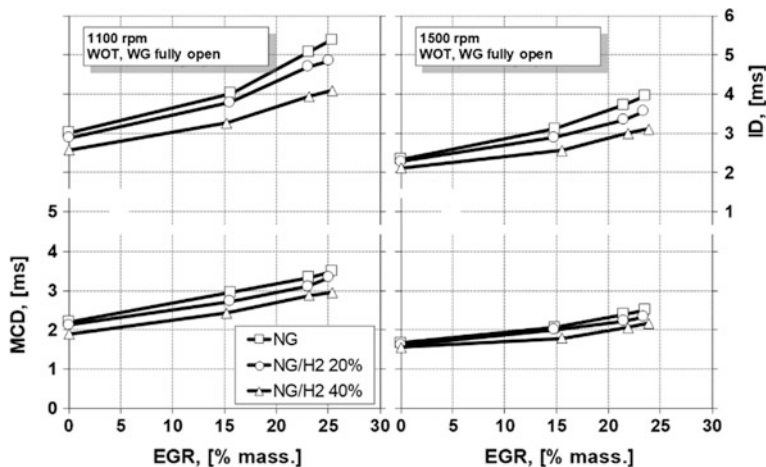


Fig. 6.10 ID and MCD duration at the two tested speeds varying EGR rate and H<sub>2</sub> for the HD engine

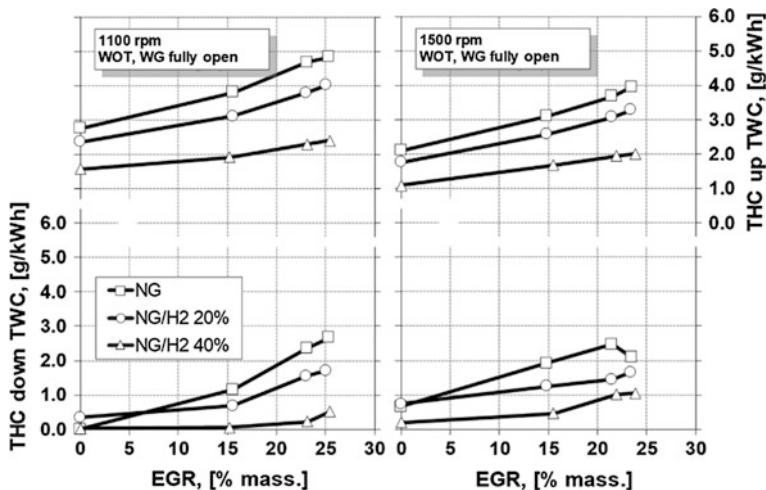
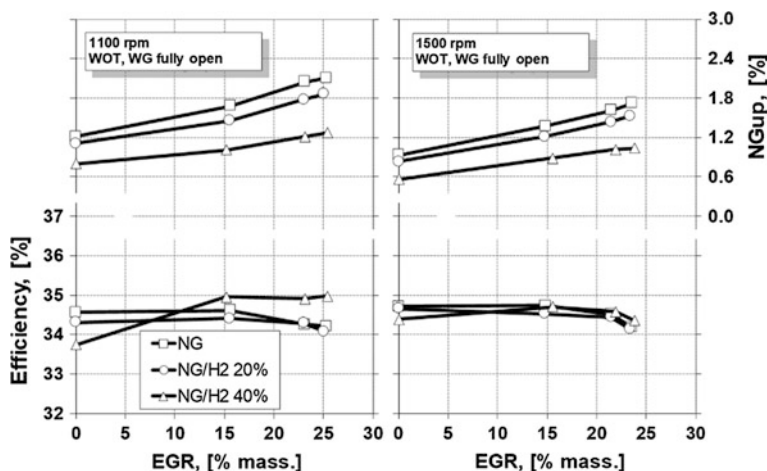


Fig. 6.11 THC up and down the catalyst at the two tested speeds varying EGR rate and H<sub>2</sub> for the HD engine

Fig. 6.10. In the same figure, a less evident effect on the MCD appears, especially at higher speed, which denotes that the effect of turbulence intensity on combustion speed increasing is higher than that of H<sub>2</sub> addition. The increase in the EGR rate worsens THC emissions, both upstream and downstream of the TWC for all three tested fuels; however, the H<sub>2</sub> content in the mixture helps to limit this drawback, as shown in Fig. 6.11.



**Fig. 6.12** Efficiency and  $NG_{up}$  at the two tested speeds varying EGR rate and  $H_2$  for the HD engine

Substituting a share of NG with  $H_2$  contributes to have a THC reduction, because the unburned  $H_2$  is not recognized by flame ionization detector instrument. Moreover, a more complete combustion also contributes to reduce THC. Therefore, the reduction of THC with  $H_2$  content, Fig. 6.11, together with the  $NG_{up}$  decreasing with  $H_2$  content, Fig. 6.12, highlights the positive effect of  $H_2$  on combustion development and propagation, which contrasts the worsening combustion conditions due to the EGR. Nevertheless, the better combustion with  $H_2$  increasing does not improve the overall engine efficiency, (Fig. 6.12). This because from one hand the improvement of combustion efficiency is of small entity, while on the other hand, a more complete combustion, reducing the thickness of the quenching zone, causes an increasing of the heat wall transfer, in an opposite way with respect to what EGR does.

The EGR rate greatly reduces  $NO_x$  formation (upstream the TWC) through lower combustion temperature. On the other hand, a slight  $NO_x$  increasing inside the combustion chamber can be observed with  $H_2$  in the blend, Fig. 6.13, due to faster combustion, which implies higher reaction temperature. At the TWC outlet,  $NO_x$  emissions are quite constant with fuel mixture composition.

## 6.5 Experimental Activity on the Light-Duty Engine

The experimental tests have been performed at a fixed throttle valve position, adjusting spark timing to have the CA50 at the optimal position. However, due to EGR flow instability, ST was adjusted with minor precision with respect to the HD case. Part-load conditions have been tested to have a pressure drop between the inlet and the outlet of EGR line. Engine speed was set at 2000 rpm.

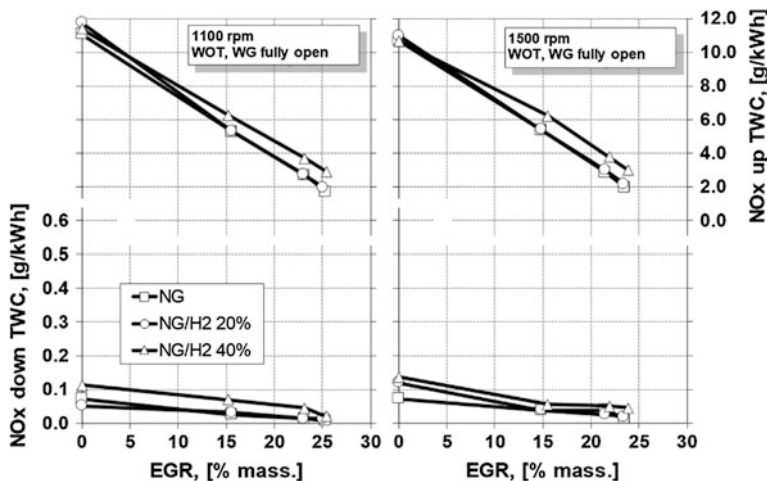


Fig. 6.13 NO<sub>x</sub> upstream and downstream the catalyst at the two tested speeds varying EGR rate and H<sub>2</sub> for the HD engine

No efficiency improvement was found with EGR. In Fig. 6.14, it is possible to compare the efficiency at EGR increasing with the case without EGR. Data were obtained as follows. The solid line represents the case without EGR, where at a BMEP increasing corresponds a TP increasing. Starting for a given TP at part load without EGR, the EGR rate was increased, acting only on the EGR valve. An increase in the EGR, at fixed TP, results in a reduction in the supplied torque. At each BMEP, engine efficiency with EGR resulted similar to that of the case without EGR, until at higher EGR rate it becomes to decrease. This behavior was imputed to the worse combustion progress, due to the presence of inert gas in the combustion chamber, that counterbalances the positive effect of lower heat losses and higher throttle valve position, at parity of BMEP. Therefore, there was a difference with respect to the tests on the heavy-duty engine, where the EGR permits a reduction of BSFC. The problem could reside in the weight that unburned hydrocarbons have on the global engine efficiency. With smaller bore engines, the effect of quenching zone is bigger with respect to larger engines, and therefore, the effect of combustion efficiency reduction, correlated with EGR rate increasing, cancels the positive effect of the EGR on BSFC.

Similarly, it is possible to compare the NO<sub>x</sub> emission at EGR increasing with respect to the case without EGR. For a given load, less NO<sub>x</sub> upstream the TWC were produced with EGR, Fig. 6.15, due to the inert gas which reduces peak temperature in the combustion chamber.

On the contrary, a higher EGR rate determines an increasing of THC upstream the catalyst, as shown in Fig. 6.16, due to the inert gas which makes worse the combustion conditions. Anyway, the presence of H<sub>2</sub> gives a positive effect on THC emissions, both without and with EGR.

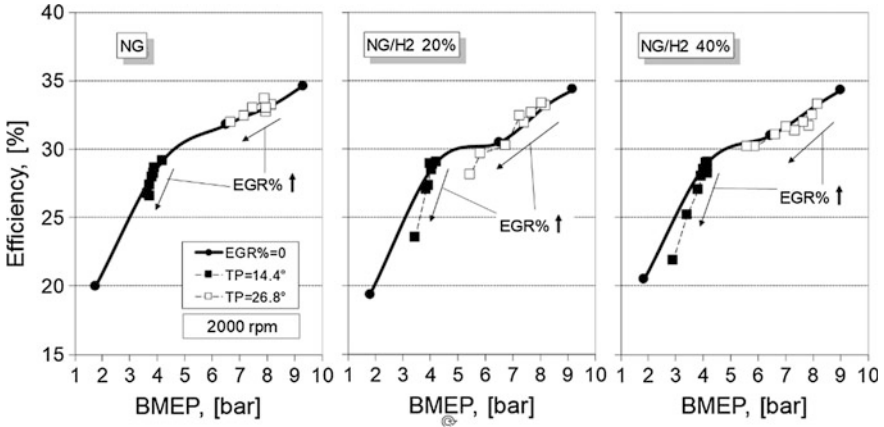


Fig. 6.14 Efficiency at the two part-load conditions varying EGR rate and H<sub>2</sub> for the LD engine

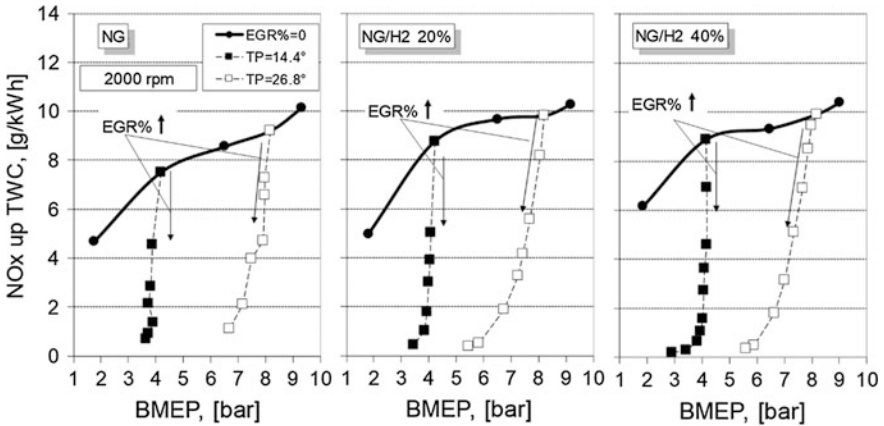
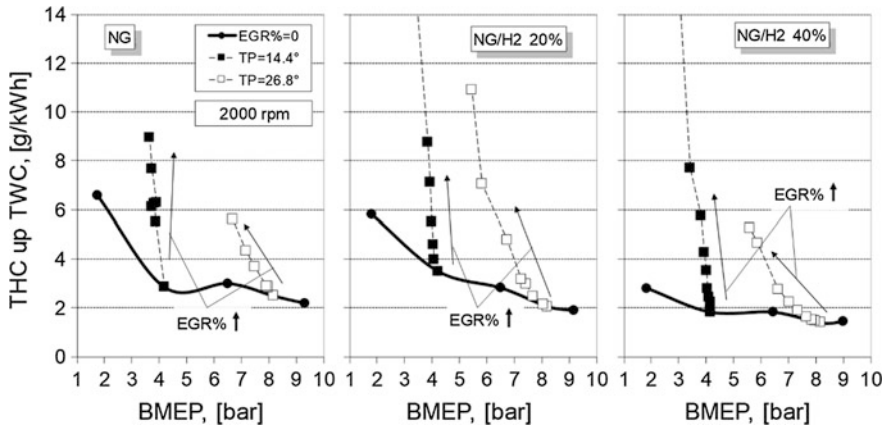


Fig. 6.15 NO<sub>x</sub> up TWC at the two part-load conditions varying EGR rate and H<sub>2</sub> for the LD engine

In Fig. 6.17, at the two considered TP, the effect of EGR on  $NG_{up}$  for the three fuels at 2000 rpm is shown. The blend of NG and 40% by volume of H<sub>2</sub>, compared to the NG case without EGR, shows a lower  $NG_{up}$  until the EGR rate was lower than 15–20%. This result clearly highlights the possibility of improve combustion condition with H<sub>2</sub> addition.

In the same conditions of Fig. 6.17, THC conversion efficiency is reduced at EGR increasing, as shown in Fig. 6.18. Anyway, NG/H<sub>2</sub> 40% shows THC downstream the TWC lower than NG case (without EGR) until 15–20% of EGR rate, Fig. 6.19.



**Fig. 6.16** THC upstream TWC at the two part-load conditions varying EGR rate and H<sub>2</sub> for the LD engine

**Fig. 6.17** NG<sub>up</sub> at the two part-load conditions varying EGR rate and H<sub>2</sub> for the LD engine

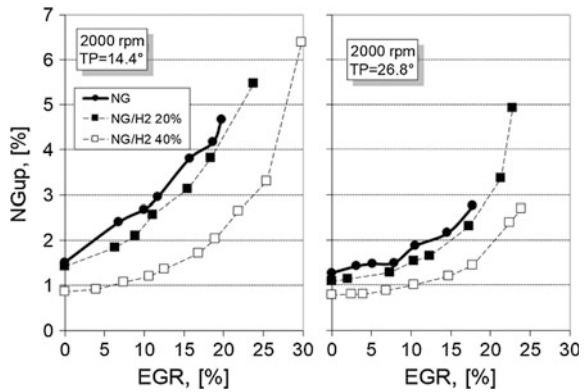


**Fig. 6.18** TWC conversion efficiency on THC at the two part-load conditions varying EGR rate and H<sub>2</sub> for the LD engine

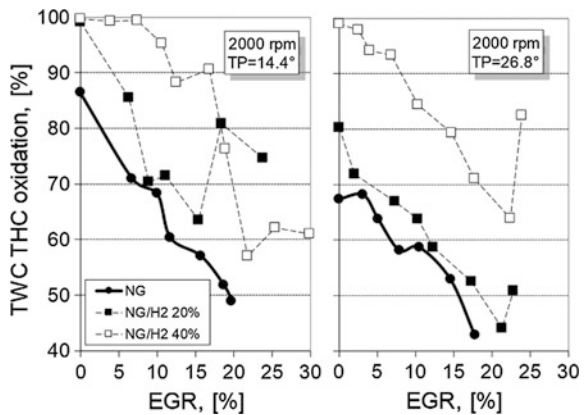


**Fig. 6.19** THC downstream TWC at the two part-load conditions varying EGR rate and H<sub>2</sub> for the LD engine

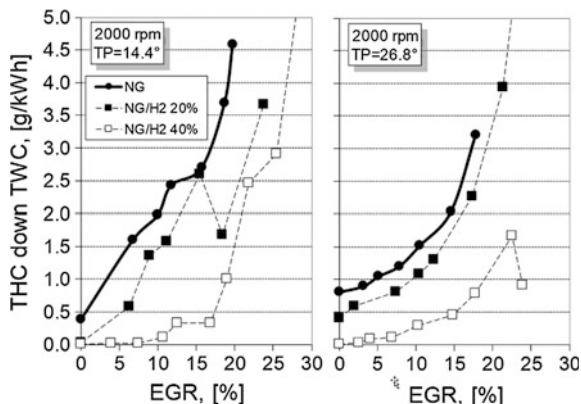
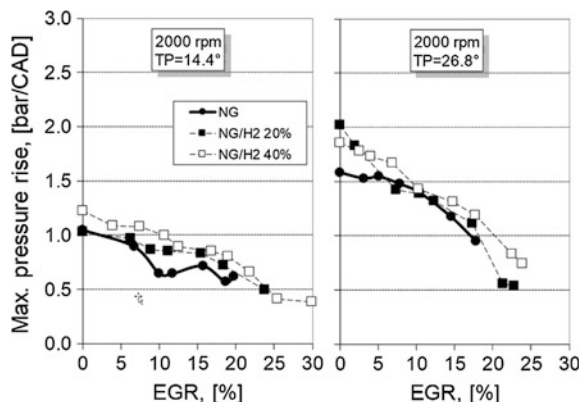


**Fig. 6.20** Maximum pressure rise rate at the two part-load conditions varying EGR rate and H<sub>2</sub> for the LD engine



EGR benefit on smoothing combustion is highlighted in Figs. 6.20 and 6.21, where, respectively, maximum pressure rise rate and coefficient of variation of indicated mean effective pressure are shown.

With H<sub>2</sub>, the pressure rise is generally slightly higher than the NG case, nevertheless the ST reducing to retain the same peak pressure position. Maximum pressure rise rate is reduced at EGR rate increasing, Fig. 6.20. This behavior could be useful, for instance, to develop turbocharged engine, with high power density, fueled with blend at high H<sub>2</sub> content, lowering maximum in-cylinder pressures and temperatures with high EGR rate. The use of high EGR rate is possible when H<sub>2</sub> is added to NG thanks to the higher capability of the engine to tolerate EGR, as shown in Fig. 6.21 by the effect of EGR on the coefficient of variation (COV) of IMEP. NG/H<sub>2</sub> 40%, with an EGR rate up to 15–20%, assures the same combustion stability of the NG case without EGR.

In Fig. 6.22, the EGR effect on the ST and the angle of the CA50 is shown, while in Fig. 6.23, the effect on ID and MCD is represented. The comparison of

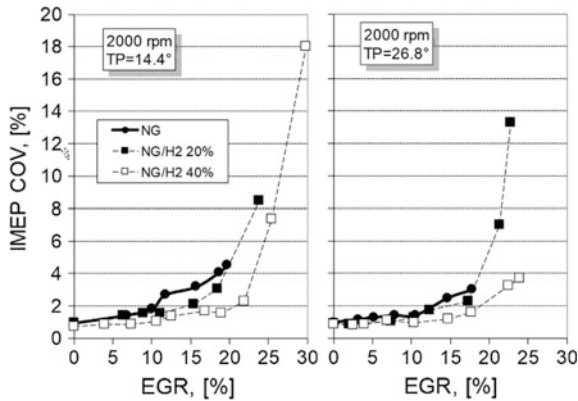


Fig. 6.21 IMEP COV at the two part-load conditions varying EGR rate and H<sub>2</sub> for the LD engine

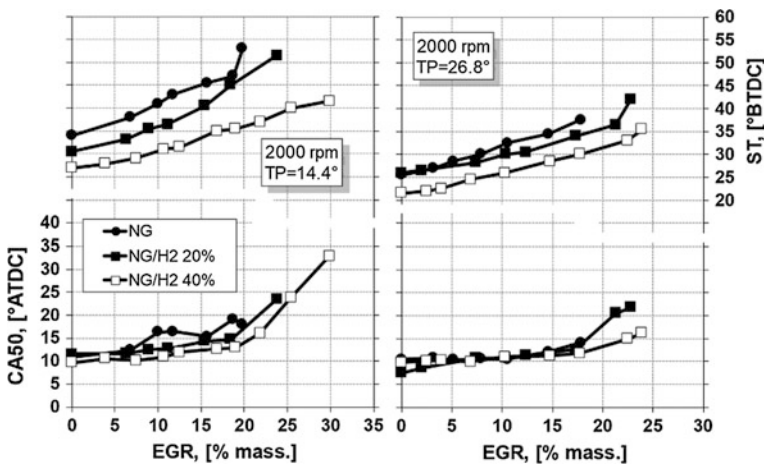


Fig. 6.22 CA50 and ST at the two part-load conditions varying EGR rate and H<sub>2</sub> for the LD engine

Figs. 6.22 and 6.23, referred to the LD engine, with Figs. 6.9 and 6.10 referred to the HD engines evidences a great congruence among the results for the two different engines.

For both the engines, a higher ST was set at EGR rate increasing to retain the CA50 close to the optimal position. Some differences can be noted at EGR rate higher than 20%. In fact, for the LD engine, it was not possible to retain the optimal CA50 position at EGR rate higher than 20%. This is mainly due to the lower LD engine load percentage, with respect to the HD engine. The connected very poor combustion conditions would have required a ST higher than the maximum allowed by the calibration tool software of the LD engine.



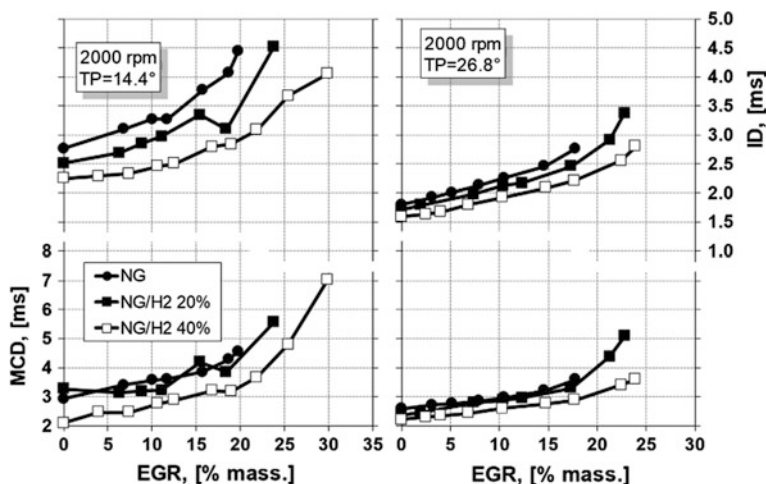


Fig. 6.23 MCD and ID at the two part-load conditions varying EGR rate and H<sub>2</sub> for the LD engine

## 6.6 Conclusions

The chapter analyses the effect of EGR and hydrogen enrichment on the performance and emission of a light-duty and a heavy-duty NG engine. EGR system for NG engines can be of different types (LPR, HPR, HLPR), due to almost soot free engine exhaust, which does not give fouling of intake system, including compressor and intercooler. EGR could be utilized to have high specific power, with low thermal stress, but also to increase efficiency. The efficiency increasing with EGR is mainly due to the reduction of thermal loss, rather than the decrease of pumping losses. Nevertheless, this last aspect could be of some interest for turbocharged engine: The main advantage could be to run un-throttled and with the wastegate closed, controlling load in a certain range (from maximum to lower torque) by adjusting the EGR rate. On the other hand, combustion propagation is worsened by EGR, which increase fuel consumption. Therefore, when unburned fuel effect exceeds the benefits associated with lower heat exchanges, efficiency gains cannot be achieved. This was the case of the LD engine compared to the HD engine. The results of the combustion process observed on the two engines were consistent with each other, although the increase of THC emissions by means of EGR is less evident on heavy-duty engine, for which the quenching zones have less effect on worsening emissions. Therefore, EGR technology is most suitable for optimizing efficiency of large bore engines.

The effect of EGR in reducing combustion speed is mitigated by hydrogen content in blend with NG. The positive effect of H<sub>2</sub> on combustion propagation is more evident at EGR rate increasing and mainly in the first stage of combustion.

EGR and hydrogen influence pollutant emissions, both upstream and downstream the catalyst. In particular, the lower temperature in combustion chamber with EGR reduces  $\text{NO}_x$  emissions formation upstream the catalyst, and since the mixture is still stoichiometric, also  $\text{NO}_x$  conversion efficiency in the three-way catalyst is very effective. Nevertheless, with EGR, the lower combustion temperature and high inert gas levels in the combustion chamber give an increment of THC. Moreover, for the lower exhaust gas temperatures and higher inert concentration, oxidation of THC in the catalyst could result in less effectiveness; for this reason, the blends with high hydrogen content, allowing a significant reduction of THC formation directly in the combustion chamber, can be a suitable opportunity for engines optimized with high EGR rates.

## References

- Arcoumanis C, Bae, C, Nagwaney A, Whitelaw J (1995) Effect of EGR on combustion development in a 1.9L DI diesel optical engine. SAE technical paper 950850
- Corbo P, Gambino M, Iannaccone S, Unich A (1995) Comparison between lean-burn and stoichiometric technologies for CNG heavy-duty engines. SAE technical paper 950057
- De Simio L, Gambino M, Iannaccone S (2007) Low-polluting, high-efficiency, mixed fuel/natural gas engine for transport application. In: Brebbia CA (ed) Urban Transport XIII: Urban transport and the environment in the 21st century, vol 96. WIT transactions on the built environment. southampton, WIT Press, UK, pp 493–502
- De Simio L, Gambino M, Iannaccone S (2009) A study of different EGR routes on a heavy duty stoichiometric natural gas engine. SAE technical paper 2009-24-0096
- De Simio L, Gambino M, Iannaccone S (2016) Using Natural Gas/hydrogen mixture as a fuel in a 6-Cylinder stoichiometric spark ignition engine. In: De Falco M, Basile A (eds) Enriched methane—the first step towards the hydrogen economy. Springer International Publishing, pp 175–194
- Dishy A, You T, Iwashiro Y, Nakayama S, Kihara R, Saito T (1995) Controlling combustion and exhaust emissions in a direct-injection diesel engine dual-fueled with natural gas. SAE technical paper 952436
- Feng D, Wei H, Pan M (2018) Comparative study on combined effects of cooled EGR with intake boosting and variable compression ratios on combustion and emissions improvement in a SI engine
- Hu E, Huang Z, Liu B, Zheng J, Gu X (2009) Experimental study on combustion characteristics of a spark-ignition engine fueled with natural gas–hydrogen blends combining with EGR. *Int J Hydrogen Energy* 34:1035–1044
- Ibrahim A, Bari S (2008) Optimization of a natural gas SI engine employing EGR strategy using a two-zone combustion model. *Fuel* 87:1824–1834
- Ibrahim A, Bari S (2010) An experimental investigation on the use of EGR in a supercharged natural gas SI engine. *Fuel* 89:1721–1730
- Jamsran N, Lim O (2016) Effects of EGR and boosting on the auto-ignition characteristics of HCCI combustion fueled with natural gas. *J Nat Gas Sci Eng* 35:1015–1024
- Kohketsu S, Mori K, Sakai K, Hakozaiki T (1997) EGR technologies for a turbocharged and intercooled heavy-duty diesel engine. SAE technical paper 970340
- Ladommatos N, Abdelhalim S, Zhao H, Hu Z (1996) The dilution, chemical, and thermal effects of exhaust gas recirculation on diesel engine emissions—Part 2: effects of carbon dioxide. SAE technical paper 961167 (1996)

- Li W, Liu Z, Wang Z, Xu Y (2014) Experimental investigation of the thermal and diluent effects of EGR components on combustion and  $\text{NO}_x$  emissions of a turbocharged natural gas SI engine
- Millo F, Ferraro C, Pilo L (2000) A contribution to engine and vehicle performance prediction. SAE technical paper 2000-01-1266
- Sen AK, Ash SK, Huang B, Huang Z (2011) Effect of exhaust gas recirculation on the cycle-to-cycle variations in a natural gas spark ignition engine. *Appl Therm Eng* 31:2247–2253
- Singh Kalsi S, Subramanian KA (2016) Experimental investigations of effects of EGR on performance and emissions characteristics of CNG fueled reactivity controlled compression ignition (RCCI) engine
- Yan B, Wang H, Zheng Z, Qin Y, Yao M (2017) The effects of LIVC Miller cycle on the combustion characteristics and thermal efficiency in a stoichiometric operation natural gas engine with EGR
- Zhang Q, Xu Z, Li M, Shao S (2016) Combustion and emissions of a Euro VI heavy-duty natural gas engine using EGR and TWC. *J Nat Gas Sci Eng* 28:660–671
- Zhang Q, Li M, Li G, Shao S, Li P (2017) Transient emission characteristics of a heavy-duty natural gas engine at stoichiometric operation with EGR and TWC. *Energy* 132:225–237

# Chapter 7

## Natural Gas Combustion in Marine Engines: An Operational, Environmental, and Economic Assessment



Roussos G. Papagiannakis, Theodoros C. Zannis, Efthimios G. Pariotis and John S. Katsanis

**Abstract** The present study contains a detailed assessment of the state-of-the-art technologies of two-stroke (2-S) and four-stroke (4-S) dual-fuel compression-ignition (CI) engines and four-stroke spark-ignited (SI) natural gas engines from technological, operational, environmental, and economic standpoints. Emphasis will be given to the examination of the effect of natural gas combustion on the performance characteristics and pollutant emissions of marine two-stroke dual-fuel engines and four-stroke dual-fuel and gas SI engines. Also, the CO<sub>2</sub> and CH<sub>4</sub> using EEDI analysis are examined for LNG carriers equipped with three different propulsion systems. The final outcome of the proposed study will be the definition of the parameters that should be taken into account to identify the optimum two-stroke and four-stroke natural gas engine technology frame, which can be used in the near future, as either main propulsion (two-stroke or four-stroke) or auxiliary (four-stroke) engines in marine applications.

**Keywords** Natural gas · Marine engines · Combustion · Emissions

### 7.1 Introduction

As known, both sulfur oxides (SO<sub>x</sub>) and oxides of nitrogen (NO<sub>x</sub>) are two critical gaseous emissions, which have a serious detrimental effect on photochemical smog and through this, on the formation of acid rain (Dieselnet 2017; Cleantech 2017; International Maritime Organization 2017). Also, SO<sub>x</sub> and NO<sub>x</sub> emissions have a

---

R. G. Papagiannakis (✉)  
Hellenic Air Force Academy, Dekelia, Attiki, Greece  
e-mail: [r.papagiannakis@gmail.com](mailto:r.papagiannakis@gmail.com)

T. C. Zannis · E. G. Pariotis · J. S. Katsanis  
Hellenic Naval Academy, Piraeus, Attiki, Greece

direct hazardous impact on human health since they are causing respiratory problems. Finally,  $\text{NO}_x$  emissions contribute significantly to eutrophication of lakes and rivers (Dieselnet 2017; Cleantech 2017; International Maritime Organization 2017). Hence, the International Maritime Organization (IMO) having acknowledged all the aforementioned negative influences of  $\text{NO}_x$  and  $\text{SO}_x$  emissions both on environment and on human health and having also convinced about the continuous deterioration of greenhouse effect has taken specific actions during recent years. Specifically, aiming to a significant curtailment of shipping-emitted gaseous pollutants, IMO has issued, during recent years, specific standards for  $\text{SO}_x$  and  $\text{NO}_x$  concentration values emitted from marine engines (Dieselnet 2017; Cleantech 2017). IMO has also launched specific measures in the form of efficiency design index (Energy Efficiency Design Index—EEDI) for new ships built after January 1, 2013, and in the form of efficiency operational index (Energy Efficiency Operational Index—EEOI) for existing ships for controlling greenhouse gas emissions with a primary interest for  $\text{CO}_2$  emissions (Dieselnet 2017; International Maritime Organization 2017).

According to IMO policy (International Maritime Organization 2017), shipping  $\text{SO}_x$  emissions are primarily controlled by fuel sulfur content. Figure 7.1a illustrates the chronological evolution from 2005 until 2025 of IMO-legislated global fuel sulfur content limit and the pertinent fuel sulfur limit, which is mandated in  $\text{SO}_x$  Emission Control Areas (SECAs) (Dieselnet 2017; Cleantech 2017; International Maritime Organization 2017). SECAs currently include Baltic Sea, North Sea, English Channel, and a 200 miles zone from North America coastline (International Maritime Organization 2017; Chryssakis et al. 2016; Diesel 2017; Chryssakis and Stahl 2013; Chryssakis and Tvete 2014). Most likely candidates for future inclusion in SECAs are Bosphorus Straits and Sea of Marmara, Hong Kong and parts of the coastline of Guangdong in China (Chryssakis et al. 2016; Diesel 2017; Chryssakis and Stahl 2013; Chryssakis and Tvete 2014). As evidenced by Fig. 7.1a, ships operating in SECAs are required to use low-sulfur fuel (0.1% S) or, in case this is not possible, to use after-treatment systems such as  $\text{SO}_x$  scrubbers. It is worth to mention that the European Union (EU) has imposed the limit of 0.1% fuel sulfur content in ports and inland waterways (Chryssakis et al. 2016; Diesel 2017; Chryssakis and Stahl 2013; Chryssakis and Tvete 2014). Also, EU will probably mandate a limit of 0.5% fuel sulfur cap in EU waters irrespective of IMO potential skepticism (Chryssakis et al. 2015, 2016).

Another category of gaseous pollutants emitted from marine engines are oxides of nitrogen ( $\text{NO}_x$ ). Nowadays, shipping-emitted  $\text{NO}_x$  is of high concern by IMO, ship owners, classes, and engine manufacturers since their control either inside or/ both outside marine engines is not directly facilitated such as in the case of  $\text{SO}_x$  emissions through fuel sulfur content. Figure 7.1b illustrates older and current IMO  $\text{NO}_x$  limits as function of engine speed “n” in RPM (Dieselnet 2017; Cleantech 2017; International Maritime Organization 2017). As evidenced by Fig. 7.1b, currently  $\text{NO}_x$  emission limits designated by standard Tier II are enforced globally, whereas the stricter standard Tier III is legislated by IMO in  $\text{NO}_x$  Emission Control Areas (NECAs) (Dieselnet 2017; International Maritime Organization 2017; Chryssakis et al. 2016). Currently, NECAs include North American ECA including

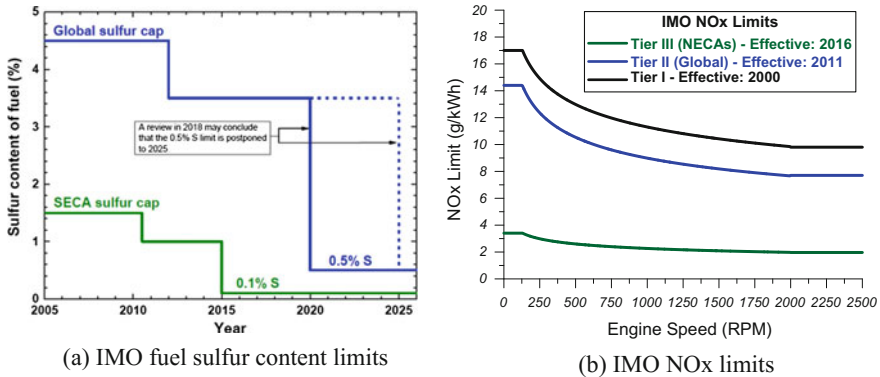


**Fig. 7.1** **a** IMO MARPOL Annex VI fuel sulfur content limits (International Maritime Organization 2017), **b** variation of IMO MARPOL Annex VI NO<sub>x</sub> limits from marine engines as function of rated engine speed. It is shown the initial NO<sub>x</sub> limits (Tier I) and the NO<sub>x</sub> limits that are currently issued globally (Tier II) and in NO<sub>x</sub> Emission Control Areas (NECAs) (Tier III) (Dieselnet 2017; Cleantech 2017; International Maritime Organization 2017)

most of USA and Canadian coast and US Caribbean ECA, including Puerto Rico and the US Virgin Islands. According to Fig. 7.1b, the most stringent NO<sub>x</sub> emission standard (Tier III) requires an approximate average reduction of shipping-emitted NO<sub>x</sub> of 80% compared to initial NO<sub>x</sub> emission standard (Tier I).

According to the Chap. 4 of IMO MARPOL Annex VI, there are two mandatory mechanisms intended to ensure an energy efficiency standard for ships: (A) the EEDI for new ships and (B) the Ship Energy Efficiency Management Plan (SEEMP) and the corresponding Energy Efficiency Operational Index (EEOI) for all ships (Dieselnet 2017; International Maritime Organization 2017). The EEDI is a performance-based mechanism that requires specified minimum energy efficiency in new ships. Ship designers and builders are free to choose the technologies to satisfy the EEDI requirements in a specific ship design (Dieselnet 2017; International Maritime Organization 2017). The SEEMP establishes a mechanism for operators to improve the energy efficiency of ships. Aforementioned regulations apply to all ships of and above 400 gross tonnages and enter into force from January 1, 2013.

As can be concluded from the aforementioned analysis, there is a very strong interest in shipping community for the actuation of immediate and drastic measures aiming to the significant curtailment of air pollutants emitted from ships and to their compliance with IMO regulations both in emission control areas and outside of them. Toward this aim, a direct mean for downplaying IMO regulated SO<sub>x</sub>, NO<sub>x</sub> and GHG emissions is the combustion of natural gas in marine main slow-speed two-stroke compression-ignition engines, in high-speed and medium-speed main and auxiliary dual-fuel CI engines and in marine main and auxiliary high-speed spark-ignition (SI) gas engines (Chryssakis et al. 2016; Diesel 2017; Chryssakis and Stahl 2013; Chryssakis and Tvette 2014; Chryssakis et al. 2015; McGill et al. 2013; Germanischer Lloyd 2013; Trauthwein 2012).

Theoretical and experimental studies conducted in the past (Murakami and Baufeld 2013; Mohr and Baufeld 2013; Tozzi et al. 2016; Moriyoshi et al. 2016; Andre 2013; Hiltner et al. 2016; Hiltner 2013; Callahan and Hoag 2013; Brynolf et al. 2014; Li et al. 2015; Wei and Geng 2016; Roecker 2016) in marine two-stroke dual-fuel and marine four-stroke dual-fuel and SI gas engines have demonstrated that natural combustion can:

- Practically eliminate  $\text{SO}_x$  emissions
- Dramatically downplay  $\text{NO}_x$  emissions allowing gas engines to directly comply with IMO Tier III regulations
- Significantly reduce  $\text{CO}_2$  emissions
- Generate extremely low PM emissions and in the cases of very small pilot diesel quantity and of SI gas engines to attain smokeless engine operation.

However, as reported in the literature (Schlick 2014; Levander 2011; Haraldson 2011; Diesel and Turbo 2017; Wartsila 2-stroke dual fuel technology 2014; Zannis et al. 2017; Yfantis et al. 2017; Kjemtrup 2015; Ott 2015; Hagedorn 2014), natural gas combustion in marine dual-fuel and gas engines is accompanied by the following environmental and operational obstacles:

- Major deterioration of total unburned hydrocarbon (THC),  $\text{CH}_4$ , and CO emissions compared mainly to conventional CI engines. Especially in the case of  $\text{CH}_4$  emissions (phenomenon of “methane slip”), dual-fuel and gas engines may provoke serious amendments of IMO GHG emissions regulations policy if not only  $\text{CO}_2$  but also methane is included in future shipping GHG picture (Murakami and Baufeld 2013; Mohr and Baufeld 2013; Hiltner et al. 2016; Brynolf et al. 2014; Schlick 2014; Levander 2011).
- Increasing risk for either knocking or flame quenching in both dual-fuel and gas engines and for misfiring mainly in dual-fuel engines. Potential avoidance of one or more of the aforementioned gas combustion-related phenomena may require the combined incorporation of various combustion chamber design technologies and in-cylinder measures (Murakami and Baufeld 2013; Mohr and Baufeld 2013; Tozzi et al. 2016; Moriyoshi et al. 2016; Schlick 2014; Levander 2011).
- High capital cost and technical complexity for retrofitting existing marine diesel engines in order to be able to operate effectively with natural gas (Murakami and Baufeld 2013; Mohr and Baufeld 2013; Tozzi et al. 2016; Moriyoshi et al. 2016; Schlick 2014; Levander 2011).

Though that in the past there have been reported extensive and elaborative studies in the literature (Murakami and Baufeld 2013; Mohr and Baufeld 2013; Andre 2013; Brynolf et al. 2014; Li et al. 2015; Wei and Geng 2016; Schlick 2014; Levander 2011), which examined thoroughly contemporary natural gas combustion technologies both in marine CI and SI engines (Murakami and Baufeld 2013; Mohr and Baufeld 2013; Andre 2013; Brynolf et al. 2014; Li et al. 2015; Schlick 2014; Levander 2011), and in other engine type (Wei and Geng 2016), there is a lack of consolidated information regarding the technological, environmental, and economic

evaluation of modern natural gas combustion technologies in main and auxiliary marine engines. Hence, the main purpose of the present study is to cover the aforementioned gap in the literature by examining thoroughly contemporary natural gas combustion technologies used in marine main and auxiliary engines on a technical, operational, environmental, and economic basis.

## 7.2 Natural Gas as Maritime Fuel

Before examining the effects of natural gas combustion on marine engines performance characteristics and pollutant emissions, it is essential to understand the main characteristics and the key advantages and disadvantages of natural gas as a maritime fuel. Hence, the advantages of the use of natural gas in marine internal combustion engines are the following (Chryssakis et al. 2016; Diesel 2017; Chryssakis and Stahl 2013; Chryssakis and Tvette 2014; Chryssakis et al. 2015; McGill et al. 2013; Germanischer lloyd 2013; Murakami and Baufeld 2013; Mohr and Baufeld 2013):

- Natural gas indicates high availability from ground reserves: The recent discovery of huge available underwater natural gas reserves in the coasts of Eastern Africa and in the Caspian Sea, for example, guarantees the unobstructed supply of the global markets for many years in the future (McGill et al. 2013).
- The competitive prices of natural gas compared to residual fuel and to distillate fuel: Natural gas is expected to have competitive cost compared to residual fuel and to distillate oil until 2035 (see Fig. 7.2). Nowadays, natural gas indicates almost 70% lower price compared to residual fuel and 85% lower price compared to distillate fuel oil (McGill et al. 2013).

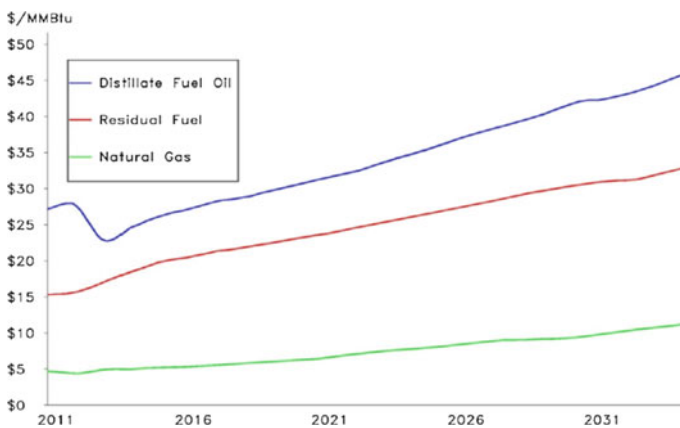


**Fig. 7.2** Chronological evolution of the prices of natural gas, residual fuel, and distillate fuel oil (McGill et al. 2013)



- Natural gas combustion can lead to approximately 20% lower CO<sub>2</sub> emissions compared to diesel oil combustion (Schlick 2014) (see Fig. 7.3). Even higher CO<sub>2</sub> reductions have been reported reaching up to 30% when burning natural gas in four-stroke lean-burn marine engines (Levander 2011). The aforementioned CO<sub>2</sub> reductions can be ascribed to the significantly lower carbon to hydrogen mass ratio of natural gas compared to diesel oil (Levander 2011; Haraldson 2011).
- Dual-fuel and natural gas engines can attain 80% lower NO<sub>x</sub> emissions compared to conventional diesel engines (see Fig. 7.3). Higher NO<sub>x</sub> reductions up to 85% compared to conventional diesel combustion can be accomplished in lean-burn gas engines, which are operating with high air–fuel ratio (Levander 2011). It has experimentally been proved that dual-fuel and spark-ignited gas engines with pre-chamber can directly comply with IMO Tier III NO<sub>x</sub> limits without the need for specially designed in-cylinder (“internal”) or after-treatment (“external”) measures (Chryssakis et al. 2015).
- Natural gas combustion in marine main and auxiliary engines can practically eliminate SO<sub>x</sub> emissions since sulfur is removed from fuel when is liquefied (see Fig. 7.3) (Chryssakis et al. 2015; Mohr and Baufeld 2013; Levander 2011).
- The use of natural gas in marine four-stroke engines can result in extremely low PM emissions especially in the case of lean-burn gas engines (Chryssakis et al. 2015). This can be attributed to lower molecular complexity of the natural gas mixture of burning gases, which generate dramatically lower polyaromatic hydrocarbons (PAHs), which are considered as primary particulate matter

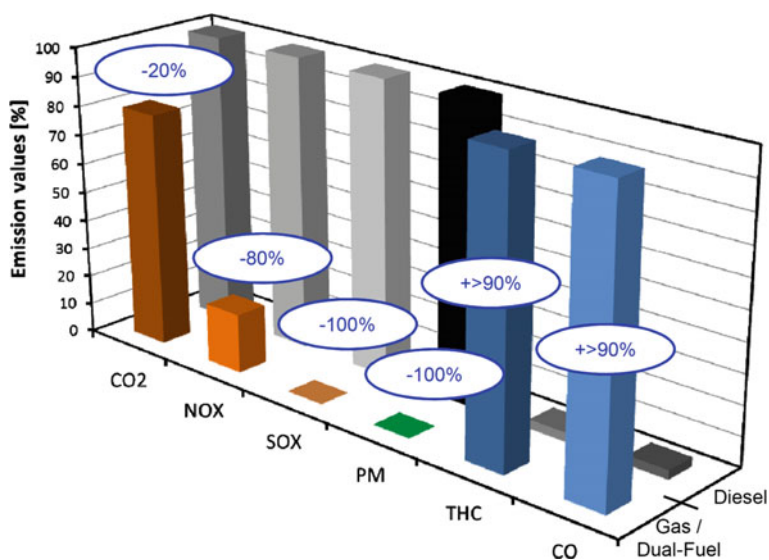


**Fig. 7.3** Comparative effect of natural gas combustion in dual-fuel and gas engines on CO<sub>2</sub>, NO<sub>x</sub>, SO<sub>x</sub>, PM, THC, and CO emissions relative to diesel combustion (Schlick 2014)

precursors, compared to conventional diesel combustion. PM emissions during dual-fuel combustion are primarily controlled by pilot diesel quantity. It is worth to mention that, according to detailed experimental studies (Chryssakis et al. 2015; Murakami and Baufeld 2013; Mohr and Baufeld 2013; Levander 2011; Haraldson 2011), natural gas combustion either under dual-fuel mode or under spark-ignited mode results in no visible smoke (“smokeless operation”).

- Finally, another virtue of natural gas combustion in marine engines is that it does not leave sludge deposits (Chryssakis et al. 2015; Mohr and Baufeld 2013; Levander 2011).
- It has been established specific rules for the construction of natural gas carriers from various classes such as DNV/GL and Lloyd’s Register (McGill et al. 2013).
- There is high availability of marine internal combustion engines operating with natural gas from many different engine manufacturers: Nowadays, there are commercially available various editions of two-stroke and four-stroke marine compression-ignition engines operating with natural gas (dual-fuel diesel/natural gas engines) and four-stroke spark-ignition marine engines operating with natural gas (McGill et al. 2013). Dual-fuel marine compression-ignition engines can be used as main engines (two-stroke and four-stroke) or as electric generators (four-stroke engines), whereas four-stroke gas spark-ignition engines can be used in passenger ships and in ferries but also as electric generators (McGill et al. 2013).
- Finally, natural gas application in shipping is also facilitated by the technical and operational experience, which has been accumulated over recent decades by ship owners, ships’ technical staff, classes, shipyards, and engine manufacturers (McGill et al. 2013).

The main disadvantages of the use of natural gas in ships are the following (McGill et al. 2013):

- Natural gas combustion in marine internal combustion engines results in higher emissions of unburned hydrocarbons and of gaseous methane compared to liquid fuel combustion. Specifically, natural gas combustion in either dual-fuel CI engines or in gas SI engines results in the deterioration of unburned hydrocarbon emissions from 70 to 90% compared to conventional engine operation (McGill et al. 2013). In addition, natural gas combustion in marine internal combustion engines results in a serious worsening of methane emissions (methane slip) compared to conventional operation. If we take into account that methane is considered as 20–25 times more detrimental global warming gas compared to carbon dioxide, then natural gas in marine engines provokes great skepticism regarding the phenomenon of methane slip. For this reason, it is expected that methane emissions will be incorporated in the future in the calculation of global warming gases and on that basis is expected the deterioration of the operational cost in ships using natural gas as marine fuel from the potential implementation of carbon tax in maritime sector (McGill et al. 2013).

- Natural gas combustion is not directly compatible with existing marine compression-ignition and spark-ignition engines and with existing marine engines' fuel supply infrastructure: Specifically, the use of natural gas as fuel in ships requires constructional modifications of existing marine internal combustion engines and requires also modifications in the fuel supply networks of main and auxiliary engines (McGill et al. 2013). Major manufacturers of marine four-stroke diesel engines have proposed certain modifications in order their engines to operate with natural gas as dual-fuel engines (Schlick 2014). Specifically, major marine CI engine manufacturers propose the reduction of compression ratio for avoiding excess in-cylinder pressures during dual-fuel operation. It is also proposed the reformulation of piston bowl design for improved fuel-air mixing and the replacement of liner honing in order to be compatible with higher in-cylinder temperatures during dual-fuel operation compared to conventional diesel operation (Schlick 2014). Regarding the cylinder head, it is proposed the installation of individual gas admission valves for each cylinder head, the installation of a pilot fuel injector, the optimization of intake process probably through increased swirl ratio for increasing in-cylinder turbulence levels and improving, thus, fuel-air mixing process. It is also proposed the modification of valve seat geometry for avoiding excessive gas leakages and the installation of a knock sensor in each cylinder for monitoring and processing in-cylinder pressure and thus avoiding pre-ignition or post-combustion knocking phenomena (Schlick 2014). In addition to engine modifications, fuel supply network modifications are required for security reasons also regarding onboard natural gas management. Of special interest are the results of a detailed study, which was performed in 2013 (McGill et al. 2013). In this study it was calculated the retrofit cost of main and auxiliary engines of three different ships in order they have the capacity to operate with natural gas as fuel. It was also calculated the pertinent retrofit cost of fuel supply networks of the main and auxiliary engines for being compatible with natural gas. The main findings of this study are summarized in Table 7.1 (McGill et al. 2013).

**Table 7.1** Retrofit costs of certain ship types for operation of their engines with natural gas (McGill et al. 2013)

Ship type	Size (tons)	Engine	Engine retrofit cost (million \$)	Engine fuel supply system retrofit cost (million \$)	Total engine retrofit cost (million \$)
Tug	150	2 × 1500 HP	1.2	6.0	7.2
Ferry	1000	2 × 3000 HP	1.8	9.0	10.8
Great lakes bulk carrier	19,000	2 × 5000 HP	4.0	20	24

- The use of natural gas as marine fuel in new buildings introduces a construction premium compared to newly constructed ships burning liquid fossil fuels in their engines. Specifically, the building cost of a gas-powered ship is considerably higher than the pertinent cost of a fossil fuel-powered ship since there is a cost increase for gas engines and for gaseous fuel system and also for LNG storage tanks (McGill et al. 2013). According to a detailed study performed by Germanischer Lloyd (Germanischer Lloyd 2013), natural gas utilization as marine fuel introduces an additional investment cost of 25% over that of the cost for constructing a typical new container ship. Also according to a recent DNV study (Schlick 2014) if a ship spends more than 30% of its operating time in ECAs the cost of gas-fueled engines can be justified (McGill et al. 2013; Zannis et al. 2017; Yfantis et al. 2017) drawback of natural gas as maritime fuel is the increased onboard space requirements for natural gas storage (McGill et al. 2013; Zannis et al. 2017; Yfantis et al. 2017). Specifically, increased onboard space requirements are necessary for the storage of the required natural gas volume for ship autonomy equal to of a conventional ship with onboard storage of liquid fuels (McGill et al. 2013; Zannis et al. 2017; Yfantis et al. 2017). A specific natural gas weight stored as liquefied natural gas (LNG) requires almost only 40% of the corresponding natural gas weight stored as compressed natural gas (CNG) at 3600 psi ( $\approx 250$  bar). Hence, LNG requires much less storage space compared to CNG, and for this reason, natural gas carriage as LNG is the preferred onboard storage and carriage technique. When natural gas is stored as LNG requires two times bigger space compared to the corresponding storage space of a liquid fuel whereas when natural gas is stored on board as CNG requires five times bigger space compared to the corresponding storage space of a liquid fuel (McGill et al. 2013; Zannis et al. 2017; Yfantis et al. 2017). Table 7.2 shows comparative examples of the minimum storage capacity and of the onboard storage volume for the carriage of residual fuel, distillate fuel, LNG, and CNG with three different ship types. In Fig. 7.3 is given the comparison of the fuel weight per equivalent gallon of distillate fuel for distillate fuel, for residual fuel, for LNG, and for CNG@3600 psi. In Fig. 7.4 is also depicted a comparison of the storage volume per equivalent gallon distillate fuel for distillate fuel, residual fuel, LNG, and CNG@3600 psi (McGill et al. 2013; Zannis et al. 2017; Yfantis et al. 2017).
- The increased ship supply time with natural gas is another serious drawback of natural gas as marine fuel. Specifically, the required supply time of a ship with natural gas is higher compared to the pertinent time for ship supply with a liquid fuel. In particular regarding the onboard storage of natural gas as CNG, it can be stated that this solution cannot be considered as more or less viable due to (McGill et al. 2013; Sarigianidis 2016):
  - Higher ship supply times compared to ship supply time with LNG.
  - Additional onboard space requirements for the CNG storage tanks.
  - Limited carriage volume, which leads to limited CNG ship autonomy.

**Table 7.2** Comparative examples of the minimum onboard storage capacity and of the onboard storage volume for the transportation of distillate or heavy fuel oil, LNG, and CNG with three different ship types (McGill et al. 2013)

Ship	Fuel type	HP	Daily fuel consumption (gal)	Typical minimum onboard storage capacity		Onboard storage volume		
				(days)	(gal)	Distillate oil (ft <sup>3</sup> )	LNG (ft <sup>3</sup> )	CNG (ft <sup>3</sup> )
Towing tug	Distillate oil	3000	1417	14	20,000	2674	4830	12,178
100-car ferry	Distillate oil	6000	2268	7	16,000	2139	3864	9742
Great lakes ore carrier	Heavy fuel oil	10,000	6934	21	145,000	19,385	38,183	92,264

Weight and Volume of One Distillate Gallon Equivalent of Different Fuels

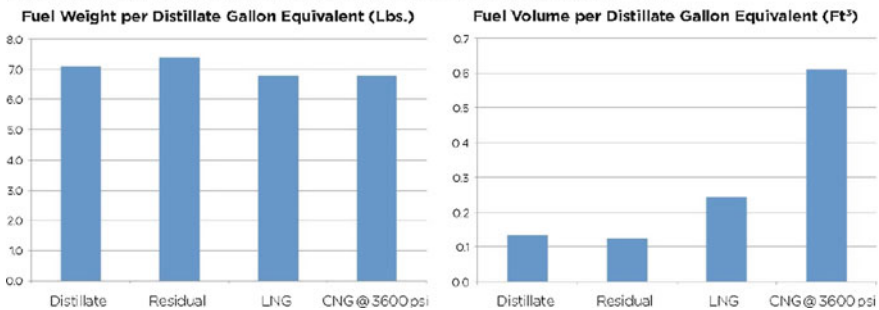


**Fig. 7.4** (Left figure) Comparison of fuel weight per equivalent gallon of distillate fuel oil for distillate fuel oil, for residual fuel, for LNG, and for CNG@3600psi. (Right figure) Comparison of fuel volume per distillate gallon equivalent for distillate fuel, for residual fuel, for LNG, and for CNG@3600 psi (McGill et al. 2013)

For the aforementioned reasons, CNG is considered as viable solution for ships doing limited-distance trips and they also have sufficient return time for ship resupply with CNG. On the other hand, the main drawbacks of the LNG are the following (McGill et al. 2013; Sarigianidis 2016):

- The liquefaction of natural gas requires the deep freezing of the gas at a temperature almost equal to  $-160\text{ }^{\circ}\text{C}$ . Nowadays, this deep freezing is attainable through technically complicated and expensive shored installations.
- LNG carriers should be equipped with technical systems of deep freezing for keeping LNG at temperatures close to  $-160\text{ }^{\circ}\text{C}$ .

- The additional onboard safety requirements of natural gas carriage ship is another obstacle to the broad use of natural gas in maritime sector. Specifically, natural gas carriage from a ship requires additional installations and safety settings, and it results in onboard constructional interventions, which lead to a higher overall constructional cost of a natural gas carriage ship compared to a conventional one (McGill et al. 2013).
- Finally, the last disadvantage of natural gas as marine fuel is the global limited number of shored infrastructures for the bunkering of ships with natural gas. Specifically, an international network of shored LNG bunkering stations should be constructed in order the LNG ship carriage and the use of natural gas as maritime fuel to be attractive for the majority of commercial ships. Today, LNG bunkering from shored LNG stations is more expensive and technically more complicated compared to liquid fuel bunkering. In addition, LNG bunkering can be accomplished by a limited number of corresponding LNG shored stations in the world (McGill et al. 2013).

In the following sections are examined the contemporary natural gas combustion technologies in marine two-stroke dual-fuel engines and in marine four-stroke dual-fuel and gas SI engines. It is also evaluated the performance of the aforementioned gas engines from technological, operational, environmental, and economic standpoints.

## **7.3 Dual-Fuel and Gas Spark-Ignition Engines: Contemporary Combustion Technologies**

### ***7.3.1 Two-Stroke Dual-Fuel Engines Technologies***

Nowadays, there are commercially available two main types of marine main two-stroke CI engines burning natural gas: The one operating according to diesel cycle and the one operating according to Otto cycle (Wartsila 2-stroke dual fuel technology 2014; Zannis et al. 2017; Yfantis et al. 2017; Kjemtrup 2015; Ott 2015). The operational principles of the two aforementioned types of two-stroke natural gas engines are shown in Fig. 7.5a and b. Regarding the “Diesel-cycle” two-stroke dual-fuel engine, it should be mentioned that the specific engine type operates according to diesel-cycle principle, which means that natural gas–diesel combustion is primarily controlled by diffusion-controlled combustion as in conventional diesel engines (Wartsila 2-stroke dual fuel technology 2014; Kjemtrup 2015; Ott 2015). Specifically, in “diesel-cycle” dual-fuel engine, a pilot diesel oil quantity of about 3%*m/m* is injected before natural gas injection both immediately before top dead center (TDC). The compression heat creates in-cylinder temperatures high enough to auto-ignite liquid fuel oil. After diesel oil ignition, a flame front is created inside cylinder, which is expanded inside the entire combustion chamber being fed by natural gas injection and combustion (Wartsila 2-stroke dual fuel technology 2014;

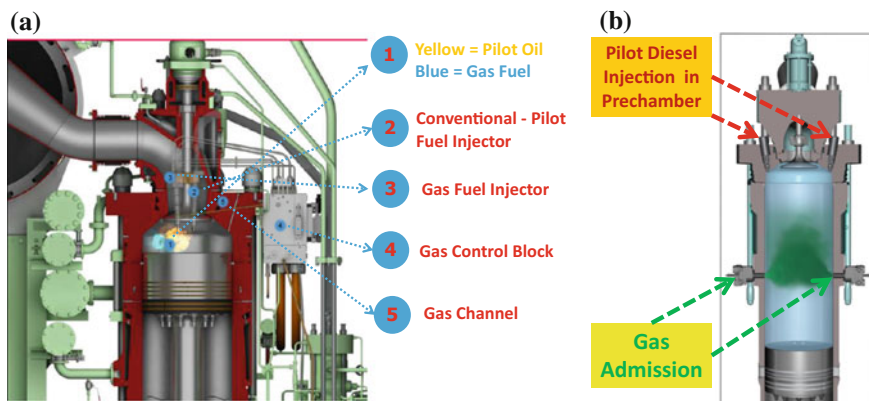


**Fig. 7.5** Operational principles of **a** “diesel-cycle” two-stroke dual-fuel engine (Kjemtrup 2015) and **b** “Otto-cycle” two-stroke natural gas engine (Wartsila 2-stroke dual fuel technology 2014)

Kjemtrup 2015; Ott 2015). Natural gas is injected in “diesel-cycle” engine at a pressure of 300bar and at a temperature of 45 °C. “Diesel-cycle” two-stroke gas engine meets  $SO_x$  requirements with LNG or low-sulfur diesel oil, and its most important virtue is that indicates a high fuel efficiency close to 50% depending on engine load (Wartsila 2-stroke dual fuel technology 2014; Kjemtrup 2015; Ott 2015). However, the “diesel-cycle” two-stroke gas engine cannot meet directly IMO Tier III  $NO_x$  limits, and thus, there is a potential need for exhaust gas recirculation (EGR) or selective catalytic reduction (SCR) (Wartsila 2-stroke dual fuel technology 2014; Kjemtrup 2015; Ott 2015).

On the other hand, the operational principle of the “Otto-cycle” two-stroke natural gas engine is based primarily on the premixed lean-burn natural gas combustion with pilot diesel ignition (Wartsila 2-stroke dual fuel technology 2014; Kjemtrup 2015; Ott 2015). Specifically, natural gas is injected at low pressure (<10 bar) at mid-stroke after scavenging. A pilot fuel oil quantity of 1%*m/m* is injected before TDC in pre-chamber, and then, it auto-ignites due to compression heat of the premixed air/gas mixture (Wartsila 2-stroke dual fuel technology 2014; Kjemtrup 2015; Ott 2015). The “Otto-cycle” two-stroke natural gas engine indicates lower fuel efficiency compared to the “diesel-cycle” engine, which is close to 47% depending on engine load (Wartsila 2-stroke dual fuel technology 2014; Kjemtrup 2015; Ott 2015). Also, the predominantly premixed-controlled natural gas combustion of the “Otto-cycle” two-stroke gas engine creates serious considerations regarding increased THC and CO emissions. It also creates skepticism regarding a significant deterioration of methane slip compared to “diesel-cycle” engine and also regarding potential undesirable pre-ignition or post-combustion knocking phenomena (Wartsila 2-stroke dual fuel technology 2014; Kjemtrup 2015; Ott 2015). The most important environmental virtues of the “Otto-cycle” two-stroke gas engine is that fulfills ECA  $SO_x$  requirements with LNG or low-sulfur

fuel oil and also meets directly Tier III NO<sub>x</sub> requirements without in-cylinder measures or after-treatment (Wartsila 2-stroke dual fuel technology 2014; Kjemtrup 2015; Ott 2015).

It is of high importance to understand the main difference in engine operational characteristics between the “diesel-cycle” and the “Otto-cycle” dual-fuel marine two-stroke engines, which are responsible for their distinctive variations in engine efficiency and NO<sub>x</sub> emissions. For this reason, in Fig. 7.6 are shown indicative predictions of mean bulk gas in-cylinder temperature obtained from the literature (Wartsila 2-stroke dual fuel technology 2014) for the “diesel-cycle” and the “Otto-cycle” dual-fuel two-stroke marine CI engines. The black color curve corresponds to the in-cylinder temperature of the “Diesel-cycle” engine, whereas the orange color curve corresponds to the cylinder temperature of the “Otto-cycle” engine. As observed from Fig. 7.6, the “Otto-cycle” indicates an earlier initiation of cylinder temperature rise during the early stages of combustion, which can be ascribed to the more homogeneous nature of natural gas combustion in this type of two-stroke marine engine. However, the “diesel-cycle” two-stroke engine indicates significantly higher peak cylinder temperatures compared to the corresponding ones of the “Otto-cycle” engine. Specifically, the “diesel-cycle” two-stroke engine demonstrates 300–500 °C higher maximum flame temperatures compared to the “Otto-cycle” engine. Also during expansion stroke, the “diesel-cycle” engine indicates higher cylinder temperatures compared to the “Otto-cycle” engine, which can be attributed to the diffusion-controlled of the fuel–air mixture, which is the dominating combustion mode in the “diesel-cycle” engine. The higher in-cylinder

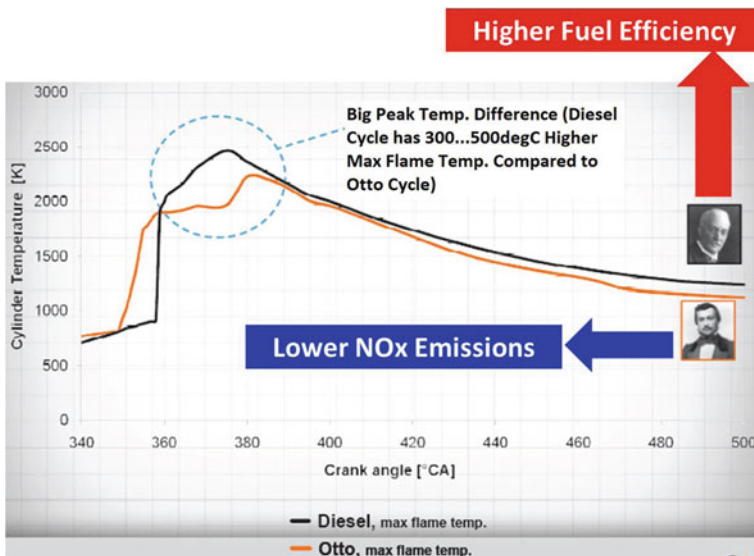


**Fig. 7.6** Comparison of in-cylinder temperature–crank angle curves between “Diesel-cycle” and “Otto-cycle” two-stroke marine engines (Ott 2015)



temperatures of the “diesel-cycle” engine, which are evidenced during combustion and expansion stroke, are responsible for the higher fuel efficiency of this type of engine compared to the “Otto-cycle” engine. On the other hand, the lower peak flame temperatures and mainly the lower cylinder temperatures during expansion stroke, which are observed in the case of the “Otto-cycle” engine, are primarily responsible for the lower  $\text{NO}_x$  emissions of the “Otto-cycle” engine compared to the ones of the “diesel-cycle” engine.

Having examined the main constructional and operational differences between the “diesel-cycle” and the “Otto-cycle” dual-fuel two-stroke marine CI engines, a question raised regarding the operational modes of the “diesel-cycle” engine and whether or not the transition from conventional diesel engine operation to dual-fuel operation is smooth and unobstructed in “diesel-cycle” engine. Toward providing answers to these questions, Fig. 7.7 is given, which provides an illustrative overview of the different operational modes of the “diesel-cycle” dual-fuel two-stroke marine CI engine (Kjemtrup 2015). As evidenced by Fig. 7.7, the “diesel-cycle” two-stroke engine can operate under three different operational modes: (a) fuel-only mode, (b) minimum-fuel oil mode, and (c) specified gas mode. Under fuel-only mode, the “diesel-cycle” engine operates as conventional two-stroke diesel engine with heavy or light diesel oil. Under minimum-fuel oil mode, the “diesel-cycle” two-stroke engine uses 97% $\text{m/m}$  natural gas with 3% $\text{m/m}$  pilot diesel oil for ignition. Under this mode, the “diesel-cycle” two-stroke marine CI engine can operate between 10 and 100% of full engine load (Kjemtrup 2015). Finally, under

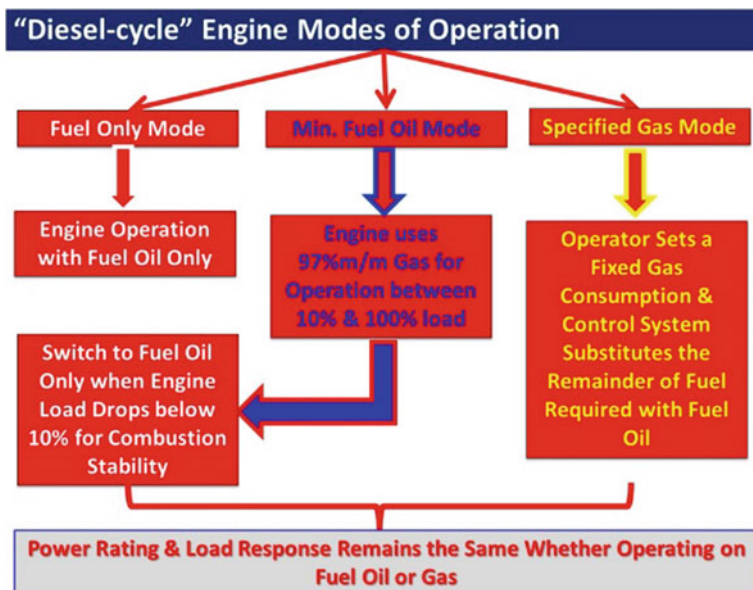


**Fig. 7.7** “Diesel-cycle” two-stroke dual-fuel marine engine modes of operation (Zannis et al. 2017; Kjemtrup 2015)

the specified gas mode, the operator of the engine specifies desirable natural gas consumption and the control system of the “diesel-cycle” engine substitutes the remained of the fuel required with heavy or light diesel oil.

Figure 7.8a and b show the variation of fuel percentage with engine load during minimum-fuel mode (Fig. 7.8a) and during specified dual fuel mode (Fig. 7.8b) of the “diesel-cycle” two-stroke marine CI engine. In both Fig. 7.8a and b with red color is showed the total fuel consumption and with green color the pilot fuel consumption. According to red area of Fig. 7.8a, the “diesel-cycle” engine under minimum-fuel mode can operate smoothly from 10 to 100% of full load (SMCR) with 97%*m/m* natural gas and with only 3%*m/m* diesel oil. As observed from Fig. 7.8b, the “diesel-cycle” two-stroke marine CI engine can also smoothly operate from 10 to 100% of full load (SMCR) with different analogies of predefined natural gas consumption and pilot diesel oil quantities. According to the literature (Kjemtrup 2015) under specified dual-mode operation, the “diesel-cycle” two-stroke dual-fuel CI marine engine experienced no fuel slip, no knocking problems and its operation was insensitive to natural gas methane number (i.e., natural gas quality). Also during specified dual-mode operation, the specific engine experienced unchanged load response, which is an important virtue of this type of engine. For this reason, the “diesel-cycle” engine managed to reduce significantly its gas mode operational load up to 10%, which is of significant importance for sustaining its high efficiency and operational smoothness under significantly low engine loads. The most important conclusion regarding “diesel-cycle” two-stroke dual-fuel CI engine is that power rating and load response remain the same whether the engine operates on diesel oil or on gas, which is extremely important for the power delivery to ship propellers.

### ***7.3.2 Four-Stroke Dual-Fuel and Gas Spark-Ignition Engines Technologies***

After examining the two types of commercially available two-stroke natural gas engines, it is of particular importance to examine the contemporary natural gas combustion technologies currently used in four-stroke dual-fuel engines and in gas SI engines, which are summarized in Fig. 7.9 (Murakami and Baufeld 2013; Mohr and Baufeld 2013). The four-stroke natural gas technologies are divided into main categories according to the constructional design of the combustion chamber and their operational principle: the open-chamber four-stroke dual-fuel and gas SI engines and the corresponding natural gas engines equipped with a divided chamber (i.e., pre-chamber and main combustion chamber) (Murakami and Baufeld 2013). The open-chamber natural gas engines are divided into two categories: The open-chamber dual-fuel engines with micro-pilot injection (OCMP) and the open-chamber spark-ignition (OCSI) gas engines (Murakami and Baufeld 2013; Mohr and Baufeld 2013). Similarly, the natural gas engines with divided chamber are divided into two categories: the pre-chamber with micro-pilot (PCMP) engines

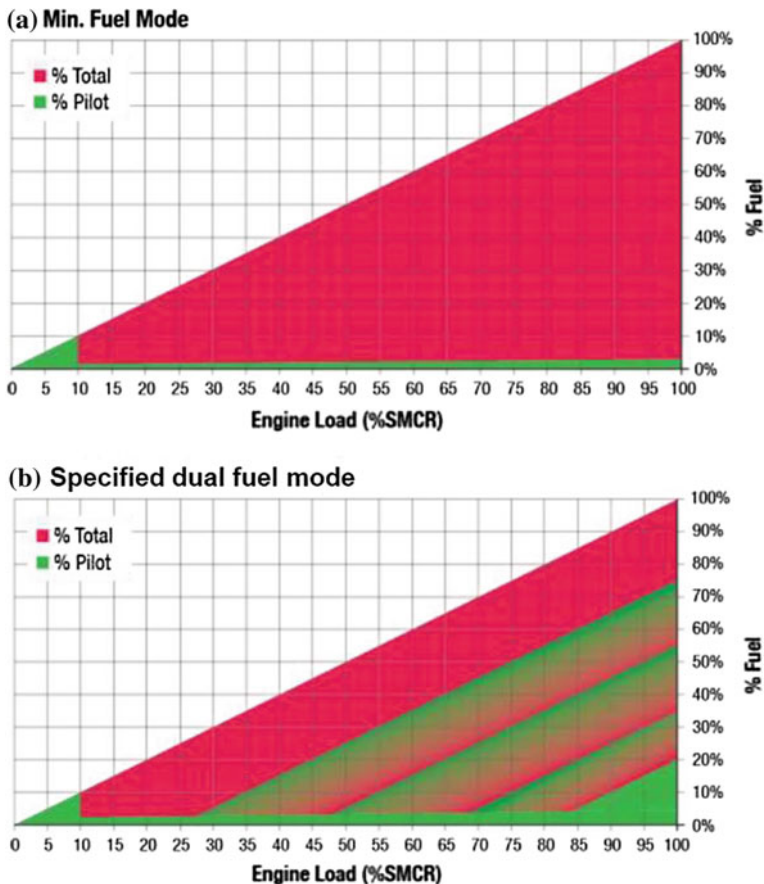


**Fig. 7.8** Variations of fuel percentage versus engine load (%SMCR) during **a** minimum-fuel mode and **b** specified dual-fuel mode of the “Diesel-cycle” dual-fuel two-stroke CI marine engine (Kjemtrup 2015)

and the pre-chamber spark-ignition (PCSI) engines (Murakami and Baufeld 2013; Mohr and Baufeld 2013; Zannis et al. 2017; Yfantis et al. 2017).

The operation principle of OCSI engines is based on the induction of a natural gas/air mixture inside the cylinder through the intake valves, which is ignited through a spark plug. The key optimization factor of OCSI engines is the piston bowl design and, specifically, the attainment of high swirl ratio and squish flow for achieving of high turbulence, which has a direct and immediate positive impact on high flame velocity (Murakami and Baufeld 2013; Mohr and Baufeld 2013; Zannis et al. 2017; Yfantis et al. 2017). However, the application of this combustion technology in large bore engines is challenging due to the increased flame travel distance, which curtails brake thermal efficiency (BTE) and worsens knocking

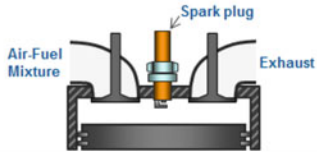
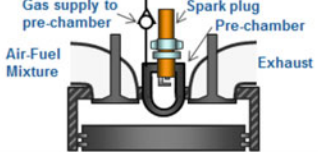
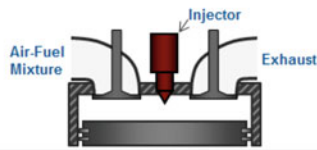
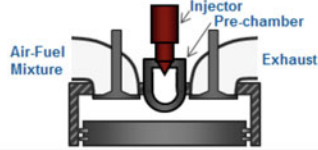
		Combustion Chamber Geometry	
		Open Chamber	Pre-Chamber
Ignition Principle	Spark Ignition	<ul style="list-style-type: none"> <li>➤ Most simple solution</li> <li>➤ Dominant in engine classes &lt; 6 liters/cyl.</li> <li>➤ Challenge: ignition &amp; combustion stability, plug life</li> </ul> 	<ul style="list-style-type: none"> <li>➤ Stable ignition &amp; combustion</li> <li>➤ High efficiency, low NOx</li> <li>➤ Dominant in engine classes &gt; 6 liters/cyl.</li> <li>➤ Challenge: complex system, plug life</li> </ul> 
	Micro Pilot Injection	<ul style="list-style-type: none"> <li>➤ Mainly used in dual fuel engines</li> <li>➤ Challenge: complex system, combustion stability, low NOx limited</li> </ul> 	<ul style="list-style-type: none"> <li>➤ Stable ignition &amp; combustion</li> <li>➤ High efficiency, lowest NOx</li> <li>➤ Long interval for injector exchange</li> <li>➤ Limited number of application</li> <li>➤ Challenge: most complex system</li> </ul> 

Fig. 7.9 Four-stroke marine dual-fuel CI and natural gas SI engines combustion technologies (Murakami and Baufeld 2013; Mohr and Baufeld 2013)

resistance (Murakami and Baufeld 2013; Mohr and Baufeld 2013; Zannis et al. 2017; Yfantis et al. 2017).

Regarding OCMF operational principle, this is based also in the induction of a natural gas/air mixture through intake valves, which is burned after injection and ignition of micro-pilot fuel oil quantity (Murakami and Baufeld 2013; Mohr and Baufeld 2013; Zannis et al. 2017; Yfantis et al. 2017). In this case, it is observed a slightly faster combustion compared to the OCSI concept due to stronger ignition source (i.e., micro-pilot fuel injection) (Murakami and Baufeld 2013; Mohr and Baufeld 2013). OCMF combustion concept is mainly applied for gas mode operation of four-stroke dual-fuel engines (Murakami and Baufeld 2013; Mohr and Baufeld 2013).

In the PCSI combustion concept, air/natural gas mixture is pushed into the pre-chamber during compression stroke with additional gas directly supplied to the pre-chamber (Murakami and Baufeld 2013; Mohr and Baufeld 2013). This provides a rich mixture close to stoichiometric, which ensures strong and stable ignition (Murakami and Baufeld 2013; Mohr and Baufeld 2013). Hence, this technology is capable of combusting very lean gas mixtures improving, thus, BTE/NO<sub>x</sub> trade-off (Murakami and Baufeld 2013; Mohr and Baufeld 2013). According to a large engine manufacturer of four-stroke dual-fuel and gas SI engines (Murakami and Baufeld 2013; Mohr and Baufeld 2013), the key optimization factors in this type of natural gas combustion technology is the pre-chamber geometry, the mixture

formation in the pre-chamber for ensuring stable combustion, and the piston bowl optimization for free flame propagation (Murakami and Baufeld 2013; Mohr and Baufeld 2013). The technical challenges of PCSI concept are the increased system complexity and the serious effort required for optimized combustion. It is noteworthy that the application of PCSI concept in smaller engines is limited due to limited installation space for pre-chamber and due to increased engine development cost (Murakami and Baufeld 2013; Mohr and Baufeld 2013).

According to PCMP concept, the liquid fuel pilot injector replaces spark plug in the pre-chamber. This combustion concept offers improved ignition stability at low  $\text{NO}_x$  levels since liquid fuel stability is not seriously affected by the high air/fuel ratio in the pre-chamber (Murakami and Baufeld 2013; Mohr and Baufeld 2013). This is an advantage of PCMP concept compared to PCSI concept which requires lean air/gas mixtures in the pre-chamber for attaining low  $\text{NO}_x$  levels worsening, thus, ignition stability (Murakami and Baufeld 2013; Mohr and Baufeld 2013). Another advantage of PCMP compared to PCSI concept is that pilot fuel injector requires longer maintenance intervals compared to the ones required for spark plug (Murakami and Baufeld 2013; Mohr and Baufeld 2013).

## **7.4 Operational, Environmental, and Economic Performance of Dual-Fuel and Gas Spark-Ignition Engines**

### ***7.4.1 Two-Stroke Dual-Fuel Engines***

This section will be devoted to the examination of the effect of natural gas combustion in the “diesel-cycle” and in the “Otto-cycle” marine two-stroke CI engines performance characteristics and exhaust emissions. Initiating with “diesel-cycle” two-stroke gas engines, an experimental investigation was performed by the manufacturer of this type of engines to evaluate the effect of natural gas combustion on performance characteristics and exhaust emissions (Kjemtrup 2015). Specifically, engine tests were performed in a “diesel-cycle” two-stroke marine CI engine under conventional diesel operation considering directly injected (DI) diesel oil and under specified dual-fuel mode with 70%*m/m* natural gas injection (GI) and 30%*m/m* diesel oil at 25, 50, 75, and 100% of full engine load (Kjemtrup 2015). In Fig. 7.10a–d are shown heat release rate profiles as mean values of all cylinders for conventional diesel operation (DI) with black color curves and for specified dual-fuel operation with natural gas injection (GI), which generated from measurements of in-cylinder pressure during the aforementioned engine tests in a “diesel-cycle” two-stroke marine CI engine. Results for heat release rates at given at 25% (Fig. 7.10a), 50% (Fig. 7.10b), 75% (Fig. 7.10c), and 100% (Fig. 7.10d) of full engine load (Kjemtrup 2015). As evidenced by the observation of Fig. 7.10a and b, natural gas combustion under specified dual-mode operation (GI) results in

more intense premixed combustion phase leading to higher peak heat release rate values for this mode compared to conventional diesel operation (GI). Especially, in the case of 50% load (Fig. 7.10b), a slightly earlier initiation of combustion is observed in the case of specified dual-mode operation with natural gas (GI). According to Figs. 7.10b and c, the combustion of natural gas in the “diesel-cycle” CI marine engine under specified dual-mode results in more intense premixed combustion, which leads to higher peak heat release rate values compared to conventional diesel engine operation (DI) and to less intense diffusion-controlled compared again to DI engine operation. As evidenced by Fig. 7.10d, there are no substantial differences in ignition point between specified dual-mode operation (GI) and conventional diesel operation (DI) of the examined “diesel-cycle” two-stroke marine CI engine. Only slightly more higher peak heat release rate values and less intense diffusion-controlled combustion phase is observed in the case of GI operation compared to DI operation at 100% of full engine load. Hence, the combustion of fuel mixture of 70%*m/m* natural gas/30%*m/m* diesel oil compared to 100% diesel oil consumption under the same engine operating conditions results in the intensification of premixed combustion phase at all engine loads with the effects to be more pronounced at low engine loads. The variations in premixed combustion phase and peak heat release rate values between GI and DI operation can be attributed to variations in the lower heating value of natural gas/diesel oil mixture and to the natural gas quality (i.e., methane number), which probably make the diesel/natural gas mixture to be more “explosive” (i.e., more intense premixed fuel burning phase with higher peak burning rate values) compared to conventional diesel engine operation.

In Fig. 7.11a and b are given experimental results of the specific fuel oil consumption (SFOC) (Fig. 7.11a) and of the specific  $\text{NO}_x$  emissions (Fig. 7.11b) from the aforementioned experimental investigation conducted in a “diesel-cycle” two-stroke marine CI engine under two different operational modes: (a) conventional diesel engine operation with directly injected fuel (DI mode) and (b) specified dual-fuel mode with 70%*m/m* natural gas and 30%*m/m* diesel oil (GI mode). In both Fig. 7.11a and b, measured SFOC and  $\text{NO}_x$  emissions are presented as functions of engine load. Also, both SFOC and  $\text{NO}_x$  values are corrected considering ISO conditions and reference peak cylinder pressure. As evidenced by Fig. 7.11a, natural gas combustion under GI mode results in significantly lower values of relative SFOC at 50, 75, and 100% of full engine load compared to conventional DI mode indicating, thus, a considerable improvement of engine efficiency in the case of dual-fuel combustion compared to conventional diesel operation. This efficiency improvement is related to the aforementioned heat release rates comparison between GI and DI modes and more specifically can be ascribed to the intensification of premixed-controlled combustion observed in the case of GI mode. In other words, as evidenced in the case of GI mode, the higher proportion of fuel mixture, which is burned under premixed conditions (i.e., homogeneously), results in the substantial improvement of engine efficiency in the case of GI mode compared to conventional DI mode. As observed from Fig. 7.11b, dual-fuel combustion under GI mode results in lower  $\text{NO}_x$  emissions at 50, 75, and 100% of full engine load compared to

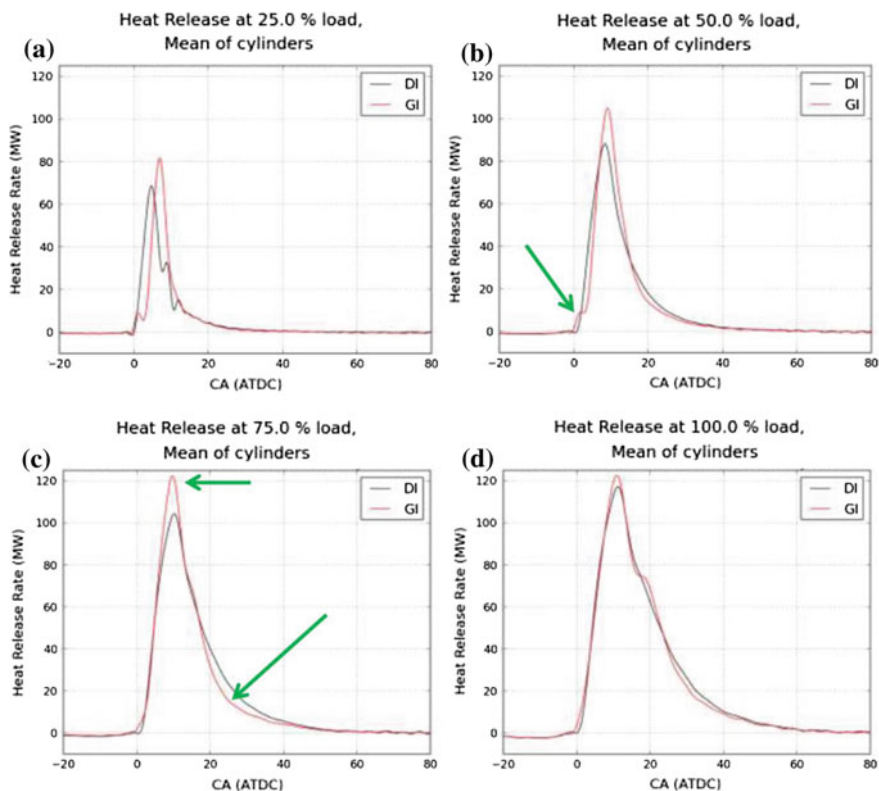


**Fig. 7.10** Comparison of heat release rates between conventional diesel operation (DI) and gas injection (GI) of a “diesel-cycle” two-stroke engine at 100% of full load (a), 75% of full load (b), 50% of full load (c), and 25% of full load (d). Data were provided from shop tests of a “diesel-cycle” two-stroke engine (Kjemtrup 2015)

conventional DI mode, whereas at 30% load, higher  $\text{NO}_x$  emissions are evidenced for GI mode compared to conventional DI mode. Also, the lower  $\text{NO}_x$  emissions observed in the case of GI mode compared to DI mode at 50, 75, and 100% load are directly related to the less intense diffusion-controlled combustion phase witnessed in the case of GI mode compared to DI mode. The less intense diffusion-controlled combustion phase during late combustion and expansion stroke resulted in lower in-cylinder temperatures in the case of GI mode compared to DI mode. According to the well-known Zeldovich thermal  $\text{NO}_x$  formation mechanism, in-cylinder temperature reduction during late combustion and expansion stroke resulted in lower specific  $\text{NO}_x$  emissions in the case of GI mode compared to DI mode. It is noteworthy to mention that despite the reduction of specific  $\text{NO}_x$  emissions, which is observed in the case of GI mode compared to DI mode, the measured  $\text{NO}_x$  values remained higher than the corresponding values dictated by IMO Tier III  $\text{NO}_x$  emission standards. Hence, the specific type of dual-fuel engines (i.e., “diesel-cycle”

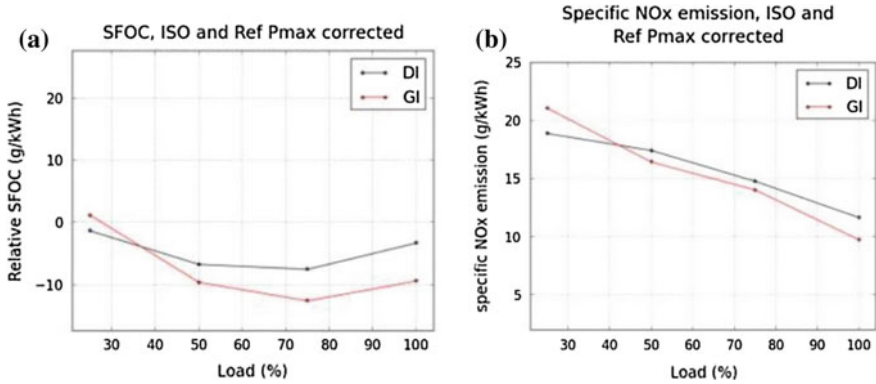


**Fig. 7.11** Comparison of relative SFOC (a) and specific NO<sub>x</sub> emissions (b) between conventional diesel operation (DI) and gas injection (GI) operation of a “diesel-cycle” two-stroke engine. Relative SFOC and specific NO<sub>x</sub> emissions are given as function of engines load. Data were provided from the shop test of a “diesel-cycle” two-stroke engine (Kjemtrup 2015)

two-stroke dual-fuel marine CI engine) cannot be directly compliant with the stringent IMO NO<sub>x</sub> standards without the implementation of either in-cylinder measures (e.g., exhaust gas recirculation—EGR) or exhaust after-treatment measures (e.g., selective catalytic reduction—SCR).

In Fig. 7.12a and b are given experimental results of the specific unburned hydrocarbon (HC) emissions (Fig. 7.12a) and of the specific carbon monoxide (CO) emissions (Fig. 7.12b) from the aforementioned experimental investigation conducted in a “diesel-cycle” two-stroke marine CI engine under two different

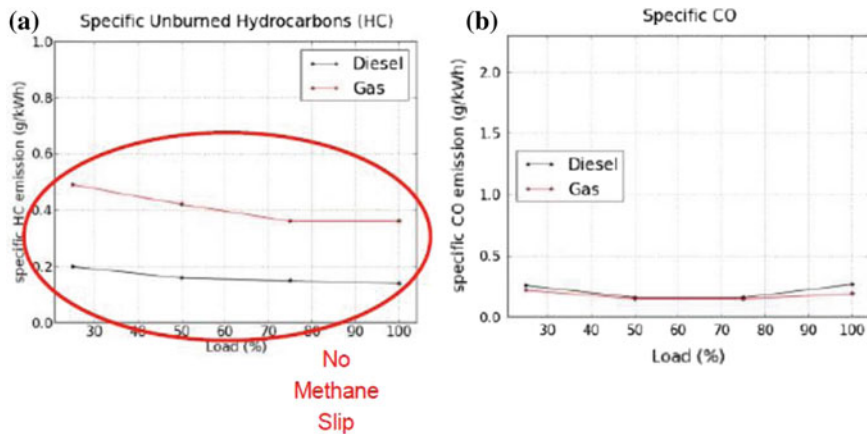


**Fig. 7.12** Comparison of specific HC emissions (a) and specific CO emissions (b) between conventional diesel operation (DI) and gas injection (GI) operation of a “diesel-cycle” two-stroke engine. Relative SFOC and specific NO<sub>x</sub> emissions are given as function of engines load. Data were provided from the shop test of a “diesel-cycle” two-stroke engine (Kjemtrup 2015)



operational modes: (a) conventional diesel engine operation with directly injected fuel (DI mode) and (b) specified dual-fuel mode with 70% m/m natural gas and 30% m/m diesel oil (GI mode). In both Fig. 7.12a and b, measured HC and CO emissions are presented as functions of engine load. As evidenced by Fig. 7.12a, the operation of the two-stroke “diesel-cycle” engine under specified dual-fuel mode with gas/diesel 70/30 resulted in the significant increase of HC emissions compared to conventional diesel engine operation (i.e., DI mode) at all loads examined. The deterioration of HC emissions with natural gas/diesel combustion compared to diesel-only combustion can be attributed as already evidenced to the intensification of the premixed combustion phase, which means that higher fuel mixture proportion is burned under homogeneous-like conditions. As expected, shift from diffusion to homogeneous (i.e., premixed) combustion results in deterioration of HC emissions. However, it is quite encouraging that the worsening of HC emissions observed in the case of GI mode compared to DI mode did not accompany by noticeable methane slip. The proven no methane slip observed in “diesel-cycle” engines is an important virtue of this type of dual-fuel two-stroke engines considering that methane emissions are almost 25 times worst greenhouse gas (GHG) compared to carbon dioxide (CO<sub>2</sub>). According to Fig. 7.12b, transition from conventional DI engine operating mode to specified dual-fuel mode (i.e., GI mode) did not accompany by substantial variation of measured CO emissions, which is another encouraging environmental finding of the aforementioned experimental investigation.

Consolidating the aforementioned observations from the experimental study performed in a “diesel-cycle” two-stroke marine CI engine, it can be concluded that the transition from conventional two-stroke diesel operation (i.e., DI mode) to specified dual-fuel mode gas/diesel 70/30 operation (i.e., GI mode) resulted in:

- More intense premixed-controlled combustion phase and less intense diffusion-controlled combustion phase, which resulted in lower in-cylinder temperatures during expansion stroke and thus to lower exhaust gas temperature values.
- Lower SFOC values (i.e., higher efficiency values) and smaller NO<sub>x</sub> emissions, which, however, remained higher than IMO Tier III limits.
- Higher HC emission values without, however, noticeable methane slip and same CO emission values.

In a second experimental investigation performed in a “diesel-cycle” two-stroke dual-fuel marine CI engine by the corresponding engine manufacturer, engine tests were performed at 25, 50, 75, and 100% of full load considering four gas/diesel (G/D) analogies: 0/100, 30/70, 70/30, and 95/5 (Zannis et al. 2017; Kjemtrup 2015). In Fig. 7.13a and b are presented heat release rate profiles, which were generated from measured cylinder pressure data for all examined gas/diesel analogies (i.e., G/D = 0/100, G/D = 30/70, G/D = 70/30, and G/D = 95/5) at 75% load (Fig. 7.13a) and at 100% of full engine load (Fig. 7.13b). As evidenced by both Fig. 7.13a and b, the increase of gas to diesel proportion results in more intense premixed

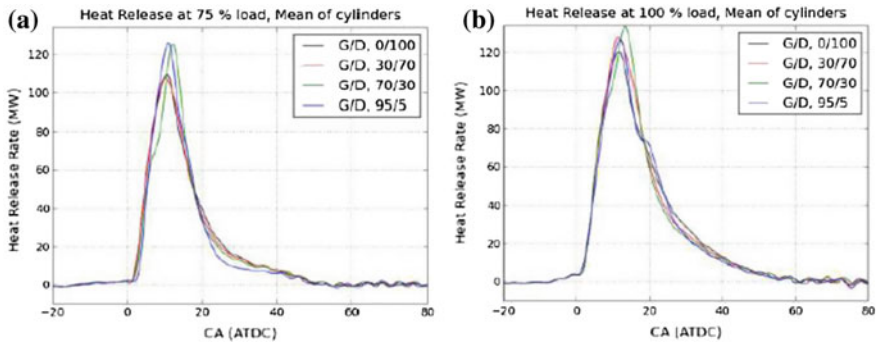


**Fig. 7.13** Comparison of heat release rates for gas/diesel (G/D) = 0/100, G/D = 30/70, G/D = 70/30, and G/D = 95/5 of a “diesel-cycle” two-stroke marine engine at 75% of full load (a) and at 100% of full load (b) (Kjemtrup 2015)

combustion phase and less intense diffusion-controlled combustion phase. Hence, the increase of natural gas quantity to diesel quantity the premixed combustion phase becomes more reactive resulting thus in higher peak heat release rate values (Kjemtrup 2015). This means that more gaseous to liquid fuel mass is physically and chemically prepared during ignition delay period leading, thus, to more reactive premixed combustion phase. The less intense diffusion-controlled combustion phase with increasing gas to diesel analogy as evidenced by Fig. 7.13a and b is expected to result in reduction of in-cylinder temperature during expansion stroke and thus to lower exhaust gas temperature values (Kjemtrup 2015).

In Fig. 7.14a–e are shown experimental results from the aforementioned investigation in a “diesel-cycle” two-stroke marine CI engine for specific  $\text{NO}_x$  emissions (Fig. 7.14a), specific HC emissions (Fig. 7.14b), and specific CO emissions (Fig. 7.14c), particulate emissions (Fig. 7.14d), and relative SFOC (Fig. 7.14e). At all Fig. 7.14a–e, measured values are given as function of engine load for four different gas/diesel (G/D) analogies, i.e., G/D = 0/100, G/D = 30/70, G/D = 70/30, and G/D = 95/5 (Kjemtrup 2015). According to Fig. 7.14a, the increase of G/D ratio resulted in a substantial reduction of specific  $\text{NO}_x$  emissions at engine loads higher than 50%. Higher reductions of  $\text{NO}_x$  emissions are observed in the case of G/D = 70/30.  $\text{NO}_x$  emission reduction with increasing G/D ratio can be ascribed with the aforementioned less intense diffusion-controlled combustion phase, which as expected resulted in reduction of in-cylinder temperature during expansion stroke (Kjemtrup 2015). An important observation here is that despite significant reduction of  $\text{NO}_x$  emissions with increasing G/D ratio compared to conventional diesel operation (i.e. G/D = 0/100), the lowest absolute  $\text{NO}_x$  values remained higher than the corresponding IMO Tier III limits indicating, thus, the necessity for additional measures implementation in order this type of engine to be IMO Tier III compliant (Kjemtrup 2015).

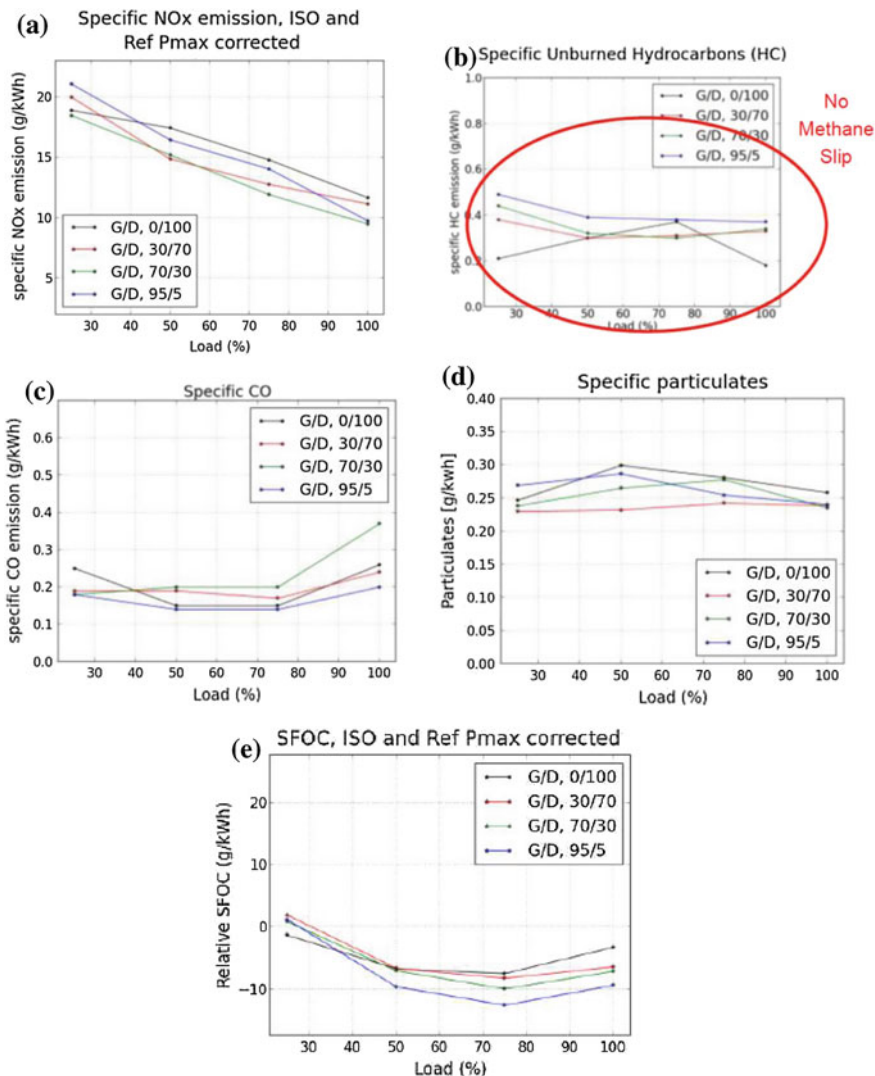


**Fig. 7.14** Comparison of specific NO<sub>x</sub>–engine load curves (a), specific HC emissions–engine load curves (b), specific CO emissions–engine load curves (c), particulates–engine load curves (d), and relative SFOC–engine load curves (e) for gas/diesel = 0/100, gas/diesel = 30/70, gas/diesel = 70/30, and gas/diesel = 95/5 of a “diesel-cycle” two-stroke marine engine (Kjermtrup 2015)

As observed from Fig. 7.14b, the increase of G/D ratio resulted in a substantial deterioration of HC emissions compared to conventional diesel operation (i.e., G/D = 0/100) at all engine loads examined. The worsening of HC emissions with increasing gas to diesel proportion is correlated with the intensification of premixed combustion phase under which fuel mixture is burned homogenously. It is

noteworthy here to mention that according to the literature (Kjemtrup 2015) the increase of HC emissions with increasing G/D ratio did not accompany by noticeable methane slip, which is a quite encouraging environmental evident for this type of two-stroke dual-fuel marine CI engine (Kjemtrup 2015).

According to Fig. 7.14c, higher values of specific CO emissions are observed in the case of G/D = 30/70 and G/D = 70/30 compared to conventional diesel operation (i.e., G/D = 0/100) at loads higher than 50%. Surprisingly, at the case of G/D = 95/5, there were not observed substantial variations in CO emissions compared to G/D = 0/100. In this case also, CO emission deterioration with increasing G/D ratio compared to conventional diesel operation is related to the intensification of the premixed combustion phase (Kjemtrup 2015).

Observing Fig. 7.14d, lower particulate emission values are witnessed for G/D ratios 30/70, 70/30, and 95/5 compared to G/D = 0/100 at engine loads examined higher than 50%. The lowest particulate values are observed in the case of G/D = 30/70. The reduction of particulate emissions with dual-fuel operation compared to diesel-only operation can be attributed to the less intense diffusion-controlled combustion phase observed with increasing G/D ratios (Kjemtrup 2015).

According to Fig. 7.14e, a clear decrease of relative SFOC (i.e., increase of engine efficiency) is observed in all cases of dual-fuel operation (i.e., G/D = 30/70, 70/30 and 95/5) compared to conventional diesel-only operation (i.e., G/D = 0/100) at engine loads higher than 50%, which is again related to the shift of combustion toward homogeneous premixed combustion (Kjemtrup 2015).

The following similarities were observed during the aforementioned investigation between diesel-only operation (G/D = 0/100) and gas/diesel operation: Same power density, same T/C, scavenging and exhaust gas temperatures, good part load SFOC, good transient engine response, gas/diesel operation was robust to gas quality changes (i.e. MN was irrelevant), simple cylinder lubrication system and use of known lube oil types and finally, regarding safety issues it was not occurred risk of misfiring or knocking and also there was no risk for explosion in scavenge receiver (Kjemtrup 2015).

As already mentioned, gas/diesel operation in “diesel-cycle” two-stroke dual-fuel engine indicated  $\text{NO}_x$  values lower than diesel-only operation but higher than IMO Tier III limits. For this reason, a second experimental investigation was performed in this type of engine considering the following operational modes: DI = conventional diesel operation, GI = gas/diesel engine operation with EGR, DI + EGR = diesel operation with EGR and GI + EGR = CNG/diesel operation with EGR (Kjemtrup 2015). In Fig. 7.15a and b are shown experimental results from this particular investigation for relative SFOC (Fig. 7.15a) and for specific  $\text{NO}_x$  emissions (Fig. 7.15b) (Kjemtrup 2015). As evidenced by Fig. 7.15a, there is a clear increase of RSFOC with EGR both for DI and GI operational modes as expected since EGR, as known, reduces in-cylinder temperature (Kjemtrup 2015). According to Fig. 7.15b, the use of EGR in gas/diesel combustion (GI + EGR) results in a substantial reduction of  $\text{NO}_x$  emissions compared to GI and DI modes

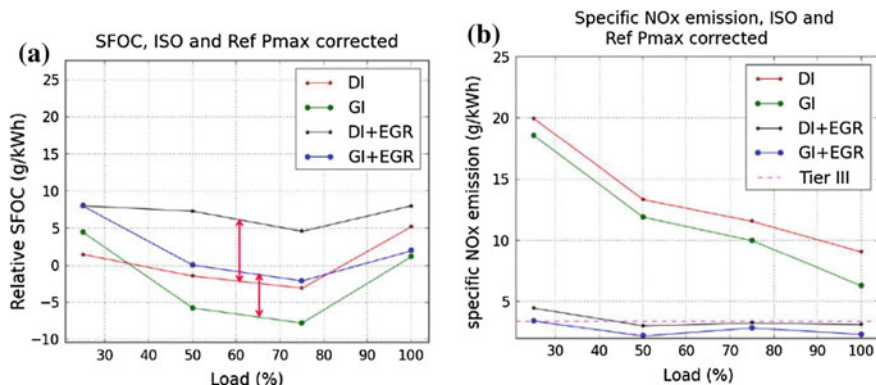


**Fig. 7.15** Experimental results for **a** relative SFOC and **b** specific NO<sub>x</sub> emissions both as functions of engine load. Results shown in both figures refer to four operational modes: DI (red curves), GI (green curves), DI + EGR (black curves), and GI + EGR (blue curves) (Kjermtrup 2015)

and most importantly leads to engine compliance with IMO Tier III limits at all engine loads examined (Kjermtrup 2015).

Having examined the operational and environmental performance of “diesel-cycle” two-stroke gas/diesel engines, it is essential to investigate the operational performance of “Otto-cycle” two-stroke dual-fuel engines. For this reason, in Fig. 7.16a is shown the effect of natural gas quality in terms of methane number (MN) on the engine power of “Otto-cycle” dual-fuel engines (Ott 2015). As evidenced by Fig. 7.16a, the maximum engine output of this type of engines may be limited by MN if engine power rating point is close to R1-R3 curve (Ott 2015). However, there is no power output limitation from MN if rating point is close to R2-R4 line (Ott 2015). It is noteworthy to mention that MN of LNG is typically between 70 and 90 and natural gases with MN lower than 70 can be burned in “Otto-cycle” dual-fuel engines by reducing engine power output (derating) (Ott 2015). However, it should be kept in mind that the operating area for low-speed two-stroke engines is typically <85% of maximum continuous rating (MCR) (Ott 2015). In Fig. 7.16b are shown two power layout diagrams: one with black line covering an orange color area, which corresponds to conventional two-stroke diesel operation and one with green color curves, which corresponds to “Otto-cycle” two-stroke dual-fuel engine operation (Ott 2015). As observed from Fig. 7.16b, the maximum rating of “Otto-cycle” dual-fuel engine is lower than conventional diesel engine due to knocking/pre-ignition limitations (Ott 2015). Green dotted lines represent selected rating point of a two-stroke diesel engine in standard ship designs, and as observed from Fig. 7.16b, “Otto-cycle” dual-fuel engine operation is covering more than 90% of these rating points (Ott 2015). According to the engine manufacturer of the “Otto-cycle” two-stroke dual-fuel engine only on exceptional cases, an additional cylinder will be needed to meet engine power output requirements (Ott 2015). Regarding an important issue of “Otto-cycle” gas engines, which is combustion stability, Fig. 7.16c shows experimental results for

the variation of indicated mean effective pressure (IMEP) with engine cycles number (300 cycles in total) for conventional two-stroke diesel engine and two-stroke “Otto-cycle” dual-fuel engine (Ott 2015). As evidenced by Fig. 7.16c, in the case of “Otto-cycle” dual-fuel engine, a stable combustion was observed since cycle-to-cycle variation of IMEP of “Otto-cycle” gas engine was comparable to pertinent IMEP variation of conventional two-stroke diesel engine (Ott 2015). Hence, in terms of combustion stability, “Otto-cycle” dual-fuel engine operation does not bring any serious problem compared to conventional diesel operation.

Regarding the environmental performance of “Otto-cycle” two-stroke dual-fuel engines, Fig. 7.17a shows measured values of NO<sub>x</sub> emissions of this type engine in contrast with IMO Tier limits (Ott 2015; Hagedorn 2014). As evidenced by Fig. 7.17a, “Otto-cycle” two-stroke dual-fuel engine clearly emits lower values of NO<sub>x</sub> emissions compared to the most stringent IMO NO<sub>x</sub> regulations (Tier III) revealing direct compliance of these engines with Tier III without any need for in-cylinder measures or after-treatment technologies. In Fig. 7.17b, EEDI value of

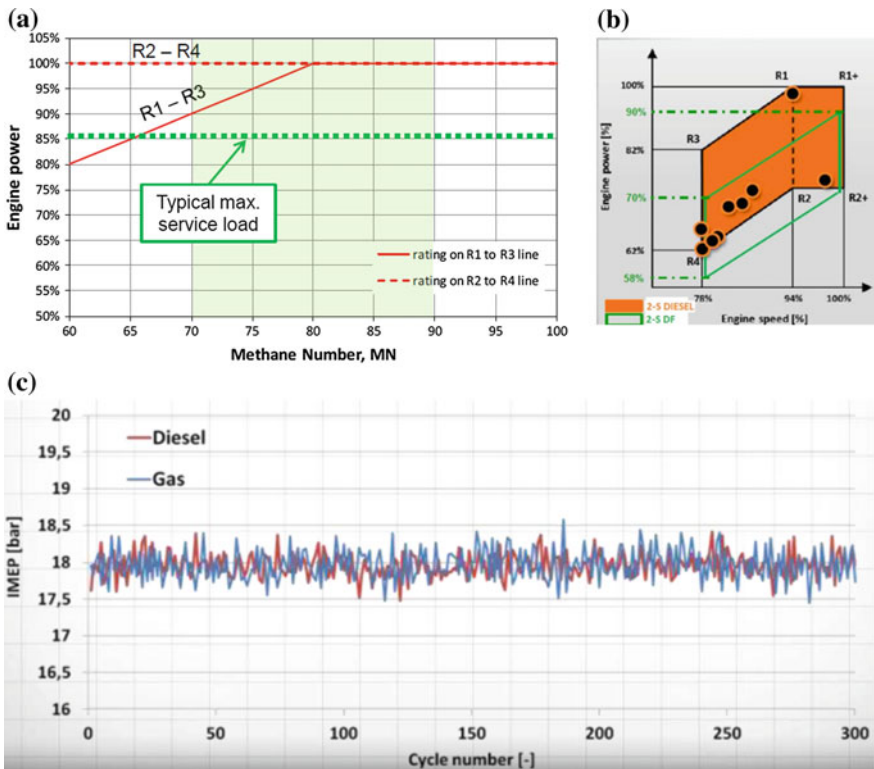


**Fig. 7.16** a Effect of natural gas MN on two-stroke “Otto-cycle” dual-fuel engine power (Ott 2015), b Power layout diagrams for two-stroke diesel engine and two-stroke “Otto-cycle” dual-fuel engine (Stiefel 2015), c IMEP variation with engine cycles number for diesel-only and “Otto-cycle” gas engine operation (Ott 2015)

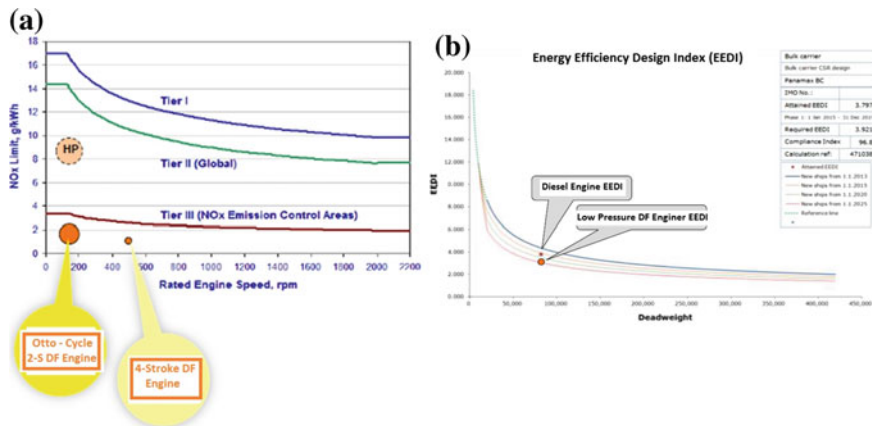


**Fig. 7.17** **a** Compliance of “Otto-cycle” two-stroke dual-fuel engine with IMO Tier III limits (Hagedorn 2014), **b** EEDI values of a conventional two-stroke diesel engine and of an “Otto-cycle” two-stroke dual-fuel engine (Stiefel 2015)

low-pressure dual-fuel engine is compared with pertinent value of a conventional two-stroke diesel engine, and as evidenced, EEDI value of the “Otto-cycle” gas engine is below conventional diesel engine EEDI point due to lower overall CO<sub>2</sub> emissions (Ott 2015; Hagedorn 2014).

#### 7.4.2 Four-Stroke Dual-Fuel and Gas SI Engines

To examine the effect of natural gas combustion in the performance characteristics and pollutant emissions of four-stroke marine dual-fuel and gas engines is described a detailed experimental investigation performed by an engine research and development company (Schlick 2014). The specific experimental investigation (Schlick 2014) was conducted in the single cylinder turbocharged (T/C) CI engine FM250. The specific engine may operate with diesel fuel only or burning almost only natural gas with micro-pilot fuel injection or as a dual-fuel engine. The maximum allowable value of peak cylinder pressure is 250 bar (Schlick 2014). AVL FM250 engine uses a high-pressure common rail fuel injection system, whereas natural gas supply can be attained either with central mixing or with gas injection in engine intake (Schlick 2014). The engine research and development company performed engine tests in FM250 engine considering the following:

- FM250 is operating according to E3 cycle. In this cycle tests, the engine is operating as main marine dual-fuel engine, whereas engine loading by the brake is following the propeller curve.

- FM250 is operating according to E2 cycle. In this cycle tests, the engine is operating as a main gas engine under constant engine rotating speed with natural gas supply in the pre-chamber.
- FM250 is operating according to D2 cycle. In this cycle tests, the engine is operating as auxiliary gas engine generating electric power under constant engine speed with natural gas supply in the pre-chamber.

In Fig. 7.18 are shown the experimental results from the CI engine FM250 for the variation of brake mean effective pressure (BMEP), brake efficiency, peak cylinder pressure, pilot fuel quantity, and 50% mass fraction burned (Fig. 7.18a). Also are shown experimental results from FM250 for air excess ratio, specific NO<sub>x</sub>, specific THC, specific CO, and smoke number (Fig. 7.18b). Experimental results shown in Fig. 7.18a and b have been obtained for E3 cycle (Schlick 2014).

From the examination of Fig. 7.18a is observed that the highest brake efficiency (almost 42.5%) of dual-fuel engine FM250 is attained at maximum engine speed and maximum power of FM250 with only 1% pilot fuel quantity (Schlick 2014). In addition, it is observed that when the engine speed is decreased the pilot fuel injection timing and the pertinent 50% mass fraction burned (MFB50%) should be decreased in order the covariance (COV) of indicated mean effective pressure (IMEP) should be lower than 2% at all examined cases. Also when engine speed is decreased, the pilot fuel quantity should be increased for effective commencement of combustion (i.e., constant NO<sub>x</sub> emissions). From the examination of the results shown in Fig. 7.18a is can be observed that the peak cylinder pressure did not

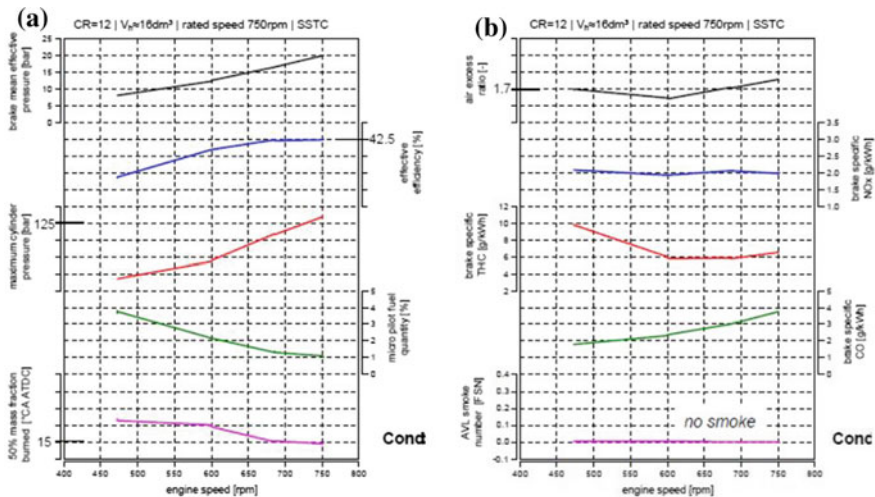


**Fig. 7.18** Experimental results from the CI engine FM250 for the variation of brake mean effective pressure, brake efficiency, peak cylinder pressure, pilot fuel quantity, and 50% mass fraction burned (a). Also are shown experimental results from FM250 for air excess ratio, specific NO<sub>x</sub>, specific THC, specific CO, and smoke number (b). Experimental results shown in figures a and b have been obtained for E3 cycle: dual-fuel operation on propeller curve (Schlick 2014)



exceed the limit of 250 bar, and thus, there was no problem with the mechanical strength of FM250 engine (Schlick 2014).

As evidenced by the examination of the experimental results shown in Fig. 7.18b, the air excess ration remains almost the same with variation of engine speed and load. This proves that FM 250 engine had the same air–fuel analogy during E3 cycle tests (Schlick 2014). According to  $\text{NO}_x$  results in Fig. 7.18b, FM 250 attained an extremely low level of  $\text{NO}_x$  emissions at all four points of E3 cycle. On the other hand, it is noteworthy to mention the high values of specific THC and CO emissions during E3 cycle tests, which are noticeably higher, compared to the ones of conventional diesel operation (Schlick 2014). Finally, it is quite encouraging that the smoke emissions are not a significant issue during FM250 operation as a main dual-fuel engine since its absolute values were almost zero (i.e., smokeless operation) (Schlick 2014).

In Fig. 7.19 are shown the experimental results from the CI engine FM250 for the variation of brake mean effective pressure (BMEP), brake efficiency, peak cylinder pressure, pilot fuel quantity, and 50% mass fraction burned (Fig. 7.19a). Also are shown experimental results from FM250 for air excess ratio, specific  $\text{NO}_x$ , specific THC, specific CO and smoke number (Fig. 7.19b). Experimental results shown in Fig. 7.19a and b have been obtained for E2/D2 cycle (Schlick 2014).

As evidenced by Fig. 7.19a, the brake efficiency is increased with engine load and its highest value is observed at highest engine load and it is equal to 46%

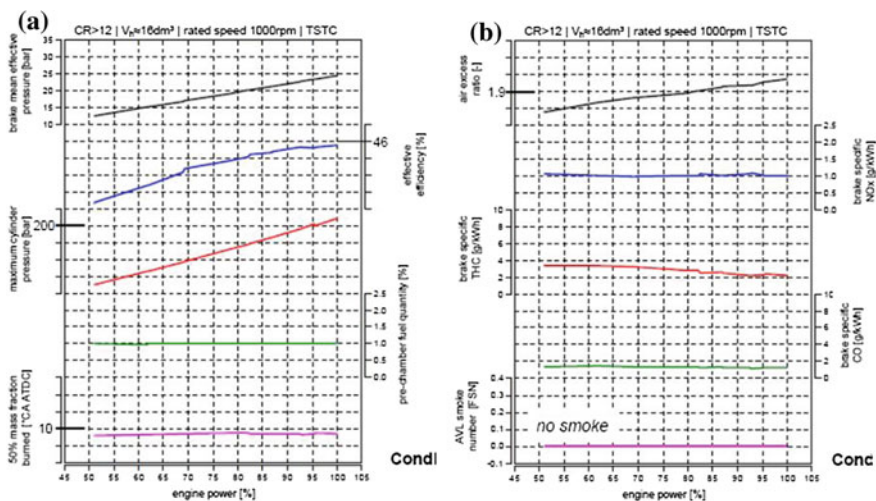


**Fig. 7.19** Experimental results from the CI engine FM250 for the variation of brake mean effective pressure, brake efficiency, peak cylinder pressure, pilot fuel quantity, and 50% mass fraction burned (a). Also are shown experimental results from FM250 for air excess ratio, specific  $\text{NO}_x$ , specific THC, specific CO, and smoke number (b). Experimental results shown in figures a and b have been obtained for E2/D2 cycle: gas engine operation with gas-fueled pre-chamber (Schlick 2014)

(Schlick 2014). Peak cylinder pressure remained at high levels at all engine loads and for load higher than 95% exceeded the limit of 200 bar (Schlick 2014). Hence, FM250 engine operation with micro-pilot injection in the pre-chamber leads to higher values of peak cylinder pressure compared to dual-fuel operation of the same engine under E3 cycle. As evidenced by the variation of 50% mass fraction burned engine operation was stable at all engine loads with IMEP covariance less than 1% at all cases (Schlick 2014). As observed from Fig. 7.19a, 1% micro-pilot fuel quantity in the pre-chamber is enough for strong ignition, which leads to fast flame propagation in the main combustion chamber (Schlick 2014). According to Fig. 7.19b, the air excess ration should be increased with engine load increase starting from 1.9 and reaching up to 2.0 at maximum engine load (Schlick 2014). During increase of air excess ration with increasing engine load, specific NO<sub>x</sub> emissions remained constant. It is of utmost importance that when FM250 engine operated as gas engine with micro-pilot injection in the pre-chamber was compliant with the most stringent IMO regulations for NO<sub>x</sub> emissions in NECAs (Tier III). In addition, it is quite important that specific THC and specific CO emissions are significantly lower compared to the values measured during FM 250 engine operation as a dual-fuel engine under E3 cycle (Schlick 2014). Finally, according to Fig. 7.19b, at all examined cases of FM250 engine operation as gas engine with micro-pilot injection in the pre-chamber, zero smoke emissions were observed (Schlick 2014).

In Fig. 7.20a is shown the variation of measured specific NO<sub>x</sub> emissions with engine speed for four-stroke main diesel engines, four-stroke pre-chamber spark-ignition (SI) engines, four-stroke main dual-fuel engines and four-stroke diesel main, and auxiliary engines (Schlick 2014). As evidenced by Fig. 7.20a, four-stroke main and auxiliary diesel engines are compliant only with IMO Tier II, which is issued worldwide outside of NECAs. On the other hand, four-stroke main dual-fuel engines and auxiliary pre-chamber SI engines are compliant with the most

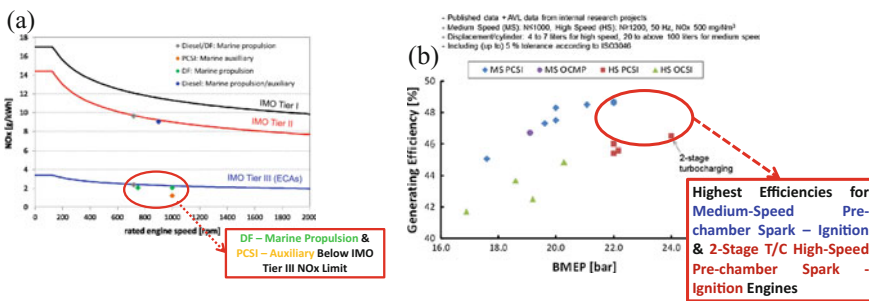


**Fig. 7.20** **a** Experimental results for specific NO<sub>x</sub> emissions for four-stroke main diesel engines, four-stroke pre-chamber spark-ignition (SI) engines, four-stroke main dual-fuel engines and four-stroke diesel main and auxiliary engines (Schlick 2014), **b** experimental results for the variation of generating efficiency with BMEP for four-stroke medium-speed pre-chamber SI engines, medium-speed open-chamber gas engines with micro-pilot injection, high-speed pre-chamber SI engines, and high-speed open-chamber SI engines (Murakami and Baufeld 2013; Mohr and Baufeld 2013)

stringent IMO NO<sub>x</sub> limits (Tier III), which are issued in NECAs (Schlick 2014). In fact, auxiliary pre-chamber SI engines are below Tier III NO<sub>x</sub> limits, which reveal the superiority of this type of marine auxiliary engines regarding their NO<sub>x</sub> performance compared to other types of marine main and auxiliary engines.

In Fig. 7.20b is shown experimental results from previous studies (Murakami and Baufeld 2013; Mohr and Baufeld 2013) for the variation of generating efficiency with BMEP for four-stroke medium-speed pre-chamber SI engines, medium-speed open-chamber gas engines with micro-pilot injection, high-speed pre-chamber SI engines, and high-speed open-chamber SI engines. As evidenced, the highest generating efficiencies are observed for medium-speed pre-chamber SI engines and for two-stage T/C high-speed pre-chamber SI engines. Specifically, the highest possible generating efficiency is close to 49% and is observed for medium-speed pre-chamber SI engines (Murakami and Baufeld 2013; Mohr and Baufeld 2013). These results reveal the superiority of pre-chamber technology in terms of generating efficiency compared to open-chamber technology (Murakami and Baufeld 2013; Mohr and Baufeld 2013).

Except the operational and environmental characteristics of four-stroke dual-fuel engines and four-stroke lean-burned gas engines, is essential to compare the usage of LNG in four-stroke marine engines compared to other available fuel types and IMO SO<sub>x</sub> and NO<sub>x</sub> limits compliant solutions. For this reason, in Fig. 7.21a–h are shown results from a detailed economic and environmental analysis performed for a Ro-Ro vessel, which was scheduled to operate in ECAs (Levander 2011; Yfantis et al. 2017). Specifically, in this particular analysis were examined three available solutions in order the specific Ro-Ro vessel to be compliant with SO<sub>x</sub> and NO<sub>x</sub> limits in ECAs: (a) combustion of marine gas oil (MGO) in main and auxiliary four-stroke engines in conjunction with SCR for reducing NO<sub>x</sub> emissions to IMO Tier III limit, (b) combustion of heavy fuel oil (HFO) in main and auxiliary engines in conjunction with SO<sub>x</sub> scrubber and SCR for reducing NO<sub>x</sub> emissions to IMO Tier III limit, and (c) use of dual-fuel main and auxiliary engines without exhaust after-treatment devices (Levander 2011). Figure 7.21a shows the relative annual fuel consumption and the corresponding relative cost with respect to MGO operation and as evidenced LNG operation indicates the lowest relative annual fuel cost compared to MGO and HFO operation (Levander 2011). Figure 7.21b shows the annual fuel, lubricant oil, and consumables (i.e., NaOH—fresh water for scrubbers, chemicals, and urea for SCR) cost (Levander 2011). As evidenced by Fig. 7.21b, the LNG solution indicates the lowest annual fuel cost compared to MGO and HFO operation. Also, LNG solution does not indicate any consumable cost since there is no need for NaOH, urea or chemicals (Levander 2011). According to Fig. 7.21c, which illustrates the machinery investment cost, LNG solution has the same total capital expenses (CAPEX) with HFO/scrubber solution whereas both LNG solution and HFO/scrubber solution have higher total CAPEX compared to MGO solution (Levander 2011). As evidenced by Fig. 7.21d, which depicts annual machinery cost for the three ECAs solutions, the LNG solution has noticeably lower operational expenses (OPEX) compared to MGO solution and HFO/scrubber solution (Levander 2011). According to Fig. 7.21e, which presents the relative payback

times (PT) of each ECA solution with respect to MGO operation, the LNG solution has higher PT compared to MGO solution and significantly lower PT compared to HFO/scrubber solution (Levander 2011). Figure 7.21f demonstrates the Net Present Values (NPV) of each ECA solution considering a 10-year operation and as evidenced, LNG solution has the highest NPV compared to MGO solution and to HFO/scrubber solution (Levander 2011). Figure 7.21g shows the relative CO<sub>2</sub>, NO<sub>x</sub> and SO<sub>x</sub> emissions of HFO/scrubber and LNG solutions compared to MGO solution. As observed from Fig. 7.21g, the LNG solution indicates the lowest CO<sub>2</sub> emissions compared to other two solutions, slightly higher NO<sub>x</sub> emissions compared to MGO/SCR solution and almost same NO<sub>x</sub> emissions with HFO/Scrubber/SCR solution. Also LNG solution does not generate any SO<sub>x</sub> emissions (Levander 2011). Finally, according to Fig. 7.21h, which depicts the EEDI values of the three examined ECA solutions, LNG alternative indicates the lowest EEDI value compared to the other two ECA solutions (Levander 2011).

### **7.4.3 Evaluation of Different Propulsion Systems of LNG Carriers Using Energy Efficiency Design Index (EEDI)**

Ekanem Attah and Rucknall (Ekanem Attah and Bucknall 2015) performed a detailed evaluation of different propulsion systems of LNG carriers using the Energy Efficiency Design Index (EEDI). In their analysis considered the impact of methane slip emissions on the calculation of overall GHG emissions. In the following sections, the alternative natural gas ship propulsion systems considered in the study of Ekanem Attah and Rucknall (Ekanem Attah and Bucknall 2015) will be described. It will be described also the EEDI analysis methodology and for each propulsion system will be discussed the main findings of the EEDI analysis.

## **7.5 Description of Alternative LNG Carriers Propulsion Systems**

*Steam Turbines Propulsion System (STPS)*. STPS ships obtain the 71% of the existing LNG carriers' fleet (Ekanem Attah and Bucknall 2015; Chang et al. 2008a; Clarksons Shipping Intelligence Network 2014a; Wayne and Hogson 2006; American Bureau of Shipping 2014; Bureau Veritas 2014), and this high percentage is attributed to the easy handling of boil-off gas (BOG) in these ships, the simple operation, and their internal safety. When the LNG tank pressure is elevated, then the steam generators are burning BOG for high-pressure steam generation, which expands in the steam turbines. Steam turbines are connected to ship propellers. When the engine load is not sufficient for burning all BOG mass, the remainder natural gas is directed to the condensers for being liquefied again. This simple

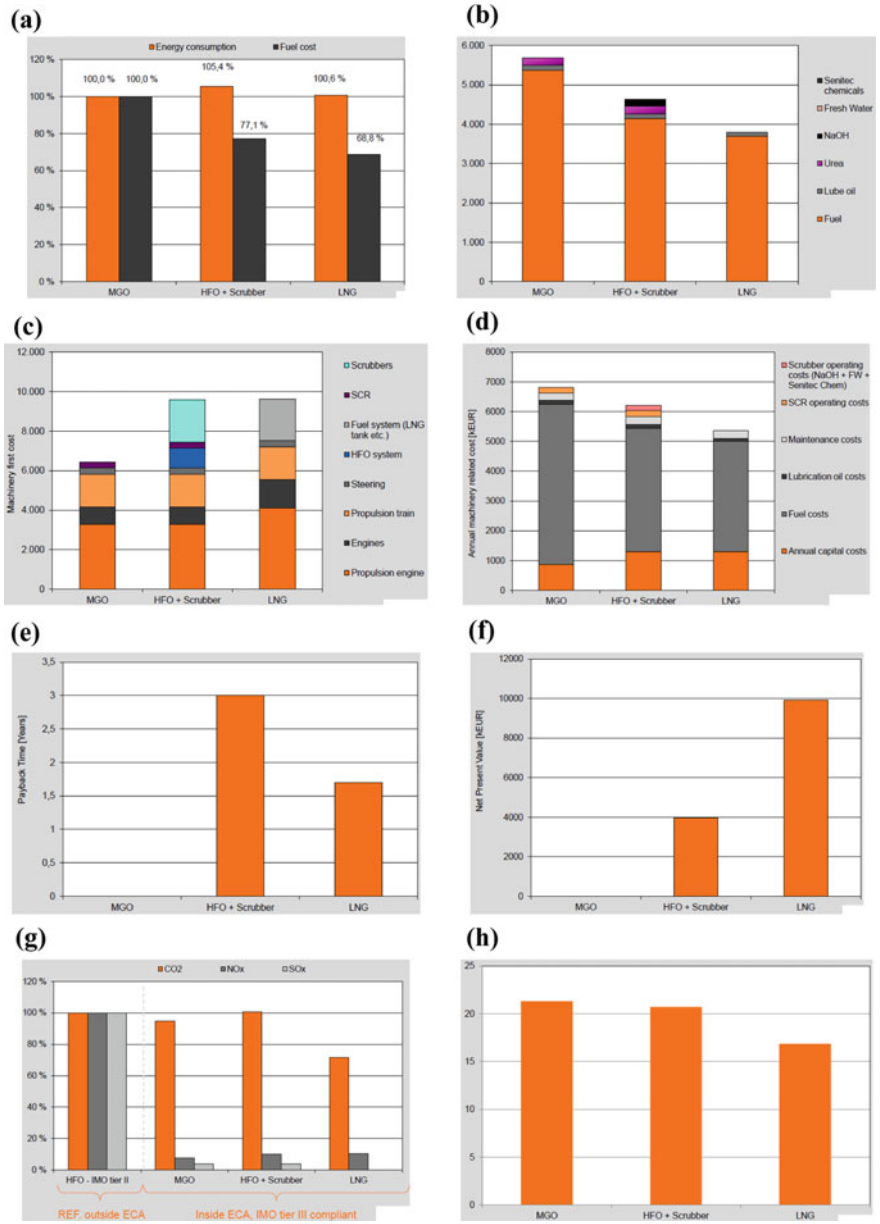


**Fig. 7.21** Results of the environmental and economic analysis of a Ro-Ro vessel operation in ECAs **a** annual fuel consumption and relative cost versus MGO operation, **b** annual fuel, lube oil, and consumables cost, **c** machinery investment cost, **d** annual machinery cost, **e** payback time (expressed as relative value with respect to MGO operation), **f** net present value assuming 10 years operation, **g** CO<sub>2</sub>, NO<sub>x</sub>, and SO<sub>x</sub> emissions relative values compared to the ones of MGO operation and **h** EEDI values (Levander 2011)

strategy eliminates the need for one gas combustion unit, which is demanded for the other two gas propulsion systems considered in the study of Ekanem Attah and Bucknall (Ekanem Attah and Bucknall 2015): the traditional slow-speed two-stroke diesel engine with re-liquefaction plant (SSDR) and the dual-fuel diesel–electric (DFDE) propulsion system. A schematic view of the LNG carrier propulsion system based on steam turbines (STPS) is given in Fig. 7.22. The specific installation is comprised of two steam generators using natural gas/heavy fuel oil as fuel. The generated steam besides expansion in steam turbines is used in auxiliary systems including electric generators and pumps (Ekanem Attah and Bucknall 2015; Chang et al. 2008a; Clarksons Shipping Intelligence Network 2014a; Wayne and Hogson 2006; American Bureau of Shipping 2014; Bureau Veritas 2014).

*Slow-speed two-stroke diesel engines with re-liquefaction of Boil-Off Gas (BOG).* The slow-speed two-stroke diesel engines installation is an integrated propulsion system with re-liquefaction installation of boil-off gas, where the BOG is liquefied and returns to storage tanks instead of being burned in the engines. The layout of the slow-speed diesel engines in such systems is usually based on the twin screw layout with two slow-speed diesel engines directly connected to two propellers as evidenced by Fig. 7.23 (Ekanem Attah and Bucknall 2015; Chang et al. 2008a; Clarksons Shipping Intelligence Network 2014a; Wayne and Hogson 2006; American Bureau of Shipping 2014; Bureau Veritas 2014; Chang et al. 2008b). This propulsion unit is also equipped with a gas control unit for selecting BOG in cases where the BOG capacity is higher than the re-liquefaction installation capacity. The BOG liquefaction installation is based on a closed nitrogen cycle

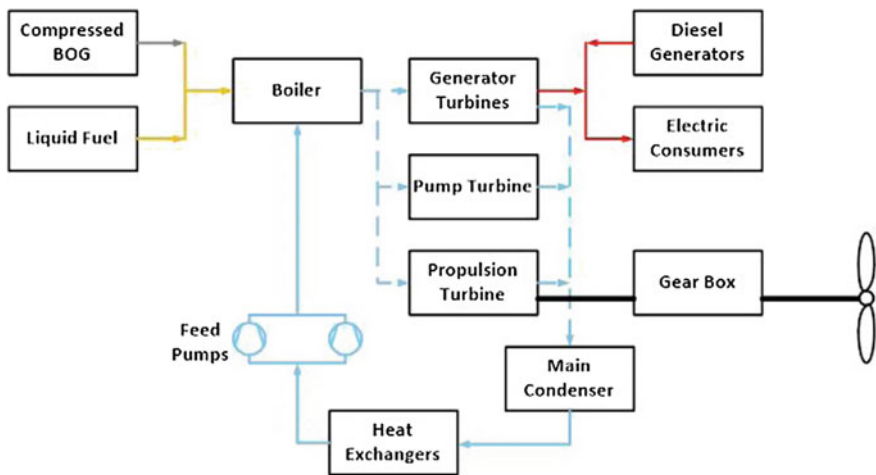


**Fig. 7.22** Schematic view of the installation of a steam turbine propulsion system (STPS) with natural gas (Ekanem Attah and Bucknall 2015; Chang et al. 2008b) “Figure reproduced from 35. Ekanem Attah, E. and Bucknall, R.: *An Analysis of the Energy Efficiency of LNG Ships Powering Options using the EEDI*. *Ocean Engineering*, Vol. 110, pp. 62–74, 2015 with permission from Elsevier”

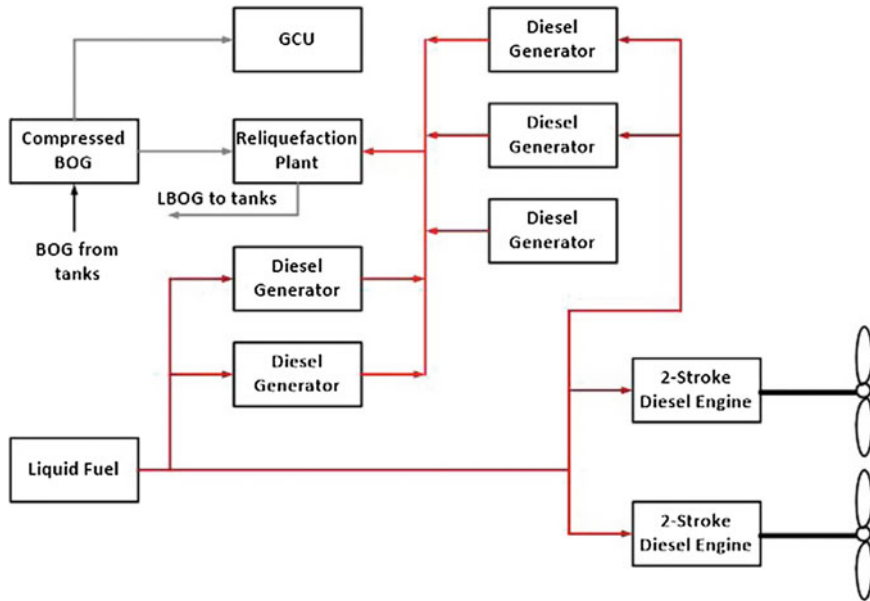


**Fig. 7.23** Schematic view of ship propulsion system with slow-speed two-stroke dual-fuel diesel engines and re-liquefaction devices of the boil-off gas (BOG) (Ekanem Attah and Bucknall 2015; Chang et al. 2008b) “Figure reproduced from 35. Ekanem Attah, E. and Bucknall, R.: *An Analysis of the Energy Efficiency of LNG Ships Powering Options using the EEDI*. *Ocean Engineering*, Vol. 110, pp. 62–74, 2015 with permission from Elsevier”

aiming to the heat extraction from the BOG. This ensures condensation of all hydrocarbons contained in the natural gas in a way that they all transformed again in LNG, whereas nitrogen and the other non-condensed gases remain as gas bubbles inside LNG. However, these gas bubbles are separated using a liquid separator where LNG is separated and is pumped back to the storage tanks and the non-condensed gases indicating high nitrogen concentration are rejected to the atmosphere or they burned in the gas combustion unit (GCU) (Ekanem Attah and Bucknall 2015). For LNG carriers, this additional re-liquefaction system will induce an additional electric power load between 3 and 4 MW though that some current LNGC propulsion installations with CI engines have gas capacities between 216,000 and 260,000 m<sup>3</sup> demanding a parasitic electric power ranging from 4.5 to 5.5 MW (Ekanem Attah and Bucknall 2015).

*Dual-Fuel Diesel–Electric Propulsion—DFDE.* This propulsion system contains retrofitted diesel engines in order they be able to burn BOG besides diesel oil as evidenced by Fig. 7.24 (Ekanem Attah and Bucknall 2015; Chang et al. 2008a; Clarksons Shipping Intelligence Network 2014a; Wayne and Hogson 2006; American Bureau of Shipping 2014; Bureau Veritas 2014; Chang et al. 2008b). This propulsion installation uses multiple diesel generators, usually four, in order all powering needs of the ship to be covered. The ship in this case contains the main

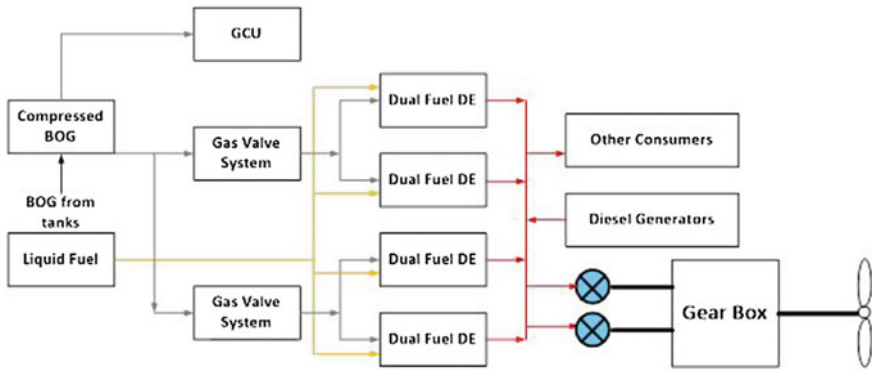


**Fig. 7.24** Schematic view of the propulsion system installation with dual-fuel diesel–electric propulsion (DFDE) (Ekanem Attah and Bucknall 2015; Chang et al. 2008b) “Figure reproduced from 35. Ekanem Attah, E. and Bucknall, R.: *An Analysis of the Energy Efficiency of LNG Ships Powering Options using the EEDI*. *Ocean Engineering*, Vol. 110, pp. 62–74, 2015 with permission from Elsevier”

system since the diesel generators produce electric energy and the electric motors use this electric energy for ship propelling (Ekanem Attah and Bucknall 2015). However, the diesel engine operates with natural gas, which is inducted in the engine through inlet valves gas, whereas ignition in each cylinder is induced using pilot diesel injection. The diesel engines of these systems can also operate under diesel-only operation. However, they cannot operate with both natural gas and diesel oil. This is a deficiency of the DFDE system compared to the STPS system, where steam generators can burn efficiently different proportions of gas and diesel simultaneously (Ekanem Attah and Bucknall 2015). Multiple diesel–electric generators operation provides operational flexibility and increased autonomy (Ekanem Attah and Bucknall 2015).

**Methodology of Comparative Evaluation of Natural Gas Propulsion Systems based on EEDI** Though that most of the energy efficiency indices are based on the simple principle of using less energy for the production of the same amount of useful energy, there is a current trend for the quantification of the energy efficiency in relevance with the corresponding environmental merits such as the reduction of anthropogenic emissions (Ekanem Attah and Bucknall 2015). This is the case with International Maritime Organization (IMO), which has defined and issued the Energy Efficiency Design Index (EEDI), which is based on mathematical formula used for the calculation of CO<sub>2</sub> mass emitted per transportation work (metric tons per nautical mile) of a specific energy production unit. Actual EEDI is calculated using mathematical formulas and directives published by IMO, and the calculated EEDI should be lower than a predefined initial value, which is progressively be reduced during a period of five years. The compliance of actual EEDI with the continuous reduced predefined limits during a period of five years is expected to trigger more effective CO<sub>2</sub> reduction methods than the initial ones considered. In



the study of Ekanem Attah and Bucknall (Ekanem Attah and Bucknall 2015), EEDI is used as an analytical tool for the evaluation of the efficiency of the current fleet of LNG carriers.

Though that the EEDI is valid only for new buildings, many studies have tried to use EEDI as a tool for the evaluation of the efficiency of existing ship projects aiming to the prediction of the impact this IMO regulation has in conjunction with specific propulsion technology or to improve EEDI values for the future energy consumption plans of the examined ship. Due to the fact that the majority of LNG carriers use unconventional propulsion systems, and thus, they were excluded from the initial EEDI regulations, and most of the studies are focused to an EEDI calculation method for these unconventional propulsion systems (Ekanem Attah and Bucknall 2015). However, there is any study analyzing EEDI of ships using steam turbines as propulsion system, which was corresponded to 80% of the ships at the moment (Ekanem Attah and Bucknall 2015). However, in 2011 were published more detailed studies covering more propulsion types (Ekanem Attah and Bucknall 2015). These studies contained publications describing an EEDI calculation method for STPS and DFDE technologies (Ekanem Attah and Bucknall 2015). Hence, these studies approved by IMO as a standard, one which the current EEDI regulations for LNG carriers are based (Ekanem Attah and Bucknall 2015).

One major advantage of the EEDI analysis is that it is based on well-established regulations, and thus, its importance for future LNG carriers (LNGC) plans should be taken into consideration. It is expected that all new LNGC EEDI regulations, which have approved in 2014, will be issued from September 2015 for all newly accepted LNGCs (Ekanem Attah and Bucknall 2015). Another virtue of LNGC EEDI analysis is that this efficiency analysis is very detailed, and it can be used effectively for assessing the efficiency and the emitted GHG values of different propulsion systems such as steam turbines (STPS), dual-fuel diesel–electric propulsion (DFDE), and slow-speed direct drive (SSDR) propulsion. EEDI analysis does not take into account other emissions except CO<sub>2</sub> (Ekanem Attah and Bucknall 2015). Though that the majority of other maritime emissions such as NO<sub>x</sub> and SO<sub>x</sub> are covered by other IMO regulations, there are GHG emissions such as methane emissions (i.e., methane slip), which at the moment are not covered by any IMO regulation (Ekanem Attah and Bucknall 2015). This observation creates the problem that there is possibility the operation of a specific propulsion system to result in reduction of CO<sub>2</sub> emissions and simultaneously to result in the deterioration of uncontrolled emissions such as methane slip. In addition, the use of a common EEDI reference value for three different propulsion technologies and their pertinent efficiencies is possible to cause a high data dispersion as we moving from the less efficient STPS to more efficient configurations such as DFDE (Ekanem Attah and Bucknall 2015).

**Analysis of EEDI Methodology** The main objectives of the Ekanem Attah and Bucknall study (Ekanem Attah and Bucknall 2015) are the quantification of the CO<sub>2</sub> values emitted from ships, and through this process, the definition of CO<sub>2</sub> reference curves for new buildings. EEDI regulations have issued for many

different ship types such as tankers, container ships, and cargo ships from January 2013, whereas LNG carriers have been excluded from these regulations due to the initial difficulties in the calculation of EEDI values for steam turbines propulsion system and diesel–electric propulsion system, which both correspond to 90% of the current LNGC fleet and of the corresponding future predictions (Ekanem Attah and Bucknall 2015). However, after an overall re-evaluation, IMO has approved amendments in MARPOL Annex VI to expand EEDI application in LNG ships and this amendment was published in April 2014, whereas its application has initiated from September 2015 (Ekanem Attah and Bucknall 2015). The baseline adopted for LNGCs is shown in Eq. (7.1), whereas details for the corresponding phase distribution can be found in Ekanem Attah and Bucknall (2015).

$$\text{Baseline value} = 2253.7 \times \text{deadweight}^{-0.474} \quad (7.1)$$

*EEDI Analysis of Current LNGC Fleet* A statistical analysis of current LNGC fleet was performed by (Ekanem Attah and Bucknall 2015) to predict effectively the repercussions of EEDI basic limits for LNGCs regarding the design of future LNG carriers. Current LNGC fleet data were obtained from Clarkson’s World Fleet Register taken into account only ships built in 2000 or later. Estimation for these ships is calculated using EEDI, which takes only into consideration the generated powers of the main and auxiliary engines, standardized fuel consumptions (based on IMO MEPC 65) (International Maritime Organization 2017; Ekanem Attah and Bucknall 2015; Clarksons Shipping Intelligence Network 2014a; Clarksons Shipping Intelligence Network 2014b), with capacity in tons deadweight and the speed of the ship, both obtained from the Clarkson’s World Fleet Register and verified from the corresponding class societies registers (American Bureau of Shipping 2014; Bureau Veritas 2014). More details about the EEDI analysis of current LNGCs fleet can be retrieved from Ekanem Attah and Bucknall study (Ekanem Attah and Bucknall 2015).

*EEDI Calculation Considering Methane Slip.* According to Ekanem Attah and Bucknall (Ekanem Attah and Bucknall 2015) though that with dual-fuel diesel–electric propulsion (DFDE) are attained lower EEDI values compared to propulsion with steam turbines and propulsion with slow-speed two-stroke dual-fuel engines, DFDE suffers from increased methane slip. The term “methane slip” corresponds to unburned methane emitted to the atmosphere from internal combustion engines. Methane (CH<sub>4</sub>) has severe negative impact on greenhouse phenomenon, and thus, this hazardous environmental impact of methane compromises seriously the environmental benefits from reduced EEDI values in CO<sub>2</sub> emissions (Ekanem Attah and Bucknall 2015). This effect is considerably worrying since methane has 20–25 times worst impact on greenhouse phenomenon compared to CO<sub>2</sub> if the effects are calculated on a life cycle of 100 years whereas the corresponding effects calculated on a life cycle of 20 years the negative greenhouse effect of methane compared to CO<sub>2</sub> is 72 times worst (Ekanem Attah and Bucknall 2015). This means that the release of even small gas volumes to the atmosphere will counterbalance all the

merits from the reduction of CO<sub>2</sub> emissions caused by the improved engine efficiency. Hence, during calculation of CO<sub>2</sub> emissions effects based on EEDI mathematical formulas, methane emissions should be taken into account as equivalent CO<sub>2</sub> emissions (Ekanem Attah and Bucknall 2015).

Methane slip issue is more intense in four-stroke engines used in dual-fuel diesel–electric propulsion compared to gas injection and diesel engines mainly because in four-stroke DFDEs the unburnt methane is trapped in combustion chamber crevices such as piston rings and valve seats. In these crevices, the fuel–air mixture equivalence ration has such a value that it cannot be totally burnt during combustion leading to methane emission with other exhaust gases through the exhaust valves during expansion stroke (Ekanem Attah and Bucknall 2015). On the other hand, natural gas injection engines operate with natural gas direct injection as in conventional diesel engines ensuring that no gas is present during compression stroke or during scavenging process reducing, thus, methane emissions to levels, which are comparable with the ones of conventional liquid fuels (Ekanem Attah and Bucknall 2015).

Considerable research has been performed aiming to the reduction of methane slip, which focuses on the use of combustion pre-chamber and on the improvement of combustion technology (optimization of injection timing, increase of injection pressure, and increase of inlet air temperature) (Ekanem Attah and Bucknall 2015). In the case that the reduction of methane slip inside the engine combustion chamber is not feasible, it has been examined the use of oxidation catalyst for methane capture in engine's exhaust. However, for most DFDE engine technologies, methane slip has been reduced to 3–4 g/kWh compared to 8–15 g/kWh of existing DFDEs (Ekanem Attah and Bucknall 2015). Having given that the mean specific fuel consumption (SFC) of DFDEs is approximately 175 g/kWh, the following formulas are used for the transformation of methane slip to equivalent CO<sub>2</sub> emissions (Ekanem Attah and Bucknall 2015):

$$\text{Methane slip} = 8 \text{ g/kWh}$$

$$\text{SFC} = 175 \text{ g/kWh}$$

$$\text{Methane equivalent of SFC}_{\text{me}} = 8/175 = 4.57\%$$

Assuming 1 ton of gas fuel containing methane is burning in DFDEs, then 2.75 tons of CO<sub>2</sub> are produced assuming 4.57% methane slip. Hence, 1 ton of fuel gas containing methane generates 2.624 tons of CO<sub>2</sub> and 0.0457 tons of CH<sub>4</sub>. Taking into account that in a life cycle of 100 years, the methane effect is 21 times higher than of this of CO<sub>2</sub> it is concluded that the total equivalent CO<sub>2</sub> emissions are (Ekanem Attah and Bucknall 2015):

$$\text{Total CO}_2\text{equiv} = 2.624 + (0.0457 \times 21) = 3.5837 \text{ tCO}_2\text{equiv}$$

Taking into consideration that in a life cycle of 20 years, the negative impact of methane slip to greenhouse phenomenon is 72 times higher than that of CO<sub>2</sub>

emissions is concluded that the total equivalent CO<sub>2</sub> emissions are (Ekanem Attah and Bucknall 2015):

$$\text{Total CO}_2\text{equiv} = 2.624 + (0.0457 \times 72) = 5.9144 \text{ tCO}_2\text{equiv}$$

Hence, the equivalent CO<sub>2</sub> emissions taking into account 1-ton methane slip to atmosphere are 3.5837 t CO<sub>2</sub> equivalent with 100 years life cycle analysis and 5.9144 t CO<sub>2</sub> equivalent with 20 years life cycle analysis (Ekanem Attah and Bucknall 2015).

**Main Conclusions of the Theoretical Analysis of Three Different Propulsion Systems of LNGCS based on EEDI** Ekanem Attah and Bucknall (Ekanem Attah and Bucknall 2015) have performed a detailed evaluation of effect of LNG transportation using EEDI. More specifically, they examined the energetic and the environmental performance of three different propulsion systems, which are used in LNG carriers in terms of CO<sub>2</sub> and CH<sub>4</sub> emissions. The three propulsion systems investigated were a steam turbines' propulsion system (STPS), a propulsion system equipped with slow-speed two-stroke dual-fuel engines (SSDR), and a propulsion system equipped with four-stroke dual-fuel CI engines (DFDE). The main conclusions of this elaborative study are the following (Ekanem Attah and Bucknall 2015):

- In terms of specific CO<sub>2</sub> emissions (in g per metric ton of ship capacity), DFDE indicates the lowest specific CO<sub>2</sub> emissions, whereas STPS indicates the highest specific CO<sub>2</sub> emissions (Ekanem Attah and Bucknall 2015).
- The current IMO EEDI limits are satisfied more or less from the 23% of the current LNG carriers' fleet. In this percentage of LNGCs, various propulsion systems are used. It is worth to mention that EEDI values corresponding to diesel–electric propulsion systems of LNGCs are considerably lower compared to the current EEDI baseline. Taking into account that 72% of future orders (reference year: 2015) for LNG carriers will have dual-fuel diesel–electric propulsion system from 2025 and onwards according to IMO dictations, they will demand additional energy efficiency improvement measures of the existing dual-fuel diesel–electric propulsion systems since they already comply with these limits (Ekanem Attah and Bucknall 2015).
- Two-stroke CI engines with natural gas injection, which correspond to the 60% of LNG carriers being ordered for construction in the near future and they will be used in direct drive propulsion systems it appears that they will offer almost 30% EEDI improvement compared to current two-stroke engines direct drive systems due to the reduction of specific fuel consumption, the reduction of CO<sub>2</sub> emissions and the elimination of the need for boil-off gas re-liquefaction installation. Such EEDI improvements of direct drive systems bring them to the same level (in terms of EEDI values) with four-stroke dual-fuel diesel–electric propulsion systems. Both two-stroke slow-speed direct drive systems and dual-fuel diesel–electric propulsion systems are fully complying with EEDI requirements from 2025 and onwards (Ekanem Attah and Bucknall 2015).

- When methane slip is taken into account in EEDI picture as equivalent CO<sub>2</sub> emissions, the energy efficiency of diesel–electric propulsion systems with dual-fuel engines is reduced. Taking into consideration a 100 years life cycle, total CO<sub>2</sub> emissions are increased by 30% compared to the corresponding EEDI value to be close or relatively lower to the current EEDI baseline curve. Oppositely considering a life cycle of 20 years, total CO<sub>2</sub> emissions are increased by 115% with the corresponding EEDI value to be considerably higher from the current EEDI baseline surpassing even the STPS, which has the lowest efficiency from all three systems examined (Ekanem Attah and Bucknall 2015).

## 7.6 Conclusions

In the present study, a detailed technological, environmental, and economic survey regarding natural gas combustion in marine two-stroke dual-fuel engines, marine four-stroke dual-fuel engines, and gas spark-ignition engines was performed. Starting from marine main two-stroke dual-fuel engines, the comparison of the “diesel-cycle” and the “Otto-cycle” dual-fuel engine types resulted in the derivation of the following conclusions:

- “Diesel-cycle” dual-fuel engine has higher fuel efficiency compared to the “Otto-cycle” dual-fuel engine type.
- “Diesel-cycle” dual-fuel engine has smoother load response and easier transition to diesel-only and back to gas/diesel operation compared to the “Otto-cycle” dual-fuel engine type.
- Unlike “Otto-cycle” dual-fuel engine, two-stroke diesel engine can be retrofitted for operating as two-stroke “diesel-cycle” dual-fuel engine.
- “Diesel-cycle” dual-fuel operation in contrast to “Otto-cycle” dual-fuel operation is not seriously affected by natural gas quality (i.e., MN).
- Both two-stroke dual-fuel engine types meet directly ECA SO<sub>x</sub> requirements
- “Otto-cycle” engine type meets directly IMO NO<sub>x</sub> Tier III limits, whereas “diesel-cycle” engine type requires EGR or SCR.
- Unlike “diesel-cycle” dual-fuel engine type, “Otto-cycle” engine type indicates a knocking risk and noticeable methane slip.

The detailed assessment of the four-stroke dual-fuel and gas SI engines on a technological, environmental, and economic basis resulted in the determination of the following conclusions:

- Modern four-stroke dual-fuel and gas SI engines have increased fuel efficiency (lower than two-stroke ones) and increased power density (higher than two-stroke ones) compared to the recent past.

- Pre-chamber technology ensures stable ignition and more complete combustion and also ensures improved combustion stability and reduced knocking risk.
- Dual-fuel marine engines and PCSI auxiliary engines meet directly ECA SO<sub>x</sub> requirements and IMO NO<sub>x</sub> Tier III limits, whereas indicate higher THC, methane slip, and CO emissions compared to conventional marine diesel engines.
- Conventional four-stroke marine CI engines can be retrofitted to dual-fuel engines
- Dual-fuel engines compared to other SO<sub>x</sub> and NO<sub>x</sub> ECA solutions indicate highest NPV and also SO<sub>x</sub> free operation.

The most promising future propulsion system solutions for LNG carriers in terms of increased energy efficiency and IMO compliance for GHG emissions are the four-stroke dual-fuel CI engines and the slow-speed two-stroke dual-fuel CI engines, whereas there is an immediate requirement for inclusion of methane emissions (i.e., methane slip) in EEDI picture.

The increasing market share of dual-fuel diesel–electric propulsion and two-stroke main dual-fuel engines in current and future LNG carriers (Stiefel 2015) is anticipated to lead to the development of future two-stroke and four-stroke dual-fuel engines with superior performance characteristics and reduced gaseous and particulate emissions compared to recent past. It should be clearly underlined that the main purpose of the present study was to consolidate and critically evaluate existing knowledge in the field of marine natural gas internal combustion engines by demonstrating the advantages and the disadvantages of each engine-type solution. Consequently, the adaptation of natural gas as marine fuel in a specific vessel is a complex and multi-variable decision, which will be determined by many technical, operational, environmental, and economic aspects on a case-by-case basis.

## References

- American Bureau of Shipping (2014) Vessel's Database. [Online] Available at: [https://www.eagle.org/safenet/record/record\\_vesselsearch](https://www.eagle.org/safenet/record/record_vesselsearch). Accessed 30 on July 2014
- Andre R (2013) Dual—fuel for maritime application. CIMAC paper no. 204, CIMAC Congress 2013, Shanghai, China
- Brynnolf S, Fridell E, Andersson K (2014) Environmental assessment of marine fuels: liquefied natural gas, liquefied biogas, methanol and bio-methanol. *J Clean Prod* 74:86–95
- Bureau Veritas (2014) Online register of ships. [Online] Available at: <http://www.veristar.com/portal/veristarinfo/generalinfo/registers/seaGoingShips>. Accessed 01 Aug 2014
- Callahan TJ, Hoag K (2013) An updated survey of gas engine performance development. CIMAC paper 277, CIMAC congress 2013, Shanghai, China
- Chang D, Rhee T, Nam K, Lee S (2008a) Economic evaluation of propulsion systems for LNG carriers a comparative life cycle cost approach. [Online] Available at: [http://osewiki.kaist.ac.kr/images/6/68/Week\\_3\\_Comparison\\_of\\_LNG\\_propulsion\\_options.pdf](http://osewiki.kaist.ac.kr/images/6/68/Week_3_Comparison_of_LNG_propulsion_options.pdf). Accessed 26 on June 2014

- Chang D, Rhee T, Nam K, Lee S (2008b) A study on availability and safety of new propulsion systems for LNG carriers. [Online] Available at: [http://ac.els-cdn.com/S0951832008001105/1-s2.0-S0951832008001105-main.pdf?\\_tid%462906dd2-26f8-11e3-a0be-00000aacb35f&acdnat%41380233579\\_df20deabaa3077eeef5702c6cc239c2](http://ac.els-cdn.com/S0951832008001105/1-s2.0-S0951832008001105-main.pdf?_tid%462906dd2-26f8-11e3-a0be-00000aacb35f&acdnat%41380233579_df20deabaa3077eeef5702c6cc239c2). Accessed 26on July 2014
- Chryssakis C, Stahl S (2013) Well-to-propeller analysis of alternative fuels for maritime applications. CIMAC paper no. 265, CIMAC congress, Shanghai, China
- Chryssakis C, Tvete H-A (2014) Alternative fuels for shipping. DNV GL strategic research and innovation, position paper 1–2014
- Chryssakis C, Brinks H, King T (2015) The fuel trilemma: next generation of marine fuels. DNV GL strategic research and innovation, position paper 03–2015
- Chryssakis C, Brinks H, Sames P, Morch C, Clausen N (2016) Feasibility and environmental impact of alternative fuels for shipping. CIMAC Paper 2016/132, 28th CIMAC world congress, Helsinki, Finland
- Clarksons Shipping Intelligence Network (2014a) LNG carrier fleet [Online]. Available at: [http://www.clarksons.net/sin2010/register/Default.aspx?sValues%4rOpt%3dregister%7crSel%3d3%7cZS0\\_SHIP\\_TYPE%3dVG9%7ctitle%3dLNG%bGas%bCarrier%bFleet%7c](http://www.clarksons.net/sin2010/register/Default.aspx?sValues%4rOpt%3dregister%7crSel%3d3%7cZS0_SHIP_TYPE%3dVG9%7ctitle%3dLNG%bGas%bCarrier%bFleet%7c). Accessed 18 on July 2014
- Clarksons Shipping Intelligence Network (2014b) LNG carrier order book [Online] Available at: [http://www.clarksons.net/sin2010/register/Default.aspx?sValues%4rOpt%3dorderbook%7crSel%3d3%7cZS0\\_SHIP\\_TYPE%3dVG9%7ctitle%3dLNG%bGas%bCarrier%bOrderbook%7c](http://www.clarksons.net/sin2010/register/Default.aspx?sValues%4rOpt%3dorderbook%7crSel%3d3%7cZS0_SHIP_TYPE%3dVG9%7ctitle%3dLNG%bGas%bCarrier%bOrderbook%7c). Accessed 18 on Aug 2014
- Cleantech (2017) <http://cleantech.cnss.no/policies-and-instruments/nox-emissions/>
- MAN Diesel (2017) <http://hhpinsight.com/marine>
- MAN Diesel and Turbo (2017) Maritime costs and benefits of alternative fuels: key results from a DNV GL and MAN diesel and turbo joint study for an LR1 product tanker 2017
- Dieselnet (2017) Emission standards, International: IMO marine engine regulations. <https://www.dieselnet.com/standards/inter/imo.php#ghg>
- Ekanem Attah E, Bucknall R (2015) An analysis of the energy efficiency of lng ships powering options using the EEDI. *Ocean Eng* 110:62–74
- Germanischer lloyd (2013) Will it be cost effective? Available at <http://www.glgroup.com>. Accessed August 8, 2013
- Hagedorn M (2014) LNG engines—specifications and economics. LNG Shipping Rostock, Wärsilä, 13/10/2014. <http://www.golng.eu/files/Main/20141017/Rostock/LNG%20Shipping%20Session%20II%20-%20LNG%20Engines-Specifications%20and%20Economics-%20W%20C3%A4rtsil%20C3%A4,Ship%20Power%20-%20Hagedorn.pdf>
- Haraldson L (2011) LNG as a fuel for environmentally friendly shipping: retrofit perspective. In: 33rd motorship propulsion & emissions conference, Copenhagen 11–12 May 2011
- Hiltner J (2013) Understanding the influence of heat transfer and combustion Behavior on end gas knock in heavy duty lean burn engines. CIMAC paper no. 36, CIMAC congress 2013, Shanghai, China
- Hiltner J, Loetz A, Fiveland S (2016) Unburned hydrocarbon emissions from lean burn natural gas engines—Sources and solutions. CIMAC paper 2016/032, 28th CIMAC world congress 2016, Helsinki, Finland
- International Maritime Organization (2017) Emission standards. <http://www.imo.org>
- Kjemtrup N (2015) Gas 2-stroke marine engine design and operation. GCA Seminar Jan 2015. [http://www.lme.ntua.gr:8080/whats-new/news-1/G2X\\_Presentations.pdf](http://www.lme.ntua.gr:8080/whats-new/news-1/G2X_Presentations.pdf)
- Levander O (2011) Dual—fuel engines: latest developments. Wartsila, 27.9.2011, Hamburg, Germany <http://www.ship-efficiency.org/onTEAM/pdf/PPTLevander.pdf>
- Li J, Wu B, Mao G (2015) Research on the performance and emission characteristics of the lng—diesel marine engine. *J Nat Gas Sci Eng* 27:945–954
- McGill R, Remley W, Winther K (2013) Alternative fuels for marine applications. A report from the IEA advanced motor fuels implementing agreement report. [http://www.iea-amf.org/app/webroot/files/file/Annex%20Reports/AMF\\_Annex\\_41.pdf](http://www.iea-amf.org/app/webroot/files/file/Annex%20Reports/AMF_Annex_41.pdf)

- Mohr H, Baufeld T (2013) Improvement of dual—fuel engine technology for current and future applications. CIMAC paper no. 412, CIMAC congress, Shanghai, China
- Moriyoshi Y, Xiong Q, Takahashi Y, Kuboyama T, Morikawa K, Yamada T, Suzuki M, Tanoue K, Hashimoto J (2016) Combustion analysis in a natural gas engine with pre-chamber to improve thermal efficiency. CIMAC paper 2016/262, 28th CIMAC congress, Helsinki, Finland, June 6–10, 2016
- Murakami S, Baufeld T (2013) Current status and future strategies of gas engine development. CIMAC paper no. 413, CIMAC congress 2013, Shanghai, China
- Ott M (2015) Low Pressure gas engines. The industry standard. CIMAC discussion Athens 22, Jan 2015 [http://www.lme.ntua.gr:8080/whats-new/news-1/03\\_MO.pdf](http://www.lme.ntua.gr:8080/whats-new/news-1/03_MO.pdf)
- Roecker R et al (2016) State-based diesel fueling for improved transient response in a dual—fuel engine. CIMAC paper no. 161, 28th CIMAC congress, Helsinki, Finland, June 6–10, 2016
- Sarigianidis C (2016) Innovative method for natural gas sea transport in compressed form (Autonomous CNG Transport Ship). (in Greek), 2016 Annual Meeting of Marine Technology, Marine Institute of Marine Technology, Athens, Greece, 2016
- Schlick H (2014) Potentials and challenges of gas and dual—fuel engines for marine application. 5th CIMAC CASCADES, Busan, Korea, 23/10/2014. [https://www.cimac.com/cms/upload/events/cascades/cascades\\_2014\\_busan/presentations/Presentation\\_Session2\\_AVL\\_CASCADES\\_Busan\\_Oct2014\\_Harald\\_Schlick.pdf](https://www.cimac.com/cms/upload/events/cascades/cascades_2014_busan/presentations/Presentation_Session2_AVL_CASCADES_Busan_Oct2014_Harald_Schlick.pdf)
- Stiefel R (2015) Low pressure gas engines, “The Industry Standard”, CIMAC discussion, Wartsila, Athens 22, January 2015
- Tozzi L, Sotiropoulou E, Beshouri G, Lepley D (2016) Novel pre-combustion chamber technology for large bore natural gas engines. CIMAC paper 2016/259. 28th CIMAC congress, Helsinki, Finland, June 6–10, 2016
- Trauthwein G (2012) Fuel for thought, maritime reporter and engineering news
- Wartsila 2-stroke dual fuel technology (2014) CIMAC NMA norge annual meeting, 22.01.2014. <https://www.sintef.no/globalassets/upload/marintek/cimac2014/6—2-s-df-technology-cimac-norway-jan-22-2014.pdf>
- Wayne WS, Hogson M (2006) The options and evaluation of propulsion systems for the next generation of lng carriers. [Online] Available at: <http://igu.dgc.dk/html/wgc2006/pdf/paper/add10055.pdf>. Accessed 26 on Sep 2013
- Wei L, Geng P (2016) A review on natural gas/diesel dual fuel combustion, emissions and performance. *Fuel Process Technol* 142:264–278
- Yfantis EA, Zannis TC, Katsanis JS, Pariotis EG, Papagiannakis RG, Mohr H (2017) Four—stroke marine natural gas diesel and spark—ignited engines: a state-of-the-art technologies evaluation. In: 3rd scientific conference SEA-CONF 2017, May 18–19 2017, Constanta, Romania
- Zannis TC, Yfantis EA, Katsanis JS, Pariotis EG (2017) Natural gas combustion in marine internal combustion engines: a technological and environmental assessment. invited lecture, Hellenic Institute of Marine Technology, January 30th 2017, Piraeus, Greece



# Chapter 8

## Advanced Combustion in Natural Gas-Fueled Engines



Ulugbek Azimov , Nobuyuki Kawahara , Kazuya Tsuboi   
and Eiji Tomita 

**Abstract** Current energy and emission regulations set the requirements to increase the use of natural gas in engines for transportation and power generation. The characteristics of natural gas are high octane number, less amount of carbon in the molecule, suitable to lean combustion, less ignitibility, etc. There are some advantages of using natural gas for engine combustion. First, less carbon dioxide is emitted due to its molecular characteristics. Second, higher thermal efficiency is achieved owing to the high compression ratio compared to that of gasoline engines. Natural gas has higher octane number so that knock is hard to occur even at high compression ratios. However, this becomes a disadvantage in homogeneous charge compression ignition (HCCI) engines or compression ignition engines because the initial auto-ignition is difficult to be achieved. When natural gas is used in a diesel engine, primary natural gas–air mixture is ignited with small amount of diesel fuel. It was found that under high pressure, lean conditions, and with the control of certain parameters, the end gas is auto-ignited without knock and improves the engine combustion efficiency. Recently, some new fuel ignition technologies have been developed to be applied to natural gas engines. These are the laser-assisted and plasma-assisted ignition systems with high energy and compact size.

**Keywords** Natural gas IC engine · Dual-fuel engine · HCCI · RCCI  
Laser-assisted ignition · Plasma-assisted ignition · PREMIER

---

U. Azimov (✉)

University of Northumbria, Newcastle upon Tyne NE1 8ST, UK  
e-mail: [ulugbek.azimov@northumbria.ac.uk](mailto:ulugbek.azimov@northumbria.ac.uk)

N. Kawahara · K. Tsuboi · E. Tomita  
Okayama University, Tsushima-Naka 3, Okayama 700-8530, Japan

## Abbreviations

ATDC	After top dead center
AFR	Air–fuel ratio
BTDC	Before top dead center
CA	Crank angle
CAD	Crank angle degree
CFD	Computational fluid dynamics
CI	Compression ignition
CNG	Compressed natural gas
CO	Carbon monoxide
CO <sub>2</sub>	Carbon dioxide
EVC	Exhaust valve closing
EVO	Exhaust valve opening
EGR	Exhaust gas recirculation
$\phi$	Equivalence ratio
IMEP	Indicated mean effective pressure
IVC	Intake valve close
IVO	Intake valve open
HC	Hydrocarbon
HCCI	Homogeneous charge compression ignition
HRR	Heat release rate
IC	Internal combustion
LES	Large Eddy simulation
LTC	Low-temperature combustion
$m_{DF}$	Mass of pilot-injected diesel fuel
NG	Natural gas
NO	Nitrogen monoxide
NO <sub>x</sub>	Nitrogen oxides
P	Pressure
PCCI	Premixed charge compression ignition
rpm	Revolution per minute
RANS	Reynolds-averaged Navier–Stokes
RCCI	Reactivity controlled compression ignition
SI	Spark ignition
SOC	Start of combustion
SOI	Start of injection
T	Temperature
$T_G$	Ignition temperature
TDC	Top dead center
UHC	Unburned hydrocarbon
V	Volume

## 8.1 Introduction

Internal combustion (IC) engines can perform more efficiently and with a lower level of toxic emissions if natural gas (NG) is used as a fuel. NG is a naturally occurring gas mixture, which consists of primarily methane and some amount of higher hydrocarbons, nitrogen, and carbon dioxide. Typical composition of a commercial NG product is shown in Fig. 8.1.

Due to the lowest carbon-to-hydrogen ratio, compared to other fossil fuels, NG emits the least amount of  $\text{CO}_2$  during its combustion. Plentiful resources, lower price, and cleaner burning compared to conventional liquid fuels have made NG a very economic fuel to be used in IC engines. Another important feature of NG, its high octane number, makes it suitable to be used in engines with high compression ratios (Zheng et al. 2005).

To meet low emission standards for IC engines, researchers have been extensively studying the low-temperature combustion (LTC) concept (Dempsey et al. 2014; Caton 2011). These studies showed that utilizing LTC strategies in engines can result in a simultaneous reduction of nitrogen oxides ( $\text{NO}_x$ ) and soot emissions and also helps achieving higher thermal efficiencies (Jia et al. 2011; Asad et al. 2013; Aoyama et al. 1996).

NG can be also used in a homogeneous charge compression ignition (HCCI) engines. In the HCCI combustion mode, a mixture of air and NG is auto-ignited due

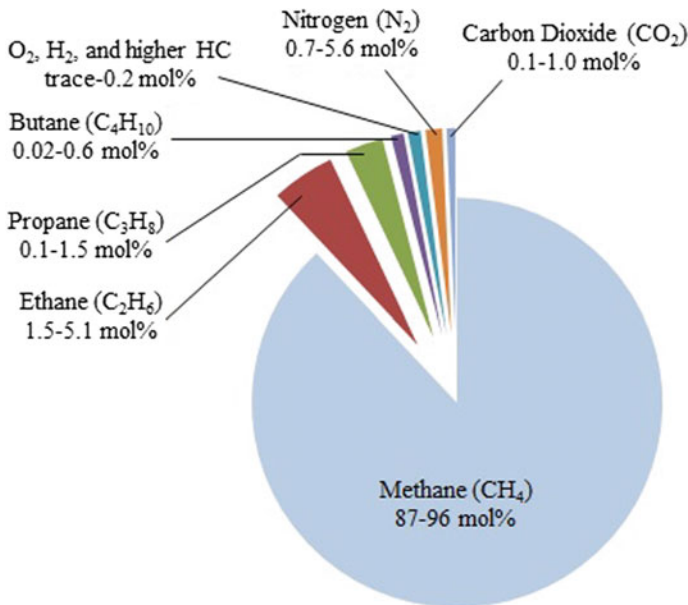


**Fig. 8.1** Typical composition of a commercial NG product (<http://www.uniongas.com/aboutus/aboutng/composition.asp>)

to the temperature increase close to the top dead center (TDC). The combustion process is significantly faster than that in either traditional compression ignition (CI) or spark ignition (SI) engines (Reitz 2013). The challenge for HCCI engine is to control auto-ignition and combustion. A new LTC concept named reactivity controlled compression ignition (RCCI) was developed by the researchers (Kokjohn et al. 2010, 2011; Splitter et al. 2010) to overcome difficulties like combustion phasing control and very high pressure rise rate (PRR), to extend engine operating limits and avoid potential combustion instability and misfire (Imtenan et al. 2014; Gharehghani et al. 2015; Zhou et al. 2015; Benajes et al. 2015; Li et al. 2015; Laguitton et al. 2007; Molina et al. 2015; Nieman et al. 2012; Paykani et al. 2015; Kakaee et al. 2015; Christensen and Johansson 1998).

The demand for high thermal efficiency can be met through ignition of lean fuel mixtures. However, lean combustion is related to slower flame propagation speeds and decreased power output. Engine power output can be elevated through boosting the initial cylinder pressure. An increase in the cylinder pressure keeping the same spark plug electrode distance would require increased secondary coil voltage, which leads to extreme erosion of electrodes over time. Flame propagation speed in lean air–fuel mixtures can be expanded whether through optimizing the position of ignition spot in the combustion chamber or with the aid of multi-point ignition. Ignition spot always stays close to the top of the combustion chamber in a traditional spark ignition engine and cannot be varied from its location. This can be resolved by using a laser as an ignition source.

In addition to the laser ignition, the possible use of non-equilibrium plasma for ignition and combustion control has also raised the increasing interest due to the possibility of plasma-assisted approaches for ignition and flame stabilization. During the past decade, significant progress has been made toward understanding the mechanisms of plasma–chemistry interactions, power redistribution, and the non-equilibrium initiation of combustion (Starikovskii 2005). Plasma application has been shown to furnish additional combustion control, which is crucial for ultra-lean flames, high-speed flows, high-pressure conditions, and distributed ignition control in HCCI engines. In addition, a wide variety of fuels have been examined for the use of various types of discharge plasmas. The following sections will describe in more detail the above-mentioned combustion and ignition technologies and techniques applied for natural gas-fueled engines.

## 8.2 Combustion of Natural Gas in Dual-Fuel Engines

To meet stringent emission standards, researchers have been developing LTC solutions to improve the traditional internal combustion engines in order to develop IC engines with higher efficiencies and cleaner combustion (Agarwal et al. 2017; Musculus Mark et al. 2013; Gharehghani et al. 2016; Scott Guerry et al. 2016).

Many different gaseous and liquid fuels have been evaluated in the dual-fuel combustion engine, and natural gas is believed to be one of the most suitable alternatives due to the low cost and excellent antiknock properties (Wagemakers and Leermakers 2012; Hosmath et al. 2016).

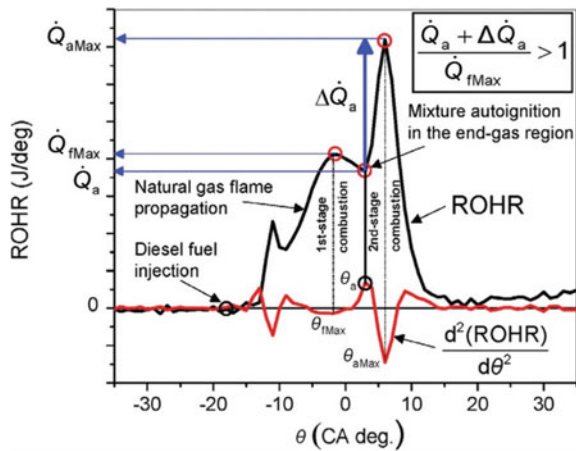
### 8.2.1 Experimental Research on Dual-Fuel Engines

Several experimental research efforts on dual-fuel engines were carried out by the authors of this chapter. The more detailed explanation can be found in references (Tomita et al. 2002, 2004, 2007; Roy et al. 2009). Tomita et al. (2009) investigated the combustion and exhaust emissions in supercharged dual-fuel natural gas engines. The authors documented the range of operating conditions under which the new higher efficiency **PRE**mixed **M**ixture **I**gnition in the **E**nd-**g**as **R**egion (PREMIER) combustion mode was experimentally tested in a pilot-ignited, natural gas dual-fuel engine. The heat release during the PREMIER combustion is presented in Fig. 8.2. The details of this combustion mode are presented in the reference (Tomita et al. 2009).

Figure 8.3 shows a schematic diagram of the experimental setup. The engine specifications and experimental conditions are given in Table 8.1 and explained in detail in the reference (Tomita et al. 2009).

Figure 8.4 shows the flame development of NG as a primary fuel ignited by micro-pilot-ignited diesel fuel. The flame area is gradually increasing in all four directions with the flame front finally reaching the cylinder wall. The flame speed is affected by the CO and CO<sub>2</sub> gases produced during the combustion. The effect of these species on fuel oxidation and flame propagation is a quite complex topic and is outside of the scope of this chapter. Figure 8.5 shows the intensity of the emitted

**Fig. 8.2** Conceptual illustration of PREMIER combustion as the rate of heat release



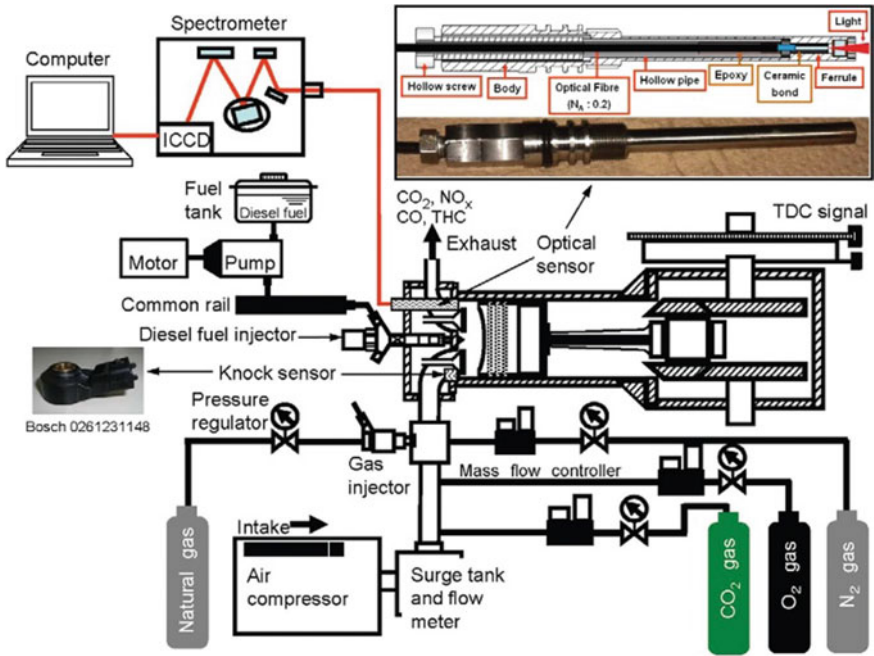
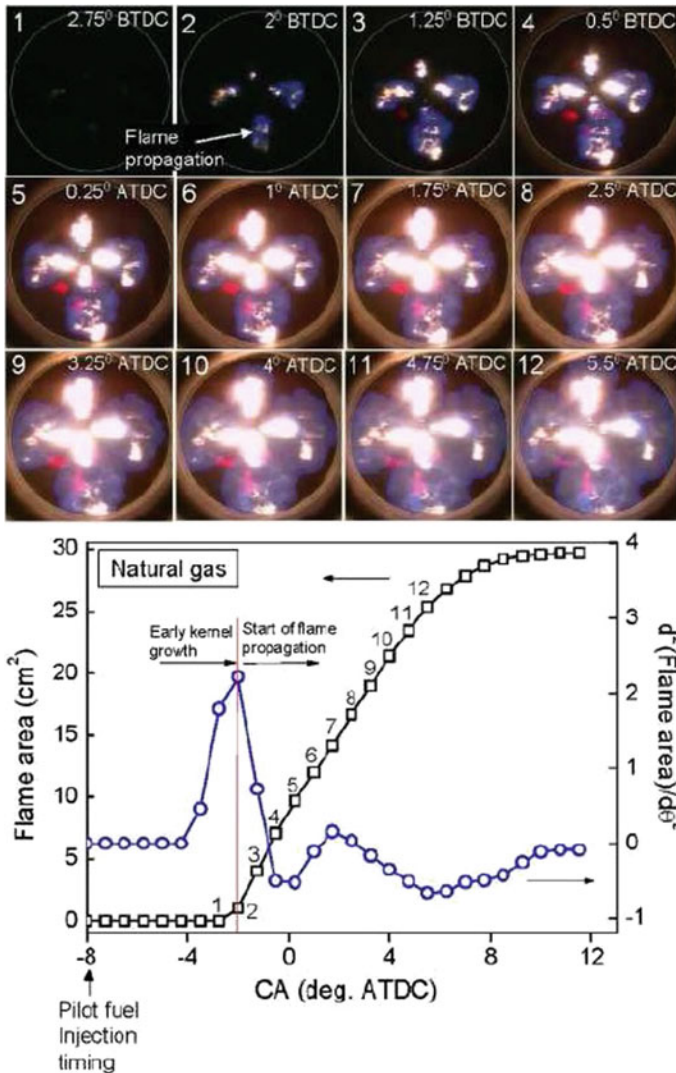


Fig. 8.3 Schematic diagram of experimental setup

Table 8.1 Engine specification and experimental conditions

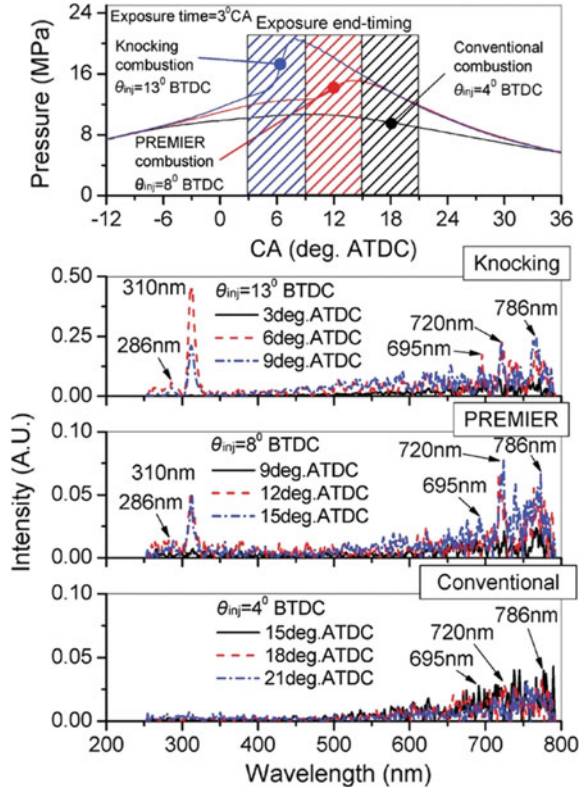
Engine type	Four stroke, single cylinder, water cooled
Bore × stroke	96 × 108 mm
Swept volume	781.7 cm <sup>3</sup>
Compression ratio	16
Combustion system	Dual fuel, direct injection
Combustion chamber	Shallow dish
Engine speed	1000 r/min
Intake pressure	101, 200 kPa
Injection system	Common rail
Nozzle hole × diameter	3 × 0.10 mm, 3 × 0.08 mm, 4 × 0.10 mm
Pilot fuel injection pressure	40, 80, 120, 150 MPa
Pilot fuel injection quantity	2, 3 mg/cycle
Injection timing	From 13° BTDC to TDC
Equivalence ratio	0.6



**Fig. 8.4** Dual-fuel combustion sequential images at  $P_{inj} = 40$  MPa,  $P_{in} = 101$  kPa,  $\theta_{inj} = 8^\circ$  BTDC,  $m_{DF} = 2$  mg/cycle,  $\phi_t = 0.6$ . Natural gas,  $CH_4 = 88\%$ ,  $C_2H_6 = 6\%$ ,  $C_3H_8 = 4\%$ ,  $n-C_4H_{10} = 2\%$

light as background-subtracted ensemble-averaged spectra at the instances the propagating flame arrives at the end-gas region where the optical sensor is installed to capture the end-gas region auto-ignition. The detailed explanations of this setup are provided in the reference (Azimov et al. 2011).

**Fig. 8.5** Detailed spectra in the end-gas region.  
 $P_{inj} = 40$  MPa,  
 $P_{in} = 200$  kPa,  
 $D_{hole} = 0.1$  mm,  $N_{hole} = 3$ ,  
 $m_{DF} = 2$  mg/cycle



To maintain PREMIER combustion in a dual-fuel natural gas engine, the effects of several operating parameters must be identified. For example, as shown in Fig. 8.6, PREMIER combustion can be achieved by maintaining certain fixed experimental conditions (Azimov et al. 2016).

The engine experimental conditions are presented in Table 8.2.

### 8.2.2 Numerical Modeling of Dual-Fuel Engines

Dual-fuel combustion is one of the efficient, clean yet difficult to model phenomenon. Dual-fuel combustion has both CI and SI characteristics in addition to its own typical behavior, which increases the complexity of the combustion process. Traditionally, in the dual-fuel combustion process, a diesel spray is introduced in a nearly homogeneous air–fuel mixture. To model dual-fuel combustion, the well-established auto-ignition models can be used. As the first stage of the dual-fuel combustion is auto-ignition, these models can be applied directly without any change under the assumption that diesel auto-ignition is not affected by the presence



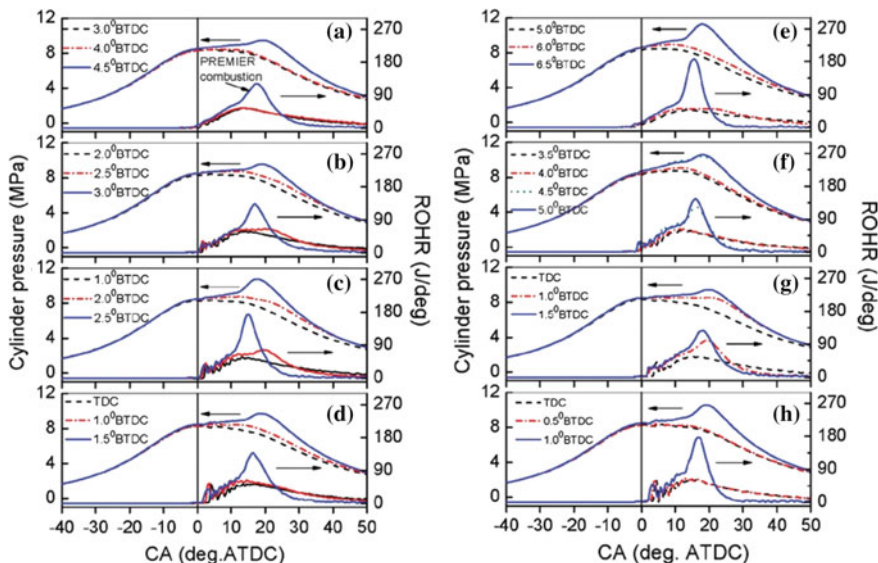


Fig. 8.6 Effect of pilot fuel injection timing on cylinder pressure and the rate of heat release

Table 8.2 Engine experimental conditions

	$P_{inj}$ (MPa)	$P_{in}$ (kPa)	$D_{hole}$ (mm)	$N_{hole}$	$m_{DF}$ (mg/cycle)
a	40	200	0.1	3	3
b	80	200	0.1	3	3
c	120	200	0.1	3	3
d	150	200	0.1	3	3
e	40	200	0.1	3	2
f	80	200	0.1	3	2
g	150	200	0.08	3	3
h	150	200	0.1	4	3

of another fuel species such as methane, and traces of ethane, propane, and iso-butane. In reality, traces of any gaseous fuel can change ignition delay, temperature of auto-ignition process, duration of first-stage ignition, and laminar burning velocity. Hence, diesel substitution ratio is very important in order to recognize the percentage of energy delivered by diesel fuel.

One of the current challenges in the 3D CFD simulation of the dual-fuel combustion is to get the correct heat release from the chemical reactions compared with the experimental data. This is important to predict knock in the dual-fuel operation. Dual-fuel engine starts combustion using pilot fuel spray, and auto-ignition of that small fuel acts as a spark energy for the lean gaseous fuel-air mixture. This mode of combustion can be investigated experimentally as was explained in earlier section,

but poses a very complicated problem for 3D CFD modeling. In SI engines, spark location is known and has precise spark energy, spark efficiency, and duration of the spark associated with it whereas dual-fuel engine heavily depends on the nature of the pilot spray to start premixed flame-type combustion.

The sequence of different types of combustion is very important for dual-fuel operation mode. For regular dual-fuel operation, the diesel pilot spray evaporates and mixes with already almost homogeneous mixture of natural gas and air. During this process, auto-ignition of diesel takes place and produces first heat release. This rate of heat release heavily depends on the quantity of diesel, compression ratio, and local equivalence ratio. First ignition starts the flame propagation and consumes most of the gaseous fuel. It is important to focus on the end-gas ignition, which follows the traditional flame propagation and has significant heat release rate compared to the first two zones, namely auto-ignition of diesel and flame front propagation in lean NG–air mixture. Hence, auto-ignition model with detailed chemistry and well-established flame propagation model hereafter mentioned as G-equation model can be used to model dual-fuel combustion in diesel engine. G-equation model is:

$$\frac{\partial \rho G}{\partial t} + \frac{\partial \rho \hat{u}_i G}{\partial x_i} = -D_t \kappa \left| \frac{\partial G}{\partial x_i} \right| + \rho_u S_t \left| \frac{\partial G}{\partial x_i} \right| \quad (8.1)$$

where  $D_t$  is turbulent diffusion,  $\kappa$  is curvature of the flame,  $\rho_u$  is unburnt density, and  $S_t$  is turbulent flame speed. Depending on the fuel composition and local equivalence ratio, ignition temperature is found to vary between 950 and 1100 K and hereafter it is denoted by  $T_G$ . This temperature ( $T_G$ ) was decided using 0D auto-ignition model for homogeneous charge in CHEMKIN.  $T_G$  changes per local equivalence ratio and fuel composition. El Merhubi et al. (2016) conducted high-pressure (40 bar) methane auto-ignition using shock tube and also validated GRI 3.0 mechanism for  $\phi = 0.5$ –1.0. At 40 bar pressure, auto-ignition temperature of methane ( $\phi = 0.5$ ) is 1560 K. Though HCCI calculations assume premixed charge, it is important to note that 1% diesel quantity by energy content significantly changes auto-ignition temperature of methane. If *n*-heptane mass fraction is less than 0.021, then  $T_G$  is on the higher side. Hence, the value of  $T_G$  needs to be determined each time when the fuel composition changes.  $S_t$  is derived from laminar flame speed  $S_l$ , when used for RANS modeling; it includes  $u'$  root mean square of turbulent fluctuation velocity as shown in Eq. 8.2 (Peters 2000).

$$S_t = S_l + u' \left( \left( \frac{-a_4 b_3^2}{2b_1} D_a \right) + \left[ \left( \frac{-a_4 b_3^2}{2b_1} D_a \right)^2 + a_4 b_3^2 D_a \right]^{\frac{1}{2}} \right) \quad (8.2)$$

where  $b_1 = 2.0$ ,  $b_3 = 1.0$ ,  $a_4 = 0.78$ ,  $D_a$ —Damkohler number.

Equation 8.3 derived by Pitch (2002) is used for LES cases to calculate  $S_t$

$$S_t = S_l \left( \left( \frac{-b_3^2 C_s \Delta}{2b_1 S_c l_F} \right) + \sqrt{\left( \frac{b_3^2 C_s \Delta}{2b_1 S_c l_F} \right)^2 + \frac{b_3^2 D_t}{S_l l_F} + 1} \right) \quad (8.3)$$

where  $S_c$  is turbulent Schmidt number,  $\Delta$  is the filter width, and  $C_s$  is dynamic Smagorinsky number. In  $G$ -equation model  $G(x, t)$  is a non-reactive scalar iso-surface for any fixed value of  $x$ . The flame front is described by  $G = 0$  surface, and the flame thickness is superimposed by  $G'$  on this iso-surface.  $G$ -equation depends on the closure solution for calculating turbulent flame speed and does not have a source term; hence,  $G$ -equation model can be easily coupled with detailed chemistry model (Yang and Reitz 2010; Liang et al. 2007; Long 2006; Tamagna et al. 2008). Positive value of  $G$  suggests burnt zone, and negative value is used for unburnt zone. In the current model, laminar flame speed is calculated using CHEMKIN 1D laminar flame speed calculations instead of Guilder's equation (Gulder 1984) as it tends to overpredict the laminar flame speed for single component fuels like methane at high pressure and temperature conditions.

Figure 8.7 shows combustion progress at 4.5° BTDC after injection has occurred at 14.5° BTDC. Formaldehyde ( $\text{CH}_2\text{O}$ ) is a main attribute of low-temperature combustion which appears not only in the vicinity of the flame kernels but on the peripheral area of entire combustion chamber. Plotted iso-surface at  $G = 0.0001$  shows predominantly low-temperature regions. The empty region in the middle of combustion chamber is a high-temperature zone, and in the third figure, OH concentration is highest in the same region. This shows the smaller high-temperature region near spray surrounded by cluster of low-temperature ignition sites.

Figure 8.8 shows the development of the initial kernel after the second micro-pilot injection is complete.  $\text{CH}_2\text{O}$  iso-surface is created for highest concentration and colored by temperature to show the sites of preignition low-temperature chemistry. Subsequently,  $G$  iso-surface at value  $1e-04$ , i.e., at 0.1 mm distance from mean flame front inside the burn zone is also colored by temperature which shows three major kernel formation zones around three spray lobes. It is very important to note that outside the flame zone, at low-temperature initial kernel development starts at various locations. This kernel depending on the location from the wall and from mean flame front either becomes auto-ignition sites or just contributes to small energy release. OH iso-surface is plotted at highest mass fraction of OH ( $1.e-03$ ) and shows the high-temperature chemistry inside the burnt zone. The heat release in case of the split micro-pilot injection is illustrated with  $\text{CH}_2\text{O}$  and  $G$  iso-surface as shown in Fig. 8.8 at 6° ATDC. The first micro-pilot injection occurs at 6° BTDC, and Fig. 8.8 shows the aftermath for flame kernel development after the second micro-pilot injection at 5° ATDC. The positive value of  $G$  suggests the burnt region, and the negative value shows the unburnt region outside the flame zone whereas  $G = 0$  is the mean flame front brush.  $\text{CH}_2\text{O}$  and  $G$ -surfaces are colored by temperature to show low-temperature flame segments.  $G = 1e-04$  shows the 0.1 mm zone inside the burnt zone after the flame front has

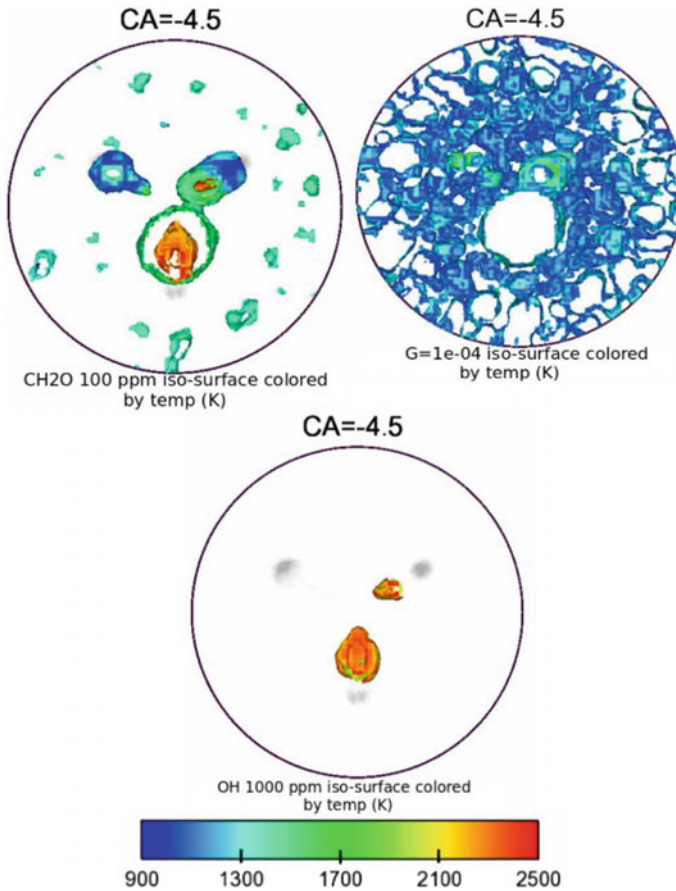


**Fig. 8.7**  $\text{CH}_2\text{O}$  and  $G$  iso-surfaces for low-temperature flame localization, and  $\text{OH}$  for high-temperature combustion (single micro-pilot injected at  $14.5^\circ$  BTDC). RPM—1000,  $P_{inj}$ —40 MPa,  $\text{CH}_4$ —25 mg/cyl, diesel—0.8 mg/cyl,  $\lambda$ —1.92, IMEP—1.5 MPa

passed.  $\text{CH}_2\text{O}$  iso-surface shows in the pre-flame chemistry occurring outside the flame front at much lower temperature of 900 K, where inside the burnt zone the temperature is 2500 K.

Figure 8.9 shows trend of local temperature, which includes single micro-pilot injection at  $14.5^\circ$  BTDC. The highest temperature is noted from preheat region (1 mm away from the flame front), and second highest temperature belongs to the burnt region (1–2 mm inside the flame front). It is also important to note that around  $6^\circ$  BTDC mean flame front ( $G = 0$ ) reaches highest temperature, and at the same time in preheat region 2–5 mm away from mean flame, there is a sudden increase in temperature. This is a very clear indication of end-gas ignition provided that temperature is much less at 0.5 mm outside the flame.

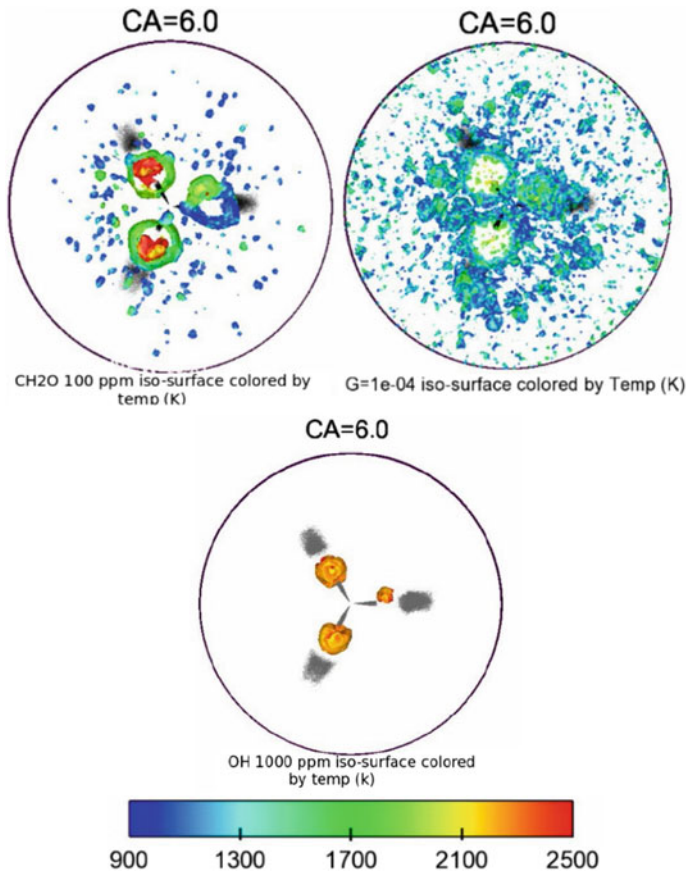


**Fig. 8.8** CH<sub>2</sub>O and  $G$  iso-surfaces for low-temperature flame localization, and OH for high-temperature combustion (the first micro-pilot injection is at 6° BTDC, and the second micro-pilot injection is at 5° ATDC). RPM—1000,  $P_{inj}$ —40 MPa, CH<sub>4</sub>—26.7 mg/cyl, diesel inj—first (6° BTDC)—0.8 mg/cyl, second (5° ATDC)—0.8 mg/cyl,  $\lambda$ —1.66, IMEP—0.82 MPa

Figure 8.10 shows the local temperature and pressure data for the same scenario, and there are two major heat release zones; the first one is at 1000 K range, and the second zone shows high-temperature end-gas heat release at 2100 K range. Both LES and RANS turbulent models with the same combustion model showed good agreement in terms of end-gas ignition.

Figure 8.11 shows the gradient  $G$  that represents the temperature profiles in three combustion regions. The positive values of  $G$  represent the temperature in the burnt zone where post-flame chemistry is dominant and has the highest temperature in the combustion chamber. Negative values of  $G$  show the preheat or pre-flame regime where end-gas ignition happens in PREMIER cases. This is an excellent way of predicting temperature in the end-gas region instead of just observing few locations for higher heat release.

**Fig. 8.9** Temperature profile for different  $G$  values with single micro-pilot injection. RPM—1000,  $P_{inj}$ —40 MPa,  $CH_4$ —25 mg/cyl, diesel—0.8 mg/cyl,  $\lambda$ —1.92, IMEP—1.5 MPa

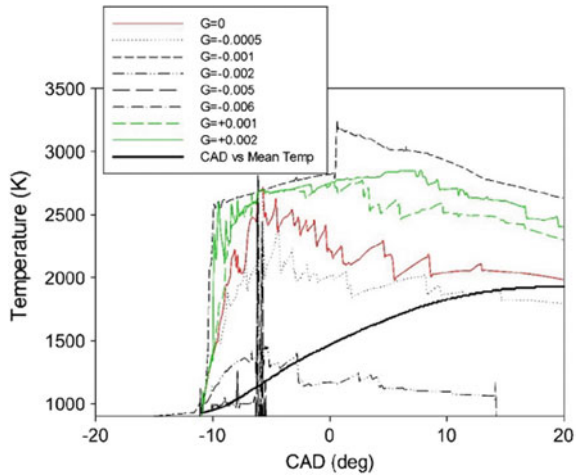


**Fig. 8.10** Local temperature–pressure relationship with single micro-pilot injection. RPM—1000,  $P_{inj}$ —40 MPa,  $CH_4$ —25 mg/cyl, diesel—0.8 mg/cyl,  $\lambda$ —1.92, IMEP—1.5 MPa

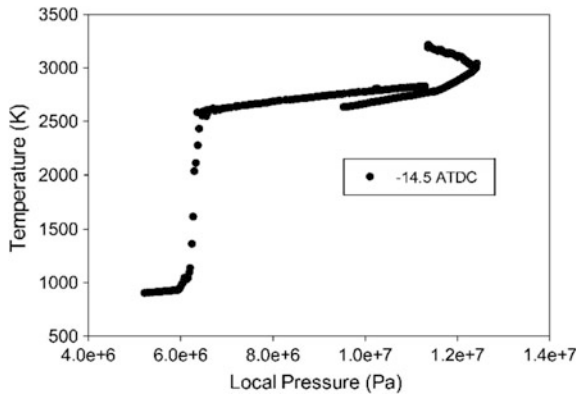
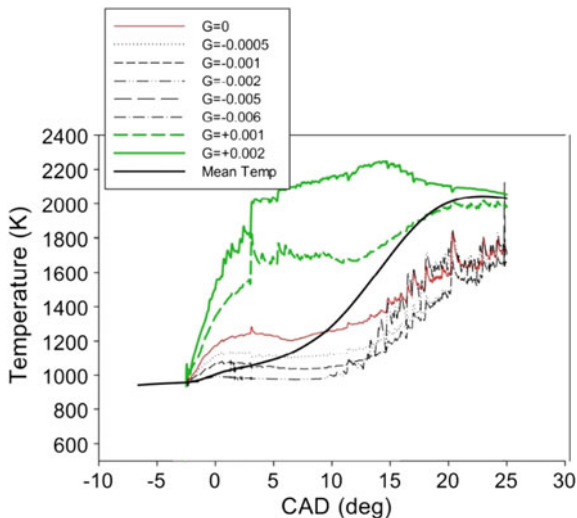
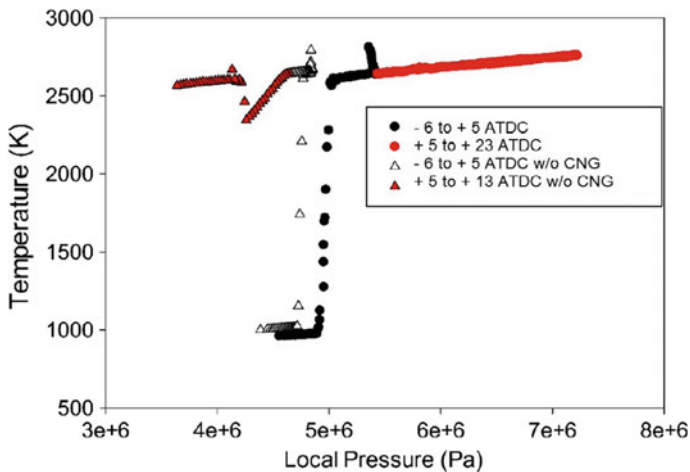


Figure 8.12 shows the effect of split micro-pilot injection. Ignition sites for split pilot injection are less in number compared to the single pilot injection case. The graph shows the effect of methane on the first ignition temperature as well as the overall temperature trend. For this case, when methane is present, first-stage ignition temperature is lower as compared to the scenario when methane is not present. On the contrary, at the second stage ignition methane burns at higher temperature compared to diesel-only case. As the second micro-pilot starts at  $5^\circ$  ATDC, for non-methane case temperature suddenly drops as spray is being injected in the developed flame kernel of the first pilot injection. Start of the second micro-pilot is visible in Fig. 8.8. This effect is reduced in case of multi-pilot injection due to the presence of methane, and flame kernel grows with steady consumption of fuel. Split injection proves to be effective in controlling end-gas ignition and growth of the flame kernel. The current way of modeling proved to be very effective in detecting changes in the end-gas ignition temperature as well as its precise location and frequency.



**Fig. 8.11** Temperature profiles for different  $G$  values for the case with the first and second pilot injection. RPM—1000,  $P_{inj}$ —40 MPa,  $CH_4$ —26.7 mg/cyl, diesel inj—first (6° BTDC)—0.8 mg/cyl, second (5° ATDC)—0.8 mg/cyl,  $\lambda$ —1.66, IMEP—0.82 MPa



**Fig. 8.12** Local temperature–pressure relationship for the case with the first and second pilot injection with and without methane/CNG

### 8.3 Combustion of Natural Gas in Homogeneous Charge Compression Ignition (HCCI) Engines

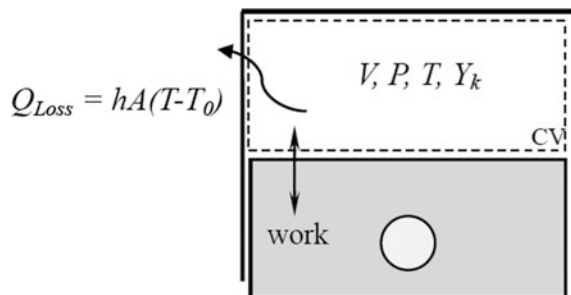
NG requires little time for mixture preparation and is chemically stable, both of which make it a suitable fuel for homogeneous charge compression ignition (HCCI) engines. NG produces less greenhouse gas emissions compared to those of petroleum-based fuels. NG also brings a few challenges for HCCI engine operations. NG has a high octane number and therefore is hard to auto-ignite. In addition, NG usually has large differences in fuel composition from field to field, which adds more uncertainties for engine applications to make universal adjustments to run on different NG types. To enable the use of NG in HCCI engines, higher compression ratios, significant amount of intake heating, some types of preignition and/or internal EGR are required to be adjusted to ensure the auto-ignition.

The use of NG in HCCI engines has been studied for over a decade. The obtained results (Ando et al. 2003; Jun et al. 2003) experimentally showed the effect of different operating parameters such as intake temperature, density, equivalence ratio, and others, on natural gas auto-ignition characteristics. Yap et al. (2004) experimentally demonstrated the decrease of  $\text{NO}_x$  emissions and increase of CO and UHC emissions with the addition of reformed EGR. The same group (Yap et al. 2006) also reported an increase in  $\text{NO}_x$  emissions with hydrogen addition at higher loads in a natural gas HCCI engine. Other groups (Doughty et al. 1992) investigated the effect of engine loads and measured the lower  $\text{NO}_x$  emissions in the exhaust gas at lower loads and at higher engine speeds.

#### 8.3.1 Single-Zone Model

To simulate NG HCCI combustion in IC engines, a single-zone model with distinct chemical kinetics in CHEMKIN can be employed (CHEMKIN-PRO 2010). The fundamental assumption that the model imposes is that the temperature and species concentrations are viewed as homogeneous throughout the cylinder. The thermodynamic system described by the model is shown in Fig. 8.13. In the cylinder, there

**Fig. 8.13** Piston–cylinder system schematics of the single-zone thermodynamic model





are four independent properties which include temperature ( $T$ ), species concentration ( $Y_k$ ), pressure ( $P$ ), and volume ( $V$ ). The heat is transferred to the cylinder wall, and the work is transferred by the piston. The main equations are described below.

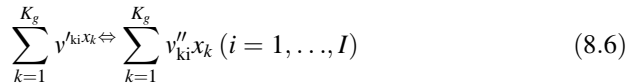
The species conservation for the system is (CHEMKIN-PRO 2010),

$$(\rho V) \frac{dY_k}{dt} = (\dot{\omega}_k V) W_k \quad (8.4)$$

where  $Y_k$  is the mass fraction,  $W_k$  is the molecular weight,  $\rho$  is the mass averaged density, and  $\dot{\omega}_k$  is the molar rate of production per volume. The energy equation for the system shown in Fig. 8.13 is the following (CHEMKIN-PRO 2010),

$$\frac{dU}{dt} = -\dot{Q}_{\text{loss}} - P \frac{dV}{dt} \quad (8.5)$$

Elementary reactions involving  $K_g$  species can be represented in the general form,



where  $\nu_{ki}^{\prime}$  and  $\nu_{ki}^{\prime\prime}$  indicates forward and reverse stoichiometric coefficients for the  $i$ th reaction, and  $x_k$  is the chemical symbol of the  $k$ th species. Then, the expression for the production rate  $\dot{\omega}_k$  can be obtained,

$$\dot{\omega}_k = \sum_{i=1}^I \left[ (\nu_{ki}^{\prime\prime} - \nu_{ki}^{\prime}) \left( k_{fi} \prod_{k=1}^{K_g} [X_k]^{\nu_{ki}^{\prime}} - k_{ri} \prod_{k=1}^{K_g} [X_k]^{\nu_{ki}^{\prime\prime}} \right) \right] \quad (k = 1, \dots, K) \quad (8.7)$$

where  $k_{fi}$  and  $k_{ri}$  are the forward and reverse rate constants of the  $i$ th reactions, and  $[X_k]$  is the molar concentration of the  $k$ th species. The forward rate constants for the reactions are generally the inputs of the model.

Arrhenius temperature dependence:

$$k_{fi} = A_i T^{\beta_i} \exp\left(-\frac{E_i}{R_c T}\right) \quad (8.8)$$

Instantaneous spatially averaged heat transfer to the cylinder wall is calculated using a version of the Woschni correlation (Heywood 1988). This version has been adjusted for HCCI combustion (CHEMKIN-PRO 2010), as shown below,

$$Nu_h = a \cdot Re^b \cdot Pr^c = 0.035 Re^{0.8} \quad (8.9)$$

where  $a = 0.035$ ,  $b = 0.8$ ,  $c = 0$ .

$$Re = \frac{\rho w B}{\mu} \tag{8.10}$$

where the local average gas velocity  $w$  is correlated as follows,

$$w = \left[ \left( C_{11} + C_{12} \frac{v_{swirl}}{\bar{v}_p} \right) \bar{v}_p + C_2 \frac{V_d T_r}{p_r V_r} (p - p_m) \right] \tag{8.11}$$

where  $V_d$  is the displaced volume;  $p$  is the instantaneous cylinder pressure;  $p_r$ ,  $V_r$ ,  $T_r$  are the pressure, volume, and temperature at the reference state;  $p_m$  is the motored cylinder pressure at the same crank angle as  $p$ . In this study,  $C_{11} = 2.28$ ,  $C_{12} = 0.308$ ,  $C_2 = 0.54$ , and  $v_{swirl} = 0$  are used. More detailed description of this heat transfer correlation can be found in (Heywood 1988).

### 8.3.2 Multi-zone Model

Multi-zone models typically require non-reacting (cold flow) fluid mechanics simulation to provide the initial temperature and concentration distributions in the cylinder. With these initial distributions, an appropriate number of zones can be determined and those zones can be established and initialized with different temperatures and concentrations. Figure 8.14 shows an example of the setup procedure where the continuous temperature distribution from the CFD simulation is converted to the zonal conditions in the multi-zone model. After the zonal initial

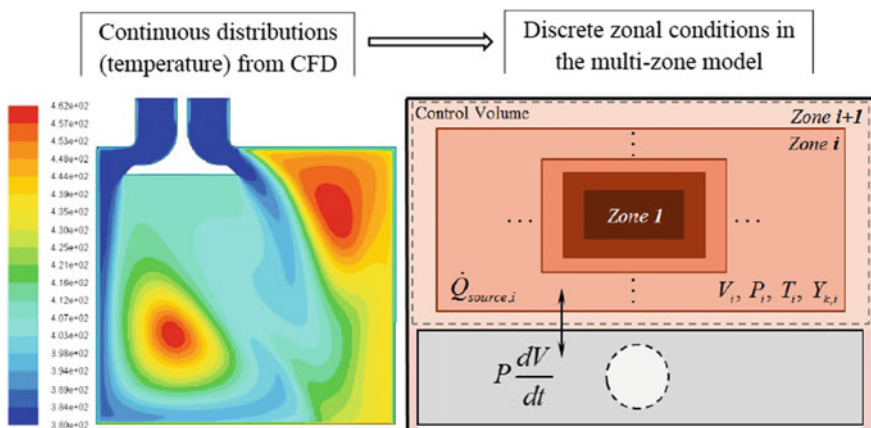


**Fig. 8.14** Illustration of the multi-zone model setup procedure, temperature distribution from CFD (left) and zonal conditions in multi-zone model (right) (CHEMKIN-PRO 2010)

conditions are set up, the detailed chemical kinetics can be applied and solved in all zones fully coupled.

The assumptions (CHEMKIN-PRO 2010) pertaining to this model formulation are as follows. First of all, all zones are assumed to have the same, uniform pressure. Second, the mass or heat transfer between zones is assumed to be negligible and the only interaction between the zones is the compression work. Third, the total volume of the zones must equal the cylinder volume computed by the slider-crank relationship used in the single-zone internal combustion engine model. This constraint is used to determine the zonal and cylinder pressure (CHEMKIN-PRO 2010).

The governing equations for the multi-zone model are similar to those for the single-zone model, except for the additional superscript “ $i$ ” which represent the zone number, as shown in Eq. 8.12 (conservation of species) and Eq. 8.13 (energy equation) (CHEMKIN-PRO 2010).

$$(\rho^i V^i) \frac{dY_k^i}{dt} = (\dot{\omega}_k^i V^i) W_k^i \quad \text{for } i = 1, 2, \dots, N \text{ zones} \quad (8.12)$$

$$(\rho^i V^i) c_p^{-i} \frac{dT^i}{dt} = -V^i \sum_{k=1}^{K_g} (h_k^i \dot{\omega}_k^i) W_k^i + V^i \frac{dP}{dt} - \dot{Q}_{\text{loss}}^i \quad \text{for } i = 1, 2, \dots, N \text{ zones} \quad (8.13)$$

The single-zone and multi-zone models have been validated against the experimental work done by Jun et al. (2003). The operating conditions at which the prediction and measurements were compared are summarized in Table 8.3. The temperatures at intake valve closure (IVC) are used to calibrate the start of combustion for both the single-zone and multi-zone simulations. Figures 8.15 and 8.16

**Table 8.3** Initial conditions for the 0D simulation and the experiments from (Jun et al. 2003)

Parameters	Single- and multi-zone models	Experiment by Jun et al. (2003)
Engine speed (RPM)	800	800
IVC timing	-132 ATDC	-132 ATDC
Intake manifold temperature (K)	N/A	380
Intake manifold pressure (K)	N/A	1.6
Temperature at IVC (K)	417	N/A
Pressure at IVC (bar)	1.6	N/A
Wall temperature (K)	450	N/A
Equivalence ratio	0.2–0.45	0.2–0.45
Natural gas composition (mole fraction)	CH <sub>4</sub> —88%, C <sub>2</sub> H <sub>6</sub> —6%, C <sub>3</sub> H <sub>8</sub> —4%, C <sub>4</sub> H <sub>10</sub> —2%	CH <sub>4</sub> —88%, C <sub>2</sub> H <sub>6</sub> —6%, C <sub>3</sub> H <sub>8</sub> —4%, C <sub>4</sub> H <sub>10</sub> —2%

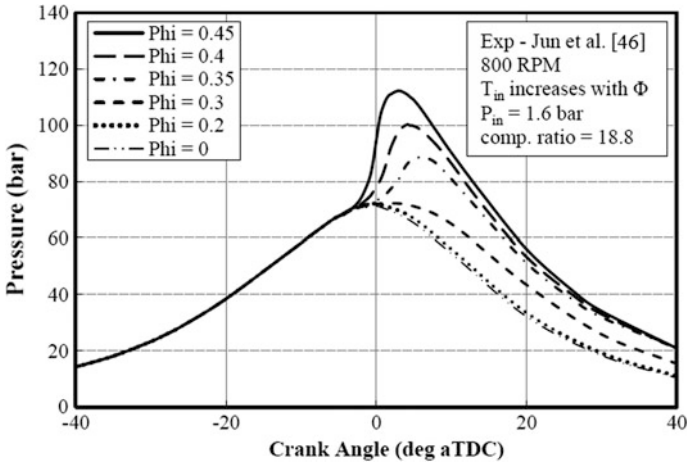


Fig. 8.15 In-cylinder pressure as a function of crank angle (Zheng and Caton 2012)

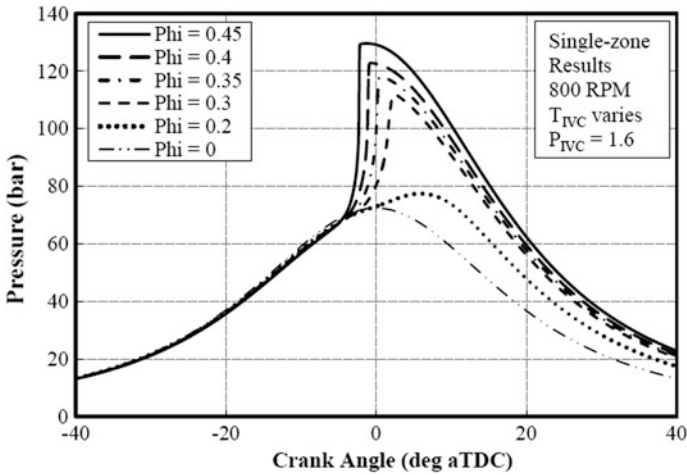


Fig. 8.16 In-cylinder pressure predicted as a function of crank angle (Zheng and Caton 2012)

show the measured and predicted pressure traces as a function of crank angle at various equivalence ratios. The results for multi-zone analysis have generally better agreement with the measurements than single-zone simulations and are provided in reference (Zheng 2012).

### 8.3.3 Engine Efficiencies for Using Natural Gas in Comparison with Gasoline

This section continues to compare natural gas with gasoline in terms of the indicated efficiency and volumetric efficiency at the best efficiency point under various operating conditions. Some of the fuel properties are shown in Table 8.4.

For all of the equivalence ratios presented here, about 3% difference in indicated efficiencies is observed between the two fuels. The efficiencies for the natural gas cases are lower largely due to the higher heat loss and lower specific heat ratio. Higher heat transfer is a direct result of higher combustion temperature. Lower specific heat ratio is caused by the higher mole fraction of the fuel species since natural gas has much lower molar stoichiometric air–fuel ratio than gasoline. A reduction of specific heat ratio reduces the amount of energy that can be extracted by the piston. At very low equivalence ratio, the chemical kinetics and combustion become slower and less complete which affects the thermal efficiency.

As the equivalence ratio increases, though combustion efficiency is improved, the heat loss as well as the fraction of heat loss out of total fuel energy is greater as a result of a higher combustion temperature. In addition, higher equivalence ratio leads to lower specific heat ratio which reduces the thermal efficiency. So the indicated efficiency reaches a peak around  $\phi$  equal to 0.3. In terms of the volumetric efficiency, it is straightforward that the gasoline cases are higher and the differences are larger at higher equivalence ratios, since volumetric efficiency is strongly affected by the intake temperature. This observation poses another issue for using natural gas in HCCI engines which is the relatively lower torque output at the same equivalence ratio due to the low volumetric efficiency (Zheng 2012).

The indicated thermal efficiency for both natural gas and gasoline increases as the engine speed increases. This increase is again related to the amount of heat transfer. Although the temperature at the IVC is higher at higher speeds, less time is allowed for transferring heat from the gas to the walls as the real time of one cycle becomes shorter as engine speed increases. The overall effect is to reduce the fraction of heat loss out of total fuel energy and to improve the thermal efficiency. The volumetric efficiency, however, decreases with the increase of engine speeds. Again, this is directly dictated by the higher IVC temperature at higher speeds. So running HCCI engines, either with gasoline or natural gas, at higher speeds could improve thermal efficiency but at the penalty of torque output (Zheng 2012).

**Table 8.4** Fuel properties of natural gas and gasoline

Fuel surrogate	Lower heating value (kJ/kmol)	Lower heating value (kJ/kg)	Stoichiometric A/F ratio, molar	Stoichiometric A/F ratio, mass	Adiabatic flame temperature (K)
Natural gas	$9.35 \times 10^5$	49,626	10.98	16.79	2596
Gasoline	$4.71 \times 10^6$	43,927	54.95	14.78	2636

The indicated thermal efficiency approximately remains nearly constant as the EGR level changes for both natural gas and gasoline cases. This might be attributed to the balance between lowered combustion temperature due to the EGR dilution effect and increased IVC temperature. Volumetric efficiency slightly drops as the EGR fraction increases and IVC temperature at best efficiency increases.

Having higher intake pressure slightly increases the indicated efficiency as a result of lower IVC temperature and corresponding lower heat loss. Furthermore, increasing intake pressure greatly improves the volumetric efficiency due to the increase in the mass of air–fuel mixture. These results imply that intake boosting is an attractive option to have for HCCI engines fueled with natural gas or other high octane fuels (Zheng 2012).

Using the single-zone model, Zheng (2012) conducted the analysis on the effect of operating conditions on the ignition characteristics, engine performance, and thermal efficiency of the HCCI engine. He found that the operating conditions, including equivalence ratio, engine speed, and intake pressure, have great influences on the HCCI ignition characteristics. The minimum required temperature at IVC for auto-ignition and complete combustion decreases as the equivalence ratio increases and the intake pressure increases, and increases as the engine speed increases. In addition to the operating conditions, compression ratio has an even greater effect on the minimum required temperature at IVC. For the natural gas case, the increase in compression ratio from 18 to 22 could reduce the requirement of the minimum required temperature at IVC by 40 K. The results imply that to reduce the intake temperature requirement for using natural gas, higher compression ratio, intake boosting, and relative lower engine speed are desirable.

The operating conditions have a great effect on the HCCI engine performance and efficiencies. The volumetric efficiency increases with the increase of equivalence ratio or intake pressure or the decrease of engine speed or exhaust gas recirculation level. The indicated thermal efficiency peaks at a certain equivalence ratio, and a higher or lower equivalence ratio than this value will decrease the indicated efficiency. The increase in engine speed improves the indicated efficiency, while the change in intake pressure and EGR level does not have a strong influence on the efficiency. In terms of the volumetric efficiency, intake boosting is a very desirable option to increase the specific power output, and operating at high engine speed is not attractive as it deteriorates the volumetric efficiency. In terms of the indicated efficiency, operating with a relatively lean mixture is still a desirable option for natural gas HCCI engines.

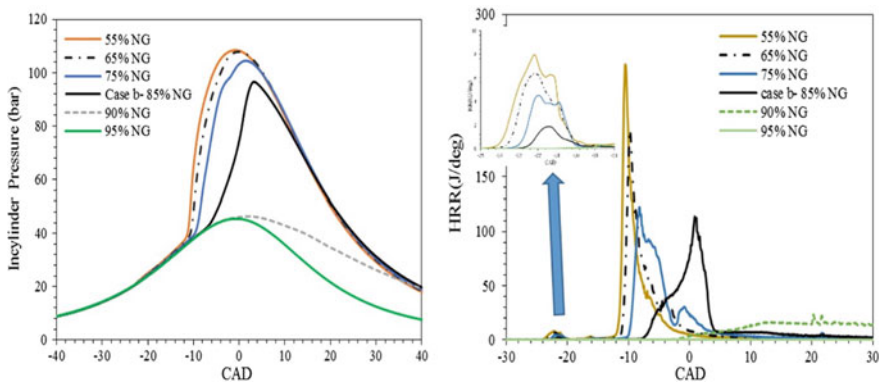
## 8.4 Combustion of Natural Gas in Reactivity Controlled Compression Ignition (RCCI) Engines

Reactivity controlled compression ignition (RCCI) concept can significantly improve the combustion process in terms of efficiency and exhaust gas emissions (Reitz and Duraisamy 2015). Recent interest has been raised to investigate RCCI combustion concept with NG/diesel fuels at different engine operating conditions (Ansari et al. 2016; Nieman et al. 2012; Zoldak et al. 2014, 2015; Doosje et al. 2014; Xu et al. 2016).

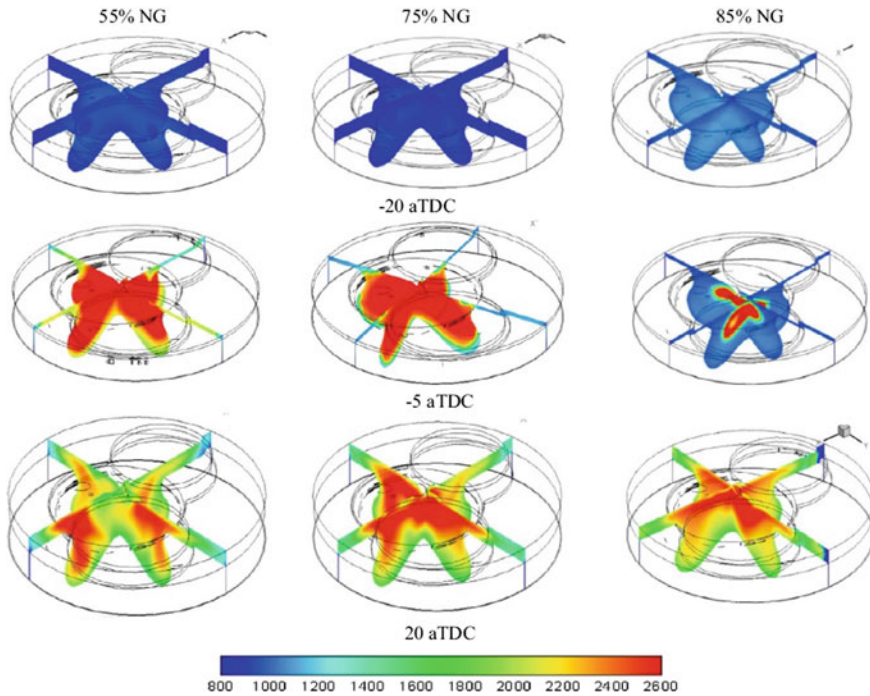
### 8.4.1 Effect of Energy-Based Premixed Ratio

Figure 8.17 shows the effect of premixed ratio (PR) on heat release rate (HRR) and in-cylinder pressure. The NG premixed ratios were composed to provide the same amount of the total energy for combustion. The graph shows that sweeping the PR from 55 to 95% increases the ignition delay and reduces the in-cylinder pressure and HRR (Poorghasemi et al. 2017).

Figure 8.18 shows that when the pressure ratio increases, the in-cylinder temperature decreases. This can result in the increase of HC emissions. It can also be explained by the fact that the crevice regions near the walls are usually colder in higher-pressure ratios. This will lower the combustion efficiency and increase the UHC emissions.



**Fig. 8.17** Effects of PR of in-cylinder mixture on in-cylinder pressure (left) and HRR (right) (Poorghasemi et al. 2017)



**Fig. 8.18** Effects of PR on in-cylinder temperature (Poorghasemi et al. 2017)

### 8.4.2 Effect of Injection Timing

#### The first injection timing

The effect of the first injection timing (SOI1) was once completed by changing SOI1 from 85° to 45° BTDC while maintaining SOI2 timing consistent at 20° BTDC. Seventy percentage of the total diesel fuel was injected at the first pulse and 30% at the second pulse. Advancing SOI1 timing from 85° to 45° BTDC results in delayed combustion and reduced peak in-cylinder pressure and HRR, as shown in Fig. 8.19. This happened due to the increase of the mixing time and better homogeneity of NG and diesel fuel, and as a result, less reactive mixture was prepared (Curran et al. 2012; Ma et al. 2013).

As the SOI1 timing is retarded,  $\text{NO}_x$  emission increases and HC and CO emissions decrease.  $\text{NO}_x$  increases due to the increase of the in-cylinder temperature. As shown in Fig. 8.20, the spray is impinged on the wall and enters the crevice cavity where due to the established lower temperature and lower volume to surface ratio zones HC and CO emissions increase. In later SOI1 at 45° BTDC, a greater



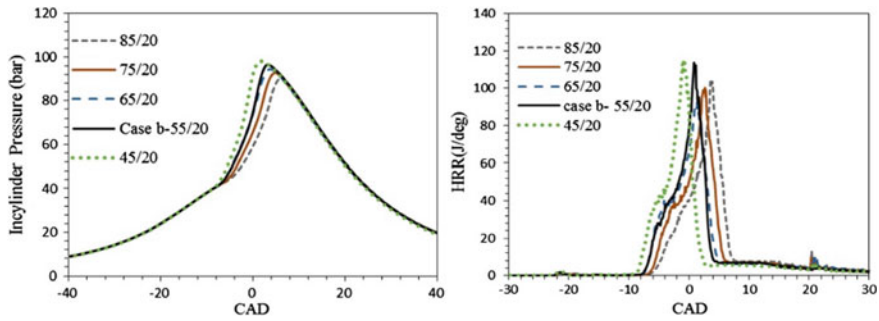


**Fig. 8.19** Effects of SOI1 timing on in-cylinder pressure (left) and HRR (right) for the engine operating condition (Poorghasemi et al. 2017)

amount of fuel is injected into the areas of piston bowl and squish areas with higher temperature and reactivity gradients, and consequently, lower levels of HC and CO produced.

### The second injection timing

The second fuel injection timing (SOI2) was changed from  $40^\circ$  to  $0^\circ$  BTDC, with constant SOI1 timing at  $55^\circ$  BTDC, as shown in Fig. 8.21. The results showed that retarding the SOI2 from  $40^\circ$  to  $0^\circ$  BTDC caused the retard of the combustion phasing, which caused the peak of in-cylinder pressure to be decreased. The second diesel injection pulse could not mix properly with in-cylinder mixture due to a very short time period, and this has caused the ignition delay to be increased.

Figure 8.22 shows the effect of SOI2 sweep on in-cylinder temperature. The simulation results showed that high local in-cylinder temperature region near TDC occurred that has caused the  $\text{NO}_x$  to be increased at earlier SOI2 timings. When SOI2 was advanced, the lowest carbon monoxide and unburnt hydrocarbon emissions were achieved. When the injection SOI2 was initiated at  $40^\circ$  BTDC, the flame could reach the whole combustion chamber, while at SOI2 at  $0^\circ$  BTDC there are more regions with lower temperatures, as shown in Fig. 8.22. This causes a lower combustion efficiency and higher levels of unburnt hydrocarbons and carbon monoxide emissions at later SOI2 timings (Paykani et al. 2015).

## 8.5 Advanced Ignition Systems for Natural Gas Combustion

Due to high octane number, natural gas engines can be operated at relatively higher compression ratios and leaner fuel–air mixtures, thus leading to higher thermal efficiencies and lower emissions. However, this can lead to considerable reduction in power density. This can be compensated by increasing the pressure of combustible charge at the end of a compression stroke. To ignite a leaner air–fuel charge

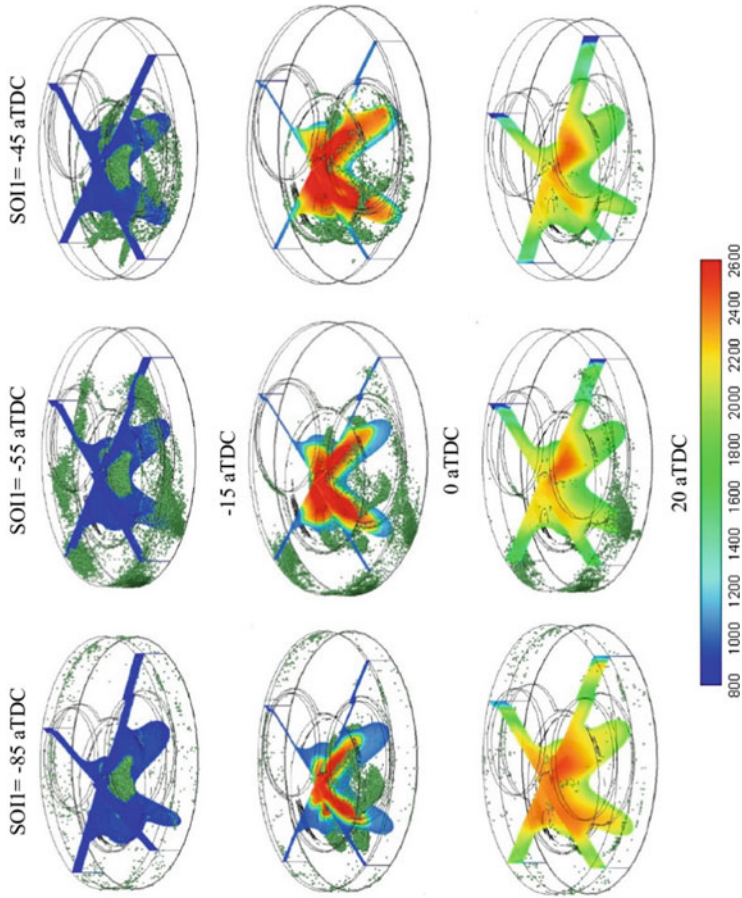


**Fig. 8.20** Effects of SOI on in-cylinder temperature for the engine operating condition (Poorghasemi et al. 2017)

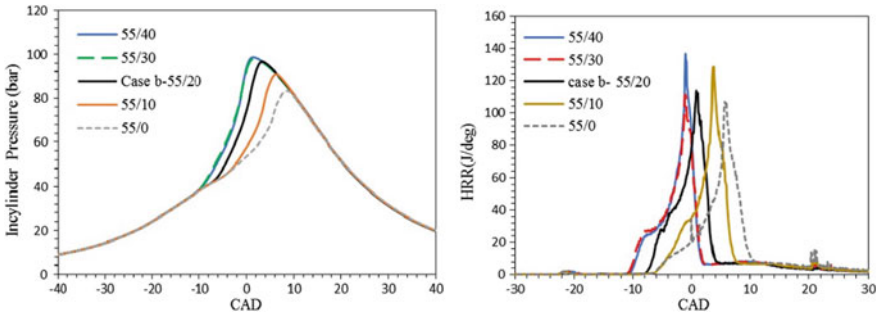


**Fig. 8.21** In-cylinder pressure (left) and HRR (right) versus SOI2 timing (Poorghasemi et al. 2017)

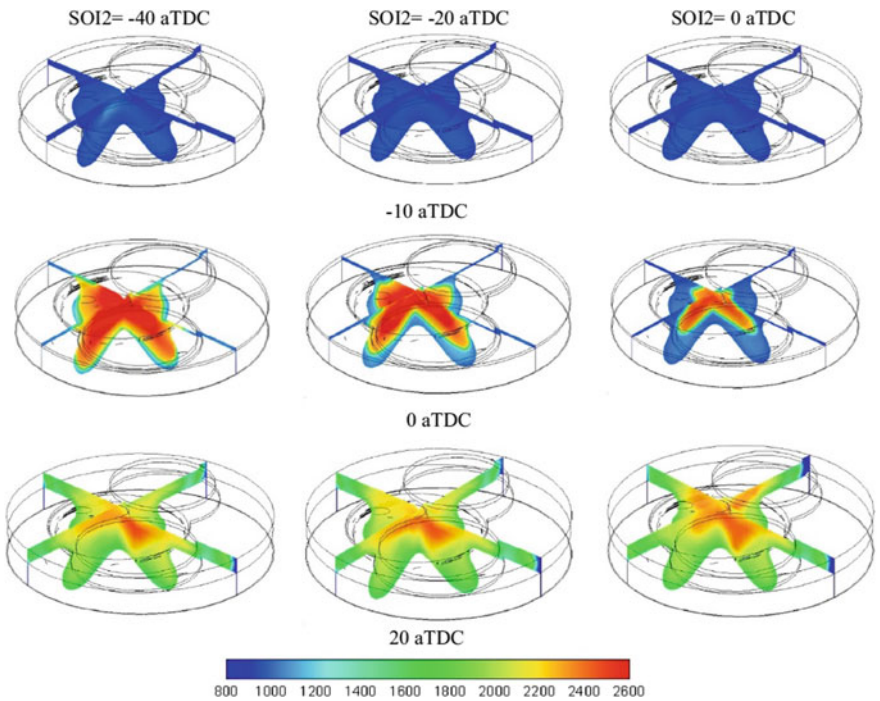


**Fig. 8.22** Effects of SOI2 on in-cylinder temperature (Poorghasemi et al. 2017)

at higher pressures requires using much higher voltage ignition systems. These high voltages significantly reduce the lifetime of spark plugs (Wienrotter et al. 2006). Such ignition systems are a laser-assisted ignition and a plasma-assisted ignition, which are discussed below.

### 8.5.1 Laser-Assisted Ignition Control

Laser can be used as an alternative ignition source for engines. Laser pulses delivered with the aid of a laser system are targeted inside the combustion chamber with fuel–air mixture. The experimental laser ignition system was designed and constructed by Srivastava et al. (2011) and is shown in Fig. 8.23.

The obtained high-speed camera images that display the development of the early flame kernel stages with time had been recorded using shadowgraphy technique. The images were obtained at 54,000 fps. The snapshots were captured at an interval of 18.5 ms for a combustion event. From these images, we can get an idea on how the flame kernel is developed with time for selected NG–air ratios ( $\lambda = 1.2$  and  $\lambda = 1.6$ ). Figure 8.24 shows the sequential snapshots of flame kernel development at unique timescales for  $\lambda = 1.2$ . Timescales of the first four snapshots were kept constant; however, the timescales for the final four snapshots were different due to the fact of longer combustion duration for the leaner mixtures. The vertical and horizontal dimensions of all images have been kept constant at 1.15 and 1.45 cm, respectively.

Srivastava et al. (2011) found that the flame kernel propagation distance was consistently decreasing with leaner mixtures  $\lambda = 1.6$ , as shown in Fig. 8.25. These findings suggest that the volumetric growth of the flame kernel reduces substantially with the reduction of NG–air mixture strength and a practical laser ignition system applied to the engine will not be able to deal with NG–air mixtures leaner than  $\lambda = 1.6$ .

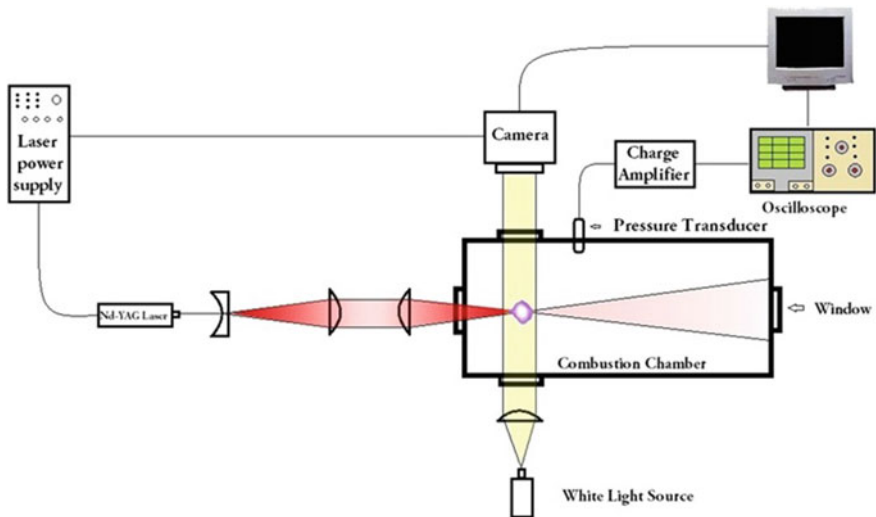


**Fig. 8.23** Schematic diagram of laser ignition shadowgraphy of NG–air mixture (Srivastava et al. 2011)

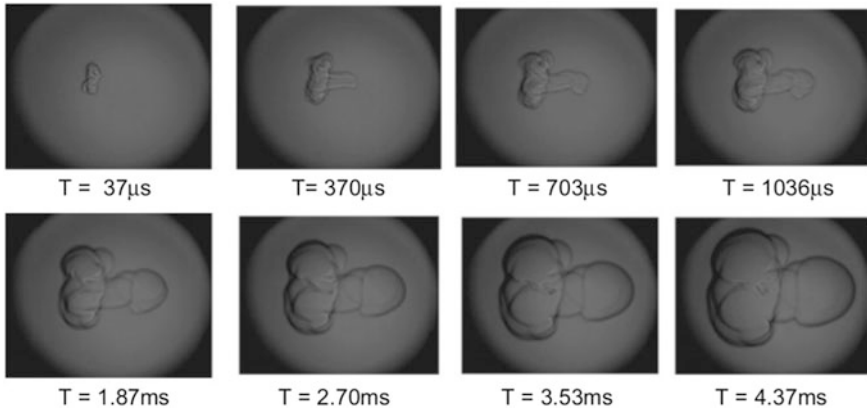


**Fig. 8.24** Shadowgraph image of flame kernel development ( $\lambda = 1.2$ ) (Srivastava et al. 2011)

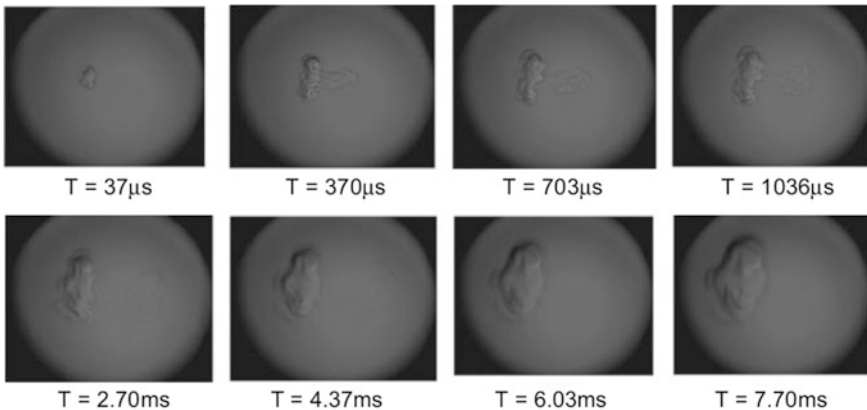


**Fig. 8.25** Shadowgraph image of flame kernel development ( $\lambda = 1.6$ ) (Srivastava et al. 2011)

To observe the laser ignition process under the reciprocating engine conditions, Dumitrache et al. (2017) used rapid compression machine (RCM) shown in Fig. 8.26. Details of this setup are given in the reference (Dumitrache et al. 2017).

The approach validated in this study used to be for a laser-ignited mixture of  $\text{CH}_4$ -air at an equivalence ratio of  $= 0.5$  (Dumitrache et al. 2017), as shown in Fig. 8.27. The lean condition used to be chosen to restrain the flame propagation speed, hence allowing capturing numerous frames of the flame propagation, given the limitations of the imaging system. In these experiments, only 30% of the mixture has been consumed by the propagating flame and the chemical heat release overcomes the heat losses to the wall that causes the flame to become turbulent with cellular structure as shown in Fig. 8.27.

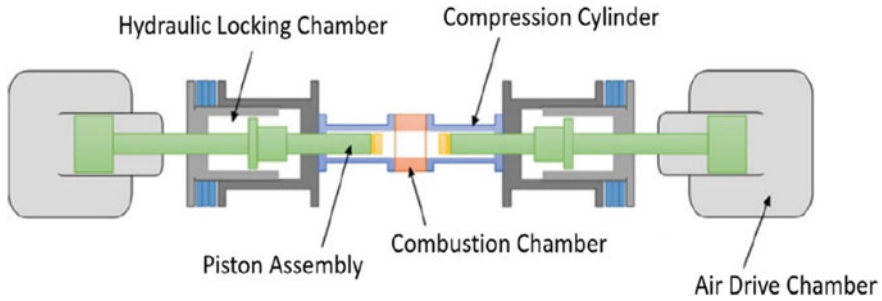


**Fig. 8.26** Schematic drawing depicting the main components of the RCM (Dumitrache et al. 2017)

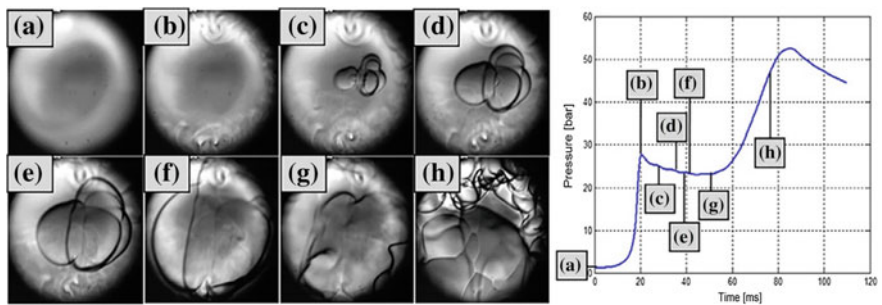


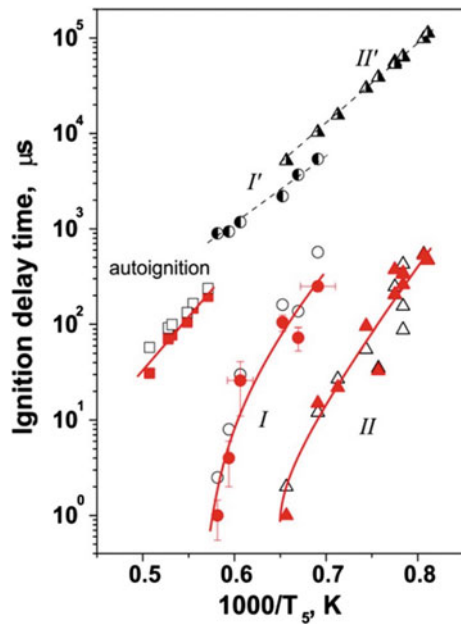
**Fig. 8.27** Schlieren high-speed photography images of a laser-ignited  $\text{CH}_4$ -air mixture ( $\phi = 0.5$ ) inside the RCM. The images show the flame development and spread. The pressure trace shown at the right is used to correlate the frames with the actual RCM firing. The field of view is 20 mm (Dumitrache et al. 2017)

### 8.5.2 Plasma-Assisted Ignition and Combustion Control

In latest years, the plasma-assisted combustion mechanisms have been validated through experimentation under controlled conditions and by the way of evaluating the effects with numerical simulations of discharge and combustion processes. Researchers became curious about non-equilibrium plasma for ignition and combustion control (Starikovskii 2005, 2006) thanks to the new potentialities for ignition and flame stabilization that are supplied by the plasma-assisted approach. The most important distinction between the traditional combustion and plasma-assisted combustion is the ignition initiation mechanism.

Kosarev et al. (2008) and Aleksandrov et al. (2009) have observed a correlation between the ignition delay time and the temperature for the  $\text{CH}_4/\text{O}_2/\text{Ar}$  mixture. The fuel discharge causes a drastic reduction in the ignition delay time and allows the mixture to ignite at notably lower temperatures. Figure 8.28 shows the ignition delay time in a  $\text{CH}_4/\text{O}_2/\text{Ar} = 3.3:6.7:90$  mixture as a function of temperature for

**Fig. 8.28** Ignition delay time in a  $\text{CH}_4/\text{O}_2/\text{Ar} = 3.3:6.7:90$  mixture as a function of temperature for auto-ignition and ignition (I–II) with the plasma discharge. The closed and open symbols correspond to measurements and calculations, respectively, and the solid curves correspond to experimental data. The dashed lines I' and II' and the semi-closed symbols correspond to the calculations of the auto-ignition delay times as those in regions I and II (Kosarev et al. 2008; Aleksandrov et al. 2009)



auto-ignition and (I–II) ignition with the plasma discharge. The diagram indicates the comparison of the measured ignition delay time with and without plasma at the equal initial gas densities. As viewed in Fig. 8.28, these times may vary by two or three orders of magnitude.

Michael et al. (2010) showed that the ignition in  $\text{CH}_4$ –air mixtures can be performed using low energy seed laser pulses and an overlapping subcritical microwave pulse. Very susceptible ionization by a laser localized the deposition of microwave energy and caused fast heating, high temperatures, and ignition. The same research team (Michael et al. 2010) also developed a coupled one-dimensional gas-dynamic/plasma-dynamic model to follow the rapidly evolving plasma and gas properties carried out through this interaction. By growing the pulse power by a factor of 3, the ignition used to be discovered alongside the seed laser path. In this case, a much larger area of strong coupling with the microwave (MW) energy was discovered in the shadowgraph snapshots as shown in Fig. 8.29 (Michael et al. 2010). For a large number of combustion-driven engines, transient plasma ignition involving quick ignition pulses (typically 10–50 ns) has been shown to efficiently minimize ignition delays and enhance engine performance compared to the conventional spark ignition.

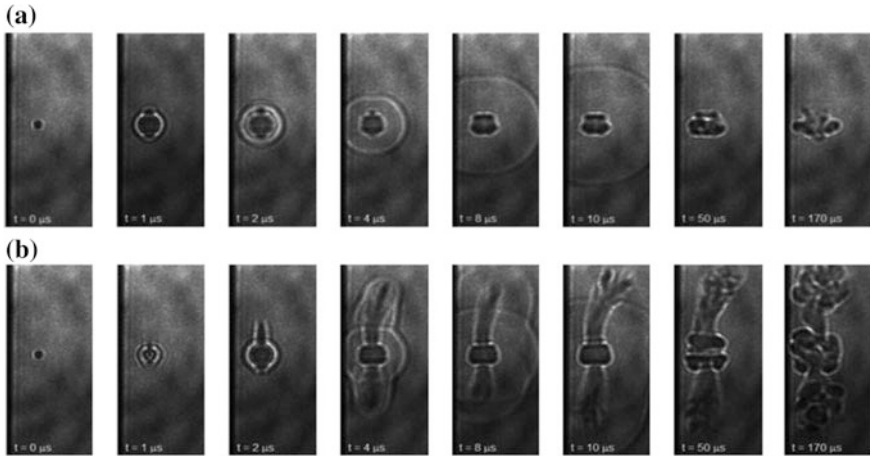


**Fig. 8.29** Laser pulse–MW evolution in air. **a** Laser spot evolution. **b** Laser + MW evolution (Michael et al. 2010)

## 8.6 Conclusion

The chapter summarizes the advanced combustion and ignition technologies with natural gas as a fuel for application in internal combustion engines. Natural gas is considered the direct alternative to replace the crude oil-derived liquid fuels for better energy efficiency and cleaner environment. It was demonstrated by several researchers that the novel combustion technologies such as PREMIER, HCCI, and RCCI can provide better fuel efficiency and emission reduction. However, these technologies should be further developed to become applicable and feasible to a wider range of engine design and operating conditions with natural gas.

These technologies will become even more useful during the transport electrification era. With the requirements to introduce more electric vehicles in transportation network, more challenges will appear to meet required power and mileage levels, especially for commercial heavy-duty vehicles and trucks. The analysis shows that in the near future it will not be possible to convert the entire heavy-duty vehicles fleet to run on electric batteries only, and therefore, the hybrid powertrain systems will have to be used to ensure the cost-effective and reliable operation. In this situation, hybrid powertrain systems with natural gas as a fuel for internal combustion engines will become a feasible solution.

Along with the novel combustion technologies for effective burning of fuel inside the engine cylinders, more advanced ignition initiation technologies are also being developed and applied to conventional and future internal combustion engines. Such technologies are laser-assisted and plasma-assisted ignition systems. Lasers are becoming feasible candidates as alternative ignition systems in internal combustion engines. This technology can be applied to initiate the combustion of high octane number natural gas mixtures. Plasma formation does not always



imply that ignition has to take place. Only if the energy content of the plasma is excessive enough, then the mixture of NG–air is ignited by a flame kernel, which may also extend or extinguish. This plasma source can be applied as a stand-alone or additional source to initiate the combustion in internal combustion engines.

Natural gas can play an important role as an actual game changer in energy and transport sectors for energy security. For the consumer’s perspectives to make a swap from current liquid fuels to compressed natural gas will be more compelling than for other alternatives such as ethanol or electricity.

## References

- Agarwal AK, Singh AP, Maurya RK (2017) Evolution, challenges and path forward for low temperature combustion engines. *Prog Energy Combust Sci* 61(7):1–56
- Aleksandrov NL, Kindysheva SV, Kosarev IN, Starikovskaia SM, Starikovskii AY (2009) Mechanism of ignition by nonequilibrium plasma. *Proc Combust Inst* 32:205–212
- Ando T, Isobe Y, Sunohara D, Daisho Y, Kusaka J (2003) *JSAE Rev* 24:33–40
- Ansari E, Poorghasemi K, Irdmousa BK, Shahbakhti M, Naber J (2016) Efficiency and emissions mapping of a light duty diesel-natural gas engine operating in conventional diesel and RCCI modes. In: SAE international powertrain, fuel and lubricants conference, 2016-01-2309
- Aoyama T, Hattori Y, Mizuta J, Sato Y (1996) An experimental study on premixed charge compression ignition gasoline engine. SAE technical paper SAE960081
- Asad U, Divekar P, Zheng M, Tjong J (2013) Low temperature combustion strategies for compression ignition engines: operability limits and challenges. SAE 2013-01-0283
- Azimov U, Tomita E, Kawahara N, Harada Y (2011) Premixed mixture ignition in the end-gas region (PREMIER) combustion in a natural gas dual-fuel engine: operating range and exhaust emissions. *Int J Engine Res* 12:484–497
- Benajes J, Molina S, Garcia A, Monsalve-Serrano J (2015) Effects of low reactivity fuel characteristics and blending ratio on low load RCCI performance and emissions in a heavy-duty diesel engine. *Energy* 90:1261–1271
- Caton J (2011) Thermodynamic advantages of low temperature combustion (LTC) engines using low heat rejection (LHR) concepts. SAE 2011-01-0312
- CHEMKIN-PRO Theory Manual, 2010
- Christensen M, Johansson B (1998) Influence of mixture quality on homogeneous charge compression ignition. SAE technical paper 982454
- Curran S, Hanson R, Wagner R (2012) Reactivity controlled compression ignition combustion on a multi cylinder light-duty diesel engine. *Int J Engine Res* 13(3):216–225
- Dempsey A, Walker N, Gingrich E, Reitz R (2014) Comparison of low temperature combustion strategies for advanced compression ignition engines with a focus on controllability. *Combust Sci Technol* 186(2):210–241
- Doosje E, Willems F, Baert R (2014) Experimental demonstration of RCCI in heavy duty engines using diesel and natural gas. SAE 2014-01-1318
- Doughty GE, Bell SR, Midkiff KC (1992) *J Eng Gas Turbines Power* 114:459–465
- Dumitrache C, Baumgardner M, Boissiere A, Maria A, Roucis J, Marchese AJ, Yalin A (2017) A study of laser induced ignition of methane–air mixtures inside a rapid compression machine. *Proc Combust Inst* 36:3431–3439
- El Merhubi H, Keromnes A, Catalano G, Lefort B et al (2016) A high pressure experimental and numerical study of methane ignition. *Fuel* 177:164–172

- Gharehghani A, Hosseini R, Mirsalim M, Jazayeri A, Yusaf T (2015) An experimental study on reactivity controlled compression ignition engine fueled with biodiesel/natural gas. *Energy* 89:558–567
- Gharehghani A, Mirsalim M, Jazayeri A (2016) Experimental study on low temperature combustion dual fuel biodiesel/natural gas engine. ASME technical paper 1:V001T03A001
- Gulder OL (1984) Correlations of laminar combustion data for alternative S.I. engine fuels. SAE technical paper 841000
- Heywood JB (1988) *Internal combustion engine fundamentals*. McGraw-Hill Book Company, New York
- Hosmath RS, Banapurmath NR, Khandal SV et al (2016) Effect of compression ratio, CNG flow rate and injection timing on the performance of dual fuel engine operated on Honge oil methyl ester (HOME) and compressed natural gas (CNG). *Renewable Energy* 93(8):579–590
- Intenan S et al (2014) Impact of low temperature combustion attaining strategies on diesel engine emissions for diesel and biodiesels: a review. *Energy Convers Manage* 80:329–356
- Jia M, Xie M, Wang T, Peng Z (2011) The effect of injection timing and intake valve close timing on performance and emissions of diesel PCCI engine with a full engine cycle CFD simulation. *Appl Energy* 88(9):2967–2975
- Jun D, Ishii K, Lida N. Combustion analysis of natural gas in a four stroke HCCI engine using experiment and elementary reactions calculation. SAE paper no. 2003-01-1089
- Kakae A, Rahnama P, Paykani A (2015) Influence of fuel composition on combustion and emissions characteristics of natural gas/diesel RCCI engine. *J Nat Gas Sci Eng* 25:58–65
- Kokjohn S, Hanson R, Splitter D, Reitz R (2010) Experiments and modeling of dual fuel HCCI and PCCI combustion using in-cylinder fuel blending. *SAE Int J Eng* 2(2):24–39
- Kokjohn S, Hanson R, Splitter D, Reitz R (2011) Fuel reactivity controlled compression ignition (RCCI): a pathway to controlled high-efficiency clean combustion. *Int J Eng Res* 12:209–226
- Kosarev IN, Aleksandrov NL, Kindysheva SV, Starikovskaia SM, Starikovskii AYU (2008) Kinetics of ignition of saturated hydrocarbons by nonequilibrium plasma: CH<sub>4</sub>-containing mixtures. *Combustion and Flame* 154:569–586
- Laguitton O, Crua C, Cowell T, Heikal M, Gold M (2007) The effect of compression ratio on exhaust emissions from a PCCI diesel engine. *Energy Convers Manage* 48(11):2918–2924
- Li J, Yang W, Ana H, Zhao D (2015a) Effects of fuel ratio and injection timing on gasoline/biodiesel fueled RCCI engine: a modeling study. *Appl Energy* 155:59–67
- Li J, Yang W, An H, Zhou D, Yu W, Wang J et al (2015b) Numerical investigation on the effect of reactivity gradient in an RCCI engine fueled with gasoline and diesel. *Energy Convers Manage* 92:342–352
- Liang L, Reitz RD, Iyer CO, Yi J (2007) Modeling knock in spark-ignition engines using a G-equation combustion model incorporating detailed chemical kinetics. SAE technical paper 2007-01-0165
- Long L (2006) *Multidimensional modeling of combustion and knock in spark-ignition engines with detailed chemical kinetics*. University of Wisconsin-Madison
- Ma SH, Zheng Z, Liu H, Zhang Q, Yao M (2013) Experimental investigation of the effects of diesel injection strategy on gasoline/diesel dual-fuel combustion. *Appl Energy* 109:202–212
- Michael JB, Dogariu A, Shneider MN, Miles RB (2010) Subcritical microwave coupling to femtosecond and picosecond laser ionization for localized, multipoint ignition of methane/air mixtures. *J Appl Phys* 108(9) (Nov 1 2010)
- Molina S, Garcia A, Pastor J, Belarte E, Balloul I (2015) Operating range extension of RCCI combustion concept from low to full load in a heavy-duty engine. *Appl Energy* 143:211–227
- Musculus Mark PB, Miles Paul C, Pickett Lyle M (2013) Conceptual models for partially premixed low temperature diesel combustion. *Prog Energy Combust Sci* 39(2–3):246–283
- Nieman D, Dempsey A, Reitz RD (2012) Heavy-duty RCCI operation using natural gas and diesel. *SAE Int J Eng* 5(2):270–285
- Paykani A, Kakae A, Rahnama P, Reitz R (2015) Effects of diesel injection strategy on natural gas/diesel reactivity controlled compression ignition combustion. *Energy* 90:814–826

- Peters N (2000) *Turbulent Combustion*. Cambridge University Press, Cambridge, ISBN 9780521660822
- Pitsch BH (2002) A *G*-equation formulation for large-eddy simulation of premixed turbulent combustion. *Cent Turbul Res Annu* 4–7
- Poorghasemi K, Khoshbakhti Saray R, Ansari E, Khoshbakht Irdmousa B, Shahbakhti M, Naber JD (2017) Effect of diesel injection strategies on natural gas/diesel RCCI combustion characteristics in a light duty diesel engine. *Appl Energy* 199:430–446
- Reitz R (2013) Directions in internal combustion engine research. *Combust Flame* 160:1–8
- Reitz RD, Duraisamy G (2015) Review of high efficiency and clean reactivity controlled compression ignition (RCCI) combustion in internal combustion engines. *Prog Energy Combust Sci* 46:12–71
- Roy MM, Tomita E, Kawahara N, Harada Y, Sakane A (2009) Effect of fuel injection parameters on engine performance and emissions of a supercharged producer gas-diesel dual fuel engine. SAE technical paper 2009-01-1848
- Scott Guerry E, Raihan Mostafa S, Srinivasan Kalyan K et al (2016) Injection timing effects on partially premixed diesel-methane dual fuel low temperature combustion. *Appl Energy* 162 (1):99–113
- Splitter D, Kokjohn S, Rein K, Hanson R, Sanders S, Reitz R (2010) An optical investigation of ignition processes in fuel reactivity controlled PCCI combustion. SAE paper 2010-01-0345
- Srivastava DK, Dharamshi K, Agarwal AK (2011) Flame kernel characterization of laser ignition of natural gas–air mixture in a constant volume combustion chamber. *Opt Lasers Eng* 49:1201–1209
- Starikovskaia SM (2006) Plasma assisted ignition and combustion. *J Phys D* 39:265–299
- Starikovskii AY (2005) Plasma supported combustion. *Proc Comb Inst* 30:2405–2417
- Tamagna D, Gentili R, Ra Y, Reitz RD (2008) Multidimensional simulation of the influence of fuel mixture composition and injection timing in gasoline- diesel dual-fuel applications. SAE technical paper 2008-01-0031
- Tomita E, Kawahara N, Piao Z, Yamaguchi R (2002) Effects of EGR and early injection of diesel fuel on combustion characteristics and exhaust emissions in a methane dual-fuel engine. SAE technical paper 2002-01-2723
- Tomita E, Kawahara N, Kinoshita Y, Komoda T, Sakane A (2004) Combustion characteristics and performance of supercharged single cylinder natural gas engine ignited with pilot injection of diesel fuel. In: FISITA 2004, World Automotive Congress, Paper F2004V229
- Tomita E, Fukatani N, Kawahara N, Maruyama K (2007) Combustion in a supercharged biomass gas engine with micro-pilot ignition-effects of injection pressure and amount of diesel fuel. *J KONES Powertrain Transport* 14(2):513–520
- Tomita E, Harada Y, Kawahara N, Sakane A (2009) Effect of EGR on combustion and exhaust emissions in supercharged dual-fuel natural gas engine ignited with diesel fuel. SAE technical paper 2009-01-1832
- Union Gas Limited, Chemical composition of natural gas. Available <http://www.uniongas.com/aboutus/aboutng/composition.asp>. Accessed 08 July 2018
- Wagemakers AMLM, Leermakers CAJ (2012) Review on the effects of dual-fuel operation, using diesel and gaseous fuels, on emissions and performance. SAE technical paper 2012-01-0869
- Wienrotter M, Srivastava DK, Iskra K, Graf J, Kopecek H, Klausner J et al (2006) Laser ignition of engines: a realistic option. *Proc SPIE* 6053:605316
- Xu M, Cheng W, Li Z, Zhang H, An T, Meng Z (2016) Pre-injection strategy for pilot diesel compression ignition natural gas engine. *Appl Energy* 179:1185–1193
- Yang S, Reitz RD (2010) A continuous multicomponent fuel flame propagation and chemical kinetics model. *Intern Combust Engines* 132(7):072802
- Yap D, Megaritis A, Peucheret S, Wyszynski ML, Xu H. Paper presented at fuels & lubricants meeting & exhibition, Toulouse, France. SAE paper no. 2004-01-1972
- Yap D, Peucheret SM, Megaritis A, Wyszynski ML, Xu H (2006) *Int J Hydrogen Energy* 31:587–595

- Zheng J (2012) The potential of using natural gas in HCCI engines: results from zero- and multi-dimensional simulations. PhD Dissertation, Texas A&M University, College Station
- Zheng J, Caton J (2012) Effects of operating parameters on nitrogen oxides emissions for a natural gas fueled homogeneous charged compression ignition engine (HCCI): results from a thermodynamic model with detailed chemistry. *Appl Energy* 92:386–394
- Zheng QP, Zhang HM, Zhang DF (2005) A computational study of combustion in compression ignition natural gas engine with separated chamber. *Fuel* 84:1515–1523
- Zhou D, Yang W, An H, Li J, Shu C (2015) A numerical study on RCCI engine fueled by biodiesel/methanol. *Energy Convers Manage* 89:798–807
- Zoldak P, Sobiesiak A, Bergin M, Wickman D (2014) Computational study of reactivity controlled compression ignition (RCCI) combustion in a heavy-duty diesel engine using natural gas. SAE paper 2014-01-1321
- Zoldak P, Sobiesiak A, Wickman D, Bergin M (2015) Combustion simulation of dual fuel CNG engine using direct injection of natural gas and diesel. *SAE Int J Engines* 8(2):846–858

## Chapter 9

# Advances of the Natural Gas/Diesel RCCI Concept Application for Light-Duty Engines: Comprehensive Analysis of the Influence of the Design and Calibration Parameters on Performance and Emissions



Giacomo Belgiorno, Gabriele Di Blasio and Carlo Beatrice

**Abstract** The increasing energy demand together with the severe emission legislation of the transportation sector requires effective solutions for automotive propulsion systems. The transportation sector is responsible for 23% of the total CO<sub>2</sub> in the European Union. Advanced combustion concepts combined with alternative fuels, if properly tuned, have the potential to increase the efficiencies and lower emissions, compared to the conventional diesel or spark-ignition combustion. This is particularly valid when natural gas (a low reactivity fuel with low auto-ignition characteristics) and fossil diesel (the high reactivity one with high auto-ignition characteristics) are fuelled together in a compression ignition engine approaching the reactivity controlled compression ignition (RCCI) combustion. However, the use of these fuels in an advanced compression ignition engine increases the degrees of freedom for the tuning of the whole system. In order to carry out robust calibrations for efficiency maximization and pollutant minimization, in the whole engine-operating area, a detailed sensitivity analysis to the functional parameters versus fuel consumption and pollutant emissions is a paramount. Based on the experiences carried out at the laboratory of Istituto Motori of CNR, the chapter analyses the correlation between the main design and operating parameters versus the engine performance, providing a scale of degree of influence of the selected parameters as useful information for the engine calibration engineers.

---

G. Belgiorno (✉) · G. Di Blasio · C. Beatrice  
Istituto Motori, Consiglio Nazionale Delle Ricerche, Via G. Marconi, 4, 80125 Naples, Italy  
e-mail: [giacomo.belgiorno@uniparthenope.it](mailto:giacomo.belgiorno@uniparthenope.it)

© Springer Nature Singapore Pte Ltd. 2019  
K. K. Srinivasan et al. (eds.), *Natural Gas Engines*, Energy, Environment,  
and Sustainability, [https://doi.org/10.1007/978-981-13-3307-1\\_9](https://doi.org/10.1007/978-981-13-3307-1_9)

**Keywords** Dual fuel · Natural gas · Engine performance optimization

## 9.1 Combustion Concepts in Compression Ignition Engines

### 9.1.1 Conventional Diesel Combustion

Due to its higher thermal conversion efficiency compared to spark-ignition (SI) engines, the compression ignition (CI) engine commonly called diesel engine (from its inventor Rudolf Diesel) is the most diffused engines for medium and heavy-duty applications like commercial vehicles, rail and marine applications. The diesel fuel is injected directly into the cylinder at the end of the compression stroke and then ignited due to the high temperature and pressure reached by the air–fuel mixture near to the top dead centre (TDC). High fuel injection pressure is used to have a desired fuel spray penetration into the combustion chamber with high velocity and good atomization levels. Figure 9.1 shows the typical heat release rate (HRR) trace from the conventional diesel combustion (CDC); the first phase is characterized by the short period called ignition delay (ID) that represents the period between the start of combustion (SoC) and the start of injection (SoI); after the ID period, a spontaneous auto-ignition process starts due to the high temperature and pressure of air–fuel mixture, and this phase is called premixed combustion characterized by the high heat-release gradient. After the premixed combustion and during the injection process, the HRR is controlled by the rate at which mixture becomes available for burning (mixing-controlled combustion phase). Finally, the heat release continues at a lower rate well into the expansion stroke (late combustion phase) (Heywood 1988).

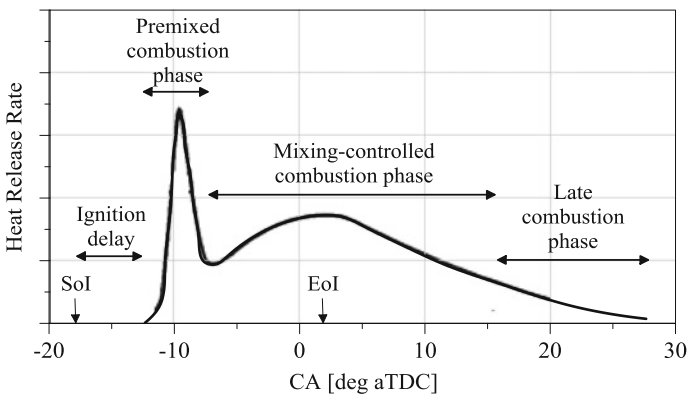


**Fig. 9.1** Typical heat release rate identifying different conventional diesel combustion phases

The CDC is characterized by several advantages compared to the SI engine. Higher combustion efficiency, with a higher brake thermal efficiency due to the higher compression ratio, adopted generally around 15:1–18:1 instead of 9:1–10:1 for SI engines. No risk of pre-ignition or knock phenomena is observed due to the different diesel fuel characteristics compared to the gasoline.

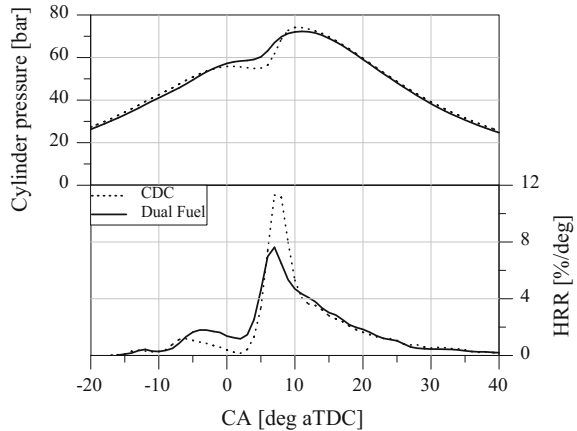
One of the disadvantages of the compression ignition (CI) engines is the complex fuel injection system that has a high impact on the complexity of the control strategy and on the cost of engines. While regarding the engine-out emissions, the CI engines have a significant problem regarding the  $\text{NO}_x$  and soot emissions trade-off (Dec 1997). This is explained by the local fuel-rich zones and high local combustion temperatures that give rise to soot and  $\text{NO}_x$ , respectively. Fuel properties are also important for the likelihood of soot production. However, Kufferath et al. present an interesting result obtained in a diesel engine for passenger cars in real driving condition, they have demonstrated that combining high level of EGR, thermal management strategy and aftertreatment systems (SCR and DPF) permits to reduce drastically the nitrogen oxide emissions under real driving conditions without penalizing the  $\text{CO}_2$  emissions as well (Kufferath et al. 2018).

### ***9.1.2 Dual Fuel Reactivity Controlled Compression Ignition (RCCI)***

Commonly, the dual fuel concept adopted the high reactive direct-injected diesel, while different low reactive fuels are used for the port injection (i.e., natural gas, ethanol and gasoline) (Di Blasio et al. 2013, 2015; Benajes et al. 2015). A dual fuel RCCI combustion process involves two different fuels with different reactivity (auto-ignition resistance). The low reactive fuel is injected via port fuel injector fitted in the intake manifold and the fuel is premixed with air during the intake stroke, while the high reactive fuel is direct injected adopting the common diesel fuel injection system.

The application of the dual fuel combustion concept consists of three main phases. A homogeneous charge of air and low reactive fuel is compressed while near the TDC a high reactive fuel is direct injected and mixed with the air–gas mixture during the ignition delay. After the ignition delay, the high reactive fuel is ignited by the high pressure and temperature from the compression, which in turn ignites the main fuel (low reactive fuel). Finally, the ensuing combustion occurs mainly through the flame propagation of the high auto-ignition fuel–air mixture (Königsson 2014; Karim 2015). Figure 9.2 shows an example of the in-cylinder pressure and HRR traces of the conventional diesel and dual fuel combustions. Both cases suppose the double direct diesel injection strategy. A substitution ratio ( $S_r$ ) equal to 50% for the DF combustion, defined as (see Eq. 9.1) the ratio between the methane fuel mass and the total fuel mass (diesel plus methane), is adopted. The DF case shows a higher low-temperature heat release compared to the CDC.

**Fig. 9.2** In-cylinder pressure and heat release rate (HRR) for CDC and dual fuel combustion ( $S_r = 50\%$ ) at 2000 rpm and 7.0 bar of IMEP



This is due to the involvement of the premixed methane during the pilot diesel combustion. As a consequence, the max peak of the premixed combustion phase lowers and the combustion speed increases leading to advantages in terms of  $\text{NO}_x$  and soot formation.

In recent years, alternative combustion concepts for dual fuel engines have been investigated. More attention to the diesel-ignited gas engine since the engine is well suited for reactivity controlled compression ignition (RCCI) combustion (Kokjohn et al. 2011). In this concept, the high reactive fuel is injected early during the compression stroke compared to the conventional dual fuel, to promote mixing within the low reactive fuel and control the combustion characteristics via the reactivity of the mixture (Valladolid et al. 2017). In contrast to the conventional dual fuel, the diesel is injected early in the compression phase with either multiple injections or one single injection. RCCI has proven to be effective in achieving high fuel efficiency and low pollutant emissions (Splitter et al. 2011). Function of the fuel reactivity, Curran et al. (2014) defined the RCCI like a combustion process between the partially premixed combustion (PPC) (Belgiorno et al. 2018a) and direct injection compression ignition (DICI) combustion. RCCI uses two fuels with varying proportions while the PPC runs efficiently on any fuel by adjusting fuel injection and other engine parameters.

One of the advantages of the dual fuel combustion engines is the application of the concept in conventional diesel engines thus without substantial hardware modification. Moreover, adopting methane as alternative fuel permits a significant  $\text{CO}_2$  emission reduction (Besch et al. 2015) with a maximum theoretical reduction of 25%, related to the chemical characteristics, supposing the same engine efficiency. However, it has to be considered that one of the main problems of the DF combustion is the  $\text{CH}_4$  slip, especially at low load condition. It has to be taken into account that the methane greenhouse gas potential (GHP) is about 25% more than that of  $\text{CO}_2$ . For this reason, a dedicated development of combustion calibration and



aftertreatment systems is necessary to reduce the CO<sub>2</sub> equivalent emission to promote the development of DF combustion engines.

Thus, the dual fuel combustion concept would permit the combination of the benefits of the high diesel engine thermodynamic efficiency with the use of alternative fuels (lower CO<sub>2</sub>). Compared to the conventional combustion, the DF exhibits same stable combustion (e.g., in terms of the cycle-to-cycle variation), and combustion noise and phasing controls thank to the flexibility of the diesel fuel injection strategies (Di Blasio et al. 2017).

As widely reported in literature, the main DF disadvantages are related to the lower combustion efficiency (typically in the range of 85–95%) due to the low reactive premixed fuel trapped in the crevice volumes and not involved by the flame front (Di Blasio et al. 2013, 2015). Additional issues derive from the non-optimized combustion chamber for DF RCCI operation as in this case study. While the DF technology is almost consolidated for the heavy-duty and marine engines (e.g., Volvo and Wartsila engines), possible engine technological and control advances still represent a challenge for the improvement of the DF concept for light-duty engines application.

## 9.2 Analysis of the Main Design and Calibration Parameters of Methane–Diesel Dual Fuel Combustion

In this chapter, some suggestions about the combustion chamber design and calibration parameters that most affect the combustion characteristics, emissions and efficiencies at low load conditions are reported. The dual fuel research activity was performed at Istituto Motori of the National Research Council of Italy. A single cylinder engine setup, equipped with a Euro 5 light duty combustion architecture, was utilized for the experimental campaign.

To make the results representative of the reference multi-cylinder engine (MCE), the boundary conditions or the control variables of the auxiliary systems (boost, EGR, oil cooling, water cooling, fuel cooling) are set as those of the reference MCE. The main engine geometrical characteristics are reported below in Table 9.1.

**Table 9.1** Single cylinder engine geometrical characteristics

Displaced volume	477.5 cc
Stroke	90 mm
Bore	82 mm
Compression ratio	16.5, 15.5, 14.5
Number of valves	4
Diesel injection system	Common rail
Diesel injector	Solenoid 7 holes microsac
PFI injector	Multihole

The indicated pressures are measured by means of a Kistler 6125B flush mounted piezo-quartz transducer, fitted inside the head glow plug hole and acquired with a resolution of 0.1 CAD. The average pressure signal, for the calculation of the indicated mean effective pressure (IMEP) and the apparent heat release (HR) and HRR, is averaged over 128 consecutive cycles. The heat release analysis is based on the first law of thermodynamics as reported by Heywood (1988). The engine-out gaseous emissions in terms of THC, MHC,  $\text{NO}_x$ , CO,  $\text{CO}_2$  and  $\text{O}_2$  are measured using an integrated emissions test bench. Two dedicated flame ionization detectors (FIDs) have been used to measure the total unburned hydrocarbons (THC) and methane unburned hydrocarbons (MHC) engine-out emissions.

The commercial EN590 compliant diesel fuel and pure methane ( $\text{CH}_4$ ) were used as direct and port-injected fuel, respectively. The fuel characteristics are listed in Table 9.2. Since natural gas is constituted by a mix of hydrocarbons, the composition and consequently its specifics are variable and dependent on the source of supply. For this reason,  $\text{CH}_4$  was used because of its fixed physical–chemical characteristics.

Common dual fuel combustion adopts a single diesel injection strategy; however, a double diesel injection strategy has demonstrated a reduction of the heat transfer loss (before the TDC) and then an improvement in terms of gross-indicated efficiency (up to 1.5% units) with a reduction of the peak pressure rise rate ( $\text{PRR}_{\text{max}}$ ) (of about 60%), THC and  $\text{NO}_x$  emissions levels (of about 10 and 30%, respectively) compared to the single injection strategy (Di Blasio et al. 2017; Belgiorno et al. 2018b). For these reasons, all the results reported in this chapter refer to the adoption of the double diesel injection strategy for both CDC and DF combustions.

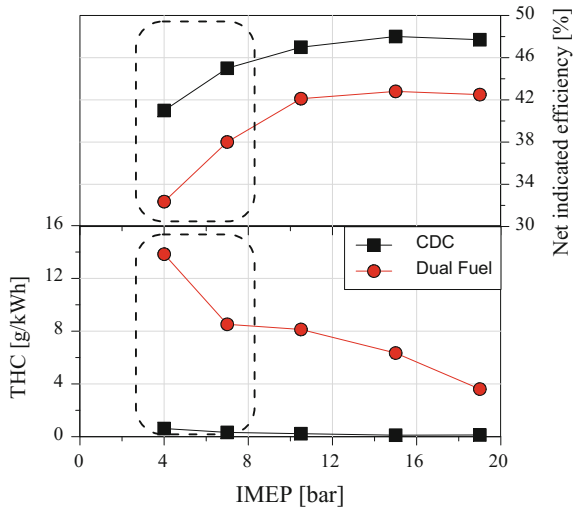
The dual fuel combustion is characterized by the high amount of natural gas not involved by the flame front that produces high emission level of MHC and then low net-indicated efficiency compared to the CDC (Fig. 9.3), especially at low load (below 7 bar of IMEP), due to not optimal combustion process (long combustion duration, high combustion and heat transfer losses), similar trend was observed in literature (Di Blasio et al. 2015; Belgiorno et al. 2018b).

As widely recognized, the main penalty of the dual fuel concept application is the  $\text{CH}_4$  emissions slip, especially at low load conditions. For this reason, the chapter mainly focuses on how the engine calibration and design parameters impact on its reduction by preserving or improving the global engine efficiency. During the

**Table 9.2** Fuel properties

Feature	Diesel fuel (EN590)	Methane
Density ( $\text{kg/m}^3$ ) STP	840	0.788
LHV (MJ/kg)	42.95	$49.5 \pm 0.2$
$A/F_{\text{stoich}}$ (–)	14.7	17.2
H/C (–)	$\sim 1.86$	4

**Fig. 9.3** THC and net-indicated efficiency trends function of IMEP for CDC and dual fuel (Sr = 50%) at 2000 rpm



parametric analysis of each of the considered variables, the combustion phasing (CA50) was kept constant and at the reference calibration value for diesel combustion, to have into a certain extent a fair comparison between CDC and Dual Fuel combustion (Di Blasio et al. 2015). The effect of each of these parameters has been investigated.

### 9.2.1 Substitution Ratio on MHC and Efficiency

In order to quantify and qualify the low reactive port-injected fuel, it is useful for defining the substitution ratio (Sr) with methane (CH<sub>4</sub>) on a mass basis according to the following equation:

$$Sr[\%] = \frac{m_{CH_4}}{m_{CH_4} + m_{diesel}} \cdot 100 \tag{9.1}$$

where  $m_{CH_4}$ ,  $m_{diesel}$  are the mass flow rates of CH<sub>4</sub>, diesel fuel, respectively.

In order to discriminate the single effect of the substitution ratio, the analysis was performed without utilizing EGR and keeping constant the compression ratio (CR=15.5), the combustion phase (MBF50), and the engine load (IMEP). The effects on the MHC and on the gross-indicated efficiency trends, at the more critical low load conditions, are reported. For a more comprehensive analysis of the regulated emissions and efficiencies, it is possibly referring to literature results (Belgiorno et al. 2018b; Papagiannakis et al. 2010; Papagiannakis and Hountalas 2003).

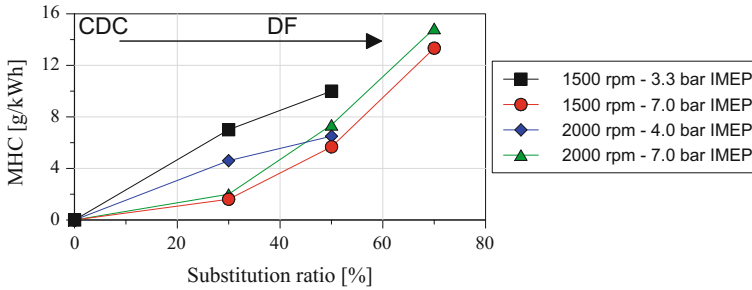


Fig. 9.4 Methane unburned hydrocarbon emissions function of substitution ratio

The CDC is characterized by very low unburned hydrocarbons emission level compared to spark-ignition and dual fuel combustion. In the DF case, most of the total unburned hydrocarbon (THC) is composed by the low reactive methane fuel (MHC), about 90–95% of the THC (Di Blasio et al. 2015; Fraioli et al. 2017), trapped in the squish and crevices volumes (Fraioli et al. 2017; Königsson et al. 2013; Di Blasio et al. 2017b). For this reason, it is fundamental to optimizing the DF combustion by reducing the MHC emission level also because the  $\text{CH}_4$  emissions contribute massively to the greenhouse gaseous emissions (GHG) and with a factor of 25 in comparison with  $\text{CO}_2$ .

Figure 9.4 reports the net-specific MHC emissions function of substitution ratio for different test points. The MHCs drastically increase passing from the CDC to DF; 30% of Sr causes a THC-increase of 3 times. In particular, the MHC trend can be divided into two steps. The first step shows a less than proportional increase when varying the Sr from 0 to 30%; this can be justified by the prevalent diesel fuel able to involve more premixed methane. The second step shows an almost linear variation from 30 to 70% of Sr that is related to the gradual increase of the trapped methane in the crevices at the expense of the diesel fuel decrease. At low load (below 4 bar of IMEP), the maximum Sr adopted was 50% because of high level of MHC up to 5000 ppm was achieved and to minimize the  $\text{CH}_4$  slip, a limit of Sr was imposed.

Regarding the gross-indicated efficiency (Fig. 9.5), passing from the CDC to DF, the thermodynamic efficiency decrease up to 15% units. This is explainable by both, the lower combustion rate that increases the heat transfer (HT) loss, and the lower combustion efficiency. For lower Sr values, the HT loss has a higher impact than the combustion loss vice versa for higher Sr values.

### 9.2.2 Effect of the Compression Ratio on MHC and Efficiency

The combustion chamber geometry is one of the most important design parameters influencing the engine performance and emission. To investigate the effect of the

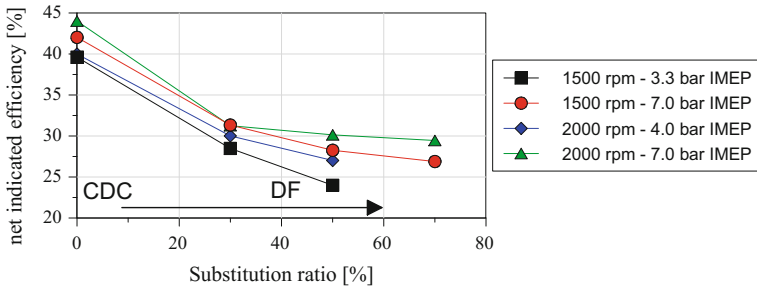
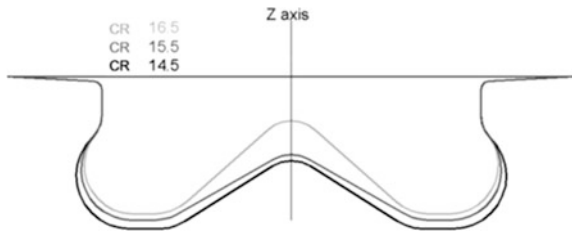


Fig. 9.5 Net-indicated efficiency function of substitution ratio

Fig. 9.6 Bowl geometries for all the compression ratio tested



CR (16.5, 15.5 and 14.5) on the DF combustion, three different piston bowl geometries have been designed. The variation of the CR target was realized by redesigning the bowl volume (Fig. 9.6). In particular, the bowl profile for each CR was defined by means of a 3D CFD simulation using the KIVA-3V code. Starting from the design of the production series piston shape (CR 16.5), the other bowl shapes were generated according to the following guidelines:

- same air flow structure at the end of the compression stroke to assure the same swirl and turbulence characteristics versus CR;
- same squish height and constant internal diameter to increase the k-factor and keep the same squish flow inside the bowl during the compression stroke;
- same bowl lip profile to guarantee the same structural robustness at the rated power.

The following analysis concentrates at low load engine operating conditions (from 3.3 to 7 bar of IMEP) at 1500 and 2000 rpm. A constant Sr and equal to 50% is adopted, employing a conventional double pulse diesel injection strategy (pilot-main) to control the combustion noise and/or the peak pressure rise rate (Di Blasio et al. 2015).

A high sensitivity of the MHC emission with the CR variation is detected independently of the engine speed and load condition in DF mode. In fact, lowering the CR, it is expected that the flame-quenching phenomenon would emphasise the MHC increase. Thus, following a rational thinking, the MHC reduction for smaller CRs is totally ascribable to the reduction of the premixed methane-air charge

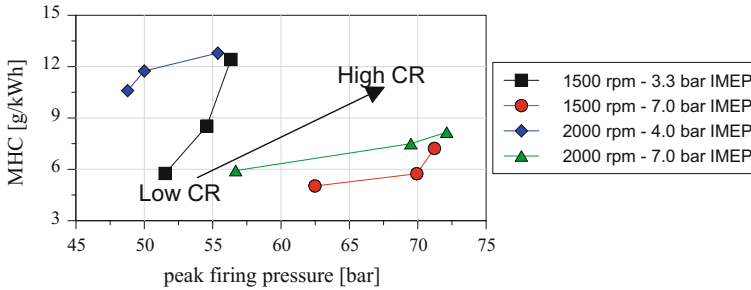


**Fig. 9.7** Methane unburned hydrocarbon emissions function of peak-firing pressure, obtained by varying the compression ratio (CR)

trapped into the crevices volumes. In this regard, the crevices volume is assumed to be the annulus volume between the piston top and the first piston ring. Since the CR variation is realised through the bowl enlargement (see test methodology section), the top land crevice volume of the three CR was the same and the variation of the bowl/crevice (b/c) up to 10% units less compared to the high compression ratio value (Belgiorno et al. 2018b) (Fig. 9.7).

As the CR reduces, the maximum in-cylinder pressure drops with a significant impact on the air-methane mixture concentration trapped into the crevice volumes. Starting from the in-cylinder pressure traces and applying the ideal gas law at TDC, reducing the CR, a methane mass reduction of about 5 and 13% at 15.5 and 14.5 compared to the CR 16.5 was calculated. Thus, for reduced CR both the increase of the bowl volume combined with the lower-trapped methane mass in the dead volumes contribute to the reduction of the MHC emissions formation.

In agreement to literature results carried out on SI-PFI engines, the observed trends of MHC reducing the CR depend on three main factors (Belgiorno et al. 2018b; Russ et al. 1995):

- the b/c ratio increment produces a higher methane mass fraction trapped in the piston bowl despite the crevice volume;
- a lower in-cylinder pressure during compression stroke reduces the methane-air mixture packaging into the crevices;
- a higher gas temperature in the late expansion stroke promotes the methane oxidation.

However, the CR has an opposite effect on the cycle conversion efficiency, indeed, a reduction of about 3.0% units is detected on the gross-indicated efficiency, passing from CR 16.5 to 14.5, related to the higher in-cylinder HT loss, lower in-cylinder thermodynamic temperature and then higher combustion duration (Di Blasio et al. 2017; Belgiorno et al. 2018b) (Fig. 9.8).

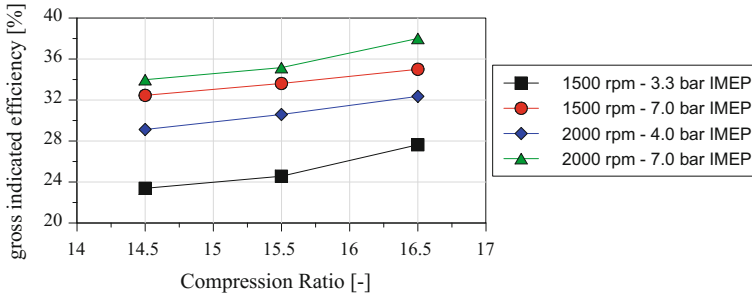


Fig. 9.8 Gross-indicated efficiency function of the compression ratio (CR)

### 9.2.3 Effect of Exhaust Gas Recirculation on MHC and Efficiency

It is worth investigating the effect of one of the most employed NO<sub>x</sub> emission technologies for CI and SI engines, that is, the exhaust gas recirculation (EGR). In particular, the EGR dilutes the in-cylinder mixture reducing the maximum in-cylinder temperatures and then the NO<sub>x</sub> formation. Additionally, for SI engines, it can permit, to some extent, the control of the knocking phenomena permitting to increase the specific rated power target. Thus, the EGR effect on efficiency and on MHC emissions is evaluated in DF mode.

The results of the EGR variation effect on MHC and gross-indicated efficiency are presented in Figs. 9.9 and 9.10. As previously explained, only the most critical low speed and load operating conditions have been considered adopting a Sr of 50%. Moreover, to discriminate the EGR effect, also the combustion phasing was kept constant, obviously, the SoIs are varied as a consequence.

Increasing the EGR rate, the MHC reduces (Fig. 9.9) and for values beyond 45%, the relative air–fuel ratio ( $\lambda$ ) reduces to 1.07 and near to the stoichiometric value and the specific MHC emission (g/kWh) drops of about 55% compared to the

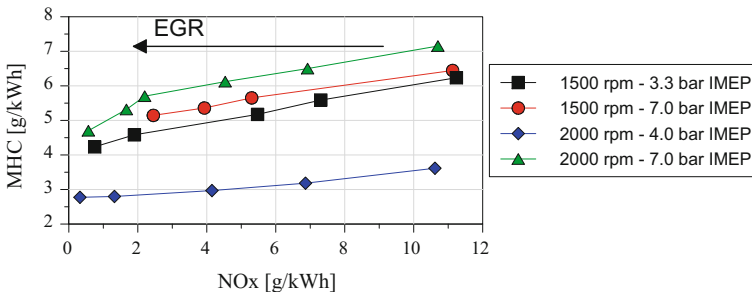
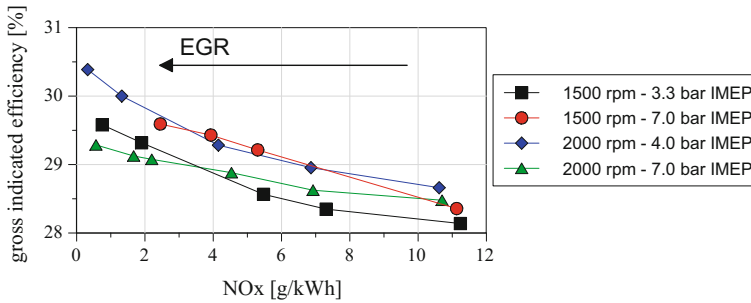


Fig. 9.9 Methane unburned hydrocarbons sensitivity versus NO<sub>x</sub> emissions changing the EGR levels



**Fig. 9.10** Gross-indicated efficiency sensitivity versus  $\text{NO}_x$  emissions changing the EGR levels

no EGR case. The difference between the specific and raw MHC emission is a consequence of the reduced exhaust mass flow rate in the presence of EGR and then of lower in-cylinder pressure that reduces drastically the methane mass trapped into the crevices volumes and a higher flame velocity that promotes the methane oxidation (Belgiorno et al. 2018b).

The EGR is increased from 0 to 45% with an increase of the gross efficiency of about 1.0% units. With a high level of EGR, the pilot-ignition delay increases, due to the lower mixture reactivity (lower in-cylinder temperature and less oxygen). This permitting to improve the efficiency by reducing the heat transfer losses during the compression stroke. The higher premixed combustion permits to release more heat closer to the TDC, improving the thermodynamic efficiency.

On this basis of the presented results, it can be drawn that the EGR represents not only an important driver to reduce the  $\text{NO}_x$  (one order of magnitude less) but also the MHC (up to 55%) while improving the gross-indicated efficiency (up to 1.0% units) compared to the no-EGR strategy, without penalization in terms of soot and combustion noise that are always below the value obtained for CDC.

### 9.2.4 Effect of Air-to-Fuel Ratio on MHC and Efficiency

Many definitions of the dual fuel combustion can be found in literature, and in general, the DF combustion can be considered as a process in between the flame propagation (SI engine) and diffusive combustion (CI engine) processes (Königsson 2014; Karim 2015; Di Blasio et al. 2017a). For this reason, the in-cylinder air-to-fuel ratio represents a fundamental parameter in the control of the combustion process and emission level. In a compression ignition engine, the air-to-fuel ratio can be varied by means of the injection quantity and thus the load or by means of reducing the intake air mass through the intake throttle valve at constant load. The latter was adopted to investigate the effect of different air-to-fuel ratio impact, keeping constant the  $S_r$  equal to 50% and the load, without EGR. The throttle



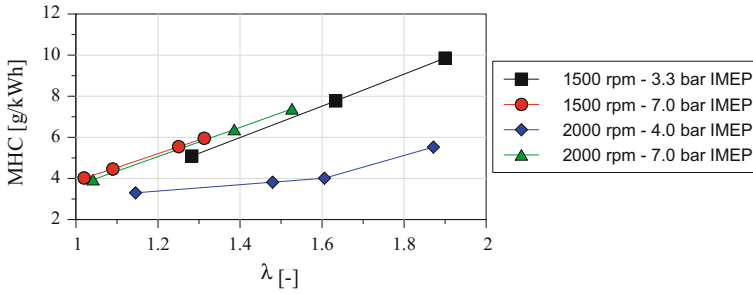


Fig. 9.11 Methane unburned hydrocarbons sensitivity versus  $\lambda$  varying the throttle valve position

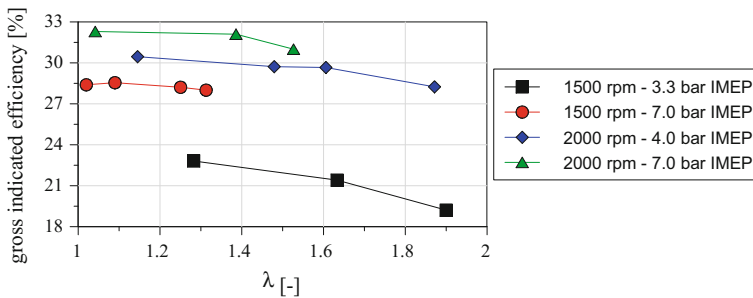


Fig. 9.12 Gross-indicated efficiency sensitivity versus  $\lambda$  varying the throttle valve position

position was varied from the fully opened condition to partialize reaching a lambda value ( $\lambda$ ), the inverse of the equivalence ratio, of 1.05.

The analysis shows that near to stoichiometric values the specific MHC emissions converge for each point towards very low level and about 35% less compared to higher lambda values (Fig. 9.11). This is because of the fastening of the combustion process that promotes the methane oxidation process, moreover, the valve throttling lowers the in-cylinder peak pressure reducing the methane mass trapped into the crevice volumes (same consideration reported in CR section).

Looking at the gross-indicated efficiency (Fig. 9.12), reducing the lambda, an improvement of the thermodynamic process is obtained (up to 3%) compared to the fully opened throttle valve, because of the lower combustion losses and lower heat transfer losses (faster combustion). However, higher pumping losses were obtained partializing the throttle valve that at the end penalize the net-indicated efficiency compared to the fully opened throttle valve.

In general, the air-throttling has a beneficial effect on the MHC reduction but at the expense of the emitted smoke and particles, especially when the  $\lambda$  value is at the limit of the diesel operation mode. Thus, since both the DF and the air-throttling act on the  $\lambda$  reduction, the last has to be opportunely calibrated as a function of the substitution ratio and the load. In particular, lower loads that employ lower

substitution ratio values require a higher air-throttling, in contrast to higher loads. Concluding, for both speeds, 1500 and 2000 rpm at 7 bar of IMEP and  $\lambda$  in the range 1.3–1.4, the MHC reduces by about 15% without penalties on the net efficiency (Di Blasio et al. 2017; Belgiorno et al. 2018b).

### 9.2.5 Summary

This chapter reports a parametric analysis of the substitution ratio, EGR, air-to-fuel ratio and compression ratio of a dual fuel combustion in a light-duty engine, at low load (till 7 bar of IMEP), since they are the most critical points for DF operation and they contribute significantly on the emissions and fuel consumption over the whole NEDC and/or WLTC emission homologation cycles for light-duty passenger car vehicles. The conducted investigation permits to evaluate the contribution factor of each analysed parameter the MHC and indicated specific fuel consumption (ISFC). Both the CH<sub>4</sub> slip and fuel consumption reduction are fundamental aspects to be faced with to promote the development of future light-duty combustion engines running in dual fuel concept. The contribution factor of each of the varied parameters on the generic output called X (e.g., MHC or ISFC) is calculated as:

$$\Delta[\%] = \frac{X_{\text{high level}} - X_{\text{low level}}}{X_{\text{low level}}} \cdot 100 \tag{9.2}$$

where the numerator represents the output increment when increasing the factor from a low to the high level (e.g., EGR from 0 to 45%). The denominator represents the output value at the starting level.

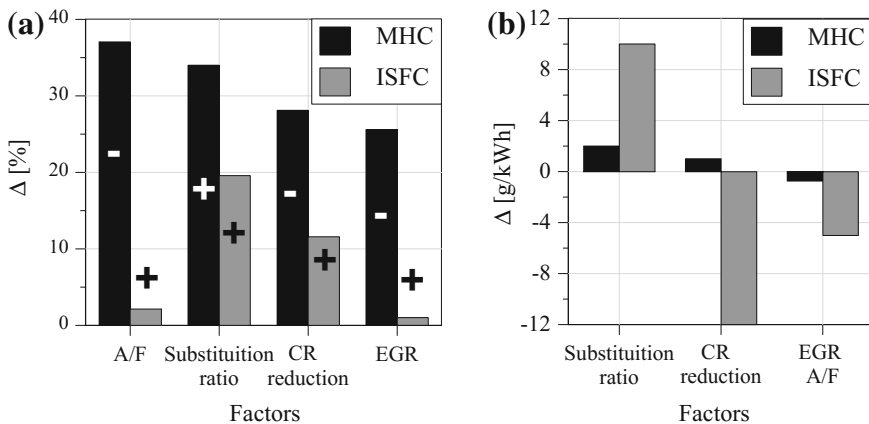


**Fig. 9.13** MHC and ISFC relative (a) and absolute (b) sensitivity versus operating parameters

The contribution factors are reported in Fig. 9.13. The analysis shows a negative impact of the substitution ratio both on MHC and ISFC, and this is mainly related to the non-optimized combustion chamber design for dual fuel operation, especially for what concerns the oxidation of methane in the peripheral and dead regions of the combustion chamber. The specific MHC (g/kWh) increase, as a function of the substitution ratio, is about 2 g/kWh/10%. Additionally, the increase of the substitution ratio leads also to ISFC penalty that is about 10 g/kWh/10%.

The CR reduction to 14.5 reduces the globally indicated efficiency of about 10% with respect to 16.5 notwithstanding the MHC reduction of about 30% due to the combined effect of the bowl/crevice volume ratio increase and peak cylinder pressure decrease. The average MHC reduction per unit of CR reduction is equal to 1.0 g/kWh. While the ISFC increases are about 12.0 g/kWh per unit of CR reduction.

An interesting result can be drawn from Fig. 9.13 in terms of MHC reduction adopting EGR and reducing the A/F without penalties in terms of ISFC. In fact, reducing the A/F, the MHC reduces up to 40% at 1500x3.3 and 2000x7, and more than 20% in the other points. The MHC reduction per units of EGR is about 0.75 g/kWh/10% of EGR while passing from  $\lambda = 1.6$  to near stoichiometric conditions an average reduction of about 5 g/kWh is detected for the load range explored.

Optimizing the combustion chamber and the fundamental DF engine operating parameters (EGR, A/F, substitution ratio, etc.), it is possible to achieve very interesting results adopting the dual fuel combustion instead of the CDC concept. Additionally, a development of the combustion chamber and a dedicated aftertreatment can help to improve the efficiency and the CH<sub>4</sub> emissions slip tailpipe to give a gain at this technology. An estimation of the outputs on the New European Driving Cycle (NEDC) shows that adopting only diesel fuel for engine load below 3.3 bar of IMEP, with high level of EGR (from 40 to 45%) while, at medium-high load, adopting a double injection strategy, maximum substitution ratio up to 70% and EGR no more than 35%, it is possible to achieve a reduction of about 6% in terms of CO<sub>2</sub> compared to the CDC under NEDC with an average substitution ratio on cycle of about 41% (Belgiorno et al. 2018b).

## References

- Belgiorno G, Dimitrakopoulos N, Di Blasio G, Beatrice C, Tunestål P, Tunér M (2018a) Effect of the engine calibration parameters on gasoline partially premixed combustion performance and emissions compared to conventional diesel combustion in a light-duty Euro 6 engine. *Appl Energy* 228:2221–2234. ISSN 0306-2619, <https://doi.org/10.1016/j.apenergy.2018.07.098>
- Belgiorno G, Di Blasio G, Beatrice C (2018b) Parametric study and optimization of the main engine calibration parameters and compression ratio of a methane-diesel dual fuel engine. *Fuel* 222:821–840. ISSN 0016-2361, <https://doi.org/10.1016/j.fuel.2018.02.038>
- Benajes J, Pastor JV, García A, Monsalve-Serrano J (2015) The potential of RCCI concept to meet EURO VI NO<sub>x</sub> limitation and ultra-low soot emissions in a heavy-duty engine over the whole engine map. *Fuel* 159:952–961. ISSN 0016-2361, <https://doi.org/10.1016/j.fuel.2015.07.064>

- Besch M, Israel J, Thiruvengadam A, Kappanna H et al (2015) Emissions characterization from different technology heavy-duty engines retrofitted for CNG/diesel dual-fuel operation. *SAE Int J Engines* 8(3):1342–1358. <https://doi.org/10.4271/2015-01-1085>
- Curran S, Gao Z, Szybist J, Wagner R (2014) Fuel effects on RCCI combustion: performance and drive cycle considerations. In: 2014 coordinating research council advanced fuel and engine efficiency workshop, Baltimore, Maryland, 24–27 Feb 2014
- Dec J (1997) A conceptual model of DI diesel combustion based on laser-sheet imaging\*. SAE technical paper 970873. <https://doi.org/10.4271/970873>
- Di Blasio G, Beatrice C, Molina S (2013) Effect of port injected ethanol on combustion characteristics in a dual-fuel light duty diesel engine. SAE technical paper 2013-01-1692. <https://doi.org/10.4271/2013-01-1692>
- Di Blasio G, Belgiorno G, Beatrice C, Fraioli V et al (2015) Experimental evaluation of compression ratio influence on the performance of a dual-fuel methane-diesel light-duty engine. *SAE Int J Engines* 8(5):2253–2267. <https://doi.org/10.4271/2015-24-2460>
- Di Blasio G, Belgiorno G, Beatrice C (2017a) Effects on performances, emissions and particle size distributions of a dual fuel (methane-diesel) light-duty engine varying the compression ratio. *Appl Energy* 204:726–740. ISSN 0306-2619, <https://doi.org/10.1016/j.apenergy.2017.07.103>
- Di Blasio G, Belgiorno G, Beatrice C (2017b) Parametric analysis of compression ratio variation effects on thermodynamic, gaseous pollutant and particle emissions of a dual-fuel CH<sub>4</sub>-diesel light duty engine. SAE technical paper 2017-01-0764. <https://doi.org/10.4271/2017-01-0764>
- Fraioli V, Beatrice C, Di Blasio G, Belgiorno G et al (2017) Multidimensional simulations of combustion in methane-diesel dual-fuel light-duty engines. SAE technical paper 2017-01-0568, 2017, <https://doi.org/10.4271/2017-01-0568>
- Heywood JB (1988) Internal combustion engine fundamentals, vol 930. McGraw-Hill, New York
- Karim GA (2015) Dual-fuel diesel engines. CRC Press
- Kokjohn SL, Hanson RM, Splitter DA, Reitz RD (2011) Fuel reactivity controlled compression ignition (RCCI): a pathway to controlled high-efficiency clean combustion. *Int J Engine Res* 12(3):209–226
- Königsson, F (2014) On combustion in the CNG-diesel dual fuel engine. Ph.D. Dissertation. KTH Royal Institute of Technology
- Königsson F, Kuyper J, Stalhammar P, Angstrom H (2013) The influence of crevices on hydrocarbon emissions from a diesel-methane dual fuel engine. *SAE Int J Engines* 6(2):751–765. <https://doi.org/10.4271/2013-01-0848>
- Kufferath A, Kruger M, Naber D, Mailander E, Maier R, Robert Bosch GmbH, Stuttgart (2018) The path to negligible NO<sub>2</sub> immission contribution from the diesel powertrain. In: 39th Internationales Wiener Motorensymposium, Wien
- Papagiannakis RG, Hountalas DT (2003) Experimental investigation concerning the effect of natural gas percentage on performance and emissions of a DI dual fuel diesel engine. *Appl Thermal Eng* 23(3):353–365. ISSN 1359-4311, [http://dx.doi.org/10.1016/S1359-4311\(02\)00187-4](http://dx.doi.org/10.1016/S1359-4311(02)00187-4)
- Papagiannakis RG, Rakopoulos CD, Hountalas DT, Rakopoulos DC (2010) Emission characteristics of high speed, dual fuel, compression ignition engine operating in a wide range of natural gas/diesel fuel proportions. *Fuel* 89(7):1397–1406. ISSN 0016-2361, <http://dx.doi.org/10.1016/j.fuel.2009.11.001>
- Russ S, Kaiser E, Siegl W, Podsiadlik D et al (1995) Compression ratio and coolant temperature effects on HC emissions from a spark- ignition engine. SAE technical paper 950163. <https://doi.org/10.4271/950163>
- Splitter D, Hanson R, Kokjohn S, Reitz RD (2011) Reactivity controlled compression ignition (RCCI) heavy-duty engine operation at mid-and high-loads with conventional and alternative fuels. SAE technical paper, no. 2011-01-0363; SAE international: Warrendale, PA, USA
- Valladolid PG, Tunestål P, Monsalve-Serrano J, García A, Hyvönen J (2017) Impact of diesel pilot distribution on the ignition process of a dual fuel medium speed marine engine. *Energy Convers Manag* 149:192–205. ISSN 0196-8904, <https://doi.org/10.1016/j.enconman.2017.07.023>

# Chapter 10

## Design and Calibration Strategies for Improving HCCI Combustion in Dual-Fuel Diesel–Methane Engines



A. P. Carlucci , A. Ficarella , D. Laforgia  and L. Strafella 

**Abstract** The interest in methane is lately increased due to power-to-gas technologies, through which green electricity in excess could be used to produce easily storable gaseous fuels. Among engines for methane exploitation, dual-fuel piston engine is a very efficient and low-impact solution. Their operation, still limited by high hydrocarbons and carbon monoxide emissions at low loads and knock at high loads, is characterized by many parameters. Besides the ones well recognized in the literature, like pilot quantity and substitution rate, other parameters, like engine volumetric compression ratio, intake charge conditions, pilot injection pressure and timing, engine load and speed, and exhaust gas recirculation (EGR), showed an impact on engine performance and emissions. This work first describes the results of a full factorial DoE in which the effects of compression ratio, intake charge pressure (ICP), pilot injection timing and pressure, and methane flow rate effect are evaluated and discussed on combustion development, engine performance, and pollutant emission levels at the exhaust. Through analysis of variance (ANOVA), the first- and second-order effects were also quantified. Moreover, the factor variation ranges leading the engine to operate in or close to HCCI combustion, i.e., guaranteeing a high conversion efficiency and low emission levels at the same time, were sought and highlighted. This suggested that not only very advanced but also retarded injection timings, combined with high ICP, determine very low levels of nitrogen oxides and maximum pressure rise rate, with little or no penalty on engine efficiency and emission levels.

**Keywords** Dual fuel · Diesel fuel · Methane · Injection pressure  
Injection timing · Volumetric compression ratio · Methane flow rate  
Intake charge pressure · HCCI combustion · MK combustion · ANOVA

---

A. P. Carlucci (✉) · A. Ficarella · D. Laforgia · L. Strafella  
Department of Engineering for Innovation (DII), University of Salento, via per Monteroni,  
73100 Lecce, Italy  
e-mail: [paolo.carlucci@unisalento.it](mailto:paolo.carlucci@unisalento.it)

© Springer Nature Singapore Pte Ltd. 2019  
K. K. Srinivasan et al. (eds.), *Natural Gas Engines*, Energy, Environment,  
and Sustainability, [https://doi.org/10.1007/978-981-13-3307-1\\_10](https://doi.org/10.1007/978-981-13-3307-1_10)

267

## 10.1 Introduction

Among all alternative fuels, methane or natural gas (NG, whose main constituent is methane) has been considered since a long time among the best solutions for fossil fuel substitution because of their availability throughout the world, inherent clean burning, favorability as fuels, and adaptability to piston (compression or spark ignition) engines in addition to turbine engines (Muhammad et al. 2016; Pali et al. 2018). The interest in natural gas is lately increased due to power-to-gas technologies, through which green electricity in excess could be used to produce easily storable gaseous fuels (McKenna et al. 2018; He et al. 2018). Focusing the attention on piston engines, it is worth mentioning that existing engines, both spark and compression ignition, can be readily converted to operate primarily on methane or NG, with the latter preferred to the former since characterized by a higher compression ratio and therefore lower fuel consumption. In this case, however, diesel (or a high reactivity fuel) must be used as a spark plug to achieve ignition, given the lower reactivity of methane; this kind of engines is referred to as “dual fuel” (DF). The substitution rates of the high reactivity fuel with a low reactivity one can overcome 90% in the currently available dual-fuel engines, so significantly reducing CO<sub>2</sub> and particulate matter (PM) emission levels. However, besides the advantages of dual-fuel combustion, some well-known drawbacks also arise, as the knock tendency at high loads and excessive total hydrocarbons (THCs) and carbon monoxide (CO) production at low loads.

Homogeneous charge compression ignition (HCCI) combustion can be a viable solution to drastically reduce these problems (Hasan and Rahman 2016). In HCCI operation—probably the first low-temperature combustion (LTC) mode introduced—air and fuel are homogeneously mixed before being ignited through compression. In this way, fuel-rich zones are avoided, local temperatures are reduced, and, overall, emissions are drastically decreased. In dual-fuel diesel–methane engines, as previously said, the ignition of a mixture of air and methane is obtained thanks to an injection of diesel fuel. Implementing HCCI in dual-fuel diesel–methane engines, therefore, requires to obtain a homogeneous mixture of air and methane as well as homogeneous distribution of diesel fuel vapor inside the cylinder before the start of ignition. While mixing homogeneously air and methane is a relatively easy task, the same cannot be said about diesel fuel. Several attempts have been documented in which the diesel fuel is fumigated along the intake duct. However, this solution, while guaranteeing a proper homogenization of the diesel fuel with air before ignition, presents as drawbacks the high PM emission levels due to poor fuel atomization conditions (Song et al. 2018).

Therefore, it is usually preferred to increase the ignition delay of the mixture, so giving more time to diesel fuel to evaporate and mix with the air. In this way, however, a perfect homogeneity is generally not obtained. The so-called partially premixed compression ignition (PPCI) or predominantly premixed charge compression ignition (PPCCI) combustion is achieved with direct injection system, where advanced multi-injection strategies lead to a certain degree of premixing of

fuel and air, although not definable as HCCI. On the other hand, the so-called reactivity-controlled compression ignition (RCCI) combustion, developed to control fuel reactivity to optimize combustion phasing, duration, and magnitude, is usually implemented in dual-fuel engines performing a very advanced pilot injection. In the open literature, the effect of the different parameters, like pilot start of injection (SOI), pilot injection pressure ( $p_{\text{rail}}$ ), pilot injection splitting, substitution rate, engine compression ratio (CR), intake charge pressure (ICP) and temperature (ICT), exhaust gas recirculation (EGR), and pilot fuel chemical composition, was evaluated with the goal of increasing the mixture ignition delay in dual-fuel conditions.

In Guerry et al. (2016), the authors varied SOI on a wide range of values, testing a single-cylinder compression ignition engine, observing that, when SOI was advanced, the ignition delay (ID) and the separation between the end of injection and start of combustion both increased; the heat release rate (HRR) curve changed from a distinct two-stage profile to a smooth single-stage profile. Correspondingly, the fuel conversion efficiency  $\eta_f$  increased together with cycle-to-cycle variability and THC and CO emission levels, while  $\text{NO}_x$  and smoke were reduced drastically. Similar results on a six-cylinder engine were reported in Doosje (2014).

In Raihan et al. (2015), the authors extended the experimental campaign reported in Guerry et al. (2016) and underlined that LTC can be established in a diesel-ignited methane dual-fuel engine setting appropriate values of SOI,  $p_{\text{rail}}$ , and ICP.

In Ibrahim et al. (2015), the authors, testing a single-cylinder compression ignition engine operated in dual-fuel diesel–biogas mode, demonstrated that, acting on SOI, ICT, and substitution rate, the engine could be effectively operated in PPCCI at low/medium loads with beneficial reduction of nitric oxides ( $\text{NO}_x$ ) and THC with respect to conventional DF combustion mode.

Srinivasan et al. (2006) studied early pilot injection strategy on a single-cylinder diesel–methane engine and discussed the effect of pilot-injected quantity and ICT on the onset of ignition and combustion.

A comprehensive work is illustrated in Napolitano et al. (2017), Di Blasio et al. (2017a, b), where the authors, testing a single-cylinder representing the technology of a modern light-duty engine operated in DF diesel–methane mode, found that CR is an important engine design parameter, which has a relevant effect on methanic THC emissions. Its effect, however, is more evident at low/medium load. A CR value of 15.5 led to the best performance in terms of pollutant emissions and  $\text{CO}_2$  saving over the New European Driving Cycle (NEDC), a test cycle. Other technologies, like double-pulse injection strategy, air throttling, and EGR, were found effective too in controlling pollutant emission levels while respecting engine functional limits, like maximum pressure rise rate (MPRR), cycle-to-cycle variability, and peak firing pressure. However, the investigated parameters were varied in a limited range of values, so that no alternative combustions like HCCI or PPCCI were observed. A similar work, limited to SOI and  $p_{\text{rail}}$  varied on a range of conventional values, led to similar results (Yang et al. 2015). In Dahodwala et al.

(2014), the authors, exploiting an optimization routine in which strategies were developed primarily involving diesel SOI and NG substitution rate, demonstrated that it was possible to achieve an average of 49% substitution across the test point map of six-cylinder engine with 15% reduction in  $\text{NO}_x$  and 43% reduction in PM emissions. At higher engine speeds, it appears that reduced time for CNG/air mixing results in a varying cylinder-to-cylinder distribution of CNG and thus deteriorated combustion stability. RCCI combustion could be achieved at low loads, which enabled even higher NG substitution and lower emissions. A maximum of 50% net indicated thermal efficiency was observed at 6 bar of brake mean effective pressure (BMEP) load point along with 75% reduction in both  $\text{NO}_x$  and PM emissions. The potential benefits of RCCI combustion were limited due to the un-optimized combustion chamber design and high compression ratio.

The effect of pilot injection pressure,  $p_{\text{rail}}$ , has been extensively studied, for example, in Hariprasad (2013). A dual-fuel single-cylinder engine was found to run smoothly with higher injector opening pressure and advanced SOI. The efficiency of the dual-fuel engine is slightly less as compared to neat diesel operation at part loads. The dual-fuel engine resulted in lower smoke and  $\text{NO}_x$  emissions as compared to neat diesel operation, but it emitted slightly higher CO and THC emissions.

Ryu (2013a, b) studied the NG dual-fuel combustion varying SOI in the range 11–23 crank angle degrees before top dead center (CAD BTDC) and  $p_{\text{rail}}$  from 30 to 150 MPa and concluded that: (1) The increase of pilot injection pressure results in lower smoke, but higher  $\text{NO}_x$  emission; (2) smoke is decreased, and  $\text{NO}_x$  is increased as the pilot injection timing is advanced; compared to diesel-only combustion, however, smoke emissions are significantly reduced over the range of operating conditions and  $\text{NO}_x$  emissions are also decreased over the range with the exception of the full load case.

In Xu et al. (2016a, b), a comprehensive study has been performed in which the pilot fuel has been injected shifted in a pre and a pilot or main injections on a very wide range of values, and the effect of  $p_{\text{rail}}$  and SOI on combustion and emission of a six-cylinder dual-fuel engine has been assessed. Results indicate that early pre-injection mode leads to lower cylinder pressure and HRR due to a decrease of combustion intensity; thereby, lower  $\text{NO}_x$  emission is obtained. In contrast, close pre-injection timing leads to large strengthening in combustion which is not beneficial for improving  $\text{NO}_x$  emission performance. Increase of pre-injection quantity ratio leads to the delayed start of combustion and slower burning rate, and thereby lower  $\text{NO}_x$  and higher THC emission. However, too high pre-injection quantity ratio leads to unstable combustion. Increasing  $p_{\text{rail}}$  leads to rapid combustion and therefore higher cylinder pressure and HRR. Consequently, in-cylinder combustion temperature increases,  $\text{NO}_x$  emission increases, and THC emission decreases.

In Ogawa et al. (2016), the authors demonstrated that, increasing the injection pressure of diesel fuel, the combustion efficiency increases with a decrease of THC and CO emissions, and the indicated thermal efficiency improves without an increase in  $\text{NO}_x$  emissions. Simultaneous reductions in the  $\text{NO}_x$ , THC, and CO emissions can be established with maintaining the equivalence ratio of NG with intake gas throttling under the 250 MPa pilot injection condition. Two-stage split



pilot injection of diesel fuel significantly reduces the maximum rate of pressure rise and  $\text{NO}_x$  emissions without deteriorations in both thermal efficiency and emissions. In Garcia and Tunestal (2015), the injection strategy, in terms of a number of injections and their timing, was varied in order to establish different combustion modes (namely conventional dual fuel, PPCI, and RCCI) on a dual-fuel methane–diesel engine. In Ansari et al. (2016), it was shown that low reactive mixture outside of the bowl at single-injection strategy showed to be the main reason for the high THC and CO at low loads. Dual-injection strategy provided a high reactive mixture inside and outside of the bowl, resulting in low CO and THC emissions.

Paykani et al. (2015) developed a simulation study on the combustion and emission performance of natural gas/diesel RCCI combustion varying SOI and pilot injection quantity in the presence of split fuel injection strategy. The results demonstrate that: (1) SOI timing of the first injection increases mixture stratification as retarded toward top dead center (TDC), and, as a result, combustion phasing is advanced and soot and  $\text{NO}_x$  increased; (2) the effect of SOI of second injection is similar to the first one, but only up to a certain point ( $-30$  after TDC, ATDC); (3) as the amount of diesel fuel injected in the second injection is increased, so is the mixture stratification, with the results already illustrated on soot and  $\text{NO}_x$ ; (4) increasing ICT, reaction rates increase, which increase  $\text{NO}_x$  and advance combustion phasing, while combustion efficiency is reduced because of lower volumetric efficiency; (5) with the explored injection strategies,  $\text{NO}_x$  and soot can be controlled, while CO and THC deteriorate.

Results of a numerical investigation are also reported in Poorghasemi et al. (2017), where the effect of diesel injection strategies, injection pressure, and spray angle on an RCCI engine performance and emission characteristics was investigated. Concerning injection strategies, results confirmed those reported in Paykani et al. (2015). Moreover, it was demonstrated that higher  $p_{\text{rail}}$  increases the spray penetration (causing wall impingement) as well as evaporation rate of diesel droplets: In this way, stratification of diesel fuel increases and combustion phasing is advanced. As a consequence,  $\text{NO}_x$ , THC, and CO all increase. A narrower spray angle determines higher values of THC and CO emissions near the cylinder wall and crevice volumes, and  $\text{NO}_x$  increases due to richer and locally higher reactive zone with higher combustion temperature. These findings have been confirmed by imaging techniques (Nithyanandan et al. 2017).

Several numerical works (Wang et al. 2016; Donateo et al. 2014) have proven the possibility to decrease both CO and THC emissions properly designing combustion chamber geometry, spray pattern, and SOI.

Finally, several benefits on DF PPCCI deriving from using biodiesel fuels were highlighted in Ghareghani et al. (2015), Hosmath et al. (2016). In Hosmath et al. (2016), the effect of CR, NG flow rate, and SOI has been analyzed on the performance of a dual-fuel engine operated on Honge oil methyl ester (HOME) and NG applying response surface methodology on the results of an experimental campaign.

As evident from the review of the open literature, a significant research activity has been performed on dual-fuel diesel–methane combustion, aiming at improving

the engine performance and reducing its environmental impact but acting on one or few controlling factors at a time. Therefore, the aim of this work is to identify the engine design and management factors—characterizing the dual-fuel combustion—most influential on engine operation outputs. In order to perform this analysis, a set of factors, namely methane flow rate, pilot injection pressure, pilot injection timing, engine volumetric compression ratio, and ICP, have been varied on different levels during an extensive experimental campaign. Their effect on engine output parameters, namely indicated mean effective pressure (IMEP), fuel conversion efficiency  $\eta_f$ , combustion start, position and duration, maximum pressure rise rate (MPRR),  $\text{NO}_x$ , THC, and CO emission levels, has been analyzed using an analysis of variance (ANOVA) approach. In this way, it was possible to recognize the factor (or combination of factors) most influential on each engine output parameter. Moreover, the factor variation ranges leading the engine to operate in or close to HCCI combustion, i.e., guaranteeing a high conversion efficiency and low emission levels at the same time, have been sought: this suggested alternative and potentially more effective ways to operate the engine closer to HCCI conditions.

## 10.2 Experimental Layout

A single-cylinder, 4-stroke, common rail diesel research engine (AVL model 5402) was used to analyze the effect of pilot injection pressure and timing, engine compression ratio, intake air pressure, and methane amount on dual-fuel diesel fuel–methane performance and emissions. The technical features of the engine are reported in Table 10.1, while in Fig. 10.1 the scheme of the experimental layout is reported. The gaseous methane has been fumigated along the intake duct of the engine by means of an injector consisting of an automatic poppet valve, with contrast spring, actuated by the methane itself introduced by a solenoid valve in a small accumulation volume (Carlucci et al. 2008). The solenoid valve was actuated using a duty cycle  $D = 50\%$  with a frequency of 30 Hz. During the tests, the injector was positioned at a distance of about 400 mm from the cylinder axis, so that a homogeneous methane–air mixture was obtained before trapping it into the cylinder. Although the engine is provided with a swirl and tumble valve, the mixture was introduced in the cylinder through the swirl valve only. This solution was chosen because it provided the best compromise in terms of engine performance and emission levels (Carlucci et al. 2009, 2010).

Table 10.2 reports the levels assigned to each factor varied during tests. The duration of the diesel fuel injection was adjusted in order to keep constant—equal to  $6 \text{ mm}^3/\text{cycle}$ —the diesel fuel amount injected per cycle. In particular, duration equal to 150 or 300  $\mu\text{s}$  was set for a diesel fuel injection pressure ( $p_{\text{rail}}$ ), respectively, equal to 1250 or 500 bar. The engine was always run at 1500 rpm. Referring to SOI variation range, more advanced SOI was not used because of either the high MPRR observed in several conditions, not tolerable by the engine structure, or the absence of combustion observed in several other conditions. On the

**Table 10.1** Single-cylinder diesel engine main specifications

Specification	Nominal value/description	
Maximum power	18 kW	
Bore	85 mm	
Stroke	90 mm	
Original compression ratio	17.1:1	
Combustion chamber	Bowl with valve pockets and flathead	
Injection system	Common rail	
Max injection pressure	1300 bar	
Valve timing	Opening	Closing
Intake	13.5° BTDC	46.5° ABDC
Exhaust	51.5° BBDC	16.5° ATDC

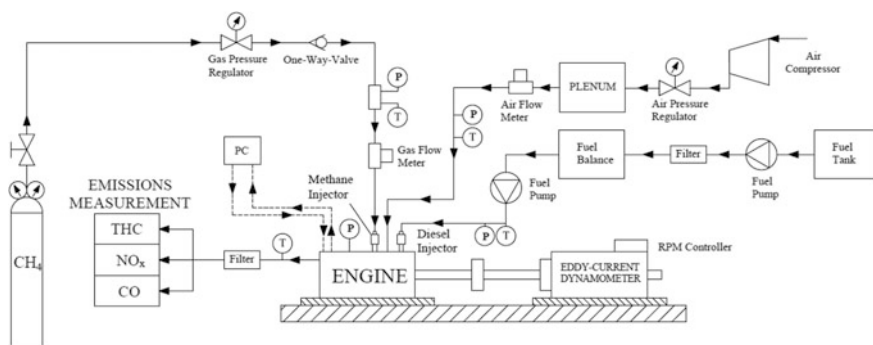


**Fig. 10.1** Experimental setup

**Table 10.2** Factors and corresponding levels varied during tests

Description	Abbreviation	Tested levels
Methane mass flow rate	$G_{gas}$	0 (kg/h)—(IMEP ≈ 0.8 bar) 0.21 (kg/h)—(IMEP ≈ 1.3 bar) 0.31 (kg/h)—(IMEP ≈ 2.4 bar) 0.37 (kg/h)—(IMEP ≈ 4 bar) 0.40 (kg/h)—(IMEP ≈ 6 bar)
Engine compression ratio	CR	14–17
Intake charge pressure	ICP	1.16–1.66 (bar)
Diesel fuel injection pressure	p_rail	500–1250 (bar)
Diesel fuel pilot injection timing	SOI	–50/–35/–20/–10/0/5/10 (CAD ATDC)

other hand, results obtained with more retarded SOI are not shown as the combustion was basically not observed.

The amount of methane introduced along the intake duct was varied acting on the duty cycle of a continuous pulse-width modulation (PWM) signal, generated by

a National Instruments High-Speed, Sourcing Digital Output NI 9474 module and controlled by means of LabVIEW software. In this way, the opening time of the gas injector was varied and so the amount of adducted methane.

The engine compression ratio was varied by changing the dead space volume of the engine. In particular, thanks to the modular composition of the engine, steel plates of a specific thickness can be inserted or removed to vary the compression ratio.

The ICP was varied by modifying the opening of a pressure-regulating valve positioned on the outflow line of an ATLAS COPCO GA 30 compressor. Also, in this case, modifying the duty cycle of a PWM signal, it was possible to modify the valve-opening degree and therefore the ICP up to the desired value. The intake charge temperature (ICT) was kept constant equal to  $314 \pm 2$  K.

Data acquisition was started only after steady conditions were reached. An AVL piezoelectric pressure sensor model QC33C was mounted in the combustion chamber. The signal sampling was triggered and synchronized with TDC by an AVL encoder model 364C with a resolution of 0.2 crank angle degree (CAD). The in-cylinder pressure transducer was characterized by a linearity error lower than 0.4%, while the sensitivity shift and the range error of the pressure amplifier (AVL model 3066A01) were less than 1%. The error associated with the A/D data conversion and acquisition was equal to 0.3%. To obtain the absolute cylinder pressure, ( $p_{\text{cyl,abs}}$ ), a pegging routine was implemented, through which the cylinder pressure measured by the in-cylinder pressure during the intake stroke was imposed equal to the average pressure measured by an absolute pressure sensor (Kistler piezoresistive sensor type 4045A2) mounted along the intake duct. Then, the absolute cylinder pressure so obtained was stored for 50 consecutive cycles, averaged and then post-processed. The gross HRR was calculated as:

$$\text{HRR} = \frac{dQ_{\text{net}}}{d(\text{CAD})} + \frac{dQ_w}{d(\text{CAD})} \quad (10.1)$$

The term  $\frac{dQ_{\text{net}}}{d(\text{CAD})}$  was estimated based on the single-zone simplified model:

$$\frac{dQ_{\text{net}}}{d(\text{CAD})} = \frac{k}{k-1} p_{\text{cyl,abs}}(\text{CAD}) \frac{dV(\text{CAD})}{d(\text{CAD})} + \frac{1}{k-1} V(\text{CAD}) \frac{dp_{\text{cyl,abs}}(\text{CAD})}{d(\text{CAD})} \quad (10.2)$$

where  $k$  is the heat capacity ratio (assumed equal to 1.38) and  $V(\text{CAD})$  is the cylinder volume variable with CAD. The term  $\frac{dQ_w}{d(\text{CAD})}$ , accounting for the heat transfer through the cylinder walls, has been estimated as:

$$\frac{dQ_w}{d(\text{CAD})} = A_{ht} h_c (T - T_w) \quad (10.3)$$

where  $A_{ht}$  is the instantaneous cylinder heat exchange surface (crown of a cylinder head, cylinder walls, and piston head),  $T$  is the instantaneous cylinder average temperature,  $T_w$  is the average temperature of the inner cylinder surface, while the total heat transfer coefficient  $h_c$  was estimated as proposed by Woschni (1967). The estimated error in this calculation, due to the errors in the absolute cylinder pressure measurement, is around 2%. Based on  $p_{\text{cyl,abs}}$ , it was possible to estimate the indicated power  $P_i$  supplied by the engine:

$$P_i = \frac{n}{n_R} \oint_{\text{cycle}} p_{\text{cyl,abs}} dV \quad (10.4)$$

where  $n$  is the engine speed, while  $n_R$  ( $=2$  in this case) is the number of crank revolutions for each power stroke. The average diesel fuel consumption was measured by means of an AVL 733S fuel balance. The methane flux was stabilized by means of a 0.8 L plenum positioned upstream the methane injector. The average methane fuel consumption  $G_{\text{gas}}$  was measured by means of a thermal mass flow, Aalborg Instruments and Controls Inc., model DFC 36 characterized by a measurement error below 1%. The measurement of the fuel consumption allowed to estimate the fuel conversion efficiency referred to the indicated power,  $\eta_f$ :

$$\eta_f = \frac{P_i}{\dot{m}_d H_{i,d} + G_{\text{gas}} H_{i,\text{gas}}} \quad (10.5)$$

where  $H_{i,d}$  and  $H_{i,\text{gas}}$  are the lower calorific values, respectively, of diesel fuel and methane. The combustion efficiency was calculated as:

$$\eta_b = 1 - \frac{\sum x_i H_{i,i}}{\left( \frac{\dot{m}_d H_{i,d} + G_{\text{gas}} H_{i,\text{gas}}}{\dot{m}_a + \dot{m}_d + G_{\text{gas}}} \right)} \quad (10.6)$$

in which  $x_i$  is the mass fractions of CO and THC measured at the exhaust,  $H_{i,i}$  the related lower calorific values, and  $\dot{m}_a$  is the consumed intake air mass measured by means of an AVL FLOWSONIX mounted between two plenums in order to stabilize the air flux. Because the composition of THC in the exhaust, and thus the related  $H_{i,i}$ , is not known, the combined mass-fraction-weighted  $H_i$  of diesel fuel and methane has been used to represent the lower calorific value of THC.

The efficiency of the thermodynamic cycle was calculated as:

$$\eta_c = \frac{\eta_f}{\eta_b} \quad (7)$$

The combustion products and therefore the pollutant emission levels at the engine exhaust have been measured by means of an AVL AMA i60 Exhaust Measurement System.

In particular, THC levels have been measured through AVL flame ionization detector (FID) analyzer, whose operation is based on the measurement of the electrical current yield by the organic carbon atoms ionized in a hydrogen flame.  $\text{NO}_x$  levels were measured through AVL chemiluminescence detector (CLD) analyzer, whose operation is based on the measurement of the light emitted during the oxidation of nitrogen oxide NO with ozone  $\text{O}_3$ , and CO levels have been measured through an infrared detector (IRD) analyzer, whose operation is based on the measurement of an infrared radiation absorption, correlated to the concentration of the component to be measured. Particulate matter at tailpipe was not measured since, as observed in several engine working conditions, the emission levels were always well below  $1 \text{ mg/m}^3$ .

## 10.3 Results and Discussion

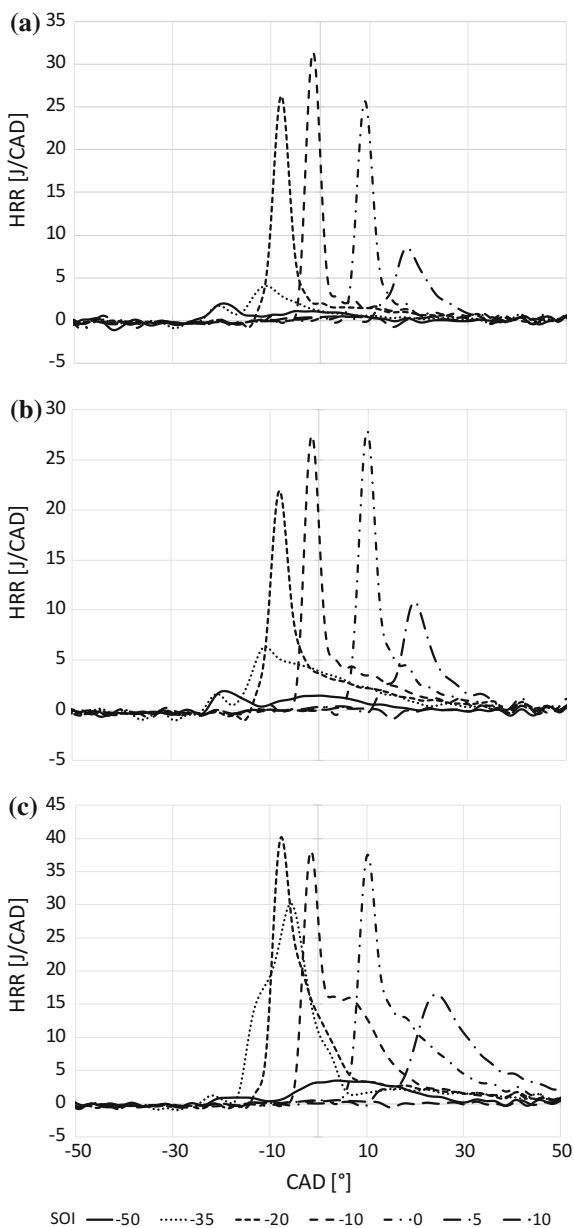
### 10.3.1 Effect of SOI Spanning on Combustion Development

Figure 10.2 shows the HRR histories calculated on the basis of cylinder pressure measured at  $n = 1500 \text{ rpm}$  for different pilot timings (varied from  $-50 \text{ CAD ATDC}$  up to  $10 \text{ CAD ATDC}$ ). Injection and engine settings were:  $\text{CR} = 17$ ;  $p_{\text{rail}} = 1250 \text{ bar}$ ;  $\text{ICP} = 1.16 \text{ bar}$ . Tests have been run injecting always the same amount of pilot diesel fuel ( $\dot{m}_d = 6 \text{ mm}^3/\text{cycle}$ ), while varying the amount of introduced methane: In detail, plot shows data (a) with no methane (OD); (b) with low/medium methane amount (LM); and (c) with medium/high methane amount (MH). The combustion development observed for all the injection and engine settings can be summarized in the following macro-trends:

- Advanced SOI and low amounts of methane (plot a) show a gradually weaker HRR, characterized by a first heat release at very advanced CAD (around  $-20 \text{ CAD ATDC}$ , likely associated with LTC) followed by a second heat release phase; as the methane is increased (plots b and c), this second heat release phase shows an increasing peak.
- Retarding SOI (plot a) leads to a HRR shape closer to the one observed with the conventional diesel combustion: a premixed peak followed by a queue characterized by a lower HRR. In this case too, this second combustion phase is more pronounced as the methane introduced in the cylinder is increased (plots b and c).

In Fig. 10.3, the above observations are summarized. In particular, referring to Fig. 10.3a, for low/medium values of methane rates, HRR peak first increases as SOI is retarded from very advanced SOI and then decreases as SOI is further retarded after TDC. This trend is still observed as the methane rate is increased; however, the SOI related to the maximum HRR is gradually advanced and

**Fig. 10.2** HRR versus CAD for variable methane rate:  
**a** OD; **b** L; **c** M. CR = 17;  
 p<sub>rail</sub> = 1250 bar;  
 ICP = 1.16 bar



maximum values globally increase. The CAD corresponding to maximum HRR is first advanced as SOI is retarded from very advanced SOI and then is delayed. Methane rate has a secondary influence on CAD corresponding to maximum HRR. This behavior, already described in the literature, is mainly due to the behavior of

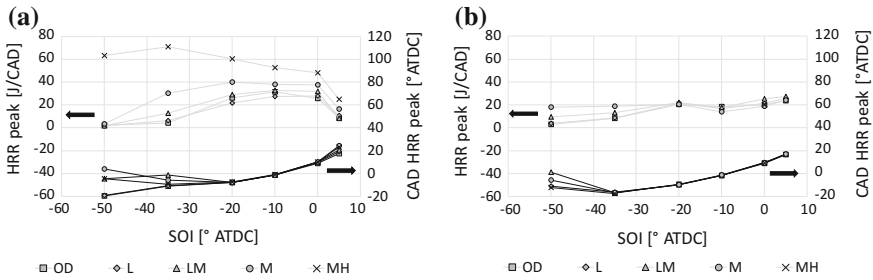


**Fig. 10.3** HRR peak and related CAD as a function of SOI for different methane rates. **a** CR = 17,  $p_{\text{rail}} = 1250$  bar, ICP = 1.16 bar; **b** CR = 17,  $p_{\text{rail}} = 500$  bar, ICP = 1.66 bar

the ignition delay combined with the equivalence ratio distribution inside the combustion chamber. As SOI is advanced, ignition delay is prolonged which can lead to overlearning of the mixture and low combustion rate. On the other hand, as SOI is retarded, ignition conditions may not be reached due to temperature reduction during the expansion phase. The combustion development just described was observed for all combinations of CR,  $p_{\text{rail}}$ , and ICP tested during the present experimental campaign with the exception of CR = 17, ICP = 1.66,  $p_{\text{rail}} = 500/1250$  bar, for which the observed behavior is reported in Fig. 10.3b. The main differences that can be noted with previous plots are: for retarded SOI, the HRR peak exhibits an increasing trend; in these conditions, the effect of increasing methane is not univocally defined.

In the following, the combustion development has been characterized in terms of: ignition delay, ID, defined as the angular difference between the SOI and the angle at which 5% of the total heat has been released; maximum pressure rise rate, MPRR; combustion beginning, CA5, defined as the angle at which 5% of the total heat has been released; center of combustion, CA50, defined as the angle at which 50% of the total heat has been released; and combustion duration, CA90-CA10, defined as the angular difference between the angles at which 90 and 10% of the total heat has been released. Then, the effects of ICP, CR, and  $p_{\text{rail}}$  on the above parameters have been analyzed. It shall be emphasized that the injection event was always decoupled from the start of combustion, due to the short duration of pilot injection. Therefore, the behavior of the difference between the start of combustion and the end of injection follows the same trend of ID assuming values always higher than zero.

### 10.3.2 Effect of Intake Charge Pressure

In Fig. 10.4, the effect of ICP (ICP = 1.16 bar, column “a”; ICP = 1.66 bar, column “b”) at different SOI and for different methane rates on ID and MPRR, plots (a’) and (b’); CA5, CA50, and CA90-CA10, plots (a’’) and (b’’), is highlighted. The engine



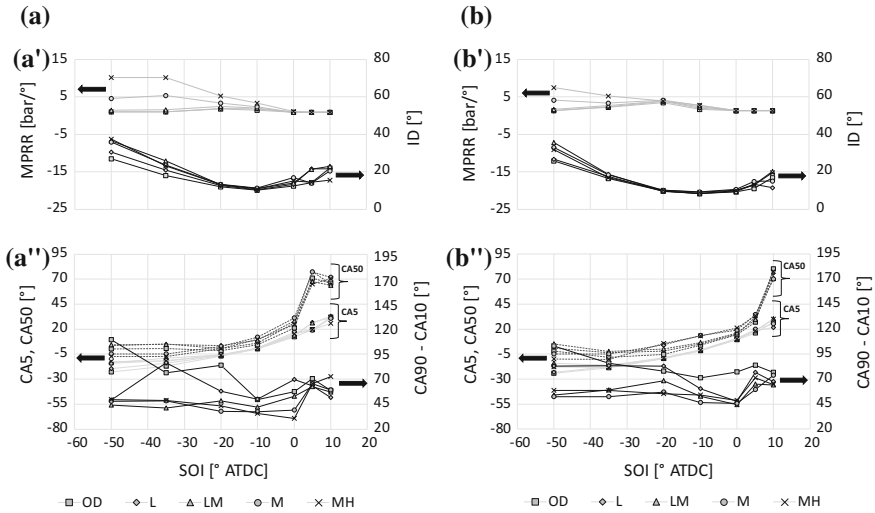


**Fig. 10.4** Effect of intake charge pressure (ICP = 1.16 bar, column “a”; ICP = 1.66 bar, column “b”) at different SOI and for different methane rates on: ID and MPRR, plots (a’) and (b’); CA5, CA50, and CA90-CA10, plots (a’’) and (b’’). CR = 14; p<sub>rail</sub> = 500 bar

volumetric compression ratio was fixed equal to 14 and the injection pressure to 500 bar.

Concerning ID (plots a’ and b’), a decreasing–increasing behavior is visible with SOI spanning. In particular, ID reaches the highest values—about 40 CAD—with the highest SOI advances, due to the low temperature at which the injection is performed. In these conditions, the limiting factor is represented by the preignition reaction rates (slower at a lower temperature), as there is sufficient time for diesel evaporation and effective mixing with the surrounding methane–air mixture. As SOI is retarded, ID decreases up to a certain value (around 10 CAD), as the temperature in the cylinder during injection is higher; then, it increases again, because the cylinder temperature during injection decreases again. This behavior has been broadly documented in the literature [see, for example, Guerry et al. (2016)] and was observed for all the other investigated combinations of engine volumetric compression ratio and pilot injection pressure. It must be specified, however, that, for the two combinations of Fig. 10.3b, the increasing trend when retarding SOI was much less pronounced.

It is visible that the methane rate has a secondary effect on ID compared to SOI. Only-pilot diesel injection condition, however, exhibits, as expected, the lowest values of ID. This behavior too has been broadly documented in the literature; see, for example, Hosmath et al. (2016).

Comparing curves varying ICP (plots a’ and b’), it can be noted that also this parameter has a secondary effect on ID. In any case, the observed trend, i.e., a reduction of ignition delay as ICP is increased, especially for central values of SOI

in the tested interval, has been already described, for example, in Guerry et al. (2016). The above conclusions that can be extended to all the other investigated combinations of engine compression ratio and injection pressure mainly occur because the in-cylinder pressure both before and during combustion is higher increasing ICP; consequently, ignition occurs earlier. Another related aspect of the ICP variation is that the overall equivalence ratio is also allowed to vary with ICP. Clearly, the temporal phasing of the HRR curves is also affected by the overall equivalence ratios.

Concerning MPRR (plots a' and b'), a strong variability is evident with SOI. At low/medium methane rate, MPRR associated with very advanced SOI is very low, then increases to higher values at intermediate SOI, and then decreases again up to very low values with retarded SOI. SOI values determining a very low MPRR are associated with a very slow combustion development, as already described in the previous section. This behavior has been documented, for example, in Raihan et al. (2015). As the amount of methane introduced in the cylinder is increased, MPRR behavior varies significantly. Values associated with very advanced SOI are very high; however, the trend becomes strictly decreasing [as shown in Guerry et al. (2016) for tests conducted at high BMEP] and MPRR values gradually reach those observed at low/medium methane rate as SOI is retarded. The effect of ICP (compare plots a' and b'), observed for all combinations of engine compression ratio and injection pressure, is to reduce significantly the absolute value of MPRR at medium/high methane rates, while there is a slight increase at low/medium methane rate. This trend is possibly due to a more limited atomization and vaporization of pilot fuel droplets acting as ignition agents for the premixed methane/air phase.

Concerning CA5 angles (plots a'' and b''), it is visible that it is advanced as SOI is advanced. For the most advanced SOI, it is visible, however, that CA5 reaches a plateau and, for several combinations of engine compression ratio and injection pressure, it actually starts increasing. This trend too has been documented in the literature [see, for example, Guerry et al. (2016)].

CA50 (plots a'' and b'') follows a similar behavior as far as SOI is between the most advanced and intermediate values. For retarded SOI, however, the difference between CA50 and CA5 increases evidently, which denotes a slower combustion development attributable to the lower pressure and temperature into the cylinder associated with very delayed SOI.

Concerning CA90-CA10 (plots a'' and b''), a trend first decreasing, then increasing, and then decreasing again when retarding SOI was observed for most of methane flow rates. This trend, observed for all combinations of engine compression ratio and injection pressure, is not in agreement with what observed, for example, in Guerry et al. (2016). It is worth noting, moreover, that the difference between CA50 and CA5, previously underlined for retarded SOI, does not excessively penalize combustion overall duration. It is also evident that the effect of methane rate is secondary and appears more evident at low/medium rates. Increasing methane amount, however, determines a reduction in combustion duration, which will lead—as analyzed in the following—to a corresponding increase in fuel conversion efficiency.

Increasing ICP very slightly decreases CA5; CA50 starts differentiation from CA5 with SOI equal to 5 at low ICP, while at high around 10. This leads to the conclusion that higher ICP sustains the combustion with more retarded SOI. Finally, combustion duration (CA90-CA10) is slightly higher at higher ICP. Again, this trend is confirmed for all combinations of engine compression ratio and injection pressure.

In Fig. 10.5, the effect of intake charge pressure (ICP = 1.16 bar, column “a”; ICP = 1.66 bar, column “b”) at different SOI and for different methane rates on  $\eta_b$  and  $\eta_f$ , plots (a') and (b'); CO and THC, plots (a'') and (b''); and  $\text{NO}_x$ , plots (a''') and (b'''), is highlighted (note that the interval of SOI has been limited to -50-0 ATDC given that, for more retarded SOI, the engine  $\eta_f$  is equal to zero and the results do not have practical sense). As for plots in Fig. 10.4, the engine volumetric compression ratio was equal to 14 and the injection pressure to 500 bar.

The behavior of  $\eta_b$  is reported in Fig. 10.5, plots a' (low ICP) and b' (high ICP). As visible, at low/medium methane rate, the behavior is increasing and then decreasing when SOI is retarded. This trend is due to the fact that, as already analyzed through HRR curves, at very advanced or retarded SOI, combustion is very poor (see Fig. 10.2a); therefore, a large amount of fuel is discharged along the exhaust line, as will be evident analyzing THC and CO emission levels in these

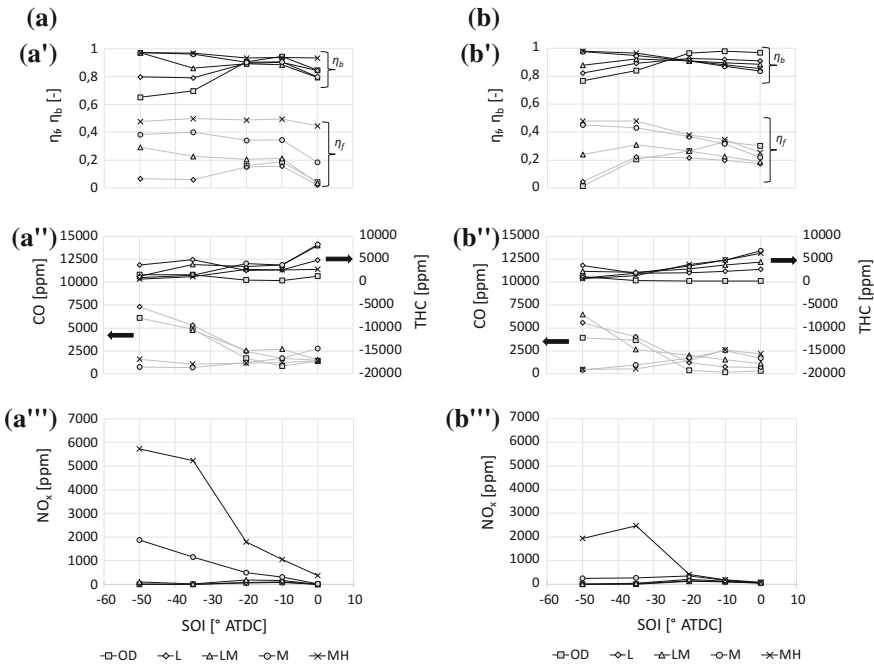


**Fig. 10.5** Effect of intake charge pressure (ICP = 1.16 bar, column “a”; ICP = 1.66 bar, column “b”) at different SOI and for different methane rates on:  $\eta_b$  and  $\eta_f$ , plots (a') and (b'); CO and THC emission levels, plots (a'') and (b'');  $\text{NO}_x$  emission levels, plots (a''') and (b'''). CR = 14;  $p_{\text{rail}} = 500$  bar

conditions. Increasing methane rate, combustion is poor only at very retarded SOI (see Fig. 10.2c): in these conditions again, a large amount of fuel is exhausted, so determining a significant reduction of  $\eta_b$ . At very advanced SOI, on the other hand,  $\eta_b$  is close to unity.  $\eta_b$  is basically unaffected by ICP being its effect evident only at low methane rate and very advanced SOI. Concerning  $\eta_c$ , the effect of methane rate is to increase  $\eta_c$ . The fuel conversion efficiency  $\eta_f$  is therefore strictly increasing at medium/high methane rates [in agreement with results reported in Guerry et al. (2016)], while it is increasing and then decreasing at low methane rates as SOI is advanced (plots a' and b'). An increase of ICP negatively affected  $\eta_f$  at medium/high methane rates and central SOI.

THC levels increase as SOI is retarded; moreover, from low to medium methane rates, THC increases, while from medium to medium/high methane rates THC decreases. If indicated specific emission levels were considered instead of [ppm], the trend would have been increasing as methane rate decreases. These trends are in agreement with results reported in Guerry et al. (2016). On the other hand, CO emission levels exhibit a more complicated behavior. They decrease as SOI is retarded at low/medium methane rate, while they show an increasing/decreasing behavior at medium/high rates. In this case too, if indicated specific emission levels were considered instead of [ppm], the trend would have been increasing as methane rate decreases.

It is widely recognized that THC emissions are determined by many causes: valve overlap, flame quenching, wall impingement, spray characteristics, crevices, in-cylinder conditions, and residence time. CO emissions, on the other hand, are mainly due to flame quenching, crevices, residence time, in-cylinder conditions. In a dual-fuel HCCI engine—with methane fumigated along the intake duct—the major sources are valve overlap, crevices, and bulk quenching of the diesel–methane–air mixture, with the in-cylinder bulk temperature having a significant influence on THC and CO oxidation rates, with the former faster than the latter.

In Fig. 10.6, the maximum in-cylinder bulk temperature is reported, at different SOI and for different methane rates (ICP = 1.16 bar, plot “a”; ICP = 1.66 bar, plot “b”).

From plot “a”, it can be observed that maximum in-cylinder bulk temperature is not sensitive to SOI for low methane rates, while it decreases as SOI is retarded at medium/high methane rates. This is consistent with the THC levels observed in Fig. 10.5 plot b”. On the other hand, from low to medium methane rates, THC increase as well as maximum in-cylinder bulk temperature, it could be argued because of crevice hydrocarbons not being oxidized because of the excessively lean methane–diesel–air mixture together to mixture escaping during valves overlap. Increasing methane rate from medium to high values, however, the mixture is not further excessively lean and crevice hydrocarbons can be—at least partially—oxidized. It is believed that no wall impingement by spray liquid phase takes place, based on data reported in Carlucci et al. (2014, 2015, 2017).

Concerning CO, a marginal increase is observed at retarded SOI, while THC increase is sharper; at very advanced SOI, CO increase is sharper than THC increase, according to results published in Guerry et al. (2016).

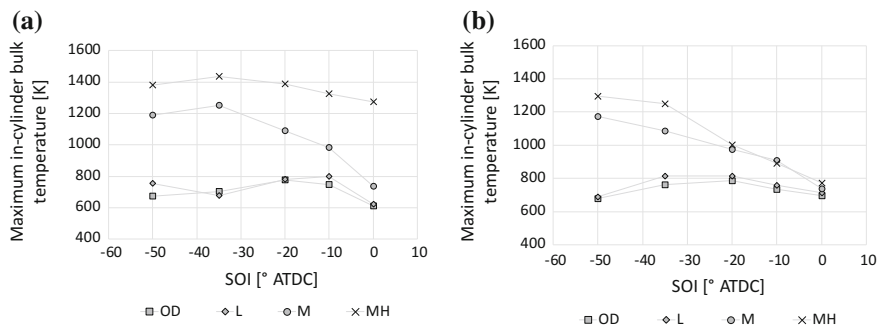


**Fig. 10.6** Effect of intake charge pressure (ICP = 1.16 bar, plot “a”; ICP = 1.66 bar, plot “b”) at different SOI and for different methane rates on maximum in-cylinder bulk temperature. CR = 14;  $p_{\text{rail}} = 500$  bar

Increasing ICP has a direct and an indirect effect on many of the abovementioned causes determining THC and CO emission levels: In particular, more oxygen is available for oxidation, but at the same time the mixture equivalence ratio decreases; more fresh methane–air mixture escapes during valve overlap; due to the different in-cylinder pressure and temperature histories, both the residence time and the diesel spray properties vary. The effect of ICP on each of these causes is hard to be quantified; the overall observed effect is that, increasing ICP, THC is reduced. On the other hand, CO emission levels decrease as ICP increases.

$\text{NO}_x$  emission levels are shown in Fig. 10.5 plot a’’. In particular, at low/medium methane rate,  $\text{NO}_x$  emissions increase and then decrease as SOI is retarded, in agreement with results reported in Guerry et al. (2016). At medium/high methane rate, the behavior is strictly decreasing as SOI is retarded.  $\text{NO}_x$  emission behavior as a function of SOI and methane reproduces the behavior of maximum bulk temperature in Fig. 10.6 being dependent, as modeled by Zeldovich mechanism, on local temperature, residence time, and oxygen availability. The effect of ICP is to significantly reduce  $\text{NO}_x$  emissions.

### 10.3.3 Effect of Engine Volumetric Compression Ratio

In Fig. 10.7, the effect of engine volumetric compression ratio (CR = 14, column “a”; CR = 17, column “b”) at different SOI and for different methane rates on ID and MPRR, plots (a’) and (b’); CA5, CA50, and CA90-CA10, plots (a’’) and (b’’), is highlighted. The injection pressure and the ICP were, respectively, set equal to 500 bar and 1.16 bar.

Comparing both ID, it is visible that the effect of compression ratio increase is to reduce both of them, for all combinations of ICP and injection pressure. Indeed, thanks to the higher in-cylinder pressure reached during compression phase,

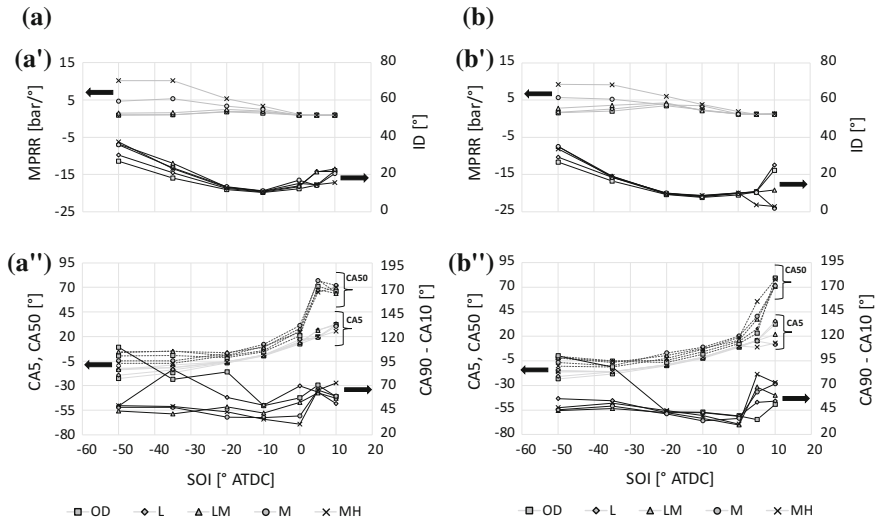


**Fig. 10.7** Effect of engine volumetric compression ratio ( $CR = 14$ , column “a”;  $CR = 17$  bar, column “b”) at different SOI and for different methane rates on: ID and MPRR, plots (a’) and (b’); CA5, CA50, and CA90-CA10, plots (a’’) and (b’’).  $p_{\text{rail}} = 500$  bar;  $ICP = 1.16$  bar

preignition reactions are accelerated and ID reduced. However, as already seen discussing the effect of ICP, ID shortening reduces the premixed combustion intensity. The result is that MPRR does not vary significantly with CR.

Increasing engine compression ratio, CA90-CA10 is reduced at low/medium methane rates, while at higher rates the values are comparable. CA5 and CA50 are similar up to  $SOI = 0$  at low compression ratio, while at high compression ratio the two angles remain similar up to  $SOI = 5$  ATDC. The observed trends are in good agreement with those presented in Hosmath et al. (2016). This leads to the conclusion that a higher CR sustains the combustion with more retarded SOI.

In Fig. 10.8, the effect of engine volumetric compression ratio ( $CR = 14$ , column “a”;  $CR = 17$ , column “b”) at different SOI and for different methane rates on  $\eta_b$  and  $\eta_f$ , plots (a’) and (b’); CO and THC, plots (a’’) and (b’); and  $NO_x$ , plots (a’’) and (b’’’), is highlighted.

The effect of increased compression ratio is to increase  $\eta_b$  at low/medium methane rates, as visible comparing plots a’ (low compression ratio) and b’ (high compression ratio) of Fig. 10.8 for all combinations of ICP and  $p_{\text{rail}}$ . The effect of compression ratio is to extend the SOI range for which fuel conversion efficiency  $\eta_f$  is high, this especially at low/medium methane rates, while at high rates the values are not sensibly affected by compression ratio, this result being confirmed by results reported in Di Blasio et al. (2017a).

THC is slightly reduced by variation of compression ratio, while CO is reduced at low/medium methane rate, especially at central values of SOI, in good agreement with results reported in Di Blasio et al. (2017a). As already discussed in

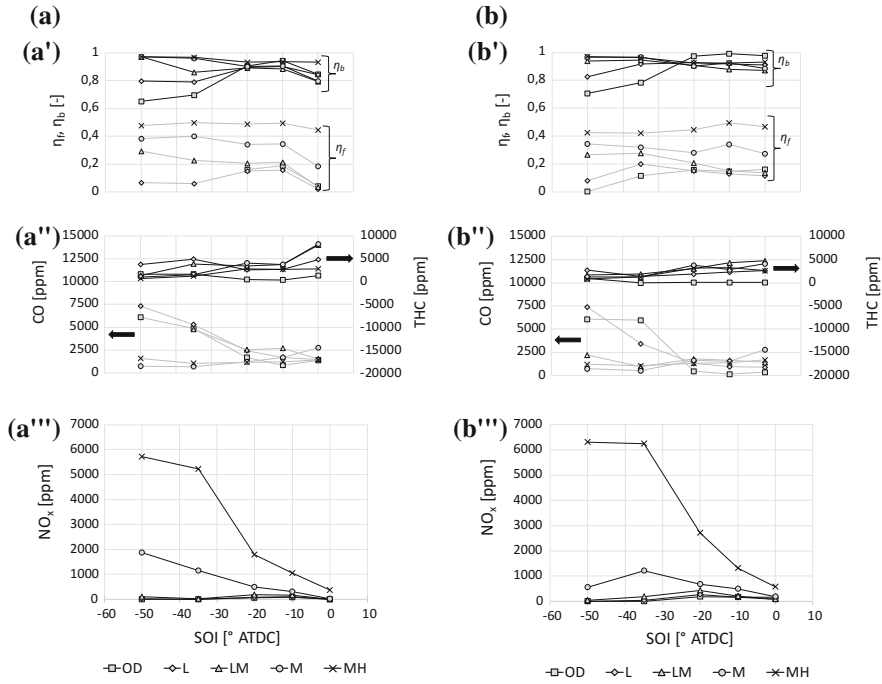


**Fig. 10.8** Effect of engine volumetric compression ratio (CR = 14, column “a”; CR = 17, column “b”) at different SOI and for different methane rates on:  $\eta_b$  and  $\eta_f$  plots (a’) and (b’); CO and THC emission levels, plots (a’’) and (b’);  $\text{NO}_x$  emission levels, plots (a’’’) and (b’’’).  $p_{\text{rail}} = 500$  bar; ICP = 1.16 bar

Sect. 10.3.2, the causes determining THC and CO are many and complex to be quantified. Among them, CR has an effect on spray properties, in-cylinder pressure and temperature histories and residence time.  $\text{NO}_x$  is increased as compression ratio is increased, due to higher in-cylinder temperature (not shown) and longer residence time.

### 10.3.4 Effect of Injection Pressure

In Fig. 10.9, the effect of pilot injection pressure ( $p_{\text{rail}} = 500$  bar, column “a”;  $p_{\text{rail}} = 1250$  bar, column “b”) at different SOI and for different methane rates on ID and MPRR, plots (a’) and (b’), and CA5, CA50, and CA90-CA10, plots (a’’) and (b’’’), is highlighted. The engine compression ratio was equal to 17, while the intake pressure was set equal to 1 bar.

Comparing ID, it is visible that the effect of injection pressure increase is to increase ID when SOI is advanced, for all combinations of ICP and engine compression ratio. The variable effect of  $p_{\text{rail}}$  with SOI is mainly due to the fact that, at

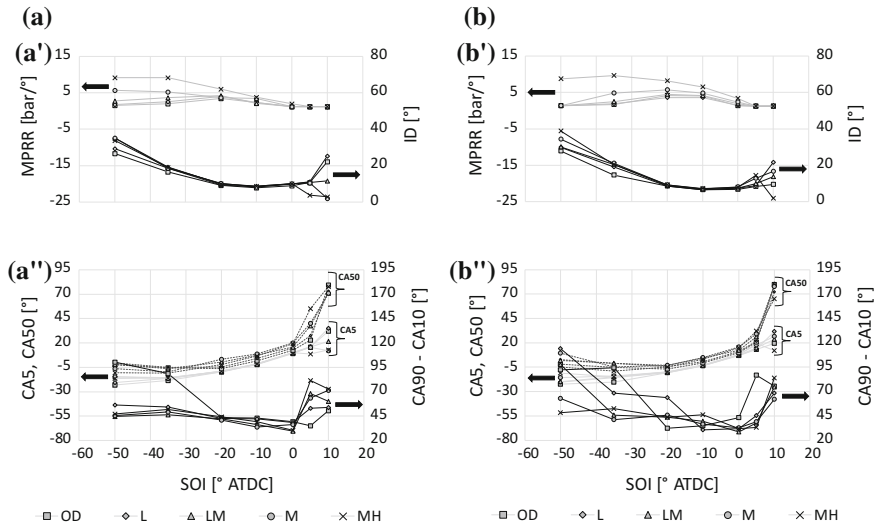


**Fig. 10.9** Effect of injection pressure ( $p_{\text{rail}} = 500$  bar, column “a”;  $p_{\text{rail}} = 1250$  bar, column “b”) at different SOI and for different methane rates on: ID and MPRR, plots (a') and (b'); CA5, CA50 and CA90-CA10, plots (a'') and (b''). CR = 17; ICP = 1.16 bar

very advanced or retarded SOI, chemical ID dominates on physical ID, while the contrary happens for central values of SOI (Carlucci et al. 2017). Concerning MPRR, the effect of injection pressure is always to slightly increase MPRR. All these trends are confirmed by data reported in Raihan et al. (2015).

CA90-CA10 is slightly reduced. CA5 and CA50 are similar up to SOI = 0 at a low injection pressure, while at high injection pressure the two angles remain similar up to SOI = 5 ATDC. Again, this suggests that with higher  $p_{\text{rail}}$  the combustion can be sustained for more retarded SOI.

In Fig. 10.10, the effect of  $p_{\text{rail}}$  ( $p_{\text{rail}} = 500$  bar, column “a”;  $p_{\text{rail}} = 1250$  bar, column “b”) at different SOI and for different methane rates on  $\eta_b$  and  $\eta_f$  plots (a') and (b'); CO and THC, plots (a'') and (b''); and  $\text{NO}_x$ , plots (a''') and (b'''), is highlighted.

A not very evident effect of injection pressure increase is observed on  $\eta_b$ , while  $\eta_f$  is increased specially at low/medium methane rates, this trend confirmed by data reported in Raihan et al. (2015). At medium/high methane rate, the values are affected by injection pressure only at very advanced SOI, where a reduction is observed when injection pressure is increased.

CO and THC emissions in ppm are reported in Fig. 10.10 plots a'' and b''. The effect of injection pressure on THC is a slight reduction, especially at low methane rates, as injection pressure is increased, in agreement with results reported in Raihan et al. (2015). An opposite behavior is observed only for advanced SOI. On the other hand, CO is increased, in agreement with results reported in Raihan et al. (2015). As already discussed in Sect. 10.3.2, the causes determining THC and CO are many



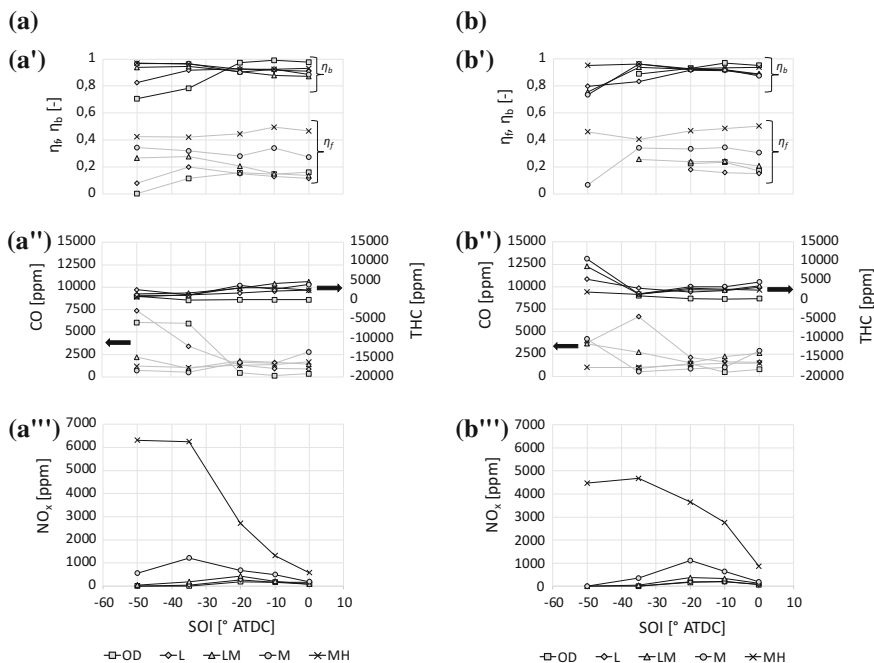


**Fig. 10.10** Effect of injection pressure ( $p_{rail} = 500$  bar, column “a”;  $p_{rail} = 1250$  bar, column “b”) at different SOI and for different methane rates on:  $\eta_b$  and  $\eta_f$ , plots (a’) and (b’); CO and THC emission levels, plots (a’’) and (b’’); NO<sub>x</sub> emission levels, plots (a’’’) and (b’’’). CR = 17; ICP = 1.16 bar

and complex to be quantified. Among them,  $p_{rail}$  has an effect mainly on spray properties and indirectly on in-cylinder pressure and temperature histories and residence time.

Finally, NO<sub>x</sub> levels are reported in Fig. 10.10 plots a''' and b'''. The effect of  $p_{rail}$  increase is to decrease NO<sub>x</sub> levels. This result, in agreement with similar data reported in Raihan et al. (2015), can be attributed to the fact that, given the little amount of diesel pilot fuel, higher injection pressures lead to faster vaporization and better fuel–air mixing which in turn facilitates better mixing of high-temperature diesel combustion zones with leaner, low-temperature methane combustion zones. Overall, this leads to a reduction in NO<sub>x</sub> at the engine exhaust.

### 10.3.5 Factor Settings Approaching HCCI Operation

As already said, the total amount of tests is very high and it is not convenient, for the sake of brevity, to report all the results. However, it is important to investigate the factor variation ranges leading the engine to operate in or close to HCCI

combustion, i.e., guaranteeing a high conversion efficiency and low emission levels at the same time.

In Table 10.3, the range of SOI able to guarantee a  $\text{NO}_x$  level lower than 2 g/kWh and  $\eta_f$  and THC values comparable with those measured for “conventional” SOI are highlighted for each combination of engine compression ratio, injection pressure, and ICP. Moreover, a cell colored in light gray, dark gray, or black means that the above result was obtained, respectively, at low, low/medium, or medium/high methane rate.

From Table 10.3, it is possible to recognize that:

- A significant reduction of  $\text{NO}_x$  levels, keeping high values of  $\eta_f$  and THC, can be obtained with very advanced pilot injections; in these conditions, however, the benefit is limited to low/medium methane rates. In order to reach these conditions, it is preferable to have lower values of engine compression ratios; the utilization of a high compression ratio was effective only with a proper choice of injection pressure and ICP.
- A significant reduction of  $\text{NO}_x$  levels, keeping high values of  $\eta_f$  and THC, can be also obtained retarding SOI after TDC. In these conditions, it is visible that the benefits are not limited only to low/medium methane rates, but are extended also at high rates. In order to reach these conditions, a high value of ICP is preferable, although good results were also reached with low intake pressure combined with a high injection pressure and a high engine compression ratio.

**Table 10.3** Factor settings guaranteeing  $\text{NO}_x$  level lower than 2 g/kWh and  $\eta_f$  and THC values comparable with those measured for “conventional” SOI

SOI [CADATDC]	-50	-35	-20	-10	0	5
14/500/1.16						
14/1250/1.16						
17/500/1.16						
17/1250/1.16						
14/500/1.66						
14/1250/1.66						
17/500/1.66						
17/1250/1.66						

Therefore, in order to obtain a homogeneous mixture and consequently a lean combustion, the longer ID obtained with very advanced or very retarded injections can be exploited. The first approach has been abundantly studied and documented in the open literature, some of which is cited in the present chapter. The second approach, on the other hand, did not receive attention so far. However, in diesel HCCI, a combustion concept exploiting very retarded injections has been already proposed, highlighting three main advantages: first, late injections are applicable with conventional technology already available for diesel engines; second, injection and combustion processes are not completely decoupled, so that combustion phasing is controlled by injection timing; third, very advanced injections determine impingement on the walls, which also shorten the average life of the lubricating oil by an excessive dilution of the fuel that wets the walls during the compression phase. This concept is the basis of the modulated kinetics (MK) combustion.

In the first generation of the MK system, success of combustion with HCCI characteristics relied on three factors. First, oxygen concentration and local temperature in the cylinder were reduced with EGR, so determining a drastic reduction in  $\text{NO}_x$  emission but also an increase in soot and THC. Second, as previously said, the fuel injection was retarded, and so the ID prolonged, which led to a more premixed combustion with lower  $\text{NO}_x$ , lower soot, but higher THC emission mainly due to wall impingement. Third, a high swirl ratio was used in order to improve the mixture formation, further reducing soot emission and avoiding wall impingement, so leading to a drastic reduction in THC (Kimura et al. 1997).

In the second generation of the MK combustion system, studied in order to broaden the load and speed range of application, the autoignition delay was increased reducing the compression ratio and cooling the EGR. Moreover, the injection duration was reduced increasing the injection pressure (Kimura et al. 2001).

It could be argued that generally, by delaying the injection, the thermal efficiency is lowered. In MK combustion, this disadvantage is compensated by the high swirl and, therefore, by the low production of THC, which brings the thermal efficiency to levels comparable or even higher than diesel conventional combustion. MK combustion, moreover, is slower in the initial phase than the conventional one—thus, a reduction of the combustion noise is obtained—however, it grows vigorously during the second part of the combustion. This means that the combustion duration for the two cases is comparable.

In DF combustion concept, however, late injection potential addressed to establish HCCI combustion has not been investigated. In Fig. 10.11, in-cylinder pressure, HRR, HRR cumulative, and in-cylinder bulk temperature curves are reported, related to two “limit” cases: in 14-500-1.16 tests with SOI at TDC, an  $\eta_f$  value close to zero was measured at low/medium methane rates, while at medium/high rates it was significantly lower than that measured at more advanced SOI (Fig. 10.5 plot a'). THC was lower as well as CO at low and medium/high methane rates (at medium rates, they slightly increased compared to more advanced SOI; see Fig. 10.5 plot a'').  $\text{NO}_x$  was almost zero (Fig. 10.5 plot a'''). In 17-1250-1.16 tests, on the other hand,  $\eta_f$  assumes values comparable to those assumed at more

advanced SOI for all methane rates, with no penalty on THC, a very little penalty at medium/high methane rates in terms of CO and low  $\text{NO}_x$  specially at low/medium rates (see Fig. 10.10, column b). Still in Fig. 10.11, the effect of the increase of methane rate is highlighted. When compression ratio, injection pressure, and intake pressure are low (plot a''), the HRR associated with diesel combustion exhibits very low HRR values; therefore, the combustion duration is several tens of CAD. This is due to lower in-cylinder local temperatures deriving from both lower CR and ICP associated with the low injection pressure leading to poor atomization and slower vaporization. The addition of methane further penalizes the pilot combustion, as the HRR further decreases in the initial stage of combustion; as a consequence, methane combustion is slow as well and can be considered complete around 60 CAD ATDC.

As CR and injection pressure are increased (plot b''), the behavior is totally different. The HRR rate associated with the diesel fuel is much higher, so the combustion duration is strongly decreased. Moreover, the addition of methane does not affect negatively the pilot combustion. On the contrary, HRR increases, which is due to the combustion of methane. The remaining part burns more slowly during the queue, but the combustion can be considered complete well before the previous case. In fact, analyzing the cumulative HRR (plots a''' and b''') highlights that, in the first case, the total heat released remains low; the presence of methane further reduces it. In the second case, on the contrary, the total heat released is significantly higher and further increases if methane is added. The analysis of in-cylinder bulk temperature, reported in plots a'''' and b''''', further confirms a more complete combustion with high values of compression ratio and injection pressure. The high-temperature values reached during the expansion stroke help the oxidation of THC and CO species without penalizing  $\text{NO}_x$  emission.

Therefore, the elements characterizing MK can be seen also in DF combustion. This, therefore, shall stimulate the study of the effect of EGR (hot and cooled) and swirl, combined with variable injection pressure and engine compression ratio, as improvers of MK combustion, whose beneficial effect has been already proved for diesel HCCI combustion.

## 10.4 Factorial Analysis

In Sect. 10.2, Table 10.2, it has been highlighted that each factor varies on a certain number of levels; being 5 the variation levels of the methane rate, 7 the variation levels of pilot injection timing and 2 the variation levels of the injection pressure, engine volumetric compression ratio, and ICP, the complete factorial plan made of  $5 * 2 * 7 * 2 * 2 = 280$  possible combinations was therefore performed. In this section, the results of the factorial analysis will be described, conducted on: IMEP,  $\eta_f$ , MPRR, THC, CO, and  $\text{NO}_x$ . Therefore, the influence of each factor (first-order effects) as well as of combinations of factors (second-order effects), on the output parameters, has been quantified. To achieve this goal, the ANOVA technique was

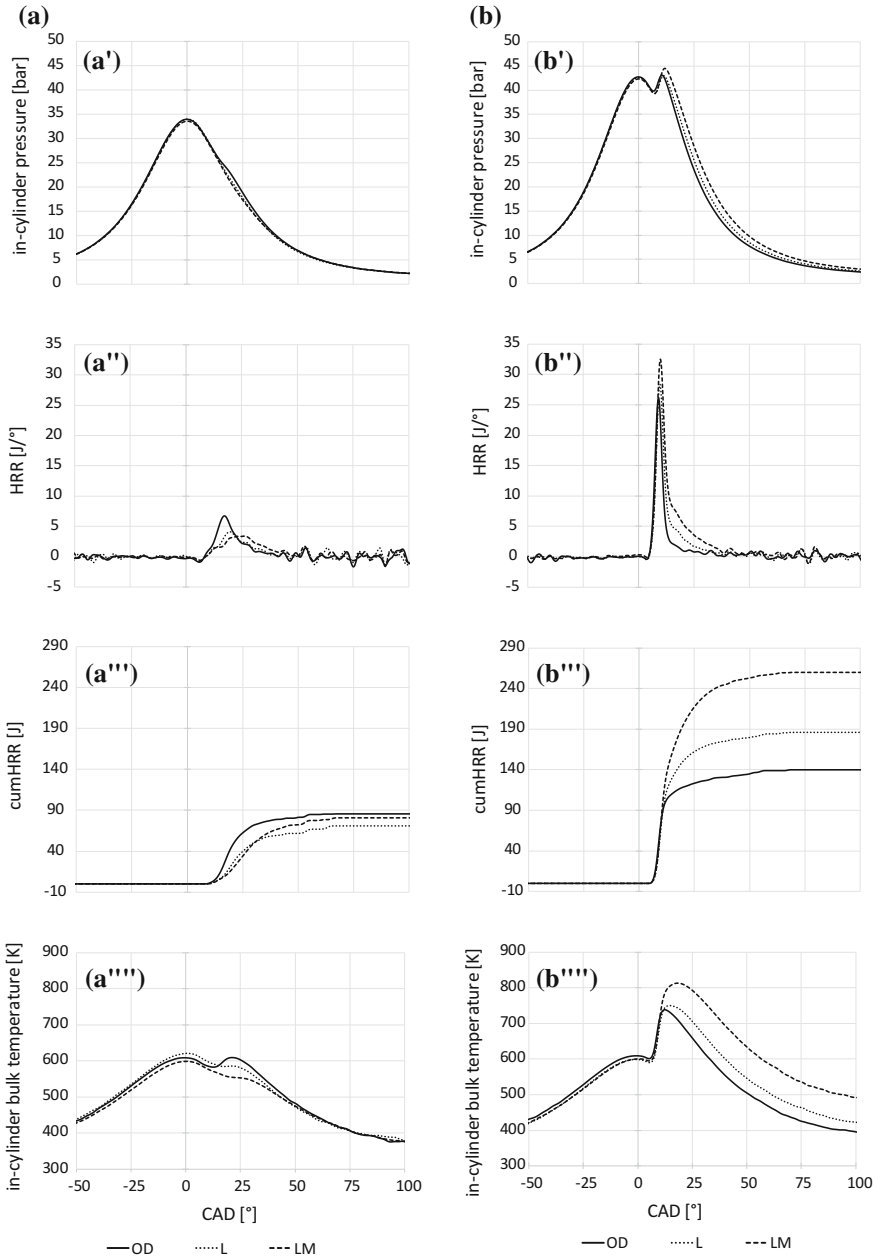


**Fig. 10.11** Comparison of in-cylinder pressure, HRR, HRR cumulative, and in-cylinder bulk temperature for different methane rates at SOI = TDC (CR = 14, p<sub>rail</sub> = 500 bar, ICP = 1.16 bar, column “a”; CR = 17, p<sub>rail</sub> = 1250 bar, ICP = 1.16 bar, column “b”)

applied and so a  $p$ -value was obtained, associated with each factor or combination of factors, for every output parameter. A low  $p$ -value means a high probability that a given output parameter is influenced by a specific factor (or combination of factors).

In Fig. 10.12a,  $p$ -values associated with each factor (CR,  $p_{\text{rail}}$ , SOI, ICP,  $G_{\text{gas}}$ ) for each output parameter (IMEP,  $\eta_f$ , MPRR, THC,  $\text{NO}_x$ , CO) are plotted. It can be easily observed that SOI is the most influential factor, as  $p$ -value is very low for all output parameters. ICP is mainly influential on engine performance (IMEP,  $\eta_f$ , MPRR) and THC emissions, while  $G_{\text{gas}}$  is more influential on both engine performance (IMEP,  $\eta_f$ , MPRR) and engine emissions (THC,  $\text{NO}_x$ , CO). The less influential factor is  $p_{\text{rail}}$ , whose slight effect is visible only on  $\text{NO}_x$  emission levels.

In Table 10.4, the effect of the increase of each factor on each output parameter is reported. The symbol “ $\uparrow$ ” means that the output parameter increases as the corresponding input increases, while the symbol “ $\downarrow$ ” means that the output parameter decreases as the corresponding input increases. The symbol “ $=$ ” associated with each of the previous symbols means that the effect is only slight. The two symbols together (as for SOI effect on IMEP and  $\eta_f$ ) means that the trend was first increasing and then decreasing.

A more detailed analysis has been conducted performing the ANOVA for each level of  $G_{\text{gas}}$ : The question was whether the  $p$ -values associated with CR,  $p_{\text{rail}}$ , SOI, ICP shown in Fig. 10.12a could be confirmed for each level of  $G_{\text{gas}}$ , i.e., varying the engine load. The analysis, not reported here for brevity, did not highlight strong differences. However, a significant effect on CO and  $\text{NO}_x$  of the ICP as the methane flow rate increases and a significant effect of pilot injection pressure on indicated mean effective pressure and fuel conversion efficiency as the methane flow rate increases were observed.

Finally, observing Fig. 10.12b, the second-order most important effects can be recognized. If the injection pressure has the least first-order effect on the output parameters, the second-order effect in combination with pilot injection timing on engine performance (IMEP,  $\eta_f$ , MPRR) and THC emissions is significant, as well as the effect on  $\text{NO}_x$  emissions in combination with ICP. Another significant

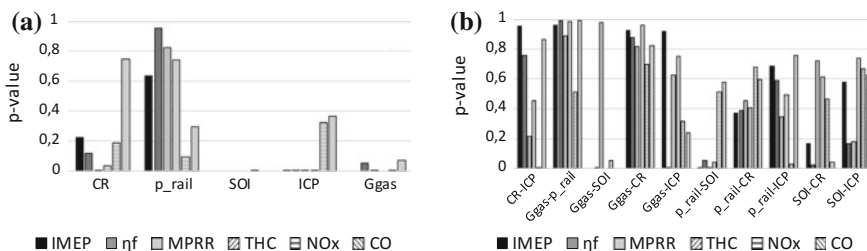


Fig. 10.12  $p$ -value associated with each factor for each engine output parameter (plot “a”);  $p$ -value associated with second-order effects for each engine output parameter (plot “b”)

**Table 10.4** Trend determined by each factor on each engine output parameter

	IMEP	$\eta_f$	MPRR	THC	NO <sub>x</sub>	CO
CR	↑	↑	↑	↓	↑	↓ =
p <sub>rail</sub>	↓ =	↓ =	↓ =	↑	↑	↑
SOI	↑ ↓	↑ ↓	↓	↑	↓	↓
ICP	↑	↑	↑	↓	↓	↓
G <sub>gas</sub>	↑	↓	↑	↑	↑	↓

second-order effect can be observed on  $\eta_f$  and CO emissions combining engine volumetric compression ratio and pilot injection timing.

## 10.5 Summary and Conclusions

In the first part of this work, a full factorial DoE has been performed on a single-cylinder diesel engine modified in order to operate in dual-fuel diesel–methane mode. The methane was fumigated along the intake duct thanks to an injector. During the experimental campaign, compression ratio, ICP, pilot injection timing and pressure, and methane flow rate were varied on several levels; this allowed to quantify the effect of each of them, as well as of their interaction, on combustion development, engine efficiency and pollutant levels at the exhaust. Results are summarized in the following:

- Pilot injection timing is the most influential factor on both engine performance and emissions. Very advanced or retarded timings (with respect to the tested range) showed potential in enabling PPCI thanks to the long ignition delay: in these conditions, very low emission levels and acceptable levels of maximum pressure rise rate with no or little penalization on fuel conversion efficiency were observed.
- Methane flow rate supplied to the engine is influential too on both engine performance and emissions; the fuel conversion efficiency and NO<sub>x</sub> levels both increase as methane flow rate increases, while CO and THC levels have a more complicated behavior, increasing when methane flow rate increases from low to medium values, decreasing from medium to high values.
- ICP mainly influences engine performance; the effect of THC is stronger, while CO and NO<sub>x</sub> are only marginally influenced. A more detailed analysis, specialized at different methane flow rates, highlighted a significant effect on CO and NO<sub>x</sub> as the methane flow rate increases. Moreover, a higher value of ICP helped in reaching PPCI with very retarded pilot injection timing.
- Engine volumetric compression ratio influences significantly only maximum pressure rise rate and THC, reducing both of them; in combination with pilot injection timing, it influences also fuel conversion efficiency and CO emissions.
- Pilot injection pressure has the weakest first-order effect on both engine performance and emissions; a more detailed analysis, specialized at different

methane flow rates, highlighted a significant effect of pilot injection pressure on indicated mean effective pressure and fuel conversion efficiency as the methane flow rate increases. Moreover, its effect increases on engine performance and THC emissions in combination with pilot injection timing.

Summarizing, a proper choice of design and calibration is necessary to reach HCCI combustion in dual-fuel engines. Besides the broadly investigated strategy based on very advanced pilot injections, retarded injection timings, combined with high ICP, determine very low levels of nitrogen oxides and maximum pressure rise rate, with little or no penalty on engine efficiency and THC and CO levels. This strategy, already investigated in diesel combustion, showed very good combustion performance at low/medium load when combined with EGR (hot and cooled) and swirl. Therefore, an ad hoc experimental campaign shall be performed also for dual-fuel combustion with the aim of evaluating EGR and swirl effects, besides the already investigated injection pressure and engine compression ratio, on engine performance and emissions abatement.

**Acknowledgements** The authors wish to thank Mr. Adriano Romano for his fundamental contribution to the present work, in particular during the ANOVA of the experimental data.

## References

- Ansari E, Poorghasemi K, Khoshbakht Irdmoussa B, Shahbakhti M et al (2016) Efficiency and emissions mapping of a light duty diesel—natural gas engine operating in conventional diesel and RCCI modes. SAE technical paper 2016-01-2309. <https://doi.org/10.4271/2016-01-2309>
- Carlucci AP, de Risi A, Laforgia D, Naccarato F (2008) Experimental investigation and combustion analysis of a direct injection dual-fuel diesel–natural gas engine. *Energy* 33 (2):256–263. <https://doi.org/10.1016/j.energy.2007.06.005>
- Carlucci A, Laforgia D, Saracino R (2009) Effects of in-cylinder bulk flow and methane supply strategies on charge stratification, combustion and emissions of a dual-fuel DI diesel engine. SAE technical paper 2009-01-0949. <https://doi.org/10.4271/2009-01-0949>
- Carlucci A, Laforgia D, Saracino R, Toto G (2010) Study of combustion development in methane-diesel dual fuel engines, based on the analysis of in-cylinder luminance. SAE technical paper 2010-01-1297. <https://doi.org/10.4271/2010-01-1297>
- Carlucci AP, Ficarella A, Laforgia D (2014) Potentialities of a common rail injection system for the control of dual fuel biodiesel-producer gas combustion and emissions. *J Energ Eng* 140(3). [https://doi.org/10.1061/\(ASCE\)EY.1943-7897.0000150](https://doi.org/10.1061/(ASCE)EY.1943-7897.0000150)
- Carlucci AP, Colangelo G, Ficarella A, Laforgia D, Strafella L (2015) Improvements in dual-fuel biodiesel-producer gas combustion at low load through pilot injection splitting. *J Energ Eng* 141(2):C4014006-1–C4014006-8. [https://doi.org/10.1061/\(ASCE\)EY.1943-7897.0000231](https://doi.org/10.1061/(ASCE)EY.1943-7897.0000231)
- Carlucci AP, Laforgia D, Ficarella A, Strafella L (2017) Improvement of a dual fuel biodiesel-producer gas engine performance acting on biodiesel injection parameters and strategy. *Fuel* 209:754–768. <https://doi.org/10.1016/j.fuel.2017.07.100>
- Dahodwala M, Joshi S, Koehler E, Franke M (2014) Investigation of diesel and CNG combustion in a dual fuel regime and as an enabler to achieve RCCI combustion. SAE technical paper 2014-01-1308. <https://doi.org/10.4271/2014-01-1308>



- Di Blasio G, Belgiorno G, Beatrice C (2017a) Effects on performances, emissions and particle size distributions of a dual fuel (methane-diesel) light-duty engine varying the compression ratio. *Appl Energ* 204:726–740. <https://doi.org/10.1016/j.apenergy.2017.07.103>
- Di Blasio G, Belgiorno G, Beatrice C (2017b) Parametric analysis of compression ratio variation effects on thermodynamic, gaseous pollutant and particle emissions of a dual-fuel CH<sub>4</sub>-diesel light duty engine. SAE technical paper 2017-01-0764. <https://doi.org/10.4271/2017-01-0764>
- Donateo T, Carlucci AP, Strafella L, Laforgia D (2014) Experimental validation of a CFD model and an optimization procedure for dual fuel engines. SAE world congress & exhibition 2014, Detroit (Michigan), 8–10 Apr 2014. SAE technical paper 2014-01-1314. <https://doi.org/10.4271/2014-01-1314>
- Doosje, E, Willems F, Baert R (2014) Experimental demonstration of RCCI in heavy-duty engines using diesel and natural gas. SAE technical paper 2014-01-1318. <https://doi.org/10.4271/2014-01-1318>
- Garcia P, Tunestal P (2015) Experimental investigation on CNG-diesel combustion modes under highly diluted conditions on a light duty diesel engine with focus on injection strategy. *SAE Int J Engines* 8(5):2177–2187. <https://doi.org/10.4271/2015-24-2439>
- Gharehghani A, Hosseini R, Mirsalim M, Jazayeri SA, Yusaf T (2015) An experimental study on reactivity controlled compression ignition engine fueled with biodiesel/natural gas. *Energy* 89:558–567. <https://doi.org/10.1016/j.energy.2015.06.014>
- Guery ES, Raihan SM, Srinivasan KK, Krishnan SR, Sohail A (2016) Injection timing effects on partially premixed diesel–methane dual fuel low temperature combustion. *Appl Energ* 162:99–113. <https://doi.org/10.1016/j.apenergy.2015.10.085>
- Hariprasad T (2013) Effect of injection pressure on performance of dual fuel diesel engines. SAE 2013-01-2887. [doi.org/10.4271/2013-01-2887](https://doi.org/10.4271/2013-01-2887)
- Hasan MM, Rahman MM (2016) Homogeneous charge compression ignition combustion: advantages over compression ignition combustion, challenges and solutions. *Renew Sust Energ Rev* 57:282–291. <https://doi.org/10.1016/j.rser.2015.12.157>
- He L, Lu Z, Zhang J, Geng L, Zhao H, Li X (2018) Low-carbon economic dispatch for electricity and natural gas systems considering carbon capture systems and power-to-gas. *Appl Energ* 224:357–370. <https://doi.org/10.1016/j.apenergy.2018.04.119>
- Hosmath RS, Banapurmath NR, Khandal SV, Gaitonde VN, Basavarajappa YH, Yaliwal VS (2016) Effect of compression ratio, CNG flow rate and injection timing on the performance of dual fuel engine operated on Honge oil methyl ester (HOME) and compressed natural gas (CNG). *Renew Energ* 93:579–590. <https://doi.org/10.1016/j.renene.2016.03.010>
- Ibrahim MM, Varuna Narasimhan J, Ramesh A (2015) Comparison of the predominantly premixed charge compression ignition and the dual fuel modes of operation with biogas and diesel as fuels. *Energy* 89:990–1000. <https://doi.org/10.1016/j.energy.2015.06.033>
- Kimura S, Ogawa H, Matsui Y, Enomoto Y (1997) An experimental analysis of low-temperature and premixed combustion for simultaneous reduction of NO<sub>x</sub> and particulate emissions in direct injection diesel engines. *Int J Engine Res* 3(4):249–259. <https://doi.org/10.1243/146808702762230932>
- Kimura S, Aoki O, Kitahara Y, Aiyoshizawa E (2001) Ultra-clean combustion technology combining a low-temperature and premixed combustion concept for meeting future emission standards. SAE technical paper 2001-01-0200. <https://doi.org/10.4271/2001-01-0200>
- McKenna RC, Bchini Q, Weinand JM, Michaelis J, König S, Köppel W, Fichtner W (2018) The future role of power-to-gas in the energy transition: regional and local techno-economic analyses in Baden-Württemberg. *Appl Energ* 212:386–400. <https://doi.org/10.1016/j.apenergy.2017.12.017>
- Muhammad IK, Tabassam Y, Muhammad IK, Muhammad F, Muhammad W (2016) Research progress in the development of natural gas as fuel for road vehicles: a bibliographic review (1991–2016). *Renew Sust Energ Rev* 66:702–741. <https://doi.org/10.1016/j.rser.2016.08.041>
- Napolitano P, Guido C, Beatrice C, Del Giacomo N (2017) Application of a dual fuel diesel-CNG configuration in a Euro 5 automotive diesel engine. SAE technical paper 2017-01-0769. <https://doi.org/10.4271/2017-01-0769>

- Nithyanandan K, Gao Y, Wu H, Lee C et al (2017) An optical investigation of multiple diesel injections in CNG/diesel. SAE technical paper 2017-01-0755. <https://doi.org/10.4271/2017-01-0755> (Dual-fuel combustion in a light duty optical diesel engine. SAE technical paper 2017-01-0755 2017. <https://doi.org/10.4271/2017-01-0755>)
- Ogawa H, Shibata G, Goto J, Jiang L (2016) Performance improvements in a natural gas dual fuel compression ignition engine with 250 MPa pilot injection of diesel fuel as an ignition source. SAE technical paper 2016-01-2306. <https://doi.org/10.4271/2016-01-2306>
- Pali R, Amit D, Saroj KM (2018) Influence of gaseous fuel induction on the various engine characteristics of a dual fuel compression ignition engine: a review. *Renew Sust Energ Rev* 82:3333–3349. <https://doi.org/10.1016/j.rser.2017.10.055>
- Paykani A, Kakaee A, Rahnama P, Reitz RD (2015) Effects of diesel injection strategy on natural gas/diesel reactivity controlled compression ignition combustion. *Energy* 90:814–826. <https://doi.org/10.1016/j.energy.2015.07.112>
- Poorghasemi K, Saray R, Ansari E, Khoshbakht Irdmousa B, Shahbakhti M, Naber JD (2017) Effect of diesel injection strategies on natural gas/diesel RCCI combustion characteristics in a light duty diesel engine. *Appl Energ* 199:430–446. <https://doi.org/10.1016/j.apenergy.2017.05.011>
- Raihan SM, Guerry ES, Dwivedi U, Srinivasan KK, Krishnan SR (2015) Experimental analysis of diesel-ignited methane dual-fuel low-temperature combustion in a single-cylinder diesel engine. *J Energ Eng* 141(2), C4014007 1–13. [https://doi.org/10.1061/\(ASCE\)EY.1943-7897.0000235](https://doi.org/10.1061/(ASCE)EY.1943-7897.0000235)
- Ryu K (2013a) Effects of pilot injection pressure on the combustion and emissions characteristics in a diesel engine using biodiesel–CNG dual fuel. *Energ Convers Manage* 76:506–516. <https://doi.org/10.1016/j.enconman.2013.07.085>
- Ryu K (2013b) Effects of pilot injection timing on the combustion and emissions characteristics in a diesel engine using biodiesel–CNG dual fuel. *Appl Energ* 111:721–751. <https://doi.org/10.1016/j.apenergy.2013.05.046>
- Song H, Liu C, Li Y, Wang Z, Chen L, He X, Wang J (2018) An exploration of utilizing low-pressure diesel injection for natural gas dual-fuel low-temperature combustion. *Energy* 153:248–255. <https://doi.org/10.1016/j.energy.2018.04.041>
- Srinivasan KK, Krishnan SR, Midkiff KC (2006) Improving low load combustion, stability and emissions in pilot-ignited natural gas engines. *Proc Inst Mech Eng D-J Auto* 220(2):229–239. <https://doi.org/10.1243/09544070JAUTO104>
- Wang B, Li T, Ge L, Ogawa H (2016) Optimization of combustion chamber geometry for natural gas engines with diesel micro-pilot-induced ignition. *Energ Convers Manage* 122:552–563. <https://doi.org/10.1016/j.enconman.2016.06.027>
- Woschni G (1967) A universally applicable equation for the instantaneous heat transfer coefficient in the internal combustion engine. SAE technical paper 670937. <https://doi.org/10.4271/670931>
- Xu M, Cheng W, Li Z, Zhang H, An T, Meng Z (2016a) Pre-injection strategy for pilot diesel compression ignition natural gas engine. *Appl Energ* 179:1185–1193. <https://doi.org/10.1016/j.apenergy.2016.07.024>
- Xu M, Cheng W, Zhang H, An T, Zhang S (2016b) Effect of diesel pre-injection timing on combustion and emission characteristics of compression ignited natural gas engine. *Energ Convers Manage* 117:86–94. <https://doi.org/10.1016/j.enconman.2016.02.054>
- Yang B, Xi C, Wei X, Zeng K, Lai MC (2015) Parametric investigation of natural gas port injection and diesel pilot injection on the combustion and emissions of a turbocharged common rail dual-fuel engine at low load. *Appl Energ* 143:130–137. <https://doi.org/10.1016/j.apenergy.2015.01.037>

# Chapter 11

## Dual Fuel (Natural Gas Diesel) for Light-Duty Industrial Engines: A Numerical and Experimental Investigation



Enrico Mattarelli, Carlo Alberto Rinaldini and Tommaso Savioli

**Abstract** This paper reviews the main results of a numerical and experimental activity, carried out on an automotive four-cylinder, common rail, 2.8 L turbocharged diesel engine, Euro IV compliant. The purpose of the project is to convert this engine, with minor hardware modifications, in order to operate in compression ignition (CI) dual-fuel (DF) mode, using natural gas (NG) as the main source of energy. The diesel injector will keep the only function to ignite the homogeneous air–NG mixture within the cylinder, injecting just a small quantity of diesel fuel. In this way, soot emissions can be almost completely eliminated, and the after-treatment system can be strongly simplified (then, its cost reduced). Other fundamental advantages in the use of NG instead of diesel are the lower emission of CO<sub>2</sub> (provided that brake efficiency is not reduced when running on DF) and the lower concentration of nitrogen oxides (NO<sub>x</sub>). This DF engine would be particularly suitable for light-duty industrial applications (power generators, small tractors, and off-road vehicles) and boats, where the installation of an additional fuel system is not limited by tight constraints. The experimental activity is supported by a comprehensive theoretical study, carried out through CFD simulation (both 1D and 3D). The numerical models are first calibrated for the standard combustion mode and then applied to get the guidelines for the development and calibration of the physical prototype. The most relevant experimental result is obtained at 3000 rpm, BMEP = 12 bar, where the DF engine can work with just a 20% of the diesel fuel required for standard operations. The following advantages are found: (1) complete elimination of soot; (2) 26% reduction of NO<sub>x</sub>; (3) 25% reduction of CO<sub>2</sub>; (4) slight improvement of brake efficiency. The only downside is the strong increase in HC and CO concentrations, which are about ten times higher. However, this issue can be addressed installing a cost-effective oxidation catalyst.

---

E. Mattarelli (✉) · C. A. Rinaldini · T. Savioli  
Department of Engineering “Enzo Ferrari”, Modena & Reggio Emilia University, 41125  
Modena, Italy  
e-mail: [enrico.mattarelli@unimore.it](mailto:enrico.mattarelli@unimore.it)

**Keywords** Dual-fuel combustion · Compression ignition · Natural gas

## 11.1 Introduction

Compression ignition (CI) engines find application in almost every industrial and transportation fields, for their intrinsic fuel efficiency, robustness, and capability to run on different types of fuels. However, their use in urban areas or indoor plants is raising concerns, mainly related to soot emissions (Lloyd and Cackette 2001; Harrod and Jaramillo 2005). The compliance to tighter regulations makes the cost of diesel engines increase significantly (Reşitoğlu et al. 2015). As a result, manufacturers are looking for alternative solutions, able to match high fuel efficiency, clean exhaust gas and relatively low costs. Among many propositions, the conversion of conventional CI engines to dual-fuel (DF) operations with natural gas (NG) is one of the most promising (Wei and Geng 2016). This conversion does not require a completely new design of the engine, but only the installation of a further gas injection system in the intake manifold. The diesel injector keeps the only function to ignite the homogeneous air–NG mixture within the cylinder, injecting just a small quantity of diesel fuel.

### 11.1.1 Dual-Fuel Combustion Fundamentals

In order to provide the same amount of heat released by a standard diesel combustion, the following mass of NG ( $m_{\text{NG}}$ ) must be introduced within the cylinder:

$$m_{\text{NG}} = \frac{(m_{\text{D}} - m'_{\text{D}}) \cdot \text{LHV}_{\text{D}}}{\text{LHV}_{\text{NG}}} \quad (11.1)$$

where  $m_{\text{D}}$  is the amount of diesel fuel injected in standard operations,  $m'_{\text{D}}$  is the mass of diesel introduced when running on DF mode, LHV stands for lower heating value, and D stands for diesel.

The residual fraction of diesel fuel, referred to as  $x$ , is defined as the ratio of  $m'_{\text{D}}$  and  $m_{\text{D}}$ .

Therefore, the amount of NG can be expressed as:

$$m_{\text{NG}} = \frac{(1 - x)m_{\text{D}} \cdot \text{LHV}_{\text{D}}}{\text{LHV}_{\text{NG}}} \quad (11.2)$$

As a first hypothesis, it is assumed that the mass of air delivered by the engine,  $m_a$ , is kept constant, when passing from standard diesel to DF operations.

Moreover, the mass of air consumed by the combustion of the injected diesel fuel is calculated as the product of  $m'_D$  and the stoichiometric air–fuel ratio of the diesel fuel,  $\alpha_{s,D}$  (typical value: 14.5).

Defining  $\alpha = m_a/m_D$ , the amount of air available for the combustion of NG,  $m'_a$ , is:

$$m'_a = m_D(\alpha - x \cdot \alpha_{s,D}) \quad (11.3)$$

Therefore, the relative air–fuel ratio of the NG–air mixture ( $\lambda_{NG}$ ) can be calculated as:

$$\lambda_{NG} = \frac{(\alpha - x \cdot \alpha_{s,D}) \cdot \text{LHV}_{NG}}{(1 - x) \cdot \alpha_{s,NG} \cdot \text{LHV}_D} \quad (11.4)$$

where  $\alpha_{s,NG}$  is the stoichiometric air–fuel ratio of natural gas (typical value: 17.1).

From Eq. (11.4), it may be deduced that the homogeneous air–NG mixture is lean for all the conditions of practical interest. In fact, considering a minimum value of  $\alpha = 16$ , a minimum value of  $x = 0.05$ , being the lower heating values of NG and diesel equal to 47.1 MJ/kg and 42.6 MJ/kg, respectively, Eq. (11.4) yields a value of  $\lambda_{NG} = 1.04$ .

As  $\alpha$  and  $x$  increase, the value of  $\lambda_{NG}$  becomes very high: As a result, the complete combustion of the NG mixture would be more and more difficult. Therefore, when the load is low ( $\alpha > 30$ ) and/or the residual fraction of diesel is high ( $x > 0.3$ ), it is probably convenient to reduce the amount of delivered air, in order to keep the value of  $\lambda_{NG}$  within an optimum range. In a turbocharged engine, this result may be achieved by controlling the boost pressure and/or by throttling the inlet flow. In a naturally aspirated engine, only the second option is possible. Moreover, there is no way to increase the amount of delivered air.

### 11.1.2 Combustion Patterns

As described in many previous papers (Wei and Geng 2016; Abdelaal and Hegab 2012; Hountalas 2003; Wannatong et al. 2007; Liu et al. 2003, 2013; Lounici et al. 2014; Papagiannakis and Hountalas 2004; Imran et al. 2014; Krishnan et al. 2004; Abd Alla et al. 2000, 2002; Singh et al. 2004; Papagiannakis et al. 2010; Egusquiza et al. 2009), the DF combustion patterns are different from standard CI engines. Typically, when  $\lambda_{NG}$  is in the range between 1.2 and 2, a single high-pressure diesel injection generates a sort of flame front, propagating from the combustion chamber core toward the cylinder walls. The shape of the heat release rate curve is quite similar to the case of a spark ignition (SI) engine, the only difference being the

higher amount of fuel burnt in the very first part of the process, after the ignition (the high chemical reactivity of diesel fuel involves a volume of premixed charge much larger than that typically ignited by a spark plug). What happens in the following depends on the composition of the charge, as well as on its thermodynamic properties (pressure and temperature). The higher is  $\lambda_{\text{NG}}$ , and the higher is the dilution with exhaust gas, and the lower is temperature, the slower will be the propagation of the flame front. In the opposite conditions, the flame front will be faster, but the end gas may auto-ignite, producing a detonation. In a regular DF combustion, the flame burns the whole charge, without knock. Moreover, it should comply with the same constraints of the standard diesel combustion, in particular with the maximum combustion pressure and the maximum pressure gradient. The injection strategy (fuel pressure, timing and duration of each single shot, number of shots) obviously plays a key role, along with intake manifold pressure and temperature, and the exhaust gas recirculation (EGR) rate. The last parameters are particularly important at both low and high loads. In the first case, without EGR,  $\lambda_{\text{NG}}$  tends to be too high: a reduction of the manifold pressure and/or an increase in temperature generally help to increase the speed of the flame front, then to achieve a complete combustion of NG. Conversely, at high load, an increase in the intake manifold pressure (thus higher  $\lambda_{\text{NG}}$ ) and/or the dilution of the charge with cooled exhaust gas help to reduce the reactivity of the end gas, therefore to lower the risk of knock.

### 11.1.3 Pollutants

Pollutant emissions are directly related to the specific combustion patterns; thus, relevant differences are expected from standard diesel operations.

Almost all the researchers agree on the strong reduction of soot, when passing from diesel to DF operations, at the same load (Wei and Geng 2016). The main reason is that soot is produced by diffusive combustion of liquid fuels, and this condition is strongly limited when the amount of injected fuel is small. Moreover, the presence of NG in the charge prolongs the diesel ignition delay; thus, it increases the lift-off length of the fuel jets, providing more favorable conditions for air and fuel mixing. The only exception to this general rule is when considering naturally aspirated (NA) engines at high loads (Papagiannakis and Hountalas 2004): Due to the volume occupied by NG in the aspirated charge, the amount of air may be so reduced that diffusive combustion is damped.

Another well-established characteristic of DF combustion is the reduction of  $\text{CO}_2$ , due to the following reasons:

- (i) NG is mainly made up of methane, featuring a H/C ratio equal to 4; the same parameter is more than halved, when considering the hydrocarbons constituting a standard diesel fuel; as a result, in DF operations, the share of  $\text{CO}_2$  in the exhaust gas composition is reduced, in favor of a larger amount of  $\text{H}_2\text{O}$ ;

- (ii) non-complete combustion often occurring in DF operations may reduce the amount of fuel terminating the oxidation process.

Obviously, the reduction of CO<sub>2</sub> is a real advantage only when combustion is complete.

Also about HC emissions, all the technical papers report the same trend (Wei and Geng 2016), that is, an increase in this pollutant, sometimes even of more than one order of magnitude. The reasons are:

- (i) low speed of the flame, propagating in a lean and/or diluted homogeneous mixture: As the cylinder volume increases, the low heat release rate makes temperature drop; therefore, the oxidation reactions freeze;
- (ii) during the compression stroke, some NG–air mixture remains trapped in the cylinder crevices, deposits, and lubricant layer: As pressure decreases, NG is released, but the low temperatures do not enable the oxidation of the fuel;
- (iii) some air–NG mixture may bypass the cylinder during the overlapping period.

Another typical trend in the DF combustion is the increase in CO, observed by all the researchers (Wei and Geng 2016). The reasons are the same described for HC, except for the bypass of fresh charge during the overlapping period. In addition, the following aspects can contribute to the increase in this pollutant:

- (i) the HC and CO oxidation reactions are competing for oxygen, but the HC oxidation rate is much faster than CO; as a result, when the cylinder temperature drops, the oxidation reactions freeze, leaving a large amount of CO in the exhaust gas
- (ii) after the ignition, the hot combustion products containing CO mix with the surrounding cooler air–NG mixture; as a result, the CO oxidation rate is damped.

The effect of DF combustion on NO<sub>x</sub> concentration is more debated: Most researchers agree that it depends on operating conditions (engine speed, load, EGR rate) and on the injection strategy; in some cases, a reduction is observed (Hountalas 2003; Papagiannakis and Hountalas 2004; Krishnan et al. 2004; Papagiannakis et al. 2010; Liu et al. 2013); in others, an increase is found (Abd Alla et al. 2000, 2002). The main reasons that bring to a reduction of this pollutant can be summarized as follows (Wei and Geng 2016):

- (i) the higher heat capacity of the air–NG mixture, in comparison to air only, makes the charge temperature drop at end of compression; lower combustion temperatures reduce the formation rate of NO<sub>x</sub>
- (ii) lean air–NG mixtures bring to a slow combustion rate, after the ignition, thus at lower combustion temperatures
- (iii) stoichiometric or rich air–NG mixtures reduce the availability of oxygen, thus the formation rate of NO<sub>x</sub>.

On the other hand, the concentration of  $\text{NO}_x$  in the exhaust gas increases when a large amount of air–NG mixture is involved in the auto-ignition of the diesel fuel, in particular when the injection advance is high. In fact, the peak of heat release, associated with the final compression of the charge up to top dead center, makes the combustion temperature increase, thus the formation rate of  $\text{NO}_x$ .

It is interesting to notice that there is a clear trade-off between  $\text{NO}_x$  and CO: The conditions yielding a peak of  $\text{NO}_x$  (fast combustion rates, with ensuing increase in the temperature peak) are the same which enhance the oxidation of CO in lean air–NG mixtures.

#### ***11.1.4 Brake Efficiency, Stability, and Performance***

The influence of DF combustion on brake thermal efficiency (BTE) depends on the specific conditions: In some cases, an improvement is found; in others, a reduction (Wei and Geng 2016). The reasons for the reduction are:

- (i) non-complete oxidation of NG, due to the lean or diluted mixture;
- (ii) higher weight of heat losses, due to the slow combustion rate after the ignition.

Both effects are observed in particular at low loads, when the air–NG mixture tends to be leaner and more diluted.

At high loads, BTE may be enhanced by speeding up the combustion of NG. This result can be obtained optimizing the injection strategy and controlling the value of  $\lambda_{\text{NG}}$ . As well known, a fast but controlled combustion helps to use all the energy of the fuel, as well as to improve the conversion from heat to piston work.

As far as combustion stability is concerned, a slight worsening is generally observed when passing to DF operations (Wei and Geng 2016). The most obvious reason is the slow combustion rate of NG, due to the lean conditions.

Finally, the maximum engine performance under DF operations is directly related to knock control. For reaching the same performance of the diesel mode, the maximum value of  $\lambda_{\text{NG}}$  is the one calculated by Eq. (11.3), provided that BTE does not change. However, for  $\lambda_{\text{NG}} < 1.5$ , the risk becomes progressively higher. All the studies reviewed in Wei and Geng (2016) show a slight reduction of brake performance.

#### ***11.1.5 Dual-Fuel Application***

The DF combustion mode may be a good alternative for several types of diesel engines, in particular for boats, trucks, commercial vehicles, and industrial applications (power generators, tractors, and off-road vehicles), where the installation of an additional fuel system is not limited by tight constraints. The most appealing



aspect is the simplification of the after-treatment system (very low concentration of soot in the exhaust flow,  $\text{NO}_x$  reduction), with minor hardware modifications. Other fundamental advantages in the use of NG instead of diesel oil are the lower emission of  $\text{CO}_2$ , the larger availability of NG (that can be obtained also from renewable sources), the lower noise due to a smoother combustion, and the strong simplification in the management of diesel fuel injection (much smaller amounts of fuel, no need of high pressures or multiple injections). Obviously, there are also some critical aspects to be addressed: The composition of the charge must be carefully controlled, in order to avoid misfires or knocking; the injection strategy must be optimized in order to achieve the best trade-off between pollutant emissions and performance; the oxidation catalyst must be designed from scratch, due to the higher concentration of HC and CO, as well as to the presence of methane in the exhaust flow.

This study reviews the main results of a numerical and experimental activity, carried out at the Department of Engineering “Enzo Ferrari” (University of Modena and Reggio Emilia), focused on a four-cylinder, common rail, 2.8 L turbocharged diesel engine, Euro IV compliant. The purpose of the project is to develop a DF-NG engine starting from this basis, minimizing the transformation costs and extracting all the potential from the new combustion concept. The choice of the engine (originally conceived for Euro IV–V passenger cars) is mainly due to the fact that it may be easily converted to other uses, with minor hardware modifications: In particular, its efficient combustion system and robust construction make the engine suitable for applications such as power generator, off-road light vehicles, boats.

First, a comprehensive CFD model of the reference automotive engine was built and experimentally calibrated: GT-Power (Gamma Technologies 2016) was used to analyze overall engine performance, as well as to provide accurate initial and boundary conditions for detailed CFD-3D analyses. A customized version of the KIVA-3V (Amsden 1997) code was then employed to investigate spray and combustion and pollutants formation.

Using the calibrated models, a CFD-3D investigation on dual-fuel combustion was carried out, in order to define the guidelines for the development of the DF combustion system, as well as to assess its potential in terms of fuel efficiency and pollutant emissions. As it will be discussed in detail in the following sections, it was found that DF CI engines can run with less than 10% of the diesel fuel required for standard operations and that a good trade-off between efficiency and emissions can be found, after a proper setup of the injection parameters, combined with a specific turbocharger control.

Finally, the diesel engine was equipped with a NG injection system and experimentally tested on a set of different operating conditions.

**Table 11.1** Main parameters of the reference engine

Engine type	HSDI 4-S diesel, EURO IV compliant
Number of cylinder	4 in-line
Total displacement (cm <sup>3</sup> )	2776
Bore (mm)	94
Stroke (mm)	100
Compression ratio	17.5:1
# of valves per cylinder	4
Air metering	Turbocharger, intercooler
Injection system	Common rail
Maximum injection press. (MPa)	160
Injector hole diameter (mm)	0.153
Number of injector holes	6
EGR system	High pressure, cooler, inlet throttle
Maximum brake power (kW@rpm)	130@3800
Maximum brake torque (Nm@rpm)	440@1750
Maximum peak cylinder pressure [bar]	150

## 11.2 CFD Modeling of the Reference Engine

### 11.2.1 The Reference Engine

The main parameters of the reference engine, manufactured by VM Motori (Cento, Italy), are listed in Table 11.1.

### 11.2.2 CFD-1D Engine Model

The GT-Power commercial software is used to build an engine model, including all the components of the gas-dynamic circuit from the inlet to the exhaust (intake and exhaust pipes and manifolds, cylinders, valves, compressor, charge cooler, variable-geometry turbine (VGT), EGR cooler, EGR valve, etc.). The experimental measure of in-cylinder pressure traces at full load enables the calculation of burn rates, entered as input data for combustion modeling, as well as the estimation of friction mean effective pressures (calculated in the model by using the Chen–Flynn correlation). The discharge coefficients of both intake and exhaust valves, measured for direct flow at a steady flow bench, are also entered in the numerical model. The VGT rack position is set by means of a PID controller, targeting the experimental boost pressure. Finally, the operating conditions are defined by considering engine speed and injected fuel mass as principal parameters.

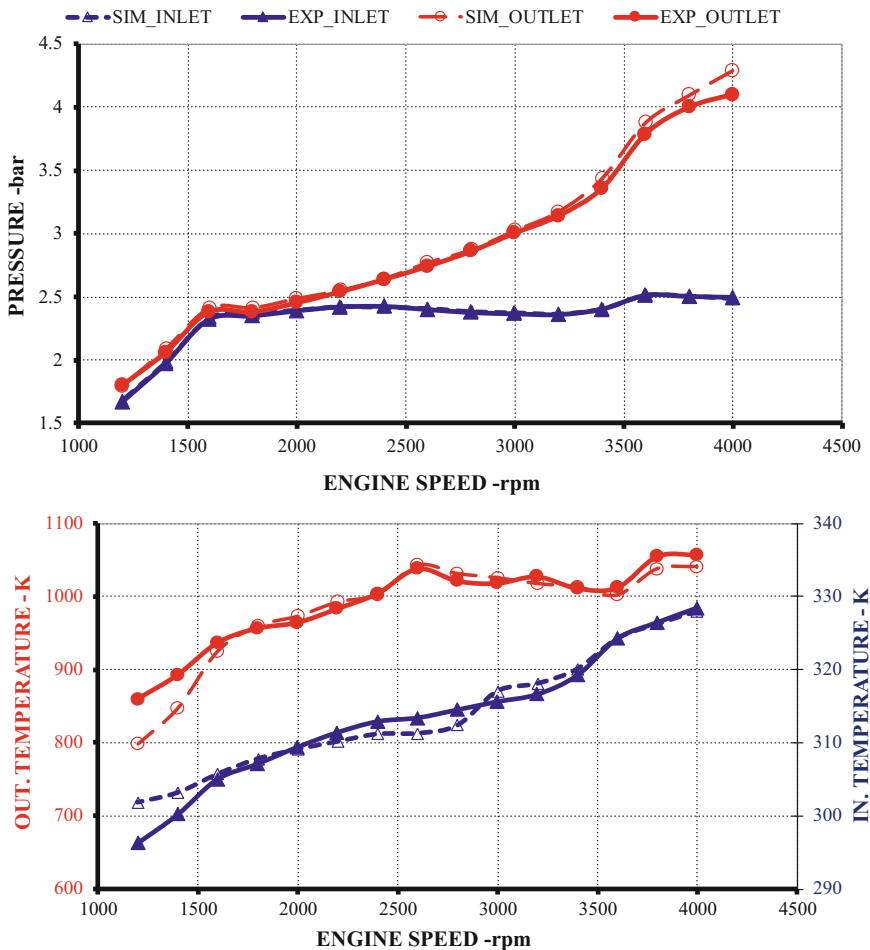


**Fig. 11.1** Comparison between CFD-1D simulation results and experiments at full load in terms of pressure and temperature, at the engine head inlet and outlet. Reprinted from Rinaldini et al. (2013a)

The model is carefully calibrated against experimental data at full load. Due to the simplifications in the modeling of some components of the gas-dynamic system (air filter, charge and EGR coolers, pipe bends, etc.), some flow and heat loss multipliers have to be specifically tuned. Also, combustion efficiency is slightly reduced (between 0.96 and 1) at a few operating points, in order to get a good correlation with experiments (in particular, with measured in-cylinder pressure traces). Further details on the building and calibration of the model can be found in (Rinaldini et al. 2013a).

Figure 11.1 shows the experimental validation of the GT-Power model, considering the gas pressure and temperature at both sides of the of the engine head

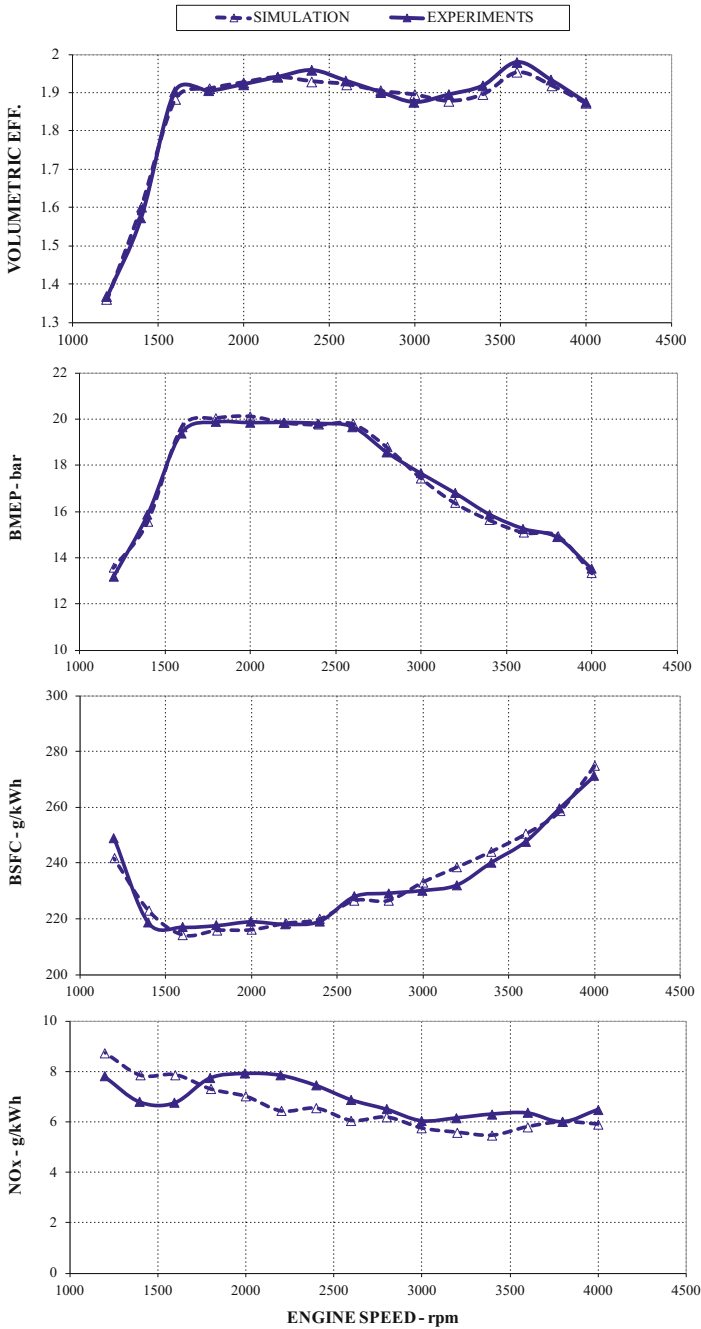


**Fig. 11.2** Comparison between CFD-1D simulation results and experiments at full load in terms of: volumetric efficiency, BMEP, BSFC, and specific NO<sub>x</sub> raw emissions

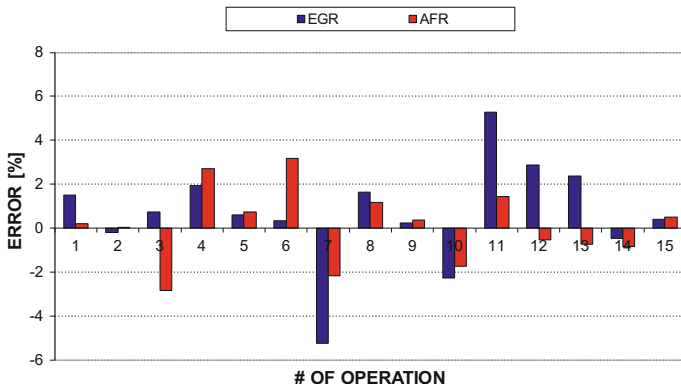


**Fig. 11.3** Accuracy of the CFD-1D model for a set of operating conditions at partial load: EGR rate and air–fuel ratio

(intake and exhaust). The good agreement between the measured and the calculated values is the evidence of the good predictive capability of the model, in terms of flow-dynamic parameters.

As a further evidence of the accuracy of the GT-Power model, Fig. 11.2 presents a comparison with experimental data in terms of the following parameters: volumetric efficiency, brake mean effective pressure (BMEP), brake specific fuel consumption (BSFC), and brake specific NO<sub>x</sub> emissions. All the parameters are referred to full load operations (Fig. 11.3).

In order to demonstrate the quality of the model also at partial load, a set of 15 operating conditions is considered. They correspond to a typical use of the engine in the New European Driving Cycle (for the details, see Rinaldini et al. 2013a). The two parameters, selected for the comparison with experimental results, are the air–fuel ratio (AFR) and the EGR rate. The reason of this choice is that both parameters have a strong impact on combustion and emissions, and they are used to define the initial conditions for the multidimensional CFD combustion analysis. As visible, the accuracy of the model is excellent also at partial load (the average error being less than 2%).

### 11.2.3 CFD-3D Cylinder Model

As already mentioned, a customized version of the KIVA-3V code has been used for analyzing combustion and predicting engine-out emissions. Besides, the standard features of the code, described in Amsden (1997), the customization includes the following aspects:

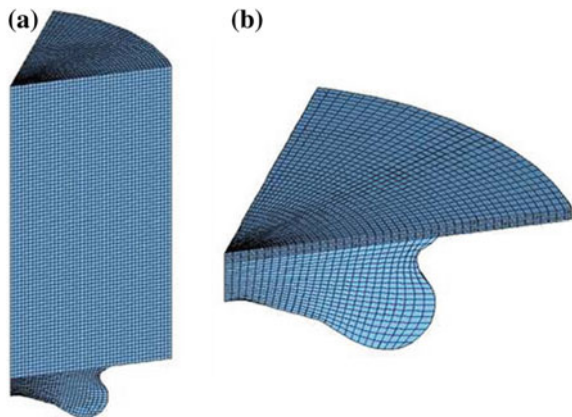
- the Kelvin–Helmholtz/Rayleigh–Taylor (KHRT) Instability model for describing the fuel droplets atomization (Patterson and Reitz 1998);

**Table 11.2** Operating conditions considered for the validation of the KIVA 3V model

	Speed (rpm)	AFR	EGR	Prail (bar)	SOI (cad ATDC)
Full load	1400	19.01	0	1460	-16.0
	2000	19.41	0	1460	-19.8
	3000	20.22	0	1600	-34.9
	4000	22.40	0	1600	-19.4
Partial load	1400	23.89	6	565	-9.3
	2000	24.27	13	1170	-23.2
	2400	25.04	35	1360	-28.1

Reprinted from Rinaldini et al. (2013a)

**Fig. 11.4** View of the optimized polar grid, adopted for CFD-3D simulations. Reprinted from Rinaldini et al. (2013a)

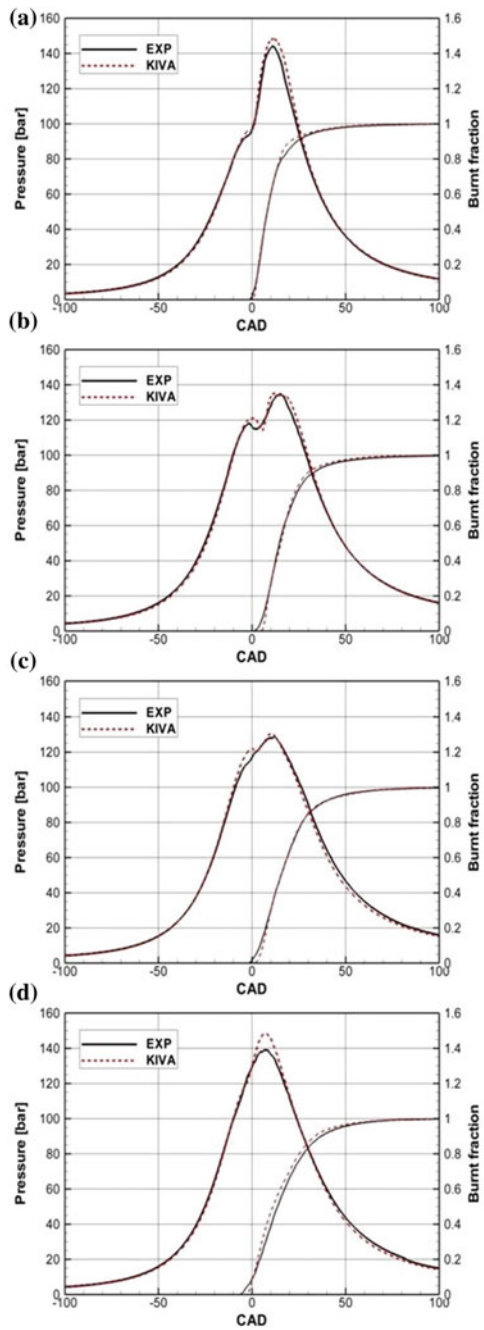


- a detailed combustion chemistry approach, coupled with a comprehensive oxidation mechanism for diesel oil surrogate (DOS) (Gustavsson and Golovitchev 2003);
- the partially stirred reactor (PaSR) model, for describing the turbulence–chemistry interaction (Golovitchev et al. 2000);
- an updated fuel library including the thermal properties of actual diesel oil.

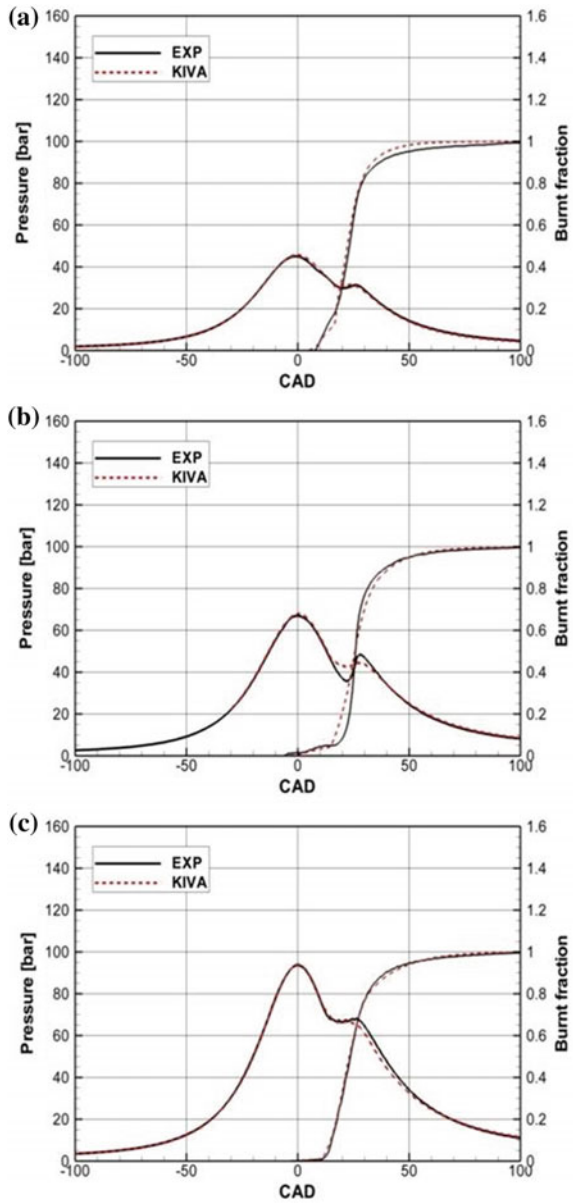
The SENKIN code (Lutz et al. 1997), of the Chemkin-2 package, was used to validate the chemical mechanism developed for DOS.

The accuracy of the customized KIVA code was tested by comparison with a set of experimental data, taken on the reference engine at seven different operating points, at both full and partial load (see Table 11.2). From the computational point of view, the most relevant difference between full and partial load conditions is the EGR rate: Simulation results are much more sensitive to modeling of chemical kinetics. Experiments are carried out by using a standard eddy-current brake, coupled to a dynamometer. The measures include the cylinder pressure, and the concentrations of  $\text{NO}_x$ , CO, and soot in the exhaust gas, before the after-treatment system. More details about the calibration/validation process can be found in Rinaldini et al. (2013a).

**Fig. 11.5** Comparison of calculated (KIVA) and measured (EXP) in-cylinder pressures and burnt fractions at different engine speeds, full load, without EGR. The operating points are:  
**a** 1400 rpm, AFR = 19;  
**b** 2000 rpm, AFR = 19.4;  
**c** 3000 rpm, AFR = 20.2;  
**d** 4000 rpm, AFR = 20.4.  
Reprinted from Rinaldini et al. (2013a)



**Fig. 11.6** Comparison of calculated (KIVA) and measured (EXP) in-cylinder pressures and burnt fractions at different partial load conditions. The operating points are **a** 1400 rpm, AFR = 28.4, EGR = 6%; **b** 2000 rpm, AFR = 24.3%, EGR = 13%; **c** 2400 rpm, AFR = 25, EGR = 35%. Reprinted from Rinaldini et al. (2013a)





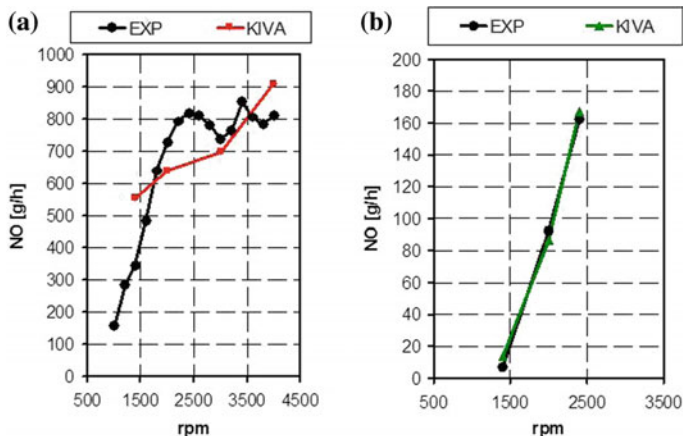


**Fig. 11.7** Comparison of calculated (KIVA) and measured (EXP) NO<sub>x</sub> mass flow rates at full load (a) and partial load conditions (b). The numerical points are the one presented in Table 11.2. Reprinted from Rinaldini et al. (2013a)

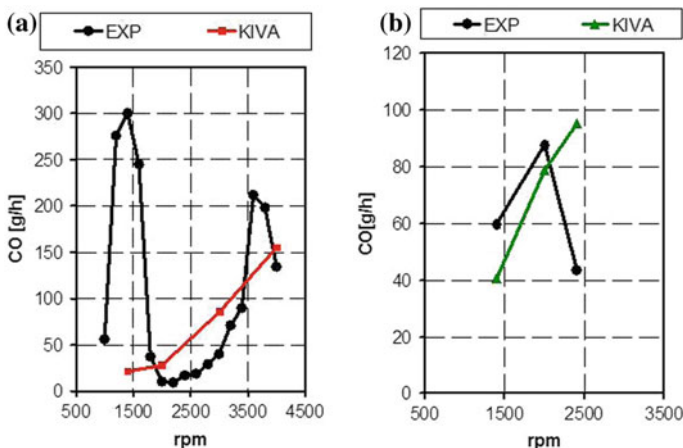
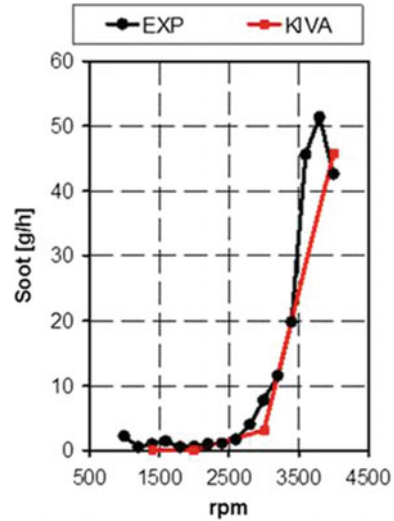


**Fig. 11.8** Comparison of calculated (KIVA) and measured (EXP) CO mass flow rates at full load (a) and partial load conditions (b). The numerical points are the one presented in Table 11.2. Reprinted from Rinaldini et al. (2013a)

The influence of the grid refinement has been investigated, comparing some alternative mesh configurations. Among them, the grid selected for the study is the best trade-off in terms of accuracy, computational demand, and physical soundness of results. This grid, shown in Fig. 11.4, is a 60° sector polar mesh made up by 140.000 hexahedral cells at BDC.

The comparison between experiments and simulation is presented in Figs. 11.5, 11.6, 11.7, 11.8, and 11.9.

**Fig. 11.9** Comparison of calculated (KIVA) and measured (EXP) Soot mass flow rates at full load. Reprinted from Rinaldini et al. (2013a)



Figures 11.5 and 11.6 show the cumulative heat release and the average cylinder pressure trace for all the operating points. The good agreement between simulation and experiments is the first evidence of the capability of the numerical model to reproduce in an accurate way the global phenomena concerning combustion and heat transfer.

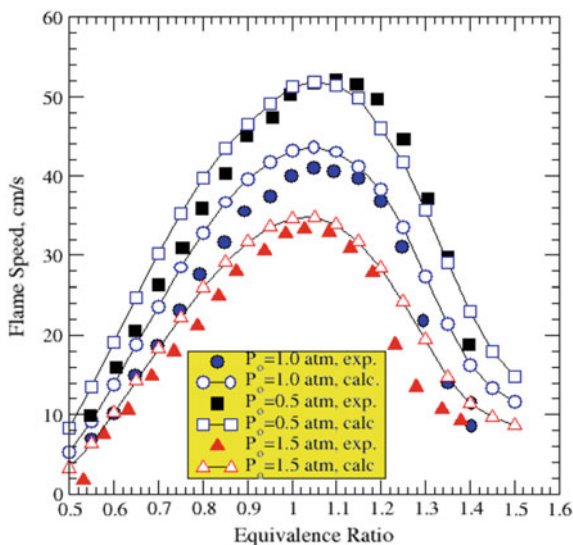
The prediction of emissions is more difficult, and it requires a specific tuning of the model, in particular for the calculation of soot. It should be noted that the same values of the calibration parameters have been employed for all the operating points. Figures 11.7, 11.8, and 11.9 show the predicted and measured mass flow rates of NO, CO, and soot. The agreement demonstrates the physical soundness of the numerical approach.

### 11.3 DF Combustion Simulation

The CFD-3D analysis of the spray and combustion processes is a fundamental step for the optimization of any new combustion system. As discussed in the first section, the trade-off between brake efficiency and NO<sub>x</sub> is far from trivial, and only simulation can provide the guidelines for a proper setting of the injection parameters.

The information deriving from simulation is also very useful to prevent mechanical failures, due to knock or simply to higher combustion temperatures and pressures.

**Fig. 11.10** Comparison of calculated (calc) and measured (exp) laminar flame speeds at different equivalence ratios. Reprinted from Rinaldini et al. (2013b)



### 11.3.1 Modeling the NG Combustion

The numerical modeling of DF combustion requires the coupling of two different modes: the PaSR mode for calculating the ignition of the diesel fuel and the flame propagation mode, for analyzing the ensuing combustion of the homogeneous air–NG mixture. Therefore, for the last mode, it is necessary to develop and validate a chemical kinetic mechanism. The validation of this mechanism is supported by experimental measures of ignition delay times, taken in shock tubes, as well as by the measure of the laminar flame speed of the main NG constituents (Golovitchev and Imren 2013). Since these experiments are carried out at temperatures lower than the ones occurring within the cylinder, the SENKIN code was used to extrapolate the data, enabling a more specific tuning of the model coefficients. Obviously, these coefficients have been modified within the limits given in the literature.

The NG components selected for the chemical kinetic mechanism are methane (>90%), ethane, propane and n-butane.

The DOS model, for the diesel fuel, considers a blend of n-heptane and toluene.

The final integrated mechanism for NG/diesel combustion features 81 species and 421 reactions. Figure 11.10 presents the experimental validation of the mechanism, in terms of laminar flame propagation speed at atmospheric conditions. The numerical values are calculated with the support of the PREMIX code (Liao et al. 2004).

### 11.3.2 Simulation Setup and Results

The DF combustion in the reference engine is analyzed at full load, at three different engine speeds (2000, 3000, and 4000 rpm). The initial and boundary conditions do not change from normal diesel operations. Due to the high values of relative air–NG ratios in the premixed mixture (lean conditions), the reduction of the amount of air related to the presence of the gaseous fuel is neglected.

All the calculations start after IVC, with identical initial flow field. The injection strategy for DF operations consists in a pilot injection that contributes only for a small fraction to the engine power output: The amount of liquid fuel that is injected is 10% of the fuel required in the corresponding normal diesel full load operation.

A set of simulations has been performed for each engine speed, varying both premixed NG concentration and start of injection (SOI). More details about the simulation setup can be found in Rinaldini et al. (2013b).

In order to compare the amount of total fuel (NG and diesel) used during DF operations to the one consumed under normal diesel (ND) full load operations, the following parameter is defined:

$$X_{\text{cng}} = \frac{m_{\text{NG,DF}} + m_{\text{Diesel,DF}}}{m_{\text{Diesel,ND}}} \quad (11.5)$$

This parameter may be used as an indicator of the efficiency of DF combustion at full load: In fact, considering all the operating conditions yielding the same brake torque of the standard diesel combustion, the lower is  $X_{\text{cng}}$  the lower is the amount of fuel required to achieve the given performance target (thus, the lower is the CO<sub>2</sub> output).

In order to represent the piston work, thus brake performance, a sort of indicated mean effective pressure (IMEP) is considered. Differently from the standard IMEP, the parameter used in this study, referred to as IMEP\*, includes only the portion of the cycle involved in the combustion process, from 40° BTDC to 110° ATDC. However, for the sake of simplicity, the pressure–volume integral is divided by the engine unit displacement.

Figure 11.11 shows the map of IMEP\* for three different engine speeds: 2000 rpm (a), 3000 rpm (b), 4000 rpm (c). The values of start of injection (SOI) are indicated on the  $x$ -axis, while  $X_{\text{cng}}$  is reported on the  $y$ -axis.

The dashed lines indicate the constant values of peak cylinder pressure. On each map, in order to directly compare DF to ND operations, the curves of IMEP\* and peak cylinder pressure corresponding to ND operations are highlighted using, respectively, a bold solid line and a bold dashed line.

The first result shown by the maps is that the values of IMEP\* corresponding to ND operations can be reached with almost every value of SOI, but within a narrow band of  $X_{\text{cng}}$ . As the injection advance increases (from right to left),  $X_{\text{cng}}$  decreases, but cylinder peak pressures tend to be higher. This trend means that increasing the injection advance less NG has to be introduced to comply with the load target; therefore, efficiency increases. However, the higher cylinder pressures are generally

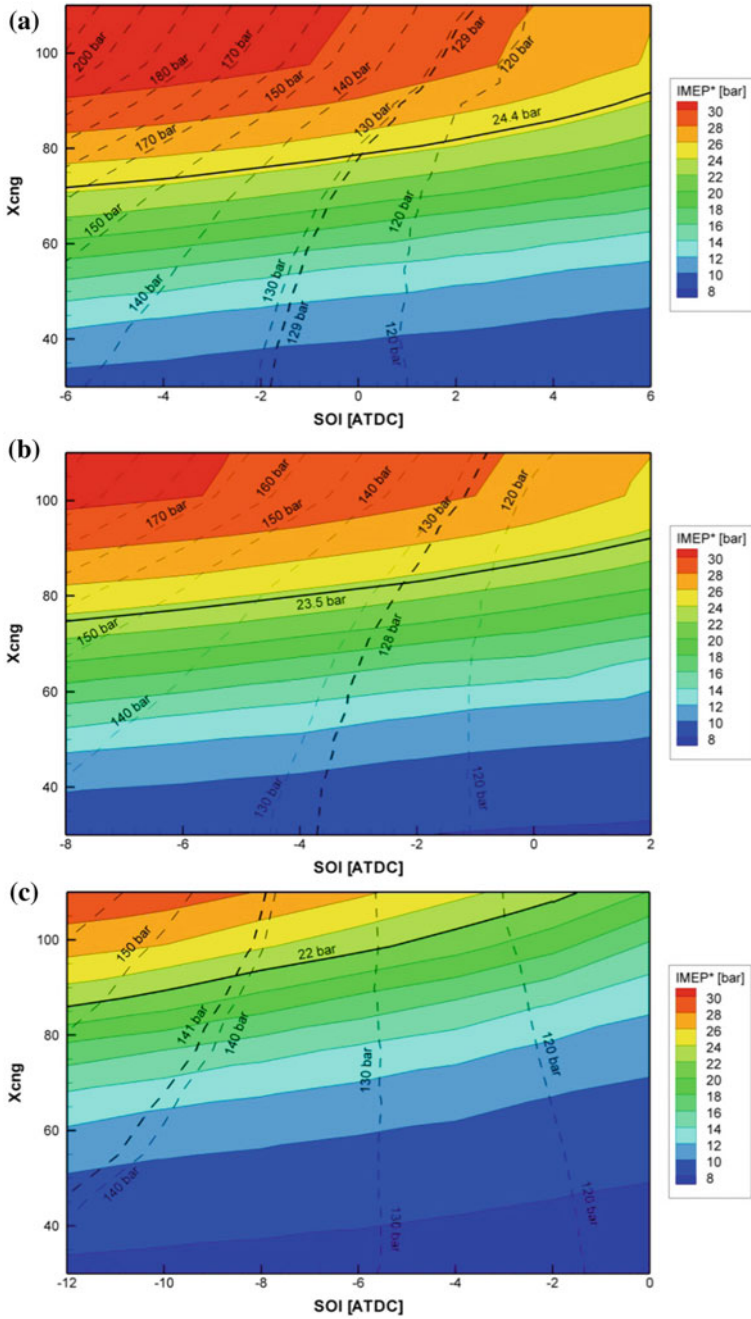


Fig. 11.11 Contours plot of IMEP\* as a function of start of injection angle (SOI) and Xcng for a 2000 rpm, b 3000 rpm, and c 4000 rpm. Reprinted from Rinaldini et al. (2013b)

**Table 11.3** Optimum setup for DF operations at full load

rpm	Operation	SOI (° ATDC)	$m_{\text{Diesel}}$ (mg/stroke)	$M_{\text{NG}}$ (mg/stroke)	$X_{\text{cng}}$
2000	Normal diesel	3 <sup>a</sup>	84.10	0	–
	Dual fuel	0	8.41	57.6	78.5%
3000	Normal diesel	–3.9 <sup>a</sup>	78.70	0	–
	Dual fuel	–2	7.78	57.2	82.6%
4000	Normal diesel	–9.1 <sup>a</sup>	69.70	0	–
	Dual fuel	–8	6.97	56.2	90.1%

Reprinted from Rinaldini et al. (2013b)

<sup>a</sup>Main injection

associated with higher temperatures and higher concentration of  $\text{NO}_x$ . The trend shown by the maps is consistent with the experiments reported in the literature (Wei and Geng 2016), showing that increasing the injection advance at constant load both brake efficiency and combustion pressure increase.

Crossing the bold solid line (ND IMEP\*) and the bold dashed line (ND peak pressure), it can be found a point on each map where the brake output and the peak cylinder pressure of DF combustion are equivalent to ND. These three conditions are reviewed in Table 11.3, and they define the optimum setup for the DF operations at full load. It may be noticed that in all the cases  $X_{\text{cng}} < 1$  (about 80% at 2000 and 3000 rpm and about 90% at 4000 rpm). Since the lower heating values of NG is about 10% higher than that of the diesel fuel, a 20% reduction of total fuel mass in DF combustion means that the efficiency is increased, whereas a 10% decrease indicates a comparable level of efficiency.

Another useful information that may be deduced from the set of simulations is the wide range of relative air–NG ratio that can be adopted, maintaining a stable and regular combustion. The values of  $\lambda_{\text{NG}}$  employed for the points reviewed in Table 11.3 are 1.58 (2000 rpm); 1.49 (3000 rpm); 1.35 (4000 rpm). However, combustion appears complete for values of  $\lambda_{\text{NG}}$  up to 2.0, while no knock is detected when  $\lambda_{\text{NG}}$  is higher than 1.3.

In Figs. 11.12, 11.13, and 14, the optimized DF combustion mode (setup reported in Table 11.3) is finally compared to ND mode. The following three parameters are chosen for the comparison, repeated at each speed: cylinder pressure, average cylinder temperature, and rate of heat release (ROHR).

The differences in terms of pressure are obviously very limited, due to the injection setup, aiming at reaching the same peak value; the slightly lower cylinder pressures (and temperatures) visible during the compression stroke of DF configuration are due to the higher specific heat capacity of the NG/air mixture

Conversely, a clear trend may be observed about temperature: DF combustion generates higher values in the first half of the expansion stroke.

As far as the ROHR curves are concerned, it should be considered that the high-frequency oscillations visible in both combustion modes are not necessarily related to an instability of the process, but they may be simply due to the computational time step (generally larger for ND mode). The average shape of the burn

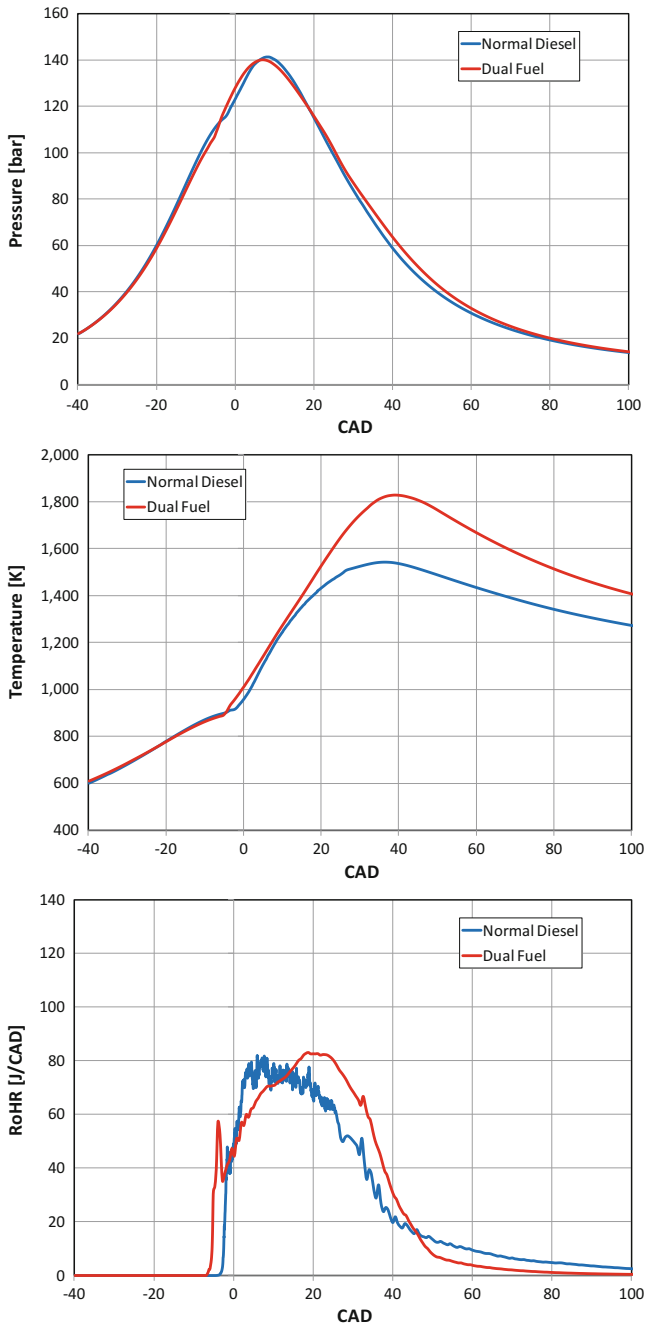


**Fig. 11.12** Comparison between normal diesel and dual-fuel operation in terms of in-cylinder pressure, temperature, and rate of heat release, at 2000 rpm, same load. Reprinted from Rinaldini et al. (2013b)

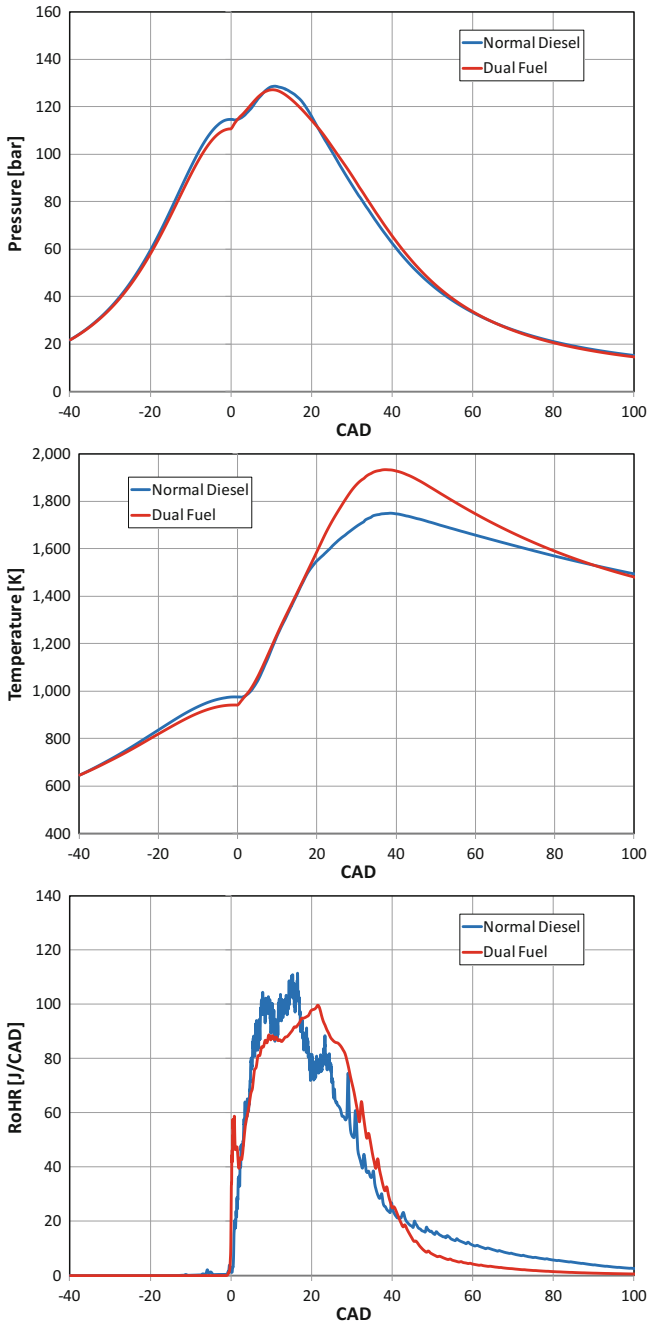


**Fig. 11.13** Comparison between normal diesel and dual-fuel operation in terms of in-cylinder pressure, temperature, and rate of heat release, at 3000 rpm, same load. Reprinted from Rinaldini et al. (2013b)



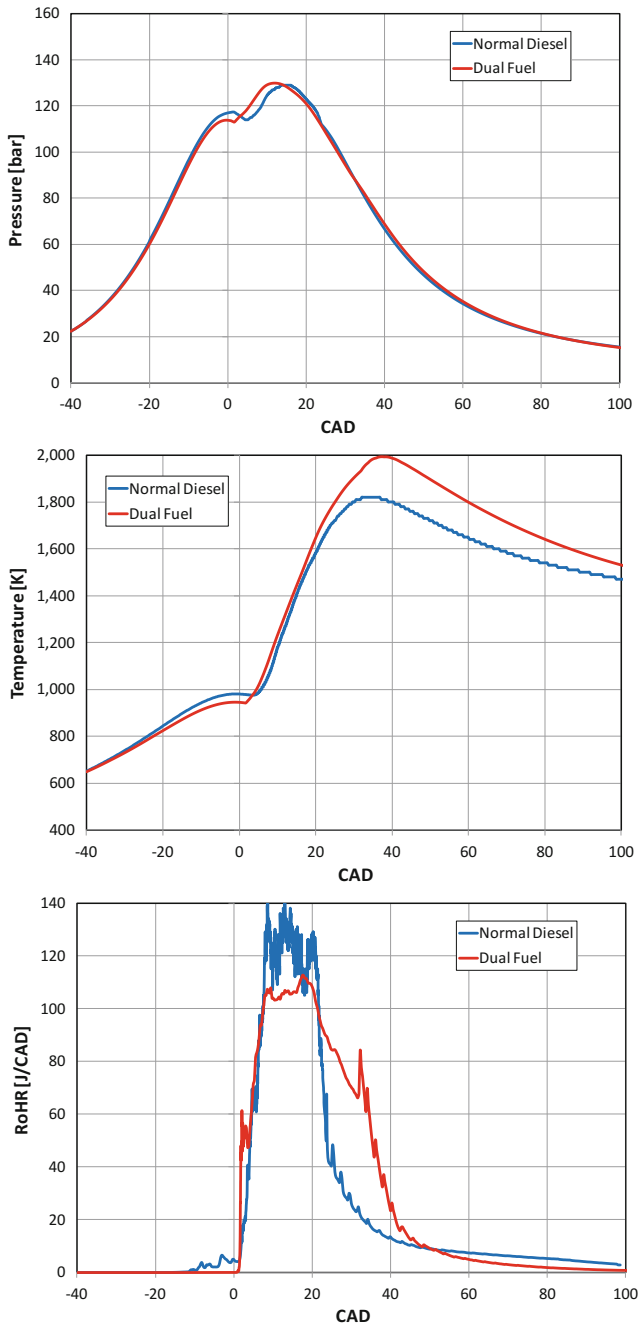
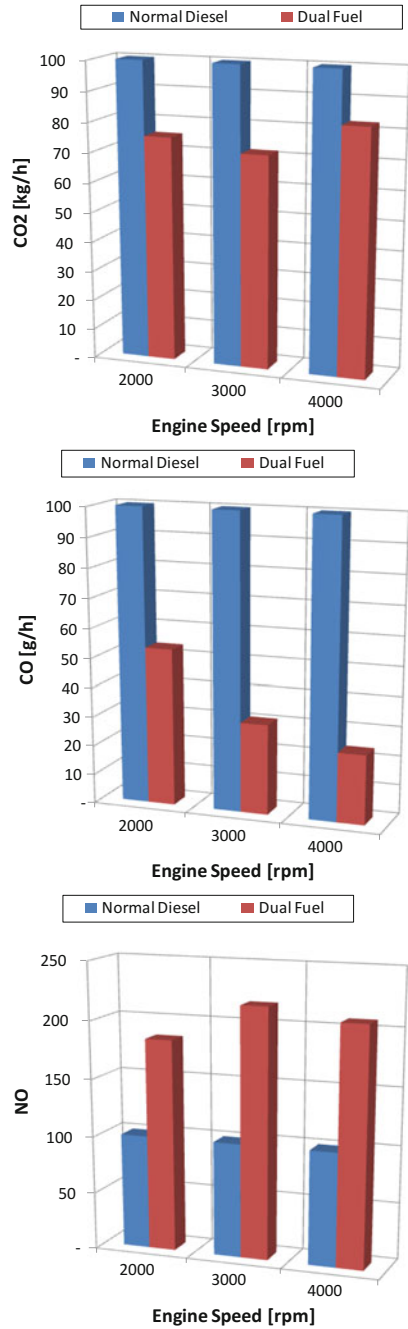


**Fig. 11.14** Comparison between normal diesel and dual-fuel operation in terms of in-cylinder pressure, temperature and rate of heat release, at 4000 rpm, same load. Reprinted from Rinaldini et al. (2013b)

**Fig. 11.15** Comparison between normal diesel and dual fuel operation in terms of CO<sub>2</sub> emissions, CO emissions, NO emissions. Reprinted from Rinaldini et al. (2013b)



rates curves is comparable at 2000 and 3000 rpm, but at 4000 rpm, the DF combustion is clearly smoother.

Figure 11.15 finally shows the comparison between optimized DF and ND operations in terms of CO<sub>2</sub>, CO, and NO. Soot is not plotted, since the values calculated during DF combustion are close to zero, as expected (no diffusive combustion, only premixed). Also, HC concentrations are not presented, remaining very low in both combustion modes.

The following advantages are observed, in comparison to the standard diesel combustion:

- (a) elimination of smoke
- (b) 25% reduction of CO<sub>2</sub> (on average)
- (c) from 40 to 80% reduction of CO
- (d) 8% improvement of fuel economy (on average)
- (e) no knock, despite the high load and high compression ratio (17.5)
- (f) similar values of UHC.

The only important drawback is the increase in NO, about doubled.

The last issue may be reduced, or even turned into an advantage, by means of a different setting of  $X_{cng}$  and SOI. This new setting would probably reduce or cancel, the improvement on CO and fuel efficiency, but it should not spoil the advantages in terms of soot and CO<sub>2</sub>.

The results obtained in this theoretical study seem quite optimistic, in comparison to the experimental values reported in the literature and discussed in Sect. 11.1. In particular, the reduction of CO and the regular operations at maximum load do not find support in previous researches. The different outcomes of this study may be explained by the following considerations:

- the engine and the operating conditions (full load, with BMEP up to 20 bar) are very unusual;
- the CFD-3D simulation enables a very effective optimization of the control parameters
- simulation is carried out in ideal conditions that may be difficult to reproduce at the dynamometer bed.

## 11.4 Experimental Setup

The experimental activity is performed at the dynamometer bench of the Department of Engineering “Enzo Ferrari,” featuring an Apicom FR 400 BRV eddy-current brake (maximum power 260 kW, maximum torque 900 Nm) and the Apicom Horus software for system control and data acquisition. Besides the standard pressure and temperature transducers, the laboratory instruments also include three flow meters, for measuring the consumption of both diesel and NG, as well as the airflow rate. Moreover, there is a set of exhaust gas analyzers (measuring the concentration of: O<sub>2</sub>, CO, CO<sub>2</sub>, NO, NO<sub>2</sub>, HC), and a smoke meter (AVL DiSmoke 4000 opacimeter).

**Fig. 11.16** Picture shows the installation of the four NG injectors (red and gray elements), between the intercooler and the intake manifold



A high-frequency indicating system has been specifically designed and installed for recording in-cylinder pressure traces; the system is made up of a Kistler piezoelectric transducer, installed on one cylinder in place of the glow plug, a charge amplifier, and an optical encoder. The National Instruments Compact RIO hardware and the Alma Automotive software (Obi) are used to acquire the in-cylinder pressure traces and to monitor the related parameters, calculated in real time.

Four NG injectors with a nominal flow rate of 1.5 g/s at 3 bar are installed on the engine inlet pipe, just downstream of the intercooler and about 500 mm before the intake manifold. The longer this distance, the better for achieving a homogeneous air–NG mixture. The position of the injectors, visible in Fig. 11.16, is carefully chosen in order to enhance the gas mixing.

## 11.5 Experimental Results

The experimental campaign covers a wide set of operating conditions. Each point was calibrated in two ways: First, boost pressure was kept constant, passing from standard diesel to DF operations (only the injection strategy was optimized); then, also the turbocharger control was modified, along with the injection parameters.

The last approach is mandatory for the operating points at low load, in order to achieve an efficient and clean combustion, whereas it is not necessary at medium-high loads.

For the sake of brevity, the paper is focused on a single point: 3000 rpm, BMEP = 12 bar. All the measures are taken setting the coolant temperature at the engine outlet at 90 °C and keeping the maximum oil temperature below 120 °C. Ambient conditions are almost identical, since the tests are performed the same day, at some minutes of distance.

Two operating modes are compared: standard diesel operations (referred to as Diesel\_100), maintaining the original engine calibration, except for the EGR valve (always shut); dual-fuel operation, reducing of 80% the diesel flow rate, and replacing it with NG (this mode is referred to as Diesel\_20). In the second case, the injection strategy is optimized, working on rail pressure, start of injection, and injection duration. In both cases, a three-pulse law is employed. Another parameter that could be modified is the pressure in the intake manifold, controlled by setting the turbine rack. In some cases, it is necessary to adjust the boost level, along with the throttle position, in order to control the composition of the charge within the cylinder. However, for the dual-fuel operation considered in the paper (Diesel\_20), a modification of boost pressure does not seem to offer particular advantages.

The goals of the optimization performed in this study are:

- regular engine operations (same or lower cycle-by-cycle variation, in comparison to Diesel\_100)
- compliance with peak cylinder pressure limit (for this point, 120 bar)
- NO<sub>x</sub> emissions as low as possible (in any case, not higher than Diesel\_100)
- brake efficiency as high as possible (in any case, not lower than Diesel\_100).

It may be noticed that the goals are often conflicting: As an example, a faster and more complete combustion normally improves brake efficiency, but it makes also increase NO<sub>x</sub> emissions and peak cylinder pressure. Therefore, the optimum injection setup is not univocal, and it depends on the specific set of constraints and goals driving the optimization process.

Figure 11.17 is showing a comparison between the original injection law (in terms of volumetric flow rate) and the one optimized for the dual-fuel condition. The profiles

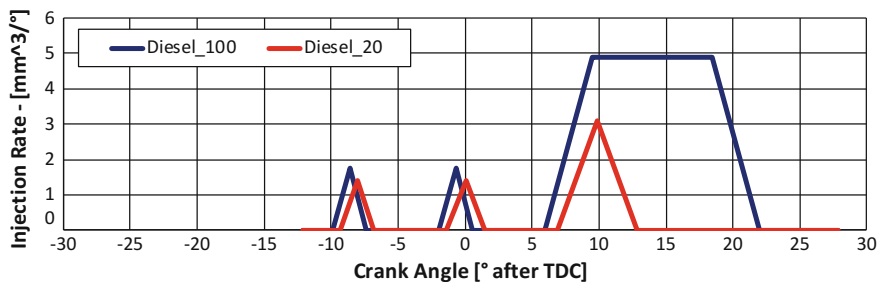
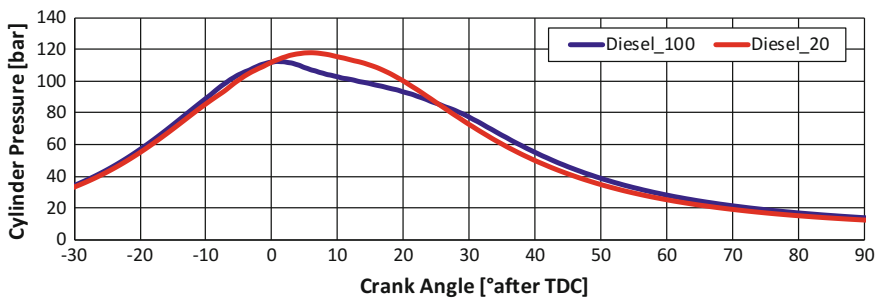


Fig. 11.17 Comparison between the injection rate profiles (3000 rpm, BMEP = 12 bar, no EGR)

are extrapolated from experimental measures, obtained at generally different rail pressures and excitation times. The extrapolation is based on simple physical correlations (as an example, the maximum flow rate is proportional to the square root of injection pressure, and the integral of the mass flow rate must yield the injected mass).

It may be noticed that the main difference consists in the shape of the third pulse, much smaller. Also, the rail pressure is halved (from 1520 to 760 bar), in order to increase the injection duration and get a smoother heat release. From this point of view, splitting the injections into three shots yields some fundamental advantages: First, the main injection releases a smaller amount of heat; second, the pilot and preinjections produce a local increase in temperature and a reduction of  $\lambda_{NG}$  that help the combustion of the lean air-NG mixture. A further reduction of rail pressure seems not convenient, probably because of the atomization worsening, increasing too much the auto-ignition retard. As far as the timings are concerned, the injection advance is limited by the constraints placed upon the peak cylinder pressure (see Fig. 11.18).

Compression is similar between Diesel\_100 and Diesel\_20, but not identical, despite the same intake manifold pressure. The reason is the different specific heat of the charge, made up of pure air (in the former case) and of air and NG in the latter. In the standard combustion, the pressure peak is located at top dead center, whereas in



**Fig. 11.18** Comparison between in-cylinder pressure traces (3000 rpm, BMEP = 12 bar, no EGR)

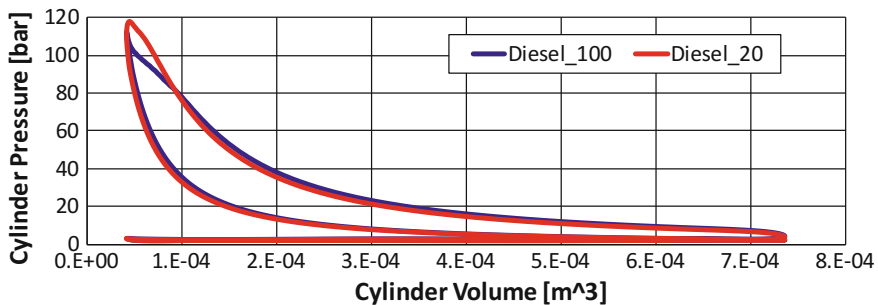


**Fig. 11.19** Comparison in terms of indicated cycle (cylinder pressure plotted as a function of cylinder volume)

Diesel\_20 is shifted toward expansion. The maximum value is slightly higher in the dual-fuel combustion, while the situation is reversed during the expansion stroke.

The energy transmitted by the charge to the piston can be estimated analyzing the pressure–volume diagram, shown in Fig. 11.19 (the indicated work is proportional to the area of the cycle). Even if the area of the indicated cycles is very similar, it is evident that dual-fuel operations are closer to an ideal Otto cycle, where combustion occurs at constant volume, at top dead center. As a result, the engine may have a higher thermal efficiency when operating on dual fuel.

The net heat release rates (i.e., the difference between the instantaneous heat released by combustion and the heat lost through the walls) are calculated on the basis of the first principle of thermodynamics, applied to the ensemble-averaged pressure trace, considering 100 consecutive cycles. The rates are presented in Fig. 11.20, while the cumulative heat curves are shown in Fig. 11.21. From both graphics, it is evident that the first part of combustion is faster in the dual-fuel mode, contributing to the enhancement of the indicated cycle efficiency. However, the maximum heat release rate is almost coincident, or even slightly lower, than the one found in standard diesel combustion. This behavior is explained by the fact that, in the D100 mode, only a small amount of fuel is available before top dead center (about 5%), whereas, in the DF mode, the very first diesel shot can ignite a relatively large amount of homogeneous air–methane charge. In this case, it is fundamental to limit the amount of diesel fuel in the first shots, in order to avoid an abrupt heat release that may also generate dangerous knocking phenomena.

Table 11.4 finally presents a comparison in terms of average cycle quantities. It may be noticed that volumetric efficiency decreases when introducing natural gas, even if the charge pressure in the intake manifold is the same. This result is explained by the fact that the gaseous fuel occupies a volume, which is subtracted to air. The total fuel energy is slightly lower in the dual-fuel operation: Since the brake output is the same, this is the clear evidence that the thermodynamic cycle is more efficient. In fact, brake efficiency is slightly higher (38.4 vs. 36.6%), and the exhaust gas temperature is slightly lower. The composition of the exhaust gas is quite different, despite a very similar relative air–fuel ratio (1.72 vs. 1.77): Soot is canceled, and  $\text{CO}_2$  and  $\text{NO}_x$  concentrations are lower, while CO and HC are ten times higher. The last values demonstrate that combustion in the dual-fuel operation is not complete; however, these

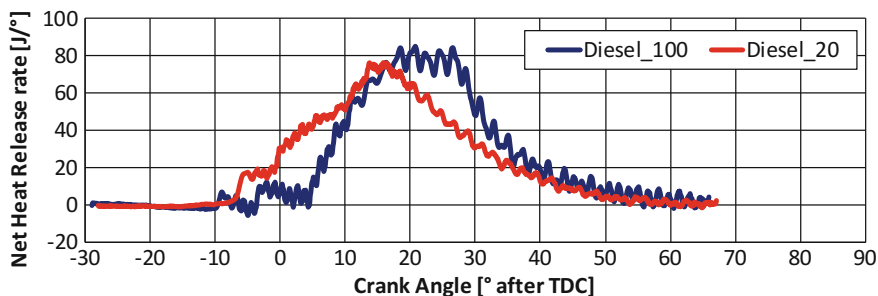


Fig. 11.20 Comparison in terms of net heat release rate (3000 rpm, BMEP = 12 bar, no EGR)

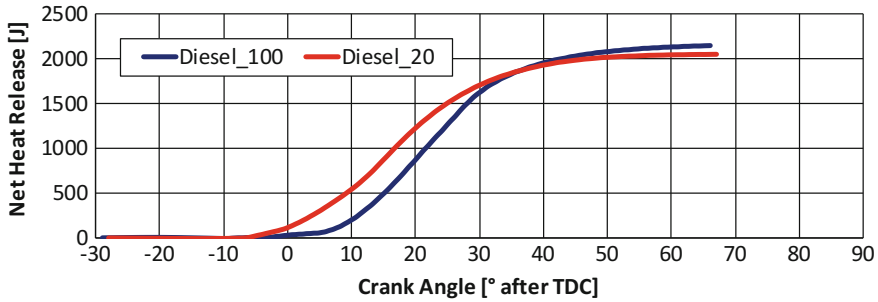


Fig. 11.21 Comparison in terms of cumulative heat release (3000 rpm, BMEP = 12 bar, no EGR)

Table 11.4 Experimental results at BMEP = 12 bar, 3000 rpm

Parameter	Unit	D_100	D_20
Diesel flow rate	kg/h	19.2	3.9
NG flow rate	kg/h	0.0	13.0
Airflow rate	kg/h	493	439
Volumetric efficiency	%	168	149
Total fuel energy	kW	227	216
Relative air–fuel ratio ( $\lambda$ )	°	1.77	1.72
Brake efficiency	%	36.6	38.4
Exhaust gas temperature	°C	444	439
O <sub>2</sub>	%	10.2	10.5
CO <sub>2</sub>	%	7.7	5.8
CO	ppm	131	1978
HC (CH <sub>4</sub> -equivalent)	ppm	630	6372
NO <sub>x</sub>	ppm	629	465
Soot	FSN	0.20	<0.01
CO <sub>2</sub>	g/kWh	720.9	482.8
CO	g/kWh	0.8	10.5
HC (CH <sub>4</sub> -equivalent)	g/kWh	2.1	19.3
NO <sub>x</sub>	g/kWh	5.2	3.4

products can be easily eliminated by adopting a standard oxidation catalyst, which has a small impact on the total cost of the engine. It is quite remarkable the fact that specific NO<sub>x</sub> and CO<sub>2</sub> emissions are strongly reduced: –35% for NO<sub>x</sub>, –33% for CO<sub>2</sub>.

## 11.6 Conclusions

This paper reviews the main results of a numerical and experimental activity, carried out at the Department of Engineering “Enzo Ferrari” (University of Modena and Reggio Emilia), focused on a four-cylinder, common rail, 2.8 L turbocharged diesel



engine, Euro IV compliant. The engine was originally conceived for automotive applications (up to Euro IV/V, adopting a diesel particulate filter and an oxidation catalyst, along with a high-pressure EGR), but it may be easily converted to other uses, with minor hardware modifications and maintaining its excellent efficiency and robustness. In particular, this study considers the implementation of a dual-fuel (natural gas diesel) combustion system, for light-duty industrial applications.

The first step of the study consisted in the construction and calibration of reliable CFD models (both 1D and 3D) of the reference engine. The calibrated KIVA-3V model of the combustion system enabled a comprehensive study on this type of dual-fuel combustion, at full and medium load, for different engine speeds. It was theoretically demonstrated that the engine can operate at full load with 10% of the diesel fuel injected in standard conditions, without generating soot and with a 20–30% reduction of CO<sub>2</sub> emissions, due to a slight improvement of brake efficiency combined to the lower concentration of carbon in the burnt fuel. However, an increase in peak combustion temperatures and NO<sub>x</sub> emissions (about two times higher) was also observed. This drawback can be probably mitigated or canceled with a new specific setup of the injection strategy.

The experimental campaign was focused on low–medium loads, in particular on the following operating condition: BMEP = 12 bar, engine speed 3000 rpm, no EGR (this point is of interest for a number of industrial applications). In the optimized dual-fuel operation, the amount of injected diesel oil is 20% of the value measured under standard conditions.

The following advantages are found, for the DF case: (1) complete elimination of soot; (2) 35% reduction of NO<sub>x</sub>; (3) 33% reduction of CO<sub>2</sub>; (4) 5% improvement of brake efficiency. The only downside is the strong increase in HC and CO concentrations, which are about ten times higher (but they can be easily eliminated adopting an oxidation catalyst, reducing a little bit the advantage on CO<sub>2</sub>).

## References

- Abd Alla GH, Soliman HA, Badr OA, Abd Rabbo MF (2000) Effect of pilot fuel quantity on the performance of a dual fuel engine. *Energy Convers Manag* 41(6):559–572
- Abd Alla GH, Soliman HA, Badr OA, Abd Rabbo MF (2002) Effect of injection timing on the performance of a dual fuel engine. *Energy Convers Manag* 43(2):269–277
- Abdelaal MM, Hegab AH (2012) Combustion and emission characteristics of a natural gas-fueled diesel engine with EGR. *Energy Convers Manag* 64(0):301–312
- Amsden AA (1997) KIVA-3V: a block-structured KIVA program for engines with vertical or canted valves. Report number: LA-13313-MS. Los Alamos National Labs, NM (USA)
- Egusquiza JC, Braga SL, Braga CVM (2009) Performance and gaseous emissions characteristics of a natural gas/diesel dual fuel turbocharged and aftercooled engine. *J Braz Soc Mech Sci Eng* 31(2):142–150
- Gamma Technologies (2016) GT-SUITE v2016 user's manual. Westmont, IL (USA)
- Golovitchev VI, Imren A (2013) Development of dual fuel combustion models for direct injected heavy duty diesel engines. In: *Diesel fuels: characteristics, performances and environmental impacts*. Nova Publisher. ISBN 978-1-62618-867-9

- Golovitchev VI, Nordin N, Jarnicki R, Chomiak J (2000) 3-D diesel spray simulations using a new detailed chemistry turbulent combustion model. SAE paper 2000-01-1891
- Gustavsson J, Golovitchev VI (2003) Spray combustion simulation based on detailed chemistry approach for diesel fuel surrogate model. SAE paper 2003-01-1848
- Harrod KS, Jaramillo RJ et al (2005) Inhaled diesel engine emissions reduce bacterial clearance and exacerbate lung disease to *Pseudomonas aeruginosa* infection in vivo. *Toxicol. Sci.* 83 (1):155–165
- Imran S, Emberson DR, Ihracska B, Wen DS, Crookes RJ, Korakianitis T (2014) Effect of pilot fuel quantity and type on performance and emissions of natural gas and hydrogen based combustion in a compression ignition engine. *Int J Hydrog Energy* 39(10):5163–5175
- Krishnan SR, Srinivasan KK, Singh S, Bell SR, Midkiff KC, Gong W et al (2004) Strategies for reduced  $\text{NO}_x$  emissions in pilot-ignited natural gas engines. *J Eng Gas Turbines Power Trans ASME* 126(3):665–671
- Liao SY, Jiang DM, Cheng Q (2004) Determination of laminar burning velocities for natural gas. *Fuel* 83:1247–1250
- Liu SH, Wang ZY, Ren J (2003) Development of compressed natural gas/diesel dual-fuel turbocharged compression ignition engine. *Proc Inst Mech Eng D J. Automob Eng* 217 (D9):839–845
- Liu J, Yang F, Wang HW, Ouyang MG, Hao SG (2013) Effects of pilot quantity on the emissions characteristics of a CNG/diesel dual fuel engine with optimized pilot injection timing. *Appl Energy* 110(0):201–206
- Lloyd AC, Cackette TA (2001) Diesel engines: environmental impact and control. *J Air Waste Manag Assoc* 51(6):809–847
- Lounici MS, Loubar K, Tarabet L, Balistrrou M, Niculescu DC, Tazerout M (2014) Towards improvement of natural gas–diesel dual fuel mode: an experimental investigation on performance and exhaust emissions. *Energy* 64:200–211
- Lutz AE, Kee JR, Miller JA (1997) SENKIN: a Fortran program for predicting homogeneous gas phase chemical kinetics with sensitivity analysis. SANDIA National Laboratories' document SAND87-8248
- Papagiannakis RG, Hountalas, DT (2003) Experimental investigation concerning the effect of natural gas percentage on performance and emissions of a DI dual fuel diesel engine. *Appl Therm Eng* 23(3):353–365
- Papagiannakis RG, Hountalas DT (2004) Combustion and exhaust emission characteristics of a dual fuel compression ignition engine operated with pilot diesel fuel and natural gas. *Energy Convers Manag* 45(18–19):2971–2987
- Papagiannakis RG, Rakopoulos CD, Hountalas DT, Rakopoulos DC (2010) Emission characteristics of high speed, dual fuel, compression ignition engine operating in a wide range of natural gas/diesel fuel proportions. *Fuel* 89(7):1397–1406
- Patterson MA, Reitz RD (1998) Modeling the effects of fuel spray characteristics on diesel engine combustion and emission. SAE 980131
- Reşitoğlu İA, Altinişik K, Keskin A (2015) The pollutant emissions from diesel-engine vehicles and exhaust aftertreatment systems. *Clean Technol Environ Policy* 17(1):15–27
- Rinaldini CA, Mattarelli E, Golovitchev VI (2013a) Potential of the Miller cycle on a HSDI diesel automotive engine. *Appl Energy* 112:102–119
- Rinaldini CA, Mattarelli E, Golovitchev VI (2013b) CFD-3D analysis of a light duty dual fuel (diesel/natural gas) combustion engine. In: *Energy procedia* 00 (2013) 12647, 68th conference of the Italian thermal machines engineering association, ATI2013
- Singh S, Krishnan S, Srinivasan K, Midkiff K, Bell S (2004) Effect of pilot injection timing, pilot quantity and intake charge conditions on performance and emissions for an advanced low-pilot-ignited natural gas engine. *Int J Eng Res* 5(4):329–348
- Wannatong K, Akarapanyavit N, Siengsanorh S, Chanchaona S (2007) Combustion and knock characteristics of natural gas diesel dual fuel engine. SAE technical paper 2007-01-2047
- Wei L, Geng P (2016) A review on natural gas/diesel dual fuel combustion, emissions and performance. *Fuel Process Technol* 142:264–278. ISSN 0378-3820

# Chapter 12

## Cyclic Combustion Variations in Diesel–Natural Gas Dual Fuel Engines



**Kalyan Kumar Srinivasan, Sundar Rajan Krishnan,  
Prabhat Ranjan Jha and Hamidreza Mahabadipour**

**Abstract** Dual fuel combustion is achieved by using a combination of two fuels with extremely different ignition characteristics. For instance, a low-reactivity fuel such as natural gas is compression-ignited using a calibrated amount of appropriately timed, high-pressure, high-reactivity diesel spray. The ensuing combustion occurs at predominantly fuel-lean conditions and is therefore devoid of soot emissions, and the relatively small amount of diesel fuel used also results in the simultaneous reduction in nitrogen oxide emissions. In addition, the use of natural gas, which is predominantly composed of methane, offers the necessary fuel flexibility required to reduce carbon dioxide emissions from conventional neat diesel fired power trains in transportation and power generation applications. The greatest reductions in carbon dioxide emissions are achieved with highest natural gas substitution. However, this also causes problems with high cyclic combustion variations leading to an increased propensity to misfire and high engine-out hydrocarbon emissions. This chapter reviews the current state of the art in strategies to mitigate cyclic combustion variations in dual fuel natural gas engines and provides substantial insights gleaned from past experimental dual fuel combustion research conducted by the authors. In particular, the chapter discusses opportunities and challenges associated with low-temperature dual fuel combustion engines.

**Keywords** Natural gas · Low-temperature combustion · Advanced combustion  
Internal combustion engines

---

K. K. Srinivasan (✉) · S. R. Krishnan · P. R. Jha · H. Mahabadipour  
Department of Mechanical Engineering, The University of Alabama,  
286 Hardaway Hall, Tuscaloosa, AL 35487, USA  
e-mail: [ksrinivasan@eng.ua.edu](mailto:ksrinivasan@eng.ua.edu)

© Springer Nature Singapore Pte Ltd. 2019  
K. K. Srinivasan et al. (eds.), *Natural Gas Engines*, Energy, Environment,  
and Sustainability, [https://doi.org/10.1007/978-981-13-3307-1\\_12](https://doi.org/10.1007/978-981-13-3307-1_12)

## 12.1 Introduction

Natural gas has been employed and studied extensively as an alternative fuel for both spark ignition (SI) and compression ignition (CI) engines (Korakianitis et al. 2011). Dual fuel engines using natural gas as the primary fuel and diesel as the secondary fuel have attracted increasing attention in recent years due to their significant performance–emissions benefits (Wei and Geng 2016). Research on dual fuel combustion has been ongoing for several decades (Boyer 1949; Elliot and Davis 1951; Felt and Steele 1962; Karim and Khan 1968; Karim 1980, 2003; Doughty et al. 1992). In particular, a preponderance of the literature is available on diesel–natural gas dual fuel combustion with a variety of fuel injection systems and operating strategies that are mostly consistent with the diesel engine architectures prevalent during the corresponding time periods. Early research efforts utilized mechanical injection systems to introduce the diesel fuel directly into the engine cylinder(s) while natural gas was fumigated in the intake manifold. In contrast, more recent studies have utilized common-rail diesel injection systems that have enabled the realization of a variety of diesel–natural gas dual fuel low-temperature combustion (LTC) strategies at low-to-medium loads (Li et al. 2016; Srinivasan et al. 2006a; Raihan et al. 2014; Guerry et al. 2016) and at high loads, including premixed mixture ignition in the end gas region (PREMIER) (Azimov et al. 2011), advanced injection low pilot-ignited natural gas (ALPING) (Krishnan et al. 2004; Srinivasan et al. 2006b), reactivity-controlled compression ignition (RCCI) (Walker et al. 2015). In addition, simultaneous direct injection of natural gas along with diesel using a specialized high-pressure direct injection (HPDI) system has been explored as a pilot-ignited nonpremixed diesel–natural gas dual fuel combustion strategy by several researchers (McTaggart-Cowan et al. 2007, 2015; Faghani et al. 2017; Neely et al. 2017) and shown capable of maintaining diesel-like performance while deriving most of the power (>90%) from natural gas.

In general, many of these studies demonstrate the potential benefits of diesel–natural gas dual fuel combustion in terms of significant reductions in engine-out emissions of oxides of nitrogen ( $\text{NO}_x$ ) and particulate matter (PM) compared to conventional compression ignition direct injection (CIDI) diesel combustion and fuel conversion efficiencies that are comparable to or slightly better than CIDI, especially at high loads. On the other hand, both conventional diesel–natural gas dual fuel combustion and dual fuel LTC strategies suffer from high cyclic combustion variations, poor combustion efficiencies, and high emissions of unburned hydrocarbons (HC) and carbon monoxide (CO) at low loads and high natural gas substitutions, and exhibit the tendency to knock with high maximum pressure rise rates (MPRR) at high loads. Comparing conventional dual fuel and dual fuel LTC strategies, it is clear that the latter provides better overall efficiency–emissions benefits. Consequently, it is imperative to identify strategies for improving cyclic variations, part-load combustion efficiencies, and high load operability issues for dual fuel LTC. It is especially important to understand and ameliorate cyclic combustion variations in dual fuel LTC because they lead to low combustion efficiencies and high HC and CO emissions.

The rest of the chapter is organized as follows. A selective review of the existing open literature on cyclic combustion variations in conventional SI, homogeneous charge compression ignition (HCCI), and dual fuel combustion is first presented. This is followed by the examination of cyclic combustion variations of diesel–methane dual fuel LTC in a single-cylinder research engine (SCRE) operating at a relatively low load of 5.1 bar indicated mean effective pressure (IMEP), a fixed engine speed of 1500 rev/min, and a methane energy fraction (MEF) corresponding to natural gas of 80% of the total fuel energy input. Methane is chosen as a practically relevant surrogate for natural gas. Despite the well-known fact that natural gas composition varies significantly across the world, its primary constituent is almost always methane. Finally, the chapter concludes by making recommendations to achieve high-efficiency dual fuel LTC by mitigating cyclic variations.

## 12.2 Selective Review of the Literature on Cyclic Combustion Variations

### 12.2.1 *Stochastic and Deterministic Features in Cyclic Variations*

Cyclic variations (or cycle-to-cycle variations) in engine combustion processes have been observed and investigated for several decades (Patterson 1966). Early studies were largely focused on cyclic combustion variations in SI engines (cf. Patterson 1966; Barton et al. 1970; Young 1981; Matekunas 1983; Ozdor et al. 1994). Many of these studies utilized normal linear statistics to characterize cyclic variations. Most of them (e.g., Young 1981; Ozdor et al. 1994) led to the understanding that cyclic variations were inherently stochastic (i.e., purely random) in nature or exhibited no statistically significant autocorrelation between one cycle and the next (e.g., Barton et al. 1970). In other words, no deterministic effects were noted in the initial studies on stoichiometric, homogeneous SI engines because they considered engine operating conditions that were far from the unstable operating limits. On the other hand, when unstable operating conditions are encountered in lean burn SI, stoichiometric SI with high levels of dilution with exhaust gas recirculation (EGR), HCCI, and dual fuel LTC, a combination of deterministic and stochastic features may be evident.

Various causes have been proposed for cyclic variations, including random turbulent fluctuations of in-cylinder fuel–air mixing processes to more deterministic prior cycle effects (e.g., residual gas effects from prior cycles). In the present context, the adjective “deterministic” may be construed as indicative of a system that follows explicit laws of cause and effect; i.e., there is at least some short-term predictability in the system’s behavior, and hence, it allows feedback-based control strategies to be used to stabilize or alter its behavior (Finney et al. 2015; Davis et al. 2001). In many situations, nonlinear dynamical systems with extreme sensitivity to

initial conditions may appear to exhibit random behavior but are actually somewhat deterministic. For example, when residual exhaust gas temperature was considered as the nonlinear coupling mechanism between successive cycles in SI engine combustion, periodic or chaotic combustion oscillations were observed under certain engine operating conditions (Kantor 1984; Daily 1988). Subsequent studies (e.g., Daw et al. 1996) suggested that residual gas composition (rather than temperature) was the most important factor vis-à-vis its nonlinear (prior cycle) impact on combustion.

In general, Finney et al. (2015) observed that there is significant experimental evidence indicating both stochastic and deterministic components in cyclic combustion variations. Stochastic variations are always apparent for nearly all operating conditions while deterministic cyclic variations typically emerge only when engine operation occurs near “a transition point” when thermal and mass feedback between successive cycles become significant (e.g., for high EGR conditions). Important factors affecting cyclic combustion variations are charge dilution (i.e., excess air or EGR) and the amount of residual gas present. For stoichiometric combustion with little or no EGR and low residual gas levels, cyclic combustion variations are generally stochastic while for higher dilution and/or residual gas levels, deterministic features become increasingly apparent. For significantly dilute operation (e.g., near lean flammability limits), the residual gas effects dominate, causing alternating misfires followed by cycles of strong combustion “recovery” or “rebound.” It is interesting to note that similar rebound behavior (i.e., partial misfires followed by cycles of intense high heat release combustion) has also been observed under dual fuel LTC conditions (e.g., Srinivasan et al. 2014). Similarly, nonlinear dynamics have also been observed in HCCI (Hellstrom et al. 2012), spark-assisted HCCI (Daw et al. 2008), and during mode transitions between standard SI and HCCI operations (Daw et al. 2007).

### *12.2.2 Cyclic Variations in SI Engines*

As discussed above, Young (1981) presented one of the early reviews of cyclic combustion variations and their influence on in-cylinder pressure evolution in homogeneous SI engines. It was reported that the main cause of cyclic cylinder pressure variations was cyclic combustion variations and faster combustion typically produced smaller pressure variations. Also, cyclic variations of velocity in the spark plug vicinity at the time of ignition were shown to result in cyclic variations later in the combustion process. To study cyclic combustion variations in an SI engine, Matekunas (1983) considered a propane-fueled single-cylinder engine with a transparent piston crown, three intake geometries, and two spark locations. It was found that cyclic combustion variations appeared in two regimes. In the first regime, away from the lean limit, the repeatability of the overall cylinder flow pattern determined the relative variations in burn (combustion) phasing. In the second regime, which corresponded to operation near misfire due to partial

quenching of the early flame, late burning in some cycles was observed. Another literature survey was performed by Ozdor et al. (1994) to assess cyclic variations in SI engines. The largest relative cyclic variations at mean best torque (MBT) spark timing were exhibited by maximum cylinder pressure while the location (crank angle) corresponding to maximum cylinder pressure exhibited cyclic variations in the initial flame kernel development stage.

Sen et al. (2011) demonstrated the influence of different EGR levels (0, 5, 10, 15, and 20%) on cyclic combustion variations in a stoichiometric natural gas-fueled SI engine at 2000 rpm. By extracting data over 200 cycles, it was revealed that cyclic variations in IMEP occurred on multiple timescales. While high-frequency intermittent fluctuations were observed for 0% EGR, more persistent frequency variations developed at higher EGR levels. Wang et al. (2008) experimentally studied the effect of hydrogen addition at different volumetric fractions on cyclic combustion variations in a natural gas-fueled SI engine. They observed that under lean mixture conditions, the cyclic variability decreased with increasing hydrogen fraction while peak pressure and MPRR increased.

The instability characteristics of a hydrogen-enriched gasoline SI engine were experimentally investigated by Wang and Ji (2012) under various operating conditions on a modified four-cylinder SI engine. They reported that hydrogen addition shortened the combustion duration, resulting in a reduction of coefficient of variation (COV) of IMEP. Also, it was shown that hydrogen addition was more effective vis-à-vis engine stability for gasoline engines at lean operating conditions, idle, and low loads compared to high loads.

Ceviz and Yüksel (2006) studied the effect of liquefied petroleum gas (LPG) on combustion variability of a lean burn SI engine. They found that with LPG as a fuel, cyclic combustion variations were lower compared to gasoline. Also, with increasing air–fuel ratio, the COV of IMEP increased for both gasoline and LPG operations; however, the increase in instability was more pronounced for gasoline.

### ***12.2.3 Cyclic Variations in HCCI Engines***

Cyclic combustion variations in gasoline-fueled HCCI combustion were studied by Agrawal (2011) on a modified CI engine. The impact of varying intake air temperature and air–fuel ratio on cyclic variations was studied at different engine speeds. In-cylinder pressure was measured for 3000 consecutive cycles, and symbol sequence statistics was used to find the stochastic and deterministic components of cyclic variability. It was found that as the fuel–air mixture became richer, the distribution of combustion timings deviated significantly from a normal distribution. Also, cyclic variations in combustion timing shifted from stochastic to deterministic behavior when the mixture became richer at all test speeds. A similar shift in cyclic variations behavior was also reported with increasing intake air temperature at a fixed air–fuel ratio. Based on modified Shannon entropy calculations, it was found that prior cycle effects on combustion timing extended back to

eight previous cycles. Therefore, it was concluded that it may be beneficial for the engine controller to have information of more than just the immediate previous cycle.

Ion current signals were investigated by Chen et al. (2016) to characterize cyclic variations in an ethanol-fueled HCCI engine by adding different CsOAc (cesium acetates) concentrations to the based fuel. Subsequently, the ion signal cyclic variations were compared with cylinder pressure variations. To identify nonlinear characteristics of ion current signals, a single-zone model was considered at different equivalence ratios. It was found from return maps, time series plots, and calculated COV that due to the low ionization energy of CsOAc, the stability of the ion signals significantly improved. It was also suggested that through the application of designed deterministic patterns, that long, consecutive symbols of the ion current signal could be reliably predicted, especially when a small amount of CsOAc was added.

Cyclic variations of IMEP and combustion duration were experimentally investigated by Maurya (2018) in a gasoline-fueled HCCI engine using symbol sequence statistics. The combustion parameters were analyzed by recording 1500 consecutive engine cycles at 1200 rpm engine speed and various engine load conditions. It was observed that at different engine load conditions, cyclic variations of IMEP and combustion duration shifted from stochastic to deterministic behavior. Also, the maximum determinism for IMEP and burn duration was observed for the leanest mixture and the richest mixture, respectively. It was concluded that information from more than just the immediate previous cycle was needed for effective HCCI engine control.

#### ***12.2.4 Cyclic Variations in Dual Fuel Combustion***

For many single fuel and dual fuel LTC strategies, since engine operation is generally very sensitive to initial charge composition and initial temperature, cyclic variations exhibit some level of deterministic behavior. Several studies have been performed on conventional dual fuel combustion as well as dual fuel LTC. A few selected publications (not an exhaustive list) on this topic are reviewed below.

Selim (2005) converted a single-cylinder, naturally aspirated Ricardo E6 engine to operate on pure diesel, diesel–methane dual fueling, and diesel–LPG dual fueling to perform a statistical analysis of cyclic combustion variations. In-cylinder pressure data were recorded for 1200 consecutive cycles to characterize combustion variations based on maximum pressure, maximum rate of pressure rise, and IMEP. Different operating and designed parameters were considered such as type of gaseous fuel, pilot fuel mass, compression ratio, engine load, pilot fuel injection timing, and engine speed. It was observed that dual fuel cyclic combustion variations strongly depended on the type and concentration of gaseous fuel used. Diesel–LPG dual fueling showed higher combustion noise compared to diesel–methane dual fueling. Advancing pilot injection timing and increasing compression ratio led



to higher cyclic combustion variations for diesel–LPG dual fueling while increasing engine speed reduced cyclic variations.

Sun et al. (2013) experimentally analyzed cyclic combustion variations in a single-cylinder, four-stroke, natural gas–diesel dual fuel engine by varying the EGR ratio, the diesel injection timing, and the pilot diesel quantity at fixed engine speed and pilot injection pressure. It was observed that, with increasing EGR, the in-cylinder peak pressure decreased and its cyclic variations increased, while the MPRR decreased. With diesel injection timing advancement, the in-cylinder peak pressure increased and its cyclic variations decreased. With increasing diesel quantity, the in-cylinder peak pressure increased while its cyclic variations decreased.

Srinivasan et al. (2014) examined experimentally the cyclic combustion fluctuations for conventional diesel–methane dual fuel combustion and partially premixed diesel–methane dual fuel combustion in a single-cylinder research engine at 6 bar brake mean effective pressure (BMEP) and 1700 rev/min engine speed. A mechanical injection system with a fixed pilot diesel injection timing (22 CAD before TDC) was used for the conventional dual fuel experiments while natural gas fueling was varied between 0 and 95% on an energy basis. For the partially premixed dual fuel combustion experiments, an electronic injection system was employed with pilot diesel injection timing varied between 20 CAD and 60 CAD before TDC and the diesel accounting for about 2% of the total fuel energy input. Cyclic variations in start of combustion (SOC), peak cylinder pressure, combustion phasing (CA50), and the separation between the diesel injection event and the combustion event were analyzed. For conventional dual fuel combustion, with increasing natural gas substitution, the peak pressure decreased, SOC and CA50 were delayed, and the COV of IMEP increased. For dual fuel partially premixed combustion, the COV of IMEP decreased from around 25% at 20 CAD before TDC to 6.2% at 40 CAD before TDC and subsequently increased to 10.6% at 60 CAD before TDC. For both conventional and partially premixed dual fuel combustion, cyclic variations were characterized by alternating slow and fast burn cycles, especially at high natural gas substitutions and advanced injection timings. Finally, using heat release return maps, it was shown that cyclic combustion variations could be decreased by adopting intake charge preheating as an effective thermal management strategy, especially for dual fuel partially premixed combustion. A similar conclusion was also reached by Srinivasan et al. (2006a) for improving COV of IMEP of pilot-ignited natural gas combustion at low loads.

Wang et al. (2016) experimentally investigated cyclic variations in diesel–methanol dual fuel combustion by considering the COV of maximum in-cylinder pressure, maximum mass-averaged temperature, and IMEP for 100 consecutive cycles. The effects of intake temperature, engine load, injection timing, and methanol substitution on cyclic variations were studied at an engine speed of 1660 rev/min and BMEPs of 3.14 and 12.52 bar. It was observed that the COV of maximum pressure and temperature increased significantly with increasing methanol substitution at low loads while at high loads, the increase of COV was negligible. At high loads, diesel–methanol dual fuel combustion was more stable

and less sensitive to methanol substitution but at low loads, the IMEP showed considerable fluctuations. It was found that COVs were more sensitive to intake temperature than diesel injection timing. Similar to the observations of Srinivasan et al. (2006a, b), with increasing intake temperature at low loads, the COVs of all combustion parameters decreased.

Cyclic variations of diesel–gasoline and diesel–ethanol dual fuel combustion were investigated experimentally and numerically by Dong et al. (2017). In-cylinder pressure was recorded for 150 consecutive cycles and cyclic variations in CA5 (ignition timing), CA50 (combustion phasing), cumulative heat release, and IMEP were reported. For both diesel–gasoline and diesel–ethanol dual fuel combustion, cyclic variations in cumulative heat release led to IMEP variations, with the latter exhibiting higher cyclic variations due to lower reactivity of ethanol and lower combustion temperatures. Also, at both high and low loads, cyclic variations of diesel–ethanol dual fuel combustion increased with increasing ethanol substitution.

### 12.2.5 Modeling Cyclic Variations

Many models, including both zero-dimensional and multidimensional models, have been proposed to simulate the dynamical character of cyclic variations. Zero-dimensional models may be broadly classified into two types (Green et al. 1999): (i) linear Gaussian random processes (LGRP) and (ii) noisy nonlinear dynamics (NND). Both LGRP and NND models presume that cyclic variations include both deterministic and random components. However, LGRP further assumes linear influences of both the deterministic (i.e., prior cycle effects) and random components; in other words, LGRP models are based on the expectation that cyclic variations occur due to noisy, linear perturbations on the combustion process (e.g., due to excited acoustic modes in the intake manifold leading to small equivalence ratio fluctuations). By contrast, NND models allow nonlinear coupling between past and future combustion cycles via some mechanism (e.g., residual gas effects), leading to “nonlinear memory” in the system. For example, Daw et al. (1996) presented a simple NND model for cyclic variations that included both stochastic and nonlinear deterministic elements. They assumed nonlinear coupling of residual gases from prior cycles as the primary mechanism for nonlinear deterministic oscillations in fuel-lean combustion while the stochastic element was modeled as random fluctuations in the important deterministic model parameters such as fuel–air ratio, residual gas fraction, and lean ignition limit. They observed deterministic behavior with dynamical noise (i.e., random fluctuations) in both experimental data and predictions from their model. More generally, based on “time irreversibility” considerations (i.e., “return maps” of cumulative heat release plotted for a given cycle  $i$  against the following cycle  $i + 1$ ) when comparing model predictions with experimental data, Green JB Jr et al. (1999) concluded that only NND models adequately reproduce the time irreversibility in cyclic combustion variations under fuel-lean operating conditions.

Recently, Sen et al. (2014) numerically studied cyclic variations in heat release in a gasoline–ethanol-fueled SI engine with wavelet analysis of 2000 consecutive engine cycles. Mixture equivalence ratio varied between 0.7 and 1, and ethanol was changed in volumetric proportions of 5–25%. It was found that cyclic variations reduced with increasing ethanol substitutions at a fixed equivalence ratio. Also, cyclic variations increased for leaner mixtures at a fixed ethanol substitution. Sjerić et al. (2015) implemented a new turbulence model in a 1D/0D cycle-simulation software (AVL BOOST) to investigate the impact of turbulence, mixture stratification, and flow angle at the spark plug on cyclic variations in SI engines. In-cylinder pressure histories for 300 consecutive cycles were recorded at a resolution of 0.1 CAD in an unthrottled CFR engine. Cyclic variations of in-cylinder turbulence had the most significant effect on cyclic combustion variations, followed by equivalence ratio variations, while flow angle at the spark plug had the lowest impact. A stochastic reactor model of iso-octane/n-heptane HCCI engine was used by Tunér et al. (2009) to investigate relation between cyclic variations and discretization as well as the effect of heat transfer and mixing on cyclic variations. A simplified mixing model was used for turbulence, and the Woschni model was used for modeling heat transfer with a stochastic approach. It was found that cyclic variations could be reduced by the presence of inhomogeneities which promote earlier ignition.

Galloni (2009) studied the parameters that affect cyclic combustion variations in a small SI engine by means of computational fluid dynamics (CFD) analysis and experimental studies of several combustion chamber geometries and part-load operating conditions. He concluded that a correlation existed between calculated mean laminar flame speed, mean turbulence intensity, and experimental COV of IMEP.

Using multidimensional simulations and monitoring the sensitivity of ignition timing to changes in initial in-cylinder temperature at IVC, Jia et al. (2015) investigated cyclic variations of various premixed compression ignition combustion strategies, focusing on dual fuel diesel–gasoline RCCI combustion. The effects of different operating parameters such as combustion mode, fuel reactivity, EGR rate, intake pressure, and injection strategies were studied using re-normalization group (RNG)  $k$ - $\epsilon$  turbulence model, Kelvin–Helmholtz–Rayleigh–Taylor (KH–RT) droplet breakup model, and improved spray–wall interaction model. Diesel–methanol RCCI combustion exhibited larger cyclic variations compared to diesel–gasoline RCCI at the same operating conditions due to lower reactivity of methanol. Also, using EGR resulted in higher standard deviations of CA50 due to retarded ignition phasing and slower burn rate. Higher intake boost pressure led to considerable reduction in cyclic variations. To reduce cyclic variations in RCCI combustion, it was found that retarded injection timing and a single high-pressure injection were helpful because the local in-cylinder equivalence ratio was sufficiently rich to promote more robust combustion. To investigate cyclic variations in gasoline-fueled HCCI and diesel–gasoline RCCI combustion, Klos and Kokjohn (2015) developed a methodology based on detailed CFD simulations. To determine the combustion characteristics and the main sources of cyclic variations, a response

surface model was fit to the design-of-experiment results to accurately predict several outputs (i.e., IMEP, CA50, MPRR, NO<sub>x</sub>, soot, and unburned hydrocarbon (UHC)). It was shown that RCCI and HCCI exhibited higher cyclic variations and much higher sensitivity to input parameters than conventional diesel combustion. Using an uncertainty propagation technique, it was found that sources of HCCI and RCCI cyclic variations were trapped gas temperature, port fuel injection mass, direct injection mass, and EGR percentage. Also, while cylinder pressure at IVC was shown to be a significant factor in HCCI combustion, its contribution to RCCI cyclic variations was minimal.

Jupudi et al. (2016) used a commercial CFD software to simulate multiple parallel single cycles of diesel–natural gas dual fuel combustion to characterize the effect of variabilities in operating parameters and boundary conditions on cyclic combustion variations. Therefore, a collection of individual cycle Reynolds-averaged Navier–Stokes (RANS) simulations was executed in parallel to evaluate cyclic variations of in-cylinder pressure in a closed-cycle simulation from IVC to 20° after TDC. It was found that the COV of in-cylinder pressure in dual fuel mode was less than half of the experimentally measured COV. Stochastic effects (e.g., in-cylinder natural gas stratification) and hole-to-hole variation in diesel injection could lead to cyclic combustion variations. Among the variabilities in operating and boundary conditions, variability in the start of diesel injection had the highest impact on cyclic combustion variations for both dual fuel and diesel combustion modes, followed by variability in diesel flow rate. These results indicated that precise fuel injection control was important to reduce cyclic combustion variations in both dual fuel and diesel combustion modes.

### 12.3 Results from Single-Cylinder Engine Experiments

In this section, selected experimental results from the authors' research group are presented. Particular reference will be made to the research conducted by Raihan et al. (2014) and Raihan (2014) on a single-cylinder research engine described in Table 12.1.

**Table 12.1** Description of the SCRE used in Raihan et al. (2014) and Raihan (2014)

Engine type	SCRE based on a Doosan DV-11 platform
Number of cylinders	1
Displacement	1.827 L
Compression ratio	17.1:1 (nominal value)
Valve train	2 intake, 2 exhaust valves
Bore × Stroke	128 × 142 mm
Connecting rod length	228 mm
IVO/IVC	4/174 CAD
EVO/EVC	503/712 CAD

Raihan et al. (2014) conducted a comprehensive experimental program that performed detailed dual fuel experiments on the effect of several parameters including diesel start of injection (SOI), intake manifold pressure (boost), and fuel injection pressure with engine speed maintained at 1500 rev/min and engine load maintained at 5.1 and 7.5 bar IMEP, respectively. In addition, the intake temperature and pressure were fixed at  $T_{in} = 30\text{ }^\circ\text{C}$  and  $P_{in} = 1.5\text{ bar}$ , respectively, the diesel injection rail pressure ( $P_{rail}$ ) = 500 bar, MEF at 80%, while the diesel injection timing was varied from SOI = 280 CAD to 355 CAD to quantify the effects of SOI variation on dual fuel combustion. Figures 12.1, 12.2, 12.3, and 12.4 discuss the performance and emissions at a particular low load condition (5.1 bar IMEP) where the unburned hydrocarbon emissions and cyclic variations pose a serious problem. From Figs. 12.1 and 12.2, several observations are in order as the SOI is advanced from 355 CAD to 280 CAD. Indicated fuel conversion efficiency and combustion efficiency increase from 29 and 56.8%, respectively, at 355 CAD SOI, reach near maximum values (42 and 79%, respectively) at 310 CAD, and then decrease to 40 and 64.3%, respectively, at 280 CAD. However,  $COV_{imep}$  exhibits the opposite trend; i.e., it decreases from 4% at 355 CAD to 1% at 330 CAD and then continues to increase to 11% at 280 CAD. Figure 12.2 shows the  $ISNO_x$ –ISHC and  $ISNO_x$ –ISCO trade-offs. It is instructive to note that engine-out smoke emissions were overall low for all SOIs (Raihan et al. 2014). As SOI is advanced from 355 CAD to 280 CAD, the  $ISNO_x$  emissions increase from 3 g/kWh at 355 CAD to 14 g/kWh at 340 CAD, then slightly decrease to 11 g/kWh at 330 CAD, and subsequently decrease sharply to 2 g/kWh at 320 CAD. Further advancement of SOI to 310 CAD results in “near-zero”  $ISNO_x$  emissions at 310 CAD. Beyond 310 CAD SOI, any further advancement does not lead to a significant reduction in  $ISNO_x$  emissions; however, the impact of SOI advancement is rather pronounced on both engine-out ISHC and ISCO emissions. Clearly, there seems to be a transition in the nature of combustion between 330 CAD and 320 CAD. It is possible that this transition signifies the start of RCCI combustion

**Fig. 12.1** Indicated fuel conversion efficiency (IFCE %), combustion efficiency (Comb. Eff %), coefficient of variation in indicated mean effective pressure ( $COV_{imep}$  %), ignition delay (CAD) trends for dual fuel combustion at diesel SOI sweep between 280 and 355 CAD, 5.1 bar IMEP, 1500 rev/min,  $P_{in} = 1.5\text{ bar}$ ,  $P_{rail} = 500\text{ bar}$ , MEF = 80%

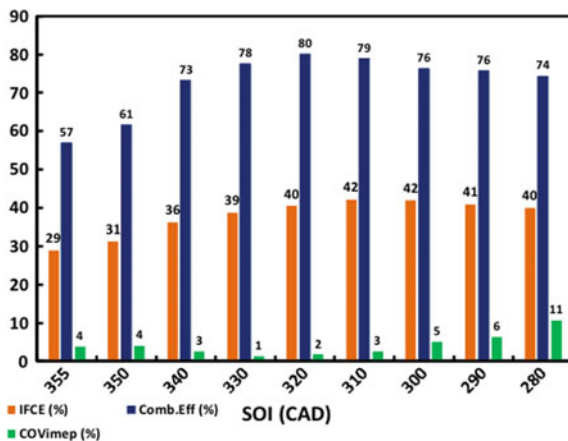
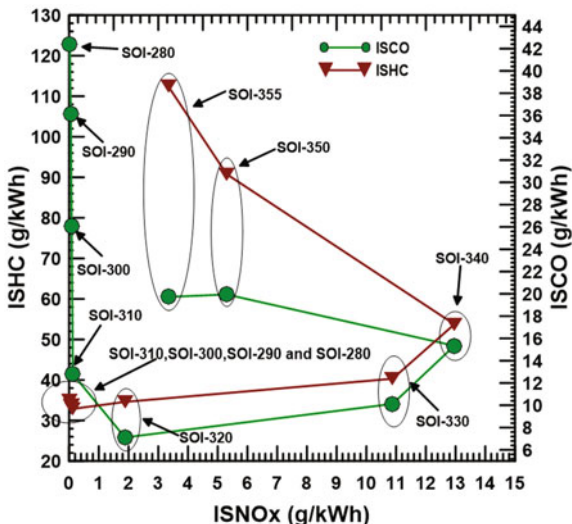


**Fig. 12.2** Indicated specific  $\text{NO}_x$ , HC, and CO emissions trends for dual fuel combustion at diesel SOI sweep between 280 and 355 CAD, 5.1 bar IMEP, 1500 rev/min,  $P_{in} = 1.5$  bar,  $P_{rail} = 500$  bar,  $\text{MEF} = 80\%$



(Walker et al. 2015) where the injected diesel has just enough time to form “pre-mixed enough” mixtures to influence local mixture reactivity to the “appropriate extent.” As a result, the combustion process is dominated by simultaneous, distributed autoignition. This observation has been recently corroborated in the computational study by Dai et al. (2018). After 320 CAD, further advancement in SOI results in very low  $\text{NO}_x$  emissions and a simultaneous increase in CO emissions, with HC emissions being relatively unaffected. This indicates that a “premixing” limit is attained, whereby any further advancement in SOI does not result in a decrease in HC emissions. However, the CO emissions continue to increase and reach a maximum of 42 g/kWh at 280 CAD. The most likely reason for this trend is due to low overall bulk gas temperatures during the expansion stroke, which essentially results in “frozen” CO kinetics (Raihan et al. 2014; Raihan 2014). These trends are further reflected in the poor combustion efficiencies as well at very advanced SOIs.

Figures 12.3 and 12.4 show the average CA50 location versus average CA5 and average CA5-90 duration versus average CA5, respectively. For reference, CA5 (or start of high-temperature autoignition or start of combustion) refers to the crank angle corresponding to the location of 5% cumulative heat release, CA50 (centroid of combustion) is the crank angle corresponding to the location of 50% cumulative heat release, and CA5-90 duration (combustion duration) is the time elapsed in CAD between 5 and 90% cumulative heat release. It is clear that when the SOI is advanced from 355 CAD to 330 CAD, the CA5 location is increasingly advanced from TDC and further SOI advancement results in CA5 being retarded closer to TDC. Similar observations can be made about the centroid of combustion or CA50 location. Interestingly, the CA50 location changes little with SOI advancement beyond 310 CAD. This explains why the IFCE magnitude does not change much despite the combustion efficiencies decreasing significantly with SOI advancement

**Fig. 12.3** CA5 versus CA50 for dual fuel combustion at diesel SOI sweep between 280 and 355 CAD, 5.1 bar IMEP, 1500 rev/min,  $P_{in} = 1.5$  bar,  $P_{rail} = 500$  bar, MEF = 80% (Note “Late” SOIs are blue-shaded circles and “early” SOIs are red inverted triangles)

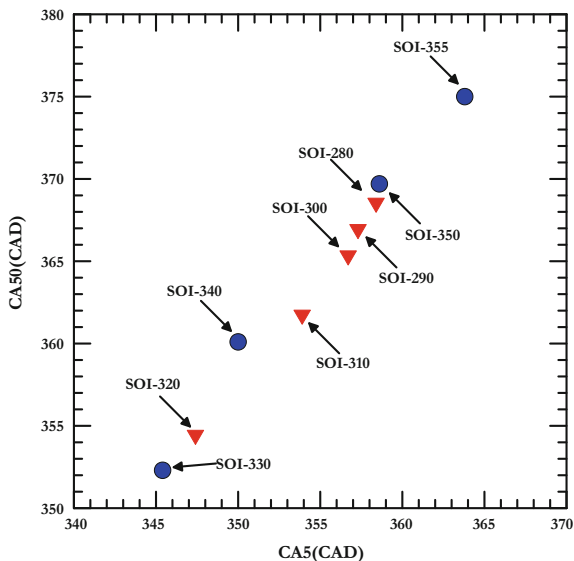
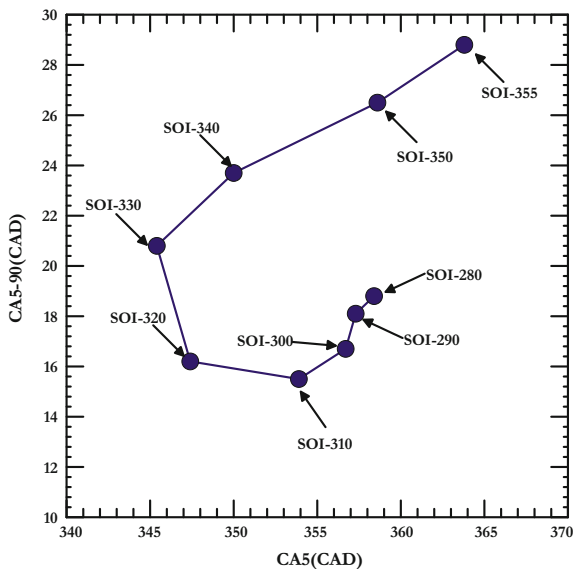


**Fig. 12.4** CA5 versus CA5-90 for dual fuel combustion at diesel SOI sweep between 280 and 355 CAD, 5.1 bar IMEP, 1500 rev/min,  $P_{in} = 1.5$  bar,  $P_{rail} = 500$  bar, MEF = 80%



beyond 310 CAD. Additionally, the CA5 and CA50 are correlated almost linearly for SOIs either advanced or retarded from 330 CAD. In other words, the occurrence of high-temperature autoignition is perhaps the most significant event in the development of both RCCI and low-temperature dual fuel combustion. Observation of the CA5-90 durations in Fig. 12.4 offers an interesting perspective on the nature of dual fuel combustion. Advancing the SOI from 355 CAD to 330 CAD decreases the combustion duration from 29 CAD to 21 CAD, respectively. Upon further advancement from 320 CAD to 280 CAD, the combustion duration is between 16 and 19 CAD. The combustion duration trend, particularly from 310–280 CAD, offers indirect evidence to support both the IFCE and HC emissions trends, which do not vary much over this range of SOIs.

While these “average” trends are certainly helpful to understand the general nature of combustion, they do not provide an in-depth understanding of the real nature of RCCI or dual fuel LTC, especially at advanced SOIs where cyclic combustion variations are observed. In particular, the very low  $\text{NO}_x$  emissions at the advanced SOIs are relatable to the “extent of premixing,” which depends on the local fluid mechanics and the residence time available for the injected diesel fuel to be spatially dispersed throughout the combustion chamber by the bulk advection of the in-cylinder charge. Given that the single-cylinder engine used in the present work is a low-swirl engine (Jha et al. 2017), the only factor that influences mixing is the diesel SOI, i.e., a more advanced SOI implies more residence time available for dispersion and local mixing. As a result, it is expected that cyclic variations will have a significant impact on the extent of premixing and local air-to-fuel ratios or local “reactivities” just before the start of combustion. In other words, CA5, CA50, and CA5-90 durations are all expected to experience significant cyclic variations, and therefore, influence the development of the overall combustion process. Since these quantities are important combustion markers, their variations can be used to quantify the nature of cyclic combustion variations.

## 12.4 Cyclic Variations in Cylinder Pressure and AHRR Schedules

In the following sections, the discussion will focus on representative SOIs, i.e., 355 CAD (retarded SOI—classical dual fuel combustion, more similar to conventional diesel combustion), 330 CAD (“premixed” enough or partially premixed combustion (PPC) dual fuel combustion, similar to RCCI combustion), 310 CAD (dual fuel LTC, where extremely low  $\text{NO}_x$  is realized), 280 CAD (dual fuel LTC characterized by significant combustion instability). All the data presented are for the same overall MEF of 80%, at a constant engine load of 5.1 bar IMEP, and engine speed of 1500 rev/min with intake charge temperature and pressure maintained at 30 °C and 1.5 bar, respectively, and with diesel injection pressure at 500 bar. The first set of plots shows the comparisons between crank-resolved cylinder pressure and apparent



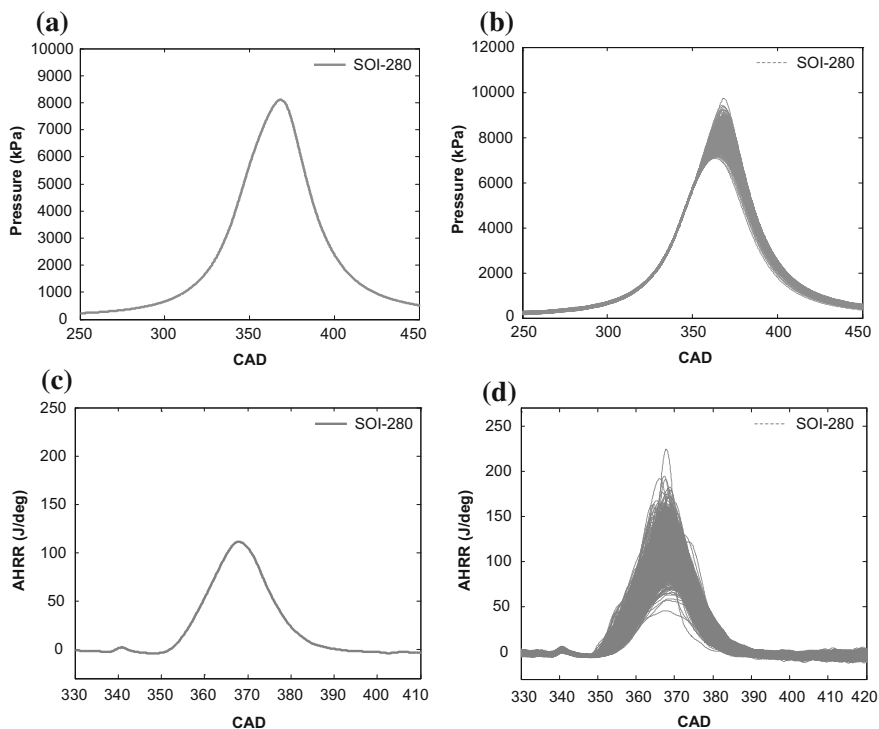


**Fig. 12.5** **a** Ensemble-averaged cylinder pressure, **b** cycle-to-cycle variations in cylinder pressure for 1000 consecutive cycles, **c** ensemble-averaged AHRR, **d** cycle-to-cycle variations in AHRR for 1000 consecutive cycles at diesel SOI = 280 CAD, MEF = 80%, speed = 1500 rev/min, load = 5.1 bar IMEP,  $P_{\text{rail}} = 500$  bar,  $P_{\text{in}} = 1.5$  bar,  $T_{\text{in}} = 30$  °C

heat release rate (AHRR) that was ensemble averaged for 1000 cycles for an “average cycle” and cycle-to-cycle variations of crank-resolved cylinder pressure AHRR over 1000 individual cycles. Figure 12.5a, b shows the differences between the cylinder pressure for an “averaged cycle” and the actual cycle-to-cycle variations for dual fuel LTC at 280 CAD SOI. The first observation that is of significant importance is about the average cycle. The typical practice of finding an “average cycle” assumes that the overall behavior of the combustion process can be adequately represented by a mathematical average cycle. While this assumption works well for conventional combustion processes that do not suffer significant cyclic variations, the assumption of an “average cycle” skews the understanding of the advanced combustion processes, particularly LTC regimes. For example, predictive CFD models that are RANS-based focus on verification and validation based on an “average cycle”; however, it is clear for advanced combustion processes such as dual fuel LTC, this practice maybe

inadequate. For instance, as seen in Fig. 12.5c, the “average cycle” AHRR shows a distinct low-temperature heat release (LTHR) and a high-temperature heat release (HTHR) phase that follows the LTHR. However, as seen in Fig. 12.5d, the cyclic variations in the magnitude of peak LTHR and in the crank angle corresponding to the start and centroid of LTHR are definitely smaller than the magnitude of peak HTHR and the crank angle corresponding to the start and centroid of HTHR. This clearly indicates that the start of HTHR development in dual fuel LTC at very advanced SOIs is strongly influenced by and particularly sensitive to the thermodynamic state, i.e., pressure, temperature, local air-to-fuel ratios, and MEF of the in-cylinder mixture while the centroid of HTHR is strongly dictated by the “local” fluid mechanic phenomena, i.e., the local mixing rates at smaller scales with “too much” mixing potentially leading to “slow” burn or “misfiring” cycles. At the same time, there exists a significant number of cycles that are “fast” burn, which have been triggered by favorable in-cylinder conditions; e.g., the correct amount of local stratification that favors autoignition.

Similar observations are in order for the cylinder pressure and AHRR results for 310 CAD SOI shown in Fig. 12.6a, b. The cylinder pressure plot indicates significant cyclic variations in the combustion process, at least until peak cylinder pressures are attained. Under these conditions, it is believed that the state of the in-cylinder mixture is “premixed enough” to support successful autoignition at 310 CAD SOI. Figure 12.6c clearly shows the average cycle for the AHRR where a distinct LTHR phase is followed by a HTHR phase. The consistent observation between Figs. 12.5c and 12.6c is that the location of the LTHR is almost unaltered but the difference is in the location of the peak HTHR, which occurs at or very near TDC at 310 CAD SOI, whereas at 280 CAD SOI, the phasing of peak HTHR is about 10 CAD after TDC. This behavior is clearly seen in the cyclic AHRR variations presented in Figs. 12.5d and 12.6d for 280 CAD SOI and 310 CAD SOI, respectively. The fact that the development of the HTHR occurs within a few crank angles after the end of LTHR indicates that the thermodynamic state of the mixture, i.e., local air-to-fuel ratio, pressure, and temperature, is most conducive to support autoignition. The only significant difference between 280 CAD SOI and 310 CAD SOI is the reduced time available for the injected diesel to mix with the surrounding premixed methane–air mixture. This observation further corroborates the fact that the extent of premixing needs to be just adequate to ensure successful HTHR development. This is further reflected in that the magnitude of variations in the crank angle corresponding to the start of HTHR and the peak AHRR and its crank angle location are not as pronounced as observed with the 280 CAD SOI case. However, this variation is sufficient for the existence of both “slow” and “fast” burn cycles.

At 330 CAD SOI, the nature of combustion is significantly different as observed from the average cycle results shown in Fig. 12.7. It is believed that this SOI is typical of RCCI combustion as observed by other researchers (e.g., Walker et al. 2015). First, while the LTHR development is similar to the 310 CAD SOI case in that its peak location occurs around 340 CAD, the interesting observation is the occurrence of HTHR immediately after the end of LTHR. This observation lends

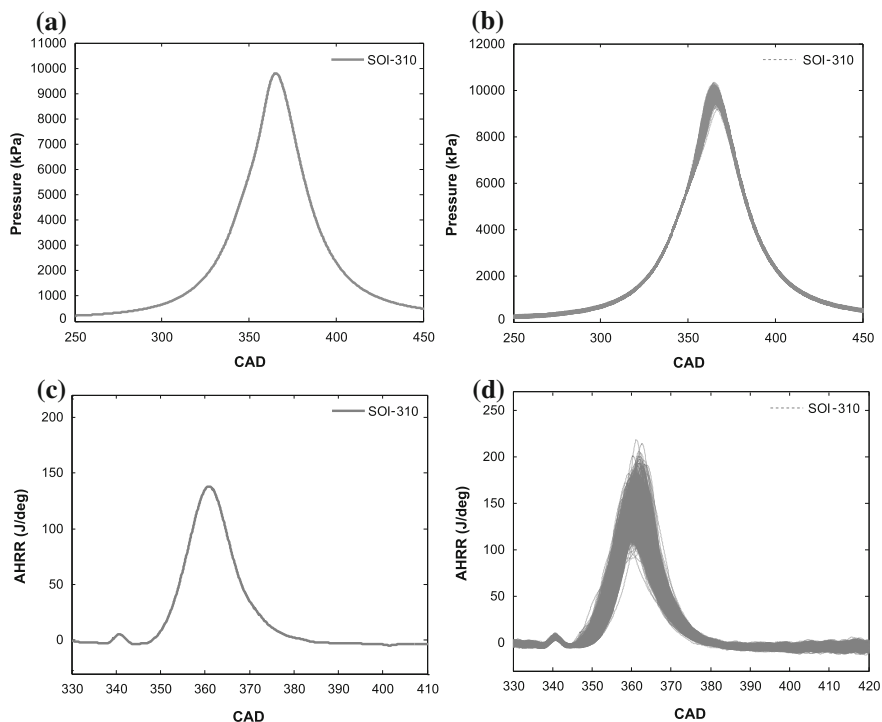


**Fig. 12.6** **a** Ensemble-averaged cylinder pressure, **b** cycle-to-cycle variations in cylinder pressure for 1000 consecutive cycles, **c** ensemble-averaged AHRR, **d** cycle-to-cycle variations in AHRR for 1000 consecutive cycles at diesel SOI = 310 CAD, MEF = 80%, speed = 1500 rev/min, load = 5.1 bar IMEP,  $P_{\text{rail}} = 500$  bar,  $P_{\text{in}} = 1.5$  bar,  $T_{\text{in}} = 30$  °C

further credence to the general observation that the local “reactivity,” which is in turn influenced by the local thermodynamic state of the mixture such as local air-to-fuel ratios, pressure, and temperature, is critical to the development of further combustion. On observing the cyclic AHRR variations in Fig. 12.7d, it is pertinent to point out that the LTHR variations are much smaller and the collective visualization lends itself to a trend very similar to the LTHR trend in the average cycle. However, the key takeaway is that the crank angle location of the start of HTHR as well as its magnitude do not exhibit much variability in comparison to both the 310 CAD and 280 CAD SOI cases. Additionally, there appears to be a distinct second phase of HTHR (similar in shape to the “mixing controlled” combustion phase in diesel combustion) after 350 CAD, which is seen to exhibit significant cyclic variability. This indicates that the local fluid mechanics plays a very important role since it directly impacts local mixing rates.

Finally, Fig. 12.8a–d discusses the nature of combustion at 355 CAD SOI. It is believed that the combustion at this SOI is closer to conventional diesel or dual fuel combustion, which likely includes the development of a lifted nonpremixed flame.

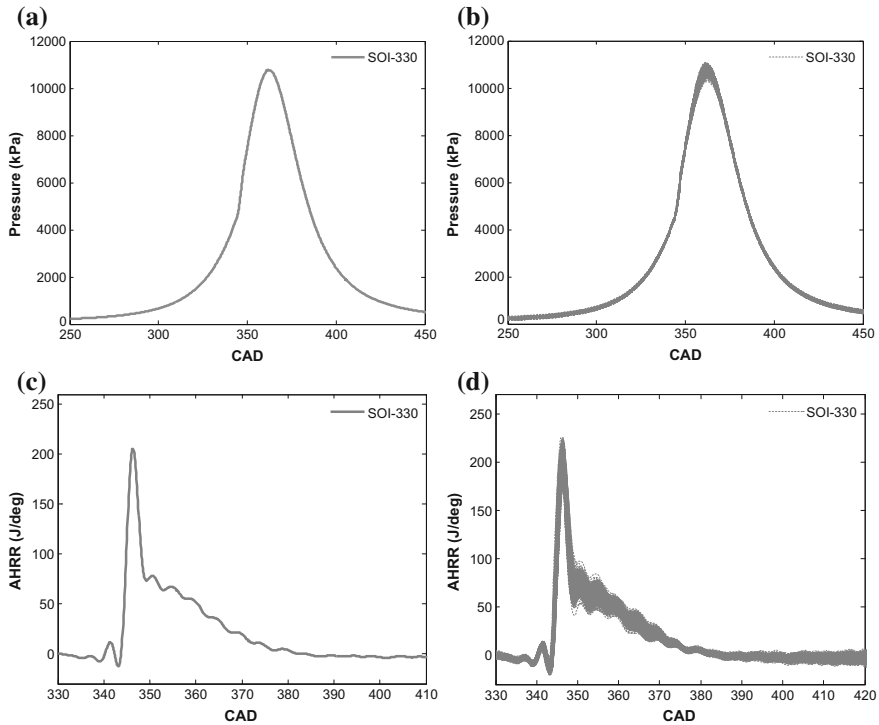


**Fig. 12.7** **a** Ensemble-averaged cylinder pressure, **b** cycle-to-cycle variations in cylinder pressure for 1000 consecutive cycles, **c** ensemble-averaged AHRR, **d** cycle-to-cycle variations in AHRR for 1000 consecutive cycles at diesel SOI = 330 CAD, MEF = 80%, speed = 500 rev/min, load = 5.1 bar IMEP,  $P_{\text{rail}} = 500$  bar,  $P_{\text{in}} = 1.5$  bar,  $T_{\text{in}} = 30$  °C

The most prominent observation here is the absence of LTHR. The development of the start of HTHR and its peak magnitude are very similar between the average cycle and the superimposed 1000 cycles, and so are the consistency and repeatability from one cycle to the next. The major variability is observed in the second phase of the AHRR curve, which is likely dominated by methane combustion. This indicates that the most important phenomenon that controls the overall AHRR development for such retarded SOIs is likely the local fluid mechanics, i.e., the local mixing rates. This observation is unique and different from all the previous SOIs, indicating that local stratification in the unburned methane–air mixture is perhaps an important contributing factor that governs the combustion process. Another important feature of the 355 CAD SOI is that it has a prolonged combustion duration compared to other SOIs.

Collectively, these observations also underline the need to adopt high-fidelity simulation approaches such as using full-scale large eddy simulation (LES) models to develop reliably predictive CFD models of dual fuel combustion, especially for conditions that encounter significant cyclic combustion variations. Additionally,

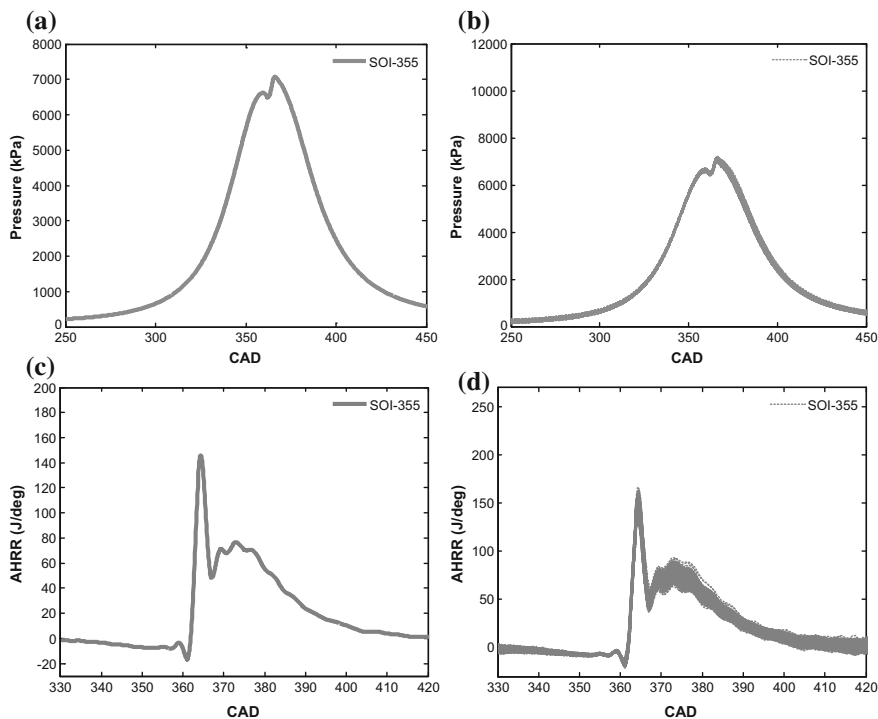


**Fig. 12.8** **a** Ensemble-averaged cylinder pressure, **b** cycle-to-cycle variations in cylinder pressure for 1000 consecutive cycles at diesel SOI = 355 CAD, MEF = 80%, speed = 1500 rev/min, load = 5.1 bar IMEP,  $P_{\text{rail}} = 500$  bar,  $P_{\text{in}} = 1.5$  bar,  $T_{\text{in}} = 30$  °C

they also indicate the need re-examine the current practice of using the “average cycle” from experiments to verify and validate RANS-based CFD models. Perhaps, a better approach maybe to validate the CFD models against the full spectrum of cyclic experimental data obtained over a statistically significant number of engine cycles. In this manner, the model predictions of cylinder pressure and AHRR histories may be compared to see if they fall within the bounds of the “maximum” and “minimum” experimental cylinder pressure and AHRR histories.

## 12.5 Parametric Characterization of Cyclic Variations

The plots in Figs. 12.9, 12.10, 12.11, 12.12, 12.13, 12.14, and 12.15 are key measures of cyclic combustion variations. For instance, based on the observations in the previous figures, i.e., Figs. 12.5, 12.6, 12.7, and 12.8, it is clear that the major cyclic variations occur in the locations of the peak pressure ( $\text{CaP}_{\text{max}}$ ), start of

**Fig. 12.9** CA5 versus CA50 for 1000 consecutive cycles at diesel SOI = 280, 310, 330, and 355 CAD, MEF = 80%, speed = 1500 rev/min, load = 5.1 bar IMEP,  $P_{rail} = 500$  bar,  $P_{in} = 1.5$  bar,  $T_{in} = 30$  °C

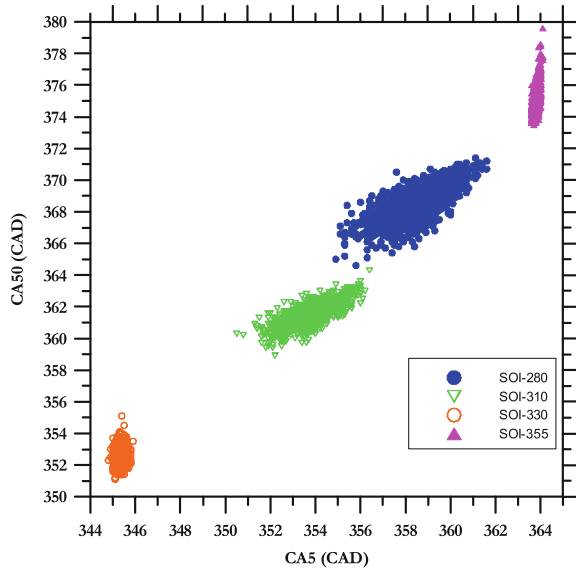
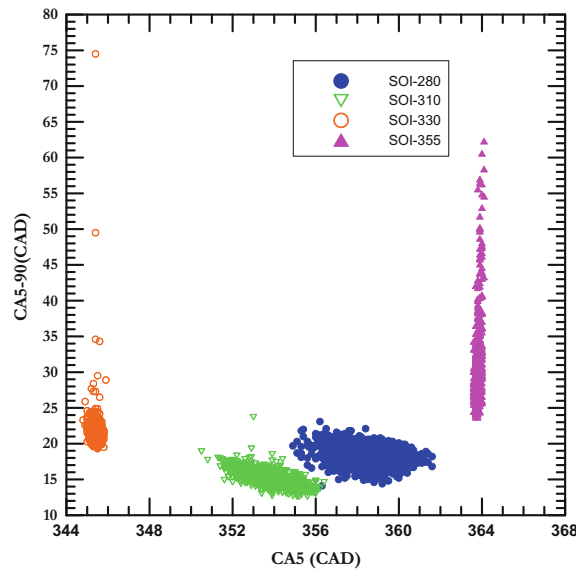


**Fig. 12.10** CA5 versus CA5-CA90 for 1000 consecutive cycles at diesel SOI = 280, 310, 330, and 355 CAD, MEF = 80%, speed = 1500 rev/min, load = 5.1 bar IMEP,  $P_{rail} = 500$  bar,  $P_{in} = 1.5$  bar,  $T_{in} = 30$  °C



HTHR (CA5), the magnitudes of peak cylinder pressure ( $P_{max}$ ), maximum pressure rise rates (MPRR), peak HTHR, and the overall combustion duration (CA5-90).

Figures 12.9, 12.10, and 12.11 discuss the trends of CA50 versus CA5, CA5-90 versus CA5,  $P_{max}$  versus  $CaP_{max}$  for the same set of SOIs (355 CAD, 330 CAD,

**Fig. 12.11**  $P_{max}$  versus  $CaP_{max}$  for 1000 consecutive cycles at diesel SOI = 280, 310, 330, and 355 CAD, MEF = 80%, speed = 1500 rev/min, load = 5.1 bar IMEP,  $P_{rail} = 500$  bar,  $P_{in} = 1.5$  bar,  $T_{in} = 30$  °C

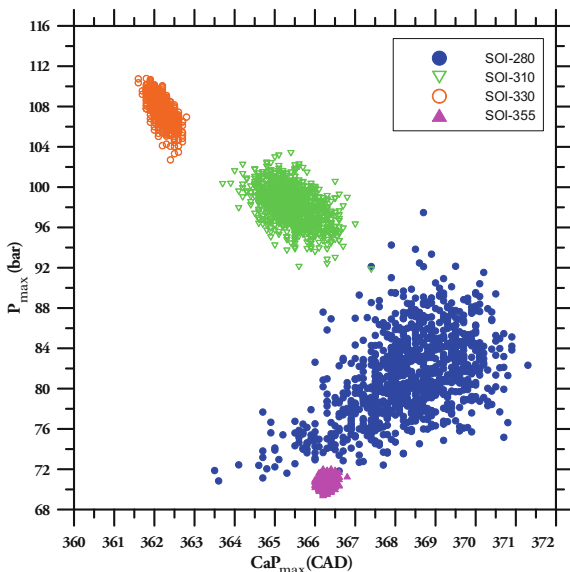
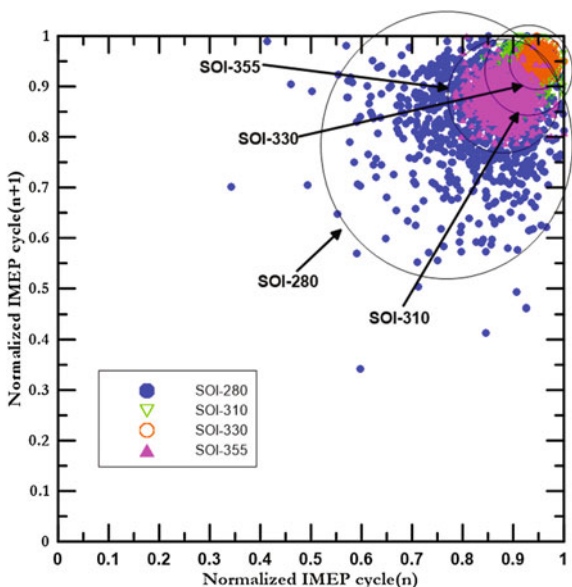


**Fig. 12.12** Normalized IMEP return maps for 1000 consecutive cycles at diesel SOI = 280, 310, 330, and 355 CAD, MEF = 80%, speed = 1500 rev/min, load = 5.1 bar IMEP,  $P_{rail} = 500$  bar,  $P_{in} = 1.5$  bar,  $T_{in} = 30$  °C



310 CAD, and 280 CAD) plotted over 1000 consecutive cycles. Figure 12.9 when viewed in conjunction with Figs. 12.5d, 12.6d, 12.7d, and 12.8d indicates that at advanced SOIs, particularly at 280 and 310 SOI, there is a positive correlation between CA5 and CA50 of each cycle for most cycles, i.e., an earlier CA5 likely corresponds to an earlier CA50, and similarly a late CA5 likely corresponds to a late CA50. However, it is to be noted that the CA50 phasing is generally between

**Fig. 12.13** Normalized CHR return maps for 1000 consecutive cycles at diesel SOI = 280, 310, 330, and 355 CAD, MEF = 80%, speed = 1500 rev/min, load = 5.1 bar IMEP,  $P_{rail} = 500$  bar,  $P_{in} = 1.5$  bar,  $T_{in} = 30$  °C

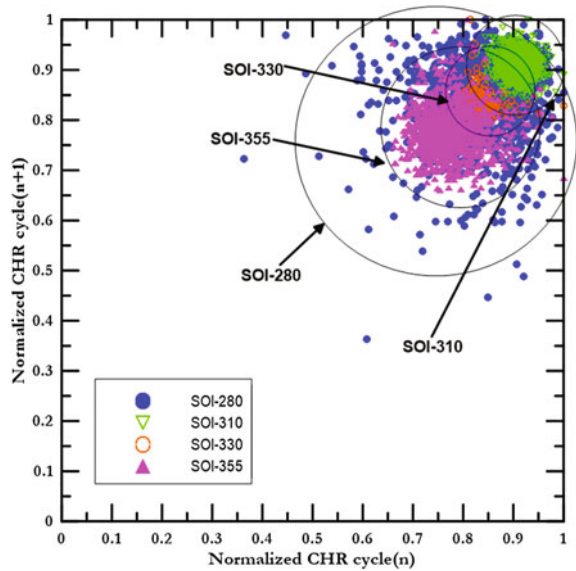
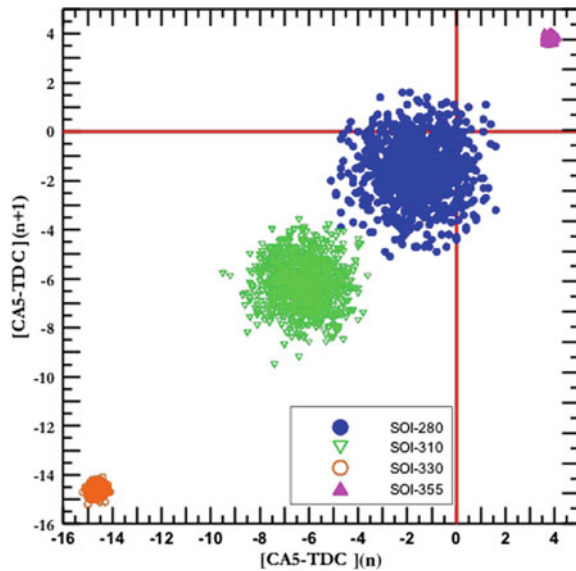


**Fig. 12.14** (CA5-TDC) return maps for 1000 consecutive cycles at diesel SOI = 280, 310, 330, and 355 CAD, MEF = 80%, speed = 1500 rev/min, load = 5.1 bar IMEP,  $P_{rail} = 500$  bar,  $P_{in} = 1.5$  bar,  $T_{in} = 30$  °C



364 and 372 CAD; as a result, the closed-cycle-indicated efficiencies are expected to be high (this was noted in the discussion of Fig. 12.1).

In contrast, at 330 CAD there is no correlation between CA50 dependence on CA5, it seems that the occurrence of both CA5 and CA50 appears somewhat “random,” indicating that the cyclic dependence of CA50 on CA5 is more



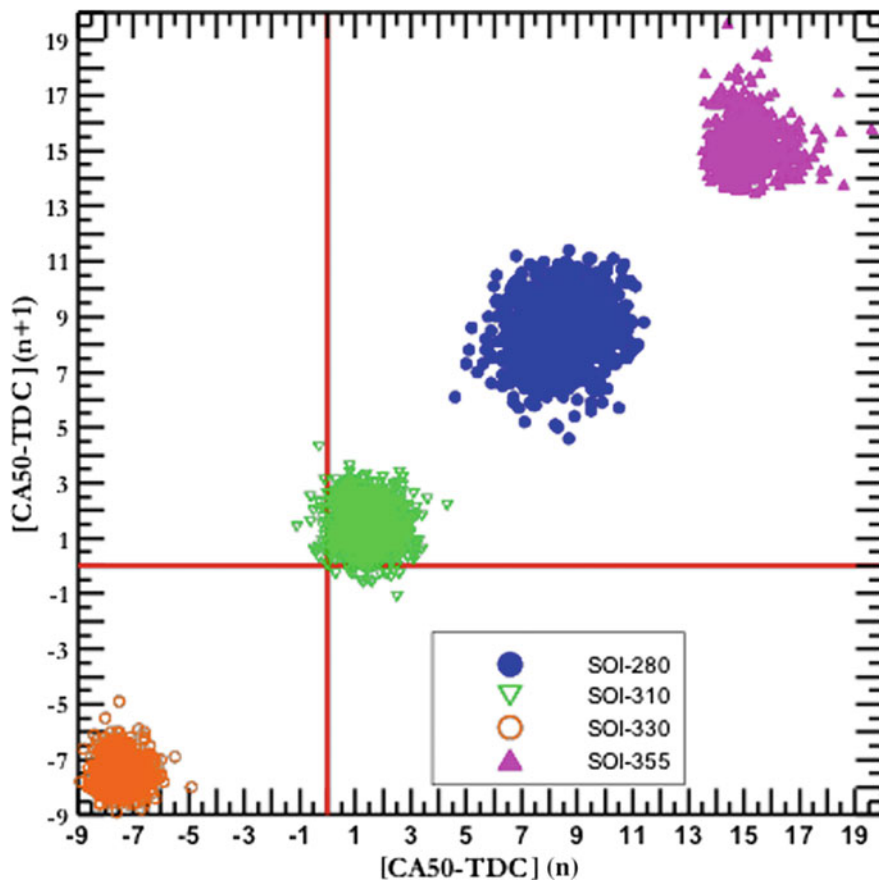


**Fig. 12.15** (CA50-TDC) return maps for 1000 consecutive cycles at diesel SOI = 280, 310, 330 and 355 CAD, MEF = 80%, speed = 1500 rev/min, load = 5.1 bar IMEP,  $P_{\text{rail}} = 500$  bar,  $P_{\text{in}} = 1.5$  bar,  $T_{\text{in}} = 30$  °C

stochastic. Also, the CA50 occurs much earlier than TDC (TDC corresponds to 360 CAD), thereby resulting in compromised closed-cycle-indicated efficiencies (confirmed by Fig. 12.1). Finally, at 355 CAD SOI, the CA5 location is consistent from one cycle to another around 364 CAD (i.e., there is very little cyclic variability in CA5) but the CA50 location is spread out between 372 and 380 CAD without any specific pattern, indicating the existence of slow burn cycles that occur despite relatively consistent diesel autoignition. As a result, the closed-cycle-indicated efficiencies for 355 CAD SOI are vastly reduced (confirmed by Fig. 12.1).

These observations are further supported by Fig. 12.10 which shows combustion duration or CA5-90 versus CA5. At 280 CAD and 310 CAD SOIs, the CA5 and CA5-90 variations are somewhat similar in magnitude. The overall spread of the combustion duration for the entire set of 1000 cycles is between 15 and 22 CAD at

280 CAD SOI and between 12 and 17 CAD at 310 CAD SOI; however, the  $COV_{imep}$  at 280 CAD SOI is 11%, while at 310 CAD SOI it is 3% indicating that the overall combustion at 280 CAD SOI is extremely sensitive to initial conditions, which are determined by the local air-to-diesel fuel ratios or local diesel energy fractions at the time of high-temperature autoignition. Interestingly, the combustion efficiency at 280 SOI is 74%, while at 310 SOI it is 79%. These trends indicate that the combustion durations are shorter at 310 SOI compared to 280 SOI but exhibit similar variability. Nevertheless, it is clear that shorter combustion durations do not necessarily translate into vastly improved combustion efficiencies, indicating that the combustion duration is not a good measure of “completeness” of the combustion process. Additionally, despite 280 and 310 CAD SOIs exhibiting similar variability in combustion durations (approximately 5–7 CAD), the impact of these fluctuations on cycle-by-cycle-indicated torque (or  $COV_{imep}$  in Fig. 12.1) is significantly higher at 280 SOI.

Figure 12.11 is a classic re-interpretation of a plot originally plotted by Matekunas in his seminal paper (25) where he discusses the modes and measures of cyclic variability in classical flame propagation-induced SI engine combustion. It is interesting to note that the shape of this plot is very similar to that observed by Matekunas. At 355 CAD SOI, the magnitude of peak cylinder pressure is fairly low, about 70 bar, and the peak occurs around 6 degrees after TDC at 366 CAD. The magnitude of variations of both  $P_{max}$  and  $CaP_{max}$  is minimal. Also,  $CaP_{max}$  occurs within a few degrees after CA5, which indicates that the maximum cylinder pressure occurs a few degrees after the high-temperature autoignition event. But, CA50 occurs around 372–378 CAD, or  $CaP_{max}$  occurs before CA50.

According to Matekunas, the occurrence of  $CaP_{max}$  before CA50 is a characteristic of “slow burning” cycles. Whereas, at 330 CAD SOI, the magnitude of  $P_{max}$  is much higher, 104–110 bar, and  $CaP_{max}$  is closer to TDC around 361–362 CAD. Also, from Fig. 12.9 it is seen that CA5 is around 345 CAD and the CA50 is around 352–354 CAD. This indicates that  $CaP_{max}$  occurs after CA50, which according to Matekunas’ observations, signifies that combustion is characterized by “fast burning” cycles. At 310 CAD, the magnitude of  $P_{max}$  is between 92 and 102 bar with  $CaP_{max}$  between 363 and 367 CAD. Also, from Fig. 12.9 CA50 at 310 CAD SOI is between 359 and 365 CAD. This indicates that for some cycles, the  $CaP_{max}$  precedes CA50 and that for other cycles  $CaP_{max}$  occurs after CA50 clearly confirming the presence of both “slow burn” and “fast burn” cycles. Furthermore, at 280 CAD SOI, the magnitude of  $P_{max}$  is between 72 and 96 bar with  $CaP_{max}$  between 363 and 371 CAD. Also, from Fig. 12.9 CA50 at 280 CAD SOI is between 364 and 372 CAD. This clearly confirms that  $CaP_{max}$  can either precede or occur after CA50 for almost any cycle with equal probability, thereby lending further credence to the observation that at 280 CAD SOI the combustion is characterized by significant cyclic fluctuations (due to the large variations seen in  $P_{max}$ ) with a wide distribution of both “slow burn” and “fast burn” cycles.

Figures 12.12 and 12.13 discuss the first-order return maps of normalized IMEP and normalized cumulative heat release (CHR) between cycle “ $n$ ” and cycle

“ $n + 1$ ” for 280, 310, 330, and 355 CAD SOIs. Before analyzing Figs. 12.12 and 12.13, we define normalized IMEP( $n$ ) and CHR( $n$ ) of the  $n$ th cycle in Eqs. 12.1 and 12.2, respectively.

$$\text{Normalized IMEP}(n) = \frac{\text{IMEP}(n)}{|\text{Max}(\text{IMEP}(n = 1 \dots 1000))|} \quad (12.1)$$

$$\text{Normalized CHR}(n) = \frac{\int_{\theta=\text{SOI}}^{\theta=\text{EOC}} \text{AHRR}(n) d\theta}{\left| \max \left( \int_{\theta=\text{SOI}}^{\theta=\text{EOC}} \text{AHRR}(n = 1 \dots 1000) d\theta \right) \right|} \quad (12.2)$$

As discussed in the literature review, return maps are excellent visual aids to identify “random” and “deterministic” patterns in cyclic variations. In particular, the information gleaned from “deterministic” patterns from return maps maybe extremely useful in designing feedback controllers (Finney et al. 2015). The patterns in both of these figures transition from being almost “triangular” at 280 CAD SOI to nearly “circular” at 330 CAD SOI, and finally to almost like a “shot gun blast” at 355 CAD SOI. It is instructive to note that Wagner et al. (2001) observed such “shotgun blast” distributions in normalized IMEP at near stoichiometric equivalence ratios in an SI engine. They concluded that such a distribution corresponded to a nearly “random” (i.e., predominantly stochastic) trend in cyclic variations, and as a result very little cyclic control may be accomplished even with a feedback controller. However, the “triangular” distribution is an artifact of a more deterministic component of cyclic combustion variability, which likely occurs at conditions that are very close to a “limiting” physical constraint.

For 280 CAD SOI, this might correspond to local air-to-diesel fuel ratios near the lean limit to support sustained autoignition. This also indicates that there are “poor” combustion cycles characterized by low IMEP (slow burn cycles) followed by cycles of “rebound” with high IMEP (fast burn). This is further corroborated by the observation in Fig. 12.13 where the CHR alternates between nearly a 50% burn to higher than a 95% burn (or vice versa), clearly indicating the presence of “slow” or “incomplete” burn and “fast” or “complete burn” cycles at 280 CAD SOI. This observed behavior also lends further credence to the very high  $\text{COV}_{\text{imep}}$  at 280 CAD SOI. At 310 CAD and 330 CAD SOIs, the patterns are more “circular” indicating that the behavior of the cyclic variations is more “random” and less “deterministic.” Again, at 355 CAD, the CHR distribution shows that a majority of the cycles are clustered around in a shot gun blast pattern with incomplete burn (centered around 75% fraction of maximum CHR). This helps clarify the reason for the high unburned HC emissions observed at 355 SOI.

Figures 12.14 and 12.15 are return maps of CA5-TDC and CA50-TDC, respectively. It should be noted that in Fig. 12.14, the CA5 is phased with respect to TDC with the understanding that for the range of SOIs swept, CA5 occurs before TDC except for the most retarded SOI of 355 CAD, where the CA5 occurs after TDC (see Fig. 12.9). As a consequence, positive values in Fig. 12.14 indicate that the CA5 for 355 CAD SOI occurs after TDC for most combustion cycles. Also,

“zero” in Fig. 12.13 indicates that the CA5 coincides with TDC. In Fig. 12.15, the CA50 is also phased with respect to TDC with the understanding that for most of the SOIs swept in this study CA50 occurs after TDC, except for the 330 CAD SOI where it occurs before TDC. As a consequence, negative values in Fig. 12.14 indicate that the CA50 occurs before TDC. Similarly, “zero” in Fig. 12.14 corresponds to CA50 coinciding with TDC. Figures 12.14 and 12.15 are important visual aids that serve to explain the evolution of combustion behavior over a wide range of SOIs. In particular, they can be used effectively to unearth the “cause–effect” relationships that govern the nature of cyclic combustion variations at LTC conditions. For instance, in Fig. 12.14 at the SOI of 355 CAD, the CA5 (or high-temperature autoignition location) is fairly consistent from one cycle to another and it occurs after TDC. This is evident from the fact that for a given value of (CA5-TDC) for cycle  $n$ , the extent of variation in the corresponding values of (CA5-TDC) for cycle  $n + 1$  is minimal. The same observation is valid for 330 CAD SOI. However, at 280 CAD SOI, for a given value of (CA5-TDC) for cycle  $n$ , the corresponding value of normalized CA5 in cycle  $n + 1$  can assume many different values, i.e., it is quite likely that there is considerable cyclic dispersion in CA5 from one cycle to the next. This reinforces the original thought process that at SOIs that are typical of LTC conditions (advanced from TDC), the critical process that drives the combustion evolution or high-temperature autoignition is extremely sensitive to local conditions, i.e., local air-to-diesel fuel ratio, and local thermodynamic conditions. The CA5 behavior at 310 CAD SOI is very similar to that at 280 CAD SOI; however, the extent of variation is considerably smaller.

Figure 12.15 discusses CA50 behavior. For instance, at 355 CAD SOI, the combustion phasing is far removed from TDC (or after TDC) and the corresponding cyclic dispersion in CA50 is minimal. This, in combination with observations from Fig. 12.11 where the  $P_{\max}$  magnitudes are low, corroborates the fact that the indicated efficiencies are expected to be low and are not likely to vary significantly from one cycle to another. Similarly, at 330 CAD, the combustion phasing is well before TDC and the corresponding cyclic dispersion in CA50 is minimal. However, the consistently high magnitudes of  $P_{\max}$  (Fig. 12.11) from one cycle to another ensure that the indicated efficiencies are not compromised severely from one cycle to another. But at 280 and 310 CAD SOI, the combustion phasing or CA50 is after TDC; however, the cyclic dispersion in CA50 is also high. When taken together with Fig. 12.14, at 355 CAD and 330 CAD, the CA5 is invariant from one cycle to another, but the corresponding variations in CA50 at these timings are non-negligible leading to the conclusion that cyclic variations in CA50 are not caused by cyclic variations in CA5. However, at 280 CAD and 310 CAD SOI, inconsistent and high cyclic variations in CA5 are correlated with inconsistent cyclic variation trends in CA50 or combustion phasing. This leads to the hypothesis that low cyclic dispersion in CA5 does not necessarily imply consistency or low cyclic dispersion in CA50; however, high cyclic dispersion in CA5 trends seems to result in high cyclic CA50. This hypothesis needs to be evaluated rigorously with additional targeted experiments and supporting high-fidelity CFD simulations to

unearth the nature of high-temperature autoignition and subsequent combustion at LTC conditions.

## 12.6 Concluding Remarks

Dual fuel engines offer a lot of promise in terms of yielding very high fuel conversion efficiencies with very low emissions. However, the limiting scenario is observed to be high cyclic combustion variations, leading to high HC and CO emissions. The primary cause of these cyclic variations is most likely “limiting” behavior brought about by inconsistent local diesel fuel–air mixing, which results in inconsistent ignition quality (CA5) from one cycle to another. Inconsistent CA5 is found to exert a cascading effect on the subsequent combustion development (CA50 and CA5-90). Strategies to mitigate cyclic combustion variations could involve ensuring a consistent level of local spatial stratification between the highly reactive (high cetane) fuel and the less reactive (low cetane) fuel. For diesel–methane dual fuel combustion, this would translate to ensuring appropriate levels of local diesel-to-methane fractions such that the dual fuel combustion process is “premixed enough” to keep  $\text{NO}_x$  and smoke emissions low while avoiding higher cyclic variability, that could lead to high HC or CO emissions. Based on the investigations presented in this chapter, it also appears that conventional RANS-based CFD investigations may prove inadequate to characterize the complete nature of dual fuel LTC.

## References

- Agarwal AK (2011) Experimental investigation on intake air temperature and air-fuel ratio dependence of random and deterministic cyclic variability in a homogeneous charge compression ignition engine. SAE technical paper no. 2011-01-1183
- Azimov U, Tomita E, Kawahara N, Harada Y (2011) Premixed mixture ignition in the end-gas region (PREMIER) combustion in a natural gas dual-fuel engine: operating range and exhaust emissions. *Int J Engine Res* 12:484–497
- Barton RK, Kenemuth DK, Lestz SS, Meyer WE (1970) Cycle-by-cycle variations of a spark ignition engine—a statistical analysis. SAE technical paper 700488
- Boyer R (1949) Status of dual fuel engine development. SAE technical paper 490018
- Ceviz MA, Yüksel F (2006) Cyclic variations on LPG and gasoline-fuelled lean burn SI engine. *Renew Energy* 31(12):1950–1960
- Chen Y, Dong G, Mack JH, Butt RH, Chen JY, Dibble RW (2016) Cyclic variations and prior-cycle effects of ion current sensing in an HCCI engine: a time-series analysis. *Appl Energy* 168:628–635
- Dai X, Krishnan SR, Srinivasan KK, Singh S (2018) Numerical study of combustion characteristics and emissions of a diesel–methane dual-fuel engine for a wide range of injection timings. *Int J Eng Res*. <https://doi.org/10.1177/1468087418783637>
- Daily JW (1988) Cycle-to-cycle variations: a chaotic process? *Combust Sci Technol* 57:149–162

- Davis L, Feldkamp L, Hoard J, Yuan F et al (2001) Controlling cyclic combustion variations in lean-fueled spark-ignition engines. SAE technical paper 2001-01-0257. <https://doi.org/10.4271/2001-01-0257>
- Daw CS, Finney CEA, Green JB Jr, Kennel MB et al (1996) A simple model for cyclic variations in a spark-ignition engine. SAE technical paper 962086
- Daw CS, Wagner RM, Edwards KD, Green JB Jr (2007) Understanding the transition between conventional spark-ignited combustion and HCCI in a gasoline engine. *Proc Combust Inst* 31 (2):2887–2894
- Daw CS, Edwards KD, Wagner RM, Green JB Jr (2008) Modeling cyclic variability in spark-assisted HCCI. *Trans ASME J Eng Gas Turbines Power* 130(5):052801
- Dong S, Ou B, Cheng X (2017) Comparisons of the cyclic variability of gasoline/diesel and ethanol/diesel dual-fuel combustion based on a diesel engine. SAE technical paper no. 2017-01-5001
- Doughty GE, Bell SR, Midkiff KC (1992) Natural gas fueling of a Caterpillar 3406 diesel engine. *Trans ASME: J Eng Gas Turbines Power* 114:459–465
- Elliot MA, Davis RF (1951) Dual-fuel combustion in diesel engines. *Ind Eng Chem* 43(12):2854–2864
- Faghani E, Kheirkhah P, Mabson C, McTaggart-Cowan G et al (2017) Effect of injection strategies on emissions from a pilot-ignited direct-injection natural-gas engine—Part II: slightly premixed combustion. SAE technical paper 2017-01-0763. <https://doi.org/10.4271/2017-01-0763>
- Felt AE, Steele WA Jr (1962) Combustion control in dual-fuel engines. *Trans Soc Automot Eng* 70:644–653
- Finney CEA, Kaul B, Daw CS, Wagner R et al (2015) A review of deterministic effects in cyclic variability of internal combustion engines. *Int J Engine Res* 16(3):366–378
- Galloni E (2009) Analyses about parameters that affect cyclic variation in a spark ignition engine. *Appl Therm Eng* 29(5):1131–1137
- Green JB Jr, Daw CS, Armfield JS, Finney CEA, Wagner RM, Drallmeier JA, et al (1999) Time irreversibility and comparison of cyclic-variability models. SAE technical paper 1999-01-0221
- Guerry ES, Raihan MS, Srinivasan KK, Krishnan SR, Sohail A (2016) Injection timing effects on partially premixed diesel–methane dual fuel low temperature combustion. *Appl Energy* 162:99–113. <https://doi.org/10.1016/j.apenergy.2015.10.085>
- Hellstrom E, Larimore J, Stefanopoulou A, Sterniak J et al (2012) Quantifying cyclic variability in a multicylinder HCCI engine with high residuals. In: *Proceedings of the ASME 2012 internal combustion engine division spring technical conference*, ASME, Torino, New York, 6–9 May 2012
- Jha PR, Srinivasan KK, Krishnan SR (2017) Influence of swirl ratio on diesel-methane dual fuel combustion. Paper no. ICEF2017-3683, pp V001T03A024; 12 pp. ASME 2017 internal combustion engine division fall technical conference, Seattle, Washington, USA, 15–18 Oct 2017. <https://doi.org/10.1115/icef2017-3683>
- Jia M, Dempsey AB, Wang H, Li Y, Reitz RD (2015) Numerical simulation of cyclic variability in reactivity-controlled compression ignition combustion with a focus on the initial temperature at intake valve closing. *Int J Engine Res* 16(3):441–460
- Jupudi RS, Finney CE, Primus R, Wijeyakulasuriya S, Klingbeil AE, Tamma B, Stoyanov MK (2016) Application of high performance computing for simulating cycle-to-cycle variation in dual-fuel combustion engines. SAE technical paper no. 2016-01-0798
- Kantor JC (1984) A dynamical instability of spark-ignited engines. *Science* 224(4654):1233–1235
- Karim GA (1980) A review of combustion processes in the dual fuel engine—the gas diesel engine. *Prog Energy Combust Sci* 6:277–285
- Karim GA (2003) Combustion in gas fueled compression: ignition engines of the dual fuel type. *Trans ASME: J Eng Gas Turbines Power* 125:827–836
- Karim GA, Khan MO (1968) Examination of effective rates of combustion heat release in a dual-fuel engine. *Proc Inst Mech Eng: J Mech Eng Sci* 10(1):13–23

- Klos D, Kokjohn SL (2015) Investigation of the sources of combustion instability in low-temperature combustion engines using response surface models. *Int J Engine Res* 16 (3):419–440
- Korakianitis T, Namasivayam AM, Crookes RJ (2011) Natural-gas fueled spark ignition (SI) and compression-ignition (CI) engine performance and emissions. *Prog Energy Combust Sci* 37 (1):89–112
- Krishnan SR, Srinivasan KK, Singh S, Bell SR, Midkiff KC, Gong W et al (2004) Strategies for reduced NO<sub>x</sub> emissions in pilot-ignited natural gas engines. *Trans ASME: J Eng Gas Turbines Power* 126:665–671
- Li W, Liu Z, Wang Z (2016) Experimental analysis and theoretical analysis of the combustion process at low loads of a diesel natural gas dual-fuel engine. *Energy* 94:728–741
- Matekunas F (1983) Modes and measures of cyclic combustion variability. SAE technical paper 830337
- Maurya RK (2018) Experimental investigation of deterministic and random cyclic patterns in HCCI engine using symbol sequence approach. *Iranian J Sci Technol Trans Mech Eng* 1–12
- McTaggart-Cowan GP, Jones HL, Rogak SN, Bushe WK, Hill PG, Munshi SR (2007) The effects of high-pressure injection on a compression-ignition, direct injection of natural gas engine. *Trans ASME J Eng Gas Turbines Power* 129:579–588
- McTaggart-Cowan G, Mann K, Huang J, Singh A et al (2015) Direct injection of natural gas at up to 600 bar in a pilot-ignited heavy-duty engine. *SAE Int J Engines* 8(3). <https://doi.org/10.4271/2015-01-0865>
- Neely G, Florea R, Miwa J, Abidin Z (2017) Efficiency and emissions characteristics of partially premixed dual-fuel combustion by co-direct injection of NG and diesel fuel (DI2)—Part 2. SAE technical paper 2017-01-0766. <https://doi.org/10.4271/2017-01-0766>
- Ozidor N, Dulger M, Sher E (1994) Cyclic variability in spark-ignition engines: a literature survey. SAE technical paper 940987
- Patterson DJ (1966) Cylinder pressure variations, a fundamental combustion problem. SAE technical paper 660129
- Raihan MS (2014) A comparative study of diesel ignited methane and propane dual fuel low temperature combustion in a single cylinder research engine. M. S. thesis, Mississippi State University
- Raihan MS, Guerry ES, Dwivedi U, Srinivasan KK, Krishnan SR (2014) Experimental analysis of diesel-ignited methane dual fuel low temperature combustion in a single cylinder diesel engine. *Trans ASCE: J Energy Eng* C4014007. [https://doi.org/10.1061/\(asce\)jey.1943-7897.0000235](https://doi.org/10.1061/(asce)jey.1943-7897.0000235)
- Selim MY (2005) Effect of engine parameters and gaseous fuel type on the cyclic variability of dual fuel engines. *Fuel* 84(7–8):961–971
- Sen AK, Ash SK, Huang B, Huang Z (2011) Effect of exhaust gas recirculation on the cycle-to-cycle variations in a natural gas spark ignition engine. *Appl Therm Eng* 31(14):2247–2253
- Sen AK, Medina A, Curto-Risso PL, Hernández AC (2014) Effect of ethanol addition on cyclic variability in a simulated spark ignition gasoline engine. *Meccanica* 49(10):2285–2297
- Sjerić M, Kozarac D, Tatschl R (2015) Modelling of early flame kernel growth towards a better understanding of cyclic combustion variability in SI engines. *Energy Convers Manag* 103:895–909
- Srinivasan KK, Krishnan SR, Midkiff KC (2006a) Improving low load combustion, stability and emissions in pilot-ignited natural gas engines. *Proc Inst Mech Eng: Part D J Auto Eng* 220 (2):229–239
- Srinivasan KK, Krishnan SR, Singh S, Midkiff KC, Bell SR, Gong W et al (2006b) The advanced injection low pilot ignited natural gas engine: a combustion analysis. *Trans ASME J Eng Gas Turbines Power* 128:213–218
- Srinivasan KK, Krishnan SR, Qi Y (2014) Cyclic combustion variations in dual fuel partially premixed pilot-ignited natural gas engines. *Trans ASME J Energy Res Tech* 136:012003
- Sun L, Zhou L, Zeng K (2013) Experimental investigation of cycle-by-cycle variations in a natural gas/diesel dual fuel engine with EGR. SAE technical paper no. 2013-01-0853

- Tunér M, Karlsson M, Mauss F (2009) Studying HCCI combustion and its cyclic variations versus heat transfer, mixing and discretization using a PDF based approach. SAE technical paper no. 2009-01-0667
- Wagner RM, Daw CS, Green JB Jr (2001) Low-order map approximations of lean cyclic dispersion in premixed spark ignition engines. SAE paper no. 2001-01-3559
- Walker NR, Wissink M, DelVescovo D, Reitz RD (2015) Natural gas for high load dual-fuel reactivity controlled compression ignition in heavy-duty engines. *Trans ASME J Energy Res Tech* 137(4):042202
- Wang S, Ji C (2012) Cyclic variation in a hydrogen-enriched spark-ignition gasoline engine under various operating conditions. *Int J Hydrogen Energy* 37(1):1112–1119
- Wang J, Chen H, Liu B, Huang Z (2008) Study of cycle-by-cycle variations of a spark ignition engine fueled with natural gas–hydrogen blends. *Int J Hydrogen Energy* 33(18):4876–4883
- Wang Q, Wang B, Yao C, Liu M, Wu T, Wei H, Dou Z (2016) Study on cyclic variability of dual fuel combustion in a methanol fumigated diesel engine. *Fuel* 164:99–109
- Wei L, Geng P (2016) A review of natural gas/diesel dual fuel combustion, emissions and performance. *Fuel Process Technol* 142:264–278
- Young MB (1981) Cyclic dispersion in the homogeneous charge spark-ignition engine—a literature survey. SAE technical paper 810020



# Chapter 13

## Emissions Control Technologies for Natural Gas Engines



A. Wahbi, A. Tsolakis and J. Herreros

**Abstract** In recent years, there has been a rising interest in alternative cleaner low-carbon fuels as they have a significant potential in decreasing the harmful exhaust emissions and contribute in decarbonising transportation. Natural gas (NG) is one of the most promising alternative fossil fuel that has been widely investigated in internal combustion (IC) engines. It is expected that global consumption of NG from 2015 to 2040 will rise 1.4% annually, accounting for the largest increase in world primary energy consumption. In this chapter, a review of the performance of NG-fuelled internal combustion engines, exhaust emissions produced from the combustion of natural gas engines and aftertreatment systems used to control those emissions is performed. In addition to the reduction of carbon dioxide (CO<sub>2</sub>) from NG fuelling, lower levels of unburnt hydrocarbons (HC) and particulate matter emissions (PM) than conventional petrol and diesel engines have also been reported. However, they tend to produce higher nitrogen oxide (NO<sub>x</sub>) and methane (CH<sub>4</sub>) emissions which are difficult to oxidise, particularly at engine operation at stoichiometric conditions. On the other hand, the slow flame speed of NG is a major problem under lean-burn operation as it increases cycle-to-cycle variations, significantly compromising engine efficiency. The addition of hydrogen enhances the combustion of NG in addition to improving engine stability and reducing exhaust emissions. The difference in combustion, emission characteristics and aftertreatment systems of stoichiometric, lean-burn and hydrogen-enriched natural gas engines is outlined.

**Keywords** Natural gas engines • Lean-burn • Stoichiometric • Emissions  
Compression-ignition • Catalyst

---

A. Wahbi · A. Tsolakis (✉) · J. Herreros  
Mechanical Engineering, University of Birmingham, Birmingham B15 2TT, UK  
e-mail: [a.tsolakis@bham.ac.uk](mailto:a.tsolakis@bham.ac.uk)

A. Wahbi  
e-mail: [AXW424@student.bham.ac.uk](mailto:AXW424@student.bham.ac.uk)

J. Herreros  
e-mail: [J.HERREROS@bham.ac.uk](mailto:J.HERREROS@bham.ac.uk)

### 13.1 Introduction

In recent years, there has been a growing concern regarding environmental pollution despite the advances in technology, with the transport sector being one of the major contributors of emitted pollutants and greenhouse gases. Emissions such as carbon dioxide (CO<sub>2</sub>), unburnt hydrocarbons (HC), oxides of nitrogen (NO<sub>x</sub>) and particulate matter emissions (PM) are all produced from the combustion of fossil fuel. Their adverse impact on climate change and human health has led to the introduction of increasingly stringent regulations that restrict the emission limits of automobiles. Accordingly, vehicle industries are continuously researching and rapidly developing emission control technologies that not only meet the rigorous emission standards introduced worldwide such as that set by the Environmental Protection Agency (EPA), and the EURO 6 standards, but also to satisfy consumer demands by delivering lower fuel consumption without compromising vehicle power or drivability.

Despite the environmental deterioration and global warming effect caused by the burning of fossil fuels, their use is projected to account for 77% of energy utilisation in 2040 (Fig. 13.1) (Eia.gov 2018). The use of gaseous and alternative fuels in internal combustion engines has therefore seen an increased interest in the last decade as they emit lower levels of exhaust emissions. Natural gas could play a leading role in the world’s transition to a cleaner energy. It is currently the third primary energy fuel globally and the only fossil fuel whose share of primary energy consumption is projected to grow with NG consumption increasing by 1.4% per year (Eia.gov 2018; World energy resources 2016).

The increased interest in NG is also due to the abundant proved reserves and increased production of NG, as shown in Fig. 13.2 making it a strong competitor to liquid fuels. Globally, there were 186.6 thousand cubic metres (tcm) of proven NG reserves in 2016, an increase of 19.2% from 2004 levels, which is sufficient to meet

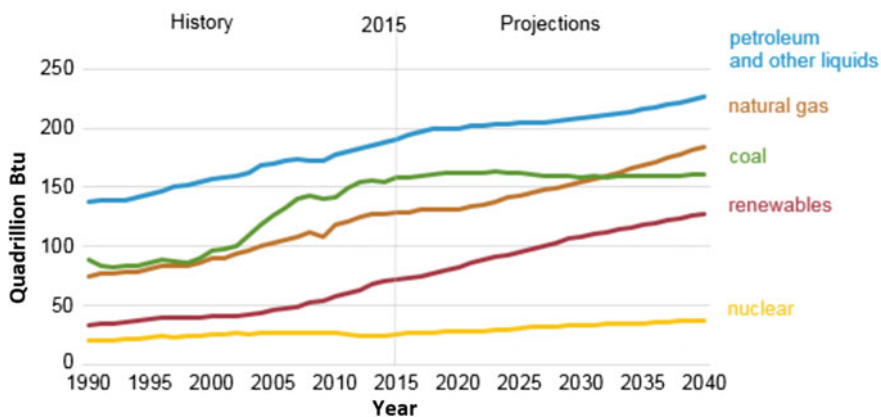
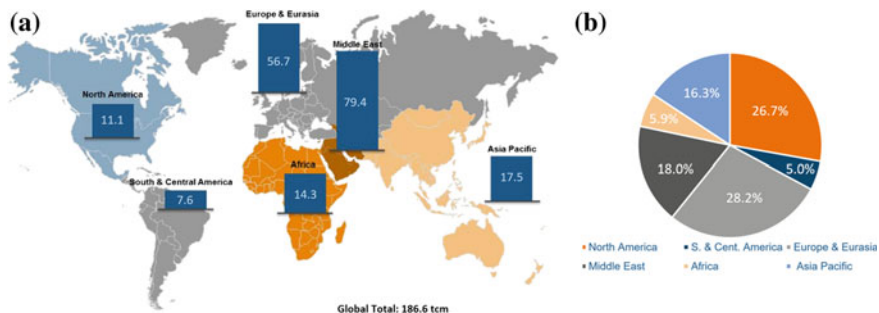


Fig. 13.1 World energy consumption by energy source (Eia.gov 2018)



**Fig. 13.2** a Global natural gas reserves (tcm), b Regional production share of natural gas. Reproduced from BP statistical review of world energy (2017), World energy resources (2016)

**Table 13.1** European emission standards for heavy-duty gas engines

Emission limits (g kWh <sup>-1</sup> )	Euro 5	Euro 6
CO	4.0	4.0
NO <sub>x</sub>	2.0	0.46
NMHC	0.55	0.16
CH <sub>4</sub>	1.1	0.5
PM	0.03	0.01
Test cycle	European transient cycle	World harmonised transient cycle

more than 50 years of current global production of NG. By region, Middle-East leads the proved reserves followed by Europe with 30% of the total reserve shares while Europe has the highest global production shares commanding up to 28.2%. Low-carbon economy maps are set out worldwide. For instance, the European Commission set out a low-carbon economy roadmap that aims to cut greenhouse gas emissions in the transport sector over 60% by 2050 from 1990 levels (Communication from the Commission to the European Parliament 2011) and using NG as vehicle fuel can help meet this aim. The Euro 5 and Euro 6 emissions standards for diesel and gas engines studied on a transient test cycle are detailed in Table 13.1. With the introduction of the new Euro 6 heavy-duty emission standards, emissions of NO<sub>x</sub> were significantly reduced by 77% from Euro 5 levels. Non-methane HCs were reduced by 71%, while methane emission from NG engines was reduced by 55% and as NG vehicles are required to meet both limits, methane emission control aftertreatment devices will be needed. In addition, the particle mass limit was reduced by 67% in the new Euro 6 emission standard which also introduced a particle number limit for the first time (not applicable for gas-fuelled engines).

These worldwide regulations will no doubt present a challenge for vehicle manufacturers to meet and will lead to the introduction of new engine technologies and aftertreatment systems or a combination of the two to guarantee the lowest

emissions, even under the most severe driving conditions. In the following sections, engine combustion and performance of natural gas in spark-ignition (bi-fuel) and compression-ignition (dual-fuel) engines are reviewed. In addition, an analysis of the exhaust products emitted from these engines and the various engine technologies and aftertreatment systems currently used to control them are described.

## 13.2 Natural Gas in Spark-Ignition (SI) Engines

### 13.2.1 Combustion of Natural Gas SI Engines

The advantage of natural gas as a vehicular fuel is that it can be utilised in both spark-ignition and compression-ignition engines. The typical combustion and physical properties of natural gas, gasoline and diesel fuels are outlined in Table 13.2. The majority of natural gas vehicles currently in use are retrofitted or converted from gasoline spark-ignition engines by adding a NG storage, supply and injection system, hence retaining the capability of being switched back to gasoline fuel (Chen et al. 2018). Although the fuel energy content in terms of mass, indicated by the lower heating value (LHV), of natural gas is higher than that of gasoline (49.5 MJ/kg for NG compared to 44.5 MJ/kg for gasoline), the engines suffer power reductions in the magnitude of 10–15% (Chen et al. 2018). This is attributed to several reasons. The volumetric heating value (VHV) of the natural gas–air mixture, which determines the amount of heat converted into mechanical work in the engine cylinder, is about 12% lower than that of gasoline–air mixture (Chen et al. 2018). In addition, the comparatively lower density of natural gas as compared to liquid fuels results in lower volumetric efficiencies (10–15% lower) as natural gas replaces a larger volume of air in the intake manifold upon injection. This limits the amount of air that can be induced into the combustion chamber and consequently less fuel is burnt leading to a reduction in power output (Korakianitis et al. 2011; Evans and Blaszczyk 1997).

Moreover, methane has a slower flame propagation speed as compared to gasoline under typical cylinder charge temperatures and pressures which extends the ignition delay time of the fuel–air mixture (Korakianitis et al. 2011; Thurnheer et al. 2009). Therefore, very advanced spark timing is employed in NG-fuelled engines which can be up to 10 CAD earlier before top dead centre (BTDC) compared to gasoline operation (Thurnheer et al. 2009). This further reduces the total power produced per engine cycle as the pre-ignited charge is working against the piston during the compression stroke. In addition, natural gas SI engines have comparatively lower thermal efficiencies to that of gasoline engines due to the relatively slower burning velocity of natural gas which reduces combustion temperatures. Therefore, gasoline engines that are converted to run on NG must be modified in order to compensate for the power loss caused by NG fuel. Engines fuelled with natural gas can run on higher compression ratios, which in combination

**Table 13.2** Typical physiochemical properties of natural gas, gasoline and diesel fuels (Kakaei and Paykani 2013)

Fuel properties	Natural gas	Gasoline	Diesel
Low heating value (MJ/kg)	48.6	43.5	42.5
Heating value of stoichiometric mixture (MJ/kg)	2.67	2.78	2.79
Cetane number	–	13–17	52.1
Octane number	130	85–95	–
Auto-ignition temperature (°C)	650	310	180–220
Adiabatic flame temperature (°C)	1890	2150	2054
Stoichiometric air–fuel ratio (kg/kg)	17.2	14.56	14.3
Flame propagation speed (m/s)	0.41	0.5	–
Flammability limit in air (vol.% in air)	5.3–15	1.4–7.6	1–6
Carbon content (%)	75	85.5	87
Hydrogen content (%)	25	12–15	16–33

with forced induction (turbocharging or supercharging) allows for increase in thermal efficiency and power output by up to 50% compared to engines that are fuelled with gasoline (Cho and He 2007). This is because the octane number of natural gas, which is defined as a measure of fuel's resistance to auto-ignition, is higher than gasoline's (120 for methane and 95 for gasoline). Fuel with high octane number is essential for SI engines in order to avoid engine knocking, which can lead to engine damage if severe. In most applications to date, the method adopted in introducing NG to the engine is through port fuel injection into the intake manifold (Korakianitis et al. 2011). However, the engine suffers a loss in volumetric efficiency due to the low density of natural gas as discussed earlier. Direct injection of natural gas into the combustion chamber after the air induction avoids the loss in volumetric efficiency associated with port fuel injection as there is no air displacement occurs in the intake manifold (Sevik et al. 2016). Moreover, the fuel-lean operating limit of natural gas engines can be extended with the adoption of direct injection with lower cycle-to-cycle variations resulted as compared to port fuel injection (coefficient of variation in indicated mean effective pressure is about 5% lower) (Korakianitis et al. 2011). This is due to an increase in charged motion as a result of the higher in-cylinder pressures caused by direct injection of natural gas, in addition to the locally fuel-rich mixtures near the spark plug which accelerates flame propagation. However, this results in an increase in combustion temperatures which favours  $\text{NO}_x$  formation.

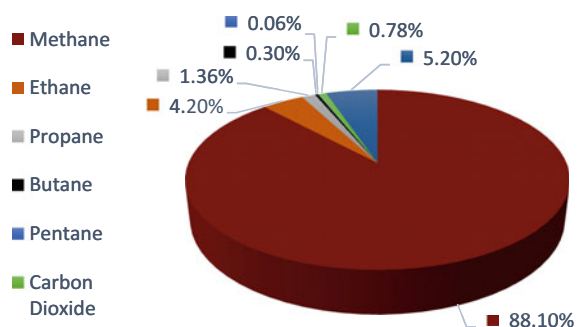
### 13.2.2 Exhaust Emissions from Natural Gas SI Engines

Natural gas is regarded as a cleaner form of energy compared to liquid fossil fuels as it emits comparatively lower  $\text{CO}_2$  levels per unit energy during combustion (by

20–30%) than coal or petroleum fuels (Kakaee and Paykani 2013; Bielaczyc et al. 2016; Semin and Bakar 2008). This is mainly due to the composition of natural gas with methane being its main constituent (typically 70–90%), leading to a low C/H ratio (1/4). A detailed composition of natural gas is given in Fig. 13.3. In addition, CO and non-methane hydrocarbon emissions produced from natural gas engines are generally lower than naturally aspirated gasoline engines (Kakaee and Paykani 2013; Korakianitis et al. 2011). The majority of CO emissions from gasoline engines are produced during cold start due to poor air–fuel mixing and incomplete atomisation and vaporisation of the liquid fuel (Jahirul et al. 2010). Conversely, the gaseous state of NG leads to a more homogenous air–fuel mixture inside the engine’s cylinder especially during cold start conditions, resulting in a more efficient combustion and significantly lower CO emissions (between 50 and 90% depending on engine calibration) (Sevik et al. 2016). The lower equivalence ratio adopted by natural gas engines results in a further reduction in CO concentrations and unburned non-methane hydrocarbon levels (by up to 55% less HC) (Semin and Bakar 2008). An opposite trend is seen at extremely low equivalence ratios because of deterioration in combustion quality. Moreover, the wall-wetting effect on intake manifold and cylinder liner is avoided due to the gaseous state of natural gas which further reduces non-methane hydrocarbon levels and reduces fuel consumption (Cho and He 2007). The comparatively higher compression ratios and advanced ignition timing adopted by natural gas-fuelled engines lead to higher  $\text{NO}_x$  emissions (by around 33%) than that of conventional gasoline engines (Aslam et al. 2006). This is due to the relatively higher in-cylinder pressure and temperature resulted which favours the formation of  $\text{NO}_x$ . The increase in  $\text{NO}_x$  emissions can be mitigated by retarding the spark timing; however, it will be at the expense of higher brake-specific fuel consumption. Therefore, a compromise among engine performance, exhaust emissions and fuel consumption have to be considered when deciding on the optimal engine operating parameters.

A major concern regarding NG engines is their methane emission as they produce large concentrations of methane gas. Hydrocarbon emissions in the USA are regulated in terms of their reactivity in the photochemical smog cycle, and although methane gas has no role in photochemistry or smog formation, it is considered a powerful greenhouse gas (global warming potential of methane is more than 20

**Fig. 13.3** Detailed composition of natural gas  
Reproduced from Kakaee and Paykani (2013)



times higher than CO<sub>2</sub> over 100 years) (US 2018). This is primarily caused by the slow flame propagation of natural gas which induces incomplete combustion and hence large amounts of unburnt natural gas escape through the combustion chamber (Ehsan 2006). This phenomenon is typical of engines converted to run on natural gas but is not optimally modified in terms of engine calibration (e.g. spark timing, injection timing) (Chen et al. 2018; Reynolds and Evans 2004). In addition, methane's reactivity is comparatively slower than most other longer-chain hydrocarbons, which makes it difficult to be removed in a typical three-way catalyst. With regard to PM, NG engines produce very low levels compared to gasoline and diesel engines (up to 95% less) as it does not contain any aromatic compounds such as benzene and has less dissolved impurities that contribute to the formation of PM (Semin and Bakar 2008). Hence, vehicles running on natural gas fuel should fulfil the emission limits of PM set out in the Euro 6 regulations. However, a new study has found that exhaust particles emitted from natural gas engines were observed to have peak diameters below 10 nm (2–5 nm range) and they were higher in number than particles with a peak diameters larger than 23 (Alanen et al. 2015). Therefore, it is important to take into consideration the peak diameter size range of 1–5 nm in order to get the full picture of natural gas emitted PM.

### 13.3 Current NG Emission Control Technologies in SI Engines

#### 13.3.1 *Lean-Burn Versus Stoichiometric Natural Gas Engines*

The control of exhaust gases emitted from natural gas internal combustion engines can be achieved through the careful control of the relative air–fuel ratio, lambda ( $\lambda$ ). Engines that run on natural gas as fuel are generally of two types, lean-burn ( $\lambda > 1$ ) and the more common stoichiometric ( $\lambda = 1$ ) combustion engines. Combustion of lean-burn NG engines can achieve lower concentrations of NO<sub>x</sub> pollutants and a better fuel economy than stoichiometric engines, but this is achieved at the expense of higher HC and CO emissions (Karavalakis et al. 2016). The control of air–fuel ratio is very important as it immensely influences engine performance and subsequently exhausts gas emissions. While running on fuel-rich mixtures results in lower NO<sub>x</sub> concentrations, significantly higher CO and unburnt HC emissions are produced due to the insufficient amount of oxygen available to oxidise the fuel. Moreover, rich engine running condition is also undesirable due to the significant fuel penalty it imposes. On the other hand, stoichiometric NG engines operate with  $\lambda = 1$  or slightly less than 1. These engines produce significantly low levels of non-methane hydrocarbons and CO emissions with some cost in fuel economy and relatively high NO<sub>x</sub> emissions. A combination of exhaust gas recirculation (EGR) and a three-way catalytic converter is used to mitigate and control exhaust

emissions from stoichiometric NG engines (Karavalakis et al. 2016; Hajbabaie et al. 2013; Einewall et al. 2005; Saanum et al. 2007).

In a lean-burn engine, the air–fuel ratio is increased beyond  $\lambda = 1.2$  in order to suppress  $\text{NO}_x$  emissions (Saanum et al. 2007). However, there is a lean operating limit beyond which acceptable engine performance can be maintained as the cycle-to-cycle variations increase significantly with leaner mixtures. Conversely, the optimal air–fuel ratio for HC emissions is reportedly between  $\lambda = 1.05$ – $1.2$  as sufficient oxygen concentration is available to oxidise the unburnt HCs, but  $\text{NO}_x$  emissions at this range (1.0–1.1) are at its highest (Einewall et al. 2005; Saanum et al. 2007; Cho and He 2008). Still, HC emissions are easier to treat in the exhaust of a lean-burn natural gas as opposed to  $\text{NO}_x$  emissions by using an oxidation catalyst. The excess of oxygen available with increasing lambda can enhance the combustion of the air–fuel mixture leading to a complete combustion of unburned HC and CO emissions. At the same time, increasing the air–fuel ratio increases the time required for the initial flame development and hinders flame propagation through the cylinder charge, causing longer ignition delay (Cho and He 2007). This results in slower heat release rate, slow combustion velocity and deterioration in combustion quality compared to that under stoichiometric conditions, thereby increasing heat transfer losses to the cylinder walls. This has an adverse effect on HC and CO emissions, as the combustion temperature in the cylinder drops hence the improvement in oxidation of HC and CO with excess of oxygen is unrealised. Even though the lean-burn engines are successful at reducing  $\text{NO}_x$  emissions, the technology is not practicable in real-life conditions as it is difficult to maintain a high air–fuel ratio at transient situations (like acceleration and low engine speed). In addition, as exhaust emissions are very sensitive to small changes in lambda value, the accuracy of the air–fuel control system is critical. The control of air–fuel ratio in a natural gas engine can be achieved using a wideband oxygen sensor. Due to its precise determination of residual oxygen content, the engine control unit can efficiently optimise fuel delivery and ignition timing for better fuel economy and emission concentrations (Heck and Farrauto 2001; Alkemade and Schumann 2006).

### ***13.3.2 Exhaust Gas Recirculation with Hydrogen Enrichment***

Exhaust gas recirculation (EGR) is an engine strategy commonly adopted by gasoline and diesel engines for the reduction of  $\text{NO}_x$  emissions. By employing EGR, a portion of the engine's exhaust gas is recirculated back to the cylinder which decreases the amount of unburned fuel and oxygen concentration in the combustion chamber, thus resulting in better fuel economy. The recirculated gas displaces some of the inlet air resulting in a dilution of the inlet charge and an increase in heat capacity which lowers the combustion temperature (Abdelaal and Hegab 2012). The use of EGR in lean-burn natural gas engines can therefore



achieve very low levels of  $\text{NO}_x$  emissions, as along with the slow flame propagation of natural gas, reduction in oxygen concentration and in-cylinder temperatures slow down the combustion of the charge mixture even further. This, however, results in higher HC, CO and PM emissions due to the colder combustion and the insufficient oxygen available to oxidise these species. The deterioration in combustion quality resulted from the EGR strategy can be ameliorated by the addition of  $\text{H}_2$ . The high flame speed of  $\text{H}_2$  has an opposite effect as it speeds up combustion of the mixture charge resulting in increased combustion temperature and more complete oxidation of HC and CO emissions. The combination of moderate EGR substitution with hydrogen in NG engines can achieve significantly lower engine-out emissions. For a 15%  $\text{H}_2$ –85% NG fuel mixture, increasing EGR substitution reduced  $\text{NO}_x$  emissions significantly as compared to the baseline NG combustion. On the other hand, HC emissions reduced with increasing EGR up to an EGR substitution of 14% but remained higher than baseline NG engine emissions (Dimopoulos et al. 2008).

### 13.3.3 Spark Timing

Modifying the spark timing can greatly influence the combustion process and engine-out emissions. In a natural gas-fuelled engine, the fuel mixture does not completely burn due to the slow flame speed of natural gas and therefore a spark advance strategy must be implemented. The advance in spark timing employed in NG engines can be between 2 and 10 CAD earlier BTDC compared to stoichiometric gasoline-fuelled engines (Evans and Blaszczyk 1997; Ji and Wang 2009). For leaner air–fuel mixtures, the spark energy transmitted to the cylinder charge in the vicinity of the spark plug is reduced at spark discharge which increases the time required for initial flame development (Cho and He 2009). In addition, the slow burning velocity of natural gas especially at lean mixtures results in an increase in combustion duration due to the low in-cylinder temperature causing a delay in ignition timing. Therefore, lean-burn NG engines require much-advanced spark timing BTDC in order to offset the ignition delay resulted with lean mixtures; however, this can also lead to knock (Cho and He 2007). The optimal MBT spark advance for better fuel economy and exhaust emissions depends on the variation of natural gas composition and the air–fuel ratio where more spark advance is needed with leaner mixtures due to the slower flame speeds (Evans and Blaszczyk 1997; Cho and He 2007). Early spark timing increases THC emissions as the fuel mixture is ignited earlier and the combustion duration is decreased. As the combustion duration is reduced, the temperature of the burned gas is lowered during the expansion stroke which further impedes the oxidation of the unburned fuel. Similarly, CO emissions follow the same trend with advancing the spark timing as the homogeneity of the air–fuel mixture is decreased due to the less mixing time. This induces incomplete combustion of the fuel in the fuel-rich or fuel-lean regions, and thus, CO emissions increase. On the other hand,  $\text{NO}_x$  emissions have a decreasing trend with early spark timings due to the lower combustion temperatures and lower burned gas temperatures resulted.

### 13.3.4 Hydrogen-Enriched Natural Gas Engines

The exhaust emissions of CO, unburned HC and CH<sub>4</sub> resulted from the slow burning rate of natural gas can be further mitigated by the addition of another fuel with a higher flame speed velocity. The combustion characteristics of natural gas engines can be enhanced by the addition of hydrogen in the intake charge (Alrazen and Ahmad 2018). The addition of small amounts of hydrogen concentrations in natural gas-fuelled combustion engines can lead to significant improvements in term of combustion stability, engine performance and levels of exhaust emissions. Table 13.3 details the combustion properties of hydrogen.

The higher burning rate of hydrogen as compared to natural gas leads to an increase in cylinder temperatures as the air–fuel mixture can be burnt more rapidly speeding up the combustion process (Açıkgöz et al. 2015). This is partially due to the increase in concentrations of H and OH radicals that increase combustion reactivity and lead to a faster flame propagation through the cylinder charge and hence more fuel is burnt (Chen et al. 2018; Korakianitis et al. 2011). This improves engine in-cylinder conditions which reduces emissions of HC and CO due to the more complete combustion. Compared to baseline natural gas engines, hydrogen-fuelled engines can have lower CO emissions depending on engine running conditions. With stoichiometric air–fuel ratio, the addition of H<sub>2</sub> leads to an increase in CO emissions while lean operating engines are expected to produce zero CO concentrations (Alrazen and Ahmad 2018; Açıkgöz et al. 2015). The higher in-cylinder temperatures resulted from the faster burn rate of the fuel mixture with the addition of hydrogen lead to a reduction in unburnt THC, although methane emissions remain high due to a big valve overlap angle (Alrazen and Ahmad 2018). The low overall carbon content of hydrogen-enriched natural gas along with the shorter quenching distance (distance between the position of flame extinguishment and the cylinder wall) induced by hydrogen addition is another reason for the reduction in HC emissions (Alrazen and Ahmad 2018; Açıkgöz et al. 2015). However, hydrogen-enriched natural gas engines produce higher NO<sub>x</sub> emissions due to increase in combustion temperature (Chen et al. 2018). The combination of hydrogen addition with lean combustion and optimal spark timing in a natural gas engine can reduce NO<sub>x</sub> exhaust emissions significantly without compromise in engine performance. Ultra-lean combustion can be attained with the addition of H<sub>2</sub>

**Table 13.3** Combustion properties of hydrogen (Mehra et al. 2017)

Fuel	H <sub>2</sub>
Flammability limit in air (%vol.)	4–75
Flammability limits ( $\lambda$ )	0.14–10
Auto-ignition temperature (°C)	585
Octane number	140
Stoichiometric air–fuel ratio	34.2
Laminar burning velocity (m/s)	2.9
Diffusivity in air cm <sup>3</sup> /s	0.63

in lean-burn NG engines due to the favourable combustion characteristics of  $H_2$ , such as its wide lean flammability limit and fast flame propagation (Lee et al. 2014). Hydrogen enrichment enhances the lean-burn capability of the NG engine and allows for more retarded ignition timing due to the shorter combustion duration, hence reducing the work done on the charge by the piston during compression (Chen et al. 2018). In addition, the deterioration in coefficient of variation (COV) of indicated mean effective pressure (IMEP) resulted from lean-burn operation is improved with  $H_2$  addition because of the more volatile fuel mixture and enhancement in combustion stability.

### 13.3.5 Aftertreatment System

As mentioned previously, lean-burn and stoichiometric combustion are the most common technologies used for the best engine performance and emission control in NG engines. However, these technologies alone cannot effectively reduce emissions to the levels acceptable to the Euro 6 emission standard, and thus, natural gas vehicles are equipped with exhaust aftertreatment technologies. In a stoichiometric NG engine (air/fuel ratio,  $\lambda = 1$ ), the abatement of methane ( $CH_4$ ) and other engine exhaust emissions (CO, NMHC,  $NO_x$ ) is achieved through a three-way catalyst (TWC) technology adapted from a gasoline TWC (Karavalakis et al. 2016). Currently, TWC technologies are very efficient in reducing exhaust emissions; however, they require a stoichiometric mixture in order to work effectively which induces drawbacks such as higher heat losses and pumping work at low-to-medium engine loads. Thus, most stoichiometric NG engines are equipped with a water-cooled EGR in order to dilute the stoichiometric mixture, allowing for a better fuel economy (i.e. lower pumping losses) and reduced emissions with combination of a TWC as compared to the lean-burn engines (Karavalakis et al. 2016; Einewall et al. 2005). The emission level of  $NO_x$  and CO can be reduced by 10–30 and 360–700 times, respectively, with the use of the combined technology as compared to lean-burn combustion (Mehra et al. 2017). Careful control of the air–fuel ratio is, however, critical for the efficient operation of the TWC as the lambda window for an acceptable trade-off between CO oxidation and  $NO_x$  reduction is very narrow ( $\pm 0.01$ ) (Einewall et al. 2005).

In addition, despite the very low HC concentrations emitted from natural gas engines as compared to gasoline engines, methane emissions remain a considerable issue. The majority of HC emissions produced by NG engines are composed of methane. As methane presents high stability of the C–H bond, it is one of the most unreactive hydrocarbons and is difficult to oxidise having a higher light-off temperature as compared to the longer-chain hydrocarbons. Therefore, platinum-group metals (PGMs), in particular palladium (Pd) and rhodium (Rh), are added to the TWC composition in order to enhance the efficiency of  $CH_4$  oxidation and meet end of life THC regulations (Raj 2016). When operating in stoichiometric conditions, a Pd–Rh catalyst with high total PGM loadings ( $>200 \text{ g ft}^{-3}$ ) can effectively remove

methane emissions. A stoichiometric air–fuel ratio is required for the TWC to simultaneously remove CO, NO and THC emissions. The performance of a bimetallic Pd–Rh catalyst on the exhaust of a conventional gasoline engine and a stoichiometric NG engine is illustrated in Fig. 13.4 as a function of engine lambda. The catalyst exhibits a similar trend overall for NO<sub>x</sub> and CO conversions in both engine cases. At stoichiometric conditions, the conversion efficiency of CO is close to 100% while higher NO<sub>x</sub> conversions can be achieved with the NG engine as they produce much lower engine-output NO<sub>x</sub> than their gasoline counterpart. In addition, HC conversion is significantly improved (95% efficiency) at stoichiometric conditions. The low HC conversion efficiency in the NG engine case in the lean condition is attributed to the poor combustion of NG at excess air, and therefore, the catalyst is exposed to high amounts of unburnt CH<sub>4</sub> which is difficult to oxidise (Karavalakis et al. 2016).

In a lean-burn NG engine, while the control of non-methane HC and CO emissions can be achieved with the use of an oxidation catalyst, NO<sub>x</sub> emissions and methane are more difficult to remove in lean conditions. Therefore, catalytic aftertreatment systems such as selective catalytic reduction (SCR) are necessary for lean-burn natural gas engines in order to comply with the Euro 6 emission standards. However, this is a rather complex and costly system and hence vehicle manufacturers could potentially favour the stoichiometric engine with TWC despite its inferior engine performance (Cho and He 2007). The coupling of an NH<sub>3</sub>–SCR (selective catalytic reduction with ammonia as reducing agent) with an oxidation catalyst based on palladium and platinum oxides has shown a great potential in the abatement of exhaust emissions produced from lean-burn NG heavy-duty vehicles (Adouane et al. 2013). The combined catalytic performance was able to achieve 40% CH<sub>4</sub> conversion at 415 °C while CO and NO<sub>x</sub> conversions reached 99 and 70%, respectively (Adouane et al. 2013). No aftertreatment systems are required for PM emissions for both lean-burn and stoichiometric NG engines due to the almost homogeneous combustion of the air–gas mixture and the absence of large hydrocarbon chains and aromatics in the fuel (Karavalakis et al. 2016).

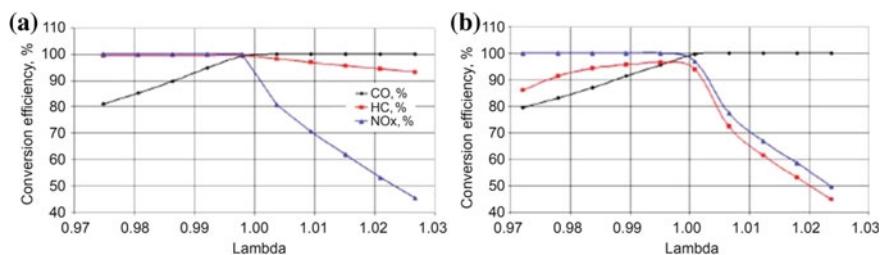


**Fig. 13.4** Performance of an aged Pd:Rh TWC at 450 °C as a function of lambda on: **a** Stoichiometric Gasoline engine, **b** Stoichiometric NG engine (Raj 2016)

## 13.4 Natural Gas in Compression-Ignition (CI) Engines

### 13.4.1 *Combustion and Performance of Dual-Fuel CI Engines*

The increasing concern regarding exhaust emissions produced from diesel engines has led to advancements in the utilisation of alternative fuels in CI engines. Natural gas has proved to be a very promising and attractive alternative fuel for both environmental and economical reasons. As compression-ignition engines employ high compression ratios, the high octane number of methane warrants its use in CI engines without experiencing the knock phenomenon (Abdelaal and Hegab 2012). However, the high auto-ignition temperature of natural gas limits its use as a 100% feasible replacement for diesel fuel in compression-ignition engines. An important fuel property for CI engines is the cetane number, which is a measure of a fuel ignition delay period; the higher the cetane number, the shorter time required for the fuel combustion process to be started. Methane, which is the main component of natural gas, has a very low cetane number compared to diesel fuel (40–55 for diesel while negligible for methane) as shown in Table 13.2, which significantly affects its ignition quality. Thus, the employment of NG fuel in CI engines requires a source of controlled ignition which aids in initiating natural gas combustion in the cylinder. This is provided by injecting small amounts of ‘pilot’ fuel with a high cetane number into the cylinder, where it blends with a premixed natural gas/air charge. This mode of operating natural gas with a pilot fuel (typically diesel or biodiesel) is commonly known as dual-fuelling in compression-ignition engines.

In the dual-fuel mode, direct injection of diesel fuel into the combustion chamber is employed late in the compression stroke, while natural gas is introduced into the intake manifold to mix uniformly with air before being introduced into the cylinder (Gogolev and Wallace 2018; Khan et al. 2015; Bhandari et al. 2005; Wei and Geng 2016). In SI engines, the low flame speed of natural gas leads to increased combustion duration as there is only one source of ignition (spark plug) and hence the flame propagates from a single point outwards through the charge (Korakianitis et al. 2011). In dual-fuel CI engines, the problem is less apparent. Dual-fuel mode combustion is characterised by two different combustion stages: non-premixed combustion of the pilot diesel fuel followed by combustion of natural gas–air mixture (Abdelaal and Hegab 2012). After an initial ignition delay, combustion of the pilot diesel fuel takes place first which then ignites the natural gas, producing multiple ignition points throughout the chamber. This instigates flame propagation, resulting in a relatively faster burn rate producing most of the energy released during combustion. It is possible to achieve more than 80% reduction of diesel fuel with the dual-fuel mode as compared to conventional diesel engines with the pilot diesel fuel accounting for 2–3% of the total injected fuel energy in some studies (Wei and Geng 2016). A schematic diagram of the dual-fuel mode is illustrated in Fig. 13.5.

With regard to combustion performance of dual-fuel natural gas CI engines, peak in-cylinder pressure and pressure rise rate for the dual-fuel are lower than

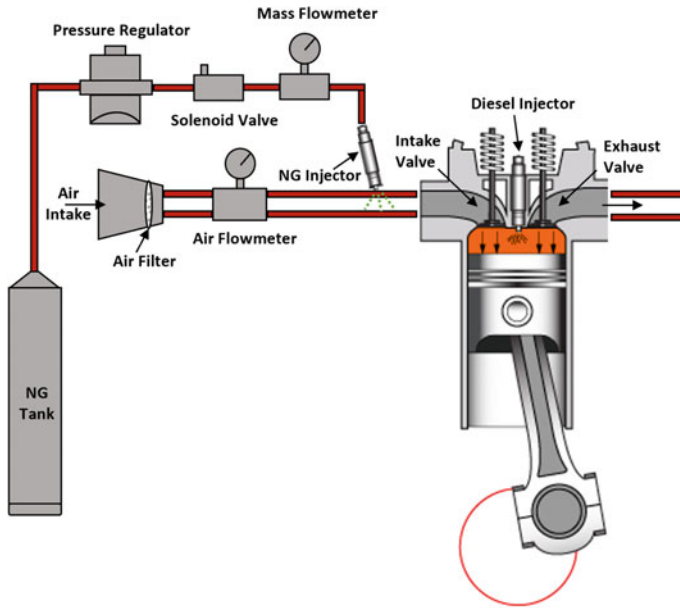


**Fig. 13.5** Natural gas/diesel dual-fuel system schematic diagram

conventional diesel engines during the initial combustion period (Sun et al. 2015), while cycle-to-cycle variations are of similar tendencies (COV of IMEP of 1%) (Korakianitis et al. 2011). This is attributed to the slower rate of natural gas combustion and longer ignition delay of the dual-fuel which shifts the combustion phase further into the expansion stroke, thus reducing peak in-cylinder pressure and pressure rise rate. As natural gas is port-injected, the dual-fuel mode suffers from significantly lower engine power output as opposed to conventional diesel engines (Gogolev and Wallace 2018). Moreover, combustion efficiency of premixed flame is very sensitive to the air–fuel ratio where it is optimal around stoichiometric conditions. However, in dual-fuel mode, premixed combustion of natural gas–air mixture suffers from very lean mixture which deteriorates combustion efficiency reducing peak value of in-cylinder pressure (Abdelal and Hegab 2012). Increasing the quantity of the pilot diesel fuel and advancing the injection timing can help in enhancing combustion of the dual-fuel due to the higher ignition source supplied to the engine cylinder and the increase in energy released during compression stroke with advanced injection. This results in an increase in heat release rate and consequently higher peak in-cylinder temperature and pressure. An alternative method of injecting natural gas into the engine cylinder is through the High-Pressure Direct Injection (HPDI) technology. In the HPDI mode, both the pilot diesel and natural gas fuels are directly injected into the combustion chamber, thus avoiding knock limitations and subsequent power losses resulted from the port injection in the dual-fuel mode (Gogolev and Wallace 2018; Wei and Geng 2016). A small quantity

of pilot diesel is initially injected into the combustion chamber which then auto-ignites under compression providing the ignition source for NG combustion. This is shortly followed by direct injection of natural gas which is then ignited by the diesel fuel's diffusion flame and burns in a predominantly non-premixed combustion event (Gogolev and Wallace 2018; Wei and Geng 2016). This mode of injecting natural gas achieves similar thermal efficiencies and power output to that of an equivalently sized diesel engine while providing better fuel economy. However, the dual-fuel injector system is more complicated as it requires a special concentric needle operating at high pressures in order to inject the two fuels. As such, combustion and emission characteristics of the dual-fuel mode will be the point of focus in this chapter.

### ***13.4.2 Exhaust Emissions from Dual-Fuel Combustion***

Depending on engine running conditions, dual-fuelling in CI engines can result in significant reduction in exhaust  $\text{NO}_x$  emissions with respect to conventional diesel engines (Korakianitis et al. 2011). In a dual-fuel engine, the production of  $\text{NO}_x$  emissions is mainly due to the combustion of the non-premixed pilot diesel fuel. As the quantity of the pilot diesel fuel is considerably small,  $\text{NO}_x$  levels are significantly lower than those of conventional diesel engines. Hence, as the combustion of natural gas occurs late in the expansion stroke, the amount of  $\text{NO}_x$  emitted from dual-fuel CI engines greatly depends on the quality and quantity of the pilot fuel (Korakianitis et al. 2011). In addition, the low flame speed of natural gas combined with the very lean mixture in the dual-fuel mode reduces in-cylinder combustion temperatures and suppresses  $\text{NO}_x$  formation. Alternatively, hydrocarbon emissions resulted from incomplete combustion of the dual-fuel engine are substantially higher than in conventional diesel engines especially at low engine loads due to low charge temperatures. While at high engine loads unburned HC concentrations decrease due to the higher in-cylinder temperatures induced by the more complete combustion, concentrations remain much higher than that of normal diesel engines. This is primarily due to the very lean air-fuel ratios adopted in CI engines which, along with the slow flame speed of NG, hinder flame propagation through the mixture charge (Korakianitis et al. 2011; Sun et al. 2015). The bulk of the HC emissions consist of unburned natural gas that might have got trapped in the crevices, survived the combustion process and escaped to the exhaust. Decreasing the percentage of natural gas substitution leads to a rapid decrease in HC concentrations. As the pilot diesel fuel quantity increases, spray atomisation characteristic is enhanced and a higher proportion of diesel fuel is ignited, leading to a more complete combustion of the air-fuel mixture. CO emissions from dual-fuel CI engines follow a similar trend to HC emissions. Remarkably higher concentrations of CO are emitted from dual-fuel combustion as compared to diesel engines. The development of flame extinct regions caused by deterioration in flame propagation favours the CO formation mechanism due to the incomplete oxidation of the

premixed natural gas–air mixture (Sun et al. 2015). Particulate matter emissions are one of the major concerns of diesel engines and the use of natural gas with pilot fuel injection may well contribute in meeting PM regulations for diesel engines. Natural gas has lower carbon atoms than diesel and does not contain aromatic compounds such as benzene which contributes to the formation of PM. Hence, most of the PM emissions formed from dual-fuel engines resulted from the combustion of the pilot diesel fuel. However, the quantity of the pilot fuel is very small, which in addition to the more homogenous air–fuel mixture caused by the longer ignition delay results in lower soot formation (Sun et al. 2015). Therefore, dual-fuel mode produces very low levels of PM emissions compared to diesel engines (up to 95% less) (Semin and Bakar 2008).

## 13.5 Current NG Emission Control Technologies in CI Engines

### 13.5.1 Exhaust Gas Recirculation (EGR)

The use of EGR in dual-fuel engines can partially enhance the lower thermal efficiency and reduce the comparatively higher CO and unburned HC emissions depending on engine running conditions while resulting in even lower NO<sub>x</sub> emissions (Abdelaal and Hegab 2012). By using EGR, the inlet charge is diluted as part of the exhaust replaces some of the inlet air which reduces oxygen levels while combustion temperature is reduced due to an increase in the heat capacity. These combined effects lead to reductions in NO<sub>x</sub> levels. In addition, with the adoption of EGR, the unburned exhaust gas is recirculated back into the engine cylinder where it is expected to reburn in the following cycle. This results in lower levels of unburned HC and a subsequent reduction in CO emissions particularly at low engine loads, while higher thermal efficiencies are also realised. Increasing EGR percentages will lead to further reductions in HC emissions as larger amounts of unburned HCs are recirculated and reburned in the mixture. The slight increase in the intake charge temperature and the reburning of the HCs resulted with EGR application induces a more complete combustion of the fuel which results in CO emission reductions. At high engine loads, HC reduction with EGR is negligible due to the reduced oxygen levels in the combustion chamber which hinders the reburning of the unburned HCs. This also has an adverse effect on CO and PM emissions due to the insufficient O<sub>2</sub> available for CO oxidation and hence an increase in these emissions is seen at high loads (Abdelaal and Hegab 2012). Moreover, the in-cylinder peak pressure reduces substantially with higher EGR percentages as more O<sub>2</sub> is replaced by carbon dioxide and water vapour which hinders the combustion of the dual-fuel and increases ignition delay.



### 13.5.2 Pilot Fuel Quantity and Type

Evidently, the pilot fuel is the main source of ignition in a dual-fuel NG engine and hence the quality and type of pilot fuel used will greatly affect engine combustion performance. In the dual-fuel natural gas engines, the bulk of the exhaust emissions are produced from the ignition of the pilot fuel. As mentioned in Sect. 13.4.2, when the pilot fuel quantity is small, unburned HC emissions as well as CO emissions are comparatively higher than that of conventional diesel engines as the flame cannot propagate throughout the whole cylinder charge in the excessively lean mixture. Increasing the quantity of the pilot fuel increases the envelope size of the pilot fuel mixture and provides a greater multitude of ignition centres that require shorter flame travel which shortens ignition delay; hence, a larger volume of the charge is ignited (Imran et al. 2014; Namasivayam et al. 2010). Moreover, the unburned fuel is compressed to a higher temperature with larger pilot energy release which increases in-cylinder temperatures and enhances the oxidation of the fuel leading to a reduction in HC and CO concentrations (Liu et al. 2013). This effect is more evident at low engine loads, whereas at high loads pilot fuel quantity has little effect as the gaseous fuel concentration in the air charge is above the lean combustion limit which leads to faster flame propagation through the cylinder charge. On the other hand,  $\text{NO}_x$  emissions increase with increasing pilot fuel quantity due to the higher charge temperatures resulted (Abd Alla et al. 2000). Similarly, increasing the NG fuel concentration in the cylinder charge leads to higher  $\text{NO}_x$  concentrations as the size of the combustion zone increases significantly (Abd Alla et al. 2000). In addition, as PM emissions from dual-fuel NG engines are mainly formed during the diffusion combustion process of the pilot fuel, an increase in pilot fuel quantity will result in a subsequent increase in PM concentrations (Liu et al. 2013).

Several alternative fuels have been investigated as potential replacement to the conventional pilot diesel fuel in dual NG engines in order to reduce exhaust emissions of HC, CO and  $\text{NO}_x$ . Biodiesel fuels such as rapeseed oil methyl esters (RME) performance as a pilot fuel is reportedly like that of diesel with both engine performance and exhaust emissions showing very comparable trends (Imran et al. 2014; Nwafor 2000). Still, the use of RME as a pilot fuel for natural gas CI engines produced lower  $\text{NO}_x$  levels compared to diesel which is attributed to the higher cetane number of RME. The higher cetane number of RME as compared to diesel results in shorter ignition delay and thus less time available for premixed combustion leading to lower in-cylinder temperature and resulted  $\text{NO}_x$  emissions (Imran et al. 2014). Other biodiesel fuels have been well researched in the literature and have also shown similar trends in terms of their performance and emissions. This is due to the similar physical and combustion properties of biodiesel as compared to diesel fuel (Abd Alla et al. 2000). On the other hand, the use of dimethyl ethers (DME) as an alternative pilot fuel showed positive reductions in  $\text{NO}_x$  emissions due to the lower combustion temperatures resulted from the cooling effect upon injection of the gaseous DME fuel. In addition, the slower flame propagation coupled with the longer ignition delay of the DME pilot fuel as compared to liquid

fuel slows down the rate of combustion and thus produce lower  $\text{NO}_x$  levels. However, this also leads to higher HC and CO levels (Namasivayam et al. 2010). These results indicate that natural gas combustion is responsible for most of the combustion enthalpy in the dual-fuel mode and the pilot fuel only acts as an ignition source to initiate combustion.

### ***13.5.3 Varying Pilot Fuel Injection Timing***

The injection timing of the pilot fuel plays a major role in defining the combustion and emission characteristics of dual-fuel NG engines. Retarding the injection timing means that the combustion of the fuel mixture occurs later in the cycle and more fuel burns after TDC which decreases the peak cylinder pressure. As the pilot fuel combustion is delayed with retarding the injection timing, incomplete combustion of the fuel mixture occurs as the in-cylinder temperature is too low for the flame to propagate throughout the combustion chamber. This leads to the production of higher HC and CO emissions (Abd Alla et al. 2002). On the other hand, slightly advancing the injection timing leads to an earlier start of the combustion process and increases the peak cylinder pressure resulting in higher peak charge temperatures as more fuel is burned before TDC (Abd Alla et al. 2002). In addition, advance in the start of injection (SOI) timing leads to a longer ignition delay as the pilot diesel fuel is injected at lower cylinder temperatures which result in a reduction in unburned hydrocarbons. This is attributed to the fact that the longer ignition delay provided more time for diesel to mix with the surrounding natural gas–air mixture which results in a more homogenous charge in the cylinder. In addition, it allowed for a fuller spray penetration and development while creating a larger amount of air–fuel mixture prior to ignition which results in multiple ignition regions throughout the cylinder (Sahoo et al. 2009; Zhou et al. 2013). These multiple ignition regions lead to an increase in flame propagation resulting in higher burning rates and shorter combustion duration. As the burning rate of the larger premixed air–fuel region increased, CO unburned HC emission levels were reduced. However, an increase in  $\text{NO}_x$  emissions is resulted with advancing the injection timing due to the higher maximum charge temperature. When the injection timing is too advanced, misfire and partial oxidation may occur as the in-cylinder temperature is not sufficiently high enough to ignite the injected fuel. In addition, excessive ignition delay will cause the diesel–air mixture to be too lean due to over-mixing of the spray which deteriorates flame propagation and prolongs the start of combustion (Zhou et al. 2013). This results in lower in-cylinder temperature and heat release rate which induces incomplete combustion of the fuel, hence increasing HC and CO emissions while reducing  $\text{NO}_x$  emissions. The effect of injection timing on the characteristics of PM emissions is apparent with a significant increase in the number of particles with advancing the injection timing while the particle mass concentration exhibits a decreasing trend. The longer ignition delay period and the more homogenous air–fuel mixture formed with advancing the

injection timing increase the formation of smaller particles while the higher in-cylinder temperatures resulted enhance the oxidation process. Thus, this leads to a reduction in the particle mass concentration but an increase in the number of particles (Zhou et al. 2013).

## References

- Abd Alla GH, Soliman HA, Badr OA, Abd Rabbo MF (2000) Effect of pilot fuel quantity on the performance of a dual fuel engine. *Energy Convers Manag* 41(6):559–572
- Abd Alla G, Soliman H, Badr O, Abd Rabbo M (2002) Effect of injection timing on the performance of a dual fuel engine. *Energy Convers Manag* 43:269–277
- Abdelaal MM, Hegab AH (2012) Combustion and emission characteristics of a natural gas-fueled diesel engine with EGR. *Energy Convers Manag* 64:301–312
- Açıkğöz B, Çelik C, Soyhan HS, Gökalp B, Karabağ B (2015) Emission characteristics of a hydrogen-CH<sub>4</sub> fuelled spark ignition engine. *Fuel* 159:298–307
- Adouane D, Capela S, Da Costa P (2013) On the efficiency of NH<sub>3</sub>eSCR catalysts for heavy duty vehicles running on compressed natural gas in synthetic gas bench scale. *Top Catal* 56 (1e8):45–49
- Alanen J, Saukko E, Lehtoranta K, Murtonen T, Timonen H, Hillamo R et al (2015) The formation and physical properties of the particle emissions from a natural gas engine. *Fuel* 162:155–161
- Alkemade UG, Schumann B (2006) Engines and exhaust after treatment systems for future automotive applications. *Solid State Ion* 177:2291–2296
- Alrazen H, Ahmad K (2018) HCNG fueled spark-ignition (SI) engine with its effects on performance and emissions. *Renew Sustain Energy Rev* 82(1):324–342
- Aslam MU, Masjuki HH, Kalam MA, Abdesselam H, Mahlia TMI, Amalina MA (2006) An experimental investigation of CNG as an alternative fuel for a retrofitted gasoline vehicle. *Fuel* 85(5):717–724
- Bhandari K, Bansal A, Shukla A, Khare M (2005) Performance and emissions of natural gas fuelled internal combustion engine: a review. *J Sci Ind Res* 64:333–338
- Bielaczyc P, Szczołka A, Woodburn J (2016) A comparison of exhaust emissions from vehicles fuelled with petrol, LPG and CNG. *IOP Conf Ser: Mater Sci Eng* 148:012060
- BP statistical review of world energy (2017). Available at: <https://www.bp.com/content/dam/bp/en/corporate/pdf/energy-economics/statistical-review-2017/bp-statistical-review-of-world-energy-2017-full-report.pdf>
- Chen H, He J, Zhong X (2018) Engine combustion and emission fuelled with natural gas: a review. *J Energy Inst* xx:1–14 (2018)
- Cho HM, He B (2007) Spark ignition natural gas engines—a review. *Energy Convers Manag* 48 (2):608–618
- Cho HM, He BQ (2008) Combustion and emission characteristics of a lean burn natural gas engine. *Int J Automot Technol* 9:415–422
- Cho HM, He BQ (2009) Combustion and emission characteristics of a natural gas engine under different operating conditions. *Environ Eng Res* 14:95–101
- Communication from the Commission to the European Parliament, the Council, the European economic and social committee and the committee of the regions: a roadmap for moving to a competitive low carbon economy in 2050', Brussels, Belgium, 8 March 2011
- Dimopoulos P, Bach C, Soltic P, Boulouchos K (2008) Hydrogen–natural gas blends fuelling passenger car engines: combustion, emissions and well-to-wheels assessment. *Int J Hydrogen Energy* 33(23):7224–7236
- Ehsan M (2006) Effect of spark advance on a gas run automotive spark ignition engine. *J Chem Eng Jpn* 24(1):42–49

- Eia.gov (2018) International energy outlook 2016-executive summary - Energy information administration. [online] Available at: [https://www.eia.gov/outlooks/ieo/exec\\_summ.php](https://www.eia.gov/outlooks/ieo/exec_summ.php)
- Einewall P, Tunestål P, Johansson B (2005) Lean Burn Natural Gas Operation versus stoichiometric operation with EGR and a three way catalyst. SAE Technical Paper No 2005-01-0250
- Evans RL, Blaszczyk J (1997) A comparative study of the performance and exhaust emissions of a spark ignition engine fuelled by natural gas and gasoline. Proc Inst Mech Eng Part D: J Automob Eng 211(1):39–47
- Gogolev I, Wallace J (2018) Performance and emissions of a compression-ignition direct-injected natural gas engine with shielded glow plug ignition assist. Energy Convers Manag 164:70–82
- Hajbabaei M, Karavalakis G, Johnson K, Lee L, Durbin T (2013) Impact of natural gas fuel composition on criteria, toxic, and particle emissions from transit buses equipped with lean burn and stoichiometric engines. Energy 62:425–434
- Heck RM, Farrauto RJ (2001) Automobile exhaust catalysts. Appl Catal A Gen 221:443–457
- Imran S, Emberson DR, Ihracska B, Wen DS, Crookes RJ, Korakianitis T (2014) Effect of pilot fuel quantity and type on performance and emissions of natural gas and hydrogen based combustion in a compression ignition engine. Int J Hydrogen Energy 39(10):5163–5175
- Jahirul MI, Masjuki HH, Saidur R, Kalam MA, Jayed MH, Wazed MA (2010) Comparative engine performance and emission analysis of NG and gasoline in a retrofitted car engine. Appl Therm Eng 30(14–15):2219–2226
- Ji C, Wang S (2009) Effect of hydrogen addition on combustion and emissions performance of a spark ignition gasoline engine at lean conditions. Int J Hydrogen Energy 34:7823–7834
- Kakaee AH, Paykani A (2013) Research and development of natural-gas fuelled engines in Iran. Renew Sustain Energy Rev 26:805–821
- Karavalakis G, Hajbabaei M, Jiang Y, Yang J, Johnson K, Cocker D, Durbin T (2016) Regulated, greenhouse gas, and particulate emissions from lean-burn and stoichiometric natural gas heavy-duty vehicles on different fuel compositions. Fuel 175:146–156
- Khan M, Yasmin T, Shakoor A (2015) Technical overview of compressed natural gas (CNG) as a transportation fuel. Renew Sustain Energy Rev 51:785–797
- Korakianitis T, Namasivayam AM, Crookes RJ (2011) Natural-gas fueled spark-ignition (SI) and compression-ignition (CI) engine performance and emissions. Prog Energy Combust Sci 37:89–112
- Lee S, Kim C, Choi Y, Lim G, Park C (2014) Emissions and fuel consumption characteristics of an HCNG-fueled heavy-duty engine at idle. Int J Hydrogen 39:8078–8086
- Liu J, Yang F, Wang HW, Ouyang MG, Hao SG (2013) Effects of pilot fuel quantity on the emissions characteristics of a CNG/diesel dual fuel engine with optimized pilot injection timing. Appl Energy 110:201–206
- Mehra RK, Duan H, Juknelevičius R, Ma F, Li J (2017) Progress in hydrogen enriched compressed natural gas (HCNG) internal combustion engines—a comprehensive review. Renew Sustain Energy Rev 80:1458–1498
- Namasivayam AM, Korakianitis T, Crookes RJ, Bob-Manuel KDH, Olsen J (2010) Biodiesel, emulsified biodiesel and dimethyl ether as pilot fuels for natural gas fuelled engines. Appl Energy 87(3):769–778
- Nwafor OMI (2000) Effect of choice of pilot fuel on the performance of natural gas in diesel engines. Renew Energy 21(3–4):495–504
- Raj A (2016) Methane emission control. Johnson Matthey Technol Rev 60(4):228 <https://doi.org/10.1595/205651316x692554>
- Reynolds C, Evans RL (2004) Improving emissions and performance characteristics of lean burn natural gas engines through partial stratification. Int J Engine Res 5(1):105e114
- Saanum I, Bysveen M, Tunestål P, Johansson B (2007) Lean burn versus stoichiometric operation with EGR and 3-way catalyst of an engine fueled with natural gas and hydrogen enriched natural gas. SAE Technical Paper No 2007-01-0015

- Sahoo BB, Sahoo N, Saha UK (2009) Effect of engine parameters and type of gaseous fuel on the performance of dual-fuel gas diesel engines—a critical review, *Renew Sustain Energy Rev* 13 (6–7):1151–1184
- Semin, Bakar RA (2008) A technical review of compressed natural gas as an alternative fuel for internal combustion engines. *Am J Eng Appl Sci* 1(4):302–311
- Sevik J, Pamminger M, Wallner T, Scarcelli R, Reese R, Iqbal A, Boyer B, Wooldridge S, Hall C, Miers S (2016) Performance, efficiency and emissions assessment of natural gas direct injection compared to gasoline and natural gas port-fuel injection in an automotive engine. *SAE Int J Engines* 9(2):1130–1142
- Sun L, Liu YF, Zeng K, Yang R, Hang ZH (2015) Combustion performance and stability of a dual-fuel diesel–natural-gas engine. *Proc Inst Mech Eng D J Automob Eng* 229(2):235–246
- Thurnheer T, Soltic P, Eggenschwiler PD (2009) SI engine fuelled with gasoline, methane and methane/hydrogen blends: heat release and loss analysis. *Int J Hydrogen Energy* 34(5):2494–2503
- US EPA (2018) Atmospheric lifetime and global warming potential defined|US EPA. [online] Available at: <https://www.epa.gov/climateleadership/atmospheric-lifetime-and-global-warming-potential-defined>
- Wei L, Geng P (2016) A review on natural gas/diesel dual fuel combustion, emissions and performance. *Fuel Process Technol* 142:264–278
- World energy resources (2016). Available at: <https://www.worldenergy.org/wp-content/uploads/2016/10/World-Energy-Resources-Full-report-2016.10.03.pdf>
- Zhou L, Liu Y-F, Wu C-B, Sun L, Wang L, Zeng K et al (2013) Effect of the diesel injection timing and the pilot quantity on the combustion characteristics and the fine-particle emissions in a micro-diesel pilot-ignited natural-gas engine. *Proc Inst Mech Eng D J Automob Eng* 227 (8):1142–1152

# Chapter 14

## A Review of Residential-Scale Natural Gas-Powered Micro-Combined Heat and Power Engine Systems



Gokul Vishwanathan, Julian Sculley, David Tew and Ji-Cheng Zhao

**Abstract** A combined heat and power (CHP) system typically employs a prime mover generator that produces electricity on-site and utilizes waste heat energy to supplement a site's thermal load requirements. Micro-CHP, notionally defined as CHP systems with a capacity lower than 50 kW, offers an alternative, and in some cases a complementary, solution to centralized power generation. A micro-CHP system would be typically installed at a residential or small commercial site where it would consume fuel such as diesel or natural gas to generate electricity locally and further use the rejected waste heat for local heating, air-conditioning, and/or humidification needs. This is in contrast to the rejected heat being dissipated at centralized power plants using cooling towers. The combined efficiency of primary energy usage for such systems can be higher than 90% on a fuel lower heating value (LHV) basis. Since a large fraction of the electricity generated from all the centralized power plants is consumed by the residential and commercial sectors, CHP implementation in these sectors can have a huge impact on both energy savings and carbon dioxide (CO<sub>2</sub>) emissions' reduction. Apart from these benefits, decentralized CHP as a form of distributed electricity generation offers numerous advantages such as reduced electrical grid stress, reduced electricity transmission and distribution losses, and potentially improved resiliency of the electricity grid. Various technologies including reciprocating internal combustion engines, Stirling engines, Brayton cycle engines, Rankine cycle engines, fuel cells, and solid-state devices such as thermoelectric generators and thermionic generators can be used as

---

G. Vishwanathan (✉) · J. Sculley  
Booz Allen Hamilton, Washington, DC 20005, USA  
e-mail: [vishwanathan\\_gokul@bah.com](mailto:vishwanathan_gokul@bah.com)

D. Tew · J.-C. Zhao  
Department of Energy, Advanced Research Projects Agency-Energy (ARPA-E)  
United States, Washington, DC 20585, USA

J.-C. Zhao  
Department of Materials Science and Engineering, The Ohio State University,  
Columbus, OH 43210, USA

micro-CHP systems. This chapter provides a detailed technological review of engine-based micro-CHP systems and further presents the challenges and opportunities for achieving high fuel conversion efficiency.

**Keywords** Combined heat and power • Internal combustion engines  
Stirling engines • Brayton cycle engines • Micro-cogeneration • Micro-CHP  
Natural gas generators • Distributed generation

## 14.1 Introduction

Micro-combined heat and power (CHP) systems have the potential to reduce the energy and emissions burdens associated with the provision of electricity, heat, and cooling services to our homes and small businesses. They also have the potential to enhance the reliability of the electricity supplies of their owners through their redundancy with the electric grid. However, the societal-level energy, emissions, and reliability value propositions that these systems could offer through their widespread deployment are currently at risk due to the high installed costs of these systems versus the energy cost savings benefits that they generally offer. This chapter offers a review of the state of the art of micro-CHP systems for residential applications and discusses several ongoing development programs that are seeking to enhance their energy and economic value propositions and thereby enable their widespread market adoption and the realization of the society-level energy, emission, economic, and reliability value propositions that they can offer.

CHP systems offer their energy, emissions, and reliability value propositions via their on-site generation of electric power and subsequent productive utilization of waste heat from the generation process for local space and/or water conditioning purposes. These systems (typically) convert the heating value of natural gas into electricity and useful thermal energy and can do so at combined overall (i.e. electricity + thermal energy) lower heating value (LHV) basis efficiencies that are in excess of 90%. This efficiency is well in excess of the average 2017 US central plant electricity generation efficiency of 33.6% (Energy Flow Charts 2018). Furthermore, a large (>60%) percentage of US utility-generated electricity is generated from fossil fuels, and the associated CO<sub>2</sub> emissions were 2 billion metric tons of CO<sub>2</sub> in 2014, which was roughly 38% of total US CO<sub>2</sub> emissions (Carbon Flow Charts 2018). Consequently, the widespread deployment of CHP systems across the residential and commercial sectors could have significant primary energy usage and CO<sub>2</sub> emissions reduction benefits, since a combined 74% of the electricity generated by centralized power plants is consumed by these sectors (Energy Flow Charts 2018).

However, despite these potential benefits, less than 500 of the 58.6 million US homes with natural gas have installed micro-CHP systems (EIA 2018; Guyer 2015). The best-performing small-scale CHP engine (~1.2 kW electrical power) has a fuel-to-electrical conversion efficiency of about 26.3% (based on fuel LHV) and a

total CHP efficiency of 92% (Honda Worldwide|Power Products 2018), but the estimated installed cost is more than \$10,000. This system is sufficient to supply the base electric load of many residences, and hence, these residences would be independent of grid electricity during off-peak periods. Tapia-Ahumada et al. (2013) performed a detailed sensitivity study of the penetration of CHP technologies over a 20-year time frame as a function of micro-CHP capital cost (product cost and not installed cost<sup>1</sup>). It can be inferred from their study that CHP systems can have a significant impact on the residential sector only when the capital cost is less than \$4,000 per kW of electricity generation. Beyond this value, the market penetration shrinks significantly as the economics of the system becomes unattractive to potential residential customers.

A recent study by the authors (Vishwanathan et al. 2018) assessed the value proposition of residential CHP in the USA. The study selected a few cities from the seven Building America Climate Zones (2018) and calculated customer payback periods using a variety of scenarios that perturbed the technical parameters of a hypothetical residential CHP system installed in a 2,500 sq. ft. single-family home. The baseline scenario assumed a variable fuel-to-electrical conversion efficiency with respect to the electrical load and a peak efficiency of 40%. The total CHP efficiency (sum of fuel-to-electrical conversion efficiency and thermal efficiency) was assumed to be 80%. It was assumed that the 1-kW system followed the residential electrical load and had a total installed cost of \$4,500. The conclusions from this study were that the tradeoffs between system size, cost, and efficiency are extremely important in developing the right product for each climate zone. The baseline scenario showed that it was possible to achieve a payback of less than 10 years in regions where the spark spread<sup>2</sup> was high (e.g. Los Angeles) or in cold climates where there was significant need for heating throughout most of the year (e.g. Boston, Denver, and Chicago), as illustrated in Fig. 14.1 (Vishwanathan et al. 2018). Finally, it was concluded that a maximum primary energy saving of 0.6 quadrillion BTU in the USA can be achieved with a total installed system cost of \$2,500.

Thus far, micro-CHP technologies have had substantially greater market success in Japan and somewhat better success in the European Union (especially Germany) (Ashurst 2016). Specifically, while the USA can claim 500 residential micro-CHP systems, roughly 50,000 units were installed in Japan in 2015 alone and Germany accounts for over 80% of the micro-CHP sales in the European Union. The enhanced market penetration in Europe and Asia is driven at least in part by supporting government policies and incentives—including net metering, tax incentives, up-front grants, subsidized natural gas (NG) prices, and favorable tariff structures. Barbieri et al. (2012) concluded that the marginal cost for a micro-CHP

---

<sup>1</sup>The gross installed cost of the CHP system includes the product cost and system installation cost.

<sup>2</sup>According to the US Energy Information Administration (EIA) Web site, spark spread is defined as “the difference between the price received by a generator for electricity produced and the cost of the natural gas needed to produce that electricity.”



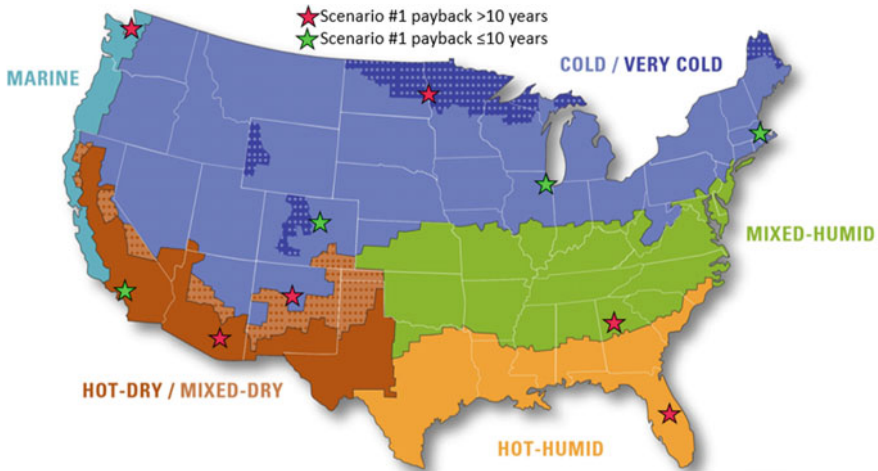


**Fig. 14.1** Customer payback analysis performed for ten cities in seven climate zones in the USA (Vishwanathan et al. 2018)

system, with respect to a traditional boiler, must be  $\sim 3,000$  €/kW for the system to be economically attractive in Italy. In their study, it is assumed that traditional household boilers will be replaced by micro-CHP systems. Their analysis evaluated a number of potential micro-CHP system technologies and predicted a  $> 20\%$  primary energy savings in two single-family home scenarios for Italy. They furthermore concluded that Stirling engine micro-CHP systems provided the most potential energy cost savings. Fubara et al. (2014) performed a mathematical modeling and optimization study at the building level and the overall energy supply network level for NG-fueled micro-CHP systems employing solid oxide fuel cells (SOFC), Stirling engines, and internal combustion engines (ICEs). At the building level, the micro-CHP system was connected to the external gas and electric networks and served the needs of the building. The overall energy supply network simulations included gas production assets, power stations, gas and electricity distribution networks, and building-level domestic energy users. A detailed case study for the UK domestic energy supply was performed for four different residential house sizes for a) cost-driven strategy, obtained by maximizing net present value, and b) primary energy-driven strategy, obtained by maximizing savings in primary energy consumption. A 3–6% reduction in primary energy (NG) consumption was estimated with the cost-driven strategy with SOFC micro-CHP systems, while a 6–10% reduction in primary energy (NG) consumption was estimated with the primary energy-driven strategy with Stirling engine micro-CHP systems.

Ren and Gao (2010) performed an economic and environmental evaluation of micro-CHP systems for residential buildings in Japan. In their analysis, they considered both a 1-kW NG engine and a 1-kW fuel cell system that were optimized to operate for (a) minimum annual energy cost and (b) minimum CO<sub>2</sub> emissions. The

fuel-to-electrical conversion efficiencies of the gas engine and the fuel cell were assumed to be 20 and 37%, respectively. When the systems were operated for minimum annual energy cost, the gas engine resulted in 24% savings while the fuel cell resulted in 26% savings. When the systems were operated with an eye on maximizing the environmental benefit, the gas engine resulted in a 2% reduction in CO<sub>2</sub> emissions while the fuel cell resulted in a 9% reduction in CO<sub>2</sub> emissions. Thus, their analysis showed that fuel cell systems were more effective than the NG engines from both an economic and environmental standpoint.

Given that there is a general consensus that micro-CHP can lead to economic and energy savings, this chapter is dedicated to the review and analysis of NG-powered micro-CHP engine systems. This chapter is organized into two main sections. Section 14.2 presents a detailed review of small-scale engines that are relevant to residential CHP, and Sect. 14.3 discusses the technical challenges and opportunities for small-scale engines. This chapter reviews ICEs, Stirling engines, Brayton cycle engines, and micro Rankine cycle engines as applicable to micro-CHP applications. It is noted here that fuel cells are one of the most sought-after technologies for CHP as they can deliver higher fuel-to-electrical conversion efficiency (30–60%) at small (1–1.5 kW) scales (Maghanki et al. 2013). However, they are not reviewed in this chapter as their economics are thought to be severely challenged at small scales due to their high capital and maintenance costs (Sevier 2015).

## 14.2 Review of the State of the Art for Small CHP Systems

The following classes of generators are reviewed in their respective subsections, viz. reciprocating ICEs, Stirling engines, Brayton cycle engines, and micro-Rankine cycle engines.

Reciprocating ICEs are good candidates for micro-CHP applications from fuel conversion efficiency and load-following capability standpoints. However, they require periodic maintenance in terms of oil change, replacement of spark plugs and/or fuel injectors, and occasional replacement of power cylinder components and emissions after-treatment devices. Spark-ignited NG ICEs can be broadly classified as stoichiometric and lean burn ICEs. Stoichiometric ICEs (without exhaust gas dilution) tend to be lower in fuel conversion efficiency as compared to lean burn ICEs (for reasons discussed in Sect. 14.3); however, stoichiometric ICEs tend to have lower tailpipe-out emissions as a low-cost catalytic converter can be used to oxidize carbon monoxide (CO) and hydrocarbons (HC) while simultaneously reducing oxides of nitrogen (NO<sub>x</sub>). Lean burn engines are plagued with higher engine-out emissions of CO and HC; however, they lead to lower engine-out NO<sub>x</sub> emissions due to lower combustion flame temperatures. Since lean burn engines are characterized by lower exhaust gas temperatures, exhaust after-treatment devices with high conversion efficiencies at traditional catalyst light-off temperatures (~200–250 °C) or even lower temperatures are required.

This is an active and ongoing research area in the ICE community. The limiting factors for high-efficiency ICEs include high heat transfer losses due to the large surface area-to-volume ratios at small scales, incomplete combustion, and friction losses. Stoichiometric ICEs are better suited for load following when compared to lean burn ICEs. Finally, ICEs are well suited to operate with NG with fairly constant composition (e.g. methane number and fuel lower heating value) and will require sophisticated combustion controls to accommodate significant variation in fuel composition. This is critical from a product development perspective as the quality of natural gas varies for each state (and sometimes with season) within the USA.

Stirling engines have the ability to operate for a long period of time without requiring significant maintenance, as evidenced by those employed in space applications, and are characterized by low noise operation. They tend to have lower fuel conversion efficiencies as compared to reciprocating ICEs and are not typically suitable for load following due to their high thermal inertia. However, since it is an external combustion engine, a Stirling engine is robust to changes in fuel composition as it is a heat engine that only requires a temperature differential to operate. In addition, the emissions generated from typical Stirling engine combustors are lower when compared to ICEs.  $\text{NO}_x$  emission formation is potentially averted due to lower combustion flame temperatures. HC and CO emissions are mitigated due to the higher residence time that is available for their oxidation, when compared to ICEs. Achieving efficient heat transfer between the combustion system and the Stirling engine working fluid is recognized as the chief limiting factor for the development of a high-efficiency Stirling engine. Consequently, the lower fuel-to-electrical conversion efficiency of a Stirling engine will lead to higher heat being rejected from the system (through exhaust gases and coolant), which can be recovered for residential heating. Hence, Stirling engines are better suited for regions with a large thermal load requirement.

Brayton cycle engines are arguably the least mature technology at residential CHP scale. Micro-turbines are the most common Brayton cycle engines employed for micro-CHP applications and are essentially low-powered versions of gas turbines that are used for power generation. Typical power outputs of micro-turbines range from tens to a few hundred kW but are generally considered more mature for applications over 20 kW. To the best of our knowledge, there is only one commercially available micro-turbine product that is less than 5 kW. Some major hurdles that make micro-turbines (employing traditional radial type turbomachinery) inefficient are: (1) small-scale effects leading to high viscous losses in the turbine passages due to low Reynolds number flow, (2) manufacturing tolerances and bearing limitations at high rotational speeds, (3) higher heat transfer due to high surface-to-volume ratios, and (4) high mechanical or parasitic losses. Recuperated Brayton cycle engines, which employ a recuperator for harvesting exhaust gas energy for heating combustion air, are more efficient and expensive as compared to non-recuperated Brayton cycle engines. Thus, Brayton cycle engines at the 1–10 kW scale have low fuel conversion efficiency when compared to ICEs and consequently are better suited for regions with a large thermal load requirement. Like Stirling engines, Brayton cycle engines are also more robust to changes in fuel

composition when compared to ICEs. The emissions generated from Brayton cycle engines are also potentially lower when compared to ICEs for the same reasons stated above for Stirling engines.

Table 14.1 provides a summary of various state-of-the-art generators in each of these categories and their performance metrics including LHV-based

**Table 14.1** Summary of the state-of-the-art generators for CHP with capacity less than 10 kW (Honda Worldwide 2018; Barbieri et al. 2012; De Paepe et al. 2006; Aisin 1.5 kW internal combustion engine CHP 2016; CP5WN 2018; CP10WN 2018; Qnergy SmartBoiler 2018; Guyer 2016; EnerTwin 2018) (<https://www.mtrigen.com/>, [http://micro-chp.com/micro\\_chp\\_products.htm](http://micro-chp.com/micro_chp_products.htm))

	Electric power (kW)	Thermal power (kW)	Fuel energy (kW)	Electric efficiency (%)	Thermal efficiency (%)
<i>ICEs</i>					
Honda Ecowill	1.0	3.3	5.0	20.0	66.0
Honda EXlink MCHP1.0K2	1.0	2.5	3.8	26.3	65.7
Aisin Coremo	1.5	3.7	5.8	26.0	64.0
AISIN SEIKI GECC46A2	4.6	10.6	18.0	25.6	58.6
Marathon Engine Systems' ecopower	4.7	12.5	18.8	25.0	65.0
SenerTec. (Dachs.) HKA G 5.0	5.0	12.1	19.2	26.0	63.1
Yanmar CP5WN	5.0	10.0	17.8	28.0	56.0
Yanmar CP10WN	10.0	16.9	31.5	31.5	53.5
M-TriGen PowerAire 45	3.4	13.0	29.6	11.5	43.9
M-TriGen PowerAire 65	6.0	16.7	37.9	15.8	44.1
M-TriGen PowerAire 85	8.0	21.5	48.9	16.4	44.0
<i>Stirling engines</i>					
Microgen	1.0	6.0	7.4	13.5	81.1
Infinia	1.0	6.4	8.0	12.5	80.0
Baxi Ecogen	1.0	5.0	6.5	15.4	77.0
Navien HYBRIGEN	1.0	5.7	6.5	15.4	88.0
Stirling systems—SOLO161	2.0	8.0	10.0	20.0	80.0
SUNMACHINE	3.0	10.5	14.9	20.1	70.5
Disenco	3.0	12.0	16.3	18.4	73.6
Qnergy SmartBoiler	7.2	39.6	47.1	15.3	84.0
<i>Brayton cycle engines</i>					
MTT EnerTwin	3.2	15.6	20.0	16.0	78.0
<i>Micro-Rankine cycle engines</i>					
Energetix	1.0	8.0	10.0	10.0	80.0
Flow energy's flow boiler	1.0	11.2	13.0	7.7	85.8
OTAG	2.0	16.0	19.1	10.4	83.6
COGEN Microsystems	2.5	11.0	13.5	18.5	81.4

Note that the M-TriGen products are micro-combined cooling, heat, and power (micro-CCHP) systems and their cooling loads are not included here

fuel-to-electrical conversion efficiency and thermal efficiency (ratio of thermal energy to fuel energy) (Honda Worldwide Honda Worldwide|Power products 2018; Barbieri et al. 2012; De Paepe et al. 2006; Aisin 1.5 kW internal combustion engine CHP 2016; CP5WN 2018; CP10WN 2018; Qnergy SmartBoiler 2018; Guyer 2016; MTT EnerTwin 2018) (<https://www.mtrigen.com/>, [http://micro-chp.com/micro\\_chp\\_products.htm](http://micro-chp.com/micro_chp_products.htm)). The total CHP efficiency is the sum of the fuel-to-electrical conversion efficiency and the thermal efficiency.

### 14.2.1 Internal Combustion Engines

ICEs are ubiquitous in numerous industrial, transportation, and power generation applications through their high fuel to shaft power conversion efficiencies and their relatively low cost. This efficiency advantage versus competing engine technologies is evident in Fig. 14.2, where the ICEs are shown to have the highest electric

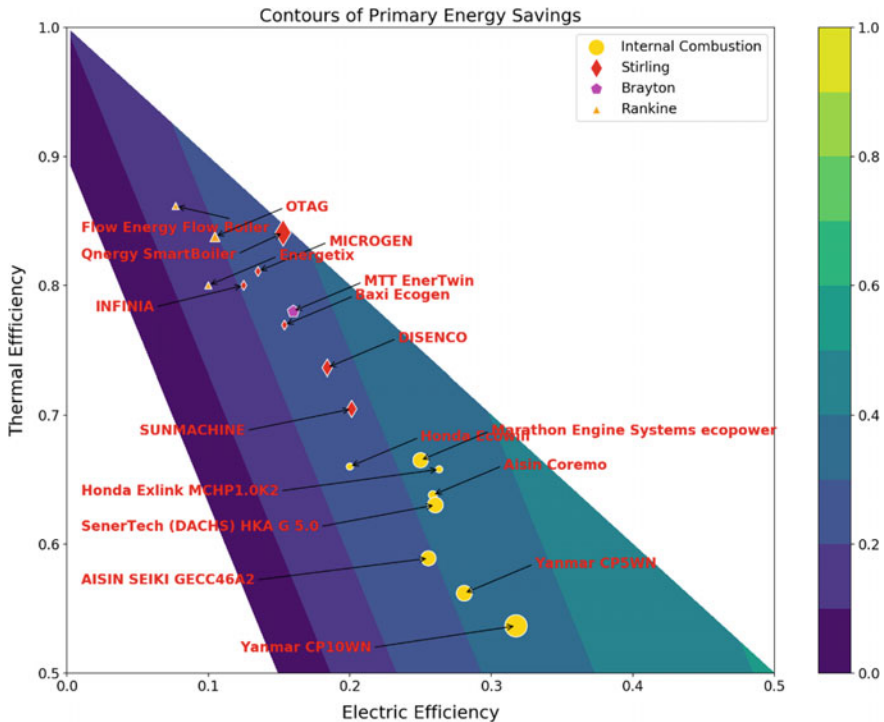


**Fig. 14.2** Scatter plot of thermal versus electric efficiency for various CHP systems listed in Table 14.1 overlaid on a contour plot of the maximum potential primary energy savings assuming a baseline electrical grid efficiency of 33.6% (the US average in 2017) and a baseline furnace efficiency of 90% (the marker size is proportional to the maximum electric output of the system)

efficiencies of the cycles represented. Two systems with industry-leading performance at small scales are the Honda EXlink at 1 kW and the Yanmar CP10WN at 10 kW.

The Honda NG or liquid propane-powered Extended Expansion Linkage Engine (EXlink) (Honda Worldwide 2018) employs an over-expanded Atkinson cycle where the expansion stroke volume ( $163 \text{ cm}^3$ ) is higher than the compression stroke ( $110 \text{ cm}^3$ ), which results in an increased in-cylinder work extraction. In addition, the shorter intake stroke also results in lower pumping losses though at a marginal cost of volumetric efficiency. Thus, the combined effects of increased expansion work and reduced pumping losses result in a higher brake thermal efficiency (defined as the ratio of the brake or shaft power to the fuel energy) for the engine. In addition, the thermal efficiency is as high as 66% by improved cooling system design and integration of the heat exchanger with the catalytic converter (or three-way catalyst). Coupled with these benefits, the system is also quiet in operation with a noise level of 43 dBA. From a reliability standpoint, the maintenance interval is around 6000 h of use or 3 years (whichever is earlier) due to the use of long-life spark plugs and high-capacity oil tank. Recently, Honda has discontinued ICEs from its portfolio of micro-CHP products in Japan as the Japanese market has largely shifted toward fuel cells (Ashurst 2016, 2018).

The Yanmar CHP family of engines (CP5WN 2018; CP10WN 2018) employs an over-expanded Miller cycle along with lean NG combustion (Yanmar mCHP 2016). The fuel-to-electrical conversion efficiencies for the 5 and 10 kW systems are 28% and 31.5%, respectively, with more than 50% thermal efficiencies. Along with high efficiency, lean NG combustion also results in low thermal  $\text{NO}_x$  emission as it reduces the in-cylinder flame temperatures. The noise levels for the 5 and 10 kW engines are 51 and 54 dBA, respectively, while the reported maintenance interval for both the products is 10,000 h of operation.

Figure 14.3a, reproduced from Cullen and McGovern (2010), illustrates the general trends in the fuel energy balance of industrial ICEs at various engine brake powers at a constant speed of 1500 rpm. Figure 14.3b, reproduced from Muccillo and Gimelli (2014), shows the estimated energy balance for a 15 kW ICE-based CHP generator.

In Fig. 14.3a, the jacket water accounts for both engine friction and engine heat transfer losses. It can be clearly seen that the heat transfer is highly nonlinear and increases significantly (>35% of the total fuel energy) at low rated powers. Moreover, the available exhaust energy has an inverse relationship with respect to heat transfer; i.e. the fraction of exhaust energy decreases with a reduction in engine power, while the converse is true for heat transfer. As the pie-chart in Fig. 14.3b shows, the total irrecoverable losses account for about 14% of the fuel energy (sum of alternator loss, wall heat transfer loss, and exhaust gas loss), thus yielding a total CHP efficiency of 86%. However, only 28% of the fuel energy is converted into electricity while the remaining energy is captured by the engine cooling circuit, exhaust gases, and the radiator heat exchanger.

More recently, Taie et al. (2018) performed detailed analyses on the 1-kW Honda Ecowill CHP system using the first and second law of thermodynamics. This

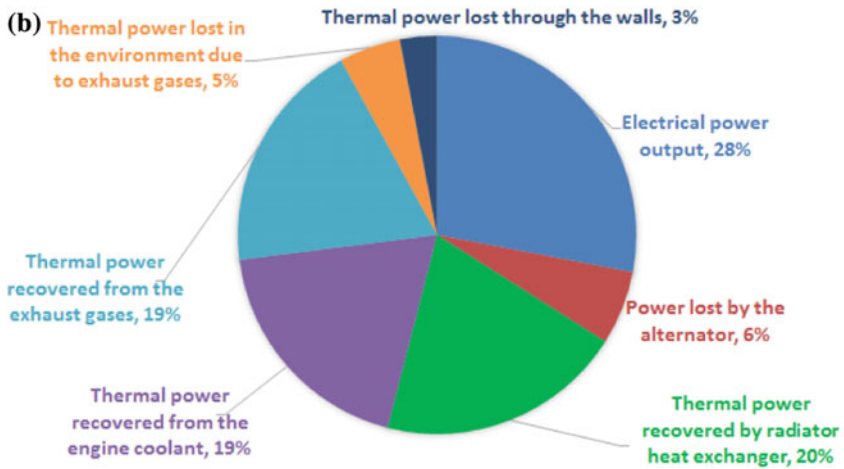
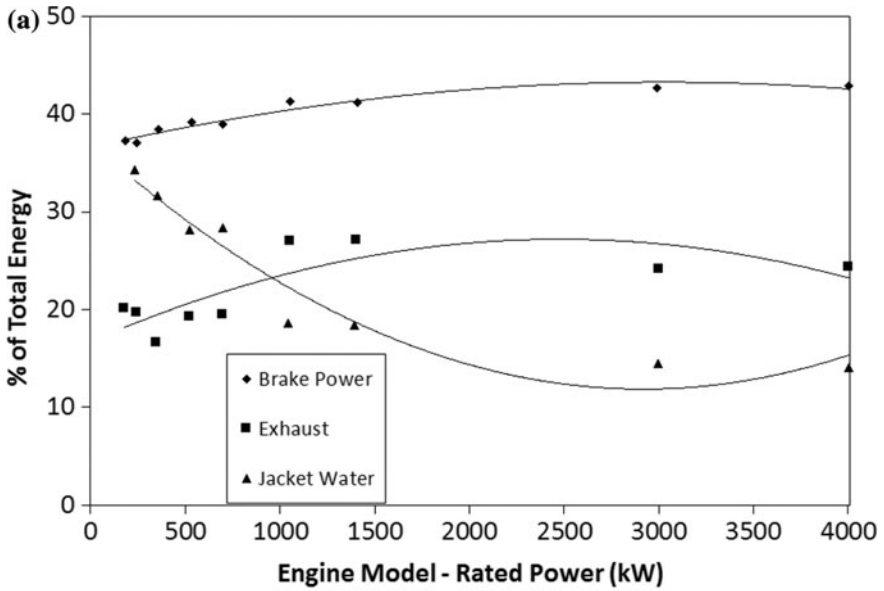
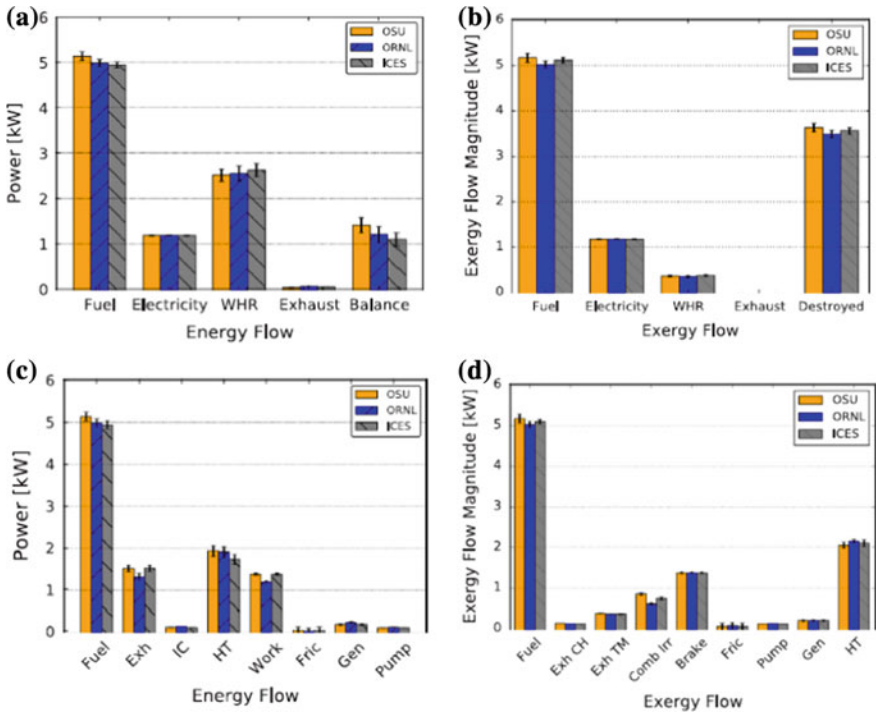


Fig. 14.3 a Energy breakdown of industrial ICES as a function of engine brake power reproduced from Cullen and McGovern (2010) and b 15 kW ICE CHP energy breakdown reproduced from Muccillo and Gimelli (2014)

work was funded by the US Department of Energy (DOE), Advanced Research Projects Agency-Energy (ARPA-E). They performed both a CHP system-level and an ICE-level energy and exergy flow analyses. Figure 14.4a–d [reprinted from Taie et al. (2018)] shows the energy and exergy flows based on the first law and second law analyses, for both the CHP and ICE systems. The three colored bars represent



**Fig. 14.4** **a** Energy flows calculated by the first law analysis for the CHP system, **b** exergy flows calculated by the second law analysis for the CHP system, **c** energy flows calculated by the first law analysis for the ICE, and **d** exergy flows calculated by the second law analysis for the ICE (Taie et al. 2018)

experimental tests that were conducted at three different facilities, illustrating the experimental repeatability. A 23% fuel-to-electrical conversion efficiency is obtained based on the first law analysis. The first law waste heat recovery (WHR) energy from Fig. 14.4a represents the energy that can be captured for hot water and space heating purposes. The WHR exergy as per Fig. 14.4b represents the maximum fraction of the WHR energy that can be converted into useful work using a bottoming cycle device such as an organic Rankine cycle. Figure 14.4c shows the energy flows for the Honda Ecowill ICE prime mover. The Work term in the figure represents the brake work, and the electrical work can be obtained after the deduction of the generator/alternator losses (Gen) from the brake work. Part of the exhaust (Exh) and heat transfer (HT) is captured as waste heat for heating. Additional loss mechanisms include powertrain friction (Fric), incomplete combustion (IC), and pumping losses (Pump). Finally, Fig. 14.4d shows the exergy flows for the ICE. The exhaust exergy is split into exhaust thermomechanical exergy (Exh TM) and exhaust chemical exergy (Exh CH). Notably, the exergy loss



due to combustion (Comb Irr) is a major loss mechanism predominantly due to flame propagation in stoichiometric combustion.

Significant challenges exist to obtain high brake thermal efficiencies (and hence high fuel-to-electrical conversion efficiency) from small-size and low-power ICES due to high surface-to-volume ratios that lead to high heat transfer. This can be shown by a simple back-of-the-envelope calculation. Consider four different ICE bore sizes ( $b = 0.1, 0.08, 0.05,$  and  $0.025$  m), a bore-to-stroke ratio of 0.8, an engine speed of 1500 rpm, a thermal conductivity ( $K$ ) of the in-cylinder fluid of  $0.06$  W/m/K, and a dynamic viscosity of the in-cylinder fluid ( $\nu$ ) of  $0.0001$  m<sup>2</sup>/s; the mean piston speed ( $S_p$ ) can be calculated using the engine speed and stroke length. The Nusselt number (Nu) and the convective heat transfer coefficient ( $h$ ) can be calculated using the Taylor correlation (Taylor 1985) as shown in Eq. (14.1).

$$\text{Nu} = \frac{h \cdot b}{K} = 10.4 \cdot \left( \frac{S_p \cdot b}{\nu} \right)^{0.75} \quad (14.1)$$

An average in-cylinder gas temperature of 1500 K and an oil temperature of 353 K were assumed for all the cases. The cycle-averaged heat transfer was calculated using Eq. (14.2).

$$Q = h \cdot A \cdot \Delta T \quad (14.2)$$

where  $A$  is the reference area calculated using the cylinder bore and  $\Delta T$  is the heat transfer potential, which is the difference between the average in-cylinder gas temperature and oil temperature. The brake power can be calculated using the engine displacement and by assuming a constant power density of 65 kW/L for all the cases. Figure 14.5 shows the ratio of the engine heat transfer to brake power as a function of engine brake power. Though the model is rudimentary, it alludes to meaningful insights into the relative contribution of fuel energy to engine heat transfer and useful brake power. It is also interesting to note that the energy associated with engine heat transfer is higher than the useful brake power for small kW engines (<5 kW), a trend that is also shown in the experimental data in Fig. 14.4c where HT is greater than the Work term. Additionally, at the small engine scales, incomplete combustion is a significant contributor to inefficiency predominantly due to flame-wall interaction (heat transfer between flame and cold wall and subsequent flame quenching) and crevice flows.

In terms of costs, the Ecowill and EXlink systems are estimated to be about \$13,000 and \$24,000, respectively, while the ecopower 4.7 kW is estimated to cost about \$24,000. These costs are based on customer input of those systems and just serve as a ballpark indicator rather than precise values. Part of the reason for the high cost of these systems is their low-volume production, which is expected to be alleviated with increased penetration of residential CHP.

Thus, novel strategies for reducing in-cylinder heat transfer, incomplete combustion, pumping, friction, and innovative combustion strategies are needed to deliver higher fuel-to-electrical conversion efficiency for small-scale ICES. In

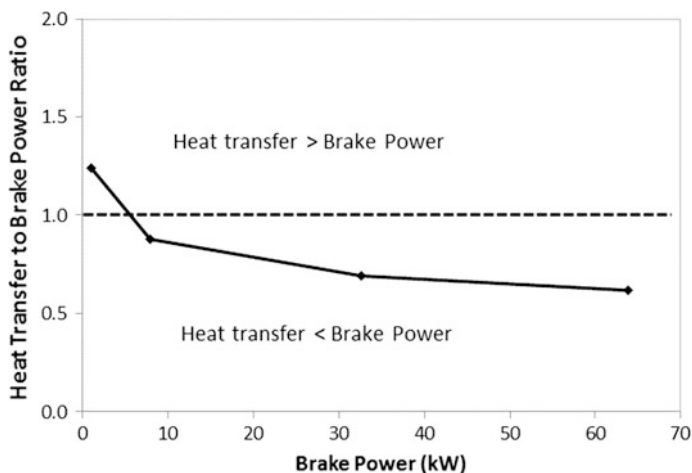


Fig. 14.5 Ratio of engine heat transfer to brake power as a function of engine brake power

addition, a significant emphasis on the reduction of the total installed cost is necessary to make these technologies feasible for residential customers. As noted by Ashurst (2016), the ICE system cost is about 60% of the total installed cost to the customer.

## 14.2.2 Stirling Engines

Stirling engines are arguably the most mature external combustion engines that have penetrated the CHP market. Table 14.1 shows the efficiency of several commercially available Stirling engines for less than 10-kW micro-CHP applications. As seen from the table, all the Stirling engines have less than 20% fuel-to-electrical conversion efficiency at 1 kW. It is important to note that the total CHP efficiency can exceed 90% for such systems. The total CHP efficiency of the Navien HYBRIGEN system is claimed to be more than 100% on a LHV basis (note the efficiency is less than 100% on a fuel higher heating value basis) due to the use of a condensing boiler for heat capture.

Figure 14.6a, reprinted from Valenti et al. (2014), shows a Sankey diagram for a Stirling engine generator with typical system losses. A significant portion of fuel energy is lost in the exhaust gases and some to the burner cooling water, while the remaining portion of the fuel energy is used as heat input to the Stirling engine. The ratio of the useful heat input to the fuel energy represents the combustor efficiency ( $\eta_{\text{comb}}$ ). Furthermore, the fraction of the useful heat input, which is converted into mechanical work by the Stirling engine working fluid (after taking into account the engine heat transfer loss) represents the Stirling engine indicated closed-cycle work. The ratio of the indicated closed-cycle work to the Stirling engine useful heat input

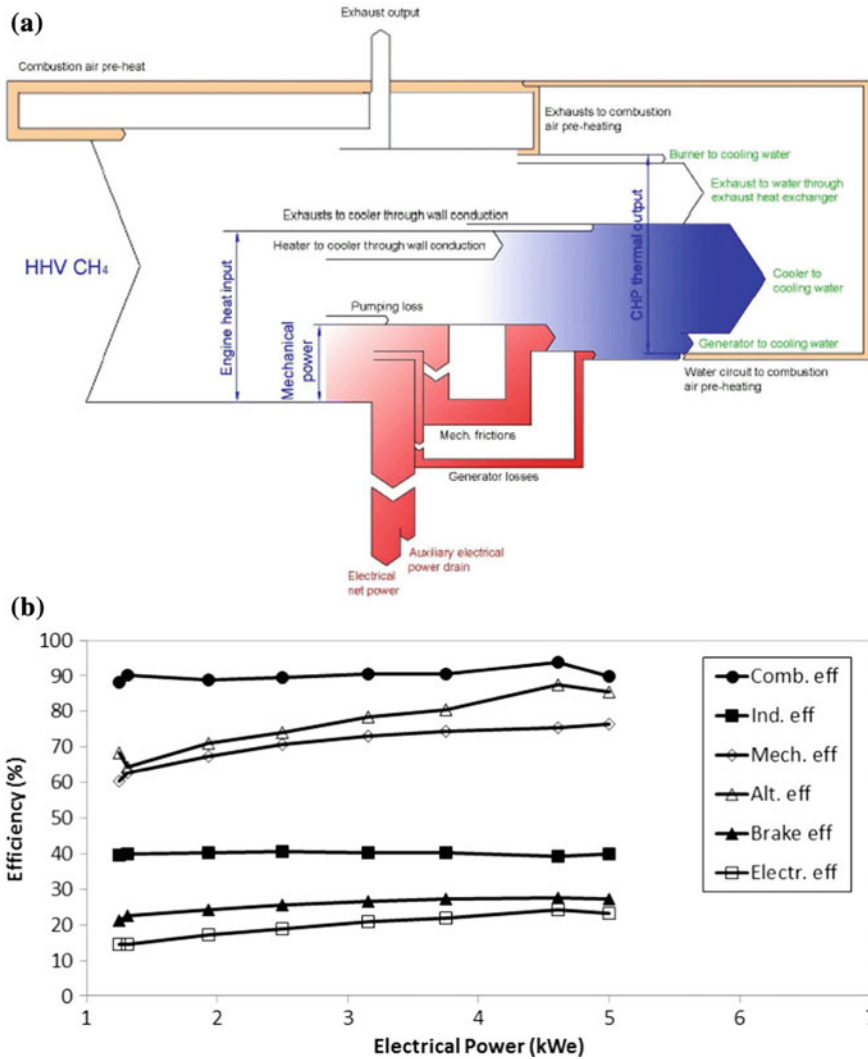


**Fig. 14.6** **a** Sankey diagram for a Stirling engine-driven CHP system from Valenti et al. (2014) and **b** typical state-of-the-art small-scale Stirling engine efficiency breakdown reproduced from García et al. (2014)

represents the indicated cycle efficiency ( $\eta_{ind}$ ). Some portion of the indicated work is further lost in pumping, friction, and other parasitic losses yielding the net shaft work. The ratio of the shaft work to the indicated work gives the mechanical efficiency ( $\eta_{mech}$ ). Finally, the alternator efficiency ( $\eta_{alt}$ ), which is the ratio of electrical power to the shaft power, represents the portion of shaft work that is converted into useful electrical power. In a typical CHP system as shown in

Fig. 14.6a, much of the energy lost in the exhaust and coolant (heat transfer and friction) is recovered for residential hot water and space heating purposes. Using a recuperator, the exhaust heat can also be used for preheating combustion air for improving the combustor efficiency. Thus, for an external combustion engine, the energy cascade gives an expression for the fuel-to-electrical conversion efficiency ( $\eta_e$ ) as shown in Eq. (14.3):

$$\eta_e = \eta_{\text{comb}} \cdot \eta_{\text{ind}} \cdot \eta_{\text{mech}} \cdot \eta_{\text{alt}} \quad (14.3)$$

Figure 14.6b, reproduced from García et al. (2014), shows the efficiency breakdown for a kinematic Stirling engine running at 1500 rpm operating with NG as fuel and helium as the working fluid with a maximum working gas temperature of 625 °C. The subsystem efficiency data were obtained by García et al. (2014) using a combination of experimental measurements (e.g. thermal and electrical power outputs) and empirical models that were developed using experimental data from different prototype Stirling engines. In their experiments, the load was varied as a function of the working gas pressure. In Fig. 14.6b, brake efficiency (or brake thermal efficiency,  $\eta_{\text{br}}$ ) can be defined as shown in Eq. (14.4):

$$\eta_{\text{br}} = \eta_{\text{comb}} \cdot \eta_{\text{ind}} \cdot \eta_{\text{mech}} \quad (14.4)$$

The indicated cycle efficiency is around 40% irrespective of the load and is primarily a function of the working gas temperature (625 °C in this case). Higher working gas temperatures can enable better indicated efficiencies due to higher Carnot cycle efficiency. In addition, the mechanical efficiency plummets at the lower power levels, which indicates that lowering engine friction (e.g. employing a free-piston Stirling engine) and parasitic losses is crucial for obtaining higher engine efficiencies. In addition, reducing the parasitic losses in power converters and power electronics will also be a key enabler for improving fuel conversion efficiency. These are accounted for in the alternator efficiency. Finally, the combustor efficiency can also be improved by improving burner design, such as employing a recuperated burner for preheating air, and by lowering the convective heat losses from the burner system. A detailed discussion of the challenges in integrating an efficient combustion system with the Stirling engine is provided in Sect. 14.3.2.

One of the reasons why Stirling engines are considered better for micro-CHP applications is that they can run continuously at steady-state conditions without needing any maintenance over a long period of time. The estimated cost of 1-kW Stirling engine CHP systems is expected to be of the same order of magnitude as an equivalent ICE and thus faces a similar challenge in achieving high market penetration. For example, a study by Ferreira et al. (2016) estimates a total capital cost of 25,880 € for a solar-powered Stirling engine with an electrical power output of 3.65 kW for residential micro-CHP. As noted by Ashurst (2016), the Stirling engine system cost is only about 30% of the total installed cost to the customer.

### 14.2.3 Brayton Cycle and Micro Rankine Cycle Engines

Recuperated micro-turbines are the most common Brayton cycle engines employed for micro-CHP applications. As noted before, major technical hurdles for micro-turbines include high viscous losses in the turbine passages due to low Reynolds number flow, manufacturing tolerances, bearing limitations at high rotational speeds, high heat transfer, and high mechanical or parasitic losses. In addition, the cost associated in manufacturing a small-scale turbine with precision tolerances is also high.

One of the smallest micro-turbine systems, a prototype 3-kW system (15 kW thermal load) for CHP applications, was built by Micro Turbine Technology BV (MTT) and is being commercialized under the name EnerTwin (2018). One of the earlier prototype systems demonstrated 16% fuel-to-electrical conversion efficiency and 80% thermal efficiency (Visser et al. 2012). Figure 14.7, reproduced from Visser et al. (2011), shows energy losses for the 3 kW micro-turbine from an experimental rig test. The numbers reported in the schematic are a percentage of fuel energy. Much of the fuel energy is lost in the exhaust (47.0%) and the rest as heat losses, friction and parasitic loads (40.8%). The international standard atmosphere (ISA) corrected values for brake and electrical powers obtained in this study were 2.98 and 2.7 kW, respectively, yielding a high value of 91% for the alternator efficiency and 13.5% for the shaft efficiency. The study reports a fuel-to-electrical conversion efficiency of only 12.3% for a recuperated cycle gas turbine system. It is believed that further subsystem improvements and optimization have resulted in an improvement in fuel conversion efficiency (Visser et al. 2012). Since there is a

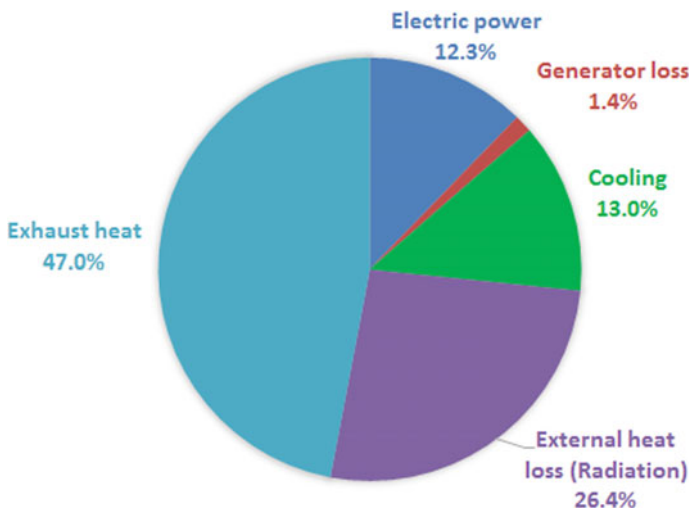


**Fig. 14.7** Typical energy losses (% of fuel energy) in a small-scale micro-turbine employing radial turbomachinery. Figure reproduced from Visser et al. (2011)

dearth of commercial technologies at this scale, the system life and product costs are uncertain at this point.

Micro-Rankine cycles are also employed for CHP applications but with much lower fuel-to-electrical conversion efficiencies of around 10–19% for 1–2.5 kW, as shown in Table 14.1. Again, the total CHP efficiency of such systems can exceed 90%. These applications are currently more suitable for replacing the household boiler. In addition, organic Rankine cycles (ORCs) are predominantly used as bottoming cycles for capturing the waste energy typically from an ICE.

### 14.3 Technical Opportunities and Challenges

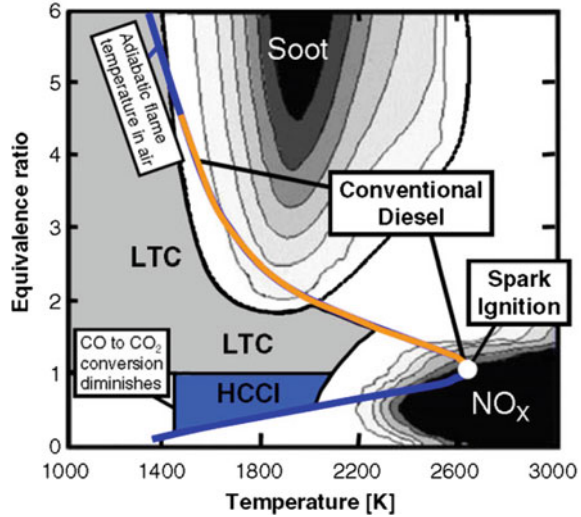
This section provides the technical opportunities and challenges for ICEs, Stirling engines, and Brayton cycle engines. The US Department of Energy, ARPA-E, initiated the GENerators for Small Electrical and Thermal Systems (GENSETS) program in 2015 (GENSETS 2018). The program is funding various mechanical and heat engine technologies with the goal of achieving 40% fuel-to-electrical conversion efficiency at 1-kW electrical output and is targeted primarily at residential CHP. Technical project highlights from the GENSETS program are included in the relevant sections.

#### 14.3.1 Internal Combustion Engines

For several decades, the ICE community has been developing low-temperature combustion (LTC) strategies such as homogenous charge compression ignition (HCCI), premixed charge compression ignition (PCCI), and high exhaust gas recirculation (EGR) LTC to achieve both high efficiency and mitigate  $\text{NO}_x$  and particulate matter (PM) emissions. Most of the LTC strategies however struggle with higher hydrocarbon (HC) and carbon monoxide (CO) emissions. Figure 14.8, reprinted from Dec (2009), shows the classic equivalence ratio ( $\Phi$ )–temperature ( $T$ ) plot overlaid with different combustion regimes. HCCI combustion has a fairly narrow operating range, and below an operating temperature of 1400 K, the conversion of CO to  $\text{CO}_2$  (through the reaction  $\text{CO} + \text{OH} \rightarrow \text{CO}_2 + \text{H}$ ) diminishes. It is also characterized by low soot and  $\text{NO}_x$  production, which makes it attractive for transportation and power generation applications. Since the operation regime is narrow and since HCCI combustion is characterized with high pressure rise rates (due to high charge homogeneity), transient and high load operation of HCCI engines are both challenging, and hence, HCCI is best suited for single-point or steady-state operation such as those seen in power generation engines and CHP applications.

Kobayashi et al. (2011) demonstrated 43.3% brake thermal efficiency and estimated a 40% fuel-to-electrical conversion efficiency for a 50-kW boosted NG

**Fig. 14.8**  $\Phi$ - $T$  plot showing HCCI and LTC combustion regimes with soot and  $\text{NO}_x$  islands (Dec 2009)

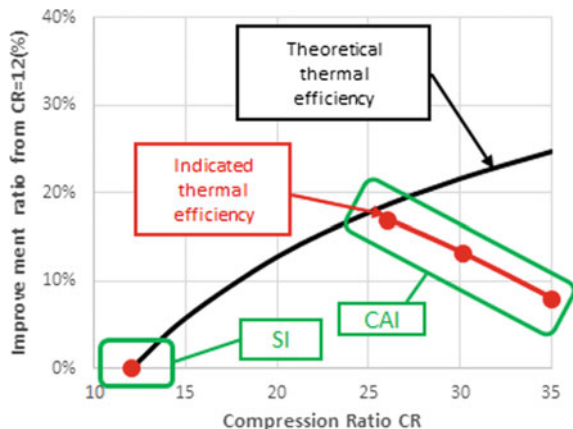


engine. The engine-out  $\text{NO}_x$  emission reported in their study, without employing an exhaust after-treatment device, was about 14 ppm. Optimizations of the compression ratio (CR) and boost pressure were performed to obtain high combustion efficiencies and low emissions of  $\text{NO}_x$  and CO. However, under high-efficiency operating conditions, the engine was also found to be sensitive to knocking. Dilution concepts such as high EGR LTC technologies predominantly reduce the heat transfer from the working fluid by operating at lower local temperatures (hence lower temperature gradients) and also by increasing the in-cylinder ratio of the specific heats ( $\gamma$ ) thus attaining higher fuel conversion efficiencies.

Caton (2014) published a study that shows potential pathways for attaining indicated efficiencies of over 50% and brake thermal efficiencies of over 45% by using a simple spark-ignited Otto cycle thermodynamic simulation for automotive engines. Key drivers for efficiency gain included increasing CR, reducing burn duration, lean engine operation (excess air ratio ( $\lambda$ )  $\sim 1.4$ ), and high EGR ( $\sim 45\%$ ). The model predicted a significant reduction in engine heat loss from 15.6% (baseline) to 5% of fuel energy. This improvement is predominantly attributed to lean combustion and high EGR operation. The main contributions to high engine efficiency were attributed to the increased ratio of specific heats and reduced in-cylinder heat transfer.

Killingsworth et al. (2011) operated a hydrogen–oxygen–argon engine and compared its performance with a hydrogen–air engine. The exhaust of the argon engine, which is composed of water vapor and argon, was condensed to recirculate the argon back into the engine intake as diluent. Since the  $\gamma$  of argon is 1.6, the hydrogen–oxygen–argon engine was more efficient than the hydrogen–air engine by about 10% points at a CR of 6. The hydrogen–oxygen–argon engine, however, could not be operated at higher CR as it was susceptible to engine knock caused by

**Fig. 14.9** Comparison of theoretical Otto cycle efficiency versus actual efficiency as a function of CR reproduced from Koga and Kiura (2013). The red line shows the effect of increasing surface area-to-volume ratio



higher local temperatures, which is again attributed to the high  $\gamma$  of the mixture. One of the issues with this approach is its limited application with hydrocarbon fuels, such as NG, as the separation of argon from the exhaust gases is challenging.

Another intriguing study by Koga and Kiura (2013) from Honda R&D Co. looked at the co-optimization of CR and stroke-to-bore ratio for increasing the efficiency for a small NG engine. This approach aimed at reducing heat transfer in, what they term as, the controlled autoignition (CAI) combustion mode (pseudonym for HCCI). It was observed that the engine efficiency improved by purely increasing the CR until a certain point (CR = 25 in their study) and then plummeted due to the subsequent high surface area-to-volume ratios (and hence high heat transfer losses), when the piston was at the top dead center. This is in sharp contrast to the monotonic increase in thermal efficiency ( $\eta_{th}$ ) that is expected from the classic Otto cycle relationship ( $\eta_{th} = 1 - 1/CR^{\gamma-1}$ ). This is illustrated in Fig. 14.9, which is reproduced from Koga and Kiura (2013).

In order to reduce the heat transfer, a simultaneous stroke-to-bore ratio optimization was also performed at a CR of 26, which reduced the surface area-to-volume ratio from 9.1 to 5.8 for a corresponding change in the stroke-to-bore ratio from 1 to 2.1. With a stroke-to-bore ratio of 2.1 and a CR of 26, the engine yielded a net brake thermal efficiency of 39.1%, which was 9.2% points higher than the baseline engine efficiency.

Gangopadhyay et al. (2012) investigated strategies to reduce engine friction using surface finishing and coating materials such as manganese-phosphate and diamond-like coating (DLC). In their study, a maximum of 17–25% friction improvement was seen at various speeds of engine operations. Further improvements could also be made with advanced lubrication technologies. To improve the efficiency of modern ICEs, Cheng et al. (2014) investigated individual lubricant formulations applicable to different engine subsystems yielding an optimum combination of lubricant formulations for the overall system. In their study, a mechanical efficiency improvement of over 5% was observed when operating a



16 hp Kohler twin cylinder diesel engine with different multi-grade oil formulations in the valvetrain and power cylinder subsystems. Furthermore, a friction improvement of over 10% was seen by altering the shear thinning characteristics of the lubricant in a motored valve train.

In terms of in-cylinder heat transfer reduction, there are numerous studies in the literature that employ thermal barrier coatings (TBCs), in an effort to mimic an adiabatic engine, with improved thermal efficiency. Parlak et al. (2005) investigated the effects of TBCs on the piston, cylinder head, and valves of a six-cylinder production diesel engine and only obtained a maximum of 2% improvement in brake thermal efficiency. However, the exhaust energy availability increased by about 3–27% depending on the operating speed and load. It was also noted that a maximum of 47% of the total exhaust energy could be extracted from an exergy standpoint. TBCs have been a long-standing topic of focus in the gas turbine industry; however, ICEs have not been able to completely leverage their advantage due to durability issues that arise from thermal cycling. The use of a bottoming cycle with a thermal barrier-coated ICE is a logical combination to yield high system efficiency.

Other recent technologies to improve brake thermal efficiency for small-scale ICEs include Miller cycle using variable valve timing (VVT) (Fontana and Galloni 2009), Atkinson cycle 10-kW ICE (Capaldi 2014), and free-piston engine linear generator (FPEG) (Kosaka et al. 2014; Goto et al. 2014). One-dimensional cycle simulation of the 10-kW Toyota FPEG (Kosaka et al. 2014; Goto et al. 2014) predicts a thermal efficiency of about 42% using a PCCI strategy.

In the ARPA-E GENSETS program, Wisconsin Engine Research Consultants, LLC (WERC), located in Madison, Wisconsin, USA, in collaboration with University of Wisconsin-Madison, Briggs and Stratton Corporation, and Adiabatics, Inc. is developing a 1-kW spark-assisted HCCI (SA-HCCI) engine (Reitz et al. 2018). The engine has a compression ratio of 17 and a stroke-to-bore ratio of 1.47 and is operated at stoichiometry with EGR dilution. SA-HCCI or spark-assisted compression ignition (SACI) uses a spark plug to initiate combustion, which subsequently leads to end-gas autoignition. In traditional HCCI, ignition is purely governed by chemical kinetics, and hence, achieving the optimum ignition timing at a particular speed and load is challenging. This is because the autoignition of the fuel-air mixture is very sensitive to initial, boundary, and in-cylinder conditions of temperature, pressure, and charge composition. In order to alleviate this problem, a spark plug is used in SACI, which provides the necessary control lever for initiating ignition. As of early 2018, the WERC team's engine has demonstrated a brake thermal efficiency of 34%. Figure 14.10 shows the pathway to 39% brake thermal efficiency and includes various updates, viz. improving cylinder head design, reducing incomplete combustion, reducing friction mean effective power (FMEP), and employing TBC. A three-way catalyst will be used for mitigating emissions of  $\text{NO}_x$ , CO, and HC. It is noted here that the next-generation Mazda SKYACTIV-X automotive engine will employ spark-controlled compression ignition (SPCCI), which is a variant of SACI (MAZDA: Next-generation technology 2018).

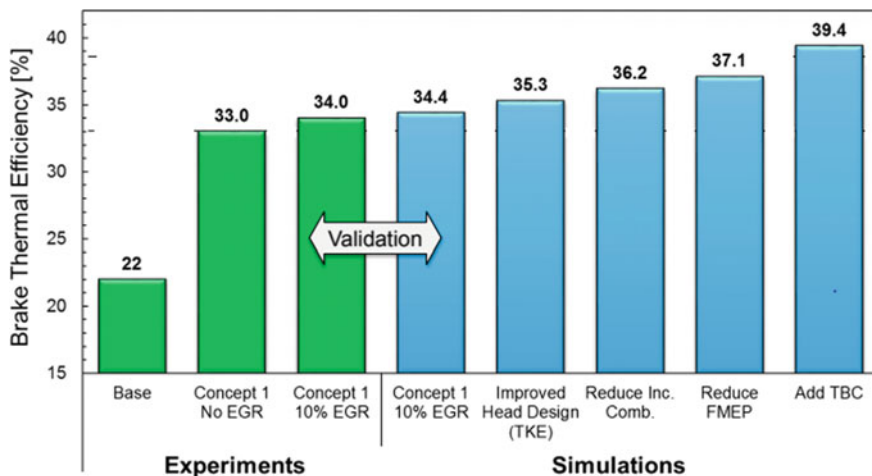


**Fig. 14.10** Technical pathway as proposed by WERC to achieve 39% brake thermal efficiency in a 1-kW ICE (Reitz et al. 2018)

Another project lead by Mahle Powertrain, LLC (Plymouth, Michigan, USA) in collaboration with Oak Ridge National Laboratory, IntelliChoice Energy, Kohler Engines, Louthan Engineering, and ExxonMobil has demonstrated, as of early 2018, a brake thermal efficiency of 32.5% at 1.7-kW brake power using their proprietary Mahle jet ignition (MJ) technology (Bunce 2018). MJ is a variant of turbulent jet ignition (TJI) technology and employs a prechamber, which is instrumented with a prechamber injector. A small quantity of fuel is injected in the prechamber where the combustion is initiated typically under rich conditions using a conventional spark plug. The resulting turbulent jets from the partially burned fuel-air mixture in the prechamber emanate into the main chamber through the prechamber nozzle. These jets act as local ignition sources for the main chamber fuel. NG is injected in the main chamber with the help of a port injector where the fuel-air mixture is kept lean. MJ is an enabling technology to extend the ICE lean limit operation, thus significantly improving the thermodynamic and brake thermal efficiencies. Other complementing technologies in this project include low-friction engine components and engine downspeeding for reducing the FMEP. For  $\text{NO}_x$ , CO, and methane emissions mitigation, the team will be employing a lean  $\text{NO}_x$  trap and a methane oxidation catalyst that is capable of operating at low exhaust gas temperatures. Figure 14.11a shows a CAD image of the MJ prechamber on the engine cylinder head, and Fig. 14.11b shows the first law energy breakdown that was achieved at a brake power of 1.7 kW and an excess air ratio ( $\lambda$ ) of 1.7.

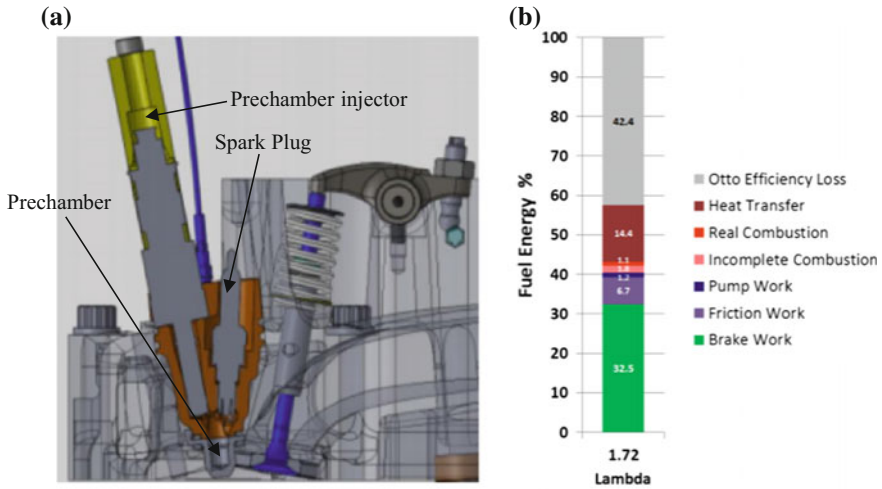


**Fig. 14.11** a CAD image of Mahle jet injection (MJ) technology and b first law energy breakdown for the MJ engine at a brake power of 1.7 kW and an excess air ratio of 1.7 (Bunce 2018)

### 14.3.2 Stirling Engines

One of the critical challenges in Stirling engines (and in other external combustion engines) is to achieve better heat transfer from the combusted fuel to the engine working fluid. The combustor efficiency ( $\eta_{comb}$ ) is a measure of effectiveness with which heat is transferred from the fuel to the Stirling engine working fluid. In order to evaluate the combustor efficiency, a simple steady-state modeling analysis was undertaken here. Consider a simple dome-shaped Stirling engine heater head design as shown in Fig. 14.12. Consider a simple NG burner mounted closely to the Stirling heater head, which is transferring heat to the Stirling engine heater head through radiation ( $Q_{rad}$ ) and convection ( $Q_{conv}$ ). Radiative heat transfer is assumed to occur between the flame and the heater head dome, while convective heat transfer is assumed to occur between the exhaust gases and the heater head along the length of the heater head. After exchanging heat with the Stirling engine, the exhaust gas is assumed to flow through a recuperator to heat the intake air for the burner (not shown in the figure). The working fluid (generally helium) is enclosed in the heater head, which performs expansion work on a power piston, which in turn drives a linear alternator to produce electricity (not shown in the figure). The details of the engine, combustion system, and the assumptions in the analysis are listed in Table 14.2. Note that the heater head dome temperature is intentionally kept at a lower temperature than the walls for preserving mechanical safety.

A steady-state energy balance analysis was performed on this recuperated burner-engine system using the parameters provided in Table 14.2. The fuel energy

**Fig. 14.12** Schematic of a simple burner and dome-shaped Stirling engine heater head configuration

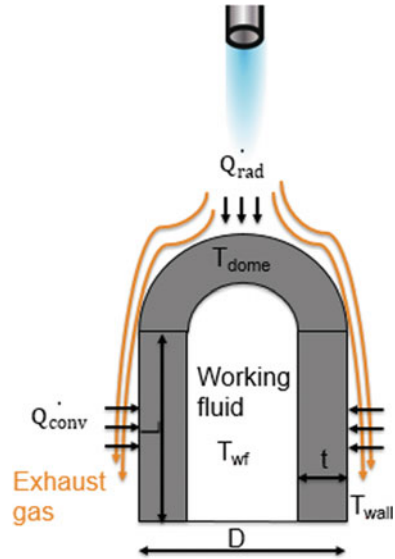


**Table 14.2** Assumptions and parameter values for Stirling engine heat transfer analysis

Parameter	Value
Burner diameter—inches	1
Diameter ( $D$ ) of heater head—mm	80–120
Length ( $L$ ) of heater head—mm	100–150
Thickness of heater head shell ( $t$ )—mm	4
Heater head wall temperature ( $T_{wall}$ )—°C	600–800
Heater head dome temperature ( $T_{dome}$ )—°C	$T_{wall} - 25$ °C
Recuperated air temperature—°C	500–615
Fuel (methane) temperature—°C	25
Excess air ratio ( $\lambda$ )	2.5
Turbulence intensity ( $Tu$ )	0.05 or 5%
Flame diameter ( $D_{flame}$ )—mm	$D + 10$ (assuming a hemispherical flame)
Heater head material and thermal conductivity ( $K_{HH}$ )—W/mK	IN718 and 23.2 at 750 °C
View factor ( $F_{12}$ ), where 1 denotes dome and 2 denotes flame	1 (Incropera and DeWitt 2002)
Emissivity of heater head material ( $\epsilon_1$ )	0.33 (Keller et al. 2015)
Emissivity of non-luminous flame ( $\epsilon_2$ )	0.20 (Sherman 1934)
Recuperator effectiveness	0.9
Heat to mechanical work efficiency of Stirling engine	65% of Carnot efficiency ( $\eta_C$ ) operating between working fluid temperature ( $T_{wf}$ ) and a cold side temperature of 60 °C
Mechanical work to electrical work efficiency or power converter efficiency ( $\eta_{pc}$ )	0.9

that is burned is used to transfer heat to the Stirling engine via convection and radiation, and the remaining energy is carried away by the exhaust gases, which is recuperated for heating the intake air from an initial temperature of 25 °C with an effectiveness of 90%. An excess air ratio of 2.5 was chosen to achieve a peak adiabatic flame temperature ( $T_{\text{flame}}$ ) below 1500 °C to mitigate  $\text{NO}_x$  emissions and to alleviate thermal stresses on the heater head material. For simplicity, the fuel was assumed to be methane (surrogate for NG), the burned gas temperature was assumed to be the same as the adiabatic flame temperature, and the exhaust gas was assumed to have the properties of nitrogen. Temperature-dependent specific heat properties were used in the analysis for the exhaust gases.

Radiation heat transfer was assumed between the flame and the heater head dome. Both the flame and dome were assumed to be concentric hemispheres, and radiation heat transfer (Watts) was calculated using Eq. (14.5) (Incropera and DeWitt 2002). In Eq. (14.5),  $A_{\text{dome}}$  is the surface area of the heater head dome hemisphere and  $\sigma$  is the Stefan–Boltzmann constant.

$$\dot{Q}_{\text{rad}} = \frac{\sigma \cdot A_{\text{dome}} \cdot (T_{\text{flame}}^4 - T_{\text{dome}}^4)}{\left[ \frac{1}{\varepsilon_1} + \left( \frac{1 - \varepsilon_2}{\varepsilon_2} \right) \cdot \left( \frac{D}{D_{\text{flame}}} \right)^2 \right]} \quad (14.5)$$

Convection heat transfer was assumed between the exhaust gases and cylindrical portion of the heater head. The turbulent Nusselt number (Nu) correlation, as shown in Eq. (14.6), was used in this case, which is applicable to a flame impinging in a direction normal to a hemi-nosed cylinder in parallel flow (Baukal and Gebhart 1996). The Reynolds number (Re) was calculated using the exhaust gas velocity, dome diameter (characteristic diameter for the flow), and burned gas properties that were evaluated at the burned gas temperature. The exhaust gas velocity was calculated using the exhaust mass flow rate (which is the sum of fuel and air mass flow rates), density of the burned gas, and the burner diameter.

$$\text{Nu} = \text{Re}^{0.5} \left[ 0.993 + 5.465 \left( \frac{\text{Tu} \cdot \text{Re}^{0.5}}{100} \right) - 2.375 \left( \frac{\text{Tu} \cdot \text{Re}^{0.5}}{100} \right)^2 \right] = \frac{h \cdot D}{K_{\text{gas}}} \quad (14.6)$$

The convection heat transfer coefficient ( $h$ ) was obtained by calculating the Nusselt number, heater head diameter ( $D$ ), and thermal conductivity of the burned gas ( $K_{\text{gas}}$ ), which was evaluated at the burned gas temperature. The convective heat transfer to the heater head surface was then calculated using Eq. (14.7) where  $A_{\text{cyl}}$  is the area of the cylinder and  $T_b$  is the burned gas temperature.

$$\dot{Q}_{\text{conv}} = h \cdot A_{\text{cyl}} \cdot (T_b - T_{\text{wall}}) \quad (14.7)$$

At steady-state conditions, the conductive heat transfer rate through the heater head surface was assumed to be equal to the sum of radiative and convective heat transfer rates as shown in Eq. (14.8). For simplicity, the working fluid was assumed

to be at the heater head inner wall temperature. Thus, by knowing the working fluid temperature from Eq. (14.8), the Carnot efficiency of the engine can be obtained. The Stirling engine heat to mechanical work efficiency ( $\eta_{\text{ind}}$ ) is then obtained from Eq. (14.9), which is assumed to be 65% of the Carnot efficiency (state-of-the-art Stirling engines are typically capable of achieving  $\sim 50\%$  of Carnot efficiency). The expression for the combustor efficiency ( $\eta_{\text{comb}}$ ) is shown in Eq. (14.10), which is obtained from the ratio of the heat transferred to the Stirling engine working fluid to the fuel energy. The fuel energy is calculated using the methane flow rate ( $m_{\text{fuel}}$ ) and methane LHV. The product of the combustor efficiency ( $\eta_{\text{comb}}$ ), engine heat to mechanical work efficiency ( $\eta_{\text{ind}}$ ), and the power converter efficiency ( $\eta_{\text{pc}}$ ) gives the Stirling engine fuel-to-electrical conversion efficiency as shown in Eq. (14.11).

$$\dot{Q}_{\text{rad}} + \dot{Q}_{\text{conv}} = -K_{\text{hh}} \cdot (A_{\text{cyl}} + A_{\text{dome}}) \cdot (T_{\text{wall}} - T_{\text{wf}}) \quad (14.8)$$

$$\eta_{\text{ind}} = 0.65 \cdot \left( 1 - \frac{60 + 273.15}{T_{\text{wf}} + 273.15} \right) \quad (14.9)$$

$$\eta_{\text{comb}} = \frac{\dot{Q}_{\text{rad}} + \dot{Q}_{\text{conv}}}{m_{\text{fuel}} \cdot \text{LHV}} \quad (14.10)$$

$$\eta_{\text{e}} = \eta_{\text{comb}} \cdot \eta_{\text{ind}} \cdot \eta_{\text{pc}} \quad (14.11)$$

Figures 14.13, 14.14, 14.15, and 14.16 show the sensitivity of the combustor efficiency and fuel-to-electrical conversion efficiency for the Stirling engine with respect to the air temperature at recuperator outlet location (Fig. 14.13), heater head area by varying the heater head dome diameter (Fig. 14.14), heater head area by varying the heater head length (Fig. 14.15), and heater head surface temperature ( $T_{\text{wall}}$ ) (Fig. 14.16). The black lines with closed square symbols in the figures show the efficiencies when both convection and radiation heat transfer are taken into account, while the black lines with closed circle symbols show the efficiencies with only convection heat transfer (i.e. neglecting radiative heat transfer).

As shown in Fig. 14.13, a higher degree of recuperation is a critical requirement to achieve a high combustor efficiency and hence a high fuel-to-electrical conversion efficiency. Increasing the area by increasing the length of the heater head (Fig. 14.15) leads to better heat transfer than that achieved by increasing the diameter of the heater head (Fig. 14.14). As expected, the effect of radiation is more pronounced by varying the diameter than by varying the heater head length. The increase in heater head temperature and its effect on the efficiencies show an interesting and perhaps counterintuitive trend (Fig. 14.16). Under the assumptions in Table 14.2, an increase in heater head temperature up to 700 °C is effective for improving the fuel-to-electrical conversion efficiency. Any further increase in heater head temperature results in a decrease in fuel-to-electrical conversion efficiency, as shown in Fig. 14.16b. This is because the combustor to Stirling engine heat transfer rate reduces with an increase in the heater head temperature, as shown in

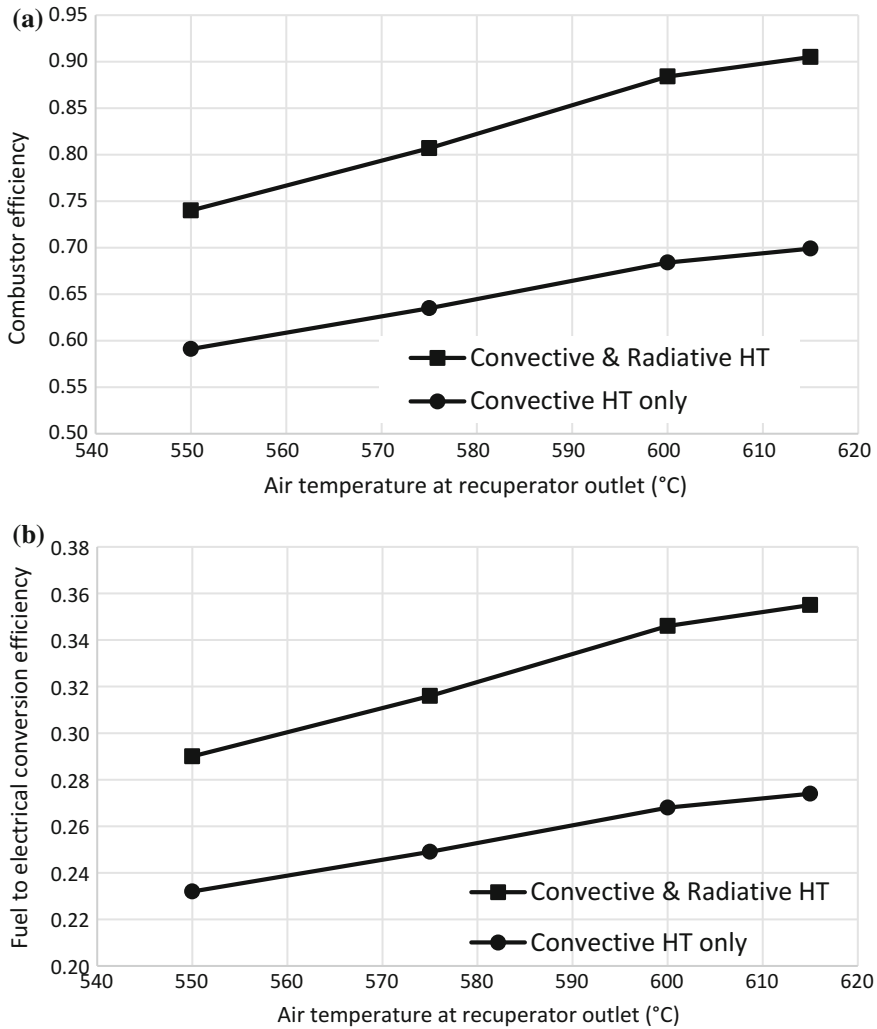


**Fig. 14.13** Sensitivity with respect to recuperator air outlet temperature for **a** combustor efficiency and **b** fuel-to-electrical conversion efficiency

Fig. 14.16a (due to reduced  $\Delta T$  between the burned fuel temperature and heater head temperature). The black dashed line with open symbols in Fig. 14.16a shows the Stirling engine heat to electrical conversion efficiency, which increases with an increase in heater head temperature. This is expected as the Carnot efficiency is expected to increase with an increase in the heater head temperature (see Eq. 14.9). The 700 °C point therefore represents an inflection point where the reduction in combustor efficiency can be compensated by the increase in the Carnot efficiency of the engine. Beyond this point, any increase in Carnot efficiency is not sufficient to

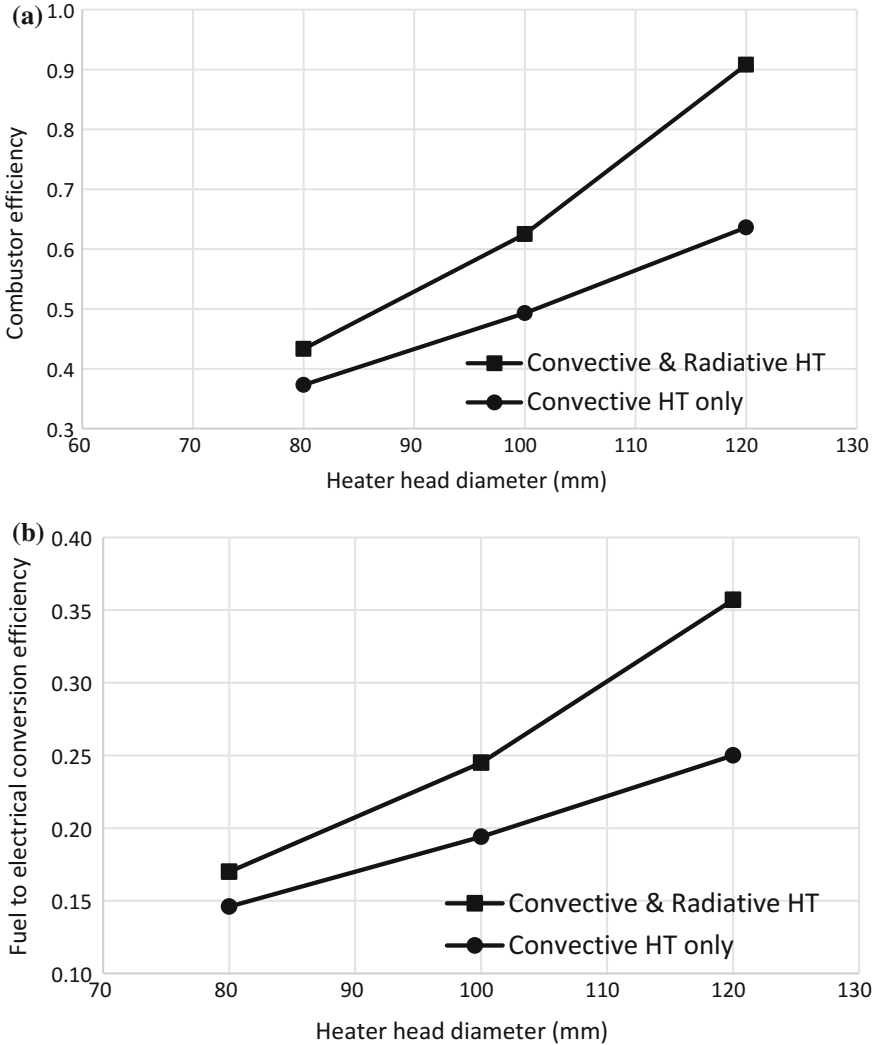


**Fig. 14.14** Sensitivity with respect to heater head diameter for **a** combustor efficiency and **b** fuel-to-electrical conversion efficiency

overcome the loss in the combustor efficiency. Note that for the scenarios in Fig. 14.16, the air temperature at the recuperator outlet was maintained fairly constant and limited to 575 °C (due to material limits), which lead to higher exhaust temperatures for scenarios with heater head temperatures greater than 700 °C. Thus, this results in lower combustor efficiencies for scenarios with heater head temperatures greater than 700 °C when compared to scenarios with heater head temperatures lower than 700 °C. Thus, the design of a combustion-driven Stirling engine



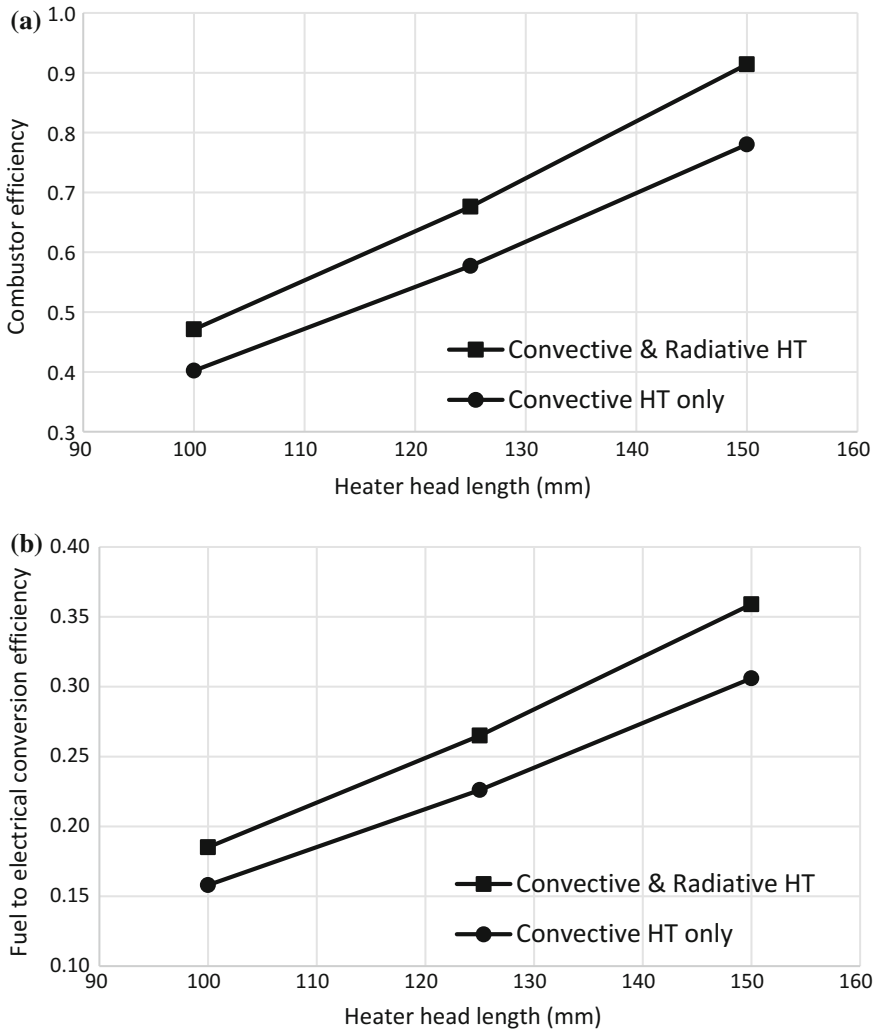


**Fig. 14.15** Sensitivity with respect to heater head length for **a** combustor efficiency and **b** fuel-to-electrical conversion efficiency

is extremely challenging and a rigorous system-level approach, which must include the co-optimization of the combustion system and the Stirling engine (rather than individual component optimization), is necessary. Radiative heat transfer is also critical for achieving a high combustor and engine efficiency for dome-shaped heater head Stirling engines.

Li et al. (2014) published a modeling study of a high-efficiency Stirling engine that showed a potential to achieve 43.9% indicated thermal efficiency while delivering a low indicated power of 33.4 W (1.88 W/cm<sup>3</sup>). The system takes

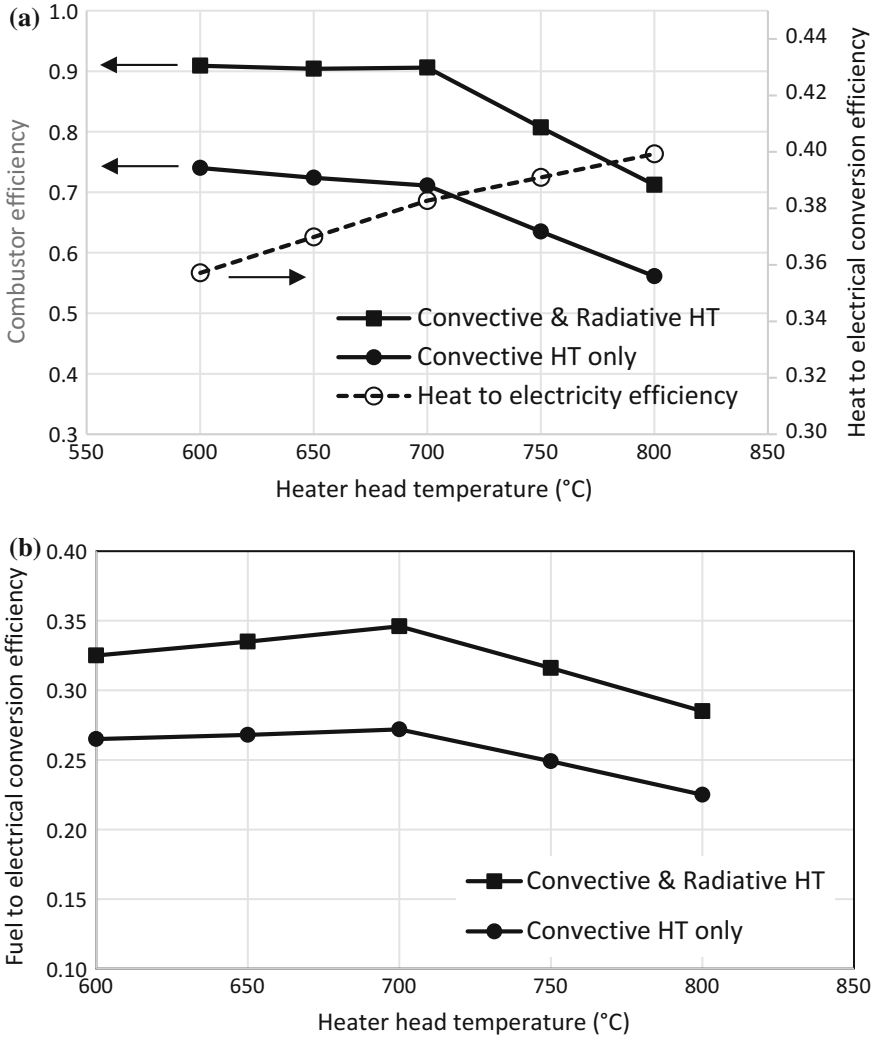


**Fig. 14.16** Sensitivity with respect to heater head wall temperature for **a** combustor efficiency and **b** fuel-to-electrical conversion efficiency

advantage of a compact porous sheet heat exchanger, which incorporates the heater, regenerator, and cooler into one assembly; the hypothesis for this approach was that a significant reduction in friction could be achieved with such a system. The major benefits of using micro-channels include reduction in flow separation and formation of wakes, low surface roughness, lower flow velocities, and lower conduction heat losses. However, this requires radical improvements in emerging micro-fabrication technologies for mass production of such heat exchangers.

Recent efforts have focused on fabricating Stirling engine components by additive manufacturing (AM) in order to increase efficiency. This is a powerful manufacturing process that can yield complex and intricate geometries, not possible by traditional manufacturing methods. In addition to increasing the effectiveness of the heat exchange process, the interfacial heat transfer losses, e.g. between the burner and the heat acceptor interface, are also projected to be minimized by additively manufacturing a single unit without using conventional joining techniques. As reported by Zelinski in *Additive Manufacturing Magazine* (*Additive Manufacturing* 2015), DEKA Research and Development is currently investigating the use of additively manufactured components, e.g. burner and Stirling engine heater head, to improve engine efficiency. Figure 14.17a, reprinted from *Additive Manufacturing* (2015), shows the additively manufactured heater head from Inconel 625 material (Stirling engine heater head on the left), which is traditionally used for high-temperature applications. DEKA is also working on additively manufacturing heater heads with Mar-M-247, which is superior in retaining high-temperature strength as compared to Inconel 625. Figure 14.17a shows also the conventional

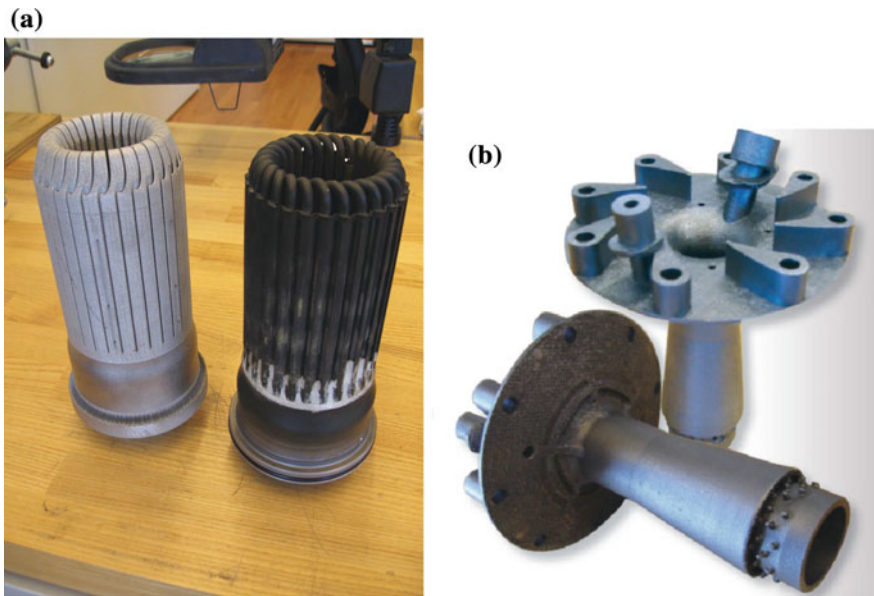


**Fig. 14.17** **a** Additively manufactured Stirling engine heater head (left) and conventional tubular heater head (right) and **b** additively manufactured Stirling engine burner (*Additive Manufacturing* 2015) manufactured by DEKA Research and Development. Originally appeared in *Additive Manufacturing Magazine*, copyright 2015 Gardner Business Media, Inc. Used with permission

heater head (on the right) which has tubes to carry the working fluid (e.g. helium) that are bent and welded at numerous places. This heater head design is called the tubular heater head. The custom shape of the fluid passages in the additively manufactured heater head is expected to better capture the heat of combustion than the conventional version of the heater head. The burner sits at the center of the heater head transferring heat to the working fluid that flows inside the tubes. One of the well-known traditional disadvantages of AM is the resulting surface roughness of the end product. As surface roughness accelerates the transition from laminar to turbulent flow, the heat transfer to the working fluid inside the tubes is also expected to be improved (Additive Manufacturing 2015). Figure 14.17b, reprinted from Additive Manufacturing (2015), shows an additively manufactured Stirling engine burner throat, where the tear-drop flanges help in fuel–air mixing, while the spout end of the burner holds a stable flame at the center of the heater head.

Song et al. (2015) achieved better heat transfer in a tubular heater head Stirling engine, similar to the one shown in Fig. 14.17a, by employing steel wool into the space between the outside of the tubes for recuperating exhaust gas energy. As expected, the steel wool resulted in increased surface area for heat transfer. In addition, the steel wool had a higher emissivity than the exhaust gas, which resulted in enhanced heat transfer between the exhaust gases and the outer surface of the tubes. The porosity of the steel wool was varied in their experiments, and it was found that the convection heat transfer coefficient ( $h$ ) increased with decreasing porosity at a constant exhaust gas velocity. However, in a typical NG-fired Stirling engine, the additional pressure drop created by the low porosity steel wool can result in higher parasitic power for the fuel and air blowers. Thus, a tradeoff in the system efficiency is expected, which will be governed primarily by improved heat transfer and a concomitant increase in parasitic power. More recently, a detailed summary of the technical challenges of Stirling engine systems has been published by Hachem et al. (2018).

Sunpower, Inc. (Athens, Ohio, USA), in collaboration with Aerojet Rocketdyne and Precision Combustion, Inc. has developed a free-piston Stirling engine (FPSE) with a recuperated two-stage catalytic combustor under the ARPA-E GENSETS program (Wood 2018). As of early 2018, the engine demonstrated a fuel-to-electrical conversion efficiency of 20.5% with a peak heat to electrical conversion efficiency of 38.8% and a peak combustor efficiency of 64%. The output power of the engine is lower than 1 kW. Further improvements in recuperator sizing and recuperator heat loss reduction are required to improve the system efficiency. Figure 14.18 shows the assembled prototype Stirling engine system (Wood 2018) that was developed by Sunpower, Inc. under the ARPA-E GENSETS program.

West Virginia University Research Corporation (WVURC) located in Morgantown, West Virginia, USA, is currently developing an additively manufactured Stirling engine heater head design under the ARPA-E GENSETS program (Qiu 2018). A computational study of the heat transfer in a stainless steel Stirling engine heater head was recently published by this team (Solomon and Qiu 2018).

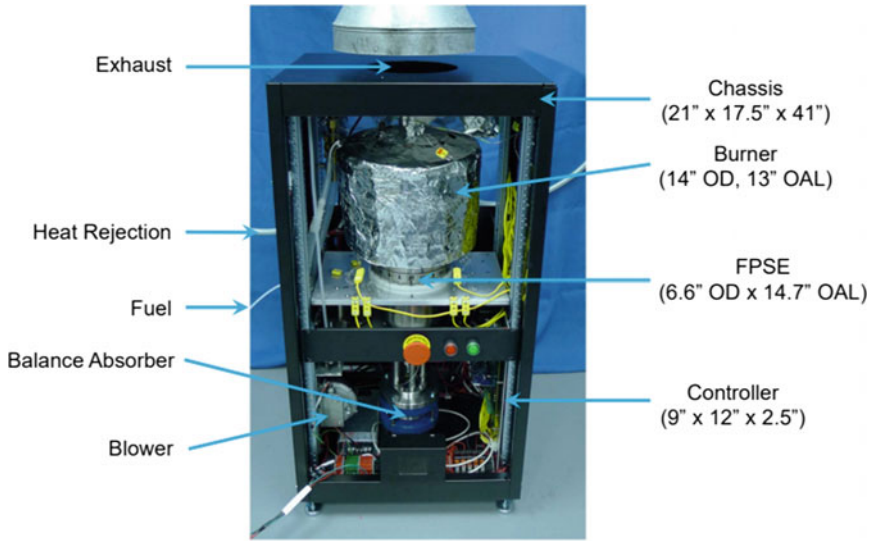


Fig. 14.18 Prototype Stirling engine system developed by Sunpower, Inc. (Wood 2018)

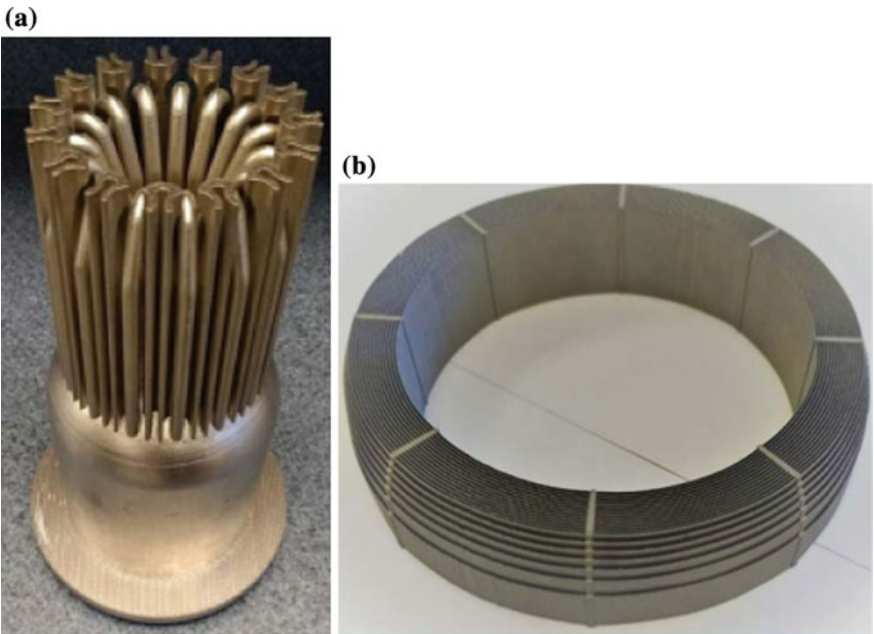
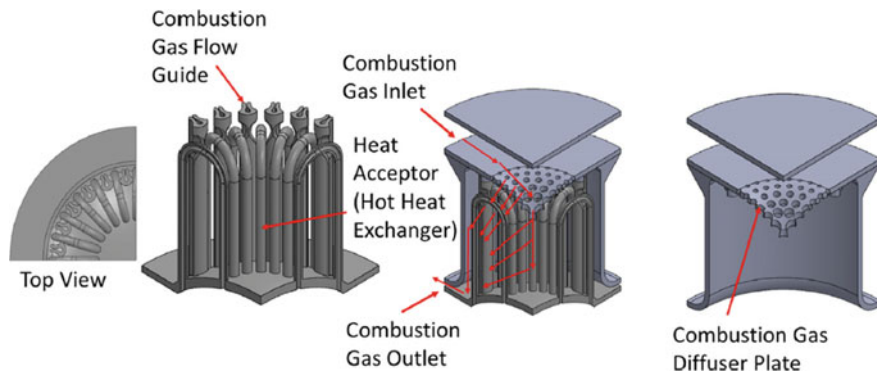


Fig. 14.19 a Image of the additively manufactured Stirling engine heater head design and b additively manufactured involute foil regenerator developed by West Virginia University (Qiu 2018)



**Fig. 14.20** Flow path of the exhaust gas through the additively manufactured heater head design developed by West Virginia University (Solomon and Qiu 2018)

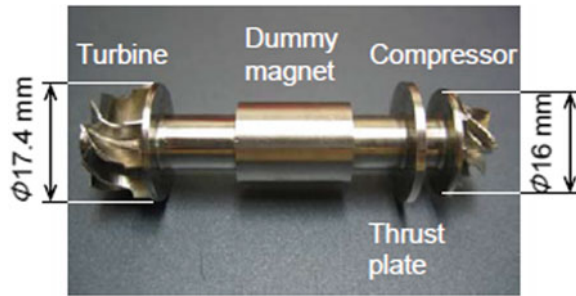
Figure 14.19a, reprinted from Qiu (2018), shows the additively manufactured heater head design, and Fig. 14.19b, reprinted from Qiu (2018), shows the additively manufactured involute foil regenerator (the regenerator is an internal heat exchanger in a Stirling engine, which stores thermal energy from the working fluid that would otherwise be rejected at the cold end of the engine and supplies that energy back to the working fluid in the next thermodynamic cycle when the working fluid shuttles to the hot end of the engine). Both designs are expected to improve the Stirling engine fuel-to-electrical conversion efficiency. Figure 14.20, reprinted from Solomon and Qiu (2018), shows the flow path of the combustion gas in the Stirling engine heater head. The combustion gas guides are provided for improving heat transfer with the tubes. The vented diffuser plate was used to provide uniform distribution of the hot combustion gas over the tubular heat exchanger.

### 14.3.3 Brayton Cycle Engines

It is more challenging for Brayton cycle engines, particularly with conventional radial turbomachinery, to be efficient at small scales due to significant flow and heat transfer losses. At the 1–10 kW scale, Brayton engines are arguably less mature than ICEs and Stirling engines.

McDonald and Rogers (2008) investigated the use of a ceramic micro-turbine concept with a ceramic combustor, ceramic radial flow turbine, and a ceramic (silicon carbide) high-effectiveness recuperator. Projected efficiency for such a system was 30% while delivering a peak power of 7.5 kW. Tanaka et al. (2007) tested what they claimed as the world's smallest turbine operating on a Brayton cycle. The engine comprised of a compressor with an impeller diameter of 16 mm, a turbine with a diameter of 17.4 mm, an annular swirl flow combustor, and a

**Fig. 14.21** World's smallest micro-turbine Brayton cycle engine reprinted from the work of Tanaka et al. (2007)



dummy electromagnetic generator. The rotor was supported with pressurized gas bearings. An image of this turbine hardware is shown in Fig. 14.21, which is reprinted from their work. The compressor was seen to approach the design adiabatic efficiency at 55% and 70% of the rated speed (580,000 rpm).

Under the ARPA-E GENSETS program, Brayton Energy, LLC (Hampton, New Hampshire, USA), is developing a rotary screw Brayton cycle engine with metallic screw compressors and ceramic screw expanders. Screw components do not suffer from flow losses that are present in conventional radial turbomachinery. In addition, the use of a ceramic expander with low coefficient of thermal expansion can lead to high-temperature tolerance and a better fuel-to-electrical conversion efficiency due to higher Carnot efficiency. A highly recuperated combustor will be used in this project. As of early 2018, Brayton Energy has demonstrated a 75% isentropic efficiency for the compressor when operated with a rotor clearance of  $68\mu$  (Kesseli et al. 2018). Figure 14.22a, b shows the coated screw compressor and ceramic rotary screw expander, respectively, developed by Brayton Energy under the ARPA-E GENSETS program (Kesseli 2018; Kesseli et al. 2018).

Metis Design Corporation (MDC), located in San Francisco, California, USA, in collaboration with Lawrence Berkeley National Laboratory (LBNL), Brayton Energy, LLC, and University of Texas—Arlington is developing a 1-kW micro-turbine with a compressor and a rotary vaneless diffuser (RVD) under the GENSETS program. The RVD rotates at a much lower speed compared to the compressor impeller and reduces the kinetic energy losses of the flow that exits at a high speed from the impeller. A recuperated low swirl burner is intended to be integrated with the micro-turbine. Figure 14.23 shows the compressor hardware with the impeller and the RVD (Keogh et al. 2018). As of early 2018, the team has demonstrated approximately 75% isentropic efficiency for the compressor at 50% of the impeller design speed (Keogh et al. 2018).

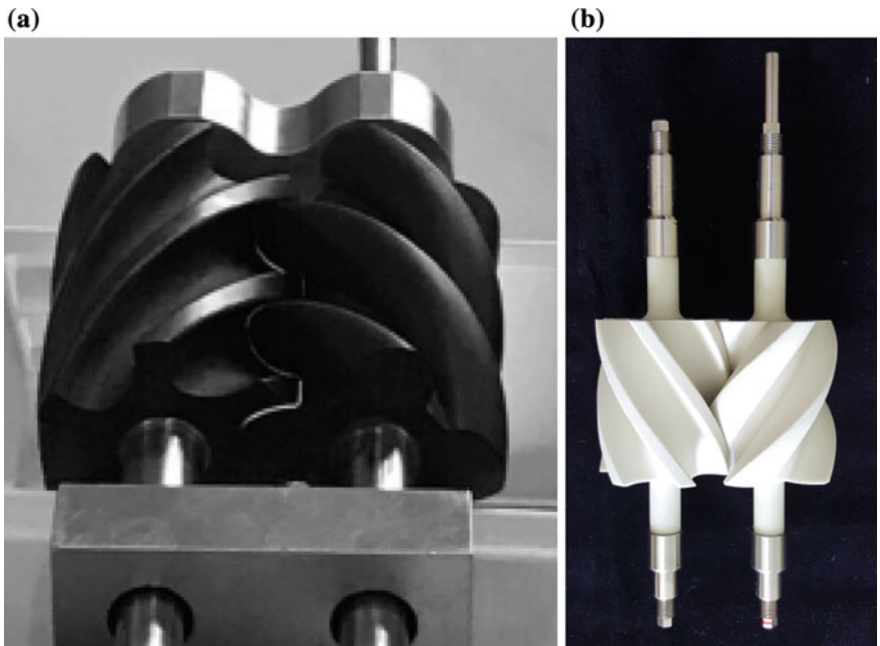


**Fig. 14.22** **a** Coated screw compressor (Kesseli et al. 2018) and **b** ceramic rotary screw expander (Kesseli 2018) as developed by Brayton Energy

**Fig. 14.23** Micro-turbine impeller and RVD as developed by MDC (Keogh et al. 2018)





## 14.4 Summary

This chapter presented a detailed review of the state-of-the-art residential CHP technologies encompassing reciprocating internal combustion engines (ICEs), Stirling engines, Brayton cycle engines, and micro-Rankine cycle engines. This was complemented by anecdotal highlights from some of the cutting-edge technologies funded by Advanced Research Projects Agency-Energy (ARPA-E). From a fuel conversion efficiency and load-following standpoint, reciprocating ICEs are considered to have the most benefits, but have some disadvantages such as regular maintenance (oil change, part replacement, etc.). Heat transfer, incomplete combustion, pumping, and friction losses at the small scale are found to be the technical hurdles for ICEs. Thus, technologies such as spark-assisted homogeneous charge compression ignition (SA-HCCI), turbulent jet ignition (TJI), and low-friction components are identified as potential enabling approaches for improving fuel conversion efficiency. Additionally, Stirling engines and Brayton cycle engines offer excellent fuel flexibility and hence are more resistant to the quality of NG as compared to ICEs.

Stirling engines have demonstrated lower fuel conversion efficiency compared to ICEs, but they can operate without maintenance for a significant amount of time. One of the biggest hurdles for improving Stirling engine fuel conversion efficiency is to achieve effective heat transfer between the combusting fuel and the working fluid of the engine. Radiation heat transfer and a high degree of intake air recuperation are found to be key mechanisms for enhancing heat transfer in dome-shaped Stirling engines. Additive manufacturing is considered to be one of the key enablers for improving tubular heater head Stirling engine efficiency by enhancing heat transfer through unique designs that are complex to fabricate by conventional manufacturing processes. Irrespective of the Stirling engine heater head design, a co-optimization of the combustion system and the Stirling engine is necessary for improving their fuel conversion efficiency.

Brayton cycle machines are the least mature technology at the 1–10 kW size as evidenced by the availability of just one commercial 3-kW micro-turbine product. Brayton cycle engines have also demonstrated lower efficiencies compared to ICEs. Challenges include achieving high compressor and expander isentropic efficiencies at the small power level.

Finally, the most important driver for customer adoption is the total installed cost of the micro-CHP system (Vishwanathan et al. 2018) and the system must be simple to install and maintain.

## References

- Additive Manufacturing—Aug 2015, <https://am.epubxp.com/i/542042-aug-2015/6>. Last Accessed 26 July 2018
- Aisin 1.5 kW internal combustion engine CHP. ARPA-E GENSETS Annual Program Review Meeting, Denver, CO, U.S (2016). URL: [https://arpa-e.energy.gov/sites/default/files/Sekihisa\\_Aisin.pdf](https://arpa-e.energy.gov/sites/default/files/Sekihisa_Aisin.pdf)

- Ashurst S (2016) Insights on the global micro-CHP market. ARPA-E GENSETS Annual Review Meeting, Denver, CO, U.S. URL: [https://arpa-e.energy.gov/sites/default/files/Ashurst\\_DeltaEE.pdf](https://arpa-e.energy.gov/sites/default/files/Ashurst_DeltaEE.pdf)
- Ashurst S (2018) E-mail Communication, 12 March 2018
- Barbieri ES, Spina PR, Venturini M (2012) Analysis of innovative micro-CHP systems to meet household energy demands. *Appl Energy* 97:723–733. <https://doi.org/10.1016/j.apenergy.2011.11.081>
- Baukal CE, Gebhart B (1996) A review of empirical flame impingement heat transfer correlations. *Int J Heat Fluid Flow* 17:386–396. [https://doi.org/10.1016/0142-727X\(96\)00003-3](https://doi.org/10.1016/0142-727X(96)00003-3)
- Bunce M (2018) Advanced lean burn micro-CHP GENSET. GENSETS Annual Program Review Meeting, Washington, DC, U.S. URL: [https://arpa-e.energy.gov/sites/default/files/8\\_Bunce-MPT\\_GENSETS\\_Annual\\_Review\\_3-2018.pdf](https://arpa-e.energy.gov/sites/default/files/8_Bunce-MPT_GENSETS_Annual_Review_3-2018.pdf)
- Capaldi P (2014) A high efficiency 10 kW microcogenerator based on an Atkinson cycle internal combustion engine. *Appl Therm Eng* 71:913–920. <https://doi.org/10.1016/j.applthermaleng.2014.02.035>
- Carbon Flow Charts, <https://flowcharts.llnl.gov/commodities/carbon>. Last Accessed 14 July 2018
- Caton JA (2014) On the importance of specific heats as regards efficiency increases for highly dilute IC engines. *Energy Convers Manage* 79:146–160. <https://doi.org/10.1016/j.enconman.2013.12.020>
- Cheng W, Wong V, Plumley M, Martins T, Molewyk M, Gu G, Park S-Y (2014) Lubricant formulations to enhance engine efficiency in modern internal combustion engines, 2014 annual merit review, vehicle technologies office. U.S. Department of Energy, Washington, DC, U.S. Climate Zones|Department of Energy, <https://www.energy.gov/eere/buildings/climate-zones>. Last Accessed 15 July 2018
- CP5WN Model CP5WN CP5WN-SNB CP5WN-SPB, <http://www.yanmar-es.com/wp-content/uploads/CP5WN-Spec-Sheet.pdf>. Last Accessed 16 July 2018
- CP10WN, <http://www.yanmar-es.com/wp-content/uploads/CP10WN-Spec-Sheet.pdf>. Last Accessed 16 July 2018
- Cullen B, McGovern J (2010) Energy system feasibility study of an Otto cycle/Stirling cycle hybrid automotive engine. *Energy* 35:1017–1023. <https://doi.org/10.1016/j.energy.2009.06.025>
- Dec JE (2009) Advanced compression-ignition engines—understanding the in-cylinder processes. *Proc Combust Inst* 32:2727–2742. <https://doi.org/10.1016/J.PROCI.2008.08.008>
- De Paepe M, D’Herdt P, Mertens D (2006) Micro-CHP systems for residential applications. *Energy Convers Manage* 47:3435–3446. <https://doi.org/10.1016/j.enconman.2005.12.024>
- EIA recs, <https://www.eia.gov/consumption/residential/data/2015/hc/php/hc1.1.php>. Last Accessed 14 July 2018
- Energy Flow Charts, <https://flowcharts.llnl.gov/>. Last Accessed 14 July 2018
- Ferreira AC, Nunes ML, Teixeira JCF, Martins LASB, Teixeira SFCF (2016) Thermodynamic and economic optimization of a solar-powered stirling engine for micro-cogeneration purposes. *Energy* 111:1–17. <https://doi.org/10.1016/J.ENERGY.2016.05.091>
- Fontana G, Galloni E (2009) Variable valve timing for fuel economy improvement in a small spark-ignition engine. *Appl Energy* 86:96–105. <https://doi.org/10.1016/j.apenergy.2008.04.009>
- Fubara TC, Cecelja F, Yang A (2014) Modelling and selection of micro-CHP systems for domestic energy supply: the dimension of network-wide primary energy consumption. *Appl Energy*. <https://doi.org/10.1016/j.apenergy.2013.09.069>
- Gangopadhyay A, Mcwatt DG, Zdrodowski RJ (2012) Engine friction reduction through surface finish and coatings. In: Conference on directions in engine efficiency and emissions research (DEER), Dearborn, MI, U.S. URL: [https://www1.eere.energy.gov/vehiclesandfuels/pdfs/deer\\_2012/friday/presentations/deer12\\_gangopadhyay.pdf](https://www1.eere.energy.gov/vehiclesandfuels/pdfs/deer_2012/friday/presentations/deer12_gangopadhyay.pdf)
- García D, González MA, Prieto JI, Herrero S, López S, Mesonero I, Villasante C (2014) Characterization of the power and efficiency of stirling engine subsystems. *Appl Energy* 121:51–63. <https://doi.org/10.1016/j.apenergy.2014.01.067>

- GENSETS, <https://arpa-e.energy.gov/?q=arpa-e-programs/gensets>. Last Accessed 21 July 2018
- Goto S, Moriya K, Kosaka H, Akita T, Hotta Y, Umeno T, Nakakita K (2014) Development of free piston engine linear generator system Part 2—investigation of control system for generator. SAE technical paper 2014-01-1193. <https://doi.org/10.4271/2014-01-1193>
- Guyer E (2015) First-hand experience with residential micro-CHP in the United States: status and challenges. ARPA-E GENSETS Program Kickoff Meeting, Chicago, IL, U.S. URL: [https://arpa-e.energy.gov/sites/default/files/Guyer\\_YankeeScientific\\_GENSETS.pdf](https://arpa-e.energy.gov/sites/default/files/Guyer_YankeeScientific_GENSETS.pdf)
- Guyer E (2016) Micro-CHP demonstration planning. A report prepared for U.S. Department of Energy, ARPA-E
- Hachem H, Gheith R, Aloui F, Ben Nasrallah S (2018) Technological challenges and optimization efforts of the stirling machine: a review. *Energy Convers Manag* 171:1365–1387. <https://doi.org/10.1016/J.ENCONMAN.2018.06.042>
- Honda Worldwide|Power products—household gas engine cogeneration unit, <http://world.honda.com/power/cogenerator/>. Last Accessed 14 July 2018
- <https://www.mtrigen.com/>, Last Accessed 11 Aug 2018
- Incropera FP, DeWitt DP (2002) *Fundamentals of heat and mass transfer*, 5th edn. Wiley, Hoboken, NJ, U.S.
- Keller BP, Nelson SE, Walton KL, Ghosh TK, Tompson RV, Loyalka SK (2015) Total hemispherical emissivity of Inconel 718. *Nucl Eng Des* 287:11–18. <https://doi.org/10.1016/j.nucengdes.2015.02.018>
- Keogh R, Kesseli J, Therkelsen P, Kim D (2018) 1 kW microturbine system. GENSETS Annual Program Review Meeting, Washington, DC, U.S. URL: [https://arpa-e.energy.gov/sites/default/files/6\\_GENSETS\\_workshop\\_2018\\_RCK\\_v5.pdf](https://arpa-e.energy.gov/sites/default/files/6_GENSETS_workshop_2018_RCK_v5.pdf)
- Kesseli J (2018) E-mail Communication, 27 July 2018
- Kesseli J, Everbeck C, Wolf T (2018) Recuperated brayton cycle engine using a screw compressor and expander. GENSETS Annual Program Review Meeting, Washington, DC, U.S. URL: [https://arpa-e.energy.gov/sites/default/files/5\\_GENSETS-2018-03-12\\_BRAYTON-Rev-3.pdf](https://arpa-e.energy.gov/sites/default/files/5_GENSETS-2018-03-12_BRAYTON-Rev-3.pdf)
- Killingsworth NJ, Rapp VH, Flowers DL, Aceves SM, Chen JY, Dibble R (2011) Increased efficiency in SI engine with air replaced by oxygen in argon mixture. *Proc Combust Inst* 33:3141–3149. <https://doi.org/10.1016/j.proci.2010.07.035>
- Kobayashi K, Sako T, Sakaguchi Y, Morimoto S, Kanematsu S, Suzuki K, Nakazono T, Ohtsubo H (2011) Development of HCCI natural gas engines. *J Nat Gas Sci Eng* 3:651–656. <https://doi.org/10.1016/j.jngse.2011.07.002>
- Koga H, Kiura T (2013) A study of controlled auto-ignition in small natural gas engines. *SAE Int J Engines* 6:2133–2139
- Kosaka H, Akita T, Moriya K, Goto S, Hotta Y, Umeno T, Nakakita K (2014) Development of free piston engine linear generator system Part 1—Investigation of fundamental characteristics. SAE technical paper 2014-01-1203. <https://doi.org/10.4271/2014-01-1203>
- Li Z, Haramura Y, Kato Y, Tang D (2014) Analysis of a high performance model stirling engine with compact porous-sheets heat exchangers. *Energy* 64:31–43. <https://doi.org/10.1016/j.energy.2013.11.041>
- Maghanki MM, Ghobadian B, Najafi G, Galogah RJ (2013) Micro combined heat and power (MCHP) technologies and applications. *Renew Sustain Energy Rev* 28:510–524. <https://doi.org/10.1016/j.rser.2013.07.053>
- MAZDA: Next-generation technology, <http://www2.mazda.com/en/next-generation/technology/>. Last Accessed 01 Aug 2018
- McDonald CF, Rodgers C (2008) Small recuperated ceramic microturbine demonstrator concept. *Appl Therm Eng* 28:60–74. <https://doi.org/10.1016/j.applthermaleng.2007.01.020>
- Micro CHP products, [http://micro-chp.com/micro\\_chp\\_products.htm](http://micro-chp.com/micro_chp_products.htm)
- MTT EnerTwin, [https://www.enertwin.com/cms/EN\\_Specifications\\_EnerTwin-2017.pdf](https://www.enertwin.com/cms/EN_Specifications_EnerTwin-2017.pdf). Last Accessed 20 July 2018
- Muccillo M, Gimelli A (2014) Experimental development, 1D CFD simulation and energetic analysis of a 15 kw micro-CHP unit based on reciprocating internal combustion engine. *Appl Therm Eng* 71:760–770. <https://doi.org/10.1016/j.applthermaleng.2013.11.025>

- Parlak A, Yasar H, Eldogan O (2005) The effect of thermal barrier coating on a turbo-charged diesel engine performance and exergy potential of the exhaust gas. *Energy Convers Manage* 46:489–499. <https://doi.org/10.1016/j.enconman.2004.03.006>
- Qiu S (2018) Advanced stirling power generation systems for combined heat and power (ASPGen). GENSETS Annual Program Review Meeting, Washington, DC, U.S. URL: [https://arpa-e.energy.gov/sites/default/files/3\\_GENSETS%20annual%20review%20meeting%20WVU%20Stirling%20S.pdf](https://arpa-e.energy.gov/sites/default/files/3_GENSETS%20annual%20review%20meeting%20WVU%20Stirling%20S.pdf)
- Qnergy SmartBoiler, <https://www.qnergy.com/wp-content/uploads/2018/01/Download-the-SmartBoiler-Brochure-Spec-Sheet.pdf>. Last Accessed 16 July 2018
- Reitz R, Wickman D, Wright C, Kokjohn S, Andrie M, Shears D, Procknow D, Kamo L (2018) Spark-assisted HCCI residential CHP. GENSETS Annual Program Review Meeting, Washington, DC, U.S. URL: [https://arpa-e.energy.gov/sites/default/files/9\\_GENSETS%20-%20WERC-Final.pdf](https://arpa-e.energy.gov/sites/default/files/9_GENSETS%20-%20WERC-Final.pdf)
- Ren H, Gao W (2010) Economic and environmental evaluation of micro CHP systems with different operating modes for residential buildings in Japan. *Energy Build* 42:853–861. <https://doi.org/10.1016/J.ENBUILD.2009.12.007>
- Sevier DK (2015) Oil & gas industry electric power for upstream operations. ARPA-E GENSETS Program Kickoff Meeting, Chicago, IL, U.S. URL: [https://arpa-e.energy.gov/sites/default/files/Sevier\\_SWN\\_GENSETS.pdf](https://arpa-e.energy.gov/sites/default/files/Sevier_SWN_GENSETS.pdf)
- Sherman RA (1934) Radiation from luminous and non-luminous natural gas flames. *Trans ASME* 56:177–192
- Solomon L, Qiu S (2018) Computational analysis of external heat transfer for a tubular stirling convertor. *Appl Therm Eng* 137:134–141. <https://doi.org/10.1016/J.APPLTHERMALENG.2018.03.070>
- Song Z, Chen J, Yang L (2015) Heat transfer enhancement in tubular heater of stirling engine for waste heat recovery from flue gas using steel wool. *Appl Therm Eng* 87:499–504. <https://doi.org/10.1016/J.APPLTHERMALENG.2015.05.028>
- Taie Z, West B, Szybist J, Edwards D, Thomas J, Huff S, Vishwanathan G, Hagen C (2018) Detailed thermodynamic investigation of an ICE-driven, natural gas-fueled, 1 kW micro-CHP generator. *Energy Convers Manag* 166. <https://doi.org/10.1016/j.enconman.2018.04.077>
- Tanaka S, Hikichi K, Togo S, Murayama M, Hirose Y, Sakurai T, Yuasa S, Teramoto S, Niino T, Mori T et al (2007) World's smallest gas turbine establishing Brayton cycle. *Tech Dig PowerMEMS* 2007:359–362
- Tapia-Ahumada K, Pérez-Arriaga JJ, Moniz EJ (2013) A methodology for understanding the impacts of large-scale penetration of micro-combined heat and power. *Energy Policy* 61:496–512. <https://doi.org/10.1016/j.enpol.2013.06.010>
- Taylor CF (1985) *The internal-combustion engine in theory and practice: Volume 1: Thermodynamics, fluid flow, performance*, 2nd edn. MIT press, Cambridge, Massachusetts, U.S
- Valenti G, Silva P, Fergnani N, Di Marcoberardino G, Campanari S, Macchi E (2014) Experimental and numerical study of a micro-cogeneration Stirling engine for residential applications. *Energy Procedia* 45:1235–1244
- Vishwanathan G, Sculley JP, Fischer A, Zhao J-C (2018) Techno-economic analysis of high-efficiency natural-gas generators for residential combined heat and power. *Appl Energy* 226:1064–1075
- Visser WPJ, Shakariyants SA, Oostveen M (2011) Development of a 3 kW microturbine for CHP applications. *J Eng Gas Turbines Power* 133:042301. <https://doi.org/10.1115/1.4002156>
- Visser WPJ, Shakariyants S, de Later MTL, Ayed AH, Kusterer K (2012) Performance optimization of a 3 kW microgasturbine for CHP applications. In: *Proceedings of ASME Turbo Expo 2012: turbine technical conference and exposition*, pp 619–628. American Society of Mechanical Engineers, Copenhagen, Denmark
- Wood G (2018) Free piston stirling engine based 1 kW generator. GENSETS Annual Program Review Meeting, Washington, DC, U.S. URL: [https://arpa-e.energy.gov/sites/default/files/1\\_Sunpower\\_2018-03-19\\_GENSETS\\_Year\\_2\\_review\\_final.pdf](https://arpa-e.energy.gov/sites/default/files/1_Sunpower_2018-03-19_GENSETS_Year_2_review_final.pdf)
- Yanmar mCHP, <http://www.yanmar-es.com/wp-content/uploads/YANMAR-mCHP-Catalog-2016-Update.pdf>. Last Accessed 20 July 2018